Metallization and Metal–Semiconductor Interfaces

NATO ASI Series

Advanced Science Institutes Series

A series presenting the results of activities sponsored by the NATO Science Committee, which aims at the dissemination of advanced scientific and technological knowledge, with a view to strengthening links between scientific communities.

The series is published by an international board of publishers in conjunction with the NATO Scientific Affairs Division

A	**Life Sciences**	Plenum Publishing Corporation
B	**Physics**	New York and London
C	**Mathematical and Physical Sciences**	Kluwer Academic Publishers
D	**Behavioral and Social Sciences**	Dordrecht, Boston, and London
E	**Applied Sciences**	
F	**Computer and Systems Sciences**	Springer-Verlag
G	**Ecological Sciences**	Berlin, Heidelberg, New York, London,
H	**Cell Biology**	Paris, and Tokyo

Recent Volumes in this Series

Volume 189—Band Structure Engineering in Semiconductor Microstructures
edited by R. A. Abram and M. Jaros

Volume 190—Squeezed and Nonclassical Light
edited by P. Tombesi and E. R. Pike

Volume 191—Surface and Interface Characterization by Electron Optical Methods
edited by A. Howie and U. Valdrè

Volume 192—Noise and Nonlinear Phenomena in Nuclear Systems
edited by J. L. Muñoz-Cobo and F. C. Difilippo

Volume 193—The Liquid State and Its Electrical Properties
edited by E. E. Kunhardt, L. G. Christophorou, and L. H. Luessen

Volume 194—Optical Switching in Low-Dimensional Systems
edited by H. Haug and L. Bányai

Volume 195—Metallization and Metal-Semiconductor Interfaces
edited by I. P. Batra

Volume 196—Collision Theory for Atoms and Molecules
edited by F. A. Gianturco

Series B: Physics

Metallization and Metal-Semiconductor Interfaces

Edited by

Inder P. Batra

IBM Almaden Research Center
San Jose, California

Plenum Press
New York and London
Published in cooperation with NATO Scientific Affairs Division

Proceedings of a NATO Advanced Research Workshop
on Metallization and Metal-Semiconductor Interfaces,
held August 22-26, 1988,
at the Technical University of Munich,
Garching, Federal Republic of Germany

ISBN-13: 978-1-4612-8086-6 e-ISBN-13: 978-1-4613-0795-2
DOI: 10.1007/978-1-4613-0795-2

Softcover reprint of the hardcover 1st edition 1989

Library of Congress Cataloging in Publication Data

NATO Advanced Research Workshop on Metallization and Metal-Semiconductor Interfaces (1988: Technical University of Munich)
Metallization and metal-semiconductor interfaces / edited by Inder P. Batra.
p. cm.—(NATO ASI series. Series B, Physics; vol. 195)
"Proceedings of a NATO Advanced Research Workshop on Metallization and Metal-Semiconductor Interfaces, held August 22-26, 1988, at the Technical University of Munich, Garching, Federal Republic of Germany"—T.p. verso.
"Published in cooperation with NATO Scientific Affairs Division."
Includes bibliographical references and index.

1. Semiconductor-metal boundaries—Congresses. 2. Metallizing—Congresses. I. Batra, Inder P. II. North Atlantic Treaty Organization. Scientific Affairs Division. III. Title. IV. Series: NATO ASI series. Series B, Physics; v. 195.
TK7872.C68N37 1988 89-31077
621.3815/2—dc19 CIP

© 1989 Plenum Press, New York
A Division of Plenum Publishing Corporation
233 Spring Street, New York, N.Y. 10013

All rights reserved

No part of this book may be reproduced, stored in a retrieval system, or transmitted in any form or by any means, electronic, mechanical, photocopying, microfilming, recording, or otherwise, without written permission from the Publisher

SPECIAL PROGRAM ON CONDENSED SYSTEMS OF LOW DIMENSIONALITY

This book contains the proceedings of a NATO Advanced Research Workshop held within the program of activities of the NATO Special Program on Condensed Systems of Low Dimensionality, running from 1983 to 1988 as part of the activities of the NATO Science Committee.

Other books previously published as a result of the activities of the Special Program are:

Volume 148	INTERCALATION IN LAYERED MATERIALS edited by M. S. Dresselhaus
Volume 152	OPTICAL PROPERTIES OF NARROW-GAP LOW-DIMENSIONAL STRUCTURES edited by C. M. Sotomayor Torres, J. C. Portal, J. C. Maan, and R. A. Stradling
Volume 163	THIN FILM GROWTH TECHNIQUES FOR LOW-DIMENSIONAL STRUCTURES edited by R. F. C. Farrow, S. S. P. Parkin, P. J. Dobson, J. H. Neave, and A. S. Arrott
Volume 168	ORGANIC AND INORGANIC LOW-DIMENSIONAL CRYSTALLINE MATERIALS edited by Pierre Delhaes and Marc Drillon
Volume 172	CHEMICAL PHYSICS OF INTERCALATION edited by A. P. Legrand and S. Flandrois
Volume 182	PHYSICS, FABRICATION, AND APPLICATIONS OF MULTILAYERED STRUCTURES edited by P. Dhez and C. Weisbuch
Volume 183	PROPERTIES OF IMPURITY STATES IN SUPERLATTICE SEMICONDUCTORS edited by C. Y. Fong, Inder P. Batra, and S. Ciraci
Volume 188	REFLECTION HIGH-ENERGY ELECTRON DIFFRACTION AND REFLECTION ELECTRON IMAGING OF SURFACES edited by P. K. Larsen and P. J. Dobson
Volume 189	BAND STRUCTURE ENGINEERING IN SEMICONDUCTOR MICROSTRUCTURES edited by R. A. Abram and M. Jaros
Volume 194	OPTICAL SWITCHING IN LOW-DIMENSIONAL SYSTEMS edited by H. Haug and L. Bányai

PREFACE

This book represents the work presented at a NATO Advanced Research Workshop on "Metallization and Metal-Semiconductor Interfaces", held at the Technical University of Munich, Garching, W. Germany from 22-26 August 1988. The major focus of the workshop was to evaluate critically the progress made in the area of metal-semiconductor interfaces. The underlying theme was the mechanism of Schottky barrier formation and a serious assessment of the various models. A significant fraction of the workshop time was also spent in discussing the interaction of alkali metals with semiconductors. Alkali metals on semiconductors form ordered overlayers and the resulting system often exhibits one-dimensional metallic properties. The nature of their interaction has introduced new and exciting complexities and this was pursued at length during the lively discussions at the workshop. A half a day was devoted to Scanning Tunneling Microscopy, the emphasis being on its utility in providing structural and electronic character of low-coverage regime. The book should provide readers with the most current status of the research activity in the general area of metal-semiconductor interfaces at an international level. It should also serve as an excellent introduction to the field, since sufficient review type of material has also been included

The workshop organizers, Dr. I. P. Batra (Director), IBM Almaden Research Center, San Jose, Prof. S. Ciraci, Bilkent University, Ankara, Prof. C. Y. Fong, University of California, Davis, Prof. Dr. F. Koch (Local Chairman), Technical University Munich, Garching, Dr. H. Rohrer, IBM Research Laboratory, Zurich, and Prof. Dr. R. H. Williams, University of Wales, Cardiff, were aware of the advances taking place independently in the three related fields and felt it would be useful to bring the scientists from various countries together under one roof. The NATO workshop format was judged to be ideal for accomplishing the objectives. This format permits each participant to play an active role and to have close personal interaction with the other participants. To the extent that we have succeeded in fulfilling this objective, the credit is due to all the participants.

The workshop was truly international in character. It included thirty-nine participants from eleven countries. There were thirty major talks given by scientists from France (5), Federal Republic of Germany (5), Greece (1), Holland (1), Italy (1), Japan (2), Spain (2), Turkey (1), Switzerland (1), United Kingdom (2), and United States of America (9). A few other scientists were invited to be senior observers. They had expertise in closely related areas and served as referees and discussion leaders. Ample time was devoted to discussions but unfortunately it never seemed to be enough. Invariably the discussions continued well past the allotted time and at meal times.

To achieve the major scientific objectives of the workshop, the talks were grouped in fourteen technical sessions. These are listed below along with the names of the chairpersons: **I- General Schottky Barrier Mechanisms** (D. R. Hamann), **II- Role of Defects at Metal-Semiconductor Contacts** (F. Koch), **III- Metal-Covalent Semiconductors Contacts** (W. E. Spicer), **IV- Temperature as a Barrier Mechanism Probe** (W. Mönch), **V- Barrier Manipulation**

with Impurities (C. Y. Fong), **VI- Band Offsets and Barriers** (J. Tersoff), **VII- Silicon-Silicide Interfaces** (I. P. Batra), **VIII- Applications of Tunneling to Metal-Semiconductor Interfaces** (H. Rohrer), **IX- Alkali Metals/Semiconductor Interactions- Overview** (F. Flores), **X- Alkali Metals/Si Interactions** (J. H. Wolter), **XI - Alkali Metals/Compound Semiconductor Interactions** (S. Ciraci), **XII- Alkali Metals/Semiconductor Interactions- Miscellaneous** (Y. Murata), **XIII- Observations and Group Meetings** (R. Ludeke), and **XIV- Group Leaders Reports and General Discussion** (R. H. Williams).

After the presentations, which were consistently of high quality and contained a great deal of new information, the floor was opened for extensive discussions. Contrary opinions were freely expressed and taken in good spirits. It was felt that participants holding opposing view points did in fact listen to each other. Some consensus seems to have emerged. However, it would be optimistic to hope that all the controversies have been resolved. The reader will easily identify the differing views, and it is our hope, may accept some of the challenges in resolving them by independent research.

We wish to express our thanks to the North Atlantic Treaty Organization for sponsoring this meeting. We are also grateful to IBM Corporation (in particular to IBM Zurich Research Laboratory and IBM Almaden Research Center) for some financial assistance. It would be a gross omission if we did not mention the able assistance of the graduate students, M. Brandt, R. Hollenbach, F. Müller, and Ch. Wetzel from Garching.

Before closing, we thank Mrs. I. Vieregg for expert secretarial help and Mrs V. Koch who handled most of the local arrangements in Garching. We also express our appreciation to Mrs. Uma Batra and the girls Puja and Mala Batra who helped with registration, mailings, and other details which often escape the workshop Director. One of us (WES), who was not involved with the arrangements, would like to express his particular thanks to all of those who made this such a productive workshop.

Inder P. Batra
IBM Research Division
Almaden Research Center
San Jose, California 95120

William E. Spicer
Electronics Laboratory
Stanford University
Stanford, California 94305

CONTENTS

Introduction to Metallization and Metal-Semiconductor Interfaces 1
Inder P. Batra

GENERAL SCHOTTKY BARRIER MECHANISMS

Mechanisms of Barrier Formation in Schottky Contacts 11
Winfried Mönch

The Role of Defects and Metal States at the Metal-Semiconductor Interface 39
R. Ludeke

Metallization, Bonding and Energetics of Ordered Phases of Al on Si(111) 55
J. S. Nelson and Inder P. Batra

DEFECTS AT METAL-SEMICONDUCTOR CONTACTS

Factors Influencing Electrical Barriers at Metal-Semiconductor Interfaces: Gold and Antimony on Indium Phosphide and Cadmium Telluride 77
R. H. Williams

Deep Levels and Band Bending at Metal-Semiconductor Interfaces 91
L. J. Brillson and P. Chiaradia

Influence of the Atomic Scale Roughness of a Clean Si Surface on the Interface Formation with Metals 111
C. A. Sébenne

δ-Doping Layers. The Shaping of Barrier Potentials by Planar Doping 123
F. Koch and A. Zrenner

TEMPERATURE DEPENDENT METALLIZATION STUDIES

Disruption, Metallization, and Electrical Properties of Metal GaAs and InP Semiconductor Interfaces 139
W. E. Spicer, R. Cao, K. Miyano, C. McCants, T. T. Chiang, C. J. Spindt, N. Newman, T. Kendelewicz, I. Lindau, E. Weber, and Z. Liliental-Weber

Metal-GaAs(110) Interfaces formed at Low Temperature:
from Adsorbate- to Metal-Induced Gap States.....163
A. Kahn, K. Stiles, D. Mao, S. F. Horng, K. Young, J. McKinley,
D. G. Kilday, and G. Margaritondo

Thermal Effects in Silicon-Metal Interface Formation:
A Photoemission Study of Si/Gd and Si/Yb.....179
L. Braicovich and E. Puppin

SILICON-SILICIDE INTERFACES

Structures and Electronic Properties of Epitaxial Silicon-Silicide Interfaces.....195
D. R. Hamann

Calculated Electronic Structures and Schottky Barrier Heights
of (111) NiS_2/Si A− and B− Type Interfaces.....215
G. P. Das, P. Blöchl, N.E. Christensen and O.K. Andersen

Electrical Characterization of Interface States at
Schottky Contacts and MIS Tunnel Diodes.....235
Jürgen H. Werner

BAND OFFSETS AND BARRIERS

Relation Between Schottky Barrier Heights, Band Offsets and the Energy Levels
of Transition Metal Impurities.....259
M. Lannoo, C. Priester, G. Allan, I. Lefebvre, and C. Delerue

Screening Near Semiconductor Heterojunctions and Valence Band Offsets.....269
C. Priester, G. Allan, and M. Lannoo

METALLIZATION REVIEW

The Theory of Schottky Barriers: Controversy or Consensus?.....281
J. Tersoff

Metallization of Semiconductor Surfaces as a Function of Coverages.....289
G. P. Srivastava and Inder P. Batra

APPLICATIONS OF TUNNELING TO METAL-SEMICONDUCTOR INTERFACES

Fermi-Level Pinning by Oxygen and Antimony Adsorbates on the GaAs(110) Surface by
Scanning Tunneling Spectroscopy.....307
R. M. Feenstra, P. Mårtensson, and J. A. Stroscio

Initial Stages of Metal-Semiconductor Interface Formation.....315
F. Salvan, F. Thibaudau Ph. Dumas, and A. Humbert

Tunneling Spectroscopy and Potentiometry on Cleaved (Al)GaAs Multilayers 329
H. W. M. Salemink

ALKALI METALS-SEMICONDUCTORS INTERFACES

Metallization of Metal-Semiconductor Interfaces 335
S. Ciraci and Inder P. Batra

Electronic Structure and Excitations of Metal Overlayer on Semiconductor Surfaces 351
M. Tsukada, N. Shima, Z. Zhu, H. Ishida, and K. Terakura

Alkali-Metal Overlayers on Silicon Surfaces 367
Y. Murata, H. Tochihara, and M. Kubota

Present Understanding of a Model Metal/Semiconductor Junction: K/Si(001)2×1 381
E. G. Michel, M. C. Asensio, and R. Miranda

Inverse-Photoemission Studies of Clean and Metal-Covered Semiconductor Surfaces 397
B. Reihl, K. O. Magnusson, J. M. Nicholls, P. Perfetti, and F. Salvan

Influence of Overlayer Metallization on Schottky-Barrier Formation 425
C. Laubschat, M. Prietsch, M. Domke, E. Weschke, T. Mandel, G. Remmers,
J. E. Ortega, C. Xue, and G. Kaindl

On the Formation of Metal-Semiconductor Interface: The Case of K on GaAs(110) 439
J. Ortega and F. Flores

A Theoretical Study of Na Overlayers on the GaAs(110) Surface 449
C. Y. Fong, L. H. Yang and Inder P. Batra

Electronic and Structural Properties and Schottky Barrier Formation of
Alkali Metal-Semiconductor Interfaces 465
P. Soukiassian and T. Kendelewicz

Adsorption of Cs on Hydrogenated W(110) Surfaces 489
C. A. Papageorgopoulos

Participants 505

Index 509

INTRODUCTION TO METALLIZATION AND METAL-SEMICONDUCTOR INTERFACES

Inder P. Batra

IBM Research Division
Almaden Research Center
San Jose, California 95120, U.S.A.

Novel electronic properties of interfaces have enormous commercial applications ranging from infrared detectors to very large scale integrated (VLSI) circuits. One such interface is a junction between a metal and a semiconductor; the components based on these are widely used in the microelectronics industry. A junction between a metal and a semiconductor is called a Schottky junction, named after W. Schottky. Nearly half a century ago, Schottky proposed a model for describing the potential variation within the barrier region between a metal and a semiconductor. The site for the workshop on "Metallization and Metal-Semiconductors Interfaces" was chosen to be right next to the Schottky Institute, which is under construction at the Technical University of Munich in Garching. The Institute will formally open within the next few months; this workshop is the first in a series of celebrations to honor W. Schottky's lasting impact on science and technology.

Whenever two different materials are brought into contact, a potential barrier is established at the interface in equilibrium which stops the net flow of current across the junction. Clearly a potential barrier at the interface is a key parameter which determines the electrical behavior of the system. The barrier between a metal-semiconductor junction in equilibrium is also known as the Schottky barrier. Upon application of an external voltage to the junction, the distance between the semiconductor quasi Fermi level and the top of the barrier is changed. Under **forward bias** conditions, the thermal population of majority carriers which can be transmitted over the top of the barrier is enhanced, and current flows. The barrier top is firmly pinned to the metal quasi Fermi level, however, so no such effect occurs when a **reverse bias** is applied. The ability to force the current to flow in one direction and not in the other leads to junctions which are **rectifying** in nature.

The Schottky model[1] was designed originally for calculating the potential barrier for metal-semiconductor rectifiers. It assumed a depletion layer (a region devoid of mobile carriers) on the semiconducting side containing a constant density of (uncompensated) ionized donor impurities for an n-type doped semiconductor. Then from Poissons's equation it immediately follows that the electrostatic potential must vary quadratically with distance as the metal is approached from the semiconducting side. If on the other hand, the barrier region is devoid of charged impurities, as in fact was assumed by Mott[2] then the potential varies only linearly with distance. The barrier height then simply is equal to the difference between the metal work function and the electron affinity of the semiconductor. The readers should keep in mind that the above discussion of the barrier has implicitly assumed an n-type semiconductor whose work function is less than the work function of the metal with which it is in

contact. This turns out to be the most widely used case in practice and our discussion revolves around this case. However, if the values of the work functions are reversed (low work function metal in contact with a higher work function semiconductor) it is easy to see that one would get an **ohmic** contact.

In any case, the simple models for the Schottky barrier formation have been inadequate. They have given results which have not agreed with the experimental findings. In particular, the Schottky-Mott model predicts a linear dependence with unit slope for the barrier height on the metal work function but experimentally the dependence is much less pronounced. Bardeen[3] explained it in 1947 by including surface states, which are usually present on a bulk truncated semiconductor surface. In the so called Bardeen limit, the Fermi level is said to be "pinned" or permanently fixed by the high density of surface states and the barrier height is independent of the metal work function. This model obviously ignores any modification of the surface states due to the presence of the metal , which must happen in any real metal-semiconductor junction. Currently, there are several models in the literature[4,5] which attempt to identify the microscopic mechanisms controlling the barrier heights. One objective of the workshop was to critically discuss and explore the strengths and limitations of the various competing models and to develop some consensus.

The workshop attempted a three prong attack to understand the Schottky barrier formation mechanisms. First, it focussed on the conventional surface science tools to carefully examine the microscopic structure of the interface. The studies covered a range from submonolayers to multilayer growth of metal overlayers. The development of the Schottky barrier as a function of metal coverage takes us from the surface science regime to the so called device regime. The term "Metallization", which is more often used in the applied world, was used[6] to describe such a transition in the context of Schottky barriers. Several speakers defined metallization more specifically within the context of their talks. For the general purpose here, let us simply state that by metallization we mean the disappearance of the forbidden energy band gap, and the appearance of a metallic density of states at the Fermi level.

The idea of finding an all encompassing mechanism for the Schottky barrier formation was abandoned almost from the start. This point was further driven home when a careful study of some well characterized interfaces showed the dependence of the Schottky barrier on the precise atomic arrangement at the interface. The second line of attack came from the study of the alkali metals in contact with semiconductors. Alkali metals on semiconductors can serve as prototypes of metal-semiconductor interfaces. They form ordered overlayers and give rise to one-dimensional metallic properties. Several studies dealing with the fundamentals of the nature of the interaction have taken us a long way towards our goal. The third avenue we explored involved the use of the newly developed tool, namely the Scanning Tunneling Microscope[7], in resolving some key structural problems for metals adsorbed on semiconductors in low coverage regime.

In what follows, a general introduction to this volume is given highlighting some of the key results. We have also alluded to some unsolved problems which may well form a basis for new research. To accomplish this, we have freely drawn from the comments made from the floor during the workshop. An extended discussion regarding the charge transfer between alkali metals and semiconductors is presented. The aim is to reconcile different values for the charge transfer obtained by different authors. The explanation is novel and puts the issue of covalency versus ionicity of the alkali metal/semiconductor bond in perspective.

In his opening remarks, Batra appealed to all the participants to have an open and free exchange of ideas and try to arrive at some sort of consensus. Mönch gave the first technical lecture in which he thoroughly reviewed the various physical mechanisms for the Fermi level pinning. Two major pictures he emphasized were the metal induced gap states (MIGS) and the defect models. The latter case was discussed for specific defects by Spicer. Mönch traced

the origin of MIGS to Heine[8] in 1965. Heine had shown that conceptually one can think of MIGS as the tails of wave function of metal electrons, having energies in the range of the forbidden gap of the semiconductor. Mönch introduced the term ViGS (virtual gap states), which are simply the solutions of Schrödinger's equation for complex wave vector. The MIGS then can be mathematically derived from ViGS of the "complex" semiconductor band structure. He discussed at some length the consequences of the metal island formation. In particular, the barrier height in presence of well separated islands, as determined from energy-distribution curves of photoemitted electrons, will be lower in value than the true barrier height.

Ludeke felt that the division into two mutually exclusive groups (MIGS and defect model) comes about because of the coverage dependent effects which have not been fully appreciated. According to Ludeke, models which ignore the influence of the metal and attribute the Schottky barrier solely to native defects in the semiconductor are looking at the Schottky barrier formation prior to the establishment of a metallic overlayer. He discussed a model which postulated deposition-induced adsorbate states on the semiconductor surface prior to the development of metallic properties. As the overlayer becomes a metal, the adsorbate states become spatially delocalized and pin the Fermi level. He stressed that these states are definitely not MIGS, but refused to coin a new acronym (MADS) and simply referred to them as metal altered defect states. There were some questions about the calculated delocalization induced broadening of the defect level, which was found to be (0.062 eV) much narrower than intuitively expected. Nelson, Srivastava, and Batra presented theoretical studies as a function of metal coverage and showed the development of the resonant states. The metallization of Si(111), and Ge(001) surfaces was discussed using total energy minimized structures. Williams stressed the point that no single mechanism can account for the values of barrier heights in all metal-semiconductor combinations. He illustrated the role of defects by presenting experimental evidence that oxide layers have a dramatic effect on measured Schottky barrier heights. Even more interesting, was the example of Au on n-CdTe for which two different values of the Schottky barrier were found depending upon the form of the CdTe surface.

Brillson discussed a broad range of experimental data and made correspondence between data and the model which it supported. He went on to show that a Schottky type of model modified only by defects induced by interface chemical interactions and, perhaps, the semiconductor crystal quality can account for the wide range of barrier heights now observed for metals on III-V semiconductors. He concluded that the electrostatic model of interface charge transfer developed by Schottky is right! Sebenne focussed on the effect of the local surface roughness on the metal overlayer growth. He characterized Si(111)7x7 surface as rough and Si(111)2x1 as smooth.

Spicer and Kahn argued convincingly that studying Schottky barrier formation at low temperature metal deposition, to inhibit clustering and/or chemical reaction between metals and semiconductors, in addition to the normal room temperature experiments, can provide better insight into the Schottky barrier formation mechanisms. Spicer showed that both MIGS and defects can be important and echoed the theme that finding a single mechanism to explain everything is an over simplification. Some discussion arose regarding the separation of the Fermi level position in an n-type and p-type GaAs at multilayer coverages. The saturation to separate levels would support the defect model but the issue is complicated if metal clusters are present. Then as discussed by Mönch, one could end up measuring slightly higher (n-type) and lower (p-type) energies. However, Spicer presented evidence for these two separate pinning levels for Cs/GaAs with a monolayer coverage at room temperature. It is believed that under these circumstances there is no clustering and metallization of Cs overlayer has not yet occurred. Spicer described three criteria for metallization which were further discussed by Kahn, Braicovich and Laubschat.

Kahn made the point that at low coverage, the Fermi level movement is controlled by adsorbate-induced states which are donor-like with the metals and acceptor-like with O_2. Mönch as well as Kahn reported a correlation between the energy position of the donor level and the first ionization potential. Braicovich presented the results of the temperature dependent photoemission studies for Si-metal interfaces. He found that in the metallization regime (about 2 monolayers) the temperature had profound effect but had little effect below that coverage. This was interpreted in terms of weakened Si-Si bonds due to the metallic screening. He concluded by stating that the construction of a unified model for interface growth is an unrealistic goal. Koch told us that in the brave new world of epitaxial growth techniques, impurities can be introduced at will in a planar sheet whose width is much less than a Bohr radius. By placing such a δ-doping profile next to say a metal-semiconductor interface the barrier height can be controlled in a desirable fashion. He introduced us to the term "mesoscopic", a region between microscopic and macroscopic.

Lannoo presented his theoretical arguments which showed in a unified fashion the role of the dangling bond states in determining band offsets in semiconductor heterojunctions as well as Schottky barrier formation. Allan developed some of these ideas in more details. Hamann and Das theoretically treated well characterized Ni- and Co-silicides-Si interfaces using first-principles methods. Many transition metals form silicides which are metallic in nature and form Schottky barriers just like ordinary metals. It is well established that $NiSi_2$ can be epitaxially grown on Si(111) in two different orientations, known as type A and type B. Type-A silicide has the same crystallographic orientation as Si(111), but in type B the $NiSi_2$ sublattice is rotated by 180° about the [111] axis. Thus the geometry of the bonds at the $NiSi_2$-Si interface is somewhat different in the two cases. More significantly, there is reasonable evidence in the literature that type-B interface forms a Schottky barrier which is somewhat higher (~0.2 eV) than type-A. The talks by Hamann and Das discussed the interfacial bonding for the two interfaces and reported calculations of the orientation dependence of Schottky barrier heights. It was noticed that the absolute Schottky barrier heights were off by a factor of two in Das' calculations but the difference seemed to be of the right order of magnitude. Hamann also obtained total energy minimized structures and discussed ballistic transport through these interfaces. Werner discussed electrical methods suitable for obtaining the energy distribution of interface states at Schottky contacts. One significant finding he reported was that the excess capacitance at silicide/silicon Schottky contact is not caused by interface states but rather due to minority carrier injection.

The session on Scanning Tunneling Microscope (STM), chaired by Nobel Laureate H. Rohrer, fulfilled expectations that information about metal overlayers on semiconductors can be obtained from STM. This was evident from the talks by Feenstra, Salvan, and Salemink. The resulting discussions further strengthened the view that STM will prove to be a potent tool in metal-semiconductor interfaces since one would be able to detect, for example metal islands.

The talks on interaction of alkali metals on semiconductors were quite lively. The review lecture by Ciraci and Batra, where they distinguished between two types of Metallization (substrate vs overlayer), opened the doors for discussions which were to continue throughout the duration of the workshop. Ciraci and Batra could explain all observed properties of the K-Si surface based on a strong ionic bond model where the charge transfer is nearly complete. Their results were based on self-consistent field pseudopotential calculations. The thermal desorption data for K/Si presented by Miranda showed that the desorption of K continued up to the room temperature. This obviously argues against the strong bond found by Ciraci and Batra. Miranda also stressed that the proper adsorption site for K on Si(001)-2x1 is still an unsolved problem both experimentally and theoretically. The value of the charge transfer obtained by him fell in the range of ~ 0.3-0.4. The sample cleanliness was raised as an issue in Papageorgopoulos' talk. Papageorgopoulos intentionally dosed the tungsten surface with hydrogen before exposure to alkali metals. Thus he could study "impure" surface in a controlled fashion. He stressed that if the dangling bonds are unintentionally passivated due to

impurities, the thermal desorption data could give results which may be subject to misinterpretation. The strong bond projected by Batra and Ciraci requires the presence of intrinsic surface states. If somehow these are eliminated by impurities then a weak bond may result. Alternatively, the strength of the bond obtained by Ciraci and Batra may be overestimated due to the use of the local density approximation for the exchange potential. We have no definite resolution of this problem in our hands.

Tsukada presented electronic structure calculations for K-Si which qualitatively agreed with Ciraci and Batra. Although they obtained similar spatial distribution of the charge density, Tsukada presented a space partitioning scheme for calculating charge transfer from K to Si which led to a small value of charge transfer. He explained that their more refined calculations being presented here are giving results which differ from their previously published results. A partial consensus thus emerged between the two theoretical groups. The one-dimensional metallic chain and the associated plasmon dispersion curve was also presented by Tsukada. The appearance of plasmons and their origin for K-Si system was pursued at length by Murata. The angle-resolved electron energy loss measurements for the plasmon dispersion convincingly showed the one-dimensional character. Murata's ultra-violet photoemission data suggested metallicity due to the K-chains (overlayer metallization). However, he pointed out that to clearly rule out the Si substrate metallization requires the angle-resolved ultra-violet photoemission data at low photon energies on a carefully prepared sample. Soukiassian, who also discussed the nature of bond between K and Si, concluded that the bond is weak because of low temperatures at which K can be desorbed from the Si surface. Furthermore, the absence of any significant Si-2p core level shift and the SEXAFS measured value of 3.14 Å for the K-Si bond length also suggested to him that the bond is covalent in nature. Braicovich pointed out that the absence of a large chemical shift in the core levels was not in itself a proof of small charge transfer.

Reihl went on to present electronic structure results for various metal-semiconductor systems obtained using inverse-photoemission spectroscopy (IPES). Recall that in IPES one explores unoccupied electronic states and hence this technique is well suited for studying the metallization of semiconductor surfaces. If the surface states become selectively occupied upon metal deposition then they are no longer detectable in IPES. For Si(001)2×1-K surface the substrate (not the alkali overlayer) was found to be metallized up to monolayer coverages because the anti-bonding π^* state got partly filled by the alkali valence electrons. This is in accord with the results discussed by Ciraci and Batra above. Reihl also clearly demonstrated that simple metals and alkali metals have rather distinct interactions with semiconductor surfaces. For example, Al adsorbed on Si(111) gives the $\sqrt{3}\times\sqrt{3}$ R30° LEED pattern at 1/3 monolayer coverage. However for the Cs/Si(111) system this LEED pattern develops only at a monolayer coverage. This may be due to the delayed onset of overlayer metallization for alkali metals which at low coverages interact ionically with the substrate. Reihl also pointed out that STM is a nice complementary tool for unravelling unoccupied electronic states since in STM electrons tunnel from the tip into unoccupied electronic states at the sample surface.

Laubschat presented core-level photoemission (Ga-3d and As-3d) results from interfaces between alkali metals and n- as well as p-doped GaAs(110). This technique is capable of providing important information on band bending during Schottky-barrier formation. A general observation for all alkali metals was a strong asymmetry in band bending for n- and p-GaAs(110). It was noted that for p-GaAs(110) the band bending was ~1 eV at 1/100 of a monolayer coverage. The band bending was negligible for n-GaAs(110) at this coverage. This was explained by large charge transfer (~1 electron/alkali atom) to the p-type GaAs substrate but none for n-GaAs. At high coverages, the observation of a common Fermi-level position for both n- and p-GaAs(110) is consistent with the overlayer metallization[6]. According to Laubschat the alkali overlayer stays non-metallic even up to 2 monolayer coverages. Flores showed from tight binding calculations that Schottky barrier is fully established for a monolayer of K on GaAs(110). More importantly, he found the site insensitivity of the

barrier height and traced it to the large size of K. Fong theoretically obtained Schottky barrier heights for Na-GaAs(110) as a function of Na coverage which nicely explained the experimental data by Laubschat.

Here I take the liberty of adding a few remarks which might help in resolving the charge transfer debate. Values ranging from 0 to ~1 have been quoted[9] for the amount of charge transfer, ΔQ, from K to Si. Miranda and Flores have obtained, $\Delta Q \simeq 0.3$ from the experimental data on the change in work function using Helmholtz formula as well as an empirical tight binding calculation. Tsukada has concluded, from Mulliken population analysis as well as a space partitioning scheme, that $\Delta Q \simeq 0.1$. An analysis by Bagus, based on a constrained space orbital variation, led to $\Delta Q \simeq 0.9$. The constrained space orbital variation analysis avoids some of the shortcomings inherent in Mulliken type population analysis. The value of $\Delta Q \simeq 1$, stated by Ciraci and Batra is not based on any integration of the charge density. They simply examine the spatial and spectral distribution of the charge density and conclude that the charge transfer from K to Si is nearly complete. If they used the definition employed, for example by Tsukada, they would also find ΔQ much less than unity since both groups get similar distributions.

The reason for getting a small value for the charge transfer, using any of the standard definitions, is simply that K and Si nuclear centers are sufficiently close to each other (vertical separation, $r_\perp \sim$ 1-2 Å). We all agree that the alkali charge is definitely confined in the region between the overlayer and the facing top Si layer regardless of whether or not it is accommodated in the Si dangling bonds. Then any reasonable partitioning of the space should and does give a small value for the charge transfer. For the same reasons, an analysis based on Helmholtz expressions, would also give a small ΔQ. Recall that the Helmholtz formula, $\Delta\phi = N_K e\mu_\perp/\varepsilon_0$ can only give the normal dipole moment, $\mu_\perp$, given the change in work function, $\Delta\phi$. The dipole moment can also be computed accurately and can be used to predict the change in work function. However, to get charge transfer, $\Delta Q = \mu_\perp/r_\perp$, one needs to supply an appropriate value for the normal separation, $r_\perp$, between the effective centers of positive and negative charges. This is where various models enter the picture, unfortunately sometimes only implicitly, and lead to some confusion. Generally it suffices to take $r_\perp$ equal to the normal separation between nuclear centers if known, or it may be estimated from sum of covalent radii. For Si-K case then one gets $\Delta Q \simeq 0.25$ (if $r_\perp = 2$ Å) and $\Delta Q \simeq 0.50$ (if $r_\perp = 1$ Å). This model, however, implicitly assumes that the charge is lost in an isotropic fashion from one center and distributed again isotropically on the more electronegative center. For the Si-K system the actual spatial distribution of the charge density is quite anisotropic. In fact as can be seen from the papers by Tsukada as well as Ciraci and Batra, the "center" of the excess negative charge lies vertically rather close to K and away from the Si core position. This is so whether one thinks in terms of strong polarization of the charge density or in terms of actual transfer into the Si dangling bonds. The net effect is that the dipole length is reduced leading to a higher value for ΔQ. Note $\Delta Q \simeq 1$, if $r_\perp \simeq 0.5$ Å. Thus one must be careful in providing an appropriate value for the separation between positive and negative "point" charges based on the spatial distribution of charge upon adsorption. It is my impression that the values obtained by various authors are certainly correct within the framework of their models. Unfortunately, the computed charge transfer value does depend on the model used. It is therefore important that the model be stated more explicitly to avoid unnecessary confusion. Finally, for what value of ΔQ a bond is to be called ionic, is also a matter of definition. One thinks of bulk GaAs, for which ΔQ is in the range of ~ 0.1-0.3, as an ionic compound semiconductor.

The final session of the workshop was devoted to observations, evaluations, progress made and work that remains to be done. Tersoff provided a broad review of his work on charge neutrality level and heterojunction band offsets. He reminded us about the distinction between the surface science approach and the measurements made in the device mode. Tersoff concluded that we are reaching consensus in the realization that the high and low coverage regimes are different. Low coverage regime is useful since things can be done in a more

controlled fashion. Hamann noted that theory and experiment can only meet when the interface geometry is well defined. Batra and Nelson cautioned that real systems have strains due to lattice mismatch which also affect bonding. Ciraci and Flores commented on the charge transfer related issues. Ciraci also showed an example of an "unstable" bond. Mönch noted that the explanation of the observed barriers for metal-GaAs is still a challenge since the barriers seem to depend on the method of preparation. Brillson pointed out that even the bulk crystal quality may be a factor as well. Spicer suggested that calculations are now required for specific interfaces of known chemical compositions. There was general agreement that no single mechanism can explain all the available data. Brillson and Williams commented on the overall success of the workshop and expressed satisfaction with the level of consensus achieved among participants. Williams noted that he had picked up enough new ideas to keep his students busy for quite some time.

This volume offers the results of important and most current research at the forefront of metal-semiconductor interfaces. It contains experimental as well as theoretical papers written by leading authorities and active researchers in the field. This is also the only book which has managed to collect, in one place, a number of significant papers dealing with alkali metal-semiconductor interactions. The review material contained in this book should serve as an excellent introduction for research students entering the field of metal-semiconductor interfaces. It is our hope that through this volume we are able to share with you the sense of excitement which most of us felt at the workshop.

ACKNOWLEDGMENT

It is my pleasure to thank D. R. Hamann for critically reading the manuscript and for his suggestions. Useful comments by F. F. Abraham, J. A. Barker, F. Herman, and W. E. Spicer are gratefully acknowledged.

REFERENCES

1. W. Schottky, Naturwissenschaften **26**:843 (1938).
2. N. F. Mott, Proc. Cambr. Phil. Soc. **34**:568 (1938).
3. J. Bardeen, Phys. Rev. **71**:717 (1947).
4. See for example, E. H. Rhoderick and R. H. Williams, "Metal-Semiconductor Contacts," Oxford University Press, New York, (1988).
5. See for example, W. Mönch, in: "Festkörperprobleme-Advances in Solid State Phys.," P. Grosse, ed., Vieweg, Braubschweig, **26**:27 (1986); L. J. Brillson, Surf. Sci. Rep. **2**:123 (1982).
6. I. P. Batra and S. Ciraci, Phys. Rev. **B33**:4312 (1986).
7. G. Binnig and H. Rohrer, Helv. Phys. Acta **55**:726 (1982).
8. V. Heine, Phys. Rev. **A138**:1689 (1965).
9. For a general review and references, see I. P. Batra, Prog. Surf. Sci. **25**:175 (1987).

General Schottky Barrier Mechanisms

MECHANISMS OF BARRIER FORMATION IN SCHOTTKY CONTACTS

Winfried Mönch

Laboratorium für Festkörperphysik
Universität–GH–Duisburg
D–4100 Duisburg, Federal Republic of Germany

1. INTRODUCTION

Fifty years ago, in 1938, Schottky explained the rectifying behavior of metal–semiconductor contacts (Braun 1874) by a space–charge layer, which is depleted from mobile carriers, on the semiconductor side of the junction. Since then, the microscopic mechanisms determining the barrier heights at such interfaces are under discussion.

Provided, that there are no electronic interface states, the barrier height simply results as the difference between the metal work–function and the electron affinity or the ionization energy of the semiconductor depending on whether it is doped n– and p–type, respectively. This well–known Schottky–Mott rule (Schottky 1940, Mott 1938) failed to explain the experimental data. Bardeen (1947) then was the first to consider electronic interface states in metal–semiconductor contacts. The barrier heights are still expected to vary linearly as a function of metal work–function but at a reduced slope S_ϕ (Cowley and Sze 1965). Such interface states are implying an interfacial dipole–layer (Bardeen 1947).

In a conceptually simple approach, Heine (1965) identified those interface states as the wave–function tails of the metal electrons in the energy region between the top of the semiconductor valence–band and the Fermi level where the metal conduction–band overlaps the band gap of the semiconductor. That induced density of interface states (IDIS, Tejedor et al. 1977) or continuum of metal–induced gap states (MIGS, Louie and Cohen 1976) is then derived from

the virtual gap states (ViGS) of the complex band structure of the semiconductor, which are solutions of Schrödinger's equation for complex wave vector. It is in this sense that the label *virtual* is used. Depending on the boundary conditions, intrinsic surface states at clean surfaces (Maue 1935, Goodwin 1939), adsorbate–induced surface states on surfaces covered with adsorbates in submonolayer quantities (see sections 4 and 6), and metal–induced gap states in metal–semiconductor interfaces (Louis et al. 1976, Louie and Cohen 1976, Tersoff 1984) are derived from those ViGS. Initially, this MIGS or IDIS model was not widespread accepted since it predicts, as the Schottky–Mott rule did, a linear relationship of the barrier height on the metal work–function but with a slope less than unity. Meanwhile, there is, however, growing evidence that the chemical trends of barrier heights observed with different metals on a specific semiconductor as well as of the slopes S_ϕ reported for different semiconductors are well described by the MIGS or IDIS model (Mönch 1986, 1987, 1988 a). The experimentally observed deviations from what that simple model is predicting are indicative of the existence of at least one additional mechanism. This will be discussed in section 6.

In these circumstances and based on specific experimental results, which were obtained by using photoemission spectroscopy and which will be discussed in section 3, Spicer et al. (1979) proposed that during the formation of metal–semiconductor contacts native defects are generated in the semiconductor at or close to the interface. The energy levels of those defects were supposed to determine the interface position of the Fermi level within the semiconductor band–gap. This defect model has attracted much attention (for a review see, for example, Mönch 1983).

Barrier heights of metal–semiconductor contacts are generally determined from current–voltage (I/V), capacitance–voltage (C/V), or photoresponse (I/hν) characteristics of Schottky diodes. Such data will be discussed in section 6. For the same metal–semiconductor pair the barrier heights ϕ_{Bn} and ϕ_{Bp} measured with substrates doped n– and p–type, respectively, are always adding up to the band–gap energy W_g of the semiconductor (Waldrop 1984, Newman et al. 1987). Such data, however, provide no insight in the nature of the electronic interface states, the chemical composition at the interface, or the atomic arrangement at the interface.

Such information may be obtained either by following the formation or by profiling of contacts. In both cases, surface–sensitive tools such as, for example, photoemission spectroscopy, low–energy electron diffraction and electron energy–loss spectroscopy, Auger electron spectroscopy, or Raman spectroscopy, to

name a few of those techniques only, were used. With all the electron spectroscopies, the information depth is determined by the escape depths of the electrons emitted or scattered. In studies on the formation of interfaces, the thickness of the overlayers are thus limited to some nanometers. Destructive profiling by using, for example, ion milling causes an intermixing within the collision cascade and thus strongly restricts the applicability of that approach.

Variations of the interface position of the Fermi level within the band gap are mostly evaluated from substrate core–level signals in energy distribution curves of photoemitted electrons. That technique probes surface areas approximately 1 mm in diameter and, therefore, the growth kinetics of the metal evaporated has to be considered, too. A brief review of the most important aspects will be given in section 2 (see also Mönch (1988 b)). Studies with metals evaporated on substrates held at low temperatures gave new insights in the formation process of Schottky contacts (Bonapace et al. 1984, Savage and Lagally 1986, Stiles et al. 1987, Cao et al. 1987). Most importantly, those low–temperature results revealed metal adatoms to induce surface states of donor character. Metal adatoms are covalently bonded to substrate surface atoms (Batra and Ciraci 1986). Those surface states of donor type as well as surface dipoles both induced by metal adatoms on semiconductor surfaces can be described in a surface–molecule model (Mönch 1988 b, c). The experimental low–temperature results and the surface–molecule model will be discussed in sections 4 and 5, respectively.

Covalent bonds are partially ionic in character which may be estimated from the difference in electronegativities of the atoms forming the bonds (Pauling 1960). This concept is part of the surface–molecule model. In section 6, it will be also applied to metal–semiconductor interfaces. Metallic bonds are also known to be partially ionic in character (Miedema et al. 1973).

In this paper we will mostly consider data obtained with metals deposited on gallium arsenide and other III–V compound semiconductors since a large number of investigation providing a wealth of experimental data were performed with this class of semiconductors recently. The very informative low–temperature results are available for metal–covered GaAs surfaces only.

2. METAL GROWTH KINETICS AT ROOM AND LOW TEMPERATURES

In most of the past studies on the formation of metal–semiconductor interfaces, the semiconductor samples were held at room temperature during the

evaporation of metals. With non-transition metals such as, for example, Al, Ag, Au, Cu, and In deposited on cleaved (110) surfaces of III–V compound semiconductors, metallic islands were detected at nominal coverages as low as a quarter of a monolayer (ML) and the surface areas in between them were found to remain clean (Ludeke et al. 1983, Kahn 1983, Bolmont et al. 1983, Bonapace et al. 1985). In low-energy electron energy-loss spectra recorded with clean GaAs(110) surfaces, one of the most prominent features is the 20 eV energy-loss peak, which is attributed to excitonic transitions from Ga(3d) core levels into empty Ga-like surface state. As Fig. 1 shows, this energy loss still retains 20% of its initial intensity after nominal depositions of 4 ML of Al room temperature

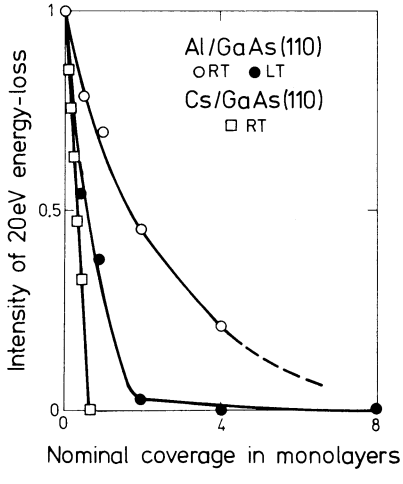

Fig. 1. Intensity of the 20 eV energy loss as a function of the amount of Cs and Al deposited on cleaved GaAs(110) surfaces. Unfilled and filled symbols are indicating depositions at room and at low temperature, respectively. After Grunwald et al. (1988) and Bonapace et al. (1985).

(Bonapace et al. 1985). After the deposition of approximately half a monolayer of Cs, on the other hand, the 20 eV energy-loss has completely vanished (Grunwald et al. 1988). Continuous films are generally not reached until an equivalent of at least some tens of metal monolayers are deposited (Savage and Lagally 1986, Rodrigues and Mönch 1987).

In photoemission experiments, the focus generally has a diameter of approximately 1 mm and, with the metals mentioned above evaporated, photo-

emission spectroscopy then probes a surface area the electronic properties of which are laterally inhomogeneous due to the presence of those metallic islands. Under metallic islands the Schottky barrier is already fully developed. The corresponding space–charge layer will also propagate around the islands. As long as those space–charge layers do not overlap, part of the uncovered surface will retain the properties of the clean surface which is flat bands for well–cleaved (110) surfaces of III–V compound semiconductors. At a nominal coverage of a few monolayers, the area–averaged barrier height as determined from energy–distribution curves of photoemitted electrons will be smaller than the true barrier height which would be measured with a continuous film of the same thickness and which is already reached under metallic islands. With well–separated metallic islands and clean semiconductor surface–areas in between them, the barrier heights determined by using photoemission spectroscopy at samples doped p– and n–type do not add up to the band–gap energy. An example is given in Fig. 2. In the past, however, many interpretations of probe–averaged changes of the Fermi–level position within the semiconductor band–gap as a

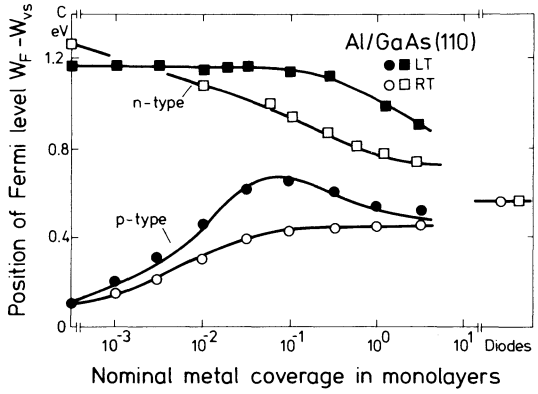

Fig. 2. Fermi–level position within the band gap as a function of the amount of Al deposited at low and at room temperature on GaAs(110) samples doped p– and n–type and determined with Al/GaAs(110) Schottky diodes prepared at room temperature. After Cao et al. (1987) and Newman et al. (1987), respectively.

function of the amount of metal deposited implicitly assumed adatoms in the submonolayer coverage–range and the growth of continuous films beyond that regime.

The growth of islands needs a large surface mobility of the evaporated adatoms which depends as $\exp(-\Delta H_m/k_B T)$ on the temperature T. For In on GaAs(110) surfaces, the enthalpy of migration ΔH_m was estimated as 0.62 eV by fitting solutions of the respective rate equations modelling nucleation and growth (Adams et al. 1988) to experimental data (Savage and Lagally 1986). Consequently, three–dimensional islands were not detected until, for example, an amount of 0.8 monolayers of In was deposited on GaAs(110) surfaces at 190 K while only 0.2 monolayers were sufficient at room temperature (Savage and Lagally 1986). For Ag and Au evaporated on GaAs(110) surfaces, the delayed formation of metallic islands at low temperatures was concluded from the broadening of the d–signals due to sd–hybridization in metallic islands (Stiles and Kahn 1988). The data for Ag are displayed in Fig. 3. With low–temperature deposits of Ag the increase of that line width sets in at 0.5 Å evaporated and is completed at 4 Å while with room–temperature deposits of 0.5 Å the metallic

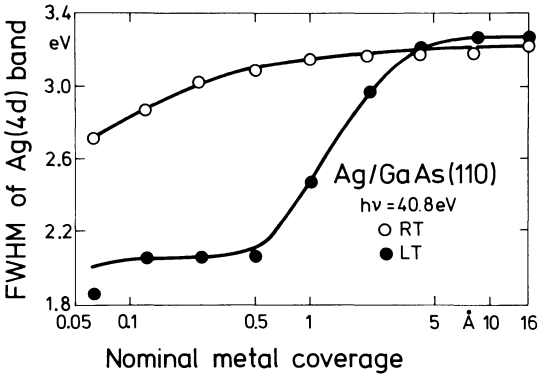

Fig. 3. Full width at half maximum (FWHM) of the Ag(4d) photoemission line recorded as a function of the amount of Ag deposited at room and at low temperature on cleaved GaAs(110) surfaces. After Stiles et al. (1988).

signal–width is almost reached. In agreement with that, a well–developed Fermi edge was already observed with 0.25 monolayers of Ag nominally evaporated on cleaved GaAs surfaces at room temperature (Ludeke et al. 1983). Indeed, the variation of the Fermi–level position within the band gap as a function of the amount metal deposited is quite different when the samples are held at low and at room temperature. An example is shown in Fig. 2 and shall be discussed in the following.

3. SURFACE BAND–BENDING AT SUBMONOLAYER COVERAGES

The barrier heights determined from I/V characteristics measured with Al/GaAs(110) diodes prepared with samples doped p– and n–type are adding up to the band–gap energy, i.e. the position of the Fermi level within the band gap as shown on the right hand side of Fig. 2 is the same for both types of doping (Newman et al. 1987). With increasing amount of Al deposited at room as well as at low temperature, the Fermi level approaches that position assumed under thick overlayers in diodes but has not yet reached it even after three monolayers of nominal coverage. The Al film is thus still non–continuous after both room– and low–temperature depositions up to at least 3 ML. This is confirmed by work–function measurements (Bonapace and Kahn 1984) where approximately 8 ML need to be deposited until the work function finally reaches the bulk Al value. In comparing the results of such experiments published by different groups, it has always to be kept in mind that the growth kinetics of metal films not only strongly depend on the surface temperature of the substrates during evaporations, which is hard to measure exactly anyway, but also on the evaporation rates.

With Al deposited on p– and on n–GaAs(110) substrates held at room temperature, and the same holds for other non–transition metals, the Fermi level almost symmetrically approaches its final position within the band gap as a function of nominal coverage. This is shown in Fig 2. Such behavior seems to be plausible since for identical growth conditions the distributions of size and shape of metallic islands should only slightly vary from one run to another. When, on the other hand, the substrates are held at low temperature during metal evaporations the Fermi level keeps its initial, clean–surface position on samples doped n–type while on substrates doped p–type a strong surface band–bending builds up. It saturates at coverages as low as 0.01 monolayers and remains constant up to 0.3 ML. Such behavior was meanwhile also reported for low–temperature evaporations of Na, K, Rb, Cs, Al, Ga, In, Sn, Ag, Au, and Mn on GaAs(110) surfaces (Stiles et al. 1987 and 1988, Cao et al. 1987, Prietsch et al. 1988 b). Such asymmetric behavior for both types of doping indicates the formation of adsorbate–induced surface states of donor character. The energy levels and the density of those extrinsic surface states will be evaluated from experimental data in the next section.

Above metal depositions in excess of approximately half a monolayer, the Fermi–level position within the band gap now moves towards its final position which is found in Schottky diodes, i.e. under thick metal overlayers, and which is the same for n– and p–type doping. In the coverage range from 0.5 to 0.8 ML

large islands were observed to grow (Savage and Lagally 1986). The surface properties then become inhomogeneous as in the case of metal deposition at room temperature. We will come back to this in section 7.

4. METAL–INDUCED SURFACE STATES

The variations of the Fermi–level position within the band gap, which is shown in Fig. 4 for In, Al, Ag, and Au deposited on p–GaAs(110) samples held at 190 K, indicate the formation of depletion layers. For a surface band–bending $e_oV_s = (W_{vb} - W_{vs})$ their space–charge density is given by (see, for example, Many et al. 1965 and Frankl 1967)

$$Q_{sc} = -\sqrt{2\epsilon_s\epsilon_o N_A e_o |V_s|}\ , \tag{1}$$

where N_A and ϵ_s are the bulk acceptor–density and the static dielectric constant of the semiconductor, respectively. Relation (1) holds to better than 10% when $|e_oV_s| \geq 6k_BT$. To guarantee charge neutrality at the surface the space charge has to be balanced by an equal amount of charge but of opposite sign in surface states. In the present case, they are adsorbate– or adatom–induced. The condition of surface charge–neutrality may be written as

$$Q_{ss}^{ai} + Q_{sc} = 0. \tag{2}$$

The energy levels of those surface states are within the band gap and they are discrete levels as long as the adatoms are well–separated and then noninteracting. The charge density in the surface states is then given by

$$Q_{ss}^{ai} = +e_oN_{ss}^{ai}\ \{1 + 2\ \exp(-\frac{W_{ss}^{ai} - W_F}{k_BT})\}^{-1}. \tag{3}$$

The nominator in the exponential may be written as

$$W_{ss}^{ai} - W_F = (W_{ss}^{ai} - W_{vs}) - e_oV_s - W_p, \tag{4}$$

where $W_p = (W_F - W_{vb})$ gives the bulk position of the Fermi level relative to the valence–band top. Combining (1) to (4) the surface band–bending and thus the Fermi–level position $(W_F - W_{vs}) = (e_o|V_s| + W_p)$ within the band gap may be evaluated as a function of the density N_{ss}^{ai} of surface states and with

the energy level W_{ss}^{ai} of the surface donors as parameter. The solid curves drawn in Fig. 4 are fits to the experimental data for Au, Ag, Al, and In deposited at low temperatures on p–GaAs(110) samples with adsorbate–induced surface donors

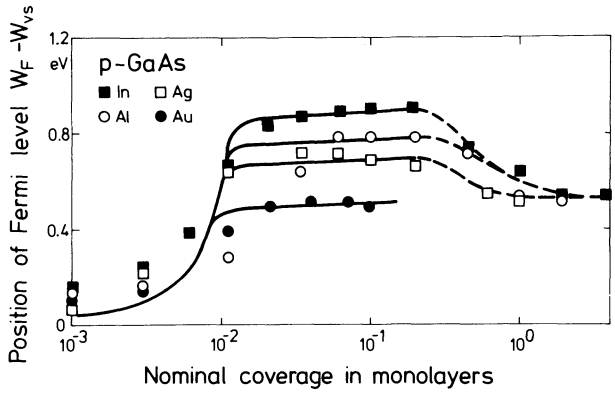

Fig. 4. Position of Fermi level above the valence–band top as a function of the amount of nominal metal coverage on clean p–GaAs(110) samples. Experimental data for In, Al, Ag, and Au deposited at low temperature from Cao et al. (1987) and curves calculated for surface donors at 0.87, 0.76, 0.68, and 0.49 eV, respectively, above the valence–band top. From Mönch (1988 b).

at 0.49, 0.68, 0.76, and 0.87 eV, respectively, above the valence–band top. It was further assumed that each metal atom deposited induces one of those surface donors, i.e.

$$N_{ss}^{ai} = N_{ad}. \tag{5}$$

The experimental data (Cao et al. 1987) are well described by the curves computed (Mönch 1988 b). For the doping level of the GaAs samples used in those experiments, the Fermi level becomes pinned for coverages above 0.01 ML. This means that in other experiments, where the approach to the respective pinning position was not monitored, the overshoot position of the Fermi level with respect to its final position under thicker overlayers may be identified as the energy position of the metal–induced surface states of donor type.

The ionization energies ($W_{cs} - W_{ss}^{ai}$) of the surface donors or, what is the same, their energy position ($W_{ss}^{ai} - W_{vs}$) above the top of the valence band linearly correlates with the ionization energies of the free metal atoms (Mönch 1988 b). This is shown in Fig. 5 which additionally contains data for some

transition metals (Ludeke and Landgren 1986, Hughes et al. 1986), the rare–earth metal Tm (Prietsch et al. 1988 a) and Ca (Ludeke and Jezequel 1987) all deposited at room temperature. The transition–metal atoms were found

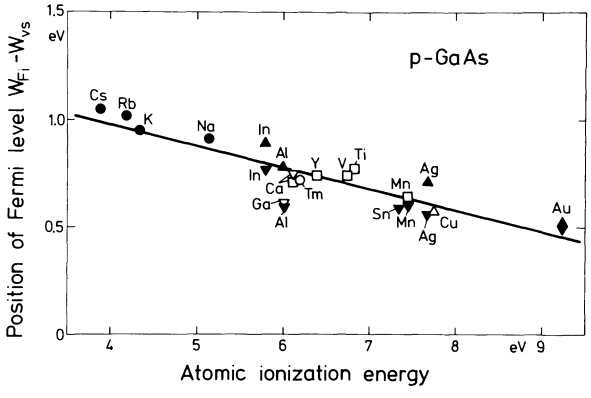

Fig. 5. Energy positions of metal–induced surface states of donor type with respect to the valence–band top as a function of the ionization energy of the free metal atoms. From Mönch (1988 c).

to replace surface gallium atoms. By this exchange reaction, the transition–metal atoms are well separated from each other and trapped so that they can not migrate on the surface and form metallic islands. The overshoot position of the Fermi level, again observed at submonolayer coverages on p–GaAs(110) samples, with respect to its final position under thick overlayers is, therefore, identified as the energy position of the metal–induced surface states of donor type. This assumption is justified by the data reported for manganese deposited at room and at low temperature (Hughes et al. 1986, Stiles et al. 1988). As Fig. 5 shows those Fermi–level positions are the same at both temperatures. The correlation between the energy positions of the metal–induced surface states and the ionization energies shall now be analyzed in a simple theoretical model.

5. SURFACE–MOLECULES IN TIGHT–BINDING APPROXIMATION

The interaction of adatoms with semiconductor surfaces may be described by covalently bonded surface molecules. Following Pauling's concept for small molecules (1960), the amount of ionic character of those bonds and with that their dipole moment is determined by the electronegativity difference between adsorbate and substrate (Clemens et al. 1978).. This concept of surface molecules

shall be illustrated by the example of cesium adatoms. Cesium is the most electropositive of the elements (X_{Cs}= 0.79) while the semiconductors are placed right in the middle of Pauling's scale ($\langle X \rangle_{sem}$= 1.95 ± 0.08). As to be expected, the ionization energies of semiconductor surfaces are drastically lowered by cesium adatoms (Allen and Gobeli 1966, Madey and Yates 1971, Spicer et al. 1975, Clemens et al. 1978). The experimental dipole moments of the cesium–induced surface dipoles may be modeled as the product of the Pauling–ionicity of such surface–molecules formed between a Cs–adatom and a substrate atom and the sum of their covalent radii (Clemens et al. 1978).

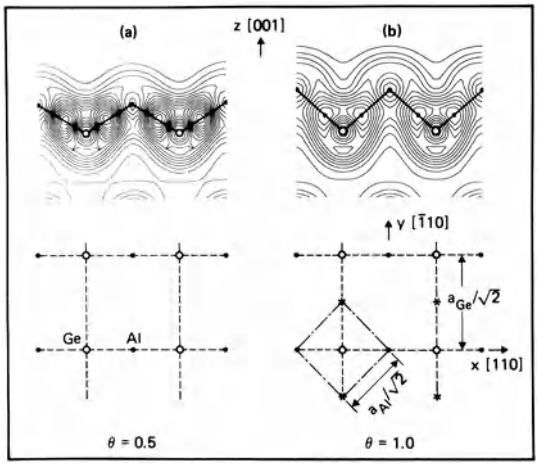

Fig. 6. Charge–density contours in the ($\bar{1}$10) plane of the Al/Ge(100) interface corresponding to Al in bridge–bonded sites for 0.5 and 1 ML. The contour spacings are 0.005 a.u. Atomic arrangements are also shown for the two coverages; the stars and filled circles represent Al atoms, and open circles Ge atoms. From Batra and Ciraci (1986) with permission.

The simple picture of surface molecules was excellently confirmed by self–consistent electronic structure calculations for Al adsorbed on Ge(100) surfaces (Batra and Ciraci 1986). At half a monolayer of coverage, each Al adatom was found to be covalently bridge–bonded to two Ge surface–atoms. As Fig. 6 shows, the centroid of the bond charges is shifted towards the Ge atoms. This result is in complete agreement with Pauling's concept of the partial ionic character of covalent bonds since Al is by 0.4 units on the Pauling–scale (Sargent–Welsh 1980) less electronegative than Ge.

The electronic levels of single–bonded surface molecules may be calculated in a tight–binding approach (Mönch 1988 c). For monovalent metal atoms, the bond orbitals are then formed by a dangling sp^3–hybrid of a substrate atom and

a s–orbital of an adatom. The energy of the bonding state is then given by

$$W_b = \frac{W_h^i + W_s}{2} - \sqrt{\left[\frac{W_h^i - W_s}{2}\right]^2 + V_2^2}\,, \tag{6}$$

where W_s is the atomic term value of the s–levels of the adatoms. The energy W_h^i of the dangling–bond sp^3–hybrid is the average

$$W_h^i = \frac{W_s^i + 3\,W_p^i}{4}\,, \tag{7}$$

of the s– and p–term value of the free atoms. The superscript i denotes whether substrate cations or anions are considered. The matrix element is obtained as

$$V_2 = \frac{-V_{ss\sigma} + 3V_{sp\sigma}/\sqrt{3}}{2}\,. \tag{8}$$

The interatomic matrix elements $V_{ss\sigma}$ and $V_{sp\sigma}$ are assumed to scale as the interatomic distances as

$$V_{ll'm} = \eta_{ll'm}\,\frac{\hbar^2}{m_o}\,\frac{1}{d^2}\,, \tag{9}$$

where m_o is the electron mass. The interatomic distances are taken as the sum of the covalent radii of the adatom and the respective substrate atom:

$$d = r_{cov}^{ad} + r_{cov}^{i}\,. \tag{10}$$

In the present approach, the same basis set of parameters is applied which was successfully used by Harrison (1981) for fitting the bands of covalent solids in a tight–binding theory. These parameters are Hartree–Fock orbital binding energies computed by Fischer (1972) and the coefficients in the interatomic matrix elements (9) proposed by Harrison (1981).

In Fig. 7, the energies of the binding states (6) calculated for surface–molecules consisting of Na, K, Rb, Cs, Cu, Ag, and Au adatoms and surface Ga atoms are plotted versus the atomic term values of the outer s–electrons of those alkali and noble metal atoms. The lower and upper boundaries of Fig. 7 are the top of the valence and the bottom of the conduction band, respectively. They were calculated using a tight–binding approach (Chadi and Cohen 1975)

and the same set of parameters utilized above. From the data displayed in Fig.

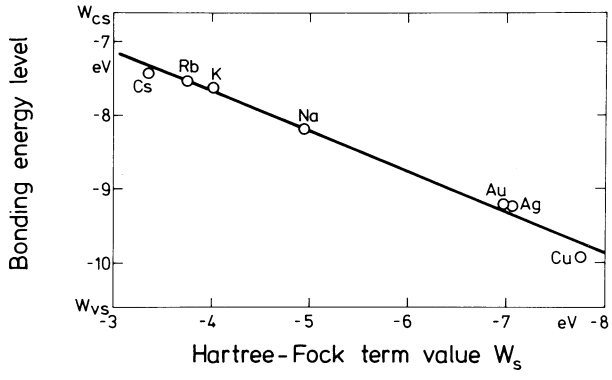

Fig. 7. Binding energy of bonding level of s–metal surface–molecules on GaAs(110) surfaces as a function of the Hartree–Fock atomic term values of the s–electrons of the metal adatoms. The vacuum level is taken as zero binding energy. From Mönch (1988 c).

7 the following conclusions may be drawn. First, the energies of the binding states calculated for the adatom–Ga surface–molecules are found to lie within the tight–binding band–gap of GaAs. Second, the minimal–basis tight–binding approach excellently confirms the linear correlation between the experimental energies of the donor–type surface states induced by metals adsorbed on GaAs(110) surfaces and the first ionization energies of the free metal atoms (see Fig. 5). The results of the calculations seem to indicate that the s–electron metal atoms predominantly bond with surface Ga atoms. This conclusion is strongly supported by the observed decay of the 20 eV energy loss after the adsorption of half a monolayer of Cs on GaAs(110) surfaces as displayed in Fig. 1 (Grunwald et al. 1988). Most recent theoretical calculations using a self–consistent field pseudopotential approach (Fong et al. 1988) and a first–principles self–consistent tight–binding model (Ortega and Flores 1988) are confirming the formation of alkali atom–Ga bonds on GaAs(110) surfaces.

6. ViGS MODEL OF METAL–INDUCED SURFACE AND INTERFACE OR GAP STATES

In the preceding section, the adsorption of metals was described in the bond picture. In the band model, the energy levels of the metal–induced surface states are found within the semiconductor band–gap and, consequently, the wave

functions of, for example, the cesium s–electrons will exponentially decay into the semiconductor. These wave–function tails are derived from the virtual gap states of the complex semiconductor band–structure. This will be explained in a one–dimensional model (see, for example, Maue 1935 and Goodwin 1939).

Let us assume a linear chain with lattice constant a and the simple periodic potential

$$V = V_0 + 2V_1 \cos(\frac{2\pi}{a} z) \ . \tag{11}$$

The resulting band structure shows an energy gap of width $2|V_1|$ at the boundary $k = \pm \pi/a$ of the 1st Brillouin zone. With an infinite linear chain, the solutions of Schrödinger's equation are Bloch waves

$$\psi_b(z) = u_k(z) \exp(ikz) \ , \tag{12}$$

i.e. plane waves modulated by a lattice–periodic function. The wave vectors k are real since for complex wave vectors (12) can not be normalized. At a surface, i.e. at the end of a semiinfinite chain, the wave functions are exhibiting exponential tails into vacuum and, therefore, wave functions exponentially decaying into the chain can be normalized. Such surface states will then have energies within the band gap and their wave vectors may be written as

$$k = \pi/a + i\gamma \ . \tag{13}$$

Solving Schrödinger's equation gives the dispersion relation

$$\frac{\hbar^2}{2m_0} \gamma^2 = -W_1 - (W - V_0) \pm \sqrt{V_1^2 + 4W_1(W - V_0)} \tag{14}$$

with

$$W_1 = \frac{\hbar^2}{2m_0} \left[\frac{\pi}{a} \right]^2 , \tag{14a}$$

and the wave functions

$$\psi_{vs} \approx e^{\gamma z} \cos\left(\frac{\pi}{a} z + \varphi\right) \text{ for } z \leq 0 \ , \tag{15}$$

which are exponentially decaying into the chain. The phase φ varies across the gap as

$$\sin 2\varphi = -\frac{4W_1}{V_1} \frac{\gamma}{2\pi/a} \ . \tag{15a}$$

gap are called virtual gap states (ViGS) of the complex band structure of the semiconductor. Whether and if so real surface states at clean surfaces, adsorbate–induced surface states at adatom–covered surfaces, and metal–induced gap states at metal–semiconductor interfaces will form is determined by the specific boundary conditions.

At the clean end of a semiinfinite chain, a wave function (15) can only be fitted to an exponentially decaying tail into vacuum if the Fourier coefficient V_1 in (11) has the correct sign. With the matching plane at $z = 0$, one obtains $V_1 < 0$ (Maue 1935, Goodwin 1939, Zak 1986). Provided that this boundary condition is met, the depth $(W_{vac} - V_0)$ of the surface potential barrier then determines the energy W_{ss} and the decay length $1/\gamma_{ss}$ of the surface state which is derived from the continuum of the ViGS (14). The character of the surface states varies across the band gap. The branch point or charge–neutrality level of the ViGS, above and below which the surface states predominantly have conduction– and valence–band character, respectively, lies at midgap position for symmetric bands. The concept outlined above for surface states shall now be utilized for adsorbate–induced surface states and metal–induced gap states.

With cesium, for example, as an adsorbate, the boundary conditions are such that negative charge is shifted into the semiconductor since adsorbed cesium lowers the ionization energy of the substrate. Those wave–function tails then need to possess acceptor or conduction–band character. The branch point or charge–neutrality level of the ViGS, above and below which surface states predominantly have conduction– and valence–band character, respectively, was computed to lie 0.5 eV above the valence–band top (Tejedor and Flores 1978, Tersoff 1986). Indeed, all metal–induced surface states are found above that energy position as can be seen in Fig. 5.

At metal–semiconductor interfaces, the continua of the metal–induced gap states and of the wave–function tails of the metal electrons have to be considered instead of discrete adsorbate–induced surface states and exponentially decaying wave functions of individual adatoms. As Fig. 6 shows, the charge distribution slightly changes by going from well–separated and noninteracting Al adatoms at half a monolayer coverage to a full monolayer of now interacting Al atoms on Ge(100) (Batra and Ciraci 1986). Other case studies investigating thick Al layers on Si, GaAs, ZnSe, and ZnS revealed the tails of the Al wave–functions to carry negative charge (Louie et al. 1977, Zhang et al. 1986). At metal–semiconductor interfaces the condition of charge neutrality (2) valid for adsorbate–covered surfaces has thus to be replaced by

$$Q_m + Q_{gs}^{mi} + Q_{sc} = 0. \quad (16)$$

Here, Q_m and Q_{gs}^{mi} are the charge densities on the metal side of the interface and in the wave–function tails of the metal electrons on the semiconductor side, respectively.

From the barrier heights in Al/GaAs(110) diodes given on the right hand side of Fig. 2, the density of states of the metal–induced gap states may be estimated. Taking into account the bulk doping levels, the space charge densities Q_{sc} amount to approximately $+3\times10^{12}$ e_0/cm^2 and -5×10^{12} e_0/cm^2 for the substrates doped n– and p–type, respectively. The positions of the Fermi level within the band gap are identical up to ±0.02 eV, the limits of experimental error, for both types of doping. Hence, the density of states of metal–induced gap sates is estimated to be $\geq 2\times10^{14}$ per cm^2 and eV. This value is in excellent agreement with results from theoretical calculations yielding 3.7 and 5×10^{14} per cm^2 and eV (Louis et al. 1976, Louie et al. 1977, respectively).

No systematic theoretical analysis of the chemical trends observed in the barrier heights of metal–semiconductor contacts has been presented up to now. From a chemical point of view, however, a charge transfer between the metal and the semiconductor is expected from the concept of the partial ionic character of chemical bonds (Pauling 1960, Miedema 1973). Therefore, the difference $(X_m - X_{sem})$ of the metal and the semiconductor electronegativities was chosen to simulate the boundary condition at the interface by the charge transfer between metal and semiconductor (Mönch 1987).

For metals deposited on cleaved GaAs(110) surfaces at room temperature, the position of the Fermi level within the band gap of GaAs is plotted versus the electronegativity difference $(X_m - X_{GaAs})$ in Fig. 8. All data shown were evaluated from photoemission spectra from substrate core–levels, i.e. the nominal coverages never exceeded some nanometers. The partially filled symbols denote experiments where the final Fermi–level positions were found to be identical on substrates doped p– and n–type. The unfilled symbols are considering data from p–GaAs samples only. The charge–neutrality level (CNL) of the ViGS is entered at $(X_m - X_{GaAs}) = 0$ since per definitionem the Fermi level and the CNL will coincide for no charge transferred between adatoms and substrate atoms at all. The data points are closely following a pronounced chemical trend which may be approximated by the straight line drawn in Fig. 8. What is most important, this chemical trend includes the charge–neutrality level predicted theoretically and by this it is confirming the ViGS model of metal–induced gap states. The figure

adsorbed on cleaved GaAs(110) surfaces (Troost et al. 1987, Koenders et al. 1988). Strictly speaking, those are no Schottky contacts and no metal adsorbates at all. Those nonmetallic adsorbates, however, were found to induce surface states of acceptor character below the CNL of the virtual gap states and to increase the ionization energy of the substrate. The acceptor–type surface states of the nonmetal adsorbates on GaAs(110) surfaces nicely correlate with the electron affinities of the respective free atoms (Koenders et al. 1988). All these

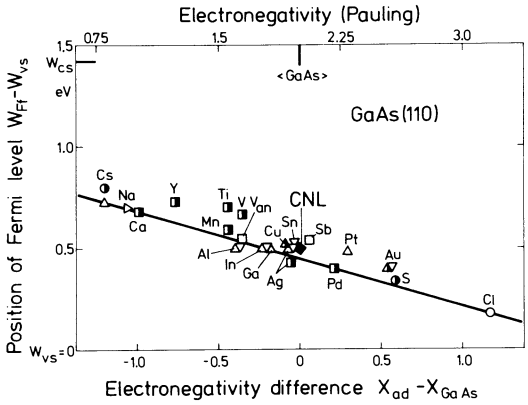

Fig. 8. Final pinning positions of the Fermi level above the valence–band top versus electronegativity difference. Unfilled and partly filled symbols are labeling data obtained with substrates doped p–type and p– as well as n–type. ▵ data from Spicer et al. (1976), Skeath et al. (1979), Pan et al. (1984), Kendelewicz et al. (1985, 1988), McCants et al. (1987), Cao et al. (1987); □ data from Hughes et al. (1986), Ludeke and Landgren (1986), Ludeke and Jezequel (1987), Ludeke et al. (1987), Schäffler et al. (1987 b); ▵ data from Stiles et al. (1987); ▹ data from McLean et al. (1987); o data from Troost et al. (1987), Koenders et al. (1988), Grunwald et al. (1988); CNL value from Tersoff (1986).

findings are also in agreement with the concepts used in the present analysis of metal–induced surface and gap states at submonolayer coverages and under continuous overlayers, respectively. It is worth mentioning that the "ViGS line" in Fig. 8 was concluded earlier from the data points for Cs:GaAs(110) and Cl_2:GaAs(110) together with the computed CNL of the ViGS of GaAs (Troost et al. 1987).

Barrier heights as determined from I/V characteristics measured with GaAs Schottky diodes are plotted versus the electronegativity difference ($X_m - X_{GaAs}$)

in Fig. 9. A data point for Ga/GaAs(110) diodes (McLean and Williams 1987) is not considered since it was evaluated from I/V curves which had extremely large electron–hole recombination currents. This was attributed to a disordered GaAs interfacial layer. Such films possibly form by reaction of evaporated Ga with excess As from the substrate. In Fig. 9, the scale given by Miedema et al. (1980) is used which relates to the one introduced by Pauling as

$$X_{Mied} = 1.93 X_{Paul} + 0.87 \ . \tag{17}$$

The straight line drawn in Fig. 9 again is the ViGS line (Troost et al. 1987) and, remarkably, it is an upper border since no data points are found above it. The same conclusion was reached from an analysis of metal– and silicide–silicon Schottky contacts (Mönch 1987).

A lowering of barrier heights with respect to the value expected from the ViGS–line is achieved by, for example, an extra positive charge at the interface. Tentatively, this will be attributed to fabrication–induced defects of donor type. In the condition of charge neutrality (16) at *ideal* interfaces, the charge density Q_{def} in such defects then has to be added and (16) may be rewritten as

$$Q_m + Q_{gs}^{mi} + Q_{def} + Q_{sc} = 0. \tag{18}$$

Let us assume donor–type defects with an energy level above the CNL of the

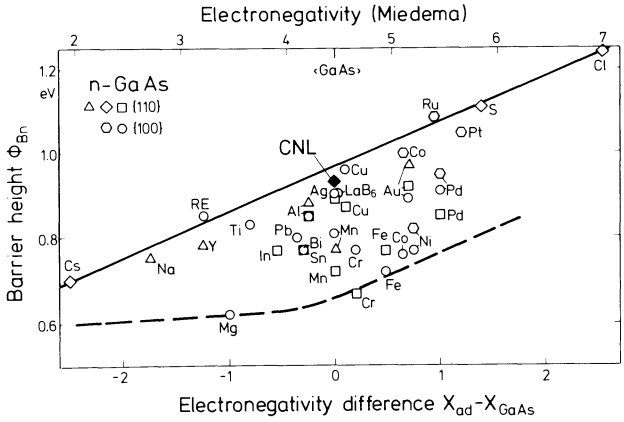

Fig. 9. Barrier heights reported for metal–GaAs contacts versus electronegativity difference (X_m–X_{GaAs}). ○ data from Waldrop (1984, 1985); □ data from Newman et al. (1986); △ data from McLean et al. (1987); ⬡ data from Ludwig and Heyman (1986) and Allongue and Souteyrand (1987); CNL from Tersoff (1986).

semiconductor ViGS. For sufficiently large transfer of negative charge into metal–induced gap states, i.e. for $\Delta X = (X_m - X_{sem}) < 0$, the ViGS model of MIGS predicts a low barrier height, in agreement with experiment, and the Fermi level shall be above the assumed donor level. All the donor defects will then be neutral. With increasing electronegativity of the metal or, in other words, with the positive charge in the metal and the negative charge in metal–induced gap states decreasing, the Fermi level moves towards the charge–neutrality level of the ViGS and by this approaches the energy level of the fabrication–induced donors. They now gradually become positively charged. The Fermi level gets pinned close to the defect level until all defects are charged and, eventually, the metal–induced gap states will again accommodate charge with further increasing metal electronegativity. The ϕ_{Bn}–versus–ΔX curve then runs parallel to that line observed with no fabrication–induced defects being present. The dashed curve in Fig. 9 gives the relationship $\phi_{Bn}(\Delta X)$ for the largest density of defects being compatible with the experimental data. The *pinned* part of that curve is determined by an assumed defect level at 0.65 eV below the conduction–band bottom.

Such a doping of metal–semiconductor interfaces was theoretically modeled (Zhang et al. 1985). A layer of positively charged donors was placed at an Al/Si interface and it was found to shift the Fermi level by 0.28 eV closer to the conduction band. This reduction of the barrier height by positively charged donors at the interface is in agreement with the conclusions drawn from the much simpler analysis of the charge–neutrality condition (18) as outlined above.

The assignment of the barrier–height lowering in Schottky diodes in comparison with what is expected from the ViGS model of metal–induced gap states to fabrication–induced defects is also supported by annealing experiments. In Fig. 8 the partly filled and unfilled data points for V:GaAs (110) were obtained immediately after the deposition of 0.1 nm of V at room temperature and after a subsequent heat treatment at 600 K, respectively (Ludeke 1987). The data point evaluated after the annealing treatment is right on the ViGS–line. This finding is suggestive for the presence of defects in the unannealed sample since excess defects are generally eliminated by thermal annealing. Similar observations were also reported for LaB_6/GaAs(100) Schottky diodes (Uchida et al. 1987) and for V:Si(111) interfaces (Clabes et al. 1982).

Furthermore, the process of metal–deposition itself seems to have a marked influence on the barrier height. Fig. 9 also exhibits results for diodes prepared by electrocrystallisation of some metals on GaAs(100) samples (Ludwig and Heymann 1986, Allongue and Souteyrand 1987). Electrodeposition always results

in larger barrier heights compared to values observed with the same metal but evaporated. The data points reported for Ru/–, Pt/–, and Co/GaAs contacts prepared by electrocrystallisation are very close to the ViGS–line.

Finally, ion bombardment of Si, GaAs as well as MoS_2 substrates (Mullin and Brunnschweiler 1976, Wang and Holloway 1984, Lince et al. 1987) prior to metal depositions was reported to reduce the barrier heights compared to untreated samples. Again, ion bombardment is considered to introduce defects.

The results of the annealing, the electrocrystallisation and the ion–bombardment experiments are supporting the assumption of fabrication–induced defects of donor type in Schottky barriers but they are are not decisive for their presence. It is conceivable that other mechanisms such as different interface structures or strains, which are both also sensitive to annealing treatments, might be responsible for reduced barrier heights.

7. FROM ADATOMS TO CONTINUOUS METAL FILMS

For metals such as Al, In, Ag, and Au deposited at low temperatures on GaAs(110) surfaces the transition from isolated adatoms to continuous and metallic overlayers occurs in the coverage range above 0.5 up to approximately 10 monolayers. This is also visible from the charge–density contour plots shown in Fig. 6. For the larger coverage, the directional covalent bonds between the Al adatoms and Ge surface atoms are still discernible but they begin to be replaced by more delocalized metallic–type interaction. It is in that coverage range that the mechanism determining the Fermi–level position within the band gap changes from metal–induced surface states of donor character to the continuum of metal–induced gap states or, with other words, the outer metal electrons become delocalized. By this, the occupied metal–induced suface states (6) of donor character as well as the related empty, nonbonding states, which were not considered here, are broadened and shifted in energy. The latter behavior is comparable to what happens in clusters of metal atoms as a function of their size. Apart from shell–structure oscillations the ionization energy and the electron affinity of spherical clusters of radius R are converging to the metal work–function ϕ_m as (Perdew 1988)

$$I = \phi_m + \frac{1}{2}\frac{e_o^2}{4\pi\epsilon_o}\frac{1}{R + r}, \qquad (19)$$

and

$$A = \phi_m - \frac{1}{2}\frac{e_0^2}{4\pi\epsilon_0}\frac{1}{R + r} . \tag{20}$$

For the monovalent metal atoms, the parameter r varies between 0.6 and 0.74 Å. A detailed analysis of the experimental ($W_F - W_{VS}$)–versus–coverage curves, however, needs the variation of the size– and shape–distribution of the islands as an input. In other cases where laminar growth might occur other models have to be developed. Similar arguments apply for metals deposited at room temperature. Here, the adatom part of the ($W_F - W_{VS}$)–versus–coverage curve is mostly not accessible since the surface mobility of the adatoms is that large and metallic islands are already forming at the lowest coverages which can be prepared experimentally.

At least at and above room temperature, dissociation of surface bonds and the formation of new compounds between ad– and substrate atoms have been reported for quite a number of metals deposited on semiconductor surfaces. Well–known examples are the transition–metal silicides on silicon. Such silicide–silicon interfaces, which are generally formed during heat treatments after metal evaporation at room temperature, are then abrupt again. One of the examples, where disruption of surface bonds was observed at low coverages, is Au on GaAs(110) surfaces. With increasing amount of gold, however, the arsenic and gallium atoms were found to segregate on top of and to incorporate in the metallic gold, respectively (Xu et al. 1987). The interface is then less distorted than to be expected from the initially occurring disruption of substrate surface–bonds. Those observations are also explaining the large barrier height reported for Au/GaAs Schottky contacts and its small deviation from the ViGS line in Fig. 9. This example indicates that the atom distributions in and on the growing films need to be studied in detail for metal–semiconductor combinations where strong surface reactions are observed at small amounts of metal deposited. A discussion of further data already available goes beyond the scope of this contribution.

8. CHEMICAL TRENDS IN THE SLOPE PARAMETER OF SCHOTTKY CONTACTS

In the analysis of chemical trends of barrier heights in Schottky contacts, the slope $S_\phi = d\phi_{Bn}/d\phi_m$ is the most important parameter. Provided the density of states D_{VS} of the continuum of metal–induced interface states is independent of the metals deposited and is constant around its charge–neutrality level

W_o, the barrier height is obtained as (Cowley and Sze 1965)

$$\phi_{Bn} = S_\phi(\phi_m - \chi_s) + (1 - S_\phi)\,\phi^o_{Bn}\,, \tag{21}$$

with the slope parameter

$$S_\phi = \left[\,1 + \frac{e_o^2}{\epsilon_o} D_{vs}\delta\,\right]^{-1}. \tag{22}$$

Here, $\chi_s = (W_{vac} - W_{cs})$ is the electron affinity of the semiconductor, and $\phi^o_{Bn} = (W_{cs} - W_o)$ is the barrier height when the Fermi level coincides with the charge neutrality level. The slope parameter is thus determined by the product of the density of states of the interface states and the width δ of the correlated dipole layer. Recently, it was found that the slopes reported for 20 different semiconductors and insulators (Kurtin et al. 1970, Schlüter 1978) are quadratically related with the electronic susceptibility of the semiconductors and insulators as (Mönch 1986)

$$S_\phi = 0.1\,(\epsilon_\infty - 1)^2\,. \tag{23}$$

This chemical trend is displayed in Fig. 10. It is not merely a coincidental fitting result but it can be given a simple physical meaning (Jaros 1988).

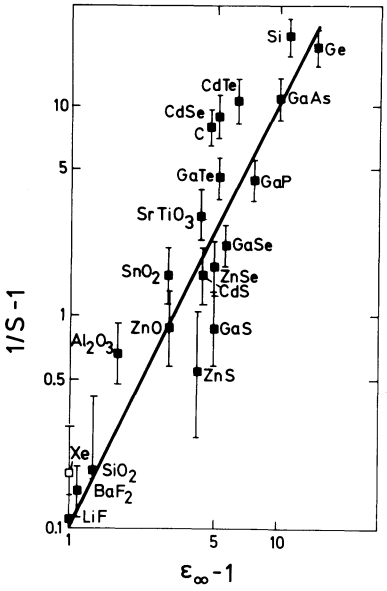

Fig. 10. Slopes $S = d\phi_{Bn}/d\phi_m$ plotted versus the electronic susceptibility $(\epsilon - 1)$ of the semiconductor. From Mönch (1986).

For a one–dimensional classical harmonic oscillator of mass m_0 and of resonance frequency ω_0, the amplitude x_0 of oscillations excited by an electromagnetic field of amplitude E_0 and frequency ω is given by

$$x_0 = \frac{e_0}{m_0} \frac{1}{\omega_0^2 - \omega^2} E_0 \ . \tag{24}$$

The polarizability is defined as the induced dipole per field $\epsilon_0 E_0$ and the susceptibility results as

$$\epsilon_\infty - 1 \propto \frac{e_0^2}{\epsilon_0 m_0} \frac{1}{\omega_0^2 - \omega^2} \ . \tag{25}$$

The quantum mechanical expression for the polarizability is obtained from (25) by replacing $\hbar\omega_0$ by the energy separation $W_{l,m}$ between the ground and the excited state and by introducing the optical matrix element $f_{l,m}$, i.e.

$$\epsilon_\infty - 1 \propto \frac{e_0^2 \hbar^2}{\epsilon_0 m_0} \frac{|f_{l,m}|^2}{W_{l,m}^2 - W^2} \ , \tag{26}$$

where $W = \hbar\omega$. Since $f_{l,m}$ is of the order 1 and $W_{l,m} \simeq W_g$, where W_g is the gap energy, one obtains for $\omega << \omega_0$

$$x_0 \propto (\epsilon_\infty - 1) \propto W_g^{-2} \ . \tag{27}$$

To get an expression for D_{vs} one can invoke quite generally the conventional Green's function theory familiar from the theory of defects (see Jaros 1982). Starting with an unperturbed Hamiltonian $\hat{H}_0$ representing the noninteracting metal–semiconductor contact, the change in the density of states due to the interaction V at the interface may be written as

$$\Delta N(W) \propto \Im \{\mathrm{Tr}\ [1 - (W^+ - \hat{H}_0)^{-1} V]\} \ . \tag{28}$$

In the present case, $\Delta N(W)$ is the density of states D_{vs} of the metal–induced gap states at the interface. W^+ is the the complex energy $W^+ = (W + i\sigma)$. Hence, D_{vs} is in the order of $\Im \{1 - [W - \hat{H}_0 + i\sigma]^{-1} V\}$ or, in the limit of small σ, simply

$$D_{vs} \propto \frac{\sigma}{(W - \hat{H}_0)^2} \propto W_g^{-2} . \tag{29}$$

Since $(\epsilon_\infty - 1) \propto W_g^{-2}$, (29) gives $D_{vs} \propto (\epsilon_\infty - 1)$. Considering also (27) and $x_0 \simeq \delta$, one obtains the relation

$$D_{vs}\delta \propto (\epsilon_\infty - 1)^2 , \tag{30}$$

i.e. the empirical trend (23), which is shown in Fig. 10, is recovered.

9. FINAL REMARKS

The formation of metal–semiconductor interfaces has turned out to be rather complex. Consequently, the same holds for the approach of the Fermi level from its initial clean–surfaces to its final interface–position within the band gap of the semiconductor. Much progress in the understanding of the build–up of barrier heights as a function of metal coverage was achieved after the growth kinetics of the metals at different temperatures as well as the adsorption of nonmetals have been taken into consideration, too. Studies at liquid nitrogen temperature strongly contributed to the separation of different mechanisms. At submonolayer coverages, isolated metal adatoms are obtained by cation–exchange reactions of transition metals evaporated at room temperature or by low–temperature depositions of group I and group III metals. The high surface mobility of the latter atoms at room temperature leads to the formation of metallic islands even for the lowest coverages practically to be achieved. The surface and it s properties then become inhomogeneous. The different contributions from surface areas still clean and those already covered with metallic islands are difficult to separate since probes averaging over larger areas were used hitherto.

Since long it has been well–known that adsorbates on semiconductors are inducing surface states as well as surface dipoles. Recent experimental studies have finally revealed that metal and nonmetal adatoms are inducing surface states of donor and acceptor character, respectively, and surface dipoles which are de– and increasing, respectively, the ionization energy of GaAs(110) surfaces. These findings may be described in a surface–molecule model. For simple monovalent metals adsorbed on GaAs(110) surfaces, the chemical trend of the energy levels of the adatom–induced surface states can be successfully modeled by a simple tight–binding approach. Additional theoretical studies are highly desirable. The chemical trends of the adsorbate–induced surface dipoles can be easily

bonds and its correlation with the difference of atomic electronegativities as well as by considering the virtual gap stale of the complex band structure of the semiconductor since the adsorbate–induced donor and acceptor levels are are found above and below, respectively, of the charge–neutrality level of the ViGS. The basic conclusion is that for adsorbates on semiconductors the boundary condition may be simulated by the charge transfer between the adatom and the adsorbate, i.e. by the difference in their electronegativities.

This concept may be also applied to abrupt metal–semiconductor interfaces. For metal–GaAs as well as metal–Si contacts, the experimental barrier heights were found to depend on the method, which was used for preparing the diodes, and they are mostly smaller than to be expected from the simple ViGS model of the continuum of metal–induced gap states. Those findings may be explained by fabrication–induced defects of donor character. The type of such possible defects could only be speculated on. Although post–fabrication annealing and pre–fabrication ion–bombardment treatments seem to support this ViGS–plus–defects model other mechanisms such as interface strain and different atomic arrangements at the interface should be also carefully considered.

Further support for the ViGS model of the continuum of metal–induced gap states in Schottky contacts comes from an analysis of the chemical trends of the slope S_{ϕ}. That parameter was found to vary as the square of the electronic susceptibility ($\epsilon_{\infty} - 1$) of the semiconductors. A simple theoretical model has recently reproduced this result.

In summary, the ViGS model of the continuum of metal–induced gap states (MIGS) together with the charge transfer across metal–semiconductor interfaces, which may be approximated by the difference in electronegativities of the metal and the semiconductor considered, are considered to provide a consistent model of the barrier heights and their chemical trends in abrupt Schottky contacts.

REFERENCES

Adams, J. B., Hitchon, W. N. G., and Holzmann, L. M., 1988, J. Vac. Sci. Technol. 6:2029.

Allen, F. G., and Gobeli, G. W., 1966, Phys. Rev. 144:558.

Allongue, P., and Souteyrand, E., 1987, J. Vac. Sci. Technol. B 5:1644.

Bardeen, J., 1947, Phys. Rev. 71:717.

Batra, I. P., and Ciraci, S., 1986, Phys. Rev. B33:4312.

Bolmont, D., Mercier, V., Chen, P., Lüth, H., and Sebenne, C. A., 1983, Surf. Sci. 126:509.

Bonapace, C. R., Li, K., and Kahn, A., 1984, J. Physique 45:C5–409.

Bonapace, C. R., Tu, D. W., Li, K., and Kahn, A., 1985, J. Vac. Sci. Technol. B 3:1099.

Braun, F., 1874, Pogg. Ann. 153:556.

Cao, R., Miyano, K., Kendelewicz, T., Lindau, I., and Spicer, W. E., 1987, J. Vac. Sci. Technol. B 5:998.

Chadi, D. J., and Cohen, M. L., 1975, phys. stat. sol. (b) 68:405.

Clabes, J. G.,Rubloff, G. W., Reihl, B., Purtell, R. J., Ho, P. S., Zartner, A., Himpsel, J., and Eastman, D. E., 1982, J. Vac. Sci. Technol. 20:684.

Clemens, H. J., v. Wienskowski, J., and Mönch, W., 1978, Surf. Sci. 78:648.

Cowley, A. M., and Sze, S. M., 1965, J. Appl. Phys. 36:3212.

Fischer, C., 1972, Atomic Data 4:301.

Fong, C. Y., Yang, L. H., and Batra, I. P., 1988, these proceedings.

Frankl, D. R., 1967, "Electrical Properties of Semiconductor Surfaces", Pergamon, Oxford.

Goodwin, E. T., 1939, Proc. Cambridge Philos. Soc. 35:205.

Grunwald, F., Fan. Y.–L., Clemens, H. J., and Mönch, W., 1988, Verhandl. DPG (VI) 23:142.

Harrison, W. A., 1980, "Electronic Structure and The Properties of Solids", Freeman, San Francisco, Ca.

Harrison, W. A., 1981, Phys. Rev. B 24:5835.

Heine, V., 1965, Phys. Rev. 138:A1689.

Hughes, G., Ludeke, R., Schäffler, F., and Rieger, D., 1986, J. Vac. Sci. Technol. B 4:924.

Jaros, M., 1982, "Deep Levels in Semiconductors", Hilger, Bristol.

Jaros, M., 1988, private communication.

Kahn, A., 1983, J. Vac. Sci. Technol. A 1:684.

Kendelewicz, T., Williams, M. D., Petro, G. W., Lindau, I., and Spicer, W. E., 1985, Phys. Rev. B 32:3758.

Kendelewicz, T., Soukiassian, P., Bakshi, M. H., Huryel, Z., Lindau, I., and Spicer, W. E., 1988, J. Vac. Sci. Technol. B 6:in press.

Koenders, L., Blömacher, M., and Mönch, W., 1988, J. Vac. Sci. Technol. B 6:in press.

Kurtin, S., McGill, T. C., and Mead, C. A., 1970, Phys. Rev. Lett. 22:1433.

Lince, J. R., Carree, D. J., and Fleischauer, P. D., 1987, Phys. Rev. B 36:1647.

Louie, S. G., and Cohen, M. L., 1976, Phys. Rev. B 13:2461.

Louie, S. G., Chelikowsky, J. R., and Cohen, M. L., 1977, Phys. Rev. B 15:2154

Louis, E., Yndurain, F., and Flores, F., 1976, Phys. Rev. B 13:4408

Ludeke, R., Chiang, T. C., and Miller, T., 1983, J. Vac. Sci. Technol. B 1:581.

Ludeke, R., and Landgren, G., 1986, Phys. Rev. B 33:5526.

Ludeke, R., 1987, private communication.

Ludeke, R., and Jezequel, G., 1987, private communication.

Ludwig, M., and Heymann, G., 1986, J. Vac. Sci. Technol. B 4:485.

Maddey, T., and Yates, J., 1971, J. Vac. Sci. Technol. 8:39.

Many, A., Goldstein, Y., and Grover, N. B., 1965, "Semiconductor Surfaces", North–Holland, Amsterdam.

Mao, D., Young, K., Stiles, K., and Kahn, A., 1988, private communication.

Maue, A. W., 1935, Z. Phys. 94:717.

McCants, C. E., Kendelewicz, T., Bertness, K. A., Mahowald, P. H., Williams, M. D., List, R. S., Lindau, I., and Spicer, W. E., 1987, J. Vac. Sci. Technol. B 5:1068.

McLean, A. B., Evans, D. A., and Williams, R. H., 1987, Semicond. Sci. Technol. 2:547.

McLean, A. B., and Williams, R. H., 1987, Semicond. Sci. Technol. 2:654.

Miedema, A. R., de Boer, F. R., and de Chatel, P. F., 1973, J. Phys. F 3:1558.

Miedema, A. R., de Chatel, P. F., and de Boer, F. R., 1980, Physica 100B:1.

Mönch, W., 1983, Surf. Sci. 182:92.

Mönch, W., 1986, in Festkörperprobleme–Advances in Solid State Phys., ed. by P. Grosse (Vieweg, Braunschweig) 26:27.

Mönch, W., 1987, Phys. Rev. Lett. 58:1260.

Mönch, W., 1988a, Phys. Rev. B 37:7129.

Mönch, W., 1988b, J. Vac. Sci. Technol. B 6:in press.

Mönch, W., 1988c, Europhys. Lett. in press.

Mott, N. F., 1938, Proc. Cambr. Philos. Soc. 34:568.

Mullin, F. M., and Brunnschweiler, H., 1976, Solid State Electron. 19:47.

Newman, N., Spicer, W. E., Kendelewicz, T., and Lindau, I., 1986, J. Vac. Sci. Technol. B 4:931.

Newman N., Spicer, W. E., and Weber, E. R., 1987, J. Vac. Sci. Technol. B 5:1020.

Ortega, J., and Flores, F., 1988, these proceedings.

Pan, S. H., Mo, D., Petro, G. W., Lindau, I., and Spicer, W. E., 1983, J. Vac. Sci. Technol. B 1:593.

Pan, S. H., Kendelewicz, T., Petro, G. W., Williams, M. D., Lindau I., and Spicer, W. E., 1984, in MRS Symp. Proc. 25:335, ed. by J.E.E.E. Banglin, Elsevier, New York.

Pauling, L. N., 1960, "The Nature of the Chemical Bond", Cornell Univ., Ithaca, NY.

Perdew, J. P., 1988, Phys. Rev. B 37:6175.

Prietsch, M., Domke, M., Laubschat, C., and Kaindl, G., 1988a, Phys. Rev. Lett. 60:436.

Prietsch, M., Domke, M., Laubschat, C., Mandel, T., Xue, C. and Kaindl, G., 1988b, Z. Physik in press.

Rodrigues, W. N., and Mönch, W., 1987, Verhandl. DPG (VI) 22:HL–18.3.

Sargent–Welch, 1980, "Table of Periodic Properties of the Elements", Sargent–Welch, Skokie, Ill.

Savage, D., and Lagally, M., 1986, J. Vac. Sci. Technol. B 4:943.

Schäffler, F., Hughes, G., Drube, W., Ludeke, R., and Himpsel, F., 1987a, Phys. Rev. B 35:6328.

Schäffler, F., Ludeke, R., Taleb–Ibrahimi, A., Hughes, G., and Rieger, D., 1987b, Phys. Rev. B 36:1328.

Schlüter, M., 1978, Phys. Rev. B 17:5044.

Schottky, W., 1938, Naturwissenschaften 26:843.

Schottky, W., 1940, Phys. Z. 41:570.

Skeath, P., Lindau, I., Chye, P. W., Su, C. Y., and Spicer, W. E., 1979, J. Vac. Sci. Technol. 16:1143.

Spicer, W. E., Gregory, P. E., Chye, P. W., Babalola, I. A., and Sukegawa, T., 1975, Appl. Phys. Lett. 27:617.

Spicer, W. E., Chye, P. W., Skeath, P. R., and Lindau, I., 1979, J. Vac. Sci. Technol. 16:1422.

Stiles, K., Kahn, A., Kilday, D. G., and Margaritondo, G., 1987, J. Vac. Sci. Technol. B 5:987.

Stiles, K., and Kahn, A., 1988, Phys. Rev. Lett. in press.

Stiles, K., Horng, S. F., Kahn, A., McKinley, J. Kilday, D. G., and Margaritondo, G., 1988, J. Vac. Sci. Technol. B 6:in press.

Tejedor, C., Flores, F., and Louis, E., 1977, J. Phys. C 10:2163.

Tejedor, C., and Flores, F., 1978, J. Phys. C. 11:L19.

Tersoff, J., 1984, Phys. Rev. Lett. 30:4874.

Tersoff, J., 1986, Surf. Sci. 168:275.

Troost, D., Koenders, L., Fan, Y.–L., and Mönch, W., 1987, J. Vac. Sci. Technol. B 5:1119.

Uchida, Y., Yokotsuka, T., and Nakashima, H., 1987, Appl. Phys. Lett. 50:670.

Waldrop, J. R., 1984, J. Vac. Sci. Technol. B 2:445.

Waldrop, J. R., 1985, Appl. Phys. Lett. 47:1301.

Wang, Y.–X., and Holloway, P. H., 1984, J. Vac. Sci. Technol. B 2:613.

Xu, F., Shapira, Y., Hill, D. M., and Weaver, J. H., 1987, Phys. Rev. B 35:7417

Zak, J., 1985, Phys. Rev. B 32:2218.

Zhang, S. B., Cohen, M. L., and Louie, S. G., 1985, Phys. Rev. B 32:3955.

Zhang, S. B., Cohen, M. L., and Louie, S. G., 1986, Phys. Rev. B 34:768.

THE ROLE OF DEFECTS AND METAL STATES AT THE METAL-SEMICONDUCTOR INTERFACE

R. Ludeke

IBM T.J. Watson Research Center
Yorktown Heights, N.Y.

INTRODUCTION

Previously proposed Schottky barrier models that attempt a microscopic description of the observed behavior fall basically into the categories of metal induced gap states (MIGS) models [1-5] and defect models.[6-9] These two types of models are mutually exclusive, as the MIGS models generally ignore the influence of defects and the defect models, for their part, ignore the importance of screening by the metal. Historically the MIGS models preceded the others and were an outgrowth of Bardeen's[10] suggestion that a large density of interface states was responsible for the generally weak dependence of Schottky barrier heights on the metal (workfunction). Bardeen's notion that these states derive from the semiconductor surface states (dangling bonds) was incorporated into the MIGS picture by Mele, et al.[3] and recently by Lefebvre, et al.[11], who considered the interaction of metallic states with the empty, cation-derived dangling bond states. The consequence of this interaction is the formation of broadened resonances which tail into the semiconductor bandgap. The rehybridization of the dangling bonds with the metallic states at the interface was not considered. In general the MIGS models encounter difficulties in the alignment of the metal-semiconductor bandstructures, a task which is model dependent.[1,4] This problem was circumvented by aligning the MIGS with the charge neutrality level (CNL) of the semiconductor.[5,12] The MIGS models are often more successful at estimating the index of interface behavior S ($S \equiv d\Phi_b^n/d\chi_m$) , where Φ_b^n represents the Schottky barrier height for an n-type semiconductor and χ_m the Pauling electronegativity of the metal[13]) since this quantity is insensitive to the magnitude of Φ_b^n , and strongly dependent only on the inverse of the interface density of states D_s.[14] Various approaches to calculate D_s have been reported, ranging from self-consistent pseudopotential methods,[2] which gave the best agreement with experiment, scaling approaches based on the mean optical gap,[3] which give poorer agreement, to one-dimensional model calculations,[4] which agree even less with experimental results.

In contrast, the defect models are based on a perceived metal independence of barrier heights, which nearly reached their full value before the development of the metallic overlayer.[6] These models are premised on the existence of unique defect levels intrinsic to the semiconductor and of sufficient density to remain unaffected by the metallic states.[15,16] Various defects have been proposed, including the anion antisite defects,[6-8] and their complexes with vacancies.[8,9] Although appealing from the point of view of their simple concept, the defect models exhibit several deficiencies which need to be addressed. Among these is their failure to account for observed variations in Schottky barrier heights in GaAs, although an

advanced version of the model partially overcomes this,[7] and corresponding variations (e.g. the index of interface behavior) for other semiconductors. In addition, there is neither a plausible explanation for the formation of a unique set of native defects removed several layers from the surface, nor evidence of their existence in sufficient densities ($\approx 10^{14}cm^{-2}$) to overcome metallic screening.[15,16] Nevertheless, there is overwhelming evidence that deposition-generated defects and impurities play the dominant role in determining the interface Fermi level E_F for metal coverages to about a monolayer (ML). We will discuss this point further in the next section, and speculate as well on the origin of defect and/or impurity levels.

The question of the role of defects at the interface beyond a ML of metal coverage, or more precisely at coverages, typically in the monolayer range, at which the overlayer develops metallic characteristics, has been addressed only recently.[17] This work, which forms the main part of this paper, will be discussed in section 3. A model will be developed based on the interaction of metallic states and localized defect states in the surface layer of the semiconductor. These interactions, a consequence of wavefunction overlap, delocalize the defect levels into broadened resonances, which can accommodate a fractional charge density. The charge sets up an interface dipole of sufficient strength to equalize the Fermi levels on both sides of the junction. The position of E_F relative to the valence band edge is determined by the degree to which the average resonance is filled by an effective charge. This charge is generally $\lesssim 0.1 \mid e \mid$, so that E_F lies low in the resonance. Thus changes in E_F can be expected following the onset of defect delocalization with metallization. Several such cases have been reported recently.[17-20] In section 4 the model is applied to the metal/GaAs interface, for which the interface Fermi level is calculated as a function of the metal workfunction ϕ_m, with the assumption that a universal defect level near the charge neutrality level characterizes all neutral deep levels in the semiconductor prior to the onset of metallic behavior. The agreement with experiment is generally good, with discrepancies attributed to alloying at the interface which alters ϕ_m. In section 5 this concept is further developed for other tetrahedrally-coordinated semiconductors, for which we calculate the index of interface behavior S with unprecedented agreement to experiment. We conclude this paper with an assessment of the principal approximations, in particular the notion of the the uniqueness of the neutral defect levels, and their energy distribution due to broadening effects other than metallization.

THE ROLE OF DEFECTS IN SCHOTTKY BARRIER FORMATION.

The observation that submonolayer coverages of metals can drastically alter the position of E_F from its clean surface position near the band edge of GaAs(110) to a position deep in the band gap was realized already a number of years ago.[21] Subsequent studies revealed this to be a general phenomenon on surfaces of several III-V semiconductors,[6] with the additional observation that the positions of E_F, although nearly the same in a given semiconductor for a number of metals, differed somewhat between n and p-type material. This observation led to the proposal of the unified defect model, with the defect associated with an intrinsic defect level of the semiconductor.[6] Subsequent studies using more diverse metals and for coverages beginning at 0.001 ML, revealed not only constantly evolving values of E_F with coverages to ~1 ML, but also final values of E_F which were metal dependent and essentially identical for n and p-type GaAs.[22,23] For an electrically active defect level (single donor or acceptor) removed several kT from the band edges and of density $\gtrsim 5 \times 10^{12}cm^{-2}$, E_F essentially determines the position of the ionized level.[24] For lower densities, the movement of E_F in the band gap as a function of increasing defect density should be parabolic for a single type of impurity level. This behavior has been observed for low temperature (LT) depositions of metals on p-type GaAs,[25] although it remains to be observed for room temperature studies. The reason for this difference is that low temperature depositions inhibit surface diffusion; consequently for low coverages ($\lesssim$0.1ML) metal atoms remain largely dispersed, rather than forming aggregates as frequently observed at RT.[26] Mönch[27] has recently shown that the band bending observed at LT can be quantitatively accounted for simply by attributing a charged donor level

to each metal atom adsorbed, which occurs up to coverages at which the motion of E_F stabilizes ($\lesssim$0.05ML). This stabilization is due to electrostatic considerations necessary to maintain E_F near the donor level, and not to the cessation of the generation process of donors for larger coverages. We may thus safely assume that additional, but on the average neutral, donor levels are formed at larger coverages. At some higher coverage atoms begin to aggregate into clusters that exhibit size-dependent ionization levels.[22] As a consequence, additional shifts in E_F may occur, a notion consistent with experimental observations.[25] At RT this process is vastly compressed in the coverage scale, which signifies that impurity levels, with the rare exception of Ga,[28] are constantly evolving with an ever deepening ionization energy. Their densities should remain proportional to the coverage, an assertion substantiated for transition metals on GaAs.[23] These metals create filled and empty gap states that are readily observed with photoemission spectroscopy for coverages as low as 0.01 ML.[23] The observed emission intensity from the impurity states is consistent with each transition metal atom producing an impurity level.

Let us next consider the origin of deep defect or impurity levels in the (110) surface layer of GaAs and similar semiconductors. Let us first consider an isolated surface adsorbate atom. Using a simple bond-orbital picture[28] schematically shown in Fig. 1, we argue that only the re-hybridization of the dangling Ga-bond can form a bonding state that lies in the gap region of the semiconductor. In this simple model rehybridized levels and the band gap, represented approximately by the interval between the As sp^3 and Ga sp^3 hybridized levels, are substantially overestimated. Interactions with the As bond are not excluded, but the typical term energies of metallic orbitals lie closer to the Ga value, so that bonding orbitals with the As lie below the As dangling bond in the valence band, and their antibonding counterpart in the conduction band. Bonding levels for single Ga-metal bonds for representative metals lie in the the GaAs "bandgap", as defined above, their energies scaling with the ionization energies.[29] For bridge-bonded configurations to both As and Ga, the levels tend to be more concentrated near midgap, marked as the CNL in Fig. 1.[29] These calculations are quantitatively a bit crude, but serve to stress the likelyhood of deep levels generated by metal adsorbates on these surfaces. Some support for the validity of these estimates is given by the total energy calculations for Al atoms on GaAs(110), which show that midgap levels are generated not only for Al atoms singly bonded to a Ga, but also if the Al is bridge bonded to both As and Ga, or has replaced the surface Ga atom.[30] The maximum density of interface states corresponds to the situation where a bond exists for each Ga surface atom, or $\approx 5 \times 10^{14} cm^{-2}$. This figure is consistent with the value of $5 \times 10^{14} cm^{-2} eV^{-1}$ calculated for GaAs,[2] with the assumption that the states are spread over $\approx$1eV of the band gap.

More frequently the metal reacts with the semiconductor by liberating predominantly Ga atoms (exchange reactions).[23,31] This arrangement would form a substitutional impurity. Tight binding calculations have shown that a number of non-metallic atoms substituting for the cation should create localized impurity states lying in the band gap region;[32] similarly, most simple metals are expected to form deep levels when substituting for the anion in the surface layer. The transition metals, which interact strongly with GaAs and other III-V's,[23,33] are well known for their ability to form deep substitutional impurities in semiconductors.[34] It is highly probable, and there is experimental evidence to support this,[23] that they generate similar levels at substitutional sites on semiconductor surfaces. In this simple model rehybridized levels and the band gap, represented approximately by the interval between the As sp^3 and Ga sp^3 hybridized levels, are substantially overestimated. Interactions with the As bond are not excluded, but the typical term energies of metallic orbitals lie closer to the Ga value, so that bonding orbitals with the As lie below the As dangling bond in the valence band, and their antibonding counterpart in the conduction band. Bonding levels for single Ga-metal bonds for representative metals lie in the the GaAs "bandgap", as defined above, their energies scaling with the ionization energies.[29] For bridge-bonded configurations to both As and Ga, the levels tend to be more concentrated near midgap, marked as the CNL in Fig. 1.[29] These calculations are quantitatively a bit crude, but serve to stress the likelyhood of deep levels generated by

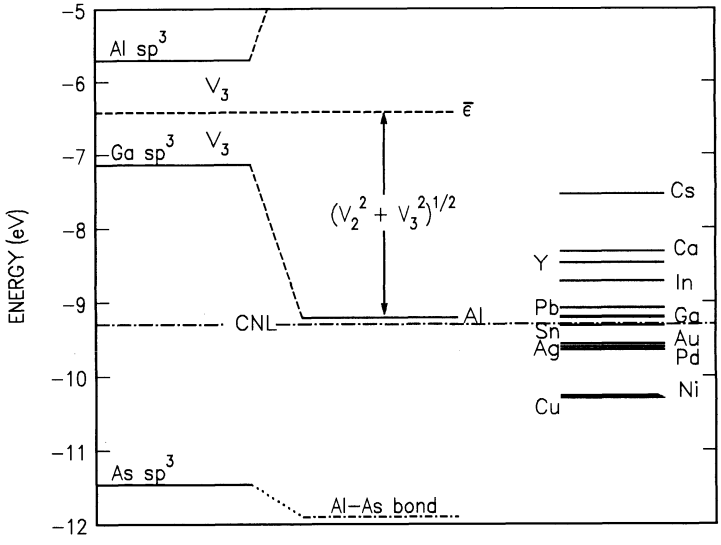

Fig. 1. Energy diagram for meta l atoms singly bonded to surface Ga atoms, in a bond orbital description (see ref. 28 for terminology). The rehybridization is drawn for an Al-Ga bond. The rehybridized levels for other metal atoms are shown on the right. Only Ga-metal ligands may form hybrid states in the band gap of the semiconductor; As-metal ligands will form states in the valence band, as schematically shown by the dash-dotted line in the lower center. The CNL is drawn half way between the As and Ga sp^3 hybrids (dangling bonds).

metal adsorbates on these surfaces. Some support for the validity of these estimates is given by the total energy calculations for Al atoms on GaAs(110), which show that midgap levels are generated not only for Al atoms singly bonded to a Ga, but also if the Al is bridge bonded to both As and Ga, or has replaced the surface Ga atom.[30] The maximum density of interface states corresponds to the situation where a bond exists for each Ga surface atom, or $\approx 5 \times 10^{14} cm^{-2}$. This figure is consistent with the value of $5 \times 10^{14} cm^{-2} eV^{-1}$ calculated for GaAs,[2] with the assumption that the states are spread over $\approx$1eV of the band gap.

More frequently the metal reacts with the semiconductor by liberating predominantly Ga atoms (exchange reactions).[23,31] This arrangement would form a substitutional impurity. Tight binding calculations have shown that a number of non-metallic atoms substituting for the cation should create localized impurity states lying in the band gap region;[32] similarly, most simple metals are expected to form deep levels when substituting for the anion in the surface layer. The transition metals, which interact strongly with GaAs and other III-V's,[23,33] are well known for their ability to form deep substitutional impurities in semiconductors.[34] It is highly probable, and there is experimental evidence to support this,[23] that they generate similar levels at substitutional sites on semiconductor surfaces.

The above discussion refers strictly to well-isolated point defects or impurities, conditions rarely achievable except at low coverages and temperatures. In practice, the defect generation is evolutionary. As defect densities increase with metal coverage, interactions among the planar defects become of increasing importance. In addition, any metal clustering about a charged defect tends to distribute the charge over a larger volume, thereby decreasing coulombic repulsion effects. This is basically an incipient screening effect which we will fully

develop in the next section. A direct consequence of the lessening of coulombic repulsion is the emergence of an amphoteric defect complex, which can act both as an acceptor on n-type and a donor on p-type material, with the consequence that the Fermi levels on n and p-type surfaces approach each other (not necessarily in a symmetric way) before the development of metallic characteristics in the overlayer. It should be recalled that before metallic screening begins to dominate, the net surface charge necessary to maintain E_F near mid gap is $\lesssim 5 \times 10^{12} cm^{-2}$ even for heavily doped semiconductors,[35] so that most impurity sites are neutral. E_F, however, is determined by the levels of the charged sites, which occupy less than 1% of the total sites at a monolayer.

Whereas isolated deep donor and acceptor levels can be found at energies spanning the band gap,[34,36] E_F is observed to lie within ± 150 meV of midgap for moderate coverages of a number of metals (and oxygen) on the GaAs(110) surface. This data is shown in Fig. 2 for two coverages of the indicated elements on n-type GaAs(110).[22,23,37] On p-type samples, the donor levels are similarly aggregated at a slightly lower energy in the gap; for reasons of clarity these are not shown. These results appear to be general and merit some speculative discussion, as the origin of this behavior is not well understood. It has recently been shown that there exists a remarkable correlation between the transition metal impurity levels in a variety of III-V compound semiconductors and the cation vacancy level,[38] or the average dangling bond energy,[39] to which the CNL was assigned. Using the defect-molecule model,[39] the neutral transition metal impurity levels were calculated to lie at this designated CNL.[38] Arguments for this agreement were based on the large, relatively unscreened coulomb integral (the Hubbard U term[34]) of the transition metal d-electrons, which imposes an effective charge neutrality by polarization of the bonds. An analogous situation appears to exist for neutral deep levels localized on the surface of the semiconductor, where charge neutrality is imposed by virtue of the electrostatics (most levels remain uncharged) and by the reduced screening which increases U. Thus we may associate a "universal" defect level with defect/impurity levels generated by a variety of different adsorbates on the semiconductor surface, which we will assign to the CNL. The error in this assumption, based on the experimental results, is less than ± 150 meV.

In summary, we have given compelling arguments in this section that metal atom induced defects or impurities determine the position of E_F at least to coverages required for the appearance of metallic character in the overlayer. Furthermore, their density at full coverage is comparable to the surface atomic density, and for GaAs their energies are within 300 meV of a "universal" level which lies near the charge neutrality level, as indicated in Fig.2. The question to be addressed next is whether the metal can completely screen these defects, as the MIGS models imply, or does not affect their energetics at all, as assumed by the defect model.

METAL-DEFECT INTERACTION.

In order to assess the effect of the metal, or more precisely the intimate presence of metallic states, on the impurity/defect levels, we will first consider an isolated "deep" level on the semiconductor side of the metal-semiconductor interface. On the free surface the defect level has atom-like characteristics, that is, it can be described by a coulombic, central core potential, which differs from the atom in that it is screened by the dielectric medium of the semiconductor. This situation may be viewed in terms of the familiar problem of the valence level of an atom, in our case the defect level, adsorbed on a metallic surface.[41,42] This approach is valid as long as the defect level is energetically far removed from the continuum states of the semiconductor (band edges). The situation before and after contact to the metal is schematically shown in Fig. 3. The atomic-like defect potential is represented by the dashed curve in Fig. 3a, with the defect level E_i^0 determining the Fermi level E_F before contact with the metal.

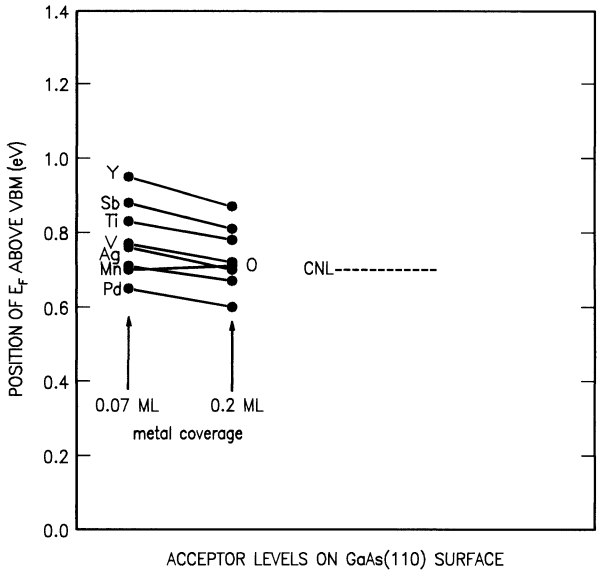

Fig. 2. Fermi level positions on n-type GaAs(110) for two coverages of indicated metals. The calculated CNL is marked by the dashed line.[5]

Let us next consider the effect of the metal approaching the defect. Near contact the wavefunctions of the defect and the metal begin to overlap, with the consequence that charge density can now be exchanged between the two systems. That is, the formerly stationary and localized defect level becomes a delocalized or virtual state, which is commonly referred to as a resonance. A charge transfer or tunneling time τ can be associated with this process, which through the uncertainty principle implies an energy uncertainty $\Delta E \sim \hbar/\tau$. The broadening can be calculated from Fermi's golden rule: $\Delta E \propto |\langle m|V|i\rangle|^2$, where $\langle m|$ and $\langle i|$ are the eigenvectors of the unperturbed metal and impurity states and $V \sim e^2/\varepsilon(r)r$ is the impurity potential screened by the dielectric function $\varepsilon(r)$ of the semiconductor. In calculating ΔE, the following approximations were made:[17] a) the metal is treated as a jellium; b) metal-semiconductor interactions (bond-formation) beyond the formation of the defect are neglected; and c) the unperturbed impurity state is isolated and represented by a single energy level. The latter approximation assumes the absence of broadening effects, which may arise both through variations in the impurity bonding environment and, to a lesser extent, from the formation of impurity bands. The underlying physics will not be changed with neglect of broadening, as the metal states delocalize all states on the semiconductor surface. This point will be considered further in the last section. The impurity wavefunction ψ_i can conveniently be represented by a hydrogenic 2s-like wavefunction $\propto(1 - ar)e^{-ar}$(where a is fitting a parameter) matched to the wavefunction of a deep level[36] in GaAs. The metal wavefunction is free-electron-like for $x > 0$ and decays exponentially for $x \leq 0$: $\psi_m = (2k_F/k_0)e^{\kappa x}e^{ik_y y + ik_z z}$. Here k_F is the Fermi wave vector, $\hbar^2 k_0^2/2m = \mu_m + \phi_m$ (μ_m is the Fermi energy of the metal measured relative to the bottom of the free electron band, and ϕ_m is the workfunction) and $\kappa^2 = k_0^2 - k_F^2$. Following a scheme similar to Gadzuk's,[42] we obtain an expression for ΔE:

$$\Delta E \equiv \frac{\Gamma_0}{\varepsilon^2} = \frac{a^4 e^2 k_F s^3 e^{-2as}}{2a_0 k_0^2 \varepsilon^2}\left[1 - \frac{4}{as} - \frac{4}{a^2 s^2} + \frac{16}{a^3 s^3} + \frac{32}{a^4 s^4}\right] \quad (1)$$

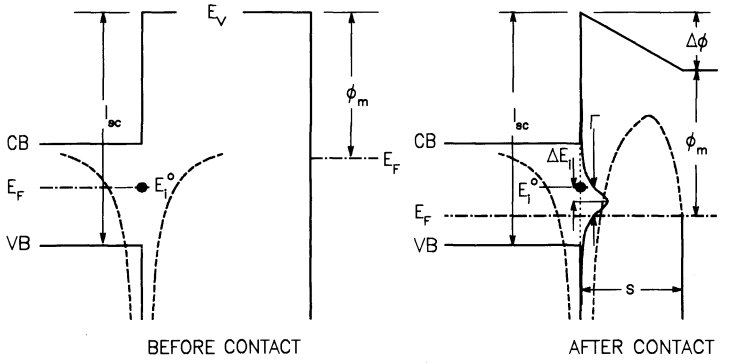

Fig. 3. Potential energy diagram s of a semiconductor with a surface defect level at E_i^0 and a metal prior to contact (a), and at intimate contact (b).

Here s is the separation between the defect/impurity site and the metal surface and a_0 is the Bohr radius. Γ_0 is the unscreened broadening due to the bare metal; its magnitude of ~1 eV is similar to the broadening of valence levels of adatoms on metal surfaces.[41,42] ε is also a function of the impurity-metal surface separation s, and must be evaluated for the appropriate value of s. We estimate its value to be half the bulk dielectric function[44] $\varepsilon_\infty(r)$ weighted by the square of the unperturbed, s-dependent impurity wavefunction $\psi_i^2(s)$.[17] In the range of $1.5 \leq s \leq 2.5$ Å, ε varies between 3.5 and 4.5 for GaAs;[17] a value of 4 being a good estimate for all cases considered here. Thus the dielectric screening by the semiconductor considerably reduces the influence of the metallic states on the impurity. However, as we shall see, these effects are nevertheless significant in affecting the ultimate position of E_F that determines Schottky barrier heights. Table I lists values of Γ_0 and $\Delta E \equiv \Gamma$ for some representative metals on GaAs. The important conclusion of this calculation is that metallic states (or equivalently MIGS) cannot totally screen out a defect level in the semiconductor surface. That is, the interface state or resonance retains considerable defect identity.

We will next address the equilibrium situation at the metal-semiconductor interface for defect densities approaching the cat- or anion dangling bond densities. The situation for intimate metal contact is shown in Fig. 3b. The delocalized level is shown to have broadened by an amount Γ (ΔE) and shifted downward in energy by ΔE_i . The shift is the consequence of metallic screening of the net charge q_{eff} in the defect level, and can be considered as an image force effect. Simultaneously, a redistribution of electronic charge between the metal and semiconductor is required to equalize the differences in their Fermi levels which existed prior to contact. This is achieved by the formation of a dipole potential $\Delta\phi$, which satisfies the energy balance $E_F = I - \phi_m - \Delta\phi$, where I represents the ionization energy of the semiconductor. $\Delta\phi = 4\pi N_i e^2 q_{eff} \lambda_{eff}$, where N_i is the surface density of impurity sites and λ_{eff} is the effective separation between q_{eff} and its counterpart near the positive ion cores of the metal. It is given by $\lambda_{eff} \sim s/\varepsilon + \xi$,[2] where ξ is the Fermi-Thomas screening length. The defect resonance, which can now accommodate fractional charge, will be interpreted as a local density of states $\rho_i(E)$, with the property $\int_{-\infty}^{+\infty} \rho_i(E)dE = 1$. The effective charge q_{eff} at the defect site can be obtained by integrating $\rho_i(E)$: $q_{eff} = \int_{-\infty}^{+\infty} F(E)\rho_i dE$, where F(E) is the Fermi function. The functional dependence of $\rho_i(E)$ is assumed to be Lorentzian, in analogy to the adsorbate-metal system:[17,43]

Table I. Parameters used to calculate the metal-dependent broadening parameter $\Gamma(s)$ for a generic deep level on the (110) surface of GaAs. The defect wavefunction fitting parameter $a = 1.24 Å^{-1}$.

metal	ϕ_m (eV)	k_F/k_0^2 (Å)	s (Å)	ε	Γ_0 (eV)	Γ (eV)
Cs	1.88	0.71	2.26	4.37	0.31	0.016
Na	2.37	0.63	1.84	4.04	1.32	0.081
Ca	2.90	0.56	1.98	4.20	0.69	0.039
Y	3.1	0.55	1.94	4.14	0.79	0.046
Al	4.06	0.42	1.76	3.95	1.19	0.076
In	4.12	0.45	1.84	4.04	0.95	0.066
Ti	4.2	0.47	1.81	4.01	1.11	0.069
V	4.3	0.47	1.77	3.96	1.27	0.081
Ga	4.32	0.43	1.77	3.96	1.17	0.075
Cu	4.48	0.44	1.76	3.95	1.26	0.081
Ag	4.52	0.48	1.84	4.04	1.01	0.062
Pd	5.12	0.42	1.81	4.01	0.98	0.061
Au	5.15	0.43	1.84	4.04	0.91	0.056

$$\rho_i(E) = \frac{1}{\pi} \frac{\Gamma/2}{\left[E - \left(E_i^0 - \Delta E_i(q_{eff})\right)\right]^2 + (\Gamma/2)^2} \tag{2}$$

The low temperature limit is assumed for convenience and simplicity, for which integration of (2) gives:

$$q_{eff} \overset{T\to 0}{=} \int_{-\infty}^{E_F} \rho_i(E)dE = \frac{1}{\pi}\left[\tan^{-1}\frac{E_F - \left(E_i^0 - \Delta E_i(q_{eff})\right)}{\Gamma/2} + \frac{\pi}{2}\right] \tag{3}$$

Both the Fermi energy, now explicitly written as:

$$E_F = (I - \phi_m) - 4\pi\lambda_{eff}e^2N_iq_{eff} \tag{4}$$

and ΔE_i depend on q_{eff}, so that eq. (2) must be solved self-consistently. The image force lowering $\Delta E_i(q_{eff})$ can be approximated by the image force potential:[45,46] $q_{eff}^2e^2/4\varepsilon(s + \xi)$. As we will determine, $q_{eff} \lesssim 0.1$ for most metals, so that $\Delta E_i(q_{eff})$ in most cases is negligible.

APPLICATION OF MODEL TO SCHOTTKY BARRIERS ON GaAs.

Reasonable estimates of all parameters in eqs. 2-4 can be made with the exception of E_i^0, which in principle is different for each metal. As discussed in section 2, experimentally its values fall within ± 150 meV of midgap for GaAs. We will make here the simplifying assumption that E_i^0 lies 0.71 eV above the valence band maximum and is the same for all metal/GaAs systems. Values for $s = r_{sc} + r_m - d_m$, where the parameters represent respectively half the GaAs bond length, the metallic radius and the metallic interplanar spacing, are readily obtained from the literature.[47,48] The electrically active density of defect states N_i is taken to be limited to 1/2 ML (4.43×10^{14} cm^{-2} for GaAs(110)[49]) With $\lambda_{eff} = 1Å$, I = 5.56 eV[50] and values of Γ from Table I, we have calculated q_{eff} and E_F for a number of metals on GaAs. The results are shown in Fig. 4. The dashed line through the data points are solutions of eqs. 2-4 with a single value of $\Gamma = 0.062$ eV, which is the average of the values for the

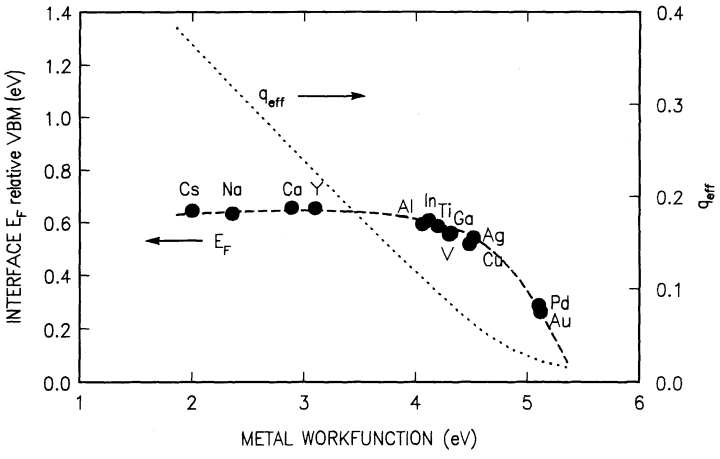

Fig. 4. Model calculation of E_F and q_{eff} for different metals on GaAs, plotted against their workfunction. The dashed line represents the results calculated with a value for $\Gamma = 0.062$ eV, the average for the metals shown.

different metals. The near coincidence of the curve and data points indicates a somewhat weak dependence of the solution on the broadening parameter. The model predicts a non-linear dependence of E_F on ϕ_m (or the electronegativity χ_m which is linearly related to ϕ_m). For $\phi_m \lesssim 4$eV the curve is essentially flat, although a slight rise in E_F is predicted with increasing ϕ_m. This rise is a consequence of the slight dominance of image force contributions due to the relatively large q_{eff} for the low ϕ_m metals. The values of the effective charges are shown in Fig. 4 as well. As can be seen, their values for $\phi_m > 4$eV are quite small, so that the resonances are essentially neutral, and coulombic effects in general can be neglected. Also in this range the position of E_F drops rapidly in the band gap as ϕ_m increases. The reason for this behavior is that only a small charge transfer is required to equalize the potentials. This charge density occupies only a fraction of the local density of states, thereby keeping E_F positioned low in the Lorentzian tails.

We are now in a position to compare the results to experimentally determined values of Schottky barriers heights Φ_b^n for n-type materials, remembering that these are related to E_F through: $E_F = E_0 - \Phi_b^n$, where E_0 is the band gap. Comparison to experimental data is shown in Fig. 5. The dashed curves are the same as the one in Fig. 4. For the photoemission data [17,29,51,52] in Fig. 5a, the model overestimates Φ_b^n for the low ϕ_m metals, although the agreement is better for the data determined by I-V and C-V measurements,[53,54] shown in Fig. 5b. Agreement is generally fair for barriers with metals of $\phi_m \approx 4 - 4.5$eV, but deteriorates for $\phi_m > 4.8$eV. An interesting data point is that for gold obtained by a high resolution transport measurement using a scanning tunneling microscope (STM).[55] Its value of $\Phi_b^n = 1.20$eV (shown as solid triangles in Fig. 5) represents the highest barrier observed at selected areas of a gold film on GaAs(100). The differences in barrier heights for Au can be attributed to inhomogeneous interface reactions[56,57] that produce locally varying workfunctions, which only the STM technique can resolve. When an alloy or intermetallic phase forms at the interface, its workfunction is intermediate between the pure constituent values, and frequently linearly dependent on the composition.[58] For most metals on GaAs, as discussed earlier, metallic Ga is liberated, which will influence the metallurgy at the interface, either by remaining in a separate phase or through alloying. In either case an effective workfunction will dominate the interface potentials. It should be re-emphasized that in the present model ϕ_m has the value for the pure metal.

Discrepancies between model predictions and experimental values can be attributed to one or more of the following considerations:
a) the assumption of a universal defect level; however, the absence of systematic deviations and a considerable scatter in the experimental data seem to suggest that this assumption is not the primary cause for the discrepancies.

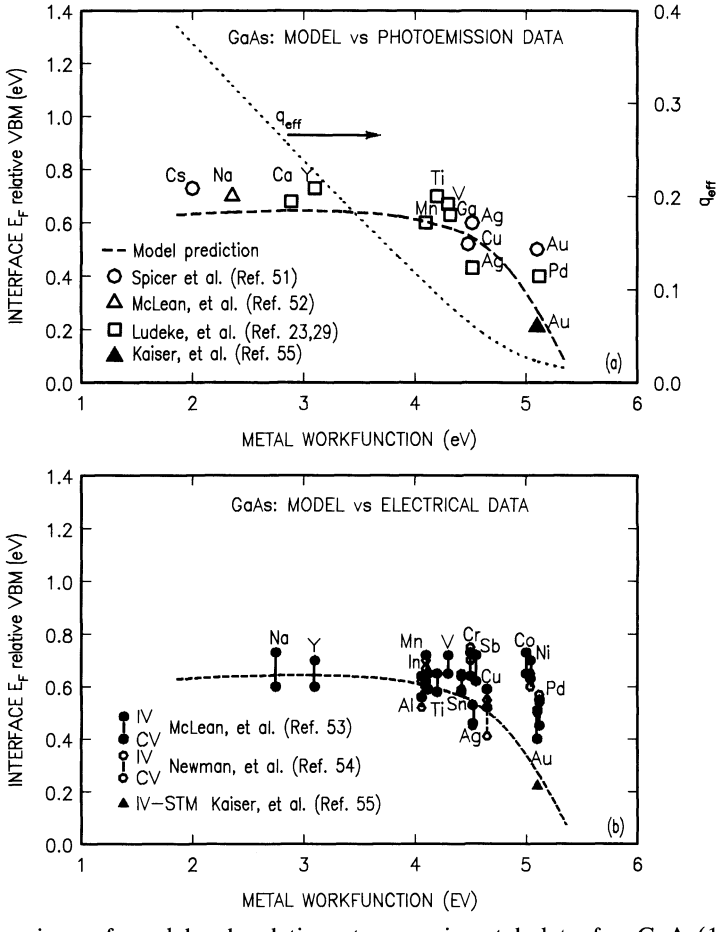

Fig. 5. Comparison of model calc ulations to experimental data for GaAs(110): (a) photoemission results; and (b) transport results. For the latter, the upper data point for each metal represents the lowest n-type barrier height measured (generally by I-V), and the lower point represents the highest barrier measured (generally by C-V).

b) alloying or formation of intermetallic phases, which are not considered in the model;
c) neglect of coulombic repulsion due to a partially charged defect level; this effect is $\propto q_{eff}$ and should raise E_i^0 for the low ϕ_m metals, for which the effective charge is relatively large. For charged bulk defects this contribution (i.e. the Hubbard U term) is of the order of an electron volt.[34] Its contribution to the present situation remains to be assessed.

APPLICATION OF MODEL TO THE INDEX OF INTERFACE BEHAVIOR.

To test further the general validity of the model we evaluate next the index of interface behavior (defined earlier as $S \equiv d\Phi_b^n/d\chi_m$) for the tetrahedrally coordinated semiconductors. Previous calculations of S were made in the framework of MIGS models; agreement with experimentally determined values ranged from fair[2,3] to poor.[4] In general a unique value of S is assumed for each semiconductor, which implies a linear relationship between Φ_b and χ_i. Existing data, which is quite scattered, do not unequivocally support this relationship; nevertheless, a single value for S is assumed and is obtained from a least square linear fit of the data.[13,59] For an abrupt, non-alloyed interface, our model does not predict a unique value for S. However, for intermediate values of $\phi_m \sim 4$eV for GaAs in Fig. 5, the effects of intermixing on $dE_F/d\phi_m$ are minimal. Consequently a comparison of model predictions and measured values of S can be attempted, keeping in mind that within this approximation trends will be more relevant than actual agreements.

Using the empirically determined relationship between electronegativity and the metal workfunction:[59] $\phi_m = 2.27\chi_m + 0.34$, the index S can be rewritten as $S = d\Phi_b^n/d\chi_m = -2.27dE_F/d\phi_m$. Solving eqn. (3) for E_F and differentiating the expression, one obtains:

$$S = \frac{2.27}{1 + [1.15\varepsilon^2(s)\lambda_{eff}N_i \sin^2\pi q_{eff}]/\Gamma_0(s)} \tag{5}$$

Here N_i is expressed in units of $10^{14}cm^{-2}$ and λ_{eff} in Å. The dominant parameter that contributes to the variation of S for different semiconductors is the square of the weighted dielectric screening function ε. Its value ε^{sc} for a given semiconductor is approximated by scaling the calculated value for GaAs ($\varepsilon^{GaAs} \approx 4$) by the ratio of the bulk dielectric constants: $\varepsilon^{sc} = 4\varepsilon_\infty^{sc}/\varepsilon_\infty^{GaAs}$. Physically ε_{sc} represents the screening response at the defect potential to the encroaching metallic states. For the less covalent semiconductors with lower ε_∞ this screening weakens and the delocalization and broadening (Γ_0/ε^2) of the defect resonance is enhanced. For a given change in q_{eff} (due to a variation in ϕ_m) a broader resonance leads to a larger variation of E_F, which signifies an increase in S.

In order to solve eqn. (5), q_{eff} must be calculated first from eqn. (2), which requires, as before, knowledge of the value of E_i^0 for each metal/ semiconductor combination. Since these values are not known, we will make the simplifying assumption that E_i^0 lies, as for GaAs, at the charge neutrality level. These levels have not been calculated for all semiconductors of interest here; the missing values need to be estimated. To facilitate this task, we have plotted in Fig. 6 the band edge positions relative to the vacuum level of 14 semiconductors, as well as Tersoff's calculated values for the CNL's relative to the valence band maxima for six III-V and four II-VI semiconductors.[61] The valence band edges were determined from measured ionization potentials.[50,62] From this figure it will be noted that all CNL's lie 5.0 ± 0.2 eV from the vacuum level. Consequently the additional assumption was made of a "universal" position for E_i^0 at 5 eV below the vacuum level for all semiconductors discussed here. This observation has a precedent with transition metal impurity levels in III-V and II-VI semiconductors, some of which exhibit a universality in energy among the different hosts when referenced to the vacuum level,[34] a feature which was used to determine empirically heterojunction band offsets.[63] The assumption of "universality" of the CNL is here only a convenience in the calculations, as the slope ($dE_F/d\phi_m$) is not significantly affected by small variations in the CNL. Thus the recent suggestion that the CNL be associated with the mean dangling-bond energies[39] would affect only the Schottky barrier heights.

The metallic parameters of Al were chosen for the present calculations. N_i was set at 1/2 the atomic surface density for each semiconductor, and $\lambda_{eff} \approx 0.6 + (0.43a_0 - 0.75)/\varepsilon^{sc}$, where a_0 is the lattice constant, was calculated for each semiconductor. The same value of $\phi_m = 4.3$eV was used throughout the computations. The model predictions for 15

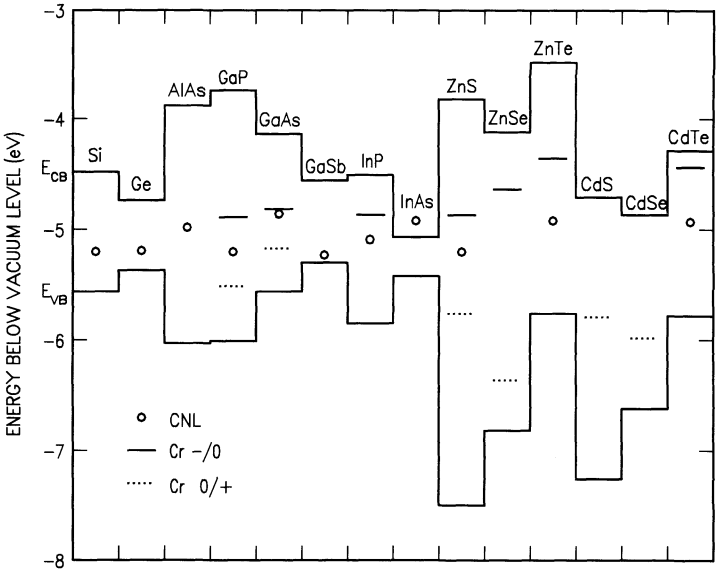

Fig. 6. Band edge diagram for in dicated semiconductors referenced to the vacuum level. Calculated CNL's are indicated when available.[5] Also shown are the experimentally determined acceptor and donor levels of Cr.[34] In general the CNL lies within these levels.

tetrahedrally coordinated semiconductors and 3 Ga chalcogenides are plotted in Fig. 7 against available experimental observations (solid circles).[64] Open circles represent model predictions. A solid data point lying on the dotted diagonal of unit slope indicates agreement between experiment and model calculation. The vertical bar through the GaSe point represents an estimated $\pm 20\%$ uncertainty in the experimental values.[59] The horizontal bar represents the range of model predictions for a variation for $4.0 \leq \phi_m \leq 4.6$eV. In general the agreement is quite satisfactory, particularly in view of the scatter of values in the data base.[13,59,64] Only ZnS and the Ga chalcogenides are outside the uncertainty range. The assumptions made here for tetrahedrally coordinated compounds may be questionable for the Ga chalcogenides, which consist of layered structures in which only the Ga is tetrahedrally coordinated. A least square fit through the solid data points exhibits a slope of 1.09 and a regression coefficient of 0.84. These two parameters suggests the absence of systematic errors in the model and attest to the general validity of the assumptions.

EPILOGUE

Arguments, substantiated by a wealth of experimental data, were given to demonstrate the existence of deep defect/impurity levels in densities approaching the cation atomic surface densities for metal coverages $\approx$1ML . These levels, generated by the metal deposition process, completely dominate the interface electronic structure and determine the Fermi level at the interface prior to the establishment of metallic characteristics in the overlayer. As these characteristics develop, the localized defect levels are drastically altered by the metallic states and become part of the non-local description of the interface density of states. However as demonstrated, the screening of the defect level by the metallic states is not complete and the former localized states retain much of of their identity, in particular their energy and total density of states. These states are definitely not MIGS in the traditional definition, but should

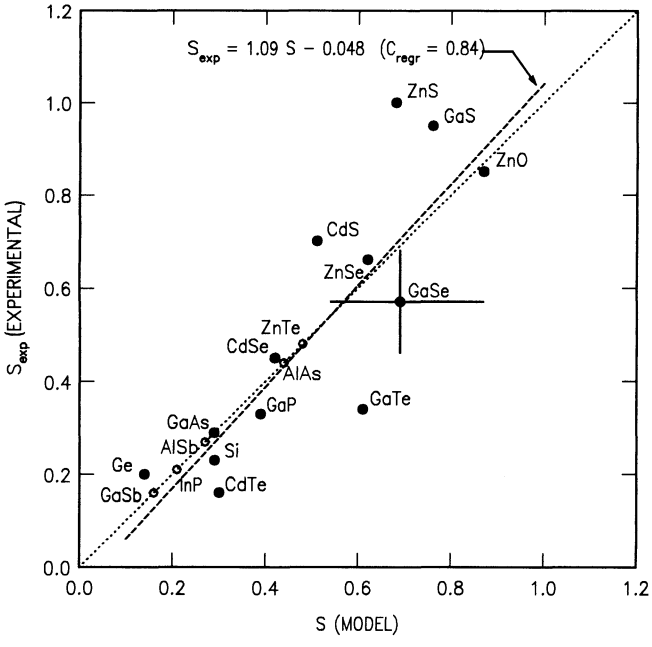

Fig. 7. Comparison of calculated index of interface behavior S to the index obtained from experimental data (solid points). Where these are unknown, model predictions were plotted on the diagonal as open circles.

perhaps be referred to as metal altered defect states; although no attempt will be made here to coin a new acronym. The isolated defect level and its evolution prior to delocalization is an aspect only during the formation of the interface, and essentially inconsequential for the macroscopic Schottky barrier. However, the observation of this evolutionary process has helped us focus on the relevant issues in the Schottky barrier description.

The assumption of an isolated and monoenergetic defect level prior to delocalization by the metal is a simplification which merits some additional comments. In principle, some degree of delocalization, or spatial extension of wavefunctions, occurs as soon as defect complexes appear on the surface, a process which is accompanied by changes in the level energies. However, in this phase of evolution the description remains essentially local. We have asserted that the limit of this phase are essentially neutral defect levels which, irrespective of their origin are located near the charge neutrality level of the semiconductor. For simplicity we have assigned a unique energy to the level, thereby neglecting defect-defect overlap (probably small because of their still localized nature even near monolayer coverages) and level variation due to local structural inhomogeneities. The latter broadening mechanism is likely to be more important and can be conveniently modeled within the present description of the interface. We have arbitrarily divided the total defect density (N_i) into a set of levels spread over a Gaussian envelope several tenth of an eV wide. Preliminary results indicate that the position of the Fermi level following delocalization is essentially the same as if the defects were concentrated in a single level, as used throughout this paper.[65]

The degree of delocalization depends directly on the screening strength of the metal, as expressed in eqn (1), and is inversely dependent on the ability ($\propto \varepsilon^2$) of the semiconductor to screen the metallic charge density. However, for a given semiconductor the Schottky barrier height is relatively insensitive to variations in the broadening parameter. The height of the barrier is mainly determined by the charge transfer required to equalize the Fermi level on both sides of the junction. The driving force for this transfer is the difference between the

ionization potential of the semiconductor and the metal workfunction. As pointed out, for a realistic comparison to most metal-semiconductor systems prepared at room temperature, an unspecified effective metal workfunction should be used. Unfortunately its value will differ for each reacted metal-semiconductor system and remains to be determined. The model may be tested more effectively with data from interfaces prepared and measured at cryogenic temperatures, conditions for which alloying reactions and interdiffusion may be suppressed altogether. The use of an STM will undoubtedly impact this field profoundly in the future, as it permits selective probing of single phase domains in an heterogenous environment. In this context the work by Kaiser and Bell is an exemplary case.[55]

ACKNOWLEDGEMENTS. The concept of delocalization evolved through extended discussions with G. Jezequel and A. Taleb-Ibrahimi following our experimental collaborations. This and subsequent concepts jelled into a cohesive model following probing questions and suggestions by J. Tersoff, A. R. Williams, J. Freeouf and W. Mönch.

REFERENCES

1. V. Heine, Phys. Rev. 138, A1689 (1965).
2. S.G. Louie, J.R. Chelikowsky and M.L. Cohen, Phys. Rev. B15, 2154 (1977).
3. E.J. Mele and J.D. Joannopoulos, Phys. Rev. B17, 1528 (1978).
4. E. Louis, F. Yndurain and F. Flores, Phys. Rev. B13, 4408 (1976).
5. J. Tersoff, Phys. Rev. Lett. 52, 465 (1984); Phys. Rev. B32, 6968 (1985).
6. W.E. Spicer, P.W. Chye, P.R. Skeath, C.Y. Su and I. Lindau, J. Vac. Sci. Technol. 16, 1422 (1979).
7. W.E. Spicer, T. Kendelewicz, N. Newman, R. Cao, C. McCants, K. Miyano, I. Lindau and E.R. Weber, to be published.
8. R.E. Allen and J.D. Dow, Phys. Rev. B 25, 1423 (1982); and S.-F. Ren and R.E. Allen, Surf. Sci. 148, L637 (1984).
9. W. Walukiewicz, J. Vac. Sci. Technol. B 5, 1062 (1987).
10. J. Bardeen, Phys. Rev. 71, 717 (1947).
11. I. Lefebvre, M. Lannoo, C. Priester, G. Allan and C. Delerue, Phys. Rev. B36, 1336 (1987).
12. C. Tejedor, F. Flores and E. Louis, J. Phys. C10, 2163 (1977).
13. S. Kurtin, T.C. McGill and C.A. Mead, Phys. Rev. Lett. 22, 1433 (1969).
14. A.M. Cowley and S.M. Sze, J. Appl. Phys. 36, 3212 (1966). Their expression is generally used by most practitioners to calculate S, with differences among the approaches arising from the source and relative magnitudes of D_s.
15. A. Zur, T.C. McGill and D.L. Smith, Phys. Rev. B28, 2060 (1983).
16. C.B. Duke and C. Mailhiot, J. Vac. Sci. Technol. B3, 1170 (1985).
17. R. Ludeke, G. Jezequel and A. Taleb-Ibrahimi, Phys. Rev. Lett. 61, 601 (1988); and J. Vac. Sci. Technol. B6, 1277 (1988).
18. K. Stiles and A. Kahn, Phys. Rev. Lett. 60, 440 (1988)
19. M. Prietsch, M. Domke, C. Laubschat and G. Kaindl, Phys. Rev. Lett. 60, 436 (1988).
20. G. Jezequel, A. Taleb-Ibrahimi, R. Ludeke and F. Schäffler, J. Vac. Sci. Technol. A6, 1561 (1988).
21. P.E. Gregory, W.E. Spicer, S. Ciraci and W.A. Harrison, Appl. Phys. Lett. 25, 511 (1974).
22. R. Ludeke, T.-C. Chiang and T. Miller, J. Vac. Sci. Technol. B1, 581 (1983).
23. R. Ludeke and G. Landgren,Phys. Rev. B 33, 5526 (1986); G. Hughes, R. Ludeke, F. Schäffler and D. Rieger, J. Vac. Sci. Technol. B4, 924 (1986); F. Schäffler, G. Hughes,W. Drube, R. Ludeke and F.J. Himpsel, Phys. Rev. B35, 6328 (1987). G. Landgren, R. Ludeke, Y. Jugnet, J.F. Morar and F.J. Himpsel, J. Vac. Sci. Technol. B2, 351 (1984); F. Schäffler, W. Drube G. Hughes, R. Ludeke, D. Rieger and F.J. Himpsel, J. Vac. Sci. Technol. A 5, 1528 (1987).

24. J.Y.-F. Tang and J. Freeouf, J. Vac. Sci. Technol. B2, 459 (1984).
25. R. Cao, K. Miyano, T. Kendelewicz, K.K. Chin, I. Lindau and W.E. Spicer, J. Vac. Sci. Technol. B5, 998 (1987).
26. Clustering is particularly pervasive for metals than interact weakly with the substrate, such as the group III and the noble metals, see for example ref. 22.
27. W. Mönch, J. Vac. Sci. Technol. B6, 1270 (1988).
28. W. A. Harrison, Electronic Structure and the Properties of Solids, W.H Freeman and Co. (San Francisco, 1980).
29. R. Ludeke, unpublished results.
30. J. Ihm and J.D. Joannopoulos, Phys. Rev. B26, 4429 (1982).
31. L. Brillson, in Handbook of Synchrotron Radiation, Vol. II, Ed. G.V. Marr (North-Holland, Amsterdam, 1985).
32. R.E. Allen and J.D. Dow, J. Vac. Sci. Technol. 19, 383 (1981).
33. M. Grioni, J.J. Joyce and J.H. Weaver, J. Vac Sci. Technol. A4, 965 (1986); J.J. Joyce, M. Grioni, M. del Giudice, M.W. Ruckman, F. Boscherini and J.H. Weaver, J. Vac. Sci. Technol. A5, 2019 (1987); C.M. Aldao, I.M. Vitomirov, F. Xu and J.H. Weaver, Phys. Rev. B37, 6019 (1988).
34. A. Zunger, Solid State Physics, Vol. 39, Ed. H. Ehrenreich and D. Turnbull (Academic Press, Orlando FL, 1986) p. 275.
35. S. Sze, Physics of Semiconductor Devices, 2nd. Edition (John Wiley & Sons, New York, 1981).
36. M. Jaros, Deep Levels in Semiconductors, (Adam Hilger Ltd., Bristol 1982)
37. G. Landgren, R. Ludeke, Y. Jugnet, J.F. Morar and F.J. Himpsel, J. Vac. Sci. Technol. B2, 351 (1984).
38. J. Tersoff and W.A. Harrison, J. Vac. Sci. Technol. B5, 1221 (1987).
39. C. Delerue, M. Lannoo and J. M. Langer, Phys. Rev. Lett. 61, 199 (1988).
40. J.M. Langer and H. Heinrich, Phys. Rev. Lett. 55, 1414 (1985).
41. A.J. Bennett and L.M. Falicov, Phys. Rev. 151, 512 (1966).
42. J.W. Gadzuk, Surf. Sci. 6, 133 (1967).
43. S.K. Lyo and R. Gomer, Topics in Applied Physics Vol 4, ed R. Gomer (Springer, N.Y., 1975) Ch 2.
44. P.K.W. Vinsome and D. Richardson, J. Phys. C, 4, 2650 (1971).
45. J.C. Inkson, J. Phys. C, 4, 591 (1971).
46. D.M. Newns, J. Chem. Phys. 50, 4572 (1969).
47. M.C. Ball and A.H. Norbury, Physical Data for Inorganic Chemists, (Longman Group Ltd., London, 1974).
48. J.C. Phillips, Bonds and Bands in Semiconductors, (Academic Press, New York, 1973).
49. The calculated values of E_F are weakly dependent for $N_i \gtrsim 10^{14} cm^{-2}$, see ref. 17.
50. A. Huijser, J. Van Laar and T.L. Van Rooy, Surf. Sci. 62, 472 (1977).
51. W.E. Spicer, P.E. Gregory, P.W. Chye, I.A. Babalola and T. Sukegawa, Appl. Phys. Lett.27, 617 (1975); K.K. Chin, S.H. Pan, D. Mo, P. Mahowald, N. Newman, I. Lindau and W.E. Spicer, Phys. Rev B32, 918 (1985).
52. A.B. McLean, D.A. Evans and R.H. Williams, Semicond. Sci. Technol. 2, 547 (1987).
53. A.B. McLean and R.H. Williams, J. Phys. C 21, 783 (1988).
54. N. Newman, M. van Schlifgaarde, T. Kendelewicz, M.D. Williams and W.E. Spicer, Phys. Rev B 33, 1146 (1986).
55. W.J. Kaiser and L.D. Bell, Phys. Rev. Lett. 60, 1406 (1988).
56. V. Mercier, C.A. Sébenne, P. Chen, D. Bolmont and F. Proix, J. Physique 46, 839 (1985).
57. Z. Liliental-Weber, N. Newman, W.E. Spicer, R. Gronsky, J. Washburn and E.R. Weber, Mat. Res. Soc. Symp. Proc. 54, 415 (1986).
58. J. Hölzl and F.K. Schulte, Workfunction of Metals, in Springer Tracts of Modern Physics, Vol. 85, Springer Verlag, Berlin (1979).
59. M. Schlüter, Phys. Rev. B 17, 5044 (1978).
60. W. Gordy and W.J. Thomas, Phys. Rev. 24, 439 (1956).
61. J. Tersoff, Phys. Rev. Lett. 56, 2755 (1986).

62. R.K. Swank, Phys. Rev. 153, 844 (1967); T.E. Fischer, Phys. Rev. 142, 519 (1966); G.W. Gobeli and F.G. Allen, Phys. 137, 245 (1965).
63. J.M. Langer and H. Heinrich, Phys. Rev. Lett. 55, 1414 (1985); J. Tersoff, Phys. Rev. Lett. 56, 675 (1986).
64. Values quoted by Schlüter (ref.59), with updated results for GaAs, CdSe, ZnO, ZnS, Si and Ge, from Landolt-Börnstein, New Series v. 17, K.H. Hellwege and O. Madelung, edtrs. (Springer Verlag, Berlin 1984).
65. R. Ludeke and V. Crespi, unpublished results.

Metallization, Bonding, and Energetics of Ordered Phases of Al on Si(111)

J. S. Nelson
Sandia National Laboratories
Livermore, CA 94550

and

Inder P. Batra
IBM Research Division, Almaden Research Center
Mail Stop k33/801, 650 Harry Road, San Jose, CA 95120

INTRODUCTION

Many models have been proposed for understanding the pinning of the Fermi energy (E_f) at the metal-semiconductor interfaces[1-3]. Each of these models is based on the general assumption that E_f is pinned in response to the presence of surface states. Bardeen[1] originally suggested that the surface states were intrinsic to the semiconductor surface, while Heine[2] proposed that the pinning was due to the tails of the metal wavefunctions decaying into the gap of the semiconductor. Since Schottky barriers are known to be developed at submonolayer coverages and many times the first adsorbed metal atoms remove the intrinsic surface states, neither model provides a universal picture of the Schottky barrier formation. Phillips[4] has pointed out that a complete picture of the Schottky barrier formation would require a description of the microscopic bonding at the metal-semiconductor interface. For each metal-semiconductor system, the surfaces states pinning E_f will depend on the bonding at the interface. Batra and Ciraci[5] recently suggested that the nature of the pinning states can also change as a function of metal coverage. Their study[5] of the pseudomorphic growth of Al - Ge(001) showed that at low coverage (1/2 monolayer (ML)) the Ge dangling bond is saturated by the formation of a strong Al-Ge chemisorption bond. At higher coverages (1 ML), the Al overlayer relaxed outward, resulting in a weakening of the chemisorption bond and an increased quasi 2D metallic character of the Al overlayer. In light of these interesting results, we have investigated the change in the bonding properties at the Si(111)-Al interface as a function of Al coverage and adatom geometry. We find that the Al adatom geometry is critically dependent on the coverage, being four-fold coordinated at 1/3 ML and evolving to single-fold on-top site configuration at 1 ML. The resulting geometries reflect the strong covalent bonding between Si and Al at each coverage.

The clean Si(111) surface is well characterized and is known[6] to reconstruct to a 2x1 surface, and then to a 7x7 surface after annealing at 800°C. The Al-covered surface structure has been examined by low energy electron diffraction (LEED)[7], high-resolution transmission electron microscopy[8], and scanning tunneling microscopy (STM)[9]. Upon adsorption of about 1/3 ML of Al, Lander and Morrison[7] found a $\sqrt{3}x\sqrt{3}$ LEED pattern, which exhibited an order-disorder transition at 800° C. At this coverage the trivalent Al atoms can naturally saturate the Si surface dangling bond orbitals. Increasing the coverage to 1 ML, Lander and Morrison[7] found several phases two of which were: (1) at temperatures below 500°C, a $\sqrt{3}x\sqrt{3}$ superstructure was seen; (2) as the temperature was raised to about 700°C this pattern changed

irreversibly to a 7x7 LEED pattern. The STM images of Hamers and Demuth[9] shown in Fig. 1a, clearly provide evidence for a change in Al adatom geometry with coverage. At 1/3 ML the Al adatom sits in a three-fold site with respect to the Si surface atoms forming a $\sqrt{3}x\sqrt{3}$ structure (Fig. 1b). While at 3/7 ML a $\sqrt{7}x\sqrt{7}$ structure is observed,with the Al adatoms occupying two-fold sites. The phase separation between the $\sqrt{3}x\sqrt{3}$ and $\sqrt{7}x\sqrt{7}$ in Fig. 1a indicates that the actual coverage is intermediate between 1/3 and 3/7 ML.

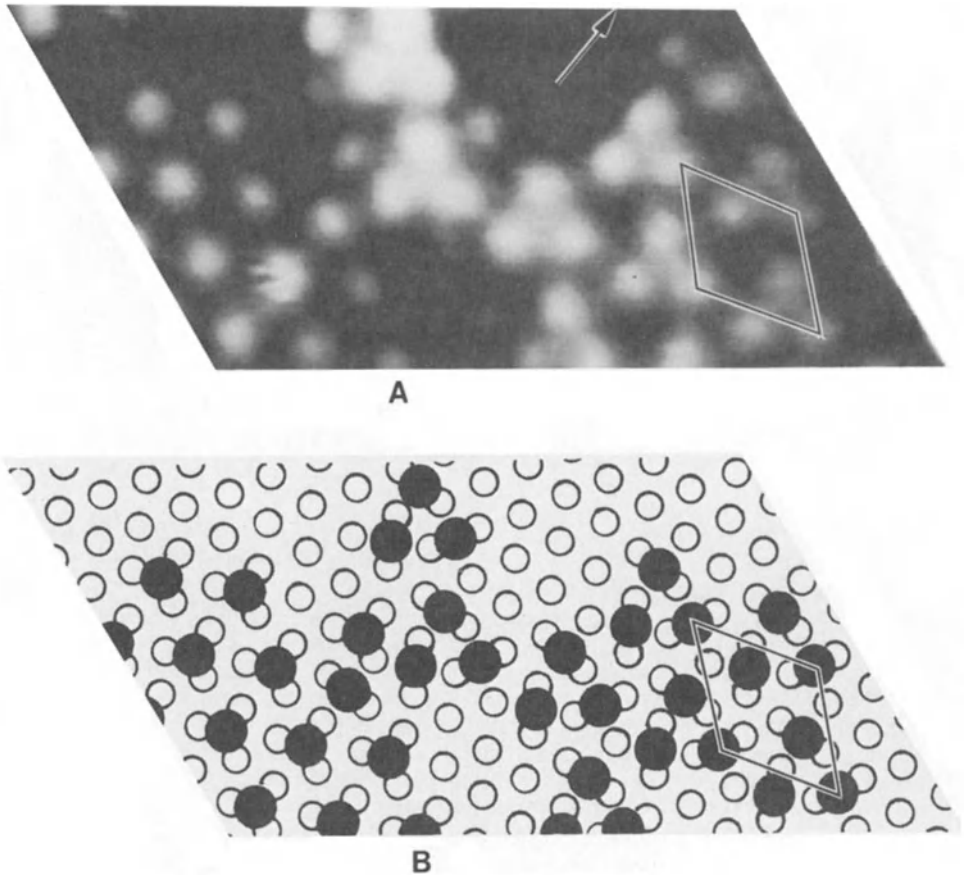

Fig. 1 Scanning tunneling microscopy profiles of Al adsorbed on Si(111) surface (A). (B) gives the Al adatom positions corresponding to the images in (A). Open circles are surface Si atoms, and filled circles are Al adatoms. The left half of (B) is at 1/3 monolayer forming a $\sqrt{3}x\sqrt{3}$ pattern, and the right half of (B) is at 3/7 of a monolayer forming the $\sqrt{7}x\sqrt{7}$ pattern indicated in (B). This figure has been reproduced from Hamers[9].

The surface states at the Si-Al interface have been extensively studied with a variety of surface sensitive experimental probes (ultraviolet photoemission (UPS)[10], electron energy-loss spectroscopy (EELS)[11], photoemission[12], Auger electron spectroscopy[12], angle-resolved photoelectron spectroscopy (ARPES)[13], Auger electron yield[12], high-resolution electron energy loss spectroscopy(HREELS)[14], and inverse angle-resolved photoemission[15]. Both the UPS[10] and the EELS[11] measurements have suggested that the local bonding at the Si-Al interface evolves with coverage. The reduction of the density of states at E_f with small amounts of Al adsorbed on the surface indicated the removal of intrinsic surface dangling bond states from the gap. The UPS measurements[10] also indicate a movement of E_f within the gap, saturating at about 1-2 ML. The movement of E_f is in conflict with Bardeen's[3] original model of intrinsic surface state pinning. However, assuming the pinning states are related to the Si-Al

bonding states, the model can be recast to account for the movement of E_f. A detailed understanding of the movement of E_f and its relationship to the Si-Al bonding states and Schottky barrier formation is one of the main objectives of our study. The HREELS[14] measurements, which can probe the states right at E_f, indicate a movement of the E_f with coverage. The tail in the HREELS spectrum has been attributed to metallic states at E_f. Kelly, et al.[14] found that the first adsorbed Al atoms removes the HREELS tail, indicating a removal of the clean metallic surface states at E_f. The metallic tail in the HREELS spectrum does not reappear until >1 ML of Al has been adsorbed. This suggests that the Schottky barrier for the Si-Al interface is not fully developed until after >1 ML of Al is deposited. Kelly, et al.[14] also concluded that the slow motion of E_f was due to a interplay between localized and non-localized states in an extended energy region. From their photoemission and Auger data Kobayashi, et al.[12] concluded that the metallic states at E_f reappear at about 1 ML.

Theoretically, the first realistic and quantitative study of the Si(111)-Al interface was made by Louie and Cohen[16] using the self-consistent pseudopotential (SCP) method. The Si-Al interface was modeled as a jellium-Si slab, with the jellium density taken to be that of Al. They showed that the metal-induced gap states(MIGS), as proposed by Heine[2], were responsible for the pinning of E_f. Later, using the SCP method, Chelikowsky[17] took into account the discrete nature of the semiconductor-metal bonding by studying the Si-Al interface in the Lander substitutional geometry[7]. Chelikowsky[17] confirmed Louie and Cohen's[16] conclusion that the pinning of E_f was due to the MIGS. Zhang and Schluter[18], also using the SCP method, studied the Si(111)-Al interface with 1 ML of Al adatoms adsorbed in different surface sites. To obtain the best agreement with the photoemission data[10], it was necessary to place the Al atom in a three-fold hollow site with a Si-Al bond length about 25% greater than the Si-Si bond length used by Chelikowsky[17]. Since total energy calculations were not done at this time, the increase in bond length was imposed in an ad hoc manner. But as will be seen below, this was an inspired guess, since the Si-Al bond length we find is very close to the increased Si-Al bond length used by Zhang and Schluter[18]. On the other hand, Platero, et al.[19], using a self-consistent tight-binding scheme, found that at ML coverage the Al adatom favors the on-top site geometry, in agreement with the measurements of Kobayashi, et al.[12]

Northrup[20] was the first to study the Si(111)$\sqrt{3}$x$\sqrt{3}$-Al interface at submonolayer coverages. Using the first principles pseudopotential total energy and atomic force calculations, for 1/3 ML, Northrup[20] was able to correlate his proposed structure of the interface with the angle-resolved photoemission measurements of Hansson, et al.[13] Northrup[20] concluded that the Al adatom sits in a four-fold site (T_4) having a Si atom in the second layer below, provided the Si substrate is allowed to relax. Kinoshita, et al.[13] performed ARPES measurements on the Si(111)$\sqrt{3}$x$\sqrt{3}$-Al interface, finding that the three-fold hollow site (H_3) gave better agreement with their occupied surface state band structure. The occupied surface states for the T_4 and H_3 sites are very similar. In order to resolve this discrepancy, Nicholls, et al.[15] performed k-resolved inverse-photoemission spectroscopy to determine the empty state surface band structure. The dispersion of the unoccupied surface state showed better agreement with the T_4 site of Northrup[20]. The experimental and theoretical results are compared in Fig. 2. Cluster calculations of Dev, et al.[21] also found that the T_4 site is lowest in energy, although the coverage can not be uniquely defined in a cluster calculation.

Theoretically, the chemical bonding at the Si-Al interface, as discussed above, seems to be well characterized at 1/3 ML (Northrup[20]) where a strong chemisorption bond is formed, and at large Al coverages where the MIGS are found to be the pinning mechanism (Louie and Cohen[16]). The goal of our calculations is to fill in the gap between these two regions where much less is known about the character and change of the Si-Al interface bond. Our results will also provide a clear physical picture of the fundamental interactions responsible for the initial formation of the Schottky barrier for this semiconductor-metal system. The rest of the paper is organized as follows: in section II the method is presented, in section III the results and discussions are given, and in section IV a summary is provided.

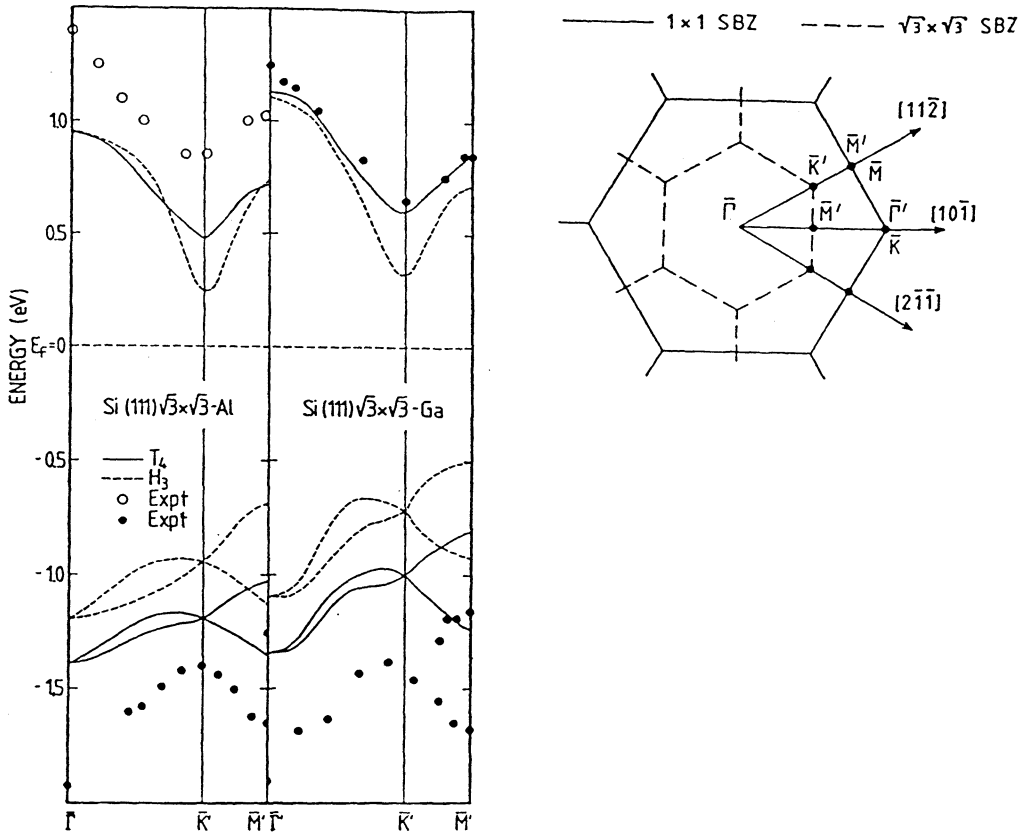

Fig. 2 Comparison between experimental and theoretical dispersion plots and surface-state bands calculated for the T_4 and H_3 models (Ref. 15). See Ref. 15 for more details.

METHOD

In order to see the initial formation and evolution of the Si(111)-Al bonding states at the interface, we have considered Al coverages of 1/3, 3/7, 2/3, and 1 ML. At each coverage several Al adsorption sites have been considered: Al adsorbed in a four-fold site (T_4, Northrup[20]); Al adsorbed in a three-fold hollow site (H_3); Al adsorbed in a two-fold bridge site (B_2); and Al adsorbed in a top-site configuration (T_1). These adatom geometries are depicted in Fig. 3. In the T_4 (H_3) site the Al adatom is placed above the second (fourth) layer Si atom. The four-fold coordination of the T_4 site is a result of the Al-Si surface atom and Al-Si second layer atom distance being nearly equal with relaxation. The B_2 site shown in Fig. 3c has recently been proposed by Hamers and Demuth[9] to explain the observed $\sqrt{7}$x$\sqrt{7}$ Scanning Tunneling Microscope images for 3/7 of a monolayer of Al on Si(111). The B_2 site is characterized by Al adatoms sitting in two-fold sites, symmetrically above two Si surface atoms, arranged in Al trimers at the corners of a $\sqrt{7}$x$\sqrt{7}$ unit cell (see Fig. 1b). The T_1 site places the Al adatom directly above the Si surface atom. In our calculations this site was only considered at 1 ML, since at lower coverages this adatom geometry would leave a portion of the Si surface atoms with unsaturated dangling bonds. The atomic arrangement of the clean Si(111) $\sqrt{3}$x$\sqrt{3}$, $\sqrt{7}$x$\sqrt{7}$, and 1x1 unit cells, corresponding to Al coverages of 1/3 and 2/3, 3/7, and 1 ML, respectively, are shown in Fig. 4. Surface unit cell parameters for the 1x1, $\sqrt{3}$x$\sqrt{3}$, and $\sqrt{7}$x$\sqrt{7}$ structures are also given in the figure. The Si(111)$\sqrt{3}$x$\sqrt{3}$ ($\sqrt{7}$x$\sqrt{7}$) is obtained from the 1x1 unit cell by a 30 (19.1) degree rotation and $\sqrt{3}$ ($\sqrt{7}$) increase in the length of the surface translation vectors. Subsurface Si atoms are indicated by their projection onto the (111) plane. The thickness of the Si slab for the $\sqrt{3}$ and $\sqrt{7}$ unit cells corresponds to four layers of Si atoms and one layer of H atoms to saturate the Si dangling bonds on the bottom

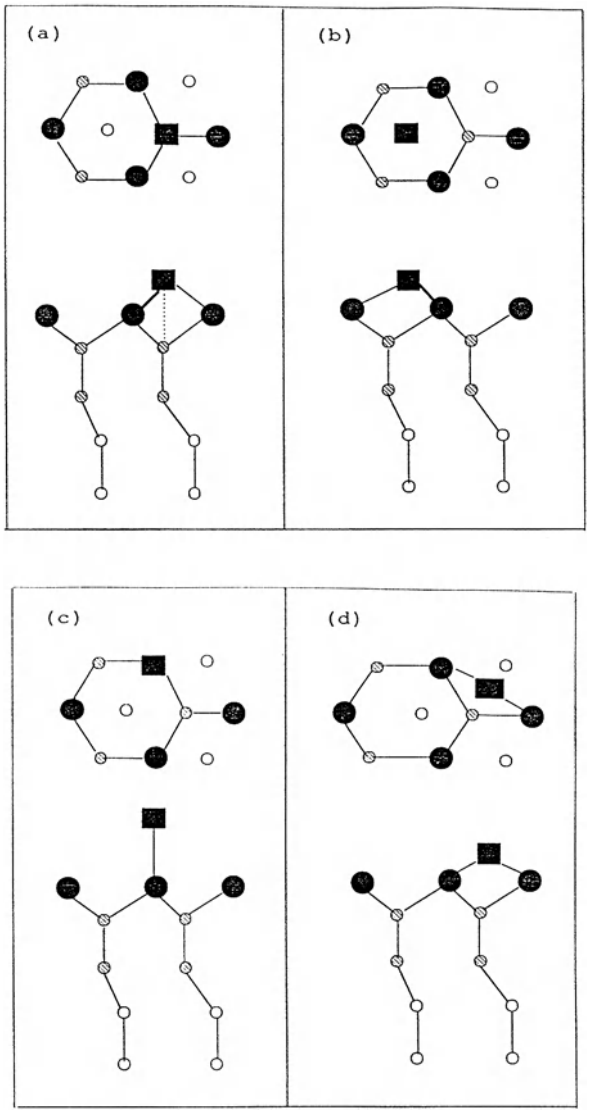

Fig. 3 Al adatom geometries for the T_4 (a), H_3 (b), T_1 (c), and B_2 (d) sites. The large filled circles represent Si first layer atoms, the large filled squares represent the Al adatoms, the small hatched circles represent second and third layer Si atoms, and the small open circles represent fourth and fifth layer Si atoms. The top (bottom) panel of each figure is a top (side) view. In the T_4 site (a) the Al adatom is directly above the second layer Si atom. In this configuration the Al adatom is bonded to three Si first layer atoms and a second layer Si atom, indicated by the dashed line in (a). In the H_3 site (b) the Al adatom is above a fourth layer Si atom. Here, the Al adatom is bonded to three Si surface atoms. The T_1 site (c) places the Al adatom directly above a Si surface atom. The B_2 site (d) is characterized by the Al adatom in a bridge-site between two Si surface atoms.

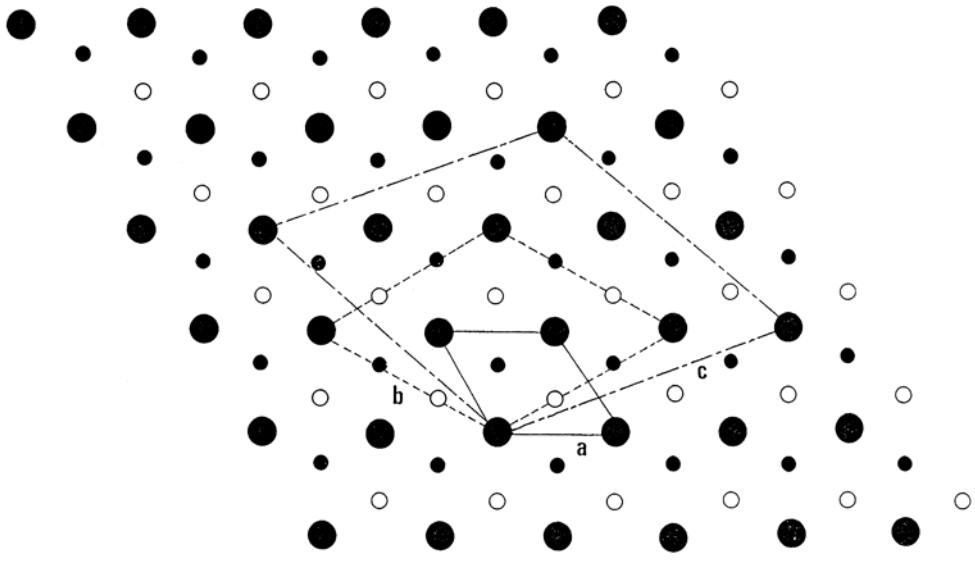

Fig. 4 The atomic arrangement of the clean Si(111)1x1 (solid line), Si(111)$\sqrt{3}$x$\sqrt{3}$ (dashed line), and the Si(111)$\sqrt{7}$x$\sqrt{7}$ (dashed-dotted line) surface unit cells. a ($A_{cubic}/\sqrt{2}$),b ($\sqrt{3}A_{cubic}/\sqrt{2}$), and c ($\sqrt{7}A_{cubic}/\sqrt{2}$) represent the length of surface translation vector for the 1x1, $\sqrt{3}$x$\sqrt{3}$, and $\sqrt{7}$x$\sqrt{7}$ unit cells, respectively. A_{cubic} is the Si bulk lattice constant (5.43 Å). The position of the subsurface Si atoms are indicated by their projection on to the (111) plane; first and sixth layer Si (large filled circles), second and third layer Si atoms (small filled circles), and fourth and fifth layer Si atoms (small open circles).

surface. The 1x1 unit cell, having only one atom per layer is modeled with six layers of Si atoms with one additional layer of H atoms. The width of the vacuum region was taken to be about 15-18 a.u.

The electronic structure is obtained using standard first principles self-consistent pseudopotential techniques, within the local-density functional theory applied in the momentum space formalism[22], using ab initio pseudopotentials[23], and the Wigner[24] exchange-correlation potential. The wavefunctions

$$\Psi_{nk}(r) = \Sigma\, a_{nk}(G)\, e^{i(k+G)\cdot r} \qquad (1)$$

were expanded in plane-waves with kinetic energy $|\mathbf{k}+\mathbf{G}|^2$ up to 4.25 Ry. **k**, **G** and n represent a reciprocal lattice point in the surface Brilloiun zone, a reciprocal lattice vector, and band index, respectively. The sum appearing in (1) is over **G**. During the self-consistency iterations the electronic valence charge density was sampled at thirteen, four, and one k-points in the surface Brillouin zone for the 1x1, $\sqrt{3}$x$\sqrt{3}$, and $\sqrt{7}$x$\sqrt{7}$ unit cells, respectively. For the $\sqrt{7}$x$\sqrt{7}$ structure the plane-wave cutoff was reduced to 3.75 Ry due to the extremely large unit cell. The adequacy of our basis set was tested by reproducing the Si-Al interlayer spacing for the H_3 and T_4 sites at 1/3 ML found by Northrup[20].

For each coverage and adatom geometry the total energy was minimized with respect to the Si-Al interlayer distance. The Si surface was held fixed during all the calculations, except for the T_4 site where it has been found by Northrup[20] to induce a large Si surface relaxation at 1/3 ML. Once the lowest energy structure is found for each coverage, the Si-Al bonding states and surface resonances can be identified by computing the local density of states (LDOS) given by the following expression:

$$LDOS_L(E) = \sum P_{k,n}(L)\, \delta(E - E_n(k)) \quad (2)$$

where

$$P_{k,n}(L) = \int_L |\Psi_{nk}(r)|^2 d^3r. \quad (3)$$

L represents the region in which the LDOS is evaluated. The sum in (2) is over all k points and bands n. The charge density corresponding to the peaks in the LDOS can be plotted in real space to provide a detailed picture of the Si-Al bonding states.

RESULTS AND DISCUSSIONS

In this section we present the results for the total energies, total valence charge densities, local densities of states(LDOS), and charge densities of the bonding states. The total energy calculations will pose some interesting questions relating to the stability of a given adatom geometry. We will try to answer these questions by analyzing the above mentioned physical properties.

In Fig. 5 the total energy differences for the Al adatom sites considered at each coverage are reported. The energy differences shown in Fig. 5 are obtained by taking the lowest energy structure for each coverage as a reference. The energy reference is chosen to be zero for all coverages. All other structures at a particular coverage are then referenced with respect to this value. At 1/3 ML, with the Si substrate held fixed, the H_3 site is about 20 mRy lower in energy than the T_4 site. If the Si substrate is allowed to relax to the geometry found by Northrup[20], labeled as T_4 (Northrup) in Fig. 5, the energy is lowered by 65 mRy. This is a large relaxation energy. Increasing the coverage from 1/3 to 3/7 ML we have investigated two Al adatom sites, H_3 and B_2. The B_2 site is found to be lower in energy than the H_3 site by about 30 mRy; in good agreement with the geometry proposed by Hamers and Demuth[9]. We have considered five different adatom sites at 2/3 ML, all of which are reasonably close in energy. The H_3 site is lowest in energy with the T_4 and B_2 sites about 5 and 15 mRy higher in energy, respectively. Simultaneous occupation of the T_4 and H_3 site at 2/3 ML increases the energy by about 5 mRy above the T_4 site, due to an increased coulomb interaction between the Al adatoms which are about 20% closer than in bulk Al. Since the T_4 and H_3 sites are so close in energy, substrate relaxation could reverse the ordering. To see if the T_4 site found by Northrup[20] at 1/3 ML is favorable at higher coverages, we have investigated this same relaxation at 2/3 ML, and find that this geometry is energetically unfavorable. When the Al coverage is 2/3 ML, two Al atoms adsorbed on the unrelaxed surface is lower in energy than two Al atoms adsorbed in Northrup[20] T_4 geometry found at 1/3 ML. The actual Si surface relaxation is probably between these two values. With 2/3 ML of Al adsorbed on the surface, two Al valence electrons are trying to saturate each Si dangling bond. This is an unfavorable situation, resulting in a small outward relaxation of the Al overlayer and a weaker interaction with the Si surface. As a result, the adatom induced relaxations of the Si surface will be smaller, favoring adsorption on the ideal surface. Similar results have been found for Na adsorption on the GaAs (110) surface[25]. At 1 ML the T_1 site is lower in energy than both the H_3 and T_4 sites, which are nearly equal in energy. This result is in agreement with the theoretical calculations of Platero, et al.[19]

The physical picture that one can obtain from the total energy calculations is the following: as the coverage is increased from 1/3 to 1 ML the coordination of the Al adatom with respect to the Si surface atoms (also including the second layer atom for the T_4 site) decreases from four-fold (T_4) at 1/3 ML to one-fold (T_1) coordinated at 1 ML. This change in coordination of the Al adatom with coverage clearly indicates that the Al adatom finds the adsorption site that can maximize its covalent bonding with Si. Al and Si atoms form a strong covalent bond at all coverages on the Si(111) surface. This fact will become clearer when we examine the charge density distributions.

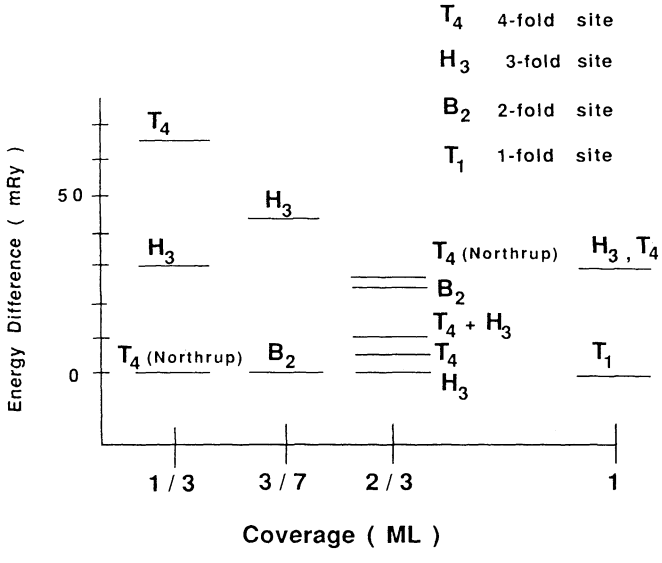

Fig. 5 Total energy differences for the adatom geometries investigated at coverages of 1/3,3/7, 2/3, and 1 monolayer (ML). The coordination of the Al adatom is also indicated for the four adatom geometries. The T_4 (Northrup) site uses the Al adatom geometry found by Northrup[20]. At each coverage the energy reference (lowest energy structure at this coverage) is taken to be equal to 0.0 mRy. The figure indicates that the coordination of the Al adatom decreases from four-fold coordinated at 1/3 ML to one-fold coordinated at 1ML.

The total energy calculations suggest some interesting questions relating to the stability of a particular adatom geometry at a given coverage:

Q1 : How does the Si-Al bond length vary with coverage and adsorption site ?

Q2 : Why is the T_4 site more stable than the H_3 site at 1/3 ML ?

Q3 : Why is the B_2 site stable at 3/7 ML ?

Q4 : Why is the T_1 site stable at 1 ML ?

By examining these questions in detail we can obtain a picture of the mechanism determining the stability of an adsorption site at a given coverage.

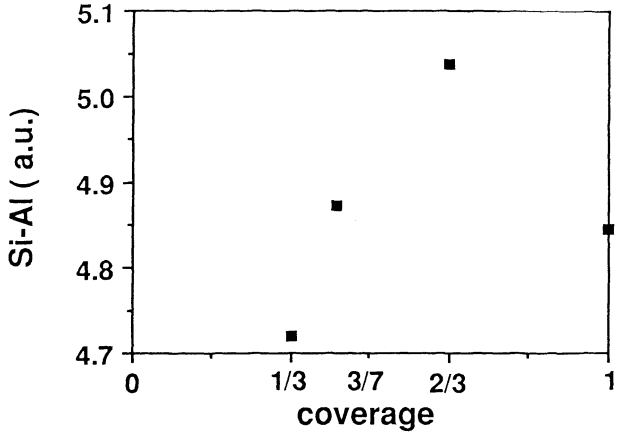

Fig. 6 Si-Al bond length versus coverage. The Si-Al bond lengths are for the minimum energy adatom geomtry at each coverage (see Fig. 5). .The variation in the Si-Al bond lengths are covalent bond at all coverages.

Q1 : How does the Si-Al bond length vary with coverage and adsorption site ?

The bond length variation versus coverage is depicted in Fig. 6. Bond lengths given here are for the lowest energy Al adatom geometries for each coverage. In the Fig. 6, we see an increase of about 0.35 a.u. in the bond length from 1/3 to 2/3 of a monolayer, then a decrease of about 0.2 a.u. at 1 ML. Overall these changes in bond length are small, so that on the average the bond length can be taken to be constant, 4.85 ± 0.15 a.u.. The sum of covalent radii of Si and Al is equal to 4.33 a.u., somewhat smaller than 4.85 a.u. The average nearest neighbor separation of Si and Al atoms in the bulk constituent crystals is 4.93 a.u., close to the value we find for the average bond length. If the Al adatom were kept fixed in a single adsorption site for all coverages, as done in our earlier work[26], the bond length variation with coverage would be considerably different. The Si-Al interlayer-distance versus coverage for the H_3 site is given in Fig. 7 . A 25% increase in the Si-Al bond length is found in going from 1/3 to 1 ML, corresponding to the 1.2 a.u. interlayer-relaxation shown in Fig. 7. This value is close to the value used by Zhang and Schluter[18]. Our results indicate that a much different picture of the bonding at a general semiconductor-metal interface can be obtained if one does not consider multiple adsorption sites at each coverage.

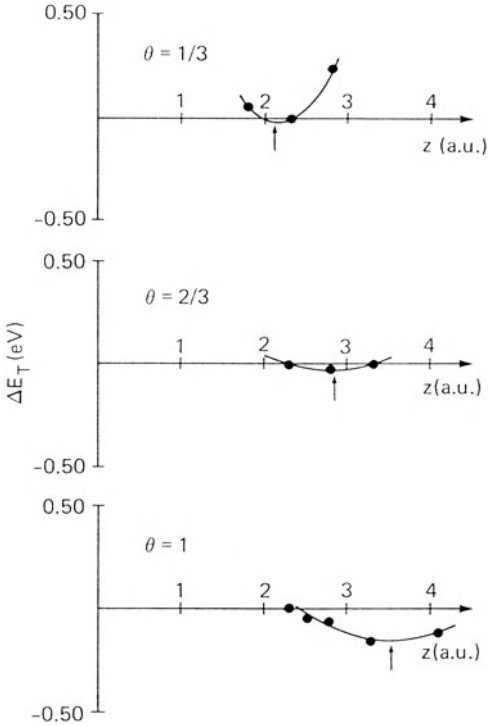

Fig.7 Total energy minimization curves for three coverages in the H_3 geometry. The arrows indicate the Si-Al interlayer-distance z which minimizes the total energy at each coverage, and the solid lines are parabolic fits to the data points. This figure has been reproduced from Fig. 1 of Ref. 26.

Q2 : Why is the T_4 (Northrup[20]) site more stable than the H_3 site at 1/3 ML ?

We can understand this by comparing the total valence charge densities, LDOS, and charge densities of the Si-Al bonding states for the two sites. The total valence charge densities, in a plane passing through the Al atom and the Si surface atom, for the T_4 and H_3 sites are given in Figs. 8a and 8c. The Si-Al bond charge maximum is 0.052 and 0.059 a.u. for the T_4 (Fig. 8c) and H_3 (Fig. 8a) sites, respectively. Although the maximum contour between the Si and Al atoms for the T_4 site is a little smaller than the H_3 site, the contour extends over a much larger area; indicating the stability of the structural unit formed between the Al adatom and the first and second layer atom in the T_4 geometry. One interesting feature of the charge density for the T_4 site can be seen by carefully examining the contours in the Si-Si backbond. This region is indicated by an arrow in Fig. 8c. In the T_4 site (Fig.8c), some of the Si-Si backbond has been transferred to the Si-Al bonding region. This charge transfer results in a strengthening of the Si-Al bond, making it closer to a Si-Si bond; the four -fold coordination of the Al atom allows for this charge transfer. Another interesting feature is that with the Al adatom in the T_4 site the second layer Si atom is five-fold coordinated. Electron energy loss spectroscopy should be able to distinguish the increased Si-Si stretch frequency associated with the five-fold Si complex. The semiconducting character of the surface can be seen by considering the charge density in a (111) plane passing through the Al overlayer (Figs. 8b and 8d). The charge densities are localized around the Al adatoms, with little overlap between the three-fold lobes of neighboring Al atoms.

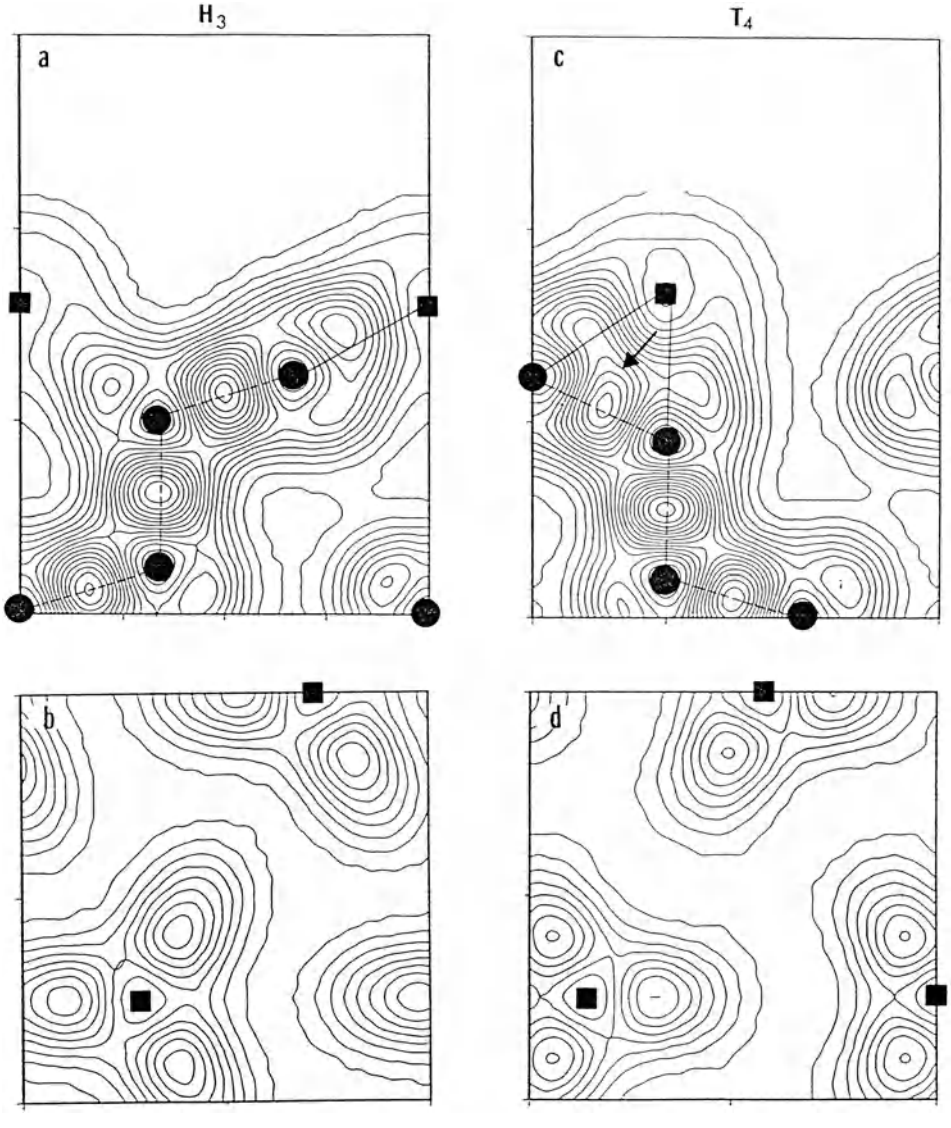

Fig. 8 Total valence charge densities for the H_3 (a,b) and T_4 (c,d) sites at 1/3 ML. The charge density contours in (a) and (c) are in a plane passing through the Al adatom and the Si surface atom, and (b) and (d) are in a (111) plane passing through the Al adatom. Filled squares represent Al atoms and filled circles Si atoms. Solid lines are along the Si - Al bond direction and dashed lines along the Si-Si bond directions. The arrow in Fig (c) indicates the transfer of charge out of the Si-Si back bond region into the Si-Al bonding region for the T_4 site. The triangle in Fig. (c) shows that in the T_4 site the Al atom is bound to both the first and second layer Si atoms. The contour spacings are 0.005 a.u.

Although the total charge density gives one information on the strength of the bond, detailed information related to the nature of the bonding states can be obtained by examining the charge densities associated with the peaks in the LDOS. The LDOS for the T_4 and H_3 sites at 1/3 ML is given in Fig. 9. The LDOS plots here are obtained by taking the difference of the LDOS in the center of the Si region (representing bulk Si LDOS) and one including the Si-Al region. The positive features in the LDOS are those relating to the Si-Al bonding states. Concentrating on the region 5 eV below E_f one can see two features, labeled P_1 and P_2, which are related to the Si-Al bond and the Si-Si backbond, respectively. P_1 and P_2 are considerably lower in energy for the T_4 site in comparison to the H_3 site. In Fig. 10 we plot the charge density associated with these peaks. For both the T_4 (Fig. 10a) and H_3 (Fig. 10c) sites, P_1 is related to the Si p_z and Al $p_{x,y}$ states. These states have been discussed previously by Northrup[20]. For the H_3 site P_1 also shows substantial charge in the Si-Si backbond region. Another interesting feature, illustrating the mixing of the Si-Al bond with the second layer Si atom in the T_4 site mentioned above, is the $p_{x,y}$ nature of P_1 with respect to the second layer Si atom (Fig. 10a). The character of the bonding state is the same in relation to both the Al adatom and the second layer Si atom.

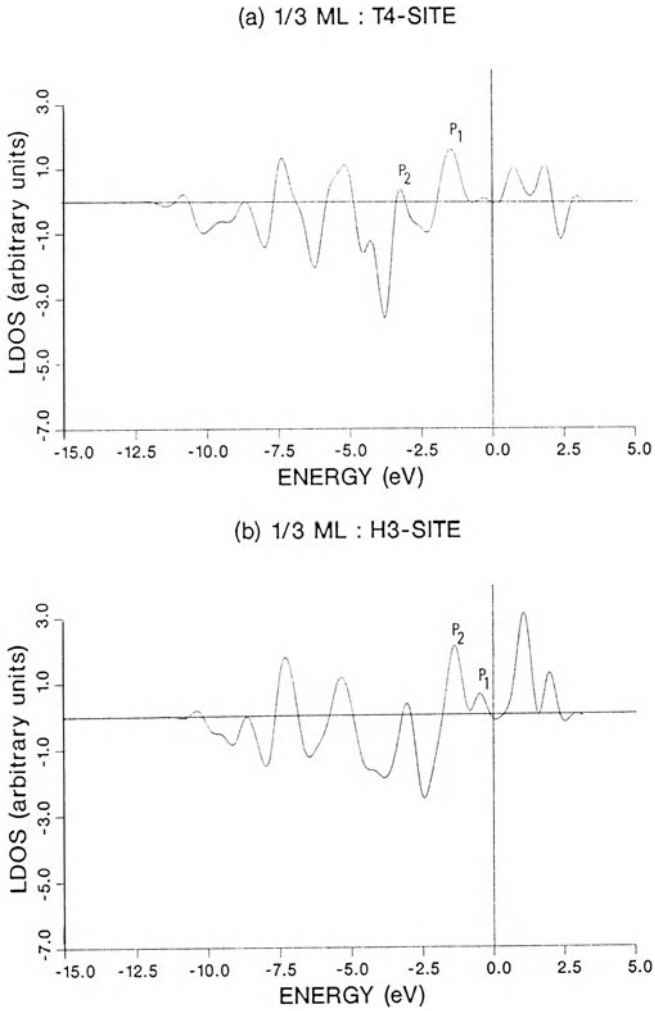

Fig. 9 Local Densities Of States (LDOS) Difference plots for the T_4 (a) and H_3 (b) sites at 1/3 ML. The positive features labeled P_1 and P_2 within 5 eV of the Fermi energy (vertical line at 0.0 eV), identify Si-Al related bonding states. See text for more details.

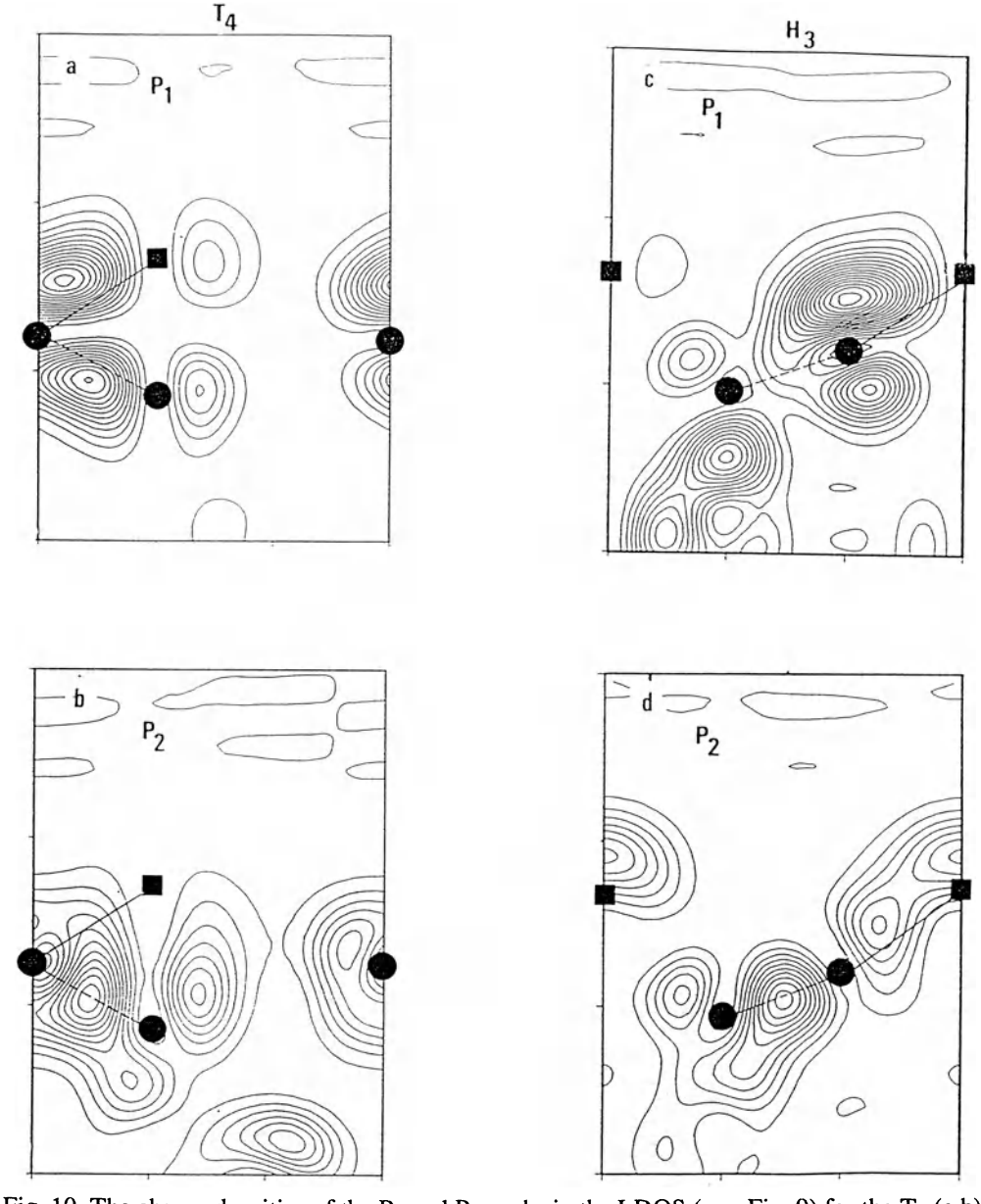

Fig. 10 The charge densities of the P_1 and P_2 peaks in the LDOS (see Fig. 9) for the T_4 (a,b) and H_3 (c,d) sites. For both sites P_1 and P_2 predominantly correspond to Si p_z - Al $p_{x,y}$ and Si-Si backbond states, respectively. The contour spacings are 0.005 a.u.

Q3 : Why is the B_2 site stable at 3/7 ML ?

The adatom geometries for the B_2 and H_3 sites at 3/7 ML are depicted in Fig. 11. The seven Si atoms per surface unit cell are labeled Si_1 - Si_7 . In the B_2 site (Fig. 11a) every Al adatom has two nearest neighbor Si surface atoms. Two of the three Al valence electrons saturate the two nearest neighbor Si dangling bonds. One of the seven Si surface atoms in the unit cell is missing a nearest neighbor Al atom, Si_7. Three Al adatoms (labeled Al_1,Al_2, and Al_3 in Fig. 11a), which are equally distant from Si_7, form the triangle shown in Fig. 11a. The third valence electron of each of these Al atoms form a cooperative delocalized bond with the dangling bond of Si_7. The cooperative bonding of Al_1 - Al_3 is clearly illustrated by the charge density contours in the plane of the Al adatoms shown in Fig. 12a. In Fig. 12b the chemisorption bonds between the Al and Si atoms are visible. In the H_3 site Si_1 - Si_4 have two nearest neighbor Al atoms, Si_5-Si_6 have one nearest neighbor Al atom, and Si_7 has no nearest neighbor Al atoms. Si_1-Si_4 have two Al atoms trying to simultaneously saturate their single dangling bond orbitals. This competition is energetically unfavorable, resulting in a small outward relaxation of about 0.5 a.u., thereby weakening the Si-Al bond in the H_3 site. In addition, the Si_7 is surrounded by a similar Al triangle as in the B_2 site, but in this case the Al adatoms are further away from Si_7, therefore, less effective in saturating the dangling bond orbital of Si_7.

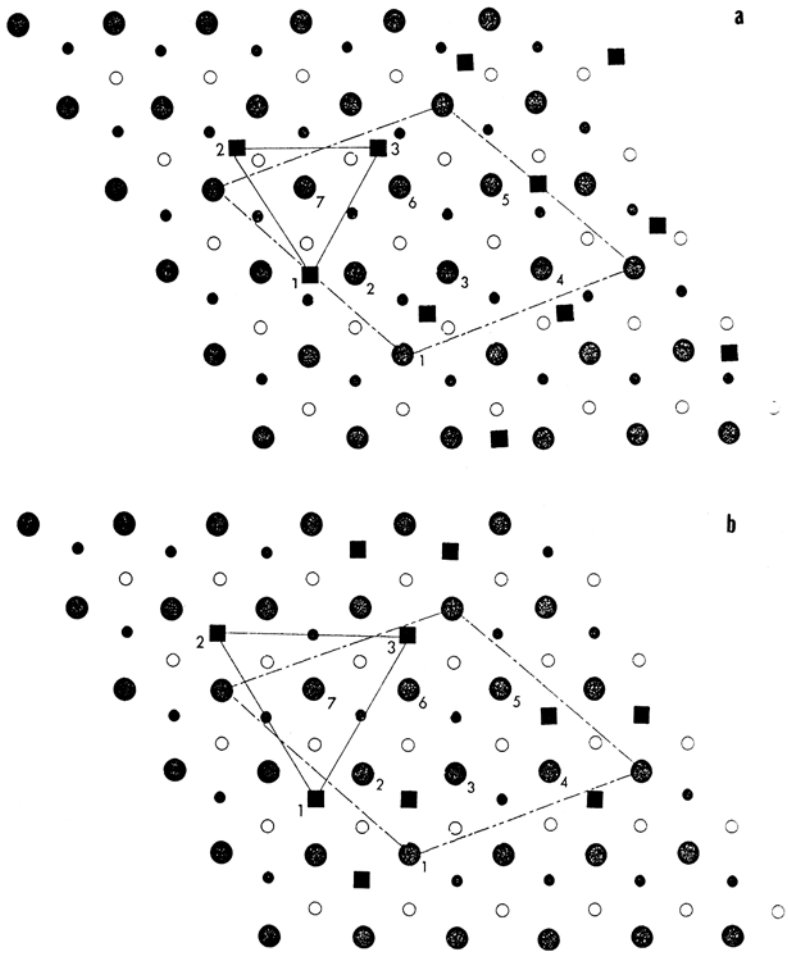

Fig. 11 Atomic arrangement of the Al adatoms in the B_2 (a) and H_3 (b) sites for the $\sqrt{7}x\sqrt{7}$ unit. The filled squares (circles) represent the Al (Si) atoms. The Si atoms in the surface unit cell are labeled 1-7, and the Al atoms 1-3. The triangle indicates the three Al atoms surrounding Si_7, which is the only Si atom in the unit cell that does not have a nearest neighbor Al atom.

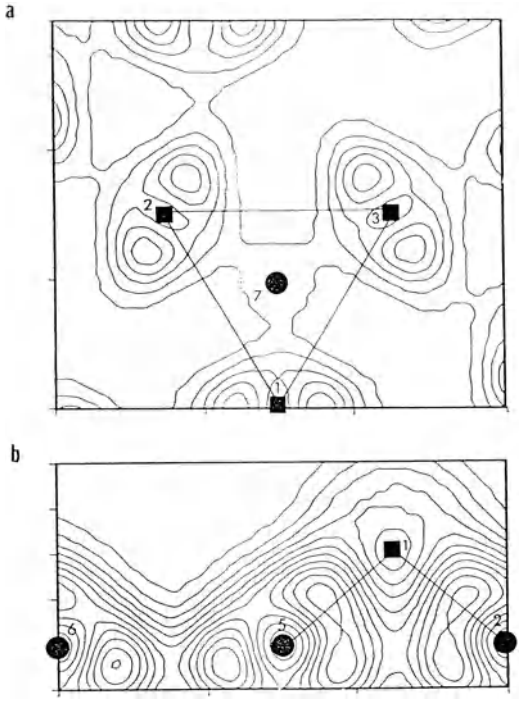

Fig. 12 Total valence charge densities for the B_2 site in a (111) plane containing the Al adatoms (a) and a plane passing through the Al and Si surface atoms (b). The filled squares (circles) represent the Al (Si) atoms. The position of the Si atom in Fig. (a), although not in this plane, is used to illustrate the cooperative delocalized bond form with the three Al atoms. The triangle in Fig. (a) correspondes to the one shown in Fig. 11. In Fig. (b) one can see a strong chemisorption bond formed between Al_1 and $Si_{5,6}$. The contour spacings are 0.005 a.u.

Q4 : Why is the T_1 site stable at 1 ML ?

Let us compare the charge density of the T_1 and H_3 sites in the plane containing the Al and Si surface atoms (Fig. 13a,c) and in a (111) plane containing the Al adatom (Fig. 13b,d). Due to the large relaxation for the Al adatom in the H_3 site at 1 ML (see Fig. 7), the bond charge between the Al and Si atom has effectively disappeared. On the other hand, in the T_1 site (Fig. 13a) one can see a strong chemisorption bond formed between Si and Al. One of the Al valence electrons forms this chemisorption bond with Si, and the remaining two valence electrons of Al form a more delocalized interaction in the plane of the Al adatoms. The charge density in the plane of the Al atoms are similar for T_1 (Fig. 13c) and H_3 (Fig. 13d) sites, with somewhat more charge in this plane for the H_3 site. This is expected since in the H_3 site the Al atom no longer forms a bond with the Si surface atoms. An interesting observation can be made by comparing the charge density, in the Al plane for the T_1 and H_3 sites with the charge density in the surface layer for an unsupported ML and seven layer Al film. This comparison is shown in Fig. 14. The T_1 site (Fig. 14a) is more similar to the ML Al film (Fig. 14c), while the H_3 site (Fig. 14b) is more like the seven layer Al film (Fig. 14d). We can then conclude that the metallic character of the charge density of the T_1 site is similar to the quasi-two-dimensional metal state seen in the unsupported ML film. This is consistent with the observations of Kelly, et al.[14] , who found that true metallic states at E_f did not appear until after 1.5 Ml of Al were deposited on Si(111). This is easily understood since at 1 ML the Al atom bond lengths are about 25% larger than in the bulk.

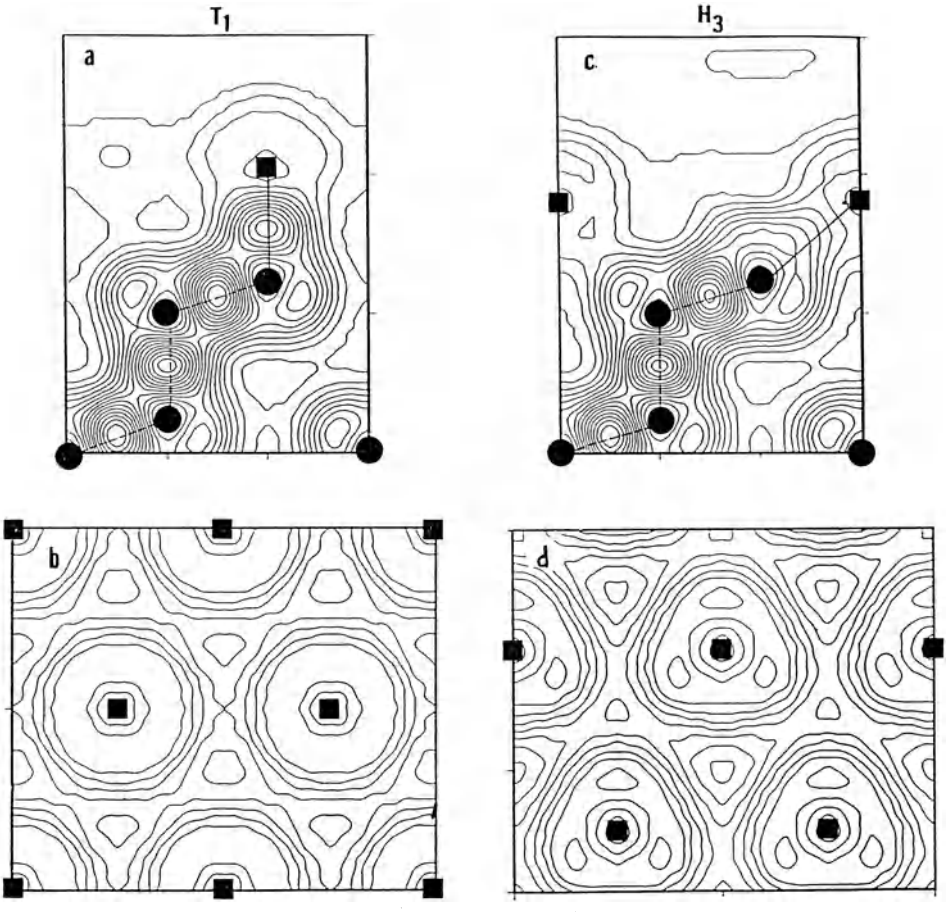

Fig. 13 Total valence charge densities for the T_1 (a,b) and H_3 (c,d) sites at 1 ML. The charge density contours in (a) and (c) are in a plane passing through the Al adatom and a Si surface atom, and (b) and (d) are in a (111) plane passing through the Al adatom. Filled squares represent Al atoms, and filled circles Si atoms. Solid lines indicate the Si - Al bond direction, and dashed lines the Si-Si bond directions. The contour spacings are 0.005 a.u.

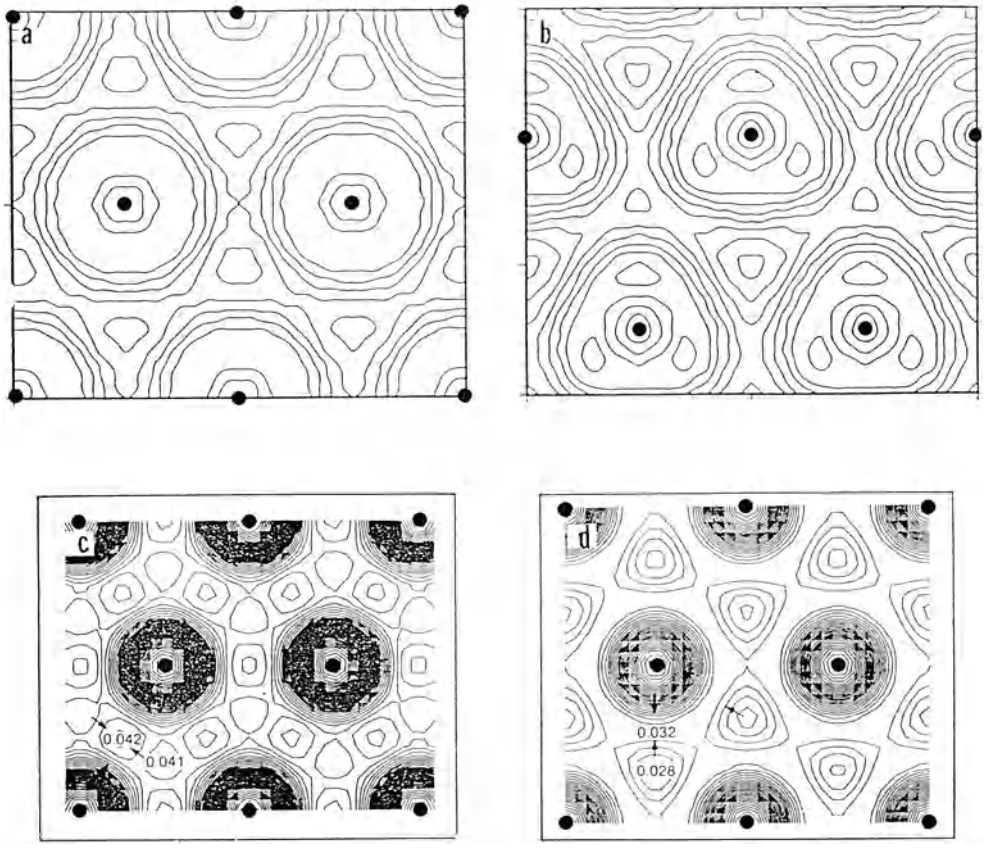

Fig. 14 A comparison between the total valence charge density, in a (111) plane passing.through the Al adatoms, for the T_1 (a), H_3 (b), unsupported ML film (c), and a seven layer Al film (d). The results for the unsupported monolayer and seven layer film are taken from Ref. 28. The contour spacings for (a) and (b) are 0.005 a.u., and in (c) and (d) 0.0012 a.u.

The LDOS for the T_1 and H_3 sites are compared in Fig. 15. The features for both sites are very similar. This may be one of the reason for the difficulties in determining the Al adatom adsorption site by comparing the LDOS to the photoemission measurements[18,19]. The local densities of states do not show significant enough variation to differentiate between these two sites. One must rely on the total energies, which we have already seen show that the T_1 site is the lowest energy. What we can say is that in comparison to Fig. 9, the main Si-Al bonding peaks labeled P_1 and P_2 in the Fig. 15 have shifted to higher energies. This result is consistent with the UPS[10] measurements showing a higher energy peak at increased coverage.

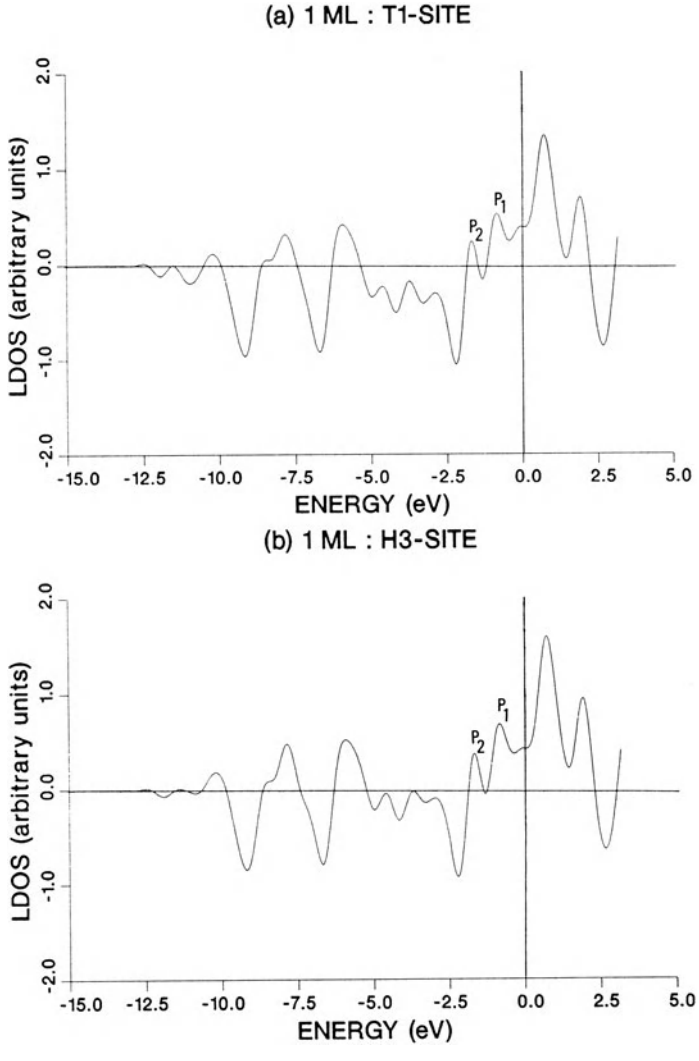

Fig. 15 Local Densities Of States (LDOS) Difference plots for the T_1 (a) and H_3 (b) sites at 1 ML. The positive features labeled P_1 and P_2 below 5 eV of the Fermi energy (vertical line at 0.0 eV), identify the Si-Al related bonding states. See text for more details.

SUMMARY

The main objective of these calculations was to try to understand the Schottky barrier formation in the Al-Si(111) system, by studying the initial evolution of the interface bonding. Our calculations have provided the following picture, summarized in schematically in Fig. 16. At 1/3 ML the strong Si-Al chemisorption bond removes the surface dangling bond state from the gap, producing a insulating surface. As the coverage is increased, we find that both the chemisorption and metallic like bonding states evolve according to the strong covalent bonding formation between Si and Al, reflected by the change in adsorption site and constancy of Si-Al bond length with coverage. Even though the Si-Al bond length stays constant, the Si/Al interlayer distance increases with coverage. At 1/3 ML the interlayer distance is about 2.5 a.u., and at 1 ML the interlayer distance has increased to 4.85 a.u. These results are consistent with the original work of Batra and Ciraci[5], which showed an increase in the metal-semiconductor interlayer distance upon metallization of the overlayer. The Si-Al bond length At coverages greater than 1/3 ML, two dimensional metallic states are developed (see for example the charge conducting channels at 3/7 and 1 ML shown in Figs. 12 and 14a, respectively.). Finally, the pinning mechanism for this metal-semiconductor system, is determined by a complicated hybridization between the local chemisorption and delocalized metallic bonds. Our picture of the barrier formation is similar to the resonant valence bond model put forth by Lannoo[28], and the conclusions of Kelly, et al.[14]

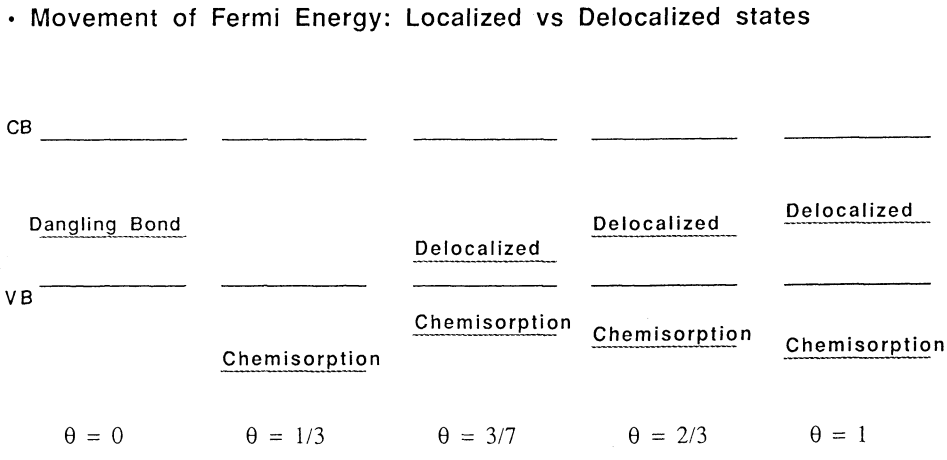

Fig. 16 Schematic summary of the Si-Al bonding states and their evolution with coverage.

Acknowledgements

We would like to thank Drs. C. Y. Fong and S. Ciraci for many useful discussions. We would also like to thank Drs. R. J. Hamers and J. Demuth for providing us with their STM results for the $\sqrt{7}x\sqrt{7}$ structure prior to publication. JSN would like to acknowledge the support of the Department of Energy, Office of Basic Energy Sciences, Division of Materials Sciences.

REFERENCES

1. J. Bardeen, Phys. Rev. 71, 717(1947).
2. V. Heine, Phys. Rev. A138, 1689(1965).
3. J. C. Inkson, J. Phys. C5, 2599(1972).
4. J. C. Phillips, J. Vac. Sci. Technol. 11, 947(1974)
5. I. P. Batra and S. Ciraci, Phys. Rev. B33, 4312(1986).
6. K. D. Gronwald and M. Henzler, Surf. Sci. 117, 180(1982).
7. J. J. Lander and J. Morrison, Surf Sci. 2, 553(1964).
8. F. K. Legoues, W. Krakow, and P. S. Ho, Phil. Mag. A53, 833(1986).
9. R. J. Hamers (in preparation).
10. G. Margaritondo, J. E. Rowe, and S. B. Christman, Phys. Rev. B14, 5396(1976).
11. J. E. Rowe, G. Margaritondo, and S. B. Christman, Phys. Rev. B15, 2195(1977).
12. K. L. I. Kobayashi, F. Gerker, J. Barth, and C. Kunz, Solid State Commun. 39, 851(1981).
13. G. V. Hansson, R. Z. Bachrach, and R. S. Bauer, Phys. Rev. Lett. 46, 1033(1981); see also G. V. Hansson, J. M. Nicholls, P. Martensson, and R. I. G. Urhberg, Surf. Sci. 168, 105(1986); in addition see also T. Konoshita, S. Kono, and T. Sagawa, Phys. Rev.B32, 2714(1985).
14. M. K. Kelly, E. Colavita, G. Margaritondo, J. Anderson, L. Pagagno, D. J. Fränkel, and G. J.Lapeyre, Phys. Rev. B32, 2693(1985).
15. J. M. Nicholls, B. Reihl, and J. E. Northrup, Phys. Rev. B35, 4137(1987); see also R. I. G, Uhrberg, G. V. Hansson, J. M. Nicholls, P. E. S. Persson, and S. A. Flodstrom, Phys. Rev. B31, 3805(1985).
16. S. G. Louie and M. L. Cohen, Phys. Rev. B13, 2461(1976).
17. J. R. Chelikowsky, Phys. Rev. B13, 3618(1977).
18. H. I. Zhang and M. Schluter, Phys. Rev. B18, 1923(1978).
19. G. Platero, J. A. Verges, and F. Flores, Surf. Sci. 168, 100(1986).
20. J. E. Northurp, Phys. Rev. Lett. 53, 683(1984).
21. B. N. Dev, S. M. Mohapatra, K. C. Mishra, W. M. Gibson, and T. P. Das, Phys. Rev. B36, 2666(1987).
22. J. Ihm, A. Zunger, and M. L. Cohen, J. Phys. C12, 4409(1979); K. C. Pandey, Phys. Rev. Lett. 49, 223(1982)., I. P. Batra and F. Herman, J. Vac. Sci. Technol. A1, 1080(1983).23.G. B. Bachelet, D. R. Hamann, and M. Schluter, Phys. Rev. B26, 4199(1982).
24. E. Wigner, Phys. Rev. 46, 1002(1934).
25. L. H. Yang, C. Y. Fong, and I. P. Batra, see this workshop.
26. J. S. Nelson, I. P. Batra, and C. Y. Fong , J. Vac. Sci. Technol. A6, 743(1988).
27. I. P. Batra, S. Ciraci, G. P. Srivastava, J. S. Nelson, C. Y. Fong, Phys. Rev. B34, 8246(1986).
28. M. Lannoo, Proc. Workshop on Metallization and Metal-Semiconductor Interfaces (Garching, Aug. 22-26, 1988), Plenum, New York, I. P. Batra, Editor.

Defects at Metal-Semiconductor Contacts

FACTORS INFLUENCING ELECTRICAL BARRIERS AT METAL-SEMICONDUCTOR INTERFACES: GOLD AND ANTIMONY ON INDIUM PHOSPHIDE AND CADMIUM TELLURIDE

R.H. Williams

Department of Physics
University College
Cardiff, U.K.

ABSTRACT

The magnitude of electrical barriers at metal-semiconductor interfaces are known to be influenced by several mechanisms, with the relative importance of these depending on the detailed nature of the interface and the way it was fabricated. Experimental programmes aimed at understanding those factors which govern these mechanisms are described, concentrating on two semiconductors, InP and CdTe, and two overlayer elements, Au and Sb. The influence of overlayer structure, interface layers, and surface stoichiometry are discussed in the context of modern theories of Schottky barrier formation.

INTRODUCTION

During the last fifteen years or so great progress has been made in our understanding of interactions at metal-semiconductor interfaces[1]. The availability of surface science techniques and small area methods such as transmission electron microscopy has enabled detailed information to be obtained in relation to chemical reactions, intermixing and ordering at interfaces. Methods such as current-voltage and capacitance spectroscopies have been combined with photoelectron spectroscopies not only to measure the magnitude of electrical barriers at metal-semiconductor interfaces but also to probe the ways the barriers develop as the thickness of the deposited contact increases. It is by now clear that the growth mode of the overlayer and the abruptness of such interfaces are significantly influenced by factors such as the substrate temperature, the deposition rate, and the stoichiometry and degree of order and cleanliness of the semiconductor surface[2]. However, despite progress in understanding growth modes and reactions, it is still the case that those processes which are responsible for establishing electrical barriers at metal-semiconductor interfaces are not thoroughly understood. The formation of Schottky barriers should, according to various models, be governed by the work function or electronegativities of the metals and semiconductors[3], and by interface states which may have a variety of origins. Interface states may arise as a consequence of the bonding between the metal and semiconductor at the interface, by the generation of

defects at the interface when the metal is deposited[4], by interface disorder , and by so called metal-induced-gap-states (MIGS)[6,7]. In the latter case the interface states arise from an effective closure of the band gap of the semiconductor near the interface, due to the presence of the metal, and the pinning energies of the Fermi levels associated with such states are not expected to vary greatly for different metal contacts on a given semiconductor, provided the density of MIGS is reasonably large ($\sim 10^{14}$ cm^{-2} eV^{-1}).In addition to these models, it has been proposed that chemical reactions at intimate metal-semiconductor interfaces often lead to new phases and that it is the work function of these interface phases that is of importance, rather than the work function of the metal forming the contact[8].

In previous publications we[9] and others[10] have argued that many processes contribute simultaneously to Schottky barrier formation and that it is too simplistic a view to expect a single model to fully account for the way electrical barriers vary for different metal-semiconductor combinations. It is a reasonable expectation that the barrier heights are determined by a linear combination of mechanisms, including those discussed above, and it is the coefficients associated with each term or mechanism that experimentalists should strive to establish. Indeed the relative importance or weighting of the different models will depend on exactly how the contact is processed and on the detailed nature of the interface. This is perhaps most vividly illustrated by the case of $NiSi_2$ contacts to silicon surfaces, where a slight rotation associated with the interface bonding appears to lead to a difference of about 0.15eV in Schottky barrier heights associated with type A and type B contacts[11].

The case of $NiSi_2$ on Si referred to above is arguably the most thoroughly investigated and best understood of all metal-semiconductor interfaces. Yet, the electrical barriers reported for nickel on n-silicon cover a range of 0.3 eV or so, and though the importance of interface bonding seems to be clear, it would be wrong to say that all processes influencing the barrier height at this interface are understood. The level of understanding for virtually all other metal-semiconductor combinations is significantly worse and there is a need to study in more detail the way different mechanisms contribute to barrier heights in a wider range of systems. In this paper we have chosen to follow this theme a little further by concentrating on two semiconductors, namely InP and CdTe, and two overlayer materials, Au and Sb. The aim is to show how barrier heights, and the balance of contributions from different mechanisms, are influenced by parameters such as the structure of the overlayer, and the nature of different surface treatment of the semiconductor. The paper considers atomically clean and chemically processed surfaces and the work reported is mostly based on investigations carried out by researchers in the author's laboratory.

A. ANTIMONY CONTACTS ON INDIUM PHOSPHIDE

2.1 CLEAN INDIUM PHOSPHIDE

Metal contacts to indium phosphide single crystals have been extensively investigated in the context of Schottky barrier formation[12,13]. For a wide range of metals on clean cleaved (110) GaAs surfaces the Fermi level is usually pinned at between 0.7 eV and 0.9 eV below the conduction band at the interface. For indium phosphide the barrier heights reported for the same range of metals show a greater variability and indeed the

literature is rather full of contradictory results even for a single metal-InP combination. One of the complicating problems is chemical reactions which tend to occur rather readily at indium phosphide interfaces[12]. To avoid these problems we have carried out extensive investigations of a non-reactive overlayer, namely antimony, on InP.

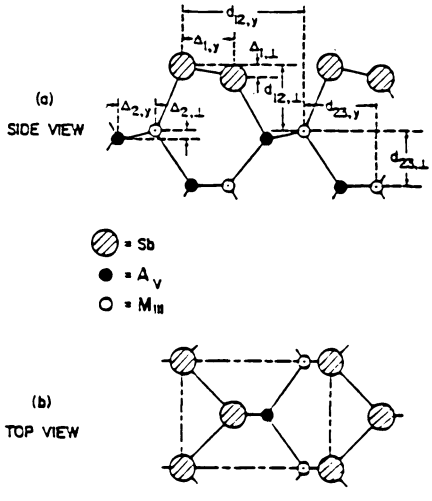

Figure 1: Proposed surface structure for one monolayer of antimony on the InP (110) surface.

It has previously been shown, first by Maani et al[14], that Sb forms an ordered monolayer when the appropriate number of atoms are incident on the clean cleaved InP(110) surface at room temperature. Using angle resolved photoelectron spectroscopy, occupied interface electron states were detected, and soft XPS investigations showed that Sb was adsorbed on two different sites on the InP surface. Duke, Kahn and co-workers[15] also investigated this system by LEED and arrived at the structural model shown in Figure 1 where Sb atoms form zig zag chains on the surface and are bonded to In and P sites. This structure also leads to an empty surface state located about 0.3 eV below the conduction band of InP[16]. Since such surface states are absent from the band gap of clean cleaved InP the adsorption of the Sb monolayer would be expected to lead to band bending on n-type crystals. This was indeed observed in the experiments of Maani et al[14].

However, transport investigations for thick Sb electrical contacts on n-InP demonstrate clearly that the contact is ohmic[17]. The I-V characteristic is shown in Figure 2 (a); here the resistance is bulk limited and any barrier height, if present, must be less than 0.3eV. In fact this is the best ohmic contact observed by our group for n-InP. To verify that the Fermi level is indeed located close to the conduction band the I-V characteristics of Sb contacts on clean cleaved p-InP have been

barrier one. This is in sharp contrast to the measurements for one monolayer where a barrier of around 0.4 eV is seen to develop[14].

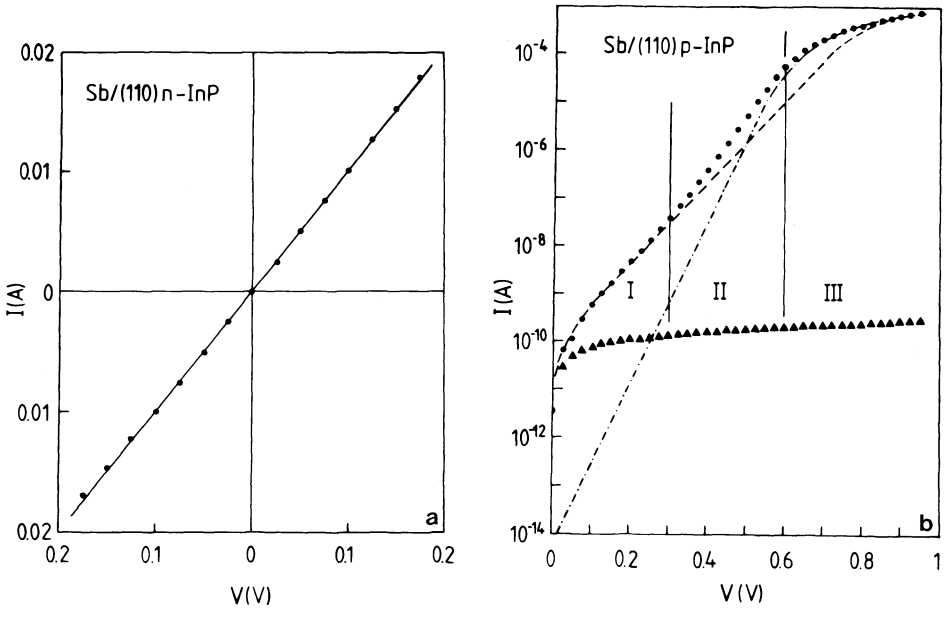

Figure 2: I-V measurements for an Sb contact on clean cleaved InP (110) surface. (a) n-type InP, (b) p-type InP. The back contact is ohmic in both cases.

This apparent transition in barrier height between thin and thick Sb overlayers on InP (110) has been studied further by Esser et al[17] using the powerful technique of electric field induced Raman spectroscopy. The band bending as a function of increasing overlayer thickness is shown in Figure 3(a); the method has the great advantage in that it can establish interface fields below overlayers several tens of Å in thickness. For n-type crystals the space charge field disappears at low coverages but is finite at a coverage of one or two monolayers, as deduced by soft XPS experiments. However, for coverages greater than about 10 ML the band bending disappears, entirely consistent with the finding of ohmic behaviour. Data for p-type crystals are also shown in Figure 3(b); here again an abrupt transition in behaviour is seen at about 10 ML coverage.

The Raman spectra produced by Esser et al[17,19] provide a further insight into the variation of barrier height with thickness for Sb on InP (110) surfaces. Figure 3(c) shows the Raman signature associated with the Sb overlayer. Initially, a small peak associated with ML adsorption (arrowed) is overtaken by a broad lineshape characteristic of amorphous Sb. For coverages in excess of 10 ML this is replaced by sharp peaks characteristic of crystalline Sb i.e. the amorphous overlayer crystallises beyond 10 ML, and it is at this point that the ohmic behaviour occurs for n-type crystals.

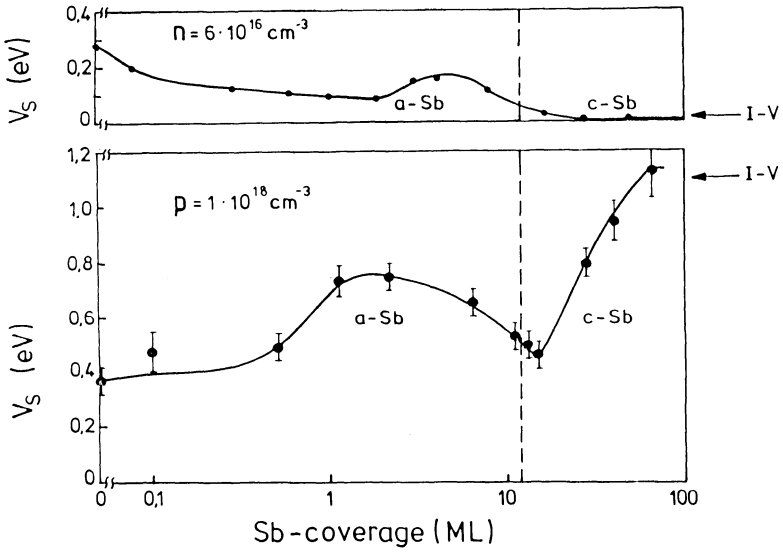

Figure 3 (a and b) Shift of the Fermi level at the surface when Sb is deposited on clean cleaved (110) InP n-type (a) and p-type (b) crystal, as determined by Raman spectroscopy.

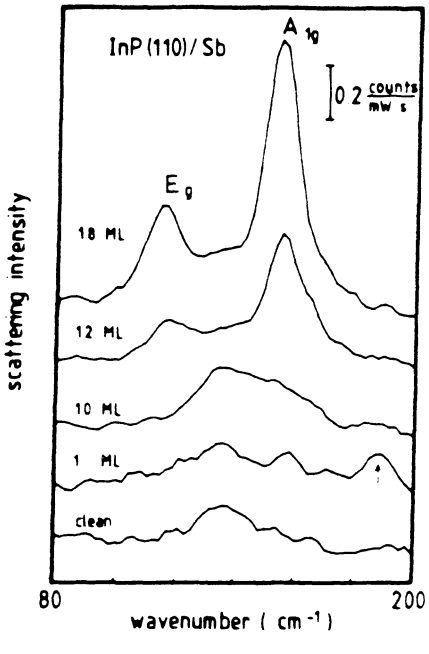

Figure 3 (c) Raman phonon spectra of Sb deposited on an InP (110) surface.

The dependence of electrical barrier height on the structure of the overlayer for Sb on InP is of particular interest, since it serves as an indicator of the applicability of various models. At first sight at least, it might be expected that the existence of metal induced gap states would be relatively uninfluenced by the ordering of the overlayer indicating that MIGS is not of primary concern in this case. The calculation of Tersoff[7] also predict a barrier height of close to 0.6 eV associated with MIGS. At least for thin coverages, the Sb overlayer does not appear to strongly dissociate the InP surface so that the influence of chemical reactions and anion rich regions is minimised. The possible effects of defects at the interface, however, cannot be eliminated. It is possible that some interface disruption takes place when the Sb overlayer thickness increases beyond 10 ML and indeed the influence of strain in the overlayer may be relevant. Unfortunately, it is not straightforward to establish the existence of interface defects when the overlayer thickness is beyond around 10 ML. It should also be remembered that the electronic structure of the overlayer will also change when its structure changes from amorphous to crystalline and at this stage it is not clear how this will influence Schottky barrier formation. In summary, therefore, though the exact mechanisms are not understood it is quite clear that electrical barrier heights at metal-semiconductor interfaces may be significantly influenced by the form of the overlayer forming the contact; this is illustrated particular clearly for Sb on InP.

2.2 OXIDISED INDIUM PHOSPHIDE

There has been some discussion in the literature regarding the way thin intermediate oxide layers influence barrier heights at metal - InP interfaces. Some workers have reported substantial effects[21] whereas others have reported minimal effects . To illustrate that major effects can occur we consider the case of Sb contacts on chemically etched n-InP crystals.

Figure 4 shows I - V characteristics for Sb contacts deposited on an InP surface chemically etched using a bromine in methanol solution followed by a water rinse[22]. The change from the ohmic behaviour associated with the clean surface is quite dramatic; in this case a barrier height of 0.7 - 0.8 eV is extropolated from the I - V measurements. XPS investigations of the chemically etched surface demonstrate that the oxide layer is extremely thin, only a few Å. The InP surface is relatively stoichiometric and there are small components of oxides of indium and of phosphorous detected in the XPS[22]. Clearly this thin intermediate layer of oxide serves to decouple the antimony from the indium phosphide surface, leading to remarkable difference in barrier height relative to that obtained for antimony on the clean surface. The detailed nature of the thin oxide layer, and the way it leads to these large effects, is at present being fully investigated.

3. METALS ON II - VI SEMICONDUCTORS: CdTe AND CdS

It has previously been reported that different metals lead to a wide range of barrier heights when deposited on clean CdTe and CdS crystals. The barriers range from ohmic to over 1 eV and attempts have been made to relate them to metal work functions and electronegativities according to a linear model[3]. Figure 5 shows barrier heights established by the I - V

technique for a range of metals on clean cleaved n-type CdTe and CdS crystals[23,25]. There are a number of important points that emerge from this data. First of all it is clear that the barrier heights do not vary in a linear fashion with metal work function. This situation also holds if metal electronegativities rather than work function are used. Precisely the same statement can be made for the case of metals on InP[12,13]. It is therefore important to repeat a point stressed by us previously[26], namely that there is little evidence that the linear model, in general,

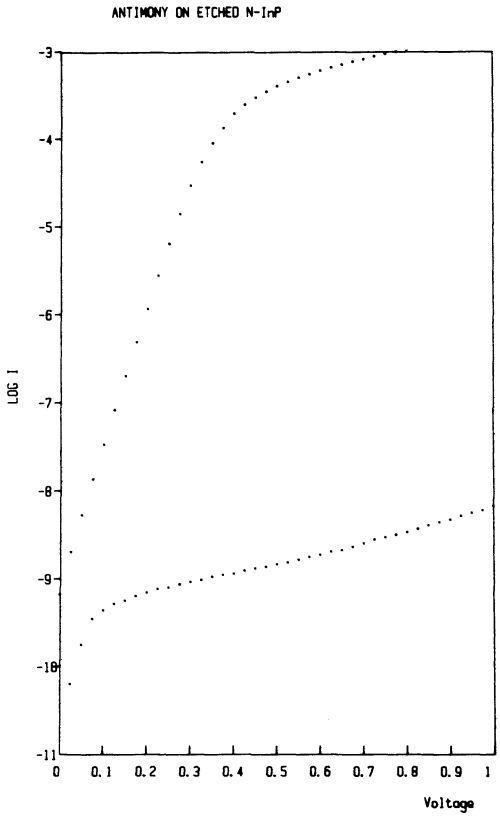

Figure 4: I-V curves for Sb contacts deposited on a chemically etched n-type InP crystal.

can be used to analyse data relating to Schottky barrier heights at metal semiconductor interfaces. The linear model is based on ther assumption of a constant distribution of interface states throughout the energy gap[27] which is clearly inapplicable for CdTe and CdS. It should be recalled that the existence of the so called covalent-ionic transition in Schottky barrier theory was based on the linear model; the existence of such a transition is clearly in doubt[28].

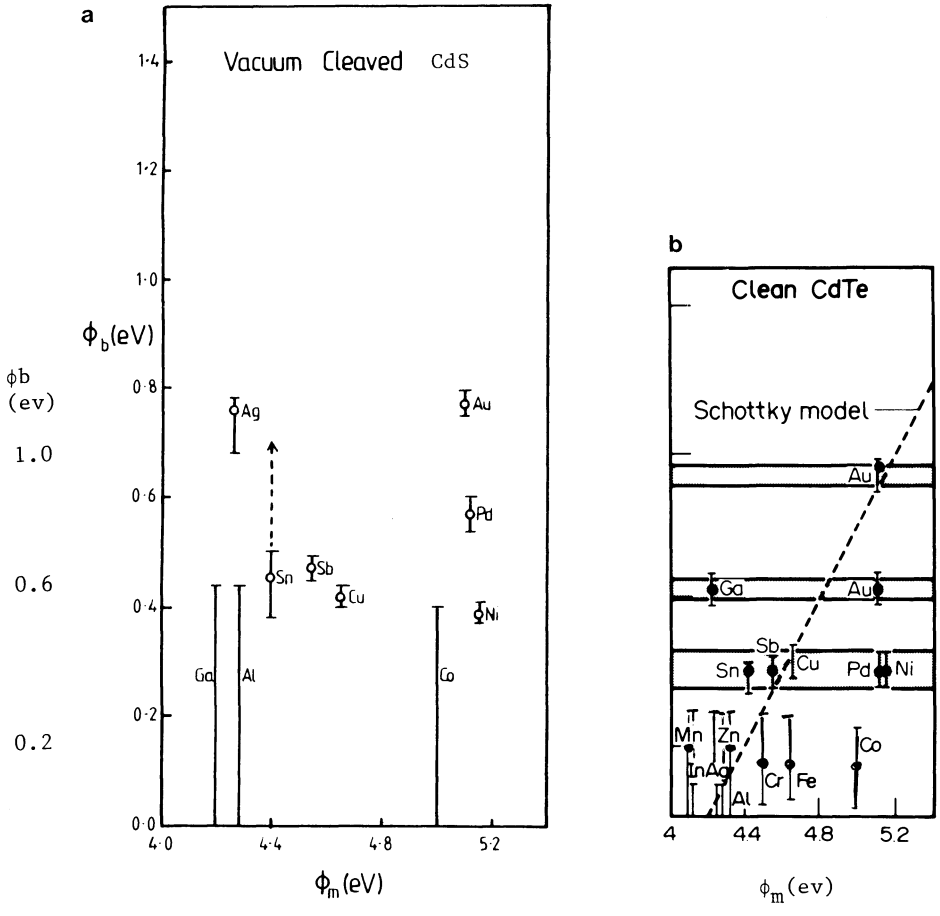

Figure 5: Barrier heights established for metals on clean CdTe and CdS cleaved surfaces, as measured by I-V methods.

A second important point to emerge from the data presented in Figure 5 relates to the reproducibility and the stability of the contacts. Many of the metals studied lead to barriers which change substantially with time and with increasing temperature (i.e. with annealing). Detailed investigations of a number of metals with clean CdS and CdTe have been carried out using XPS. A typical series of spectra for increasing thicknesses of cobalt on CdS is shown in Figure 6. Here the emission from the Cd 3d core level is clearly seen to split, indicating strong reactions at the interface. This splitting is not observed for overlayers such as Ag, Au and Sb on CdS. In general the reaction rates increase upon annealing, probably leading to the changes observed in barrier heights. A third important point is illustrated by reference to the experimental data for Au and Sb on n-CdTe surfaces. When diodes are made by depositing barrier contacts of Au under apparently identical conditions one sometimes observes barrier heights of 0.60 eV and at other times barriers 0.93 eV. The occurrence of two values of barrier height for a nominally identical preparation condition is puzzling and has been investigated further by changing the surface nature of CdTe surfaces by chemical means.

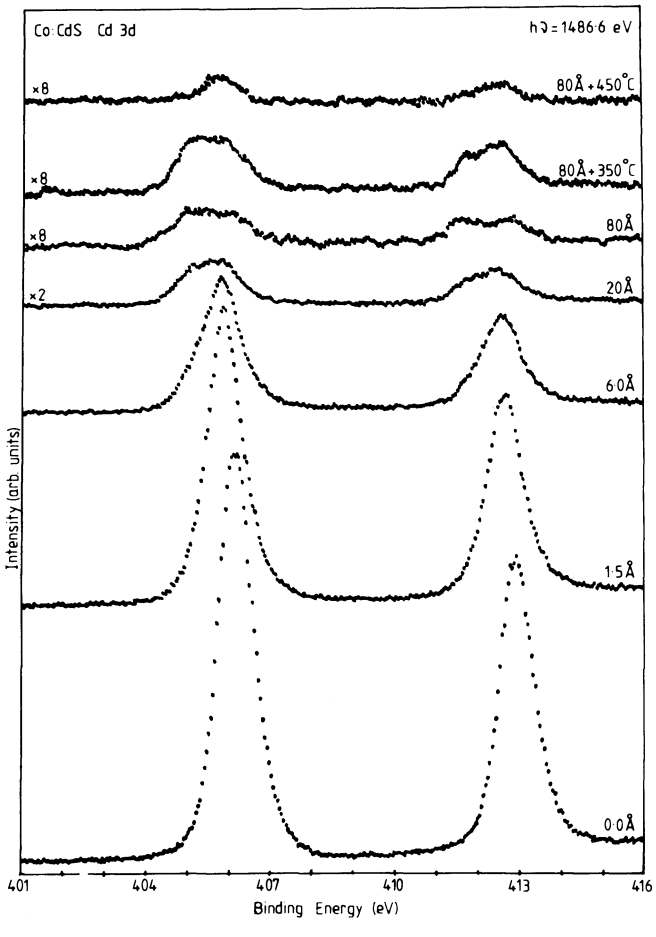

Figure 6: XPS plots of the Cd3d emission when thin Co layers are deposited on clean cleaved CdTe surfaces.

Figure 7 shows a plot of barrier height measured for a range of metals on n-CdTe crystals subjected to chemical etching in a bromine in methanol solution. Here again it is apparent that the etching treatment has led to dramatic changes of barrier heights for some metals but not for others. It has previously been shown[23,30] that many metals lead to complex reactions with the thin oxide on the CdTe surface. Here again it is clear that both Sb and Au lead to two values of barrier height, one of 0.74 eV and the other 0.93 eV. We now concentrate on the occurrence of these two valued barriers for Au and Sb on CdTe.

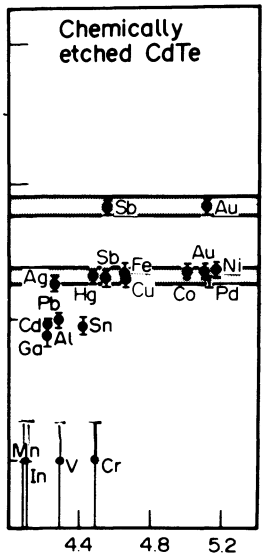

Figure 7: Schottky barrier heights measured by the I-V technique for metals on CdTe surfces chemically etched with a bromine-methonal solution.

Dharmadasa and co-workers[31] have subjected CdTe crystals to different chemical treatments before depositing Sb and Au contacts and measuring diode behaviour. They also probed the surface stoichiometry of the etched CdTe crystals using XPS. Figure 8 shows XPS spectra for three such treatments, bromine in methanol, bromine in methanol followed by hydrazene, and an oxidising plus reducing etch[31]. Comparison of the XPS peak areas with those for a clean cleaved stoichiometric surface demonstrates that the surface giving the spectrum shown in Figure 8 (a) is deficient in cadmium, whereas that of Figure 8 (c) is deficient in tellurium. Figure 9 shows I - V characteristics for Au and Sb contacts on chemically treated CdTe and clearly shows the two valued nature of the barrier heights. Upon depositing Au or Sb on surfaces characterised by the XPS spectrum of Figure 8 (a), both these I - V characteristics may be measured. However, deposition onto the tellurium deficient surface of Figure 8 (c) always yields barrier heights of 0.93 eV. Thus, a procedure has been found[31] for the reproducible generation of the highest of the two barriers. Dharmadasa et al[31] also showed that as the CdTe surface becomes less tellurium deficient the probability of the lower barrier occurring increased substantially.

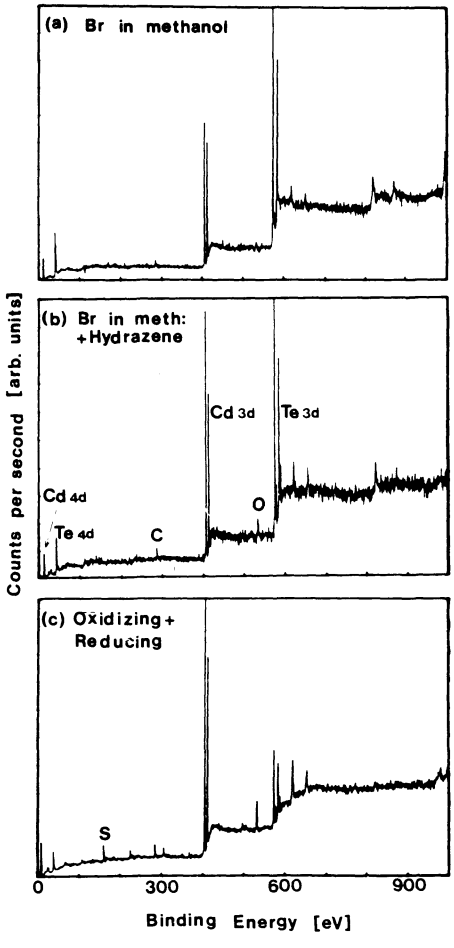

Figure 8: XPS spectra for a CdTe surface subjected to different chemical treatments.

The above example strongly suggests that the barrier heights for Sb and Au on CdTe are closely associated with the stoichiometry of the surface. It is tempting to suggest that the 0.93 eV barrier is associated with Fermi level pinning by tellurium deficiency, and indeed it has been previously suggested that tellurium vacancies form a band of deep levels at around 0.9 to 1.1 eV below the conduction band edge in CdTe[32], consistent with the possibility of pinning by tellurium vacancies in these experiments. It is also tempting to suggest that the 0.74 eV barriers are associated with Cd deficiency; again deep levels at 0.72 eV below the conduction band have previously been assigned to Cd vacancies[32]. However, this interpretation may well be too naive since gold is known to react to some extent with oxidised CdTe surfaces and the interface cocmposition may differ from that measured for the free surface. It could also be argued that the 0.72 eV barrier heights are associated with pinning by MIGS; this energy is very close to the 'mid-gap' energy calculated by Tersoff[7] for pinning by MIGS in CdTe. In this model, then, pinning by MIGS would dominate until the density of defects induced by tellurium deficiency becomes sufficient for the 0.93 eV level to dominate. Though one can only speculate about these possibilities at this stage it is certain, though, that two different values of barrier height may be observed for Au and Sb contacts depending

on exactly how the contact is made. This is a clear illustration of a situation where there is a close balance between different pinning mechanisms which themselves are process dependent. Here also it is relevant to refer to the work by Kuech[33] who made contacts to n-CdTe cleaved crystals using Cd, Au, and Au-Cd alloys. For the Au-Cd alloy contact a barrier height of 0.92 eV was consistently found whereas contacts with elemental gold and cadmium gave barriers of 0.65 eV and 0.42 eV respectively. It was suggested that the Cd in the Au overlayer for the alloy led to a change in the nature of the interface defects and that crystal defects play a key role in Schottky barrier formation. The work described in this paper fully supports that view.

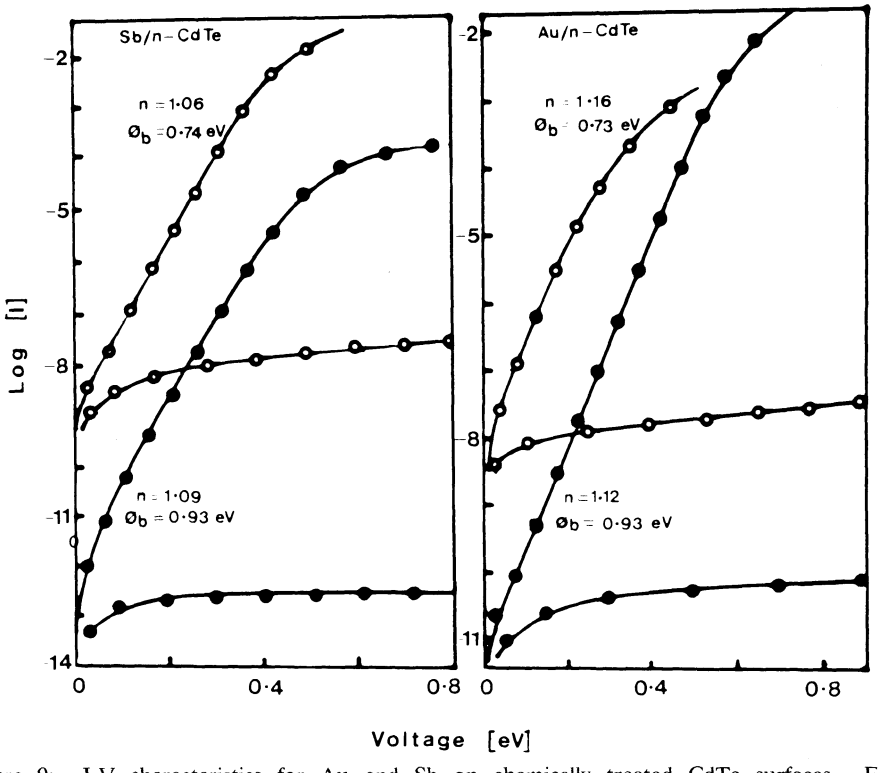

Figure 9: I-V characteristics for Au and Sb on chemically treated CdTe surfaces. Forward and reverse currents are shown.

CONCLUSIONS

In the past a number of different mechanisms and models have been proposed to account for electrical barrier formation at metal-semiconductor interfaces. In addition many of the experimental data have been interpreted in terms of a linear model where barrier heights vary linearly with metal work function or electronegativity for a given semiconductor. In this paper it is emphasized yet again that the use of this linear model, in general, is highly suspect and does not appear to be applicable

for metals on CdS, CdTe and InP. In this paper we have considered further certain factors which have a substantial influence on Schottky barrier formation, and chosen to illustrate these by reference to Sb on InP and Au and Sb on CdS and CdTe. Dramatic effects are observed which appear related to the structure of the overlayer for Sb on InP and large changes are associated with thin intermediate oxide layers at the interface. For Au and Sb on n-CdTe it is shown that two values of barrier height may be obtained and that the occurrence of one or the other of these is related to the form of the CdTe surface before the contact is deposited. The data suggest that Schottky barrier formation, in general, is associated with contributions from several mechanisms and the relative importance of each may be significantly influenced by the detailed nature of the interface and the way it is made. To expect one single model or mechanism to account for the values of electrical barrier height in all metal-semiconductor combinations is very clearly too simplistic a view, when most interfaces are not perfectly ordered, abrupt, or free of chemical reactions.

ACKNOWLEDGEMENTS

The author wishes to thank numerous people in Cardiff who have contributed to this work. In particular, Dr I.M. Dharmadasa, Dr Z. Sobiesierski, Mr D Zahn, Miss N Forsyth and Mr S Wilks have been responsible for generating much of the data which has been, or will be, published in full by them.

REFERENCES

1. R.H. Williams Chap 1 in The Chemical Physics of Solid Surfaces and Heterogeneous Catalysis -Electronic Materials (Elsvier, 1988, ed. D.A. King and D.P. Woodruff)

2. R Ludeke and G. Landgren J. Vac. Sci. Technol. 119. 667 (1981)

3. S.G. Kurtin, T.C. McGill and C.A. Mead Phys. Rev. Letts. 22 1433 (1969)

4. W.E. Spicer, I. Lindau, P.R. Skeath, C.Y. Su and P.W. Chye Phys. Rev. Letts. 44 420 (1980)

5. H. Hasegawa and H. Ohno J. Vac. Sci. Tech B4, 1130, (1986)

6. C. Tejedor, F. Flores and E. Louis J Phys C 10 2163 (1977)

7. J.Tersoff J. Vac. Sci. Tech. B4 1066 (1986)

8. J.L. Freeouf and J.M. Woodall Appl.Phys.Letts. 39 727 (1981)

9. R.H Williams Surface Science 132 122 (1983)

10. W. Monch J. Vac Sci Tech B4 1085 (1986)

11. R.T. Tung Phys. Rev. Letts. 52 461 (1984)

12. R.H.Williams, A. McKinley, G.J. Hughes, V. Montgomery & I.T. McGovern J. Vac. Sci. Tech. 21, 594 (1982)

13. N. Newman, T. Kendelewicz, L. Bowman and W.E.Spicer Appl. Phys. Letts. 46 1176 (1985)

14. C. Maani, A. McKinley and R.H. Williams J. Phys. C. 18. 4975 (1985)

15. C.B. Duke, C. Mailhiot, A. Paton, K.Li, C. Bonapeace and A. Kahn Surface Sci 163 391 (1985)

16. C. Mailhiot, C.B. Duke and D.J. Chadi Phys. Rev. Letts. 53 2114 (1985)

17. N. Esser, H. Munder, M. Hunermann, W. Pletschen, W. Richter and D.R.T. Zahn J. Vac. Sci.. Tech. B5 1044 (1987)

18. D.R.T. Zahn, A.B. McLean, R.H. Williams, N. Esser and W. Richter. Appl. Phys. Letts, 52, (1988) 739.

19. N. Esser, U. Resch, U. Rettweiler, W Richter, D.R.T. Zahn and R.H. Williams, Vacuum 38, (1988) 229.

20. N. Newman, W.E. Spicer, T. Kendelewicz and I. Lindau J. Vac. Sci. Tech. B4 931 (1986)

21. R.H. Williams, V. Montgomery, R.R. Varma and A. McKinley J. Phys. D, 19, L253 (1977)

22. S. Wilks and I.M. Dharmadasa - private communication - to be published.

23. I.M. Dharmadasa, W.G. Herrenden-Harker and R.H. Williams Appl. Phys. Letts. 48 1082 (1986)

24. R.H. Williams and M.H. Patterson Appl. Phys. Letts. 40. 484 (1981)

25. N. Forsyth, I.M.Dharmadasa, Z. Sobiesierski and R.H. Williams to be published.

26. R.H. Williams in Chapter 1 of 'Physics and Chemistry of III - V Compound Semiconductor Interfaces' (Plenum 1985 ed C.W. Wilmsen)

27. E.H. Rhoderick and R.H. Williams 'Metal-Semiconductor Contacts' Oxford University Press, 1988

28. M. Schluter Phys. Rev. B 17 5044 (1978)

29. Z Sobiesierski,. I.M. Dharmadasa, N. Forsyth and R.H. Williams to be published

30. N. Forsyth, I.M. Dharmadsaa, Z. Sobiesierski amnd R.H. Williams to be published

31. I.M. Dharmadasa, J.H. Thornton and R.H. Williams Appl. Phys.Letts. in press.

32. K. Zanio 'Semiconductors and Semimetals - Cadmium Telluride' Vol 13 (Academic Press) p. 160 and 162 (1978)

33. T.F. Kuech J. Appl. Phys. 52 4874 (1981)

DEEP LEVELS AND BAND BENDING AT METAL-SEMICONDUCTOR INTERFACES

L.J.Brillson

Xerox Webster Research Center
Webster , NY 14580

P. Chiaradia

Istituto Struttura Materia of CNR 38
Via E. Fermi, Frascati, 00044, Italy

Introduction

Over the past several decades, a common theme of metal-semiconductor interface studies has been the insensitivity of semiconductor band bending to the properties of different metal overlayers and the physical mechanisms responsible for this Fermi level "pinning". Hampering efforts to identify the nature of charge transfer at these electronic junctions has been the narrow ranges of reported Fermi stabilization energies themselves, which permit a number of quite dissimilar explanations. Furthermore, evidence for charge states at metal-semiconductor junctions has been indirect for the most part, relying heavily on electrostatic measurements. Experimental and theoretical work over the last few years has contributed new information which challenges the commonly accepted view of semiconductor contact rectification. First of all, experimental evidence now exists to show that semiconductors, even those previously thought to be strongly "pinned", exhibit wide ranges of Fermi level stabilization with different metal overlayers. Secondly, it is now possible to observe interface states directly by optical techniques and to demonstrate their direct relationship to Fermi level stabilization at the microscopic electronic junction. Furthermore, these states confirm the predictions of a microscopic electrostatic model for the detailed band bending measurements over wide energy ranges. Recent developments have also highlighted the importance of surface processing and bulk crystal quality in terms of the deep levels formed and their subsequent role in rectification at less than-ideal interfaces. In

contrast, experiments performed at low temperature on high quality interfaces permit a closer approach to ideal chemical junctions and a striking contrast with more conventional measurements of the same systems. Given the much wider array of band bending and deep level information now available, it is now possible to draw sharp distinctions between many of the various models which have been advanced to describe the charge transfer between metals and semiconductors. What emerges is a picture similar to that advanced fifty years ago by Schottky in terms of macroscopic electrostatic parameters, but complicated by the formation of chemically-induced native defects and interfacial phases.

Band Bending and Interface States: Historical

Two basic elements of contact rectification at metal-semiconductor interfaces are 1) the physical nature of the electronic states at the interface and 2) the relative magnitudes of the interface and surface space charge dipoles which together comprise the potential difference between the initial interface components. Dipoles form at free semiconductor and metal surfaces due to the charge distributions which extend into vacuum. A new dipole forms at the metal-semiconductor junction which can involve tunneling as well as discrete localized charge states. The latter can be due to: changes in semiconductor lattice bonding, adsorbate-semiconductor bonding, surface defects, bulk defects segregated to the surface, native defects induced by a metal-semiconductor reaction or diffusion, impurities, extended lattice imperfections, as well as new interface chemical phases. There is now extensive evidence[1-3] to show that metals and semiconductors can interact strongly, thereby giving rise to one or more of these extrinsic interface state phenomena.

The charge in the interface states will determine the magnitude of the interface dipole and thereby the portion of the junction electrostatic potential difference which falls across the semiconductor's band bending region. For tunneling states, the magnitude of the dipoles and their change upon junction formation can be determined via a variety of microscopic model calculations. However, the results depend sensitively upon the detailed boundary conditions chosen, which can produce completely disparate conclusions. For example, the boundary condition of a relatively constant barrier height itself necessitates a large interface dipole for tunneling calculations involving a charge neutrality level.[3-5] Calculations which model the metal electronic density as "jellium" and impose bulk lattice properties at the interface also obtain large interface dipoles which dominate the charge transfer.[6,7] Here the total voltage change is required to occur completely at the microscopic junction. In contrast, a

microscopic model which allows a self-consistent "jellium" density and a voltage split into long- and short-range components obtains relatively small changes in dipole strength before and after contact.[8,9] This last result implies that the difference between the observable metal work function and semiconductor electron affinity, e.g., the "Schottky barrier",[10] provides a good approximation to the interface barrier height. In fact, the accuracy of such calculations as well as the overall importance of electronic *vs.* atomic relaxations at the metal-semiconductor interface can now be judged on the basis of experiment.

Wide Range of Band Bending

Over the past three years, soft x-ray photoemission spectroscopy (SXPS) and electrical measurements have revealed far wider ranges of band bending for metals on III-V compound semiconductors than had hitherto been believed possible. Figure 1 illustrates the range of barrier heights for metals on clean, ordered $In_xGa_{1-x}As$ (100) ($0 \leq x \leq 1$) surfaces prepared by molecular beam epitaxy (MBE) and thermal desorption of a protective As cap.[11,12] These surfaces are characterized by sharp valence band features which, for the binary compounds, closely resemble the analogous spectral features for high-quality, cleaved (110) surfaces. The data points shown span ranges of 0.6 - 0.7 eV for each of the pseudobinary alloys studied. In the case of InAs, the Fermi level (E_f) stabilization energies extend across the entire band gap. Furthermore, the trend of these Fermi levels for a given metal across the pseudobinary alloy series is contrary to that predicted by various defect calculations, for which the energy levels parallel the valence rather than the conduction band. Likewise, the trend of the Au barriers differs substantially from that measured for air-exposed pseudobinary alloys. We have in fact reproduced representative portions of these earlier results by intentionally exposing our specimens to air.

Interestingly, the energy trends for $In_xGa_{1-x}As$ ($x>0$) suggest that the chemical composition of the interface plays a role in determining the Fermi stabilization energy. The heavy dashed lines in Fig. 1 follow the Au data points between Φ_{As} and Φ_{Au} and the In and Ga data between Φ_{Au} and $\Phi_{In,Ga,Al}$. SXPS measurements of anion and cation core level intensities confirm the As-rich nature of the In and Al interfaces with InAs relative to GaAs and the As-deficient nature of the Au interface with InAs relative to GaAs. Our measurements for metals on GaAs[13,14] in fact suggest that the completeness of As decapping can affect the E_f stabilization energy. Such process variations may well extend the range of energies for the ternary alloys even further.

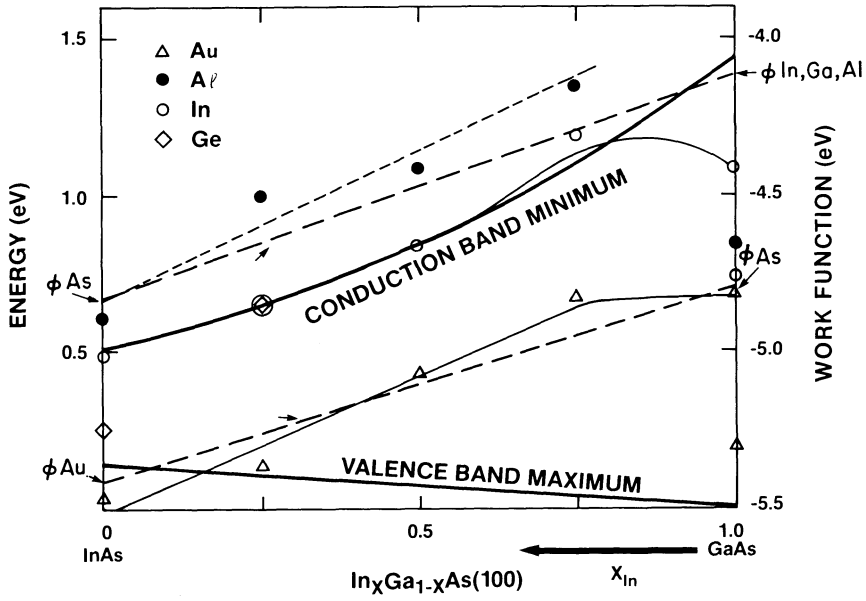

Fig. 1. Fermi level stabilization positions for metals on clean, MBE-grown $In_xGa_{1-x}As$ (100) ($0 \leq x \leq 1$) surfaces with respect to the semiconductor conduction and valence band edges.The energy ranges for metals on a given semiconductor span a wide energy range. After Ref. 12.

The Fermi level movements induced by metal deposition on MBE-grown GaAs(100) surfaces are in striking contrast to earlier studies for melt-grown GaAs(110) surfaces using similar measurement techniques.[15,16] Figure 2 shows that various common metals produce a range of 0.7 eV or more,[13,14] as opposed to the 0.2 - 0.3 eV reported for the cleaved material. Also different is the fact that the same metal on n-type and p-type GaAs (100) stabilizes the Fermi level at the same energy in the band gap, whereas a gap of 0.2 eV or more has been reported for a number of metals on GaAs (110).[15,16] Finally, the stabilization of the Fermi level on the MBE-grown GaAs (100) surface occurs over metal coverages of several monolayers or more, depending on the particular metal, in contrast to the submonolayer stabilization often reported for the cleaved GaAs (110) surface.[15,16] These qualitative differences and the expanded range of E_f behavior now demonstrated for the MBE-grown GaAs (100) surfaces contradict the common assumption that adsorbates on GaAs "pin" the Fermi level in a narrow range of energies. Reasons for this marked improvement in barrier behavior follow in subsequent sections.

Figure 3 illustrates the contrast in barrier height behavior for MBE-grown (100) vs. melt-grown (110) GaAs surfaces as a function of metal work function.[14] Here the Fermi energies are plotted on an absolute scale (left side) with respect

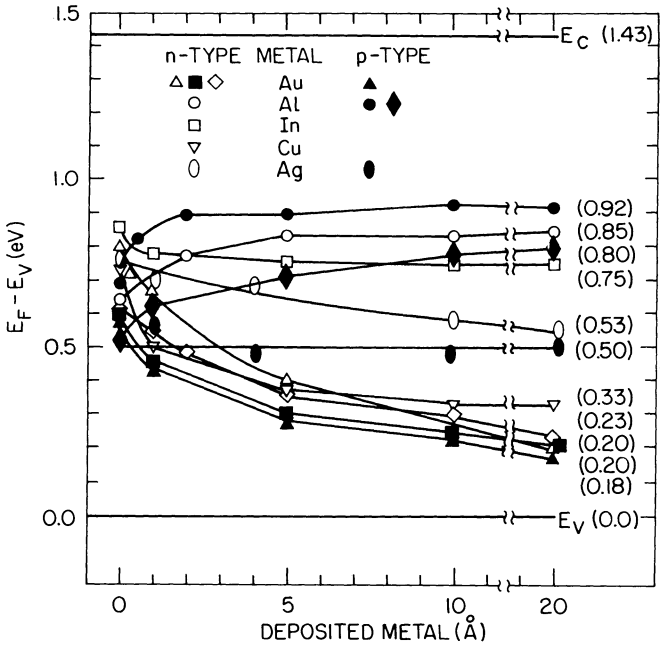

Fig. 2. Fermi level movements for metals on clean, MBE-grown GaAs (100) surfaces as a function of metal coverage. A wide energy range of stabilization values evolve over multilayer coverages with n-and p-type results coinciding. After Ref. 13.

to the vacuum level (see inset) as well as with respect to the conduction band edge (right side). For a wide range of common metals, the Fermi level is constrained to the narrow range of energies indicated by the dashed lines for melt-grown GaAs (100) surfaces. For MBE-grown GaAs (100), the metals In, Al, Ag, Cu, and Au stabilize E_f over a much wider range which encompasses the GaAs (110) range and which extends to within 0.2 eV of the valence band edge. Despite this wider range however, the functional dependence of the MBE-grown GaAs (100) data still deviates from ideal Schottky behavior, which is represented by the diagonal, dashed line extending from the lower left to the upper right corner.

In order to describe the interface charge states responsible for the barrier dependence in Fig. 3, we have employed the self-consistent electrostatic analysis developed by Duke and Mailhiot.[8,9] Here one assumes charged states as a consequence of atomic relaxations and/or chemical reactions without necessarily assigning a microscopic nature and origin.This calculational method takes both the local dipoles as well as the band bending across the surface space charge region into account explicitly and yields barrier height *vs.* metal work function

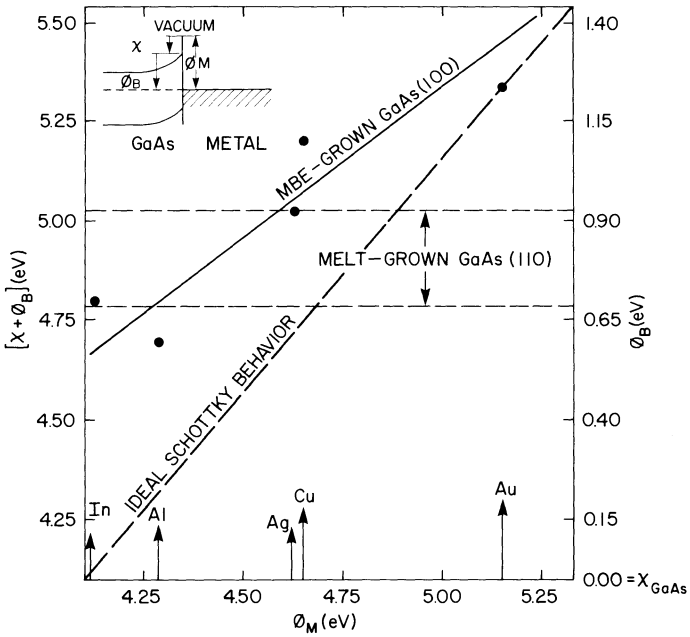

Fig. 3. Barrier heights and energies relative to ideal Schottky behavior plotted vs. metal work function. The inset illustrates the macroscopic parameters and the Schottky condition. Barrier heights for MBE-grown GaAs(100) surfaces span an energy range which extends beyond that of cleaved, melt-grown GaAs (110) surfaces. After Ref. 14.

curves whose detailed features are sensitive to the energy levels, surface densities, and donor / acceptor nature of the interface charge states. Indeed the shapes of these curves provide a characteristic "fingerprint" of a specific set of interface charge centers.

For the data in Fig. 3, a good fit is obtained using only a single acceptor level located 0.2 eV above the valence band edge (E_{VBM}) with a surface density of 3.1 x 10^{13} cm^{-2}. [14] However, when metals such as Sm and Yb are included, this analysis must be extended. Figure 4 illustrates the n-type barrier heights for all metals we have studied to date on MBE-grown GaAs (100) surfaces.[17] In contrast to the metals shown in Fig. 3, the Sm and Yb data suggest a minimum $\Phi^n{}_B$ above 0.5 eV. This necessitates the introduction of a second acceptor level located 0.8 eV above E_{VBM}. (In general, the choice of energy levels depends sensitively on the data, the densities less so. For the data shown in Fig. 4, the choice of energy and density for one level has little effect on the fit near the other level, suggesting that the two do not arise by the same physical mechanism.) In contrast to the data for Au, Cu, Ag, In, and Al, which conform to

a single acceptor level of constant density, the data for the more reactive metals offer no unique fit by curves of various 0.8 eV acceptor level densities. These features are represented in Fig. 4 by the family of curves for the same 0.2 eV and different 0.8 eV acceptor level densities which overlap for the higher work function metals. It is evident that densities of 10^{14} cm^{-2} or more are required to fit the Sm and Yb data points, as opposed to the 10^{13} cm^{-2} or less required for the In and Al data points in the same Φn_B energy range. This contrast in behavior between the low and high work function metals suggests that the 0.8 eV acceptor level density is sensitive to the particular metal -GaAs interaction. This is consistent with the fact that pronounced chemical reaction and diffusion occur for the low work function metals, particularly so for Sm and Yb. Interestingly, the lower apparent density of 0.8 eV acceptors needed to fit the Al point agrees with the lower chemical disruption expected since Al can grow epitaxially on GaAs (100) surfaces.[18]

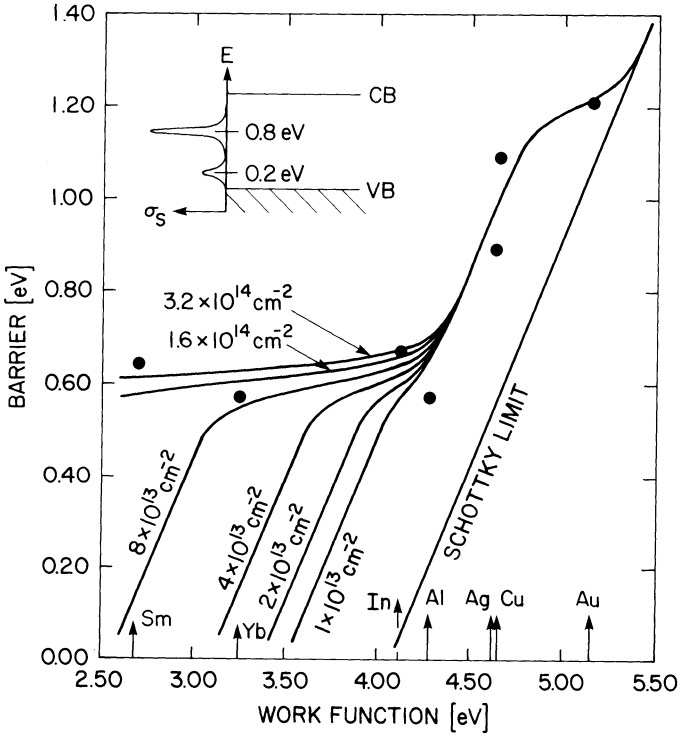

Fig. 4. Self-consistent electrostatic modelling of the charge states required to account for the SXPS-measured barrier heights on the metal work function. For metals on clean, MBE-grown GaAs (100) surfaces, an acceptor at E_{VBM} + 0.2 eV with density 3.1 x 10^{13} cm^{-2} and an acceptor at E_{VBM} + 0.8 eV with metal-dependent density fit the data points. CLS measurements confirm the existence of these levels. After Ref. 39.

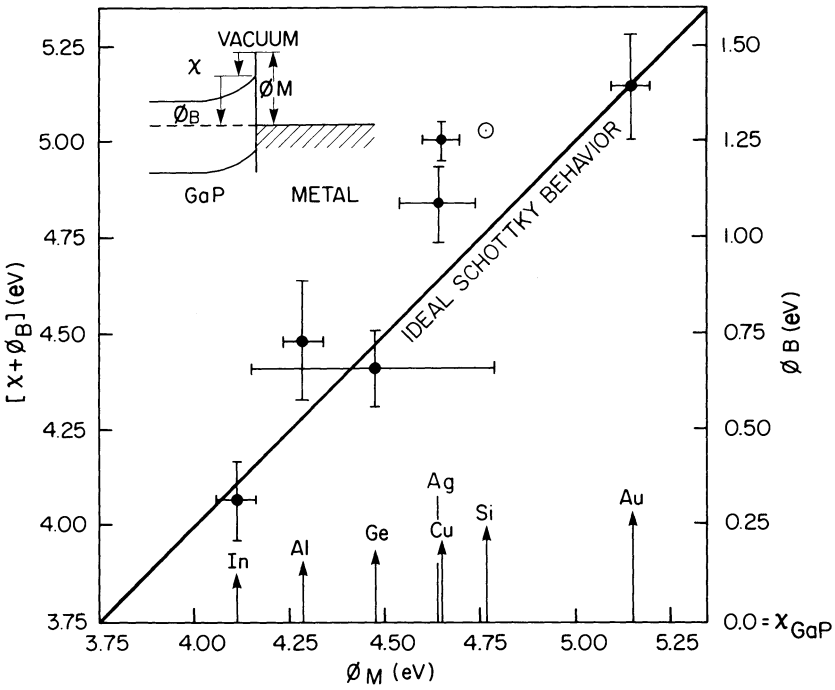

Fig. 5. Barrier heights and energies relative to ideal Schottky behavior plotted vs. metal work function. Barrier heights for UHV-cleaved GaP (110) span a 1.1 eV range and match closely with the ideal Schottky line. After Refs. 19-21.

Results of the self-consistent electrostatic analysis described in Fig. 4 account for the SXPS barrier height data in terms of a low acceptor density at 0.2 eV above E_{VBM} and a metal-dependent acceptor density at 0.8 eV above E_{VBM}. In a subsequent section, we will present optical evidence for the existence of these discrete levels and will show that the the density of the 0.8 eV feature is in fact sensitive to the chemical interaction between the metal and the semiconductor substrate.

Perhaps the most dramatic example of "unpinned" band bending is shown in Fig. 5 for metals on cleaved GaP (110) surfaces. Here the range of barrier heights extends over 1.1 eV and closely follows the diagonal line of ideal Schottky behavior, that is, $\Phi n_B = \Phi_M - X_{SC}$.[19-21] This agreement is particularly significant, given the absolute scale of the plot and the fact that there are no adjustable parameters. Furthermore, the only significant deviations from ideal behavior occur for Cu and Al, metals observed to have pronounced interface chemical reactions. Indeed, both metals produce an accumulation of As near the interface, and an increase of metal work function toward that of As[22,23] serves to move these data points toward the line of ideal behavior. The data set in Fig. 5 represents SXPS work performed both in the United States and Italy. Besides

displaying internal consistency, it provides an existence proof that near-ideal Schottky barrier formation can be achieved.

Besides InAs (100), $In_{0.25}Ga_{0.75}As$ (100), $In_{0.5}Ga_{0.5}As$ (100), $In_{0.25}Ga_{0.75}As$ (100), GaAs (100), and GaP (110), SXPS measurements reveal wide ranges of E_f stabilization for InAs (110)[11] and, most recently, InP (110) surfaces.[24] Added to this are the results obtained by photoelectrochemical etching[25] or Na_2S passivation,[26] which appear to "unpin" the Fermi level of GaAs as well. Of the remaining III-V compounds, there is insufficient data for GaSb, InSb or the Al compounds. Only the cleaved GaAs (110) surface, which has been studied extensively, appears to show pronounced evidence of Fermi level "pinning". Reasons for the behavior of these GaAs (110) surfaces are discussed in a following section. Overall, the measurements of band bending over the last three years for high-quality clean interfaces demonstrate that Fermi level "pinning" is not characteristic of metal/III-V compound semiconductor junctions.

Direct Observation of Interface States

The wide range of band bending observed for compound semiconductors demonstrates the sensitivity of interface charge exchange to the properties of the metal. However, a number of physical mechanisms can contribute to this metal-dependent charge transfer, particularly since both the band bending and any chemical interactions can evolve over multiple metal overlayers. In order to link the electrostatic behavior of these interfaces with their microscopic electronic structure, we have performed direct observations of metal-semiconductor interface states using low energy cathodoluminescence spectroscopy (CLS).[27, 28] The CLS technique involves incident electrons of energy ~500 -5000 eV, which excite electron-hole pairs within the near-interface region of the semiconductor, giving rise to luminescence associated with band-to-band, impurity level, native defect, or new compound transitions. As shown in Fig. 6, the CLS technique provides direct evidence for sub-band gap transitions involving discrete energy levels induced by metallization. For Au on UHV-cleaved InP (110) surfaces (Fig. 6a), two emission peaks appear near 0.8 and 1.0 eV which evolve in energy and intensity with metal coverage.[29] By varying the surface sensitivity of the CLS technique as a function of incident electron beam energy, one can establish that these feature are in fact localized near the metal-semiconductor interface. Furthermore, the gradual disappearance of the band-to-band luminescence at 1.35 eV signals a large increase in band bending within the surface space charge region since the associated electric field serves to decrease free carrier recombination. Figures 6a-d illustrate that the energies, densities, band bending,and their rate of evolution with overlayer coverage depend sensitively upon the particular metal. Furthermore, the energies of

these emission features correlate with the E_f stabilization energies observed by SXPS measurements.[30] Even the metal coverages over which these Fermi levels reach their final position agree in detail with the SXPS results.[30]

CLS measurements of MBE-grown GaAs (100) surfaces and interfaces reveal the presence of discrete states within the band gap as well. Figure 7a illustrates the emission for a GaAs (100) surface prior to decapping of the protective As layer.[31] A relatively broad emission structure is evident at sub-band gap

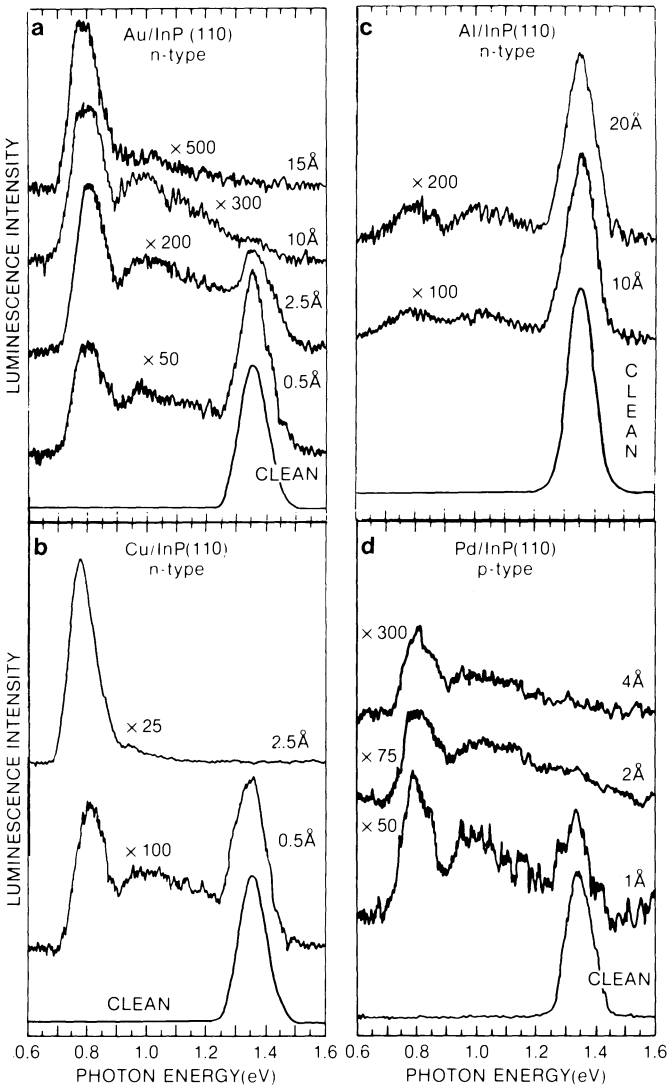

Fig. 6. Cathodoluminescence spectra for metals on UHV-cleaved InP (110) surfaces. Discrete, metal-dependent interface states features evolve with multilayer coverages to energies consistent with the stabilized Fermi level. After Ref. 29.

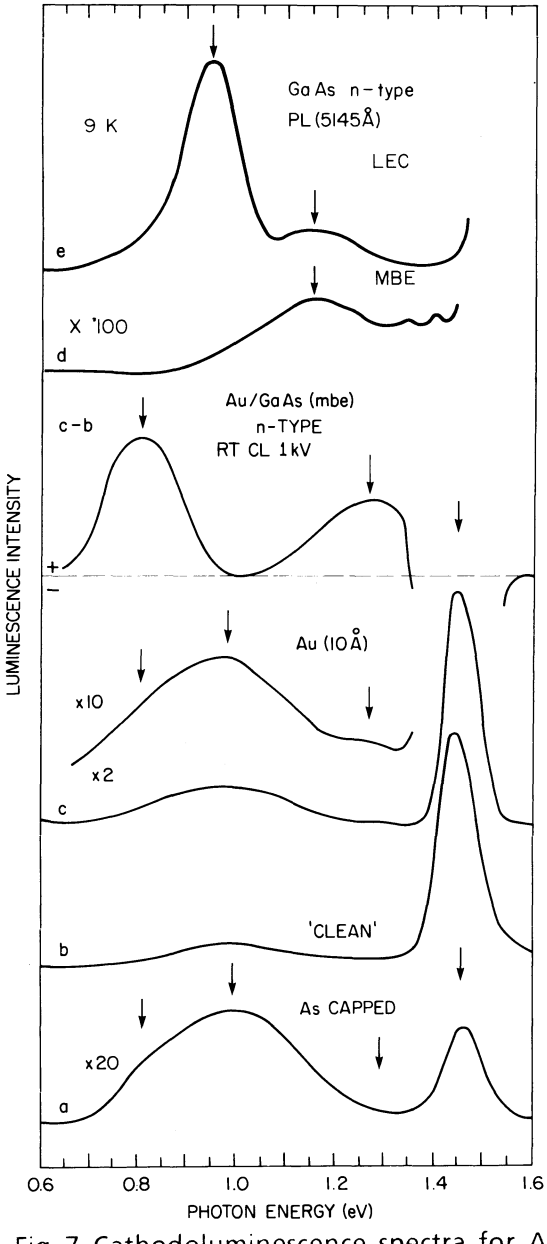

Fig. 7. Cathodoluminescence spectra for As-capped, thermally-decapped, and Au-covered GaAs (100) surfaces. Both As and metal produce additional, discrete features. The metal-derived features confirm the self-consistent electrostatic calculations in Fig. 4. After Ref. 31.

energies, in addition to the band edge emission at 1.45 eV. Upon thermal desorption (Fig. 7b), the low energy shoulder at 0.8 eV disappears and the band edge emission increases substantially. Figures 7a and 7b indicate that the MBE-grown GaAs contains a relatively small density of bulk defects, which are not removed by thermal decapping of the As overlayer. The disappearance of the 0.8 eV shoulder suggests that the As cap produces a discrete state near mid-gap, near the "pinning" position of melt-grown GaAs (110) surfaces as well as near the Fermi level expected for bulk As.

Deposition of a 10Å Au layer on this clean GaAs (100) surface produces new emission below the band edge as well as decreasing the intensity of band edge emission (e.g., increasing the band bending). The difference spectrum 7c-b reveals two new emission features at 0.8 and 1.25 eV. For n-type band bending, the most probable recombination channels involve transitions from mid-gap to the valence band and from the conduction band to a shallow acceptor respectively.[28,29] With these band edge assignments, the CLS peak features indicate discrete gap states located 0.8 eV and 0.18 eV above the valence band. The energies of these states are in excellent agreement with the predictions of the self-consistent electrostatic analysis discussed in Fig. 4.

The correspondence between the 0.8 eV features induced by both As and Au overlayers suggests that this metal-semiconductor interface level may be related to a local As excess. For Al on a similar GaAs (100) surface, the analogous difference spectrum yields the same two peak features, but with a significant reduction in the 0.8 eV peak amplitude.[31] Furthermore, when this Al interface is annealed, the 0.8 eV peak decreases further. Since Al bonds strongly with As and annealing promotes this reaction even more, the continued decrease in the 0.8 eV emission intensity with Al metallization and then annealing is consistent with an As scavenging process. More generally, these results show that the same two discrete levels are present for both Au and Al metals and that the 0.8 eV level is sensitive to the chemical interaction between metal and GaAs, just as was inferred from Fig. 4.

CLS emission from melt-grown GaAs (110) surfaces and interfaces differ both in magnitude and nature from those of MBE-grown GaAs (100). UHV-cleaved surfaces exhibit a higher emission intensity from bulk states, and metals on this surface result in higher intensities of interface state emission.[31] Furthermore, metals produce an additional intense emission which peaks beyond the cutoff of the CLS (Ge) detector, at 0.6 -0.7 eV.[31]

In addition to surface and interface state differences, photoluminescence spectroscopy (PLS) of these two GaAs materials reveal major differences in their

bulk states. Figure 7d and e show that deep level emission from native defects are two to three orders of magnitude more intense for liquid-encapsulated Czochralski (LEC) than for MBE-grown crystals.[31] Furthermore, the LEC GaAs exhibits emission from states located closer to mid-gap, where E_f "pinning" takes place. Corrected for the low temperature increase in the band gap, this lower energy emission would lie at 0.85 eV at room temperature, near the 0.8 eV energy discussed already for the As and metal-dependent peak features. Thus, there are ample electronic features detected by optical techniques to account for the pronounced differences in MBE-grown GaAs (100) vs. melt-grown GaAs (110) barrier formation.

Interface and Native Deep Levels

There is now considerable evidence to suggest that native deep levels, present in the semiconductor bulk or modified upon surface metallization, can play a role in the interface charge transfer. Besides GaAs, CdTe provides an excellent example of this extrinsic phenomena. Compared with MBE-GaAs, CdTe has a relatively high density of bulk traps deep within its 1.55 eV band gap.[32,33] PL spectra reveal a number of deep level emission features whose energies and relative intensities depend on the growth technique and subsequent processing. SXPS measurements of band bending with metal deposition show E_f movements from energy to energy, corresponding to the positions of these deep levels. For example, a 20Å Au deposition on a UHV-cleaved, n-type CdTe (110) surface moves E_f to 0.5 eV above E_{VBM}, consistent with a Schottky barrier $\Phi n_B = \Phi_{Au} - X_{CdTe}$. However, with aging in UHV and subsequent laser annealing, E_f moves back toward the conduction band and stabilizes at E_{VBM} + 1.5 eV, nearly coincident with a deep level at E_{VBM} + 1.55 eV, whose emission dominates all radiative recombination.[33] Associated with this E_f movement is a pronounced anion-rich outdiffusion of both semiconductor constituents into the metal overlayer. Similarly, laser annealing of In / p-CdTe (110) interfaces promotes several stages of chemical reaction, characterized by well-defined chemical shifts of the cation core levels, and a discontinuous movement of E_f from E_{VBM} + 0.5 eV in three stages to E_{VBM} + 1.55 eV - a movement of over 1 eV. Here, the energy plateaus correspond to the energy of deep levels luminescing to the valence band.[33] This correspondence between E_f position and deep level energies suggests that the deep levels strongly affect the interface band bending.

The same metal on UHV-cleaved CdTe with different bulk defect densities produces dramatic differences in electrical barrier formation. Figure 8 shows PL spectra for two CdTe crystals, one with a high density of state emission at 1.0 and 1.4 eV (B), the other with only a weak emission at 1.4 eV (A).[34] Internal

photoemission of the high trap density crystal yields Φ^{n}_{B} = 0.67 eV, e.g., $E_f \sim E_{VBM}$ +0.95 eV (roughly the deep level energy). In contrast, the internal photoemission barrier for the low trap density crystal is Φ^{n}_{B} = 0.91 eV, e.g., $E_f \sim E_{VBM}$ +0.65 eV (roughly the energy expected from Φ_{Au} relative to X_{CdTe}. Thus, by lowering the density of deep traps, one can move from the "pinned" E_f regime toward the Schottky limit.

Interfacial chemistry can serve to suppress the formation of deep level due to diffusion. A 2 monolayer (ML) Yb interlayer introduced between Au and CdTe blocks the outdiffusion of Te noted above.[35] As a result, PL spectra show a strong reduction in deep level emission near 1.1 eV relative to a similar interface with no diffusion barrier. In-situ SXPS measurements of band bending on the same interfaces reveal an E_f position 0.5 eV above E_{VBM} for the diffusion-blocked interface, in contrast to an E_f position 1.1 eV above E_{VBM} for the interdiffused junction. Thus, the 2 ML Yb interlayer stabilizes the Fermi level at the classical electrostatic value.

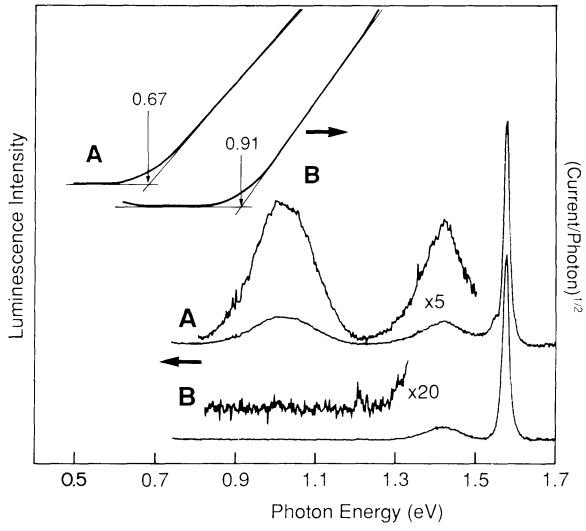

Fig. 8. Photoluminescence spectra and internal photoemission plots for Au on UHV-cleaved CdTe (110) with different densities of deep levels. The barrie for the low trap density CdTe is near the Schottky value, the barrier for the nigh trap density CdTe nearly coincides with the mid-gap level. After Ref. 34.

To summarize, CdTe typically exhibits a multiplicity of deep traps whose energies are specimen-dependent. With low native defect densities, a Schottky relation appears to hold, whereas high native defect densities lead to "pinning" at these deep level energies. Interfacial chemistry is responsible for creation of additional native defects[36,37] at the same as well as new energies, and these

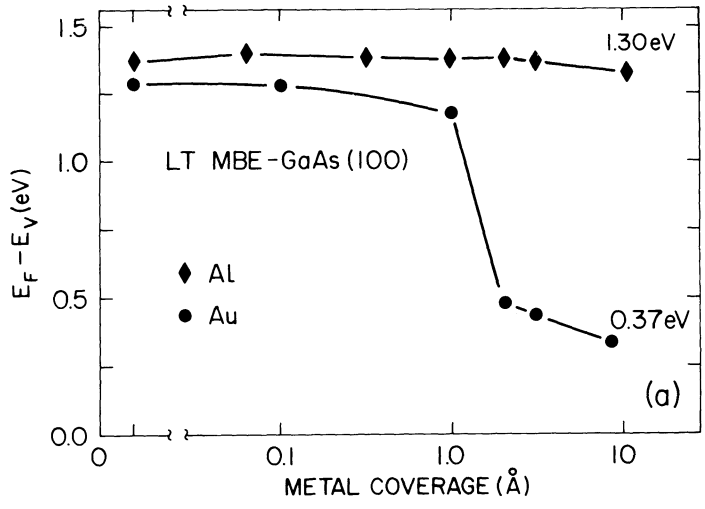

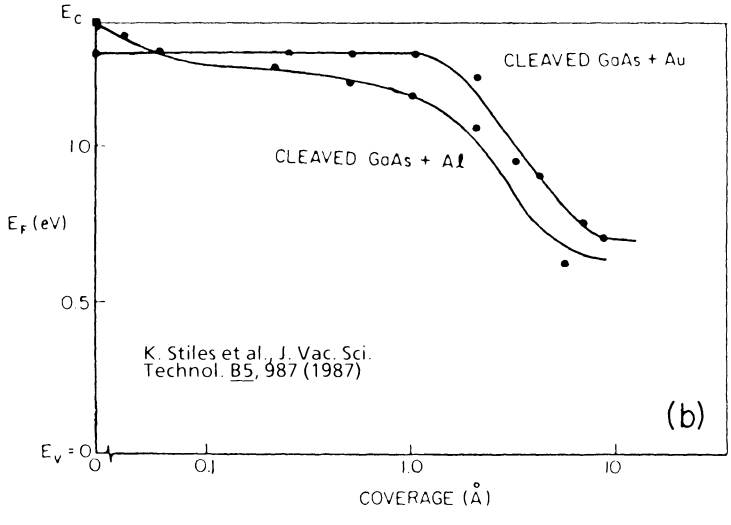

Fig. 9. Low temperature Fermi level movements for Au and Al on clean, MBE-grown GaAs (100) (a) and UHV-cleaved, melt-grown GaAs (110) (b) as a function of metal coverage. In (a), the two metals span a range of nearly 1 eV; in (b) only 0.2 eV. Both exhibit a characteristic low temperature delay in Fermi level movement until "metallic" coverages.

states can alter the interface barrier height. Finally, interfacial chemistry can be modified to block the formation of native defects, thereby stabilizing the Fermi level at the Schottky limit. All of these results serve to highlight the major role which native defects in the bulk and at the interface can play in the charge transfer process.

Low Temperature Metallization

In contrast to native defects, which represent a movement away from the ideal metal - semiconductor interface, low temperature metallization represents an opportunity to suppress chemical interactions and move toward more ideal behavior. Figure 9 illustrates E_f movements for Au and Al deposited at 80 - 100 K for both MBE-grown GaAs (100) (a)[38] and melt-grown GaAs (110) (b)[39] surfaces. Both metals on both GaAs speciments exhibit delayed E_f movements to their final energy positions, consistent with the onset of metallization at multilayer coverages. However, for the Stiles *et al.* data[39] in (b), these final stabilization energies both lie close to the "pinning" position established for UHV-cleaved GaAs (110) surface, whereas the E_f positions for the MBE-grown GaAs (100) surfaces in (a) exhibit a wide energy range of almost 1 eV. In both experiments, chemical interactions were strongly suppressed so that all of these interfaces represent near-ideal chemical systems. However, whereas the narrow E_f range for the GaAs (110) experiment is consistent with tunneling state[4-7,40], defect[15,16,40], or effective work function[22,23] models, the wide E_f range for the GaAs (100) experiment is not.

In fact, the GaAs (100) results in Fig. 9a represent near-ideal electrostatic interface behavior. Figure 10 illustrates the E_f stabilization energies for Au and Al at low temperature (LT) as well as the E_f values at room temperature (RT) taken from Fig. 2. The excellent agreement between the LT values and the Schottky values expected indicates that this near-ideal chemical interface exhibits near-ideal electrostatic behavior. For comparison, the RT values exhibit a deviation from ideal behavior, presumably due to chemical interactions. Thus, MBE-grown GaAs (100) represents a case where chemically-inert interfaces exhibit Schottky-like behavior.

Implications for Interface Theories

In the previous sections, we have discussed a number of new observations which bear on the variety of interface theories and models for electrical barrier formation. These observations are: (a) a wide range of barrier heights for different metals on a given semiconductor, (b) discrete interface states at the E_f

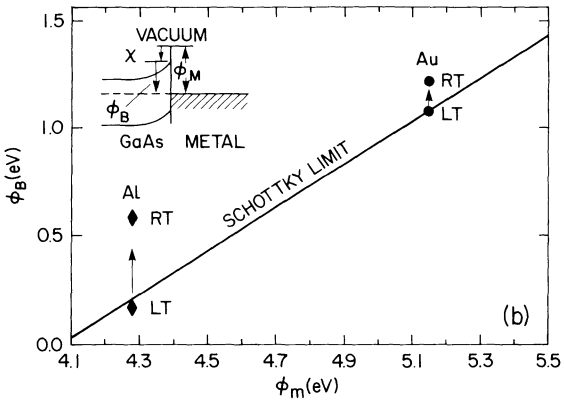

Fig.10. MBE-grown GaAs (100) barrier heights and energies relative to ideal Schottky behavior plotted vs. metal work function. Barrier heights at low temperature (LT) coincide with the Schottky limit whereas interfaces formed at room temperature (RT) deviate, suggesting that the reduced LT chemical activity results in more Schottky-like behavior.

stabilization energy, (c) $\Phi n_B + \Phi p_B = E_g$, (d) barrier formation at metallic coverages, (e) low temperature-delayed onset in barrier formation, and the Φ_B shift to $\Phi_M - \Phi_{SC}$ at low temperature.

The wide Φ_B range for different metals supports the Schottky model plus its microscopic derivation[8,9] and is in conflict with the MIGS[3-7], VIGS[41], DIGS[41], unified defect[15,16], chemical dipole[42], and effective work function models[22,23], since all of the latter predict only a narrow range of E_f stabilization. Discrete interface states at E_f support the adsorbate induced resonance model[43,44] as well as models which involve defects, such as the VIGS, unified defect, reaction-induced defect[36,37], and bulk defect[14,33-35] pictures. Discrete states are in conflict with the MIGS and DIGS models, which predict only a continuum of states. Observation of $\Phi n_B + \Phi p_B = E_g$ is in conflict with the unified defect and chemical dipole model. Barrier formation at metallic coverages supports all models but the DIGS and unified defect model. The low temperature-delayed onset in barrier formation can be construed as support for all models. The Φ_B shift to $\Phi_M - \Phi_{SC}$ at low temperature supports only the Schottky model and, by inference, a reaction-induced defect picture. It is conflict with all other models. Overall, the experimental observations strongly support the Schottky model as modified by the formation of reaction-induced or resident native defects. Only

the adsorbate-induced resonance model appears to be a reasonable alternative, given its first-order dependence on the properties of the metal.

The success of the Schottky phenomenology carries additional implications. The demonstration of near-ideal interface behavior as well as interface behavior which can be accounted for by intermediate densities of directly observable deep levels supports the microscopic, self-consistent electrostatic calculations of Mailhiot and Duke[8,9]. Within this model, a self-consistent evaluation of the electron charge redistribution reveals that the overall change in dipole strength from free metal and semiconductor surfaces to the metal-semiconductor interface is small. This result suggests that atomic rather than electronic relaxations are responsible for E_f "pinning". The success of this calculational scheme in predicting the deep level energies for metals on MBE-grown GaAs (100) surfaces indicates its significant predictive power based on direct optical measurements.

Epitome

Modern analysis of metal-semiconductor interfaces took an initial step forward here in Germany fifty years ago with the work of Schottky. High-purity semiconductor crystals free of complicating bulk effects were only then starting to become available for interface studies. However, atomically-clean interfaces were not available until decades later, largely through the use of silicide reactions or, for compound semiconductors, by cleavage and metal deposition in high vacuum. By the early 1970's, surface science techniques had revealed the presence of metal-semiconductor diffusion and reactions on an atomic scale for these clean interfaces, even at room temperature, which could affect the junction electrostatics. By the early 1980's, workers had begun to modify macroscopic electronic properties using atomic -scale techniques. Coming full circle with early work, the recent use of further improved semiconductor materials and processing has led to wide ranges of band bending for different metals on the same semiconductor. Likewise, the use of new interface techniques has provided direct and detailed observations of the interface states which can modify the otherwise ideal behavior.

In this paper, we have demonstrated that a wide range of band bending is possible for metals on III-V and II-VI compound semiconductors. Direct optical methods show that the interface states which stabilize the Fermi level are discrete and depend sensitively on the metal-semiconductor interaction. Bulk native defects at the interface or additional native defects produced by chemical interaction can "pin" the Fermi level in a narrow range of energies or at a set of well-defined deep level positions. Finally, chemically-inert interfaces appear to

exhibit Schottky-like behavior. All of these observations confirm the electrostatic model of interface charge transfer developed by Schottky five decades ago.

Partial support by the Office of Naval Research and the Army Research Office is gratefully acknowledged. It is a pleasure to thank Drs. C. Mailhiot and R. E. Viturro for valuable conversations.

References

1. L. J. Brillson, Surface Sci. Repts. **2**, 123 (1982); L. J. Brillson and G. Margaritondo, in The Chemical Physics of Solid Surfaces and Heterogeneous Catalysis, Eds. D.A. King and D.P. Woodruff (Elsevier, Amsterdam, 1988), Vol. 5, p. 119.
2. J. H. Weaver, Treatise on Mater.Technol. **27**, 15 (1988).
3. V. Heine, Phys. Rev. **138**, A1689 (1965).
4. F. Flores and C. Tejedor, J. Phys. C: Solid State Physics **20**, 145 (1987).
5. J. Tersoff, Phys. Rev. **B32**, 6968 (1985).
6. M. L. Cohen, Adv. Electron. Elect. Phys. **51**, 1 (1980).
7. J. Tersoff, Phys. Rev. Lett. **52**, 465 (1984).
8. C. B. Duke and C. Mailhiot, J. Vac. Sci. Technol., **B3**, 1170 (1985).
9. C. Mailhiot and C. B. Duke, Phys. Rev. **B33**, 1118 (1985).
10. W. Schottky, Z. Physik **113**, 367 (1939).
11. L. J. Brillson, M. L. Slade, R. E. Viturro, M. Kelly, N. Tache, G. Margaritondo, J. Woodall, G. D. Pettit, P. D. Kirchner, and S. L. Wright, J. Vac. Sci. Technol. **B4**, 919 (1986).
12. L. J. Brillson, M. L. Slade, R. E. Viturro, M. Kelly, N. Tache, G. Margaritondo, J. Woodall, G. D. Pettit, P. D. Kirchner, and S. L. Wright, Appl. Phys. Lett. **48**, 1458 (1986).
13. R. E. Viturro, L. J. Brillson, J. L. Shaw, C. Mailhiot, N. Tache, J. McKinley, G. Margaritondo, J. M. Woodall, P. D. Kirchner, G. D. Pettit, and S. L. Wright, Appl. Phys. Lett. **52**, 2052 (1988).
14. L. J. Brillson, R. E. Viturro, J. L. Shaw, C. Mailhiot, N. Tache, J. McKinley, G. Margaritondo, J. M. Woodall, P. D. Kirchner, G. D. Pettit, and S. L. Wright, J. Vac. Sci. Technol. **B6**, 1263 (1988).
15. W. E. Spicer, I. Lindau, P. Skeath, and C. Y. Su, J. Vac. Sci. Technol. **17**, 1019 (1980).
16. W. E. Spicer, I. Lindau, P. Skeath, and C. Y. Su, and P. Chye, Phys. Rev. Lett. **44**,420 (1980).
17. R. E. Viturro, C. Mailhiot, and L. J. Brillson, Proc. 19th Int. Conf. on the Physics of Semiconductors (DHN Ltd., Warsaw, 1988), in press.
18. A.Y. Cho and P. D. Dernier, J. Appl. Phys. **49**, 3328 (1978).
19. P. Chiaradia, R. E. Viturro, M. L. Slade, L. J. Brillson, D. Kilday, M. Kelly, N. Tache, and G. Margaritondo, J. Vac. Sci. Technol. **B5**, 1075 (1987).
20. L. J. Brillson, R. E. Viturro, M. L. Slade, P. Chiaradia, D. Kelday, M. Kelly, and G. Margaritondo, Appl. Phys. Lett. **50**, 1379 (1987).
21. P. Chiaradia, M. Fanfoni, P. De Padova, P. Nataletti, L. J. Brillson, R. E. Viturro, M. L. Slade, G. Margaritondo, M. K. Kelly, D. Kilday, and N. Tache, Proc. 14th Int. Symposium on GaAs and Related Compounds (Heraklion, Crete, 1987). Institute of Physics Conf. Series, in press.
22. J. L. Freeouf and J. M. Woodall, Appl. Phys. Lett. **39**, 727 (1981).
23. J. M. Woodall and J. L. Freeouf, J. Vac. Sci. Technol. **19**, 794 (1981).
24. C. M. Aldao, I. M. Vitomirov, F. Xu, and J. H. Weaver, Phys. Rev. **B37**, 6019 (1988).
25. S. D. Offsey, J. M.Woodall, A. C. Warren, P. D. Kirchner, T. I. Chappell and G. D. Pettit, Appl. Phys. Lett. **48**, 475 (1986).

26. E. Yablonovitch, H. M. Cox, and T. J. Gmitter, Appl. Phys. Lett. **52**, 1002 (1988).
27. L. J. Brillson and R. E. Viturro, Scanning Electron Microsc. **2**, 789 (1988).
28. L. J. Brillson, R. E. Viturro, J. L Shaw, and H. W. Richter, J. Vac. Sci. Technol. **A6**, 1437 (1988) and references therein.
29. R. E. Viturro, M. L. Slade, and L.J. Brillson, Phys. Rev. Lett. **57**, 487 (1986).
30. L. J. Brillson, C. F. Brucker, A. D. Katnani, N. G. Stoffel, R. Daniels, and G. Margaritondo, J. Vac. Sci. Technol. **21**, 564 (1982).
31. R. E. Viturro, J.L. Shaw, and L.J. Brillson, J. Vac. Sci. Technol. **B6**, 1397 (1988).
32. J. L. Shaw, R. E. Viturro, L. J. Brillson, D. Kilday, M. K. Kelly, and G. Margaritondo, J. Electron. Mat. **17**, 149 (1988).
33. J. L. Shaw, R. E. Viturro, and L. J. Brillson, D. Kilday, M. Kelly, and G. Margaritondo, J. Vac. Sci. Technol. **A6**, 1579 (1988).
34. J. L.Shaw, R. E. Viturro, L. J. Brillson, G. Margaritondo, and J. M. Woodall, J. Electron. Mat., in press.
35. J. L. Shaw, R. E. Viturro, L. J. Brillson, and D. LaGraffe, unpublished.
36. R. H. Williams, J. Vac. Sci. Technol. **18**, 929 (1981).
37. L. J. Brillson, C. F. Brucker, A. D. Katnani, N. G. Stoffel, and G. Margaritondo, Appl. Phys. Lett. **38**, 784 (1981).
38. R. E. Viturro, C. Mailhiot, and L. J. Brillson, unpublished.
39. K. Stiles, A. Kahn, D. G. Kilday, and G. Margaritondo, J. Vac. Sci. Technol. **B5**, 987 (1987).
40. W. Mönch, Phys. Rev. Lett. **58**, 1260 (1987).
41. H. Hasagawa and T. Sawada, Thin Solid Films **103**, 119 (1983).
42. L. J. Brillson, J. Vac. Sci. Technol. **16**, 1137 (1979).
43. R. Ludeke, G. Jezequel, and A. Taleb-Ibrahimi, Phys. Rev. Lett. **61**, 601 (1988).
44. R. Ludeke, J. Vac. Sci. Technol., in press.

INFLUENCE OF THE ATOMIC SCALE ROUGHNESS OF A CLEAN Si SURFACE ON THE INTERFACE FORMATION WITH METALS

C.A. Sébenne

Laboratoire de Physique des Solides, UA 154
Univ. Pierre et Marie Curie,
75252 Paris Cedex 05, France

INTRODUCTION

In order to study the influence of surface roughness on the formation of a metal-semiconductor interface, it is necessary, to start with, to have a strong control over the basic properties of the chosen couple, namely (i) the knowledge of the surface structure and properties of the perfect semiconductor substrate, (ii) the ability to master reproducibly its degree of roughness, as it will be defined below, (iii) the knowledge of the expected interface formed with the metal.

The first point is already strongly limiting since the choice is left between the (111) and the (100) faces of Si and Ge and the cleavage face of several 3-5 or 2-6 compounds. In spite of their practical interest, the (100) faces of GaAs and InP cannot be considered since their composition-dependent structures are not yet fully established.

Before discussing the second point, we must define what we mean here by surface roughness. We start with the ideal surface structure obtained by considering the bulk atomic positions along a given crystallographic plane. Then, any departure from these ideal positions involving displacements smaller than a bond length and forming a perfect two-dimensional lattice gives a reconstructed surface which we define as perfectly smooth : for example, we take as such the perfectly cleaved Si(111)-2x1, Ge(111)-2x1, GaAs(110)-1x1 and InP(110)-1x1 reconstructed surfaces as well as the perfect Si(100)-2x1. On the contrary any surface where adatoms or vacancies, or any combination of these, can be defined with respect to the above ideal crystallographic plane, displays some degree of roughness : it is the case of the 7x7 reconstructed Si(111) surface which combines vacancies and adatoms among others (1), as well as of stepped surfaces. Coming back to the choice of substrates where roughness can be tentatively controlled, in order to escape compositional problems, it is clear that only elemental semiconductors such as Si and Ge are acceptable. Therefore, in this work we shall limit our discussion to the cases of (i) Si(111)-7x7, well known rough surface which can be compared to the smooth Si(111)-2x1 and (ii) Si(100), the roughness of which can be approximately calibrated using vicinal surfaces, as shown recently (2).

The choice of the metal is now open. Let us simply recall that one can distinguish several typical cases as the ultimate structure of metal-semiconductor interfaces after deposition of the metal on the clean surface and proper annealing of the system. A first one corresponds to the formation of abrupt interfaces, where the metal atoms stay outside the

surface envelope of the substrate atoms ; on silicon it is the case of Ga, In, Sn, Pb for example. A second one corresponds to the formation of a two-dimensional mixed layer, a few angstroem-thick at most, where metal atoms are embedded in the last atomic plane(s) of the substrate ; it seems the case of the annealed Ag-Si(111) system for example. A third case corresponds to the formation of a three-dimensional mixed layer, which may form epitaxially or not and may have a well defined composition or not : it is the case of many transition metals on Si such as Fe, Ni, Co, Pt, Pd, Cr, Mo, W, Ta, Ti, etc... The resulting silicide-silicon interface in the last case should be less sensitive to the initial density of substrate surface defects and will be kept out of the present discussion.

We shall focus our attention here on two typical examples illustrating the first two cases, first the system Si(111)-Ag which has been thoroughly studied in the last ten years and has known recently renewed interest and, second, the system Si-Ga both along the (111) and (100) faces together with some comparisons with In, Sn and even Ge in spite of not being a metal. The paper will therefore be divided into three parts dealing successively with Si(111)-Ag, Si(111)-Ga and Si(100)-Ga before getting to some conclusions.

THE Si(111)-Ag SYSTEM

This system is particularly interesting because, when Ag is deposited at room temperature on Si(111), being 2x1 or 7x7 reconstructed, it forms an abrupt interface. Then, after annealing it is transformed into a seemingly two-dimensional mixed layer. This example is used here to illustrate the different behaviours between the smooth 2x1 reconstructed surface and the rough 7x7 one.

Vacuum deposition of Ag on a clean cleaved 2x1 Si(111) substrate kept at room temperature has been studied by a few groups including our own (3). The main points can be summarized as follows, using the monolayer unit 1ML of Ag coverage as the density of Si atoms along the ideal (111) plane, that is 7.8×10^{14} cm^{-2}. The interface forms in a two-stage process. The first one corresponds to the appearance of a $\sqrt{7} \times \sqrt{7}$ - R19.1° surface unit mesh in coexistence with the 2x1 initial one. This new structure is the sharpest around 2/3ML of Ag. At this coverage Auger signals indicate a two-dimensional Ag layer and photoemission yield spectroscopy shows (i) the completion of a parallel decrease of both the work function (initially 4.87 eV) and the ionization energy (initially 5.30 eV) by the same amount of 0.35 eV, that is with no band bending change, (ii) the change of the double-peak surface state band (at 0.2 and 0.6 eV below the valence edge E_{VS}, or 0.65 and 1.05 eV below E_F) which characterizes the clean cleaved surface, into a single band, may-be smaller, 0.5 eV below Evs.Then at higher coverages, LEED spots of Ag(111) metal come up while the two other structures remain visible : they still coexist nicely at 1.3 ML of Ag. However no change in both the work function and band bending are observed while the density of surface states shows an increase towards E_F, which indicates the appearance of some metallic character in a relation with the growth of flat and oriented silver islands. At coverages beyond 2ML, the island growth becomes slightly three-dimensional. It is interesting to see in this case that the smoothness of the surface allows fairly long displacements of Ag atoms, as demonstrated by the coexistence of various reconstructions along the surface : the result is a highly inhomogeneous Ag distribution. Therefore the actual number of Ag atoms per $\sqrt{7} \times \sqrt{7}$ surface unit mesh is only known with a large margin of error and the actual surface structure within the $\sqrt{7} \times \sqrt{7}$ cell is not known.

Let us consider now room temperature deposition of Ag on 7x7 reconstructed Si(111). Most of the work has been devoted to the annealed system, which we shall examine later, but only a few papers deal with the room temperature growth (4, 5). Fortunately a recent study made on samples prepared at 90 or 130°C, and using a scanning tunneling microscope (6) brings much light to understand the earlier results which are the following. LEED observations show the persistence of the 7x7 diagram beyond 1ML Ag coverage. Around 1.3ML, only the Si(111) 1x1 spots remain while Ag(111) 1x1 spots start to appear. No Ag-induced intermediate structure is observed. Auger behaviour is qualitatively the same as for the 2x1 substrate, as shown in Fig. 1. However the curves demonstrate that in

the first stage the Ag layer is more uniform on the 7x7 substrate than on the 2x1 while the islands are more three-dimensional on the 7x7 in the second stage. In the 1ML coverage range, photoemission yield spectra show the completion of the same decrease of the ionization energy (initially 5.30 eV) by 0.35 eV as on the 2x1 substrate, but this time, the work function (initially 4.60 eV) remains practically constant (0.05 eV decrease) which means a band bending change by 0.30 eV. This change is related to the removal of the upper peak of the filled surface state band, which comes higher into the gap in the clean 7x7 than in the 2x1, while the lower peak of the band, within the valence band, is only decreased. Tunnel

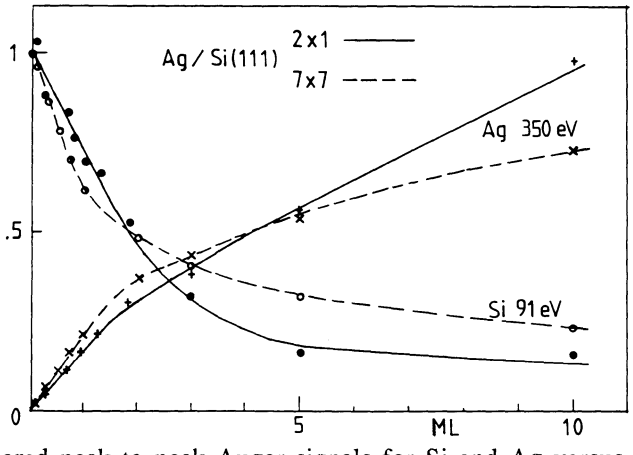

Fig. 1 : Compared peak to peak Auger signals for Si and Ag versus Ag coverage in monolayer units (1ML=7.8×10^{14} at/cm^2) after deposition on an unheated substrate initially either 2x1 or 7x7 reconstructed. E_p=2 kV, I_p=5×10^{-6}A, 5V peak to peak modulation (CMA with a coaxial electron gun).

microscope observations (6) explain these results since they show that 1/3ML of Ag distributes orderly and respects the 7x7 surface unit by making Ag atom flat packs, from a ring-like structure containing at most 36 Ag atoms, located preferentially on top of the faulted triangular part of the 7x7 initial structure. We understand then why the 7x7 reconstruction is preserved beyond 1ML Ag without formation of large two-dimensional islands and why the ionization is decreased (dipole effect) while the dangling bond band is non-uniformly changed is spite of the apparent conservation of the 7x7 structure. As compared to the 2x1 case, the roughness of the 7x7 surface unit cell plays the important role of stopping any long distance

diffusion of Ag atoms which must then find their best arrangement within the 7x7 cell up to coverages close to 1ML : within the evaluation given in reference 6, a "perfect" arrangement could be found at 36/49ML, that is roughly at 3/4ML.

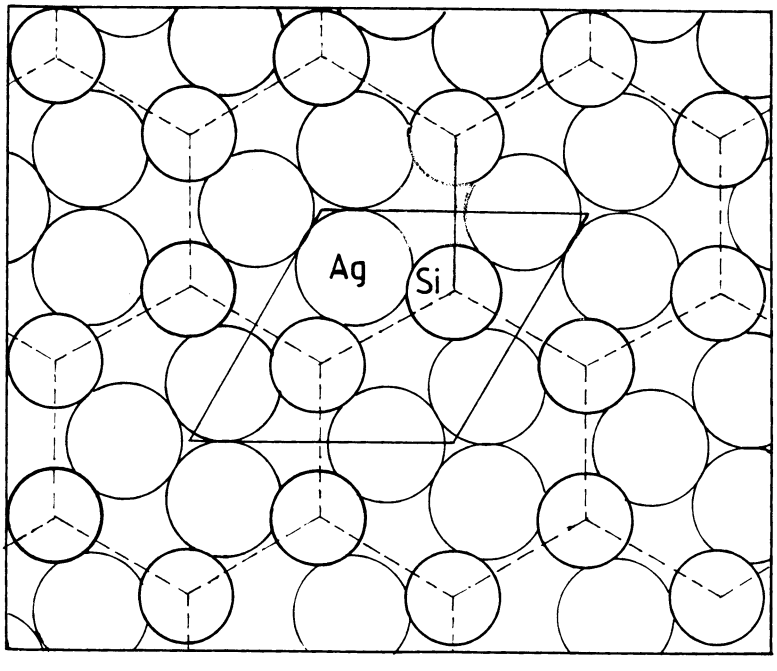

Fig. 2 : Top view of the √3x√3-R30° Ag-Si(111) surface model with Ag trimers embedded in a honeycomb Si top layer ; the side of the √3 unit mesh is taken as 6.65A ; the atomic diameters of Si and Ag are 2.35 and 2.88A respectively. Deeper Si layers are not shown.

The last point which must be discussed is to check if the two different structures which characterize Ag deposition on Si(111)-2x1 and 7x7 at room temperature, that is respectively "large" and "7x7" inhomogeneities have a consequence on the annealed interface. In both cases, it is well known that upon annealing beyond 250°C, a √3x√3-R30° surface structure developes, above which purely three-dimensional Ag clusters are formed. This √3 structure has been widely studied in order to determine its actual Ag content and atomic arrangement. First a honeycomb model with 2/3ML Ag on top was proposed (4, 7). Then arguments were given in favor of Si forming the last layer (8, 9) also with 2/3ML Ag. Then recently, tunnel microscopy came to the subject and two models remained : either Ag-trimers (1ML) situated below Si atoms which form a honeycomb (2/3ML) (10) or Ag atoms (2/3ML) forming a honeycomb above the Si atoms (11). The latest work, which used Impact Collision Ion Scattering Spectrometry (12), agrees well with the model of embedded Ag trimers in a Si honeycomb. This model looks presently like the most probable one and we take it as the actual structure, shown in Fig. 2. The positions of the Si atoms in the next layers with respect

to first ones is not shown. Then our discussion will be based on two points : first the temperature at which the √3 structure establishes itself and second the quantitative aspect of the accepted model of the structure.

There is no full study dealing with both coverage and annealing temperature parameters. While annealing is usually made in the 500°C range, sometimes it is kept in the 250-300°C range and gives apparently satisfactory samples. We know that a LEED pattern is not a reliable proof of a surface uniformity but it proves the existence of ordered domains large enough to give a diagram. Therefore the √3 Ag structure can be induced at temperatures quite comparable to the one needed to induce the transformation from the 2x1 clean cleaved Si into the 7x7. This is remarquable because we know in the latter case that such a low temperature is far below any bulk recrystallization or surface melting temperature. However the change occurs, and it is clear that a perfect Si(111)-2x1 surface cannot transform easily into a 7x7 for the simple reason that the latter (1) contains in its last three atomic planes, from the inside, 48+42+12 atoms against 49+49 atoms for the corresponding area along a 2x1 . It means that 4 atoms per 7x7 unit mesh have to be found somewhere for the transformation to occur, which can only come from step edges. This is the reason why depending on the cleave, the switching temperature may increase wildly and, in the worst cases, one must go even above about 900°C in order to pass the apparent 1x1 LEED pattern, which shows surface disorder at the LEED scale, and to get a nice 7x7 reconstruction, usually at the expense of large scale smoothness. In the case of the √3 Ag, we have to deal with a very similar situation and if the lowest switching temperatures can be expected in the case of deposition on the 7x7 structure since the Ag first layer is more uniform than on the 2x1, the √3 structure cannot form itself uniformly. The reason is that 2/3ML of Si cannot be extracted from below without picking atoms along existing steps or creating extra vacancies : in the best cases, the existence of domains is therefore unavoidable, and they were indeed observed by tunnel microscopy (13).

Following the same idea, the situation is not better when starting with a 2x1 substrate since the formation of the √3 Ag structure needs the existence of some surface roughness before and/or after structural transformation. Experimental evidence is not easy to get in that case and in future work, before dealing with the roughness effects on Si(111)-Ag, it would be probably better to go back to a detailed analysis of the 2x1 into 7x7 transformation.

THE Si(111)-Ga SYSTEM

With Ga, we enter the family of abrupt interfaces and the discussions should be more conclusive. In the present case, we compare the same roughness effects as for silver, that is room temperature deposition of the metal either on the cleaved 2x1 or on the 7x7 reconstructed Si(111) surface.

Without trying to be exhaustive in reviewing the literature, let us simply recall first the main characters of the Ga/Si(111)-2x1 interface formation (14), the case of the smooth surface. Upon increasing Ga coverage, at room temperature, one can distinguish three stages. In the first one, from 0 to 1/3ML (1ML is here again $7.8 \times 10^{14} cm^{-2}$), the 2x1 LEED diagram vanishes progressively to become unobservable beyond 0.3ML while a √3x√3-R30° diagram shows up at 0.1ML, to be fully established at 0.3ML and beyond. Auger lines show a two-dimensional deposition. Photoemission yield spectroscopy shows (i) a decrease of the ionization energy by 0.4 eV and a lesser decrease of the work function by 0.3 eV which means that E_F at the surface comes closer to the valence band edge E_{vs} by 0.1 eV, (ii) a removal of the filled surface state band of Si which is replaced by a single narrow peak about 0.1 eV below E_{vs} in the valence band. In the second stage, at coverages from 1/3 to about 1.5ML the √3 LEED diagram vanishes progressively to be replaced at, and beyond, 1ML by a 1x1. Auger analysis shows that the Ga layer is still two-dimensional but not necessarily uniformly distributed and more like a patchwork. This is consistent with photoemission results where no significant changes occur except may-be the appearance of some metallic

character close to E_F. The third stage, beyond 1.5ML, is characterized by the growth of relatively flat Ga islands. Let us note that In has a qualitatively similar behaviour (14) with a $\sqrt{3}$ structure showing up at even lower coverages (it has a higher surface mobility than Ga on Si) and with a larger decrease (0.7 eV) of the ionization energy since its covalent diameter (2.88A) is larger than the Ga one (2.52A) ; however the $\sqrt{3}$ structure is replaced at 0.5ML by a 2x2 which demonstrates the increase of lateral interactions in the case of a bigger atom.

Room temperature deposition of Ga on Si(111)-7x7 has not been studied in detail. However the behaviour has some common features with the room temperature deposition of Ag (see above) or Ge (15) on Si(111)-7x7. In particular, the 7x7 reconstruction persists up to monolayer coverage without any trace of a $\sqrt{3}$ diagram. The layer is inhomogeneous but statistically two-dimensional in that range. Photoemission yield spectra show (i) the same decrease of ionization energy and a smaller decrease (0.1 eV) of the work function as compared to the 2x1 and (ii) a removal of the filled surface state band at and below the valence band edge. As for silver, the local roughness of the 7x7 reconstruction refrains Ga mobility along the surface and consequently, the early development of a metallic character in the growing layer, while its relative stability blocks the formation of the $\sqrt{3}$ structure which formed spontaneously at room temperature on the cleaved surface. In order to induce the $\sqrt{3}$ structure at 1/3ML on the 7x7 surface, annealing is necessary. The actual temperature needed to get the structural change is in the 300°C range, as in the case of silver. However, in the case of Ga, an activation is needed only for the rough surface since the transformation is easy on the smooth 2x1 surface. This is easy to understand if we refer to the actual structure of the $\sqrt{3}$ reconstructed Ga-Si(111) surface which is fairly well knwon : Ga atoms sit in ternary T4 sites on the Si surface, more or less equally bonded to four Si atoms, three in the first plane of the ideal (111) clean Si surface and one in the second plane, as shown in Fig. 3. Actually on the 2x1 surface, Ga adsorption in the proper site needs only a small redistribution of the electron density with slight displacements of the Si atoms underneath.

On the contrary, an initial 7x7 structure which contains vacancies and adatoms along the surface implies large Si atom displacements to switch to the smooth $\sqrt{3}$ structure : one can expect, as in the case of Ag, the creation and/or the survival of defects along the interface even after long annealings at relatively high temperatures. This has been demonstrated recently in the equivalent case of Al-Si(111)-7x7 by tunnel microscopy (16) where the presence of surviving Si adatoms within the $\sqrt{3}$-Al layer has been observed, associated with the corresponding electron localized filled state.

One can wonder what happens at the interface at high metal coverages : there is no evidence of any local conservation of the $\sqrt{3}$ structure itself ; however once a rough surface has been made, with its specific electron state disorders, it seems very unlikely to have it removed upon metal thickness increase, especially in the case of abrupt interfaces.

THE Si(100)-Ga SYSTEM

On a very general basis, the Si(100) face may be considered as one of the best to study intrinsic surface defects (geometry, electronic properties, consequences on adsorption, effects on Schottky barrier formation, etc...) for various reasons. Besides the general reasons given in the introduction, the clean Si(100) face has an undisputable, simple and unique elementary atomic arrangement, called the dimer, where two neighbour Si atoms of the ideal (100) plane bend towards each other to make a bond, which suppresses one of the two dangling bonds per atom of the ideal surface. The question of the symmetry of the dimer and the possibility to get larger unit meshes by an irregular but periodic distribution of the dimers do not involve significant energy differences and do not influence much the defect problem. Then following the definition of the introduction, a Si(100) surface with a uniform array of dimers along a single crystallographic plane is smooth. Now, considering surface defects, besides ordinary point defects which can be found along this surface (single vacancy in the surface plane, single adatom above it), some specific ones are : the in-plane unpaired Si atom (it should be very mobile), the missing dimer and the ad-dimer and all their associations including

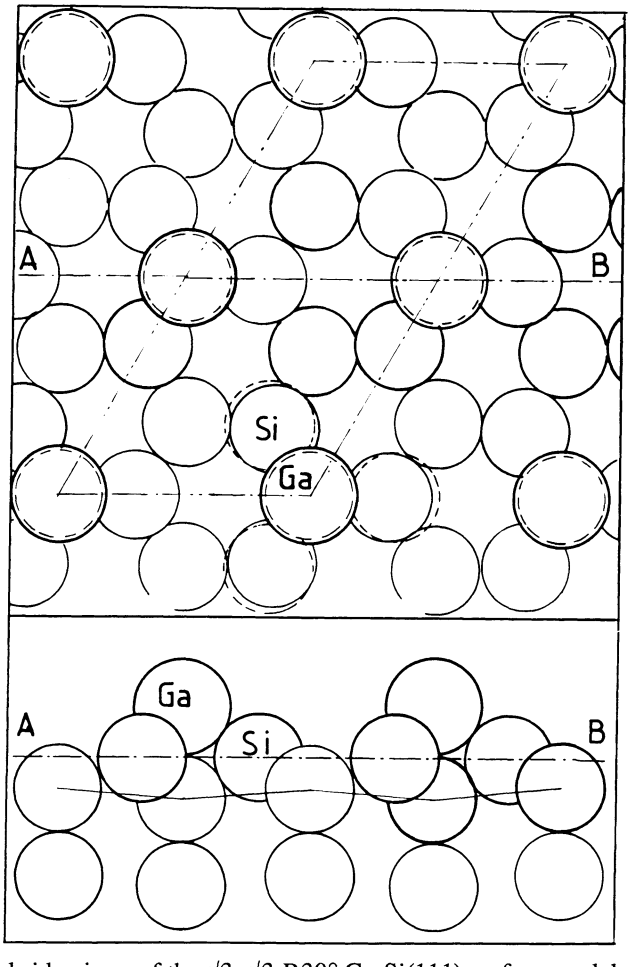

Fig. 3 : Top and side views of the √3x√3-R30° Ga-Si(111) surface model with Ga adatoms in T4 surface sites and the adequate distorsions conserving the covalent diameters of Si(2.35A) and Ga(2.52A).

step-limited islands and dips. Whatever tempting this system might be, the work on its surface defects and their consequences is still at present very scarce and the present discussion will be based on very partial and preliminary results which we have obtained recently.

In our approach, the first step has been to get a relatively accurate information about the averaged surface roughness of a given clean Si(100) sample. We all know that LEED or RHEED measurements are not reliable for that, while photoemission techniques are recognized to be very sensitive to surface preparation. We have therefore taken advantage of the high sensitivity and high energy resolution of photoemission yield spectroscopy (17) to try and, obtain some correlation between the degree of roughness of a surface, as it can be controlled through its preparation, and its electronic properties, that is the shape of its filled surface state band, its work function and its ionization energy. This approach has been found very promising (2) since not only such a correlation has been shown but surface smoothing or roughening procedures and a crude evaluation of the density of edge atoms along the surface can also be proposed.

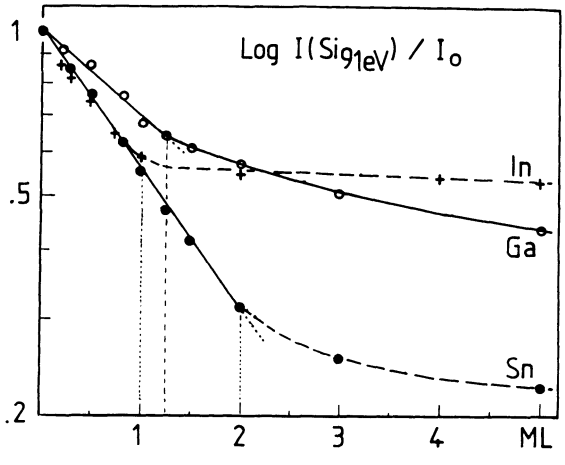

Fig. 4 : Relative Si(91 eV) Auger signals as a function of metal coverage in monolayer units (1ML=6.8x10^{14} at/cm^2 on Si(100)) for Ga, In and Sn deposited at room temperature on a clean Si(100) 2x1 reconstructed surface, under ultrahigh vacuum.

The adsorption of Ga (18), In (19) and Sn(20) on such surfaces at room temperature has also started to be studied and in the present state of the work, it is only in the case of Ga that the influence of the substrate surface roughness has been shown to play a role. In the following, we shall discuss the three cases because their comparison will help in understanding how roughness influences the interface formation.

In all three cases, the formation of an abrupt interface is obvious and the usual two-main-stage process is demonstrated by the behaviour of the Auger peak intensities ; the decrease of the Si (91 eV) signal is shown as a function of coverage for the three metals in Fig. 4 and indicates clearly at what coverages the three-dimensional metal islands start to

form. In order to get into the details of the first stage (the two-dimensional layer) where roughness effects should manifest themselves, one has to rely on structural and electronic information. LEED measurements are interesting but reveal a complicated situation. For example, the annealed Si(100)-Sn system displays several diagrams upon increasing coverage (21, 22, 23) but it is almost impossible to assign a precise coverage to a given diagram and any modelization is therefore difficult. The situation may be less complicated in the case of Ga and In where, besides the initial 2x1 diagram and a final 1x1, only a 2x2 is observed at intermediate coverages (around 1/2ML) at room temperature (18, 19) as well as after annealing (24), but definite conclusions cannot yet be drawn. Complementary information can be obtained from photoemission measurements. From the yield spectra, we can deduce the work function, the ionization energy and the filled surface state density changes as a function of metal coverage up to the one monolayer range ; for the three cases discussed here, the first two quantities are presented in Fig. 5. New break points appear on these curves, namely at

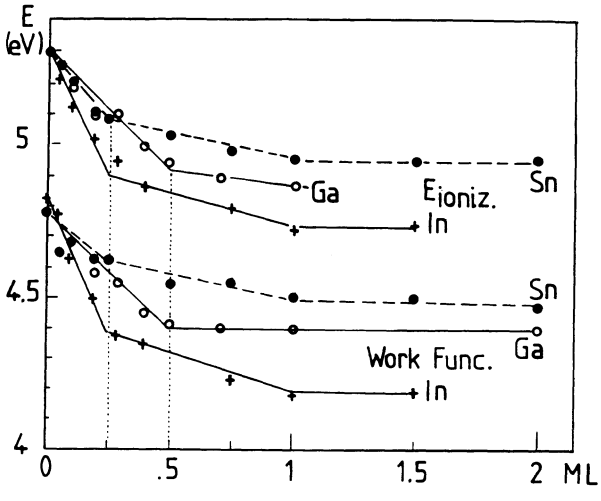

Fig. 5 : Work function and ionization energy of an initally clean Si(100)-2x1 surface versus coverage of Ga, In or Sn, as in Fig. 4.

0.25ML for both In and Sn or at 1/2ML for Ga. The filled surface state band goes through series of deformations and only in the case of In its integral seems to pass through a minimum around 0.2-0.3ML. The data in Fig. 5 are more interesting because they show (i) a decrease of the ionization energy occuring at low coverage, which means that whatever the metal, its atom binds covalently to the Si surface atoms with the tendency to stay out of plane (dipole with the plus on the outside), (ii) the first break point is the same for In and Sn and different for Ga, which means that common size is the dominant parameter against common valency, (iii) the break point occurs at 1/4ML for the "large atoms" against 1/2ML for the "small one". It may mean that what can be made by one large atom needs two small ones, that is Ga probably prefers to adsorb as dimers. Fig. 6 illustrates possible adsorption sites.

Let us come back now to the roughness influence we are dealing with. The above observations in which roughness may be involved in the case of Ga are as follows : the LEED 2x2 is at its best around 3/4ML while electronic properties break at 1/2ML ; the two-dimensional growth (Fig. 4) goes up to 5/4ML with no metallic character. If the surface were smooth the coverages at which the changes of properties occur would not be all different. Within a Ga dimer model for example, each Ga dimer would remove four Si dangling bonds and the surface state band, work function, ionization energy would break at 1/2ML where the 2x2 diagram would be the sharpest. Then, the metallic character should appear beyond 1ML. Only the surface roughness is able to explain the delay in the establishment of some of the properties. It is indeed the case and the analysis of the initial roughness of the samples enlightens the situation : the shape of the density of filled states of

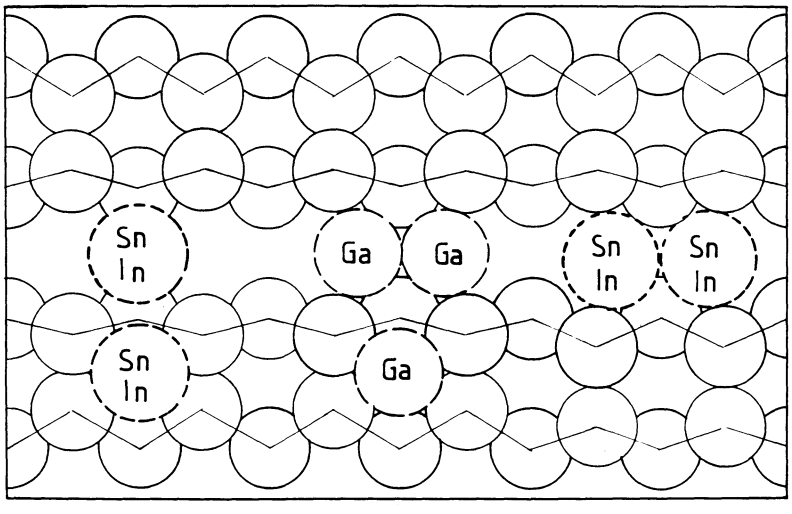

Fig. 6 : Top view of a reconstructed Si(100) surface with possible adsorption sites for Ga, In or Sn atoms. The actual covalent diameters of the atoms (Si : 2.35 ; Ga : 2.52 ; Sn : 2.80 ; In : 2.88A) and their relative distances are on scale.

the clean surface (18) shows that in the present case it has between 20 and 30 percents of its atoms in edge positions. Then, 1/4ML of Ga seems to be needed first to sit along these edges probably because there, one Ga atom can easily remove three Si dangling bonds. Next, another 1/4ML or so is sufficient to saturate the electronic properties while an extra 1/4ML is needed to form a regular array of Ga dimers. Such effects are not very likely to occur in the case of In or Sn which are more than 20 percents bigger than Si atoms, against about 7 percents for Ga, and cannot take substitutional-like surface sites as easily as Ga : on the contrary, their size can render possible top site which are excluded for Ga since it would induce too much distorsion, (Fig. 6). This discussion will not be pushed too far because it rests on scarce and preliminary experimental data. It remains that in the case of randomly distributed surface irregularities, some evidence on their role in the formation of a metal-Si(100) interface has already been obtained.

CONCLUSION

It is obvious that structural irregularities at metal-semiconductor interfaces play an important role in the transport properties of the corresponding Schottky barriers : a simple proof is given by the extreme rarity of the cases where the so-called "ideality factor" is found strictly equal to one in electrical measurements. In order to overpass the phenomenological understanding of transport properties and to get a more fundamental one, the detailed knowledge of both of the various atomic geometries at the interface and the local electronic properties, in particular at defective sites of the initial surfaces is absolutely necessary, just as it is in the semiconductor bulk. We have shown through the discussion of a few examples of metal adsorption on silicon substrates, that such a goal is not out of reach anymore. In particular, it has been shown here that some interfaces cannot form without some degree of roughness because a sizable density of surface defects must be generated or anihilated especially when the atomic geometry differs markedly from the clean to the covered surface as in the case of Ag on Si(111) or Ga on Si(111) 7x7.Of course an important amount of work has to be done but the conjugation of a well-chosen set of metal-semiconductor system such as the ones we dealt with here, on the one hand, and a well chosen set of complementary experimental techniques, including of course scanning tunneling microscopy and spectroscopy, on the other hand, should be very fruitful within the next few years.

ACKNOWLEDGMENTS

The use of published and unpublished results obtained with passed and present coworkers Ping Chen, D. Bolmont, I. Andriamanantenasoa and J.P. Lacharme is gratefully acknowledged.

REFERENCES

1. K. Takayanagi, Y. Tanishiro, M. and S. Takahashi, J. Vac. Sci. Technol. **A3**, 1502 (1985).
2. I. Andriamanantenasoa, J.P. Lacharme, C.A. Sébenne and F. Proix, Semicond. Sci. Technol. **2**, 145 (1987).
3. D. Bolmont, Ping Chen, C.A.Sébenne and F. Proix, Phys. Rev. **B24**, 4552 (1981).
4. G. Le Lay, PhD Thesis, Université Marseille III (1977) unpublished.
5. D. Bolmont, Ping Chen and C.A. Sébenne, unpublished (see D. Bolmont, PhD Thesis, Université Pierre et Marie Curie, 1982).
6. St. Tosch and H. Neddermeyer, Phys. Rev. Lett. **61**, 349 (1988).
7. G. Le Lay, M. Manneville and R. Kern, Surface Sci.**72**, 405 (1978).
8. M. Saitoh, F. Shoji, K. Oura and T. Hanawa, Surface Sci. **112**, 306 (1981).
9. D. Bolmont, Ping Chen and C.A. Sébenne, J. Phys. C **14**, 3313 (1981).
10. E. J. Van Loenen, J.E. Demuth, R.M. Tromp and R.J. Hamers, Phys. Rev. Lett. **58**, 373 (1987).
11. R.J. Wilson and S. Chiang, Phys. Rev. Lett. **58**, 369 (1987).
12. T.L. Porter, C.S. Chang and I.S.T. Tsong, Phys. Rev. Lett. **60**, 1739 (1988).
13. R.J. Wilson and S. Chiang, Phys. Rev. Lett. **59**, 2329 (1987).
14. D. Bolmont, Ping Chen, C.A. Sébenne and F. Proix, Surface Sci. **137**, 280 (1984).
15. Ping Chen, D. Bolmont and C.A. Sébenne, Solid State Comm. **46**, 689 (1983).
16. R.J. Hamers and J.E. Demuth, Phys. Rev. Lett. **60**, 2527 (1988).
17. C.A. Sébenne, D. Bolmont, G.M. Guichar and M. Balkanski, Phys. Rev. **B12**, 3280 (1975) and C.A. Sébenne, Nuovo Cim. **B39**, 768 (1977).
18. I. Andriamanantenasoa, J.P. Lacharme and C.A. Sébenne, The Structure of Surfaces II Van Der Veen and Van Hove Ed. Springer Series in Surface Science 11, (1988) p. 363.
19. I. Andriamanantenasoa, J.P. Lacharme and C.A. Sébenne, unpublished (see I. Andriamanantenasoa, Thesis, Université Paris 7, 1987).
20. I. Andriamanantenasoa, J.P. Lacharme and C.A. Sébenne, Surface Sci. **189/190**, 563 (1987).

21. N. Kuwata, T. Asai, K. Kimura and M. Mannami, Surface Sci. **143**, L393 (1984).
22. K. Ueda and K. Kinoshita, Surface Sci. **145**, 261 (1984).
23. D.H. Rich, T. Miller, A. Samsavar, H.F. Lin and T.C. Chiang, Phys. Rev. **B37**, 10221 (1988).
24. J. Knall, J. Sundgreen, G. Hansson, J. Green, Surface Sci. **166**, 512 (1986).

δ-DOPING LAYERS. THE SHAPING OF BARRIER POTENTIALS BY PLANAR DOPING

F. Koch and A. Zrenner

Physik-Department E 16
Technische Universität München
D-8046 Garching, Fed. Republic of Germany

ABSTRACT

Electronic potential barriers, in the interior of a semiconductor, at metal-semiconductor interfaces, as well as at heterostructure interfaces, can be made and shaped using dopant impurities. The dipole layers created by doping involve the spatially separated ionized donors, acceptors and their respective, mobile screening charges. We consider the δ-function doping layer, which is a sheet of impurities introduced during epitaxial growth in a single atomic layer. For such 2D doping the mobile charge screening the ions is contained in subbands with binding lengths determined by the quantum-mechanical motion of the effective mass carriers. As a result the δ-doping dipole has a length intermediate between that of the interfacial atomic layer and a typical depletion layer. We discuss the technology of growing such δ-layers, the electronic properties of the layer and their role in shaping potential barriers.

1. INTRODUCTION

Doping a semiconductor in order to achieve specific electronic functions is a standard and straightforward step in the making of devices. One can create p-n junctions or make ohmic contacts by properly designed doping strategy. For Schottky barriers the lowering induced by the image effect is a subject to be found in the textbooks together with the necessary formulas and tables /1/. Even Capasso's DID (doping interface dipole), proposed as an instrument for tuning heterostructure band-offsets /2/, is thoroughly classical in the sense of textbook electrostatics. We have taken the liberty in Fig. 1 to include it in the classical doping strategies for the making and breaking of electronic potential barriers in a semiconductor. Nevertheless DID highlights the capabilities of modern crystal growth, the deliberate and controlled layer-by-layer growth techniques that allow the introduction of dopants with atomic-plane precision.

The traditional tools of impurity engineering are based on diffusion, implantation-anneal sequences, and incorporation during bulk crystal growth. These methods result in the random, statistical placement of the donors and acceptors with a depth resolution of not much better than ~ 0.1 μm. By contrast, in the brave new world of planar, layer-by-layer

epitaxial growth techniques, impurities can be introduced at will with near atomic-layer precision /3/. Confinement of the impurity ions in a layer whose width is much less than a Bohr radius, has dramatic consequences for the arrangement of the compensating mobile charge. In such so-called δ-function doping layers the effective mass carriers occupy distinct quantum-mechanical subbands. Their quantum properties were first recognized in Ref. /4/ and have since been explored in a number of publications.

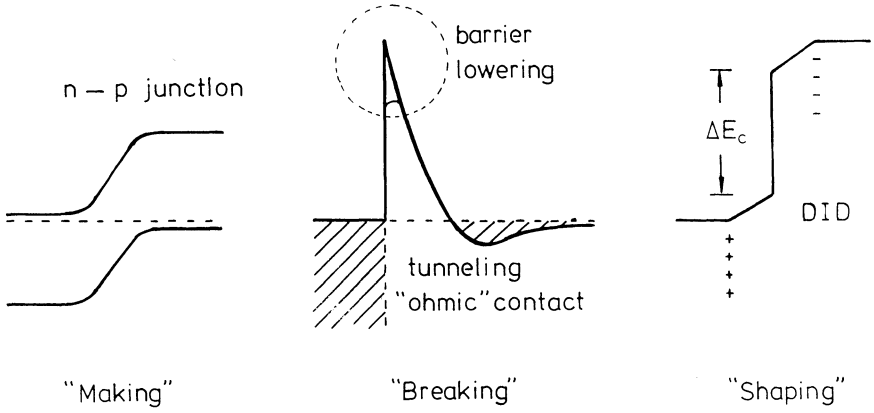

Fig. 1. Classical doping strategies employed in the making, breaking, and shaping of barrier potentials in a semiconductor. The p-n junction and ohmic contact are well known examples. Barrier adjustment of the Schottky contact is based on shaping the tip of the potential maximum to change image and tunneling effects.

In the context of the workshop theme of metal-semiconductor and heterostructure interfaces, we aim here to explore how the quantum aspects of layer doping enter in the consideration of barrier tuning. The distinctive quantum characteristics of the δ-layer become apparent in the listing and comparison in Fig. 2 of the different dipoles contributing to the potential barrier. In planar electrostatics potential variations are linked to dipole layers. In that sense the metal work function, the semiconductor electron affinity, and the heterostructure band-offset can be understood in terms of the interfacial atomic dipole layer. This microscopic dipole consists of each of the 10^{15} atoms per cm^2 each displacing a charge of order e by a length of order 1 Å. The resulting potential barrier height is of order 1 eV. On the other extreme of the scale of lengths is the macroscopic distribution of charges in the depletion zone of a p-n junction. In this case in Fig. 2, some 10^{11} charges per cm^2 are separated by a length of order 10^4 Å to make up a macroscopic dipole layer. The rise in the potential occurs on a much larger scale. Its magnitude, however, is again ∿ 1 eV. In the same sense, the semiconductor depletion layer of the Schottky barrier forms a

macroscopic dipole sheet. Capasso's DID /2/ is an extreme case of "macroscopic" electrostatics, one that exploits the possibilities of modern growth technology.

The case of the degenerately doped δ-layer in Fig. 2 is genuinely different in that the separation of the electronic screening layer from the ionized donors is determined by the quantum-mechanics of binding in the asymmetric, self-consistent potential well. The dipole moment reflects the quantum confinement length of the effective-mass electrons and is of order 100 Å. The potential varies on a scale of length which is intermediate to the microscopic interface dipole and the macroscopic depletion

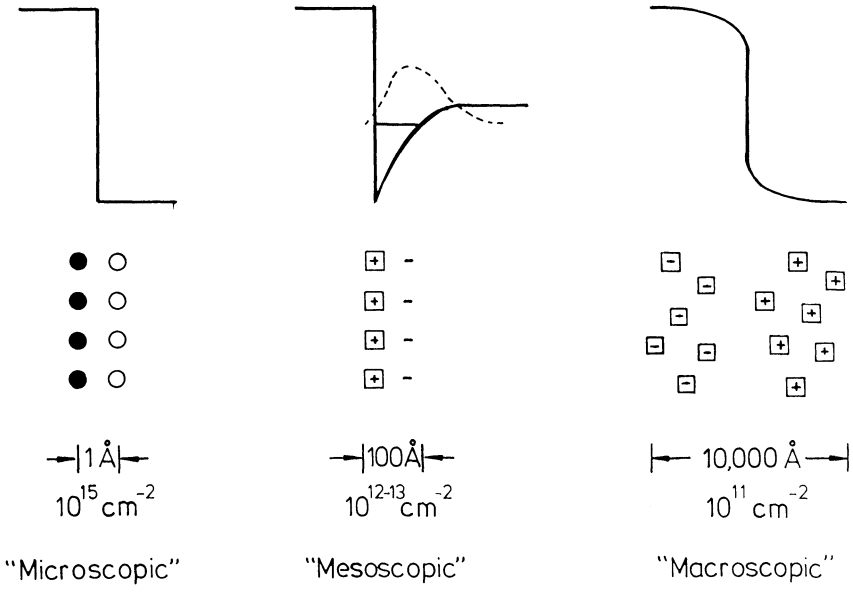

Fig. 2. Dipole layers with different physical lengths. The "mesoscopic" dipole of the δ-doping layer has a length depending on the quantum-mechanical confinement of the effective mass electrons.

layer. We refer to this case as a mesoscopic dipole layer. Its characteristic features are determined by the quantum mechanics of effective-mass motion of confined carriers. The number of carriers N_s in the doping layer can be of order 10^{13} cm^{-2}. Together with the binding length of ∿ 100 Å this makes for potentials of order 1 eV. The knowledgeable reader will recognize in this example the essence of 2D subband physics as introduced by F. Stern and others /5/ in the late 1960s.

In the following section we examine the growth technologies that have been used to achieve near atomic-layer confined doping. Sec. 3 reviews relevant electronic properties of the δ-layer. In Sec. 4 we examine the role of doping layers in shaping barrier potential structures

2. DOPING TECHNOLOGY. HOW TO GROW A δ-LAYER?

How does one achieve an ideal, atomically confined sheet of dopant atoms? Given the planar, 2-D epitaxial growth technologies of molecular-beam-epitaxy (MBE), of metal-organic chemical-vapor-deposition (MOCVD) or atomic-layer epitaxy (ALE), the answer appears straightforward and obvious. It is not at all so. The experimental realization of a true δ-layer is complicated by the details of incorporation kinetics, by segregation mechanisms, by clustering of the impurities and other processes.

The original approach to δ-doping is the stop-and-go method as introduced by C. Wood to produce a sheet of Si atoms in MBE-grown GaAs. In this method growth is interrupted by shutting off the flow of Ga atoms. The surface is As-stabilized, while Si atoms are deposited in the desired concentration. Typical interrupt times are of the order of ∿ 100 sec. Thereafter growth at the typical rate of 1 Å/s is continued. The substrate temperature is kept constant throughout. It has since been proven that serious ion-spreading in the direction of growth results /6,7/ when the usual, optimal growth temperature of 550° C or above is used. As discussed in a recent paper on a SIMS-study of the Si layer /8/, the incorporation of the dopant into the GaAs during the continued growth phase is

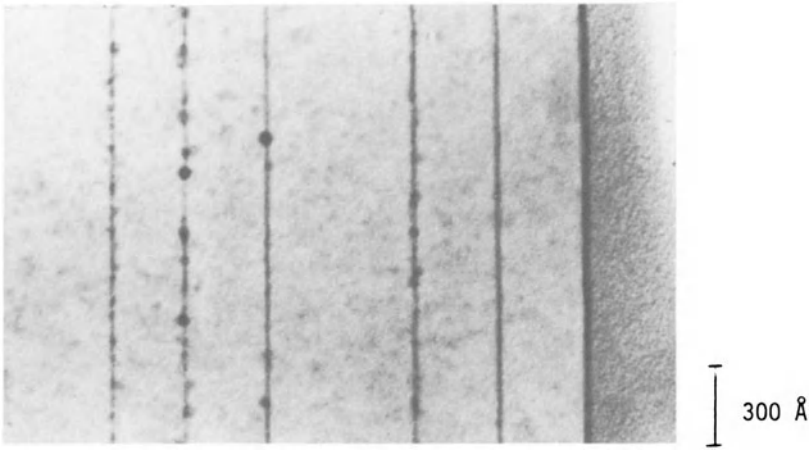

Fig. 3. δ-layers of Sb in (100) Si epitaxially grown by MBE. The bright-field TEM images have a resolution of order 20 Å. Note the clustering for increasing Sb densities(after Ref. /13/).

a complicated kinetic process which depends sensitively on parameters of the growth procedure. Substrate temperature, growth rate and possibly the partial Ga and As pressures will influence the result. Very good confinement has been achieved in a sample grown near 450° C with substantially higher than usual As pressure /9/. For densities in the 1×10^{13} Si cm^{-2} range and above there is serious clustering of the dopant atoms and autocompensation results /10/.

In Si MBE growth the incorporation of a donor like Sb is greatly complicated by a low sticking coefficient and substantial segregation. Sb atoms accumulate in large numbers on the growing interface. Only a small fraction is built into the epitaxial layer as the growth front advances. To deal with this problem in producing a sharp layer, Jorke et al. /11/ have introduced a "soft" secondary-ion implantation technique. A low voltage

applied to the substrate causes charged Si atoms to bombard the Sb-rich surface layer. By means of knock-on collision the dopant is gently implanted just beneath the surface. A large and fairly well localized enhancement of the Sb atomic density can be achieved in this way.

Even more successful has been the solid-phase-epitaxy (SPE) introduced by H.P. Zeindl et al. /12,13/ to produce Sb δ-layers in Si. In this approach, Sb is deposited in the desired concentration onto the substrate cooled to near room temperature after growth interruption. The dopant is then buried in a cover of ∿ 40 Å of amorphous Si before reheating to the growth temperature (∿ 650°C) and continuing the epitaxial growth cycle. Densities of order 5×10^{13} cm^{-2}, which represents ∿ 10^{-2} monolayers of Sb have been grown confined to better than a few lattice constants (< 20 Å). Using bright-field imaging in TEM-microscopy, the layer has been made visible with a resolution of ∿ 20 Å. On the way to achieving higher Sb densities, possibly even near mono-layer coverage, it has been noted that the Sb will cluster. The continuous doping layer in Fig. 3 will break up into distinct droplets when the density is raised too much.

The CVD epitaxy permits neither the growth interruption nor cooling of the substrate. Nevertheless, using a very low growth rate together with the highest possible doping rate, D. Grützmacher and his coworkers have achieved sharp S doping layers in InP /14/ that have shown distinct quantum characteristics. It appears that other techniques like metal-organic MBE, or the ALE can also produce layers with δ-like properties.

3. ELECTRONIC PROPERTIES OF THE δ-LAYER

What for the isolated donor impurity is the hydrogenic energy level scheme, is the subband spectrum for the doping layer. The subbands are the quantum states of the self-consistent potential well formed by the sheet of ionic charge and its complementary mobile screening charge. To understand the essential properties of the δ-layer we consider a sheet of Si donor atoms in GaAs. The density of Si per cm^2 is chosen sufficiently large so that strongly overlapping Bohr orbits guarantee a metallic system and a homogeneous distribution of the electronic charge in the plane. This condition is satisfied when $N_D \geqq a_B^{-2}$. For Si in GaAs, the necessary density is of the order 2×10^{11} cm^{-2}. The δ-layer is equivalent to a one-dimensional effective mass atom with the electrons moving in the self-consistently screened potential of the N_D ions. The electron density N_S equals this N_D, when there is no external perturbing influence.

The one-dimensional Hamiltonian of the δ-layer assumes the ionic charge to be uniformly spread over a distance "dz". For the model calculation in Fig. 4 this length has been taken as 5 Å to represent a near ideal case for which there is no growth- or diffusion-caused spreading of the donors. Because of the high values of the Fermi energy of the degenerate electron system it is necessary to include nonparabolicity of the GaAs band structure in the calculation / 7 /. A correction term for the exchange-correlation contribution to the energy has actually been included in the result of Fig. 4. The figure shows the potential well, energy levels and quantum-mechanical distribution of the charge for $N_D = N_S = 1.1 \times 10^{12}$ cm^{-2}. We note three occupied subbands each containing a fraction of the charge. Each level represents a 2-D continuum of occupied states starting at energy E_i and going up to the Fermi energy E_F. The levels are subbands of the type familiar from inversion layers in MOS-devices. In Fig. 4 the layer has inversion symmetry in $\hat{z}$ and no net dipole moment. The conduction band edge has the same

height before and after the layer when there is neither an electric field, a nearby interface nor other asymmetric external influence. The electron charge is spread about the ion sheet by a length of order 100 Å.

In a number of recent publications the quantum features and transport characteristics of the 2-D subband electrons have been thoroughly studied. One experiment, in particular, has served to demonstrate the quantum nature of the electronic levels and to measure the partial subband occupations N_S^i. It is the well-known Shubnikov-de Haas oscillatory magnetoresistance. Its period in reciprocal magnetic field applied normal to the layer plane is simply related to the N_S^i. The reader will find numerous examples in the literature / 4, 6, 7/.

Knowing the N_S^i and comparing these with an accurate and detailed model calculation has provided a measure of the ionic spreading / 6, 7/. In this way a very effective check on the growth technology has been possible. The original conclusion, that for conventional MBE growth

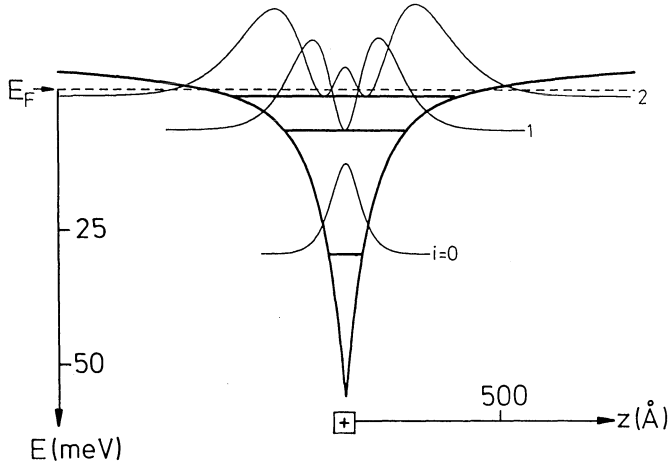

Fig. 4. Energy levels and potential well for a δ-layer (dz = 5 Å) with $N_D = N_S = 1.1 \times 10^{12}$ Si cm^{-2} in GaAs. Nonparabolicity and exchange-correlation correction to the potential are included. Fractional occupations: $N_S^0 = 0.87$, $N_S^1 = 0.20$, and $N_S^2 = 0.03$ in units of 10^{12} cm^{-2}.

procedures and substrate temperature of 550° C and above there is a finite spreading of the Si donors, has since been confirmed with high resolution SIMS / 8/. The alternative approach, to measure the ion-spreading by capacitance-profiling /15/ of the doping layer, is not meaningful for values of dz that are less than the quantum confinement length of the lowest subband. A recent experiment makes use of hydrostatic pressure in order to lower the DX-center energy in GaAs until it coincides with the E_F of the δ-layer. In this way it provides a caliper measure of the potential well depth and is sensitive to ion spreading on a scale less than the width of the i = 0 subband / 9/.

The level scheme and other properties of the δ-layer will vary widely with the choice of the host material. Thus the Sb-layer in (100) Si has a different subband structure which, in particular, must account for the multi-valley nature of the conduction bands. δ-doping in Si requires an up-scaling of the N_D by a factor of order 25 in order to satisfy the

degeneracy criterion. The δ-layer assumptions are satisfied for Si only with $N_D \gtrsim 1 \times 10^{13}$ Sb per cm^2. This makes transport experiments much more difficult. Energy levels and quantization has been demonstrated in tunneling spectroscopy experiments /12,16/. Very recently the far-infrared resonance excitation of Si subbands has been observed /17/. Because of the high N_D and strong confinement potential in Si, there is considerable band-mixing involved in the calculation of the δ-layer states.

Returning to the transport experiments on δ-layers, it remains to mention the diamagnetic-shift experiments done in parallel magnetic fields /18,19/. These have provided a measure of the extent of the wavefunction in the $\hat{z}$-direction. The quantum-Hall-effect has recently been observed for δ-layers in GaAs /20,21/. Of particular interest for the metal-insulator transition problem appears to be the current work on δ-layers in the low N_D limit. For the case of high N_D, the physical limits of planar Si-doping in GaAs have been explored in Ref. /10/.

It is a simple extension of the present discussion to consider a superlattice of periodically spaced δ-layers. For an example of successive Si-layers with $N_D = 3 \times 10^{12}$ cm^{-2} and spaced 100 Å apart, the electronic band structure has been calculated in Ref. /22/.

This rapid scan of δ-layer physics has served to acquaint the reader with the electronic properties of the layer. In the next section we turn to the applications.

3. MAKING, BREAKING, AND SHAPING POTENTIAL BARRIERS

Given the δ-layer growth technology and the understanding of relevant electronic properties we are ready to explore the role that δ-doping layers play in modern electronic device structures. We deliberately avoid discussion of the merits of the δ-doped MESFET /23/, of the saw-tooth nipi laser diode /24/, of the non-alloyed contacts /25/, and of the implanted base structure in HBT (heterobipolar transistor) technology /26/. For these the reader will find adequate references in the literature. Instead we highlight a few current examples that best illustrate the principles involved.

Using δ-layers together with the precision and control of MBE-growth it is possible to form and finely sculpture potential variations to suit a given electronic purpose. The principle is quite similar to that expressed in the camel-back transistor structure /26/ and in the hot-electron-spectrometer arrangement of Levi et al. /27/. The ultimate limit is an arrangement of successive δ-layers with a separation comparable to electron wavelengths - a quantum version of the familiar p-n junction and transistor, so to say. The small distances separating the emitter, base, and collector would make possible ballistic transport together with the quantization of energies.

We show in Fig. 5 an MBE-grown Si structure in which the base is a δ-layer with 2.0×10^{13} Sb cm^{-2}. It is followed by a 100 Å wide p-type barrier layer uniformly doped with Ga at the 3-D density of 1×10^{18} cm^{-3}. The emitter contact is a metal with Schottky-barrier height 700 meV. In the figure the potential profile and quantum levels in the δ-layer base are shown. Ground state levels i = 0 and 0', of the 2- and 4-fold degenerate valleys respectively, are found to be occupied. The calculation has assumed a forward biased emitter with voltage V_{BE}. The potential distribution is shown for three different values of the collector voltage. In this structure the δ-layer base is sufficiently close to the

metal surface that tunneling occurs. There are expected resonant structures in the tunnel current as electrons tunnel into the unoccupied 1 and 1' levels or out of the occupied 0 and 0' states. We note the small length of order 100 Å that carriers must traverse in order to reach the potential barrier maximum on the way to the collector. This is what makes ballistic transport of the carriers possible and assures fast transit of the base region. It is true that the proposed transistor structure in Fig. 5 is difficult to realize in practice because the proximity of the layers makes strategies for external contacts very elaborate. In particular, the potential drop along the base contact when there is current flow will cause a breakdown between the base and collector regions outside the active region of the transistor unless the two layers are additionally insulated somehow. Nevertheless, the transistor arrangements in the figure serves well to make a point. Potential variations on a length scale comparable with carrier wavelengths can be created at will using the δ-layer doping technology.

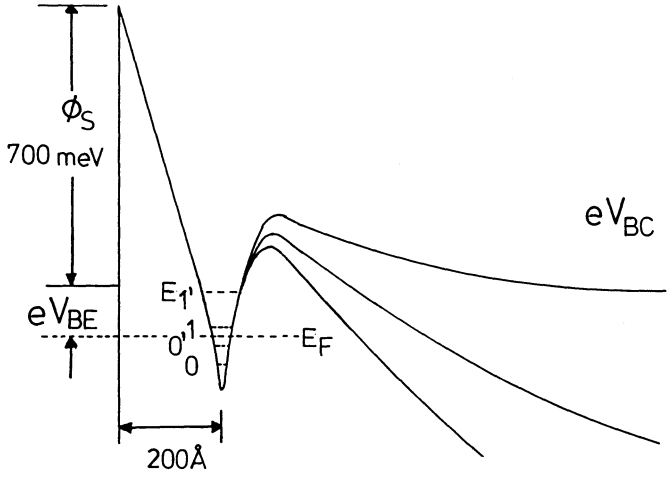

Fig. 5. Band edge variation diagram for a transistor structure employing a δ-doping layer as a base

For the second example we consider a δ-layer placed at a small distance from the interfacial barrier to the metal. Given that a high density of interface state pins the Fermi energy at a constant barrier height, we must expect a number of free electrons to be transferred from the δ-layer to the metal. In Fig. 6 we recognize that this number is inversely related to the distance separating metal and δ-layer. Enough electrons are transferred to provide the fixed barrier height. The electric field at the surface is related directly to the transferred charge. Knowing the metal to δ-layer distance together with the occupation of the subbands it is straightforward to reconstruct the barrier height. In that sense the δ-layer can be used as a probe of the surface potential barrier. Aside from the image potential effect, the charge transfer will not substantially change the barrier because the density of interface state is much higher than the δ-layer density N_D. For an electrically passive interface, such as a lattice-matched heterostructure, the situation is quite different. This will be considered later.

In Fig. 6 the self-consistent potential for 1.3 x 10^{13} Sb cm^{-2} at 200 Å from the interface has been calculated (assuming fixed barrier height). Electrons can be exchanged between the metal and the semiconductor by either thermal emission over the barrier or by tunneling. At low temperatures the tunnel current derivative, as observed for the arrangement in Fig. 6, has distinct structures that reflect the quantized bands in the δ-layer. Electrons tunneling from the metal give evidence for empty levels in the well. Conversely the peaks that occur when tunneling is from the δ-layer into the metal, are linked to the occupied subbands. The tunneling current component can be tailored to suit by properly positioning the doping layer. In this way the effective barrier can be made arbitrarily small. We recognize that the case discussed here is only a quantum version of the ohmic contact formation by heavy doping. It is distinct from its classical counterpart only by the discrete structures in the current.

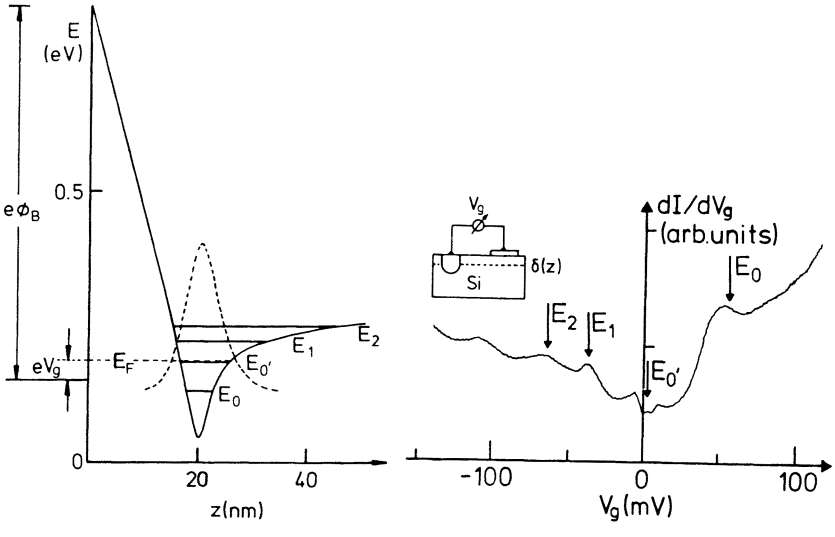

Fig. 6. Tunneling structure involving a Sb δ-layer with density 1.3 x 10^{13} cm^{-2} in (100) Si and a metallic surface layer. The current shows distinct structures that relate to the subbands (after Ref. /12/).

The example in Fig. 6 also serves to illustrate the principle involved in barrier lowering by the image effect. Thus a carrier approaching the interface from the semiconductor side senses the electric field that exists in the region between the δ-layer and the metal. As a point charge, the hot electron participating in the thermoemission process causes a surface charge to be induced in the metal. The resultant attraction reduces the barrier potential by an amount that increases with the surface electric field according to the standard Schottky-barrier lowering theory. In this way the δ-layer serves to tune the barrier height for thermal emission.

The most significant application of the doping layer, one where its quantum-mechanical dipole characteristics are essential, is in the doping

of heterostructures. In contrast to the metal-semiconductor interface, the lattice-matched heterointerface has almost no defect states at the bounding surface. For a dopant placed inside the lower-gap material the electronic state is confined mostly to that material. Donors near the interface of GaAs and AlGaAs will have the electron charge displaced such that its center lies ∿ 50 Å within the GaAs. The result is a large dipole moment for each of the N_D donors.

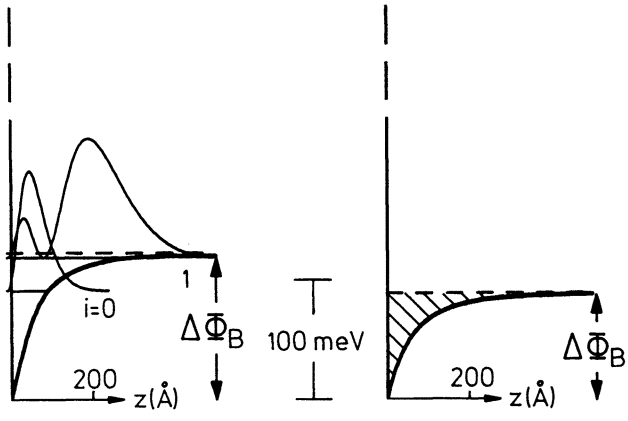

Fig. 7. Comparison of the dipole layer potential $\Delta\Phi_B$ calculated quantum-mechanically and classically for T = 0 K. The ionic charge is 1 x 10^{12} cm^{-2} at the interface. The barrier height is chosen so large (2 eV) that there is insignificant penetration of the wavefunction. Parameters are for GaAs.

To illustrate the effect and calculate the potential caused by the dipole layer at the heterointerface we consider in Fig. 7 the case of 1 x 10^{12} cm^{-2} donors at an abrupt and impenetrable barrier (actually 2 eV). The change in barrier potential $\Delta\Phi_B$ caused by the dipole layer depends sensitively on the quantum nature of the bound states. To demonstrate this point we compare in the figure the "classical" calculation (that assumes degenerate Fermi statistics for T ∿ 0 K and uses a 3-D density of states proportional to $E^{1/2}$) with the proper quantum result. Screening in the non-quantum case is provided by charge moving right up to the surface. Only Fermi-statistics and the finite $E^{1/2}$density of states keeps the average negative charge at a finite distance. The value of $\Delta\Phi_B$ is 87 meV for GaAs. Repeating the calculation using quantum mechanics gives two discrete occupied subbands and gives $\Delta\Phi_B$ = 122 meV. The difference is mainly caused by the larger quantum confinement length. The charge at the interface is minimal. The dipole moment is correspondingly greater.

The example in Fig. 7 has been calculated to make a point that has long since been recognized with regard to inversion layer subband physics. It applies equally well to doping whenever lengths of the order of a Bohr radius are involved. In this sense the δ-layer is a mesoscopic, quantum object. That is all the more reason to include in a calculation

of barrier lowering all the quantum refinements. For the finite 290 meV barrier between our AlGaAs and GaAs, there is a substantial penetration of charge into the large gap material. Nonparabolicity needs to be included as well as the many-body, exchange-correlation energy. With all these refinements we arrive at the result of Fig. 8. The dipole energy is so that after doping the net barrier height is only 196 meV. The barrier tuning effect of dopants, although well known in principle, has not always been accounted for in the experimental determination of band-offsets. One reason for this is the often unknown and possibly inhomogeneous distribution of defects at the interface. Thermoemission or internal photoemission will exponentially weight local potential variations caused by doping dipoles. This has been beautifully demonstrated by spatially

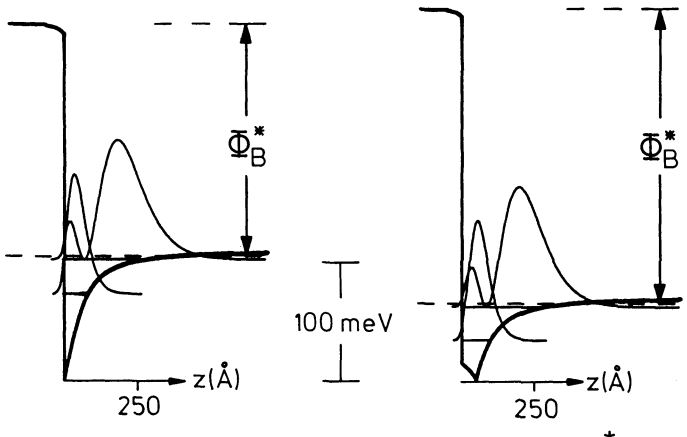

Fig. 8. Calculated effective barrier height Φ_B^* in the presence of interface donors for AlGaAs/GaAs with offset 290 meV. Note that the correct quantum calculation allows penetration into the AlGaAs and gives ∿ 10 meV of rise in the conduction band. For donors displaced by 50 Å into the GaAs the barrier lowering is substantially smaller.

resolved photoemission work on the Si-SiO_2 interface doped with Na^+-ions /28/. Fig. 8 also illustrates how sensitive the barrier lowering effect is to the positioning of the donor ion. Repeating the calculation when the donor sheet is displaced inward by only ∿ 10 lattice constants (50 Å), gives a Φ_B^* = 247 meV. In this case electron charge is both to the right and left of the donor ions. The dipole layer reverses sign and has a substantially smaller net effect on the barrier height. The calculation shows a lowering from 290 meV to 247 meV instead of the 196 meV.

5. CONCLUSION. ACKNOWLEDGEMENTS

In considering the effects that dopants near an interface have on the shape and magnitude of the barrier potential we have made the point that this involves mesoscopic, quantum physics. The classical concepts of p-n junctions, ohmic contacts via doping and barrier tuning that we introduced at the outset merit reexamination when there is sharply

defined, planar doping. Throughout, we have only needed to apply concepts that are well established in the physics of the 2D-electron gas.

We acknowledge financial support for this work from both the Deutsche Forschungsgemeinschaft and the Siemens Company (A.Z. is an Ernst v. Siemens research fellow). Several coworkers have contributed to this paper. The calculation of the Si transistor structure in Fig. 5 was provided by G. Tempel. Figures 4, 7, and 8 have been supplied by G. Müller from his thesis research.

REFERENCES

1. See for example S.M. Sze "Physics of Semiconductor Devices" (John Wiley and Sons, N.Y. 1981)
2. F. Capasso, K. Mohammed, and A.Y. Cho, J. Vac. Sci. Technol. B 3(4), 1245 (1985)
3. C.E. Wood, G. Metze, J. Berry, and L.F. Eastman, J. Appl. Phys. 51, 383 (1980)
4. A. Zrenner, H. Reisinger, F. Koch, and K. Ploog, Proc. 17th Int. Conf. on the Phys. Semicond., San Francisco 1984; ed. J.P. Chadi and W.A. Harrison (Springer, New York), p. 325
5. T. Ando, A.B. Fowler, and F. Stern, Rev. Mod. Phys. 54(2), 437 (1982)
6. A. Zrenner, F. Koch, and K. Ploog, Inst. Phys. Conf. Ser. 91, 171 (1987)
7. A. Zrenner and F. Koch, Surf. Sci. 196, 671 (1988)
8. R.B. Beall, J.B. Clegg, and J.J. Harris, Semicond. Sci. Technol. 3, 612 (1988)
9. A. Zrenner, F. Koch, R.L. Williams, R.A. Stradling, K. Ploog, and G. Weimann, Semicond. Sci. Technol. (in press) (1988)
10. A. Zrenner and F. Koch, Proc. 3rd Int. Conf. on Shallow Impurities in Semicond. (Linköping 1988) (to be published)
11. H. Jorke, H.-J. Herzog, and H. Kibbel, Appl. Phys. Lett. 47, 511 (1985)
12. H.P. Zeindl, T. Wegehaupt, I. Eisele, H. Oppolzer, H. Reisinger, G. Tempel, and F. Koch, Appl. Phys. Lett. 50, 1164 (1987)
13. H.P. Zeindl, G. Tempel, B. Bullemer, and I. Eisele, Proc. 2nd Int. Symp. on Si MBE, Honolulu 1988, ed. J.C. Bean, L.J. Schowalter
14. Wenchao Cheng, A. Zrenner, Qiu-Yi Ye, F. Koch, D. Grützmacher, and P. Balk, Sem. Sci. Technol. (in press) (1988)
15. E.F. Schubert, J.B. Stark, B. Ullrich, and J.E. Cunningham, Appl. Phys. Lett. 52, 1508 (1988)
16. G. Tempel, F. Koch, H.P. Zeindl, and I. Eisele, J. de Physique 48, C5-259 (1987)
17. N. Schwarz, G. Tempel, and F. Koch, Semicond. Sci. Technol. (submitted for publication)
18. H. Reisinger and F. Koch, Surf. Sci. 170, 397 (1986)
19. A. Zrenner, H. Reisinger, F. Koch, K. Ploog, and J.C. Maan, Phys. Rev. B 33, 5607 (1986)
20. G. Gillmann, P. Bois, E. Barbier, B. Vinter, D. Lavielle, M. Stohr, S. Najda, A. Briggs, and J.C. Portal, Semicond. Sci. Technol. 3, 620 (1988)
21. A. Zrenner, F. Koch, R.L. Williams, R.A. Stradling, K. Ploog, and G. Weimann, Sem. Sci. Technol. (in press) (1988)
22. F. Koch, A. Zrenner, and M. Zachau, in "Two-Dimensional Systems: Physics and New Devices", ed. G. Bauer, F. Kuchar, and H. Heinrich (Springer, Berlin 1986); Solid State Sciences 67, 175 (1986)
23. E.F. Schubert and K. Ploog, Jpn, J. Appl. Phys. 24, L 608 (1985)
24. E.F. Schubert, J.E. Cunningham and W.T. Tsang, Phys. Rev. B 36, 1348 (1987)

25. E.F. Schubert, J.E. Cunningham, W.T. Tsang, and T.H. Chiu, Appl. Phys. Lett. 49, 292 (1986)
26. J.M. Shannon and A. Gill, Electronics Lett. 17, 620 (1981)
27. A.F.J. Levi, J.R. Hayes, P.M. Platzmann, and W. Wiegmann, Phys. Rev. Lett. 55, 2071 (1985)
28. T.H. Di Stefano, Appl. Phys. Lett. 19, 280 (1971)

Temperature Dependent Metallization Studies

DISRUPTION, METALLIZATION, AND ELECTRICAL PROPERTIES OF METAL GaAs AND InP SEMICONDUCTOR INTERFACES

W. E. Spicer, R. Cao, K. Miyano, C. McCants,
T. T. Chiang, C. J. Spindt , N. Newman, T. Kendelewicz,
and I. Lindau

Stanford Electronics Laboratories
Stanford University, Stanford, CA 94305-4055

E. Weber and Z. Liliental-Weber

Lawrence Berkeley Laboratory
University of California,
Berkeley, CA 94720

I. INTRODUCTION

Despite dedicated efforts of many people over many decades, we are still struggling with the problem of Schottky barrier formation [1-11]. Perhaps this is because the emphasis has been on discovering a single mechanism which could explain everything. Mönch [12] has already suggested the importance of multiple mechanisms, and this approach will be emphasized in this paper.

Rather than beginning by focusing on detailed mechanisms and models, we divide the mechanisms into two general categories: extrinsic and intrinsic. The intrinsic category will include all proposed mechanisms compatible with a perfect, undisturbed semiconductor in contact with the metal. MIGS and VIGS are the primary examples. For brevity these will be called "MIGS" [6-9,12]. For the extrinsic category, we must include all mechanisms which depend on defects or impurities in the semiconductor or other layers between the semiconductor and the metal. For brevity this will be termed "defect" mechanism [4,5]. Separating possible mechanisms into intrinsic (MIGS) and extrinsic (defect) helps in distinguishing between the two categories based on experiments. For most metals it now appears well established experimentally that deposition at room temperature (RT) causes chemical reactions which measurably disrupt the GaAs or InP and produce new compounds. (Among the exceptions are Ag, Sn, Cs, In, and Ga.) However, recent experiments in which the semiconductor is cooled to low temperature (LT) before the metal deposition and kept at that temperature for photoelectron spectroscopy (PES) and other studies have the potential for distinguishing between extrinsic and intrinsic mechanisms by suppressing the extrinsic at LT [13-15]. Even where new chemical compounds are not formed, defects may be produced by the heat of condensation, chemisorption, or other adsorption phenomena [4,16,17] which release energy. The probability of such defect formation will be reduced at LT. Because much of the data is new, we will pay particular attention to LT studies in this paper.

MIGS requires metallization of the deposited metal atoms, while the defect mechanism does not. Thus, we will also pay special attention to the question of

metallization and its correlation with Fermi level movement. At LT, evaporated metal thin films tend to be uniformly distributed whereas this is often not the case at RT. The criteria which we develop apply most easily for uniform coverages and, thus, to the LT data. At RT, where islands of metal may form, leaving some semiconductor surface uncovered, special care must be taken in applying any criteria of metallicity.

A very important criterion is the comparison of the "pinning" position of the Fermi level (E_{ff}) in the thin film measured by PES with that obtained from thick metal overlayers (e.g. 1000 ML) by electrical measurement, such as the I-V method. Differences can be important. For example, if a MIGS mechanism is indicated at LT with thin films and a significantly different E_{ff} position is found by I-V, the results suggest that a defect mechanism may dominate in the thick case. Another important test can be made with the thick diodes. Chemical reactions at the interface can be enhanced by thermal annealing. If this causes a significant change in E_{ff}, a defect mechanism must be considered. Further discussion of the possible causes of annealing shifts is given in Section IV D. In this process, the effect of chemical reactions at the interface must be taken into account.

We will start this paper by examining the case where PES on RT and LT thin films seems to give the clearest example of a reaction being suppressed at LT with a corresponding change in E_{ff}. A large amount of new data with a large number of metals on GaAs will then be presented and discussed. In this context criterion for metallization will be presented and applied. Comparison will also be made with thick diode values of E_{ff}; the strength of the metal/semiconductor reaction will be considered as well as changes in E_{ff} due to annealing. From this, judgment will be made as to the mechanism (defect or MIGS) taking place for a number of metals on GaAs. Relationships between the direction of movement of E_{ff} on annealing and one specific defect mechanism will also be examined.

II. METALLIZATION AND FERMI LEVEL MOVEMENT: CRITERIA OF METALLICITY

For studies involving deposition of metal atoms, it is important to develop satisfactory criteria for the development of metallicity in the deposited films, i.e. how does one determine when a collection of metal atoms organizes itself so that it becomes a metallic film. Can the film be characterized by Fermi-Dirac statistics and in general demonstrate the properties of a Fermi liquid? The criteria we will develop for metallicity will be closely tied to the metallic behavior of the "free electrons". However, as will be discussed at the end of this section, it is ultimately important that any correlation of metallicity with other properties, e.g. the appearance of MIGS, relates the criteria for metallicity to the phenomena (MIGS in this case) of interest. This is particularly important when the morphology of the film is less than ideal, e.g. it may have a non-uniform thickness.

We suggest three criteria for metallicity which are particularly applicable to PES. For two of these there are sufficient experimental data to allow us to apply them in the present paper. The first is the development of a Fermi surface as seen by PES. This is illustrated by Figure 1. For a metal there is a Fermi cutoff of the electron distribution which coincides with the Fermi level. This will show thermal broadening; however, for the temperature lower than RT, the thermal broadening (0.025 eV or less) is negligible compared to the instrumental broadening (usually greater than 0.1 eV). Thus, the Fermi cutoff will be instrumentally broadened about the Fermi energy as shown in Figure 1 with the Fermi level bisecting the broadened cut off.

In Figure 2 we show data for Cs. Cs was chosen because, of all the metals studied, it has the least tendency to form lateral non-uniformities such as clumps or islands. Thus, it provides the least ambiguous data on metallization. The right and left hand panels of Figure 2 show the high binding energy cutoffs and the Fermi level from the Cs after the indicated amount was deposited. Using the definition of metallicity developed above, we find that the Cs film is not metallic at 1.5 ML but is at 2 ML of Cs. (1 ML = 4.4×10^{14} atoms/cm^2 for Cs on GaAs (110)).

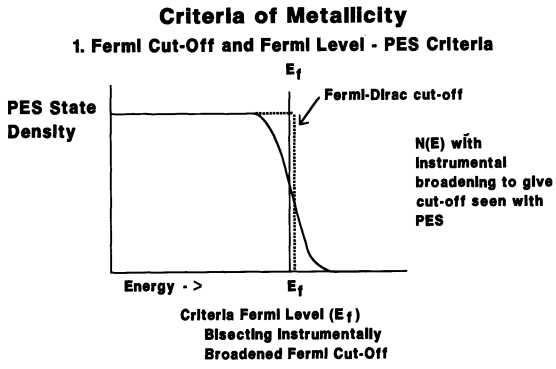

Figure 1. Full establishment of metallicity is characterized by a Fermi cutoff convoluted with thermal and instrumental broadening (with PES). The experimentally broadened Fermi cutoff is bisected by the Fermi level.

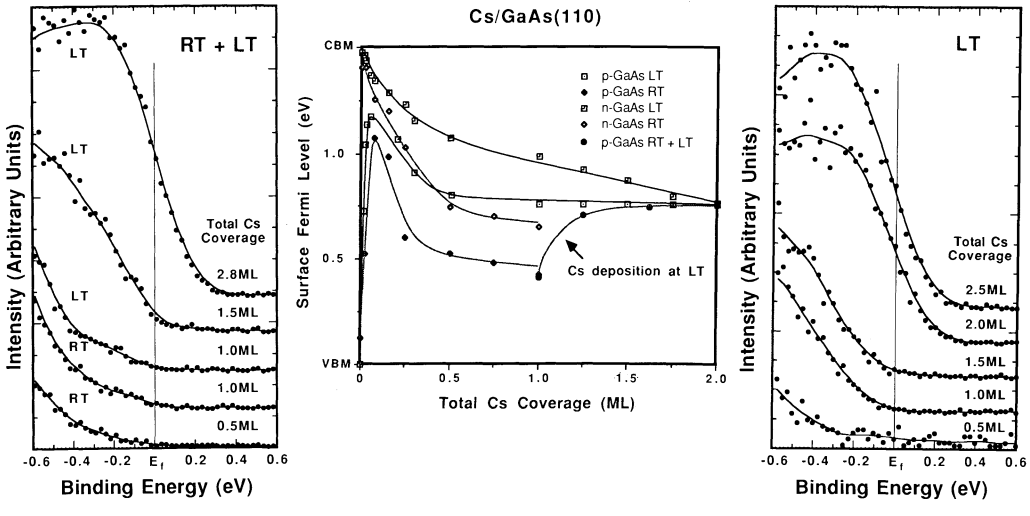

Figure 2. Development of the Fermi cutoff and surface Fermi level for Cs/GaAs(110) at RT and LT. The metallicity is fully established with Cs coverage greater than 2ML, where the E_{ff}'s are pinned at the same position (0.75 eV above the VBM). In contrast 1 ML Cs/GaAs does not show metallic feature, and two pinning positions are observed correspondingly.

A second criterion of metallicity of the overlayer is that the interface Fermi levels in the semiconductors with n- and p- type doping must coincide. Zur et al.[19] discuss this criterion. If charge can "flow" between the metal and the semiconductor, then the charge will adjust itself to satisfy this condition. In the center panel of Figure 2, we present data on the surface Fermi level (E_{fi}) for n- and p-GaAs (at LT or RT) as Cs is deposited (note the distinction between E_{ff}, which denotes a final stabilization (pinning) position and E_{fi},

which represents a metal coverage dependent band bending). As can be seen, the n- and p-values of E_{fi} coincide at approximately 2 ML. This measure of metallicity is in agreement with the Fermi cutoff criterion discussed before.

At RT only a monolayer of Cs is thermally stable. This is due to the large difference in binding energy of Cs bound directly to the GaAs substrate relative to Cs bound to Cs [20]. To deposit more than one ML, it is necessary to cool the sample. Thus, as indicated by Figure 2, a metallic Cs overlayer can only be obtained at reduced temperature (LT = 80°K in this case). As can be seen, E_{fi} for the p-GaAs changes strongly due to the deposition of metallic Cs. We will discuss this in the next section.

In Figure 2 there is reasonable agreement between these two criteria - the Fermi cutoff and the coincidence criterion. However, as will be apparent in the next section, this is not always the case. More typically, we find the coincidence criterion is usually satisfied noticeably before the Fermi cutoff criterion. However, both criteria usually indicate metallization occurring at several monolayers, never at less than a monolayer.

This paper will present E_{fi} versus metal coverage for a wide range of metals. We will indicate the coverage at which the Fermi cutoff criterion indicates that the overlayer is metallic. The coverage at which the coincidence criterion indicates a metal will be apparent from the E_{fi} versus coverage plots. The use of both criteria should give more certainty as to the occurrence of the metallicity.

Applying both criteria can be important. For example, for Ag at LT, it has been argued that the first criteria may not be applicable below several ML because of "instantaneous charging" of the Ag in the photoemission event. In such a case, one can examine the second criteria which would not be affected by this "charging". Since this criteria also finds the Ag film to not have metallicity, the situation is made clear. A second criterion is for Al, In, or Ga on GaAs at RT where the metal deposition is established to be non-uniform with the metal forming clumps or islands which only partially cover the surface. In this case the first criterion indicates metallicity whereas the second does not. This is explained by the fact that the islands are metallic, but the uncovered GaAs surface is not. Thus, the situation becomes clear when both criteria are applied.

A third criterion which we would suggest is the appearance of free electron plasma loss features in the PES spectra. Unfortunately, such data are presently available only for the alkali metals on GaAs(110). The Cs data show no such plasma loss for 1 ML of Cs, good indications of losses at 1.5 ML, and a well-developed loss structure by 2 ML. Thus, a very good agreement with the other criteria is found. One reason for mentioning this criterion here is the need for more plasma loss data which can provide important information on metallization.

III. Ag AND Cu ON InP: THE ROLE OF INTERFACIAL REACTIONS IN THE FERMI LEVEL PINNING

Ag and Cu on InP give an ideal case where cooling to LT (80°K) stops the chemical reaction between InP and Ag, and the E_{ff} pinning position moves from a position which can be correlated with defect formation to a new position which is close to the calculated MIGS "pinning" position. In contrast cooling does not prevent the reaction with Cu, and the E_{ff} remains unchanged at the "defect" position [21,22].

Figure 3 shows the In 4d core level for both LT and RT depositions as a function of the Ag coverages. At RT the new structure is clearly observed. This is due to elemental or metallic In which has been removed from InP by the chemical reaction. A curve fitting program was used to separate the In 4d components as shown in Figure 3. At LT there is no evidence of the chemical reaction. In Figure 4 we indicate E_{fi} position versus coverage for Cu and Ag. As can be seen, the "pinning" position at high coverages moves from 0.95 eV at RT to 0.7 eV above the valence band maximum (VBM) (later in this paper all the E_{fi} positions are measured from the VBM) at LT. As will be discussed in more detail below, the 0.95 eV is associated with defects and the 0.7 eV with MIGS.

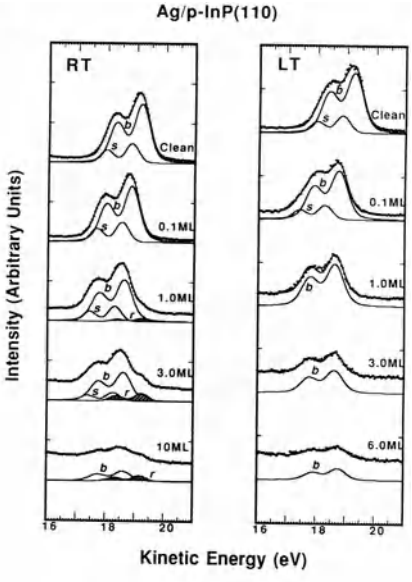

Figure 3. In 4d core level spectra (hv = 40.8 eV) for RT and LT Ag/p-InP(110) at selected Ag coverages. The spectra are decomposed into bulk (b), surface (s), and reacted (r) components. Note the disapperance of the reacted component at the LT interface.

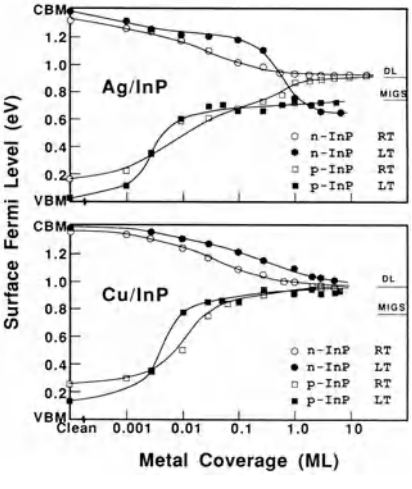

Figure 4. Surface E_{fi} positions at the RT and LT interfaces of Ag and Cu on InP(110) as a function of metal coverage. The pinning position for defects (DL), metal induced gap states (MIGS) and by I-V measurement (I-V) are marked. The two interfaces show different temperature dependences on the Fermi level pinning.

Ag: Reactive @ RT; Non-reactive @ LT

Cu: Reactive @ RT and LT

In Figure 5 we present data for Cu on InP. As can be seen, a chemical reaction is taking place for coverages of 1 ML or greater. Note that this chemistry is not removed by cooling to LT. As Figure 4 shows, the "pinning" position is also unchanged by cooling.

We associate the position at 0.95 eV with defects. For example, heating cleaved (110) p-type InP in vacuum below the decomposition temperature, it is possible to move E_{fi} for p-InP from the original position near the VBM to 0.95 eV [23, 24]. Based on a number of studies involving metals on InP the range of pinning for defects has been identified as lying between 0.85 and 1.05 eV [25]. The 0.7 eV position is located outside that range and coincides reasonably close to the E_{ff} position position of 0.76 eV calculated theoretically by Tersoff [26]. Thus, it would appear that defects pin the Fermi level at RT for Ag, and that cooling removes the chemical reaction necessary to produce defects in this case, and that MIGS then do the pinning. The Cu/InP pinning is associated with defects since the reaction remains almost unchanged at LT

One reason that the InP results are so clear cut is that the defect pinning positions and the pinning position for MIGS are far away from each other, experimental distinction between the two possible. Unfortunately, this is not the case for GaAs as will be seen in the next section.

Several things are indicated in the right margin of Figure 4. Since we will also use this nomenclature for GaAs, we will explain it here in some detail. The line labeled DL indicates the energy level associated with a defect. For GaAs two lines will be used since two defect levels are important [4,5,27]. The theoretical MIGS position is indicated by the line labeled MIGS.

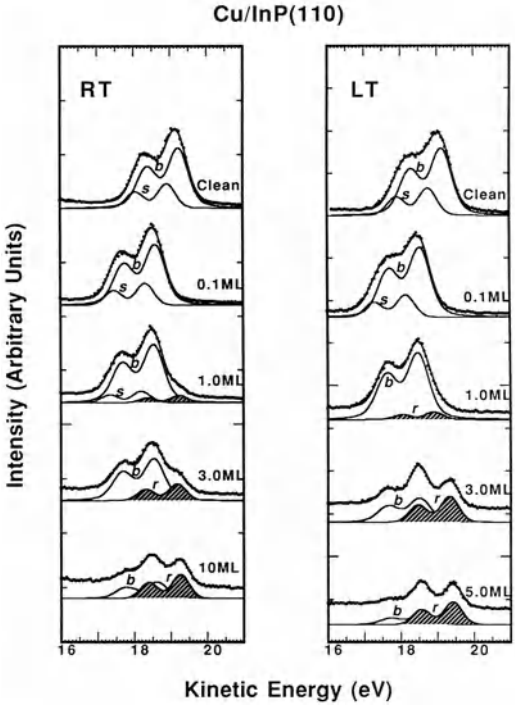

Figure 5. In4d core level spectra (hν = 40.8 eV) for RT and LT Cu/p-InP(110) at selected Cu coverages. The difference in temperature causes no drastic change in the interfacial reaction.

Also included is a line labeled I-V. This is the E_{ff} position obtained from I-V measurements of thick metals (1000Å) on the semiconductor. This is important because it locates E_{ff} after the RT coverage has been increased from a few to hundreds of monolayers. Usually it closely coincides with the PES E_{ff} position at RT. This is the case for Cu for Ag. Rather the latter moves close (0.8 eV) to the calculated MIGS position (although it is still well above the LT PES E_{ff} position.) This suggests that both MIGS and defects are playing a role in determining E_{ff} for the thick diodes. For some interfaces, where annealing of the diode has performed, the values from the I-V measurement before and after annealing are also indicated.

Unfortunately, our Fermi level cutoff data was not good enough for inclusion of the metallicity data in Figure 4. However, the Fermi levels for n- and p-type InP coincides for coverages greater than approximately 2 ML. Thus, it is reasonable to assume that metallicity is present at that coverage.

The curves of Figures 3 and 5 are important in that they illustrate the manner in which PES can be used to follow chemistry. Similar studies have been done on most of the metal/GaAs systems to be discussed. For brevity, we will not present such data much pf it has been in the literature but will just indicate the strength of the GaAs/metal interfacial chemical reaction on the basis of it.

IV. METALS ON GaAs

A. Introduction

This section will make up most of this paper. This is due to the fact that more data is available for metals on GaAs than for any other system and because the metal/GaAs system seems so complicated. Fortunately, it appears that considerable sense can now be made from this data if we take the approach outlined in the introduction in which both defects and MIGS mechanisms are considered to exist.

The problem is separating out MIGS and defect effects. Since metallicity is necessary for MIGS but not defects, we will start by examining the results for a nonmetallic overlayers of Sb on GaAs. In this sense it is representative of other non-metals, e.g. oxygen, Ge, and Si on GaAs which have been studied. In addition, much is known about the way 1 ML of Sb organizes itself epitaxially on GaAs. Thus, thin Sb provides a good example of a non-metal film on GaAs. Next we will examine Sn which can be either metallic or non-metallic. In this work, it seems to have a rather abrupt phase transition, becoming a metal at coverages of about 3 ML.

In a separate section we will discuss data for column IIIB metals (Al, Ga, In) which span a broad range of reactivities and tend to cluster on the GaAs surface. For Al the exchange reaction is well documented while In is the least reactive in the series. In a separate section we will discuss very insightful new data on Cs overlayers which served to develop the criteria of metallicity presented in the previous section. New data on the transition and noble metal overlayers at low temperatures will be treated in a separate section and discussed in the context of competition between MIGS and defect mechanisms. The transition metals, in particular, tend to have a very strong chemical reaction with GaAs and "tear it apart". In contrast, the noble metals do not react so strongly. Ag, in particular, is quite non-reactive.

In Section IVC, we will examine changes in E_{ff} due to thermal annealing of thick metals on GaAs. This gives another way of distinguishing between defects and MIGS. A detailed model for the key defects near the GaAs interface will also be introduced since, it will enable us to correlate the direction of motion of E_{ff} and the interfacial chemistry. Finally, a section will be given in which the results from the various metal GaAs interfaces are tabulated and a suggestion given as to the relative importance of MIGS and defects for each system.

B. CASE STUDIES OF OVERLAYERS ON GaAs

1. Sb and Sn on GaAs

Figure 6 shows the movement of the E_{fi} from the bulk position into its final "pinning" position as a function of Sb coverage. (1ML = 8.85 x 10^{14} atoms/cm^2 on GaAs(110) except Cs). Also drawn in Figure 6 and all the figures of surface Fermi level (E_{fi}) versus coverage are the positions of the two defect levels characterizing the Unified Defect Model [4] and the new Advanced Unified Defect Model (AUDM) [5]. The AUDM will be discussed in more detail in Section C. As can be seen, the "pinning" positions roughly coincide with the two defect levels. It was this type of data which played an important role in developing the UDM and defining these defect energy levels

Note that the E_{fi} versus coverage data is the same at LT and RT for Sb/GaAs. We attribute this to the fact that the Sb on Ga and As chemisorption surface atoms is to a large extent independent of temperature. The energy released by this chemisorption process is assumed to be large enough to produce the 10^{12}-10^{13}/cm^3 defect level density necessary to pin the E_{fi} independent of temperature [27]. Note that since thin Sb film on GaAs is not a metal, one does not have to worry about metallic screening of the defects [19,28] so that a relatively small number should be able to do the pinning.

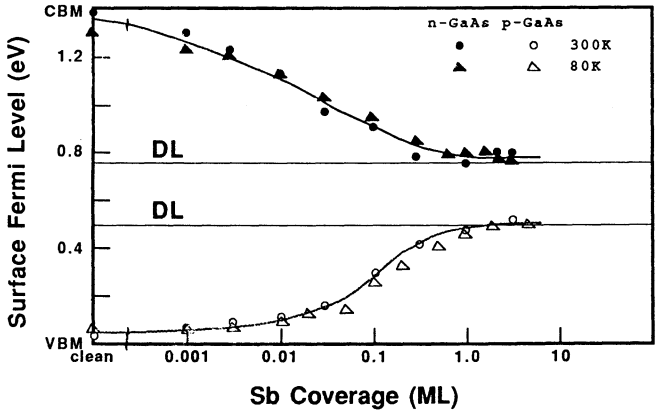

Figure 6. Evolution of Surface E_{fi} versus Sb coverage at the RT and LT Sb/GaAs(110) interfaces. The lack of temperature dependence is expected for this chemisorption system. Two distinct pinning positions which coincide with defect levels (DL) are found.

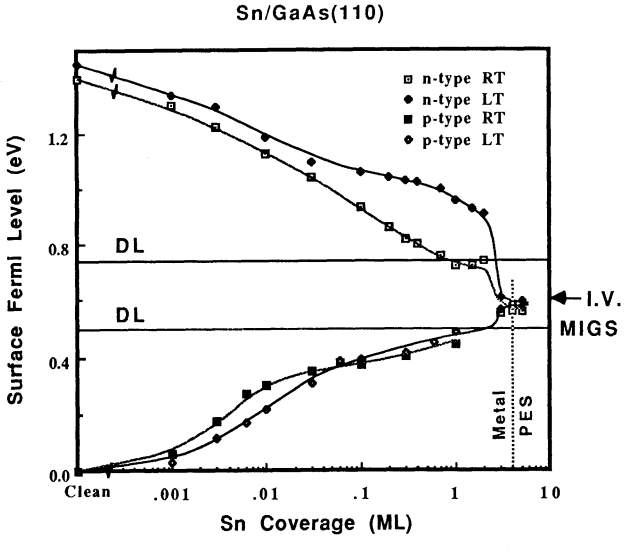

Figure 7. Evolution of surfaces E_{fi} at the RT and LT Sn/GaAs(110) interfaces. The abrupt change in the E_{fi} position at high coverages is related to the development of metallicity in the Sn overlayer, which is marked by the vertical dash line (same for most figures shown later).

In Figure 7 we show E_{fi} versus coverage for Sn. Particularly at RT there are similarities between this data and that for Sb for coverages less than about 2 ML. At the higher coverages, where our criterion indicates that Sn becomes a metal, the E_{fi}'s come together and the pinning position is at 0.6, eV close to that predicted for MIGS (0.5 eV) which is indicated in the figure. Also shown is the E_{ff} position obtained from I-V measurements of thick Sn on GaAs. As can be seen, this coincides quite nicely with the PES "pinning" position. This data strongly suggests the importance of MIGS in pinning the Fermi level for this system [28,29,30]. In so far as E_{ff} by PES or I-V deviates from the MIGS position, defects may also be playing a role.

2. Column IIIB metals on GaAs

Data for In/GaAs is presented in Figure 8. Here we see very fascinating behavior at LT for p- GaAs. The rapid rise of E_{fi} at low coverages is clearly due to isolated In atoms [31] on the surface donating their electrons to acceptors in the p-GaAs as suggested by Mönch, Kahn, and others [31,32,33]. We will see this behavior for a number of other metals. This and other low coverage behaviors will be treated by the authors in separate publications. Here we will concentrate on the behavior at coverages above 1 ML. At RT, the behavior is similar to that of Sb. This is surprising because PES gives clear indication of metallic In at the highest coverages. We can only understand this in terms of the strong and well established tendency for In to form islands rather than a continuous film in this coverage range [18,34]. The area between the islands would dominate the "pinning" as seen by PES. Thus the observed RT pinning behavior is attributed to defects between the islands [35].

The behavior of LT E_{fi} data near a monolayer coverage is quite different from that at RT. Here the E_{fi} curves drop rather abruptly and come together near the metallization coverages. This behavior is very suggestive of MIGS and the "pinning" position is in good agreement with the theoretical MIGS position. Thus, it appears that the MIGS mechanism is operative at LT.

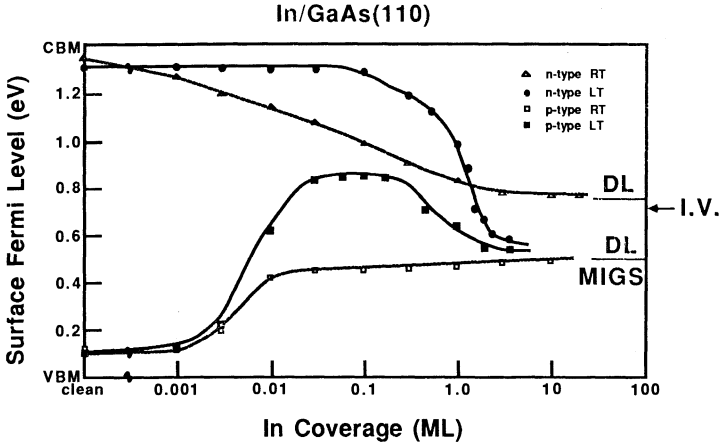

Figure 8. Evolution of surface, E_{fi} at the RT and LT In/GaAs(110) interfaces. Different pinning behavior appears at RT and LT, which corresponds to different dominant pinning mechanisms.

Very recent studies [36] have found that, by warming the LT p-GaAs sample with coverages near 2 ML, it is possible to move E_{fi} from the MIGS position up to the position

of the plateau which appears at LT for .02 <θ <0.1 ML. This is attributed to island formation removing the metallic In and leaving free areas in which isolated In atoms donate their electrons to acceptors in the GaAs. It illustrates the interplay between MIGS and other mechanisms where islanding is possible.

The I-V position for n-GaAs reported by [37] is also shown in Figure 8. This is sufficiently far from the LT-PES MIGS. However, this work should be repeated and extended to p- GaAs.

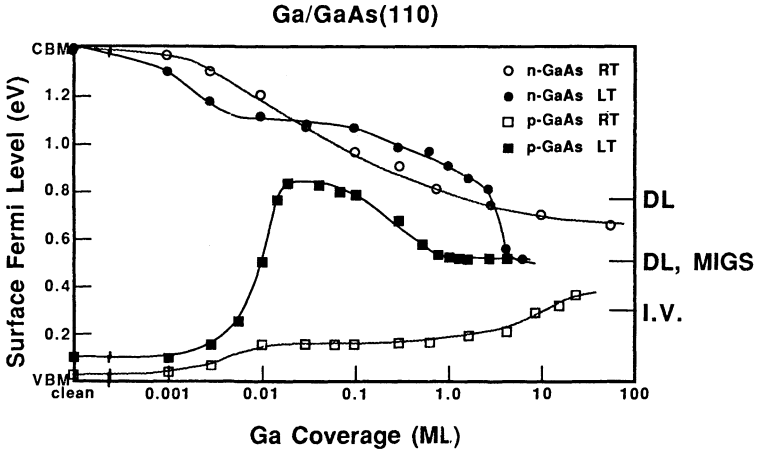

Figure 9. Evolution of Surface E_{fi} at the RT and LT Ga/GaAs(110) interfaces. It is similar to that at the In/GaAs(110) interface shown in Figure 8.

Ga is a system of great interest because of its relation to the new AUDM. Band bending data is shown in Figure 9 which is qualitatively consistent with the previous study [38]. At RT the data is similar to that for In; however, at LT the data beautifully illustrates the pattern expected for a MIGS mechanism. No PES Fermi cutoff data has been published. However, our studies indicate metallization by the PES Fermi cutoff criterion takes place at a coverage where the MIGS mechanism takes place at LT.

The pinning behavior of Ga on GaAs at RT and higher temperatures (including MBE and thick Ga I-V data) has recently been briefly reviewed by our group [39]. We will not reproduce this here. Rather we simply point out that the thick I-V data shows a pinning position about 0.3 eV above the VBM and that the other data is consistent with this. This is the only metal we know where the thick I-V data indicates a pinning position below the defect and MIGS levels indicated in the figure. However, as will be covered in Section III D, the explanation for this comes naturally from the AUDM. In any case, it seems safe to say that this pinning position can only be explained with a defect mechanism.

Fermi level movement versus coverage for Al/GaAs is shown in Figure 10. The Fermi level movement pattern for Al/GaAs at RT is similar to that for In and Ga. We would suggest that the defect mechanism works for all three metals at RT for the same reason as discussed above for In. The data is not as complete as would be desired. However, it seems to show metallicity by the coincidence criterion at about 5 ML at LT. This and the E_{fi} data indicate a MIGS mechanism at LT. However, a defect mechanism is indicated by the data for the "free" GaAs seen by PES at RT.

The thick I-V data for Al is interesting. It gives a pinning position at 0.65 eV for the diode formed at RT. This suggests that defects, as well as MIGS mechanisms, are important. Further evidence consistent with a defect mechanism is given by changes in E_{ff} upon annealing the diodes [40]. A movement of E_{ff} from 0.65 to 0.55 eV due to annealing has been found. The direction of movement will be explained in terms of the AUDM in Section IV C.

3. Cs overlayers on GaAs

The data for Cs/GaAs are shown in Figure 11. There is general agreement between this data and that of Prietsch et al.[41], although there are differences in detail. The very complex and interesting behavior below 1 ML will be discussed elsewhere [42]. Here we will concentrate on the E_{fi} movement near and above 1 ML. At RT the behavior up to 1 ML (the highest possible RT coverage in a vacuum) is similar to that for the systems discussed

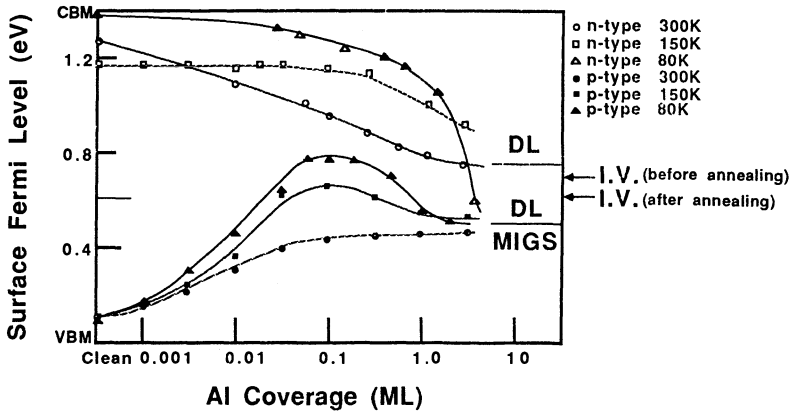

Figure 10. Evolution of Surface E_{fi} at the RT and LT Al/GaAs(110) interface data of 80 K LT Al/n-GaAs from ref. 15. Although data is not as complete as desired, the overall pattern is similar to In and Ga/GaAs(110).

above except high overshoot for p-GaAs at very low coverages. At LT the n- and p-GaAs coincide near 0.75 eV. The behavior is quite consistent with a MIGS mechanism except that the "pinning" position lies 0.25 eV above the MIGS position. This may be due to the extremely low electronegativity of Cs and charge transfer from Cs to GaAs [42], however, more theoretical and experimental work should be done to test this. The fact that the p-GaAs reaches its "pinned" position at a coverage of 0.5 ML well before metallicity occurs is hard to understand in terms of MIGS.

The E_{ff} for bulk Cs on p-GaAs by I-V which we could find in the literature gives a value of 0.63 eV [43]. This would suggest a defect mechanism at RT and/or further question the MIGS explanation at LT. However, the thick Cs should be redone and extended from p- to n- GaAs before the value of E_{ff} for thick Cs in Figure 11 is taken too seriously.

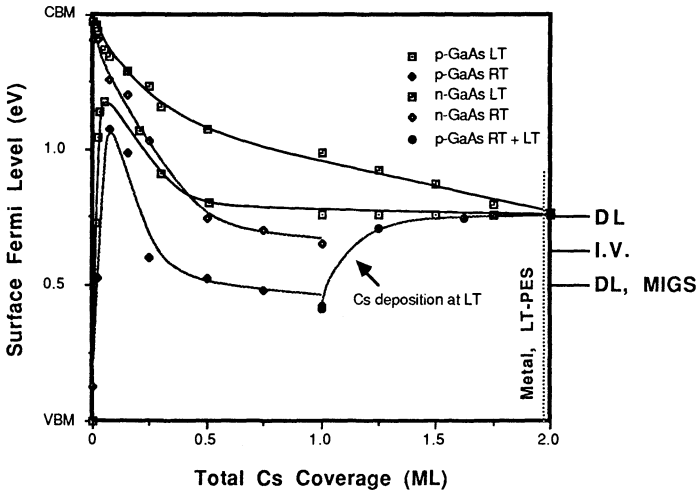

Figure 11: Surface E_{fi} position at Cs/GaAs(110) interface. It shows the largest overshoot for p-type GaAs of all metals studied so far. Two stabilized E_{ff} positions are found at RT with 1 ML saturation coverage. With more Cs deposition at LT only one pinning position is observed.

4. Noble metals on GaAs

Data for Ag on GaAs is presented in Figure 12. The LT curves and the I-V data are consistent with a MIGS mechanism [44]. The p-type RT data is also consistent with this; however, the n-type RT position deviates significantly from the MIGS position even at the highest coverage. This probably indicates islanding (well established for Ag) and a mild defect mechanism at RT for PES conditions [17,18]. However, the PES plus I-V data indicate the MIGS mechanism when the Ag is in good contact with the GaAs.

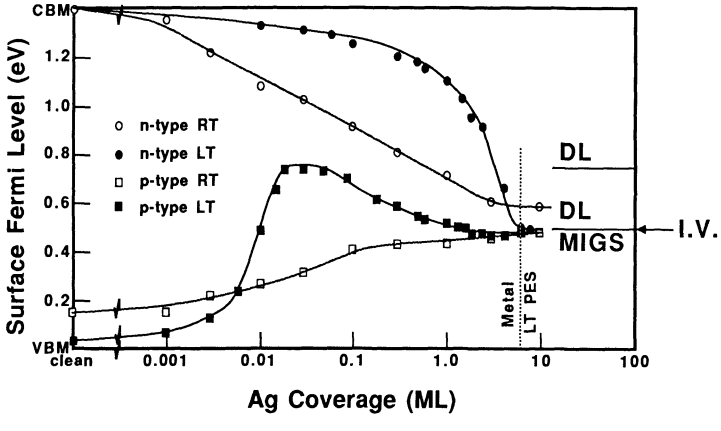

Figure 12: Surface E_{fi} position at the RT and LT Ag/GaAs(110) interfaces. Strong temperature dependence is observed.

Chiang et al. [45] have found that by heating Ag/GaAs in vacuum, the Ag forms a few well isolated islands, and the E_{fi} moves from the positions shown in Figure 12 for high Ag coverage back almost to the original position near the CBM (n-GaAs) or VBM (p-GaAs). Thus, the Ag is removed from most of the surface and the "pinning" disappears. This can be most easily explained by the MIGS mechanism disappearing as the metal is removed from contact with GaAs. However, the possibility of annealing away defects must also be considered.

Ag is the only metal studied to date which shows no tendency to chemically bond (chemisorption) to or react with GaAs [46,47]. This non-reactivity is consistent with thermodynamic data . There is also no change in E_{ff} on annealing thick Ag on GaAs [48]. This is also consistent with the AUDM prediction if no reaction is present and MIGS dominate.

In Figure 13 we present data for Au/GaAs. Although this data is not as complete as desired, it appears to agree with a MIGS model as does the I-V value of E_{ff}. However, annealing moves the Au/GaAs diode E_{ff} up from 0.5 to 0.6 eV above the VBM measured by I-V. This additional movement can be easily explained in terms of defects but not MIGS. In fact, this E_{ff} movement can be well correlated with the interfacial chemistry and experimentally seen excess (free) As [49]. Thus, for Au it appears that defects as well as MIGS are important.

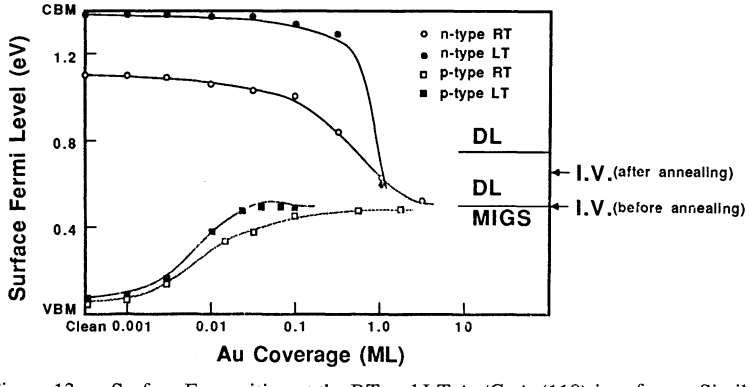

Figure 13. Surface E_{fi} position at the RT and LT Au/GaAs(110) interfaces. Similar behavior (except much less overshoot for LT p-type GaAs) as Ag/GaAs(110) in Figure 12 is observed. However, a change in the E_{ff} position during annealing was found [48].

For brevity, the Cu data is not shown. The E_{ff} position is found to be 0.55 eV independent of the type of doping or temperature [14].

5. Data for representative transition metal overlayers.

Data for a transition metal, Ti, is presented in Figure 14. Unfortunately, RT n-GaAs data is missing from this set. However, we have established that E_{ff} for that case is the same as for the cases shown [50]. As in the case of Cs, the observed behavior is consistent with a MIGS behavior except that E_{ff} is about 0.2 eV higher than the MIGS position. If the electronegativity argument were used for MIGS on Ti, it would be inconsistent with such an argument for Cs and also inconsistent with the In and Ga results. Thus, we do not believe this can be explained solely in terms of electronegativity arguments [51].

The annealing I-V data shows a downward shift of E_{ff} for Ti. This is consistent with a defect mechanism and, in fact, can be well explained by the AUDM and established interfacial chemistry. This will be discussed in more detail in the next section. It should also be noted that Ti reacts very strongly with GaAs. Thus, we suggest a defect mechanism for this material.

As mentioned above, agreement is obtained between the Ti E_{ff} data and the AUDM. However, Ludeke et al. have suggested that another type of defect may be important for Ti and other strongly reacting transition metals [52,53]. In this case the defect is the transition metal moving into GaAs and forming a deep impurity level. This model should be considered for Ti and related metals as well as the AUDM.

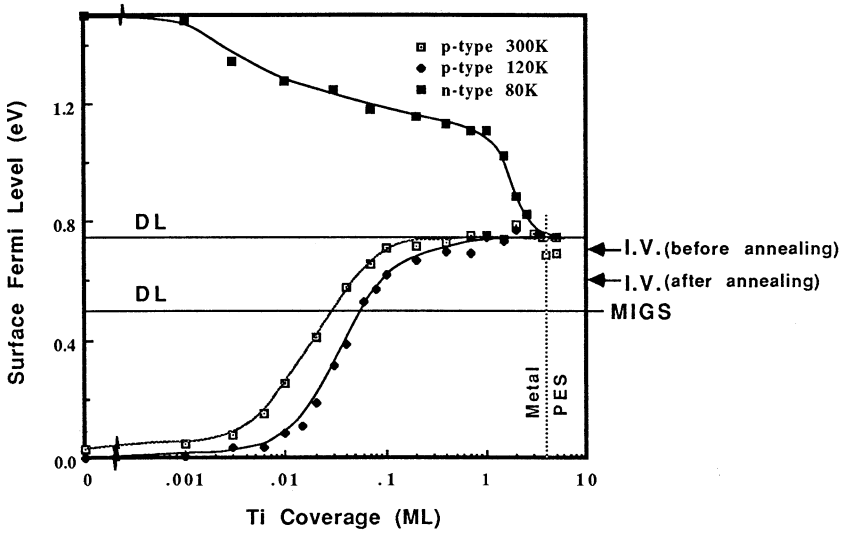

Figure 14. Surface E_{fi} position at the RT and LT Ti/GaAs(110) interfaces. One pinning position (0.75 eV above the VBM) is found for RT n- and p-GaAs and LT n-GaAs. The change in the E_{ff} position upon annealing is marked.

We have studied Cr but for brevity will not display the data. It is similar to that for Ti except that E_{ff} is 0.65 eV. For Cr, E_{ff} is not moved by annealing [48]. Defect mechanisms including that of Ludeke et al. and the AUDM should be considered for Cr.

Data for Pd is shown in Figure 15. E_{ff} by all methods lie at or slightly below 0.5 eV. This is roughly consistent with a MIGS mechanism. However, due to the reactivity of Pd with GaAs [54], and the lack of annealing data, defect mechanisms should not be ruled out until further study is done.

The results for Ni/GaAs are shown in Figure 16. The PES pinning positions shown are in good agreement with MIGS. However, some prior PES/RT studies have reported E_{ff} as high as 0.7 eV [55]. In addition, note the rather bizarre behavior of the n-type data just before metallization. This suggests that both MIGS and defects may be important. The fact that the E_{ff} position of 0.7 eV by I-V [56] is well above the MIGS position reinforces this conclusion. The present data suggests that both MIGS and defects are important for Ni. Further studies should be carried out before any final judgements are made.

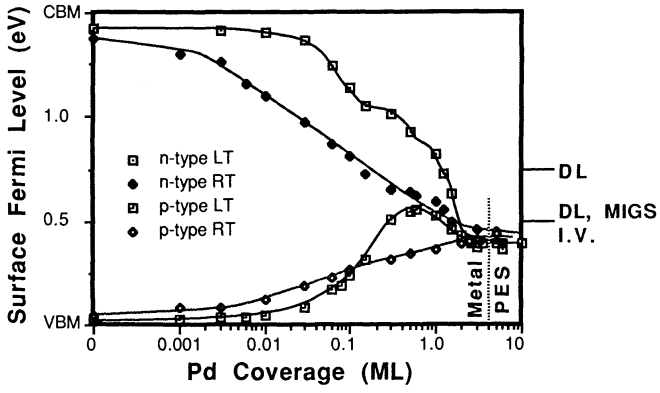

Figure 15. Surface E_{fi} position at the RT and LT Pd/GaAs(110). A final pinning position which is lower than those due to defects and MIGS appears.

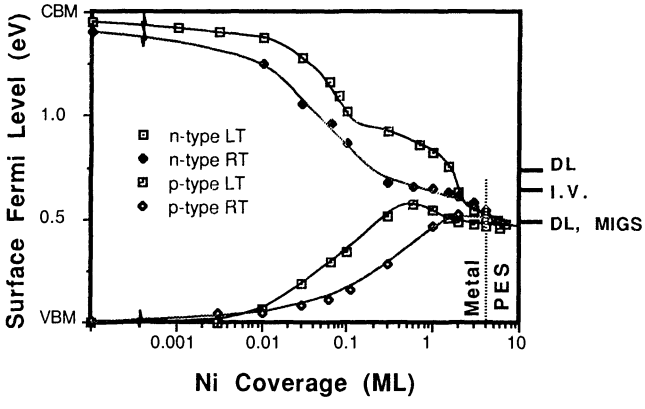

Figure 16. Surface E_{fi} position at the RT and LT Ni/GaAs(110). A similar pattern is obtained as that of Pd/GaAs(110) in figure 15 except a little higher E_{ff} position.

C. Thick Diodes, Changes Due to Annealing and the Advanced Unified Defect Model (AUDM)

As mentioned earlier, it is important that thin film values of E_{ff} be related to those obtained from thick (100's of ML) film studies. This is particularly true since it is such thick layers which are usually of practical interest. In the curves of E_{fi} vs. metal coverage presented earlier, we indicated the value of E_{ff} obtained for RT depositions where it was available. In this section, we will examine changes in E_{ff} which can be produced by annealing carefully prepare diodes of this type [5,25,39,49] and show how this can be explained in the context of a specific defect model - the Advanced Unified Defect Model (AUDM). The AUDM gives a semi-quantitative explanation for the I-V annealing data. The AUDM and the experimental data on which it is based have been described in two recent publications [5,39]. We will only briefly describe AUDM and its genesis here.

In 1982, Weber et al. proposed energy levels for As_{Ga} antisite defects in GaAs [57]. This was done principally in relation to the EL-2 center responsible for semi--insulating GaAs. Weber et al. proposed that the As_{Ga} antisite was responsible for the energy levels suggested in 1979 for the UDM. Figure 17 shows data from the 1979 paper [58] with the proposed defect model as well as the levels of Weber et al. from their 1982 paper [57]. As can be seen, there is surprisingly good agreement between the two sets of energy levels. The As_{Ga} energy levels of Figure 17 have stood the test of time well.

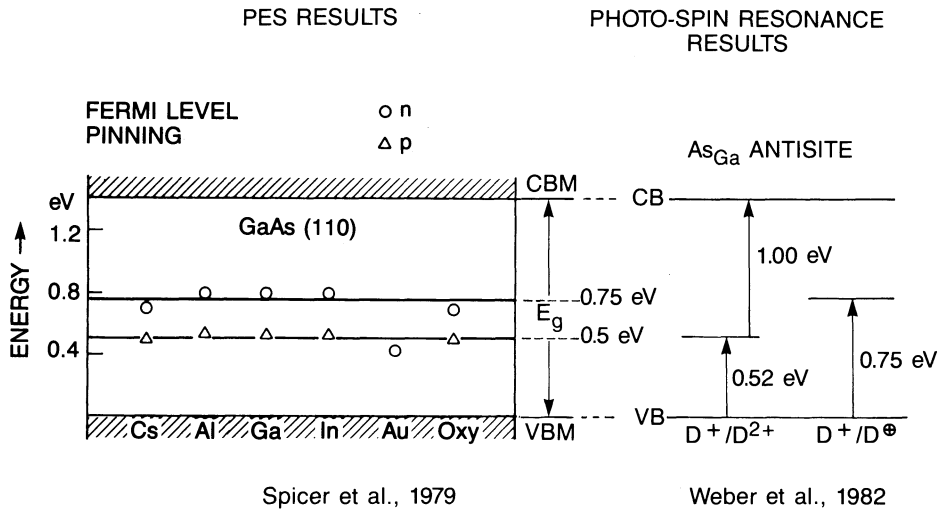

Figure 17 . The diagram to the left is taken from a 1979 paper (Ref 58). This energy level diagram indicates the pinning positions obtained on n- and p-GaAs with very low coverages (order 1 ML or less) of the indicated element measured at room temperature (Eg = 1.42 eV). The pinning positions are identical within experimental error to those obtained in the present work for Al, Ga, In, and Sb. (See Figure 6, 8, 9, and 10 of this paper). The vertical lines through those data points indicate the defect energy levels deduced in 1979. The right diagram indicates the energy of the As_{Ga} antisite levels from the VBM measured at 8 K (Eg = 1.52 eV) by Weber, et al. in 1982 (Ref. 57). As can be seen, the two sets of levels are found to agree.

A problem with using the As_{Ga} alone to explain the GaAs/metal E_{ff} data or the EL-2 /semi-insulating GaAs phenomena is that the As_{Ga} antisite is a double donor. To explain the data, a lower lying minority acceptor is needed. For the interface have an acceptor, and perhaps for EL-2, the best choice is a Ga_{As} antisite defect which is known to have acceptor state below the lowest As_{Ga} level of 0.5 eV [59]. This is the combination used for the AUDM as shown in Figure 18. Usually the density of Ga_{As} antisite defects must be considered smaller than that of As_{Ga} antisites. The only strong exception is

Ga/GaAs where it is necessary to assume that the Ga_{As} density is larger. As described in more detail in Ref. 5 and 39, the starting GaAs crystals are grown from the As side of the phase diagram. As a result, it is not surprising that the interfaces are As rich. Independent evidence for this has been found in the experimental work of Liliental-Weber et al. [49].

The defect levels (DL) indicated in Figures 6-16 were taken from the original Unified Defect Model. These levels are the same in the AUDM.

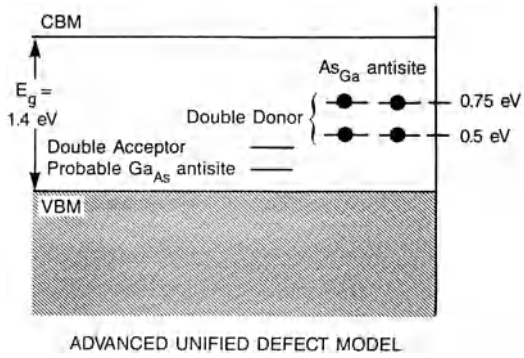

Figure 18. This energy level diagram for the Advanced Unified Defect Model (AUDM). The As_{Ga} antisite double donor with levels of 0.75 and 0.5 eV and the compensating acceptor (probably the Ga_{As} antisite) with energy levels below 0.5 eV are shown. Both defects are located in the same spacial region near the surface. The surface Fermi level position, E_{fi}, for the free surface will be determined by the relative densities of the two defects in the near surface region. In the usual case where $E_{fi} > 0.5$ eV, the density of $As_{Ga} > Ga_{As}$.

Since the As_{Ga} antisite donor levels are to some extent compensated by the Ga_{As} acceptors, the value of E_{ff} is set by the relative numbers of the two type of antisites and by any charge which flows into the defect levels from the semiconductor and the metal. In Figure 9 we indicated that Ga on GaAs was very unusual in that it had the E_{ff} position measured for thick Ga diodes which is well below the 0.5 MIGS or defect levels. This can now be explained easily in terms of the AUDM if we assume that for thick Ga on GaAs, sufficient Ga moves in significant quantity into the interfacial region of GaAs so as to make the Ga_{As} antisite the dominant defect.

The relationship between E_{ff} movement through interfacial chemistry and the AUDM is outlined in Table 1. As can be seen, the direction of motion of the Fermi level prediction in this agrees well with the experimental results. Note that the Al, Au, and Ti [39,60] results are for annealing of a thick diode above RT. The Ga results are for going from a few ML of Ga on GaAs at LT to the thick I-V condition at RT. Independent evidence has been obtained of the increase or decrease of excess As at the interface on annealing [5,39,49,63]. This is in agreement with the chemistry indicated in Table 1.

In the course of investigating the changes due to annealing, alternative explanations of the effect of annealing have been investigated. For Au/GaAs it was originally suggested that the movement of E_{ff} on Au due to annealing was explained in terms of Ga alloying with Au reducing the electronegativity. However, detailed investigation gave no evidence of sufficient Ga concentrations in the Au to explain this [49,63] in the diodes for which the changes were observed.

For the Al/GaAs case, it was first thought that the change in E_{ff} was due to an increase in band gap due to replacing Ga in GaAs by Al to form $Al_{1-x}Ga_xAs$. However, studies on p-GaAs showed that the sum of barrier heights on n- and p-GaAs was not increased on annealing as is necessary if the band gap was increased [40]. One importance of the AUDM is that it gives a mechanism by which the Fermi level motion can be explained in terms of the interfacial chemistry.

Table I. Movement of the Fermi Level (E_{fi}) According to the AUDM

- Position of E_{fi} depends on Antisite Ratio $\frac{N(As_{Ga})}{N(Ga_{As})}$
  - If $\frac{N(As_{Ga})}{N(Ga_{As})}$ increases (i.e. As excess),E_{fi} moves up (i.e. toward CBM)
  - If $\frac{N(As_{Ga})}{N(Ga_{As})}$ decreases (i.e. Ga excess)E_{fi} moves down (i.e. toward VBM)

4 Reactions

Reaction	Product	Predicted Direction	Observed Direction
Ga + GaAs	Ga excess	VBM	VMB(>0.2 eV)
Au + GaAs	GaAu + Au	CBM	CBM(0.1 eV)
Al + GaAs	AlAs + Ga	VBM	VBM(0.1 eV)
Ti + GaAs	TiAs + Ga	VBM	VBM(0.1 eV)

Explanation of the E_{fi} movement from the thin interface positions to that of thick diodes and for diode annealing. The key parameter is the density ratio between the two types of antisite defects. Four interfaces are listed here with the reaction and the product during thick diode formation and annealing. The experimental findings are in good agreement with the AUDM predictions.

D. Summary and Discussion

In this section we summarize the results of the previous sections in Table 2. All the results were obtained by the Stanford group except those marked. In the first and second columns the semiconductors and all the metals mentioned in this paper are listed. Barrier heights for RT and LT thin interfaces measured by PES, and for RT and annealed thick diodes measured by I-V are listed. All the values are referred to the VBM. Where appropriate for thin-PES, the pinning for n- and p-GaAs are indicated. At LT, only one pinning position is observed. RT positions for most metals on GaAs are consistent with the defect levels, in particular, for those which have two pinning positions. The calculated pinning position due to MIGS [9,26] is also listed in this table. Good agreement between most LT PES measurements and the MIGS prediction is seen, indicating that MIGS are dominant there. For the rest, we believe both defects and MIGS are operative with the defect usually dominating. Metal electronegativities for different metals are included here. The additional change in the E_{ff} movement upon annealing and that from thin Ga to thick Ga overlayers follow the direction predicted by AUDM, suggesting that the interfacial reaction and defect formation have to be taken into account for thick diodes. In the last two columns, the occurrence of interface chemistry and the suggested dominant mechanisms are indicated. Where interface reactions occur, defects tend to dominate; while MIGS dominate where reactions are not observed. The disappearance or suppression of this reaction enhances the role of MIGS.

Flores [64] has pointed out that the MIGS pinning position can change due to different preparation if this causes the metal atoms to bond strongly with either Ga or As dangling bonds. It is important that this be investigated. At present some examination of this suggestion can be made in terms of the present data. First note that the Column III metals all pin near the MIGS position at LT. For thick diodes the Ga position (~0.3 eV) is

Table II. Fermi Level Position (E_f - VBM) (eV) and Mechanisms of Schottky Barrier Formation

S.C.	Metal	Thin-PES RT	Thin-PES LT	MIGS	Metal Electro-negative	Thick-I.V. R T	Thick-I.V. Anneal	Chemistry seen RT	Chemistry seen LT	Suggested Dominant mechanism RT	Suggested Dominant mechanism LT
InP	Ag	0.95	0.7	0.7	(1.9)	0.8	–	Y	No	D/M	M
	Cu	0.95	0.95	0.7	(1.9)	0.9	--	Y	Y	D	D
GaAs	Cs	0.73(n) 0.5(p)	0.75	0.5	(0.7)	0.65[a]	--	No	No	D/M	M
	Ti	0.7	0.7	0.5	(1.5)	0.7	0.6	Y	Y	D	D/M
	Al	0.75(n) 0.5(p)	~0.55	0.5	(1.5)	0.65	0.55	Y	Y	D	---
	Ga	0.75(n) 0.5(p)	0.5[b]	0.5	(1.6)	~0.3[c]	--	No	No	D	M
	Cr	0.65	0.65	0.5	(1.6)	0.65	0.65	Y	Y	D/M	D/M
	In	0.75(n) 0.5(p)	0.5	0.5	(1.7)	0.7[d]	Ohmic n-GaAs	No	No	D	M
	Ni	0.5(0.7)	0.5	0.5	(1.8)	0.7	-	Y	Y	D/M	D/M
	Sn	0.6	0.6	0.5	(1.8)	0.65	-		Chemisorp	M/D	M
	Cu	0.55	0.55	0.5	(1.9)	0.5	-	Y	Y	D/M	D/M
	Ag	0.65(n) 0.5(p)	0.5	0.5	(1.9)	0.5	0.5	No	No	M/(D)	M
	Pd	0.45	0.45	0.5	(2.2)	0.55	-	Y	Y	D/M	D/M
	Au	0.5	0.5	0.5	(2.4)	0.5	0.6	Y	No	D/M	M

D = Defect
M= MIGS

Measured Fermi level positions relative to the VBM for thin interfaces at RT and LT (by PES), thick diodes (by I-V) and diode annealing. All work was done at Stanford except those marked.
a. reference 42: b. reference 37: c. reference 60,61: d. reference 36

quite different from that of In and Al even, though one would expect the bonding of these three metals to the GaAs to be similar. However,the AUDM gives an explanation in terms of Ga_{As} antisite formation. The change of pinning position for thick Al, Ti, and Au on annealing can be explained in terms of interfacial chemistry and the AUDM as described in the text; however, it is important to see if MIGS with bonding taken into account can also give an explanation.

V. CONCLUSIONS

We have studied a variety of metals on GaAs(110) at both RT and LT as well as thick diode annealing. Our study shows that both extrinsic (defects) and intrinsic (MIGS) states at the interfaces can be important in determining the final Fermi level position (or the Schottky barrier height) at the interfaces. Most metals strongly disrupt III-V semiconductors when deposited at RT and during the course of annealing so that defects become important. For near perfect interfaces usually obtained by preparation at LT, defect formation may be largely suppressed. With the near uniform metallic overlayers formed in this case, MIGS can play a dominant role determining the E_{ff} position. However, one should be cautious in assigning a MIGS mechanism just because the calculated charge neutrality position is close to the pinning position [26] since defect positions may accidentally fall near that energy. This is particularly true for GaAs. The development of the metallicity in the overlayer has to be closely examined. To understand the physical nature of Schottky barrier formation, careful studies are needed, e.g the effect of the electronegativity of metal atoms, charge transferring between overlayers and semiconductors, the effect of interfacial chemistry, etc. Careful studies of well characterized thick diodes (including annealing study) need more attention and must be strongly correlated with thin film (PES) studies. Particularly important is annealing of thick diodes where changes in chemistry, interfacial stoichiometry and the resultant change of the barrier height can help us understand the interplay between different mechanisms. Techniques such as TEM and STM combined with conventional techniques such as I-V, CV measurements and PES are needed to provide more insight into this many-decade old and fundamental problem.

This work is supported by ONR under contract No. N00014-86-K-0736, DARPA and ONR under contract No. N00014-83-K-0073, and Air Force Office of Scientific Research under contract AFOSR-86-0263.

References

1. W. Schottky, Z. Physik. 113:367 (1939).

2. N. F. Mott, Proc. Roy. Soc. (London) A 171:27 (1929).

3. J. Bardeen, Phys. Rev. 71: 727 (1947).

4. W. E. Spicer, I. Lindau, P. Skeath, C. Y. Su, and P. Chye, Phys. Rev. Lett. 44:420 (1980).

5. W. E. Spicer, T. Kendelewicz, N. Newman, R. Cao, C. McCants, K. Miyano, I. Lindau, Appl. Surf. Sci. (in press). and references therein.

6. V. Heine, Phys. Rev. A 138:1689 (1965).

7. G. Louie and M. L. Cohen, Phys. Rev. B 13:2461 (1976).

8. C. Tejedor, F. Flores, and E. Louis, J. Phys. C: Solid State Phys. 10:2163 (1977).

9. J. Tersoff, Phys. Rev. Lett. 52:465 (1984).

10. J. M. Andrews and J. C. Philips, Phys. Rev. Lett. 35:56 (1975).

11. J. L. Freeouf and J. W. Woodall, Appl. Phys. Lett. 39:727 (1981).

12. W. Mönch, J. Vac. Sci. Technol. B 4:1085 (1986).

13. R. Cao, K. Miyano, T. Kendelewicz, K. K. Chin, I. Lindau and W. E. Spicer, J. Vac. Sci. Technol. B 5:998 (1987).

14. R. Cao, K. Miyano, T. Kendelewicz, I. Lindau, and W. E. Spicer, Appl. Phys. Lett. 53:210 (1988).

15. K. Stiles, A. Kahn, D. Kilday, and G. Margaritondo, J. Vac. Sci. Technol. B 5:987 (1987).

16. W. Mönch, R. S. Bauer, H. Gant, and R. Murschall, J. Vac. Sci. Technol. 21:498 (1982).

17. A. Zunger, Phys. Rev. B 24:4372 (1981).

18. R. Cao, K. Miyano, I. Lindau, and W. E. Spicer, J. Vac. Sci. Technol. (to be published).

19. A. Zur, T. C. McGill, and D. L. Smith, Phys. Rev. B 28:2060 (1983).

20. J. Derrien and F. Arnaud D'Avitoya, Surf. Sci. 65:668 (1977).

21. R. Cao, K. Miyano, I. Lindau, and W. E. Spicer, J. Vac. Sci. Technol. (to be published).

22. R. Cao, K. Miyano, T. Kendelewicz, I. Lindau, and W. E. Spicer, (submitted for publication).

23. K. K. Chin, R. Cao, K. Miyano, T. Kendelewicz, J. J. Yeh, I. Lindau, and W. E. Spicer, Phys. Rev. B 36:5914 (1987); Mat. Res. Soc. Symp. Proc. 77:429 (1987).

24. L. Koenders and W. Mönch, Proc. of 17th International Conference on the Physics of Semiconductors, edited by D. J. Chael: and W. A. Harrison (Springer, New York 1985) p. 85.

25. N. Newman, W. E. Spicer, T. Kendelewicz, and I. Lindau, J. Vac. Sci. Technol. B 4:931 (1986); T. Kendelewicz, N. Newman, R. S. List, I. Lindau, and W. E. Spicer, J. Vac. Sci. Technol. B 3:1206 (1985).

26. J. Tersoff, Phys. Rev. B 30:4874 (1984).

27. R. Cao, K. Miyano, I. Lindau, and W. E. Spicer, Appl. Phys. Lett. 53:137 (1988).

28. S. B. Zhang, M. L. Cohen, and S. B. Louie, Phys Rev B 32:3955 (1985).

29 K. Stiles, A. Kahn, D. Kilday, J. McKinley, and G. Margaritondo, J. Vac. Sci. Technol. A 6:1462 (1988).

30. R. Cao, K. Miyano, I. Lindau, and W. E. Spicer, J. Vac. Sci. Technol. (to be published).

31. R. Cao et al (in preparation).

32. W. Mönch, J. Vac. Sci. Technol. B 6:1270 (1988).

33. A. Kahn, (this proceeding).

34. D. E. Savage, and M. G. Lagally, Phys. Rev. Lett. 55:959 (1985).

35. K. E. Miyano, R. Cao, T. Kendelewicz, C. J. Spindt, P. H. Mahowald, I. Lindau, and W. E. Spicer, J. Vac. Sci. Technol. B 6:1403 (1988).

36. K. Miyano, R. Cao, T. Kendelewicz, I. Lindau, and W. E. Spicer, J. Vac. Sci. Technol. (to be published).

37. B. L. Smith "Metal Contacts", edited by E. H. Roderick Clarendon press, Oxford (1978) p. 68.

38. K. Stiles, S. F. Horng, A. Kahn, J. McKinley, D. G. Kilday, and G. Margaritondo, J. Vac. Sci. Technol. B 6:1392 (1988).

39. W. E. Spicer, Z. Liliental-Weber, E. R. Weber, N. Newman, T. Kendelewicz, R. Cao, C. McCants, K. Miyano, P. H. Mahowald, and I. Lindau, J. Vac. Sci. Technol. B 6:1245 (1988) and references therein.

40. N. Newman, W. E. Spicer, and E. R. Weber, J. Vac. Sci. Technol. B 5:1020 (1987).

41. M. Prietsch, M. Domke, C. Laubschat, T. Mandel, C. Xue, and G. Kaindl, Z. Physik (in press).

42. R. Cao, K. Miyano, T. Kendelewicz, I. Lindau, W. E. Spicer (submitted for publication).

43. J. J. Uebbing, and R. L. Bell, Appl. Phys. Lett. 11:357 (1967).

44. K. Stiles and A. Kahn, Phys. Rev. Lett. 60:440 (1988).

45. T. T. Chiang, C. J. Spindt, W. E. Spicer, I. Lindau, and R. Browning, J. Vac. Sci. Technol. B 6:1409 (1988).

46. R. Ludeke, T.-C. Chiang, and D. E. Eastman, J. Vac. Sci. Technol. 21:599 (1982).

47. K. K. Chin, S. H. Pan, D. Mo, P. Mahowald, N. Newman, I. Lindau, and W. E. Spicer, Phys. Rev. B 32:918 (1985).

48. N. Newman, Z. Liliental-Weber, E. R. Weber, J. Washburn, and W. E. Spicer, Appl. Phys. Lett. 53:145 (1988).

49. Z. Liliental-Weber, E. R. Weber, N. Newman, W. E. Spicer, R. Gronsky, and J. Washburn. "Defect in Semiconductor", Edited by H. J. von Bardeleben, Mat. Sci. Forum 10-12:1223 (1986).

50. C. McCants, G. P. Carey, R. Cao, K. Miyano, M. D. Williams, P. H. Mahowald, I. Lindau, and W. E. Spicer, J. Vac. Sci. Technol (to be published).

51. W. E. Spicer, S. Pan, D. Mo, N. Newman, P. Mahowald, T. Kendelewicz, and S. Eglash, J. Vac. Sci. Technol. B 2:476 (1984).

52. R. Ludeke, Surf. Sci. 168:290 (1986);

53. R. Ludeke, D. Straub, F. J. Himpsel, and G. Landgren, J. Vac. Sci. Technol. A 4: 874 (1986).

54. T. Kendelewicz, W. G. Petro, S. H. Pan, M. D. Williams, I. Lindau, and W. E. Spicer, Appl. Phys. Lett. 44:113 (1984).

55. T. Kendelewicz, M. D. Williams, W. G. Petro, I. Lindau, and W. E. Spicer, Phys Rev. B 32:3858 (1985).

56. N. Newman, M. van Schilfgaarde, T. Kendelewicz, M. D. Williams, and W. E. Spicer, Phys. Rev. B 33:1146 (1986).

57. E. R. Weber, H. Ennen, V. Kaufmann, J. Windschief, J. Schneider, and T. Wosinski, J. Appl. Phys. 53, 6140 (1982); E. R. Weber and J. Schneider, Physica 116B:398 (1983).

58. W. E. Spicer, P.W. Chye, P. R. Skeath, C. Y. Su, and I. Lindau, J. Vac. Sci. Technol. 16:1427 (1979); 17:1019 (1980).

59. T. Figielski, Appl. Phys. A 35:255 (1984).

60. C. E. McCants, T. Kendelewicz, P. H. Mahowald, K. A. Bertness, M. D. Williams, N. Newman, I. Lindau, and W. E. Spicer, J. Vac. Sci. Technol. A 6:1466 (1988).

61. R. Reinke and Meming, Surf. Sci. 192:66 (1987).

62. A. B. McLean and R. H. Williams, Semicond. Sci. Technol. 2:654 (1987).

63. J. B. Pallix, C. H. Becker, and N. Newman, MRS Bulletin, 12:52 (1987).

64. F. Flores (private communication).

METAL-GaAs(110) INTERFACES FORMED AT LOW TEMPERATURE: FROM ADSORBATE- TO METAL-INDUCED GAP STATES

A. Kahn, K. Stiles*, D. Mao, S.F. Horng and K. Young

Department of Electrical Engineering
Princeton University, Princeton, NJ 08544

and

J. McKinley, D.G. Kilday and G. Margaritondo

Department of Physics and Synchrotron Radiation Center
University of Wisconsin, Madison, WI 73506

I. INTRODUCTION

After two decades of research on metal-semiconductor interfaces, the problem of the formation of Schottky barriers is still very much present (and controversial)[1]. The origin and nature of the interface states which pin the Fermi level (E_F) at metal-semiconductor interfaces remain uncertain. The difficulty in resolving this issue stems from the diversity of metal-semiconductor interfaces and from the complexity of their chemistry, morphology and atomic structure. Progress has been made in the understanding of the microscopic structure of some of these interfaces with low energy electron diffraction (LEED)[2,3], ion channeling[4], total energy minimization calculations[5,6] and with the recent development of scanning tunneling microscopy[7]. Enough remains unknown, however, that interface structure, interdiffusion, defects or metallization still raise unanswered questions about the pinning process. In addition, Vitturo et al. have recently indicated that deep levels in the bulk of the materials used for most Schottky barrier formation studies, i.e. liquid-encapsulated Czochralski GaAs, might be responsible for the narrow range of E_F pinning in the gap, and that pinning occurs in a much wider range on (100) surfaces of substrates grown by molecular beam epitaxy[8]. This result adds another dimension to an already difficult and overly discussed subject.

From the point of view of electronic and atomic structures, the best understood semiconductor surface is GaAs(110)[2]. It has no intrinsic surface states in the gap, and this has led to extensive work on the formation of metal-GaAs(110) interfaces. These prototypical interfaces exhibit a wide range of structural and chemical behaviors. Some are abrupt (In, Ag)[9] or interdiffused (Au)[10], reacted (Mn, Ca, Ti)[11,12] or chemically inert (In, Ag, Ga)[9,11], quasi two-dimensional (Sb, Sn)[13–15] or composed of three-dimensional clusters (Ag, In)[9]. Yet, the rate of band bending and the final pinning position of the Fermi level are quite

* Present address: ATT Bell Laboratories, 555 Union Bld., Allentown PA 18103

comparable at all these interfaces. The simultaneity of various interface events such as reactions, metal clustering or atomic relaxation has so far obscured the identification of the dominant E_F pinning mechanisms. With low metal coverage, during the initial stages of the formation of the barrier, the experimentalist deals with systems which are far removed from the ideal, and often atomically ordered, interface modeled by the theorist. It is indeed far too difficult at this time to do theory on these real interfaces.

One of the techniques used in the past few years to circumvent this difficulty is the formation of metal-semiconductor interfaces at low temperature (~70-100 K)[9,11,15-18]. It is expected, and verified in most cases, that interface reaction, interdiffusion and clustering are considerably inhibited at LT and that the complex interface is "simplified". Although the interface formed at LT is "frozen", and is therefore somewhat different from its RT counterpart, valuable information on the overall E_F pinning process can be obtained. In particular, LT provides a more accessible step-by-step formation of interfaces and helps identify more readily the dominant pinning mechanism(s) for various coverage regimes.

During the past three years, we have investigated interfaces formed between LT GaAs(110) and Al[9,19], In[9], Ag[9,17,20], Au[9,20], Pd[21] and Sn[15]. A trend in band bending, different from the room temperature (RT) band bending, was observed at all these interfaces. This forced a reevaluation of the Schottky barrier formation problem in a way which tends to reduce the role of interface defects and emphasize the importance of adsorbate-induced states and overlayer metallization. More recently, we studied LT interfaces between GaAs and Mn[11], Ga[11] and O_2[22], and a RT interface with Ca[12]. The results obtained with this group of interfaces are in full agreement with the earlier results. We attempt to establish in this paper a coherent picture of these results, to discuss them in terms of the main Schottky barrier models, and to draw some conclusions on the mechanisms which most likely induce and determine band bending at the GaAs(110) surface in various metal coverage regimes.

II. EXPERIMENTAL CONSIDERATIONS

The experiments were performed on (110) n-GaAs ($1\text{-}5\times10^{17}/cm^3$) and p-GaAs ($5\times10^{17}/cm^3$) surfaces cleaved in-situ. The temperature of the sample was maintained at RT or LT during metal deposition or exposure to O_2, and during the measurements. Metallization was obtained by resistive evaporation of metals from W baskets. The evaporations were done in incremental coverages ranging between 10^{-2}ML and 10-20ML (1ML = one monolayer = $0.89\times10^{15}atm/cm^2$), and were controlled with a quartz crystal thickness monitor. Nominal thicknesses of 1ML Ga, Mn and Ca on GaAs(110) are 1.7Å , 1.1Å and 3.8Å respectively. Exposures to unexcited molecular oxygen were measured with a cold cathode gauge. Band bending at the GaAs surface was obtained from the rigid shift of the photoemission Ga-3d and As-3d core levels as a function of metal coverage. The soft X-ray photoemission spectroscopy (SXPS) measurements were done at the Synchrotron Radiation Center of the University of Wisconsin. The ultra-violet photoemission spectroscopy (UPS) measurements on Ca- and O_2-GaAs were done with a conventional He discharge lamp. In addition, low energy electron diffraction (LEED) and Auger electron spectroscopy (AES) were used to investigate overlayer morphology, structure and composition at some of these interfaces.

III. RESULTS

1. Temperature Effects on Overlayer Morphology and Interface Chemistry

The primary effect of LT on the formation of the metal-semiconductor interface is the reduction of the hopping frequency and mobility of adatoms deposited on the surface. The thermal energy of incident adatoms is very rapidly transmitted to the substrate, and the surface mobility depends essentially on adatom substrate bonding and substrate temperature. The hopping frequency is $F_H = \nu.\exp(-\phi/kT)$ where ν is an attempt frequency ($\sim 10^{12}-10^{13}$Hz), ϕ is the potential barrier seen by an adatom moving from one unit cell to the next and T is the substrate temperature. ϕ was estimated to be between 0.3eV and 0.6eV for

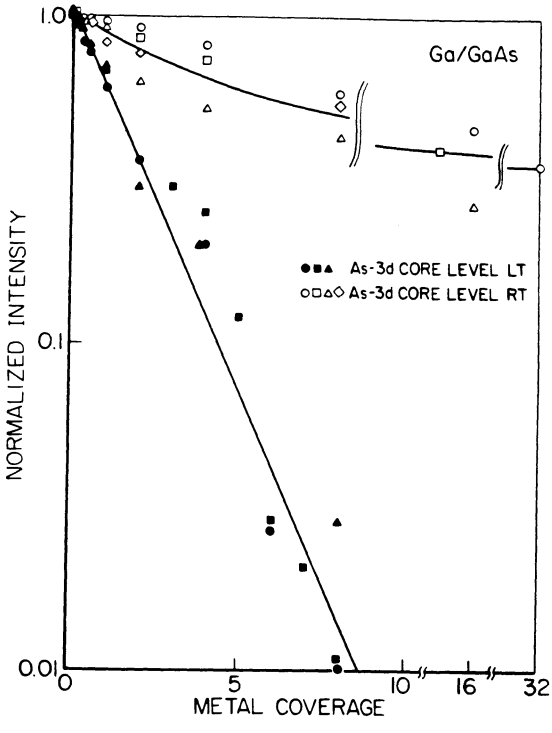

Fig. 1. Amplitude of the As-3d photoemission peak as a function of Ga coverage on RT and LT GaAs(110) (After K. Stiles[21], with permission).

Al on GaAs(110), depending on the migration path between unit cells[23]. Both numbers do lead to a reduction of F_H by many orders of magnitude when the substrate temperature is reduced from 300 K to 80 K. The temperature effect is particularly drastic with metals which have a tendency to cluster at RT, e.g. In, Ag or Ga. At these interfaces, metal-metal bonding is energetically more favorable than metal-semiconductor bonding, and there is little directional covalent metal-

substrate bonds. Large areas of the surface remain uncovered up to equivalent metal coverages of tens of Å . In addition, LEED indicates that the atomic structure of the semiconductor between clusters is that of the clean surface. For characterizing the interface and measuring initial band bending, severe clustering poses several problems: 1. band bending can be very inhomogeneous, especially with high substrate doping; great care must be taken in the interpretation of data on E_F movement collected with probes which average over macroscopic areas of the sample[24] 2. information on the structure and chemistry of the interface between the clusters and the semiconductor, and at the edges of the clusters, is considerably more difficult to obtain than at a laminar interface[25]; 3. clusters become metallic after the deposition of equivalent metal thicknesses far below what is generally considered sufficient to produce a metallic overlayer (a large fraction of Ag clusters appear to be metallic after the deposition of ~0.1ML on RT GaAs(110)[17]).

The effect of LT on the morphology of In, Al, Au and Ag overlayers on GaAs(110) has been presented elsewhere[9]. At the non-reactive RT Ga/GaAs interface, Ga clusters extensively, as demonstrated by the slow attenuation of the As-3d core level photoemission peak (Fig.1). At LT, clustering is inhibited and the overlayer grows in a quasi laminar fashion. The attenuation of the substrate peak is exponential with a characteristic escape depth of 2Å for 35eV kinetic energy electrons. This morphological change is also reflected in the chemical shift between the 3d core level peaks of the Ga adatom and Ga-in-GaAs (Fig.2). The Ga adatom is less tightly bound than Ga in the crystal and thus has a 3d peak on the low binding energy side of the Ga-in-GaAs peak. At RT and above 0.5Å , the shift between the two peaks is 0.9eV, characteristic of metallic Ga on GaAs[26]. At LT the shift remains smaller (~0.4-0.6eV) up to 2Å . This larger binding energy can be accounted for in two ways: by initial state effects, which would correspond to a real change in the binding energy of the 3d electrons as a function of Ga coordination; or by final state effects, corresponding to surface charging of the small Ga cluster due to screening of the core hole by the cluster conduction electrons[27]. The latter has been suggested for supported clusters when electrons from the substrate cannot discharge the cluster in a time short with respect to that of the emission of the photoelectron. In any case, both processes are consistent with the fact that, at low coverage, Ga on LT GaAs is distributed in small clusters or isolated atoms. The shift reaches 0.9eV between 2Å and 6Å when the average Ga coordination in the overlayer becomes comparable to that of the metallic layer, or when final state charging becomes insignificant in large clusters or in the extended metallic overlayer. This point will also be important for the analysis of E_F pinning at LT in the discussion part of this paper.

A second effect of LT is to reduce or inhibit interface chemical reactions. We show here the example of Mn on GaAs. Mn reacts with GaAs, liberating Ga in the process[11,12]. Probable reaction products are MnAs and Ca_3As_2. The effect of the reaction is illustrated in Fig.3a. At RT, there is a Ga peak, clearly resolved at 2Å Mn and above, on the low binding energy side of the Ga-in-GaAs peak. This peak corresponds to Ga freed by the exchange reaction and diluted in, or segregated on top of, the Mn layer. Dilution of Ga in another metal with different electronegativity increases the chemical shift over and beyond the 0.9eV corresponding to metallic Ga on GaAs. This additional shift due to a charge transfer between the two species should be approximately 0.4eV for Ga in Mn[26]. The total shift of ~1.0eV (Fig.3a) indicates therefore that Ga is largely metallic with little effect of dilution in Mn at 8Å coverage. In contrast to the RT behavior, Fig.3b shows that the reacted peak is much smaller, albeit not completely eliminated at LT. The Ga-3d and As-3d core levels are attenuated more rapidly with increasing Mn coverage, indicative of less segregation at LT. We get an estimate of the interface reactivity from the heat of reaction ΔH_R[28]. At moderately reactive interfaces such as Al/GaAs (ΔH_R = -10.8kcal/mole[29]) or Mn/GaAs (ΔH_R = 3kcal/mole[29]), the

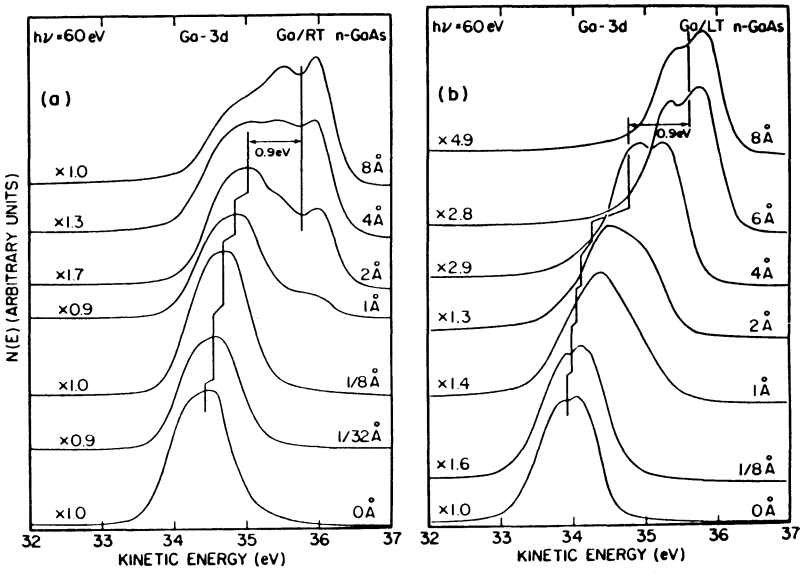

Fig. 2. Ga-3d core level as a function of Ga coverage on (a) RT and (b) LT GaAs(110).

reaction is considerably inhibited by depositing at 80-100 K. At very reactive interfaces such as Ca/GaAs (ΔH_R = -120kcal/mole[30]) or Ti/GaAs (ΔH_R = -18kcal/mole[29]), little effect is observed[21]. Depositions at lower temperatures will have to be investigated for these latter interfaces.

The adsorption of O_2, or other electronegative elements such as Cl[31], is not central to the problem of Schottky barrier, but gives important informations on the nature of electronic states induced by the adsorption of various species on the semiconductor surface. This aspect of the adsorption will be discussed in the next section. We focus here on the chemical characteristics of the interface and show that the oxidation of GaAs(110) is also slowed down at LT. Valence band (VB) spectra of GaAs(110) as a function of O_2 exposure at RT are shown in Fig.4a. The main feature in the VB spectra is the broad peak at ~5eV below the VB maximum (VBM); this peak is attributed to chemisorbed atomic oxygen; there are indications that there is more than one chemisorbed state[32,33]. The VB spectra in Fig.4b show that the adsorbtion state is different at LT. Rather than a broad peak centered at 5eV below VBM, there is a sharper feature at ~7eV, which grows larger up to exposures of 10^4L. At higher exposures, a second peak appears at 5.5eV and grows larger than the 7eV peak at 10^6L. Both features merge into one broad peak at 10^8L. From the analysis of Frankel et al.[32,33], we tentatively attribute the 7eV peak to chemisorbed molecular oxygen, a state which is not stable at RT and which reflects the slow-down of the oxidation of the GaAs surface at LT. Fig.4b indicates that this state and the atomic chemisorbtion state coexist while the concentration of atomic chemisorbed oxygen increases at higher exposures.

2. Temperature Effects on Band Bending

The RT deposition of Ga and Mn on n- or p-GaAs(110) induces band bending at the lowest coverages investigated, ~10^{-2}ML (Figs. 5 and 6). The stabilization of E_F occurs above 1Å with Ga, at lower coverage with Mn. The rate of band bending vs. metal coverage is approximately the same for both doping types. This behavior is common to most metal-GaAs(110) interfaces and has been

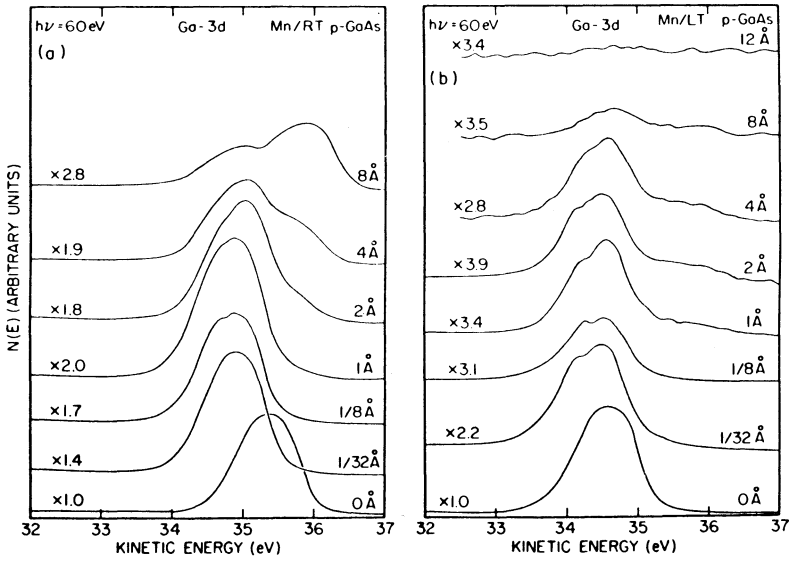

Fig. 3. Ga core level as a function of Mn coverage on a) RT and b) LT GaAs(110).

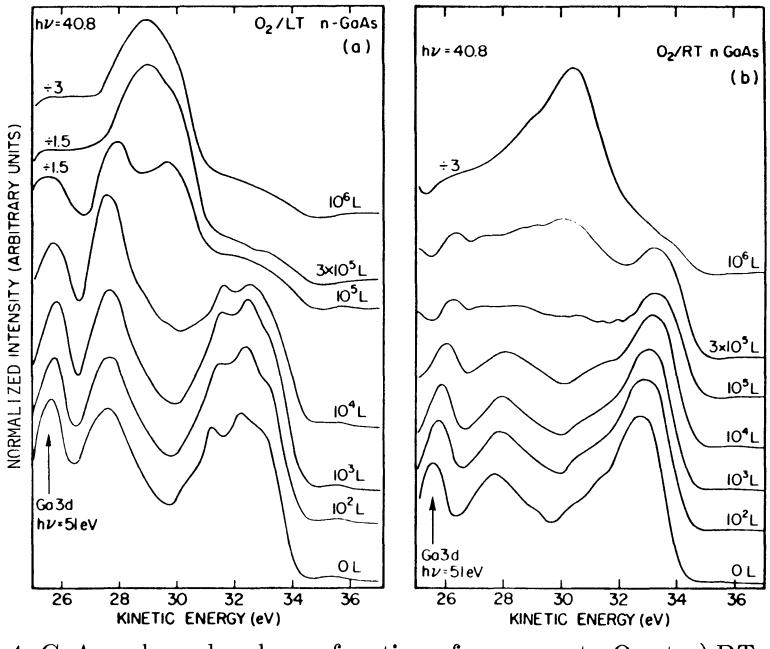

Fig. 4. GaAs valence band as a function of exposure to O_2 at a) RT and b) LT (After Stiles et al.[22], with permission).

documented at length[34]. In particular, this rapid and symmetric E_F movement and quasi metal independent final band bending has been at the foundation of E_F pinning models based on deposition-induced interface defects[35]. Deviations from this trend are seen mostly in the metal coverage necessary to produce final E_F pinning. It is observed that with metals such as In or Ga, a 0.2eV difference in the position of E_F measured with photoemission on n- and p-GaAs persists up to coverages of several ML (Fig. 5). This difference is believed to be due to

inhomogeneous band bending at clustered interfaces. Electrical measurements of Schottky barrier heights indicate that this small gap disappears at high coverage[35].

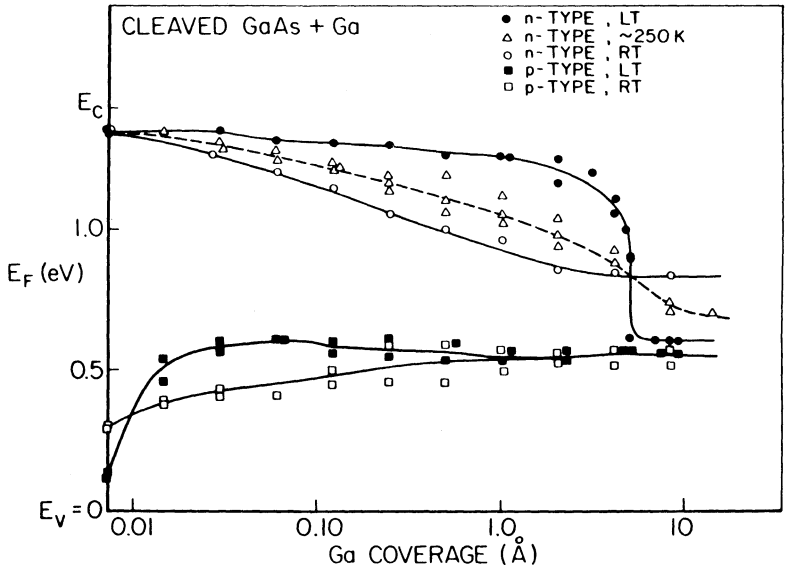

Fig. 5. Surface E_F position in the gap of n- and p-GaAs(110) as a function of Ga coverage at RT and LT (After Stiles et al.[11], with permission).

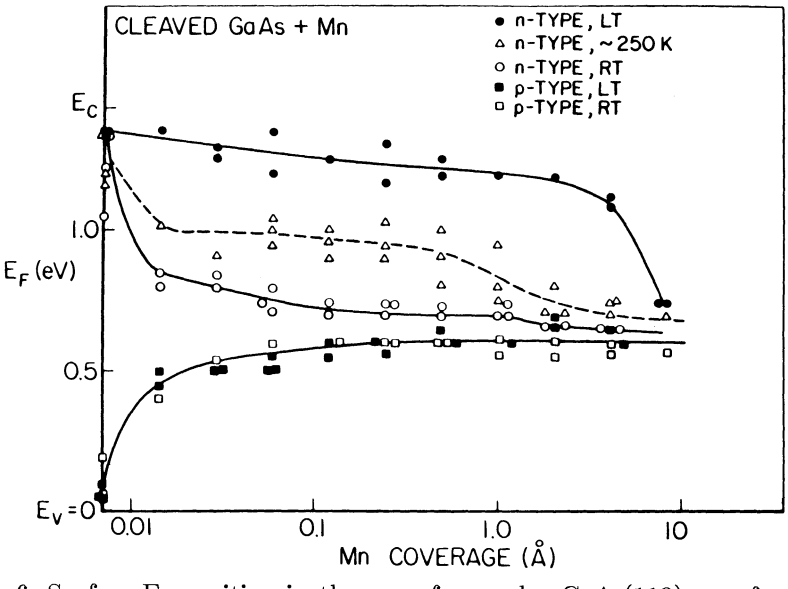

Fig. 6. Surface E_F position in the gap of n- and p-GaAs(110) as a function of Mn coverage at RT and LT (After Stiles et al.[11], with permission).

The typical LT band bending induced by the deposition of most metals investigated evolves in a completely different fashion with a total break of the n- vs. p- symmetry. It is illustrated in Fig.7. On n-GaAs, the movement of E_F down from the conduction band is considerably slower than at RT until the coverage exceeds ~2ML (the exact coverage varies with the metal). Then E_F moves rapidly

towards its final position. On p-GaAs, the movement of E_F up from the valence band is very fast, and an overshoot with respect to the final position can occur, depending on the metal. Figs. 5 and 6 show specific examples for Ga and Mn. E_F overshoots slightly its final position with Ga (~50meV). Large overshoots are observed with other metals: 0.2-0.3eV with In and Al[9,16], and up to 0.4eV with Cs and Rb[36,37]. The overshoot is central to our analysis of the low coverage band bending; we argue in the next section that it is related to the energy position of gap states induced by the adatoms adsorbed on the surface. One should also note that, with Ga, the gap between the positions of E_F on n- and p-GaAs has all but disappeared at 6Å . This presumably results from increased homogeneity in the overlayer at LT and in the band bending across the area sampled by photoemission spectroscopy.

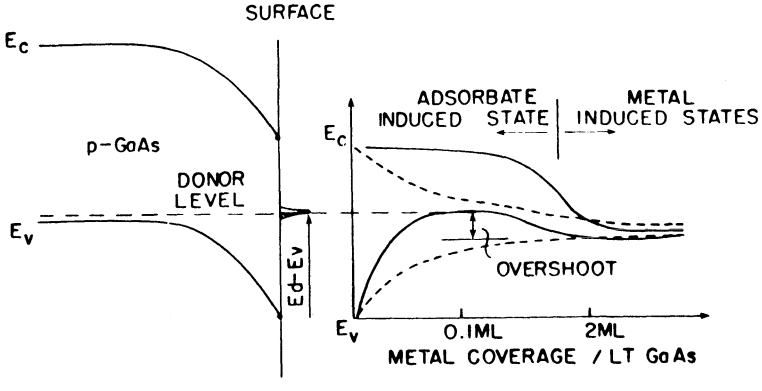

Fig. 7. Right: typical E_F movement as a function of metal deposition on RT (dashed line) and LT (full line) GaAs(110). Left: adsorbate-induced donor at the GaAs surface. Dominant band-bending mechanisms are indicated.

Band bending at the RT O_2/GaAs interface has been extensively studied[38,39]. Little band bending is observed on p-GaAs at low exposures ($<10^3$L) whereas a 150meV band bending on n-GaAs is already obtained at 5L. E_F pinning on n- and p-substrates takes place after 10^6L exposures. Pinning is explained in terms of defects introduced by the exothermic oxidation of the upper GaAs layers[39]. The RT asymmetry is considerably amplified at LT. While E_F moves down from the conduction band on n-GaAs at the lowest exposure investigated, no significant change in band bending occurs up to $5x10^3$L on p-GaAs, and an increase of only 150meV is obtained at 10^8L (Fig.8). The full RT band bending is recovered only after warm up to RT. This situation originates from a similar slow down of the interface formation process as was described above: inhibition of clustering or reaction for metals, of reaction and oxidation for O_2. The evolution of the bands is also entirely analogous to that obtained with Cl, another electronegative element, adsorbed on GaAs(110)[31].

Finally, we examine the case of Ca on RT GaAs. The LT data are not presented in this paper. From the point of view of morphology and E_F pinning, these data are very similar to the RT data. This results presumably from a limited change in the rate of chemical reaction at 80-100 K. The movement of E_F, however, is very peculiar. It follows a two-step process (Fig.9). First, band bending develops on p- as well as n-GaAs, with a well defined plateau in the movement of E_F on p-GaAs between 0.02ML and 0.5ML (1ML Ca = 3.8Å). Band bending on n-GaAs is smaller than with other metals. Second, an additional 0.25eV move-

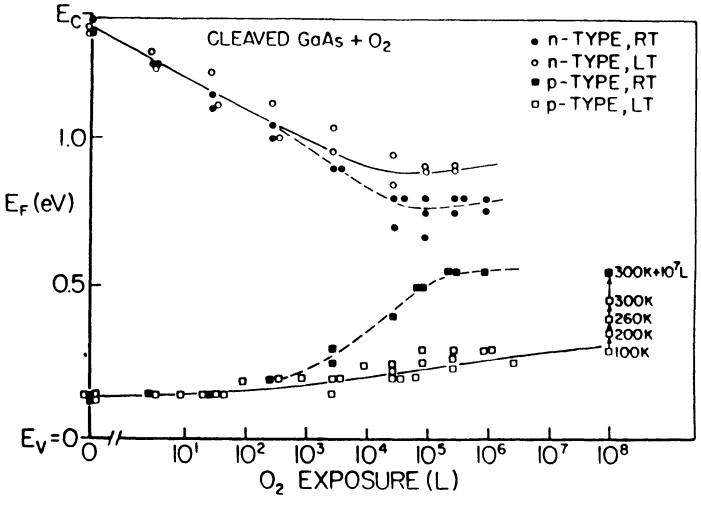

Fig. 8. Surface E_F position in the gap of n- and p-GaAs(110) as a function of exposure to O_2 at RT and LT (After Stiles et al.[22], with permission).

ment of E_F toward the VB occurs when the coverage reaches 1ML. The final pinning position for n- and p-GaAs is 0.55eV above the VBM. We believe that the reversal of the E_F movement seen with Ca is the manifestation of the same phenomenon which produces the E_F overshoot described above. We suggest in the next section that it is due to two competing band bending mechanisms: the formation of adsorbate states at low coverage, and the metallization of the overlayer at high coverage.

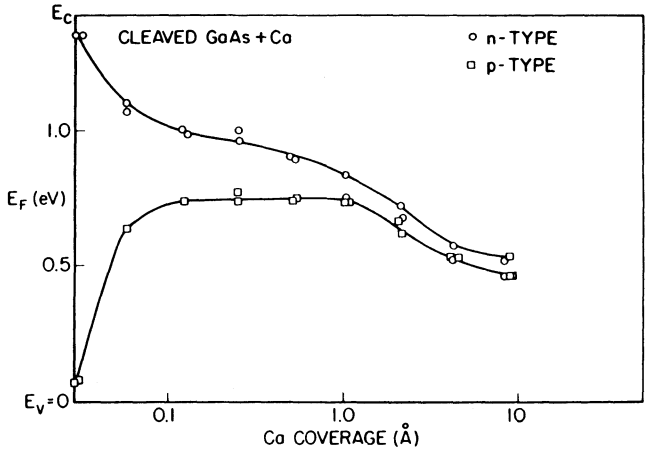

Fig. 9. Surface E_F position in the gap of n- and p-GaAs(110) as a function of Ca coverage at RT (After Mao et al.[12], with permission)

IV. DISCUSSION

1. Low Coverage: Adsorbate-Induced States

The metal overlayers on LT GaAs, as was discussed above, consist predominantly of isolated atoms or very small non-metallic clusters at low coverage. Interdiffusion and reactions are inhibited and the rate of formation of interface defects in expected to be reduced. The asymmetry of the band bending on n- and p- samples at LT indicates that defects of the type considered in the unified defect model (UDM) of Schottky barriers[40] cannot play a predominant role here. The reduced rate of defect formation is incompatible with the increased rate of band bending observed on p-GaAs with Ga (Fig.5), as well as In, Al and Ag[9]. Within the framework of the defect model, the lack of band bending on n-GaAs would indicate a drastically different rate of formation for acceptor and donor defects which form at the same rate at RT, a situation which is very unlikely for GaAs. Finally, native defects in GaAs should give metal-independent levels in the gap, and cannot explain the low coverage metal-dependent E_F overshoot mentioned above and illustrated in Fig.7.

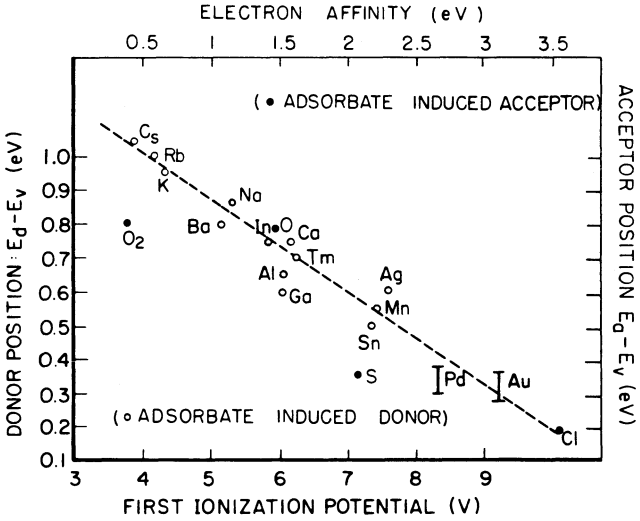

Fig. 10. Adsorbate-induced donor (acceptor) level position, extracted from initial E_F movement on LT p-GaAs (n-GaAs), as a function of adatom first ionization energy (electron affinity) (Tm[43]; Cs, Rb, K, Na[36,37]; Cl[31]; S[45]).

Absent a metallic layer at very low coverage, the initial movement of E_F at the Ga and Mn interfaces, as well as at interfaces with In, Al, Ag, Au and Sn, can be explained in terms of adsorbate-induced *donor* states[11,12,17,31]. We will assume that all adatom-substrate interactions are inhibited, other than simple chemisorption and atomic surface unrelaxation. If the adsorbate-induced donor level is fairly narrow, its position above the valence band, E_d—E_v, can be inferred from the maximum level reached by E_F in the p-GaAs gap during the initial band bending (Fig.7). By analogy with models developed for adsorption on ionic surfaces[41], and following the model presented by Mönch[42], we relate this position to a specific parameter of the adatom, namely the first ionization energy E_I. The smaller E_I,

the higher the level above the valence band maximum. The first ionization energies for Ga and Mn are 6.0eV and 7.43eV, and the corresponding donor level positions are 0.62eV and 0.55eV respectively. Fig.10 shows E_d-E_v as a function of E_I for a number of metals we deposited on LT GaAs(110) as well as for Tm[43], Cs, Rb, K and Na[36,37]. Although there is some scatter in the plot, the correlation is very clear.

The very small low coverage band bending on LT n-GaAs is compatible with the donor-like character of these states and indicates that acceptor levels induced by these adsorbates must be located near or above the conduction band minimum. If native defects are responsible for the initial band bending on RT n-GaAs, it is clear that the formation of these defects is greatly inhibited at LT.

A similar analysis applies to Ca/RT GaAs, although some exchange reaction takes place at RT. Ca adatoms can be viewed as dispersed at very low coverage on the RT surface, and as such fulfill the condition of 2-D homogeneous distribution of isolated adatoms imposed by LT on other overlayers. The first ionization energy of Ca is 6.1eV. The E_F plateau (Fig.9) corresponds to a donor level located at 0.75eV above the valence band maximum. Low coverage band bending on n-GaAs could result from defects induced by the RT Ca-Ga exchange reaction, and perhaps from the presence of some oxygen contamination on the very reactive Ca.

The real value of the LT data depends in part on our ability to extrapolate these results and conclusions to the problem of formation of Schottky barriers at RT. What are the essential differences between the RT and LT situations ? From the point of view of band bending at RT, the initial E_F movement is much faster on n-GaAs, and there is little or no overshoot on p-GaAs. Both can be explained in terms of increased clustering and/or defect formation at RT, depending on the type of interface under investigation. At interfaces with In, Ga or Ag for example, the increase in surface clustering and in the density of multi-adatom centers at RT can modify the adsorbate induced states, reduce the gap between adatom-induced donor and acceptor states, and thus induce early band bending on n-GaAs. Similarly, it is reasonable to assume that the LT adsorbate-induced state, which gives rise to the E_F overshoot, is modified and is overcome early on by the onset of metallic character in the clusters. At RT and at reactive interfaces, the density of defects is bound to be larger and these presumably play a more important role, inducing quasi symmetric band bending.

We now consider how the oxygen data fit in this analysis. Fig.10 shows a relationship between donor level and metal ionization energy, relationship which is characteristic of the interaction between isolated adatoms and the substrate. Similarly, at temperature and O_2 exposures low enough that surface disruption by oxidation is eliminated, the E_F movement is due to an adsorbate-induced state in the gap. The state is acceptor-like, as expected from the large electronegativity of oxygen. As a result, E_F drops into the gap on n-GaAs and flat band conditions are preserved on p-GaAs. This is in excellent agreement with the interpretation of STM data for O/GaAs(110)[44]. It is also entirely compatible with the band bending obtained with Cl and S on GaAs[31,45]. It underscores the importance of adsorbate-induced states for these elements and for the metals considered above. For O, Cl and S, the analogy with the theory of adsorption on ionic surfaces brings forth the electron affinity of the species as a guide to the energy position of the level (Fig.10). It is understood, however, that ionization energy or electron affinity alone are insufficient to describe accurately the energy level induced by these adatoms. In order to predict energy levels more realistically, calculations should include information on chemisorption site and local bonding coordination, information which is unfortunately not available at present.

2. High Coverage: Metallization

With Ga, Mn and most metals deposited on LT n-GaAs(110), an abrupt increase in band bending occurs when the coverage exceeds 2-3ML. A decrease in band bending occurs on p-GaAs when E_F initially overshoots its final pinning position (particularly visible with In, Al, Ag and the alkali metals). The simultaneity of these two E_F movements suggests that the final pinning mechanism is common to both n- and p-substrates. In accordance with previous studies of Ag and Au on LT GaAs(110), we propose to link this delayed pinning to the delayed formation of multi-adatom centers and onset of metallic character in the interface region. We now justify this correlation for Ga, Mn and Ca.

For Ga/LT GaAs, we obtain indirect evidence of metallic character from the shift of the adatom Ga 3d core level with respect to that of Ga-in-GaAs. From Fig.2, we see that the shift (the binding energy of the 3d electrons) remains low (high) up to 2Å at LT, and reaches the value characteristic of large clusters only after deposition of 4-6Å . It is difficult to point out the precise coverage at which the Ga layer becomes metallic. Yet, regardless of which of the two phenomenon underlined above controls the binding energy of Ga in the cluster, i.e. initial state or final state effects, the sudden shift of the Ga adatom 3d binding energy indicates a transition between an overlayer predominantly formed of single adatoms, or very small clusters, and multi-adatom clusters with development of a metallic-like state in the overlayer. This increase coincides with the abrupt movement of E_F toward final pinning position.

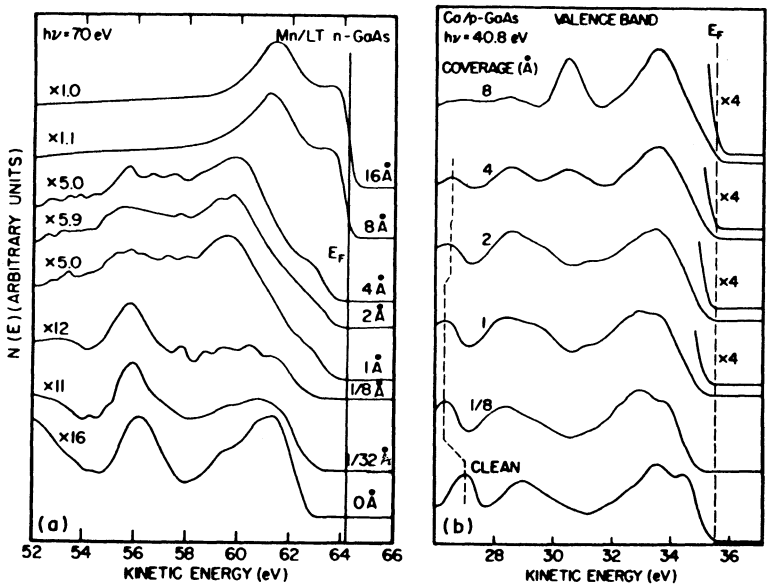

Fig. 11. Valence band photoemission spectra for: (a) Mn on LT GaAs; (b) Ca on RT GaAs.

The evidence is more direct with Mn. The photoemission spectra of the top of the GaAs valence band (Fig.11) shows the appearance of a density of states at the Fermi level between 4Å and 8Å . This signals the transition to metallic character in the overlayer. It coincides precisely with the coverage range where E_F exhibits the shift to its final position on n-GaAs. The second shift does not appear on p-GaAs because the adsorbate-induced E_F position coincides within 50meV with the final pinning position.

The case of Ca is somewhat different: the metal is deposited on RT GaAs and induces low coverage band bending on the n-type substrate. Yet, Fig.9 shows that a second E_F shift occurs on both n- and p-GaAs above 2-4Å . This second shift, which moves E_F to its final pinning position, also coincides with the appearance of a density of states at E_F in the photoemission spectra (Fig.11).

These data indicate that metallization plays an important role in the establishment of the final Schottky barrier and confirm the conclusions drawn from several recent experimental studies[17,43]. As the density of metal atoms deposited on the surface increases, the size of the clusters or of the 2-D layer increases. At low coverage, the gap between adsorbate-induced donor and acceptor levels is large (the acceptor states are at or above the conduction band minimum). At higher coverage, the levels broaden and the gap decreases as the band structure of the metal forms. The semiconductor gap ultimately overlaps with the continuum of metallic states, leading to the well known concept of metal induced gap states (MIGS). First introduced by Heine[46], MIGS were later used by several theorists to explain Schottky barriers[47–50]. Near the interface, the wave functions of the metal electrons with energy in the semiconductor gap are matched in amplitude and phase with wave functions which decay into the semiconductor gap. The penetration depth depends on the boundary conditions and on the semiconductor gap. E_F stabilizes in a position where charge neutrality is conserved, taking into account the occupation of the conduction- and valence-like complex states of the gap and the charge transfer between the metal and the semiconductor[51]. Our LT results are in qualitative agreement with predictions of barrier heights based on MIGS calculations: final pinning when metallic character appears, final E_F position within 0.1eV of the charge neutrality level calculated by Tersoff[49].

Another model based on the development of a metallic layer was recently presented by Ludeke et al.[52]. This model, which explains data for Ag + V / GaAs(110), considers the delocalization of impurity or defect levels in the gap (created by the very reactive V) by a metallic overlayer (Ag). The model, however, assumes the existence of defect levels in the gap, defects presumably created during the low coverage deposition of the reactive metal. In the case of In, Ga, or Ag on LT GaAs(110), however, the data presented above show that the existence of defect acceptor states near the GaAs gap is unclear.

The high coverage MIGS constitute a natural extension of the low coverage adsorbate-induced gap states[11,12,17,31,45,51]. The combination of the two leads to a coherent description of the formation of the Schottky barrier on LT GaAs(110). Secondary effects due to interface defects cannot be ruled out, but it is clear that defects as they are described in the UDM model cannot explain the LT data presented and discussed in this paper. The most compelling reason pertains to the fast rise of E_F on p-GaAs and the asymmetry between n- and p-substrate E_F movements at low coverage, as was discussed in section 4a. The second is that at reactive interfaces which show delayed E_F pinning, the reaction products, i.e. free Ga, is detected well before final pinning occurs. This is verified for the LT Mn-GaAs interface and for the RT Ca-GaAs interface. One can therefore argue that defects invoked in the UDM, which are presumably created in part by these reactions, are created in sizable density before, and thus are not responsible for, final pinning. Third, the LT pinning behavior described in this paper occurs at reactive as well as totally unreactive interfaces like Ga-, In- and Ag-GaAs where defect formation mechanisms such as clustering are all but suppressed. A recent STM study of an unreactive and abrupt interface, Sb/GaAs(110), has shown that unsaturated dangling bonds at the periphery of Sb 2-D islands, rather than defects induced by the adsorption of Sb, were responsible for E_F pinning[7].

The analysis of these LT data leads to the picture of a double pinning mechanism: adsorbate-induced states plus MIGS. The role of defects is contained

to the most reactive interfaces. It is likely, however, that defects do play a more important role at RT, even at interfaces which are not considered highly reactive[37,38]. At high coverage, the extrapolation of this model to the interface formed at RT should therefore include a modulation of the final pinning position primarily imposed by metallization, as was proposed by Mönch[51]. A sensible modulation of this position, however, should result only from the presence of a large density of defects, comparable to the density of MIGS. We can therefore expect to see in most cases the effect of metallization on the pinning process. The Ca/GaAs(110) and Tm/GaAs(110) RT data are clear examples of the validity of this LT to RT extension[12,43].

V. SUMMARY

The study of metal-GaAs(110) interfaces formed at low temperature shows that the position of the Fermi level is controlled by coverage-dependent mechanisms. At low coverage, we find adsorbate-induced donor states. Deep acceptor states result from the adsorption of electronegative element such as O or Cl. The position of the metal-induced donors depends quite sensitively on electronic characteristics of the adatom. Defects may also be important in the initial band bending on n-GaAs(110), at reactive interfaces in particular. At high coverage, final E_F pinning is related to the onset of metallic character at the interface. The experimental evidence of the role of metallicity has now been obtained for a number of interfaces and bring support to Schottky barrier models based on gap states induced or modified by the metal.

ACKNOWLEDGMENTS

This work was supported by a grant of the National Science Foundation (DMR-8709531) and by the Office of Naval Research. Partial support was also provided by General Electric and General Motors Corporation through the Presidential Young Investigator Award program.

REFERENCES

1. see for example: Proceedings of the 15th Conference on the *Physics and Chemistry of Semiconductor Interfaces*, J. Vac. Sci. Technol. B **6** (1988).
2. A. Kahn, Surf. Sci. Repts. **4/5** 193 (1983).
3. C.B. Duke, in *Surface Properties of Electronic Materials*, D.A. King and D.P. Woodruff edts. (Elsevier 1986) Chap. 3.
4. L. Smit and J.F. van der Veen, Appl. Surf. Sci. **26** 230 (1986).
5. D.J. Chadi, Phys. Rev. Lett. **41** 1062 (1978).
6. C. Mailhiot, C.B. Duke and D.J. Chadi, Phys. Rev. B *31* 2213 (1985).
7. R.M. Feenstra and P. Martensson, Phys. Rev. Lett. **61** 447 (1988).
8. R.E. Vitturo, J.L. Shaw, C. Mailhiot, L.J. Brillson, N. Tache, J. McKinley, G. Margaritondo, J.M. Woodall, P.D. Kirchner, G.D. Pettit and S.L. Wright, Appl. Phys. Lett. **52** 2052 (1988).
9. K. Stiles, A. Kahn, D.G. Kilday and G. Margaritondo, J. Vac. Sci. Technol. B **5** 987 (1987).

10. P.W. Chye, I. Lindau, P. Pianetta, C.M. Garner, C.Y. Su and W.E. Spicer, Phys. Rev. B **18** 5545 (1978).
11. K. Stiles, S.F. Horng, A. Kahn, J. McKinley, D.G. Kilday and G. Margaritondo, J. Vac. Sci. Technol. B **6** 1392 (1988).
12. D. Mao, K. Young, K. Stiles and A. Kahn, J. Appl. Phys. (in press).
13. J. Carelli and A. Kahn, Surf. Sci. **116** 380 (1982).
14. P. Skeath, I. Lindau, C.Y. Cu and W.E. Spicer, J. Vac. Sci. Technol. **19** 556 (1981).
15. K. Stiles, A. Kahn, D.G. Kilday J. McKinley and G. Margaritondo, J. Vac. Sci. Technol. A **6** 1462 (1988).
16. R. Cao, K. Miyano, T. Kendelewicz, K.K. Chin, I. Lindau and W.E. Spicer, J. Vac. Sci. Technol. B **5** 998 (1987).
17. K. Stiles and A. Kahn, Phys. Rev. Lett., **60** 440 (1988).
18. R. Cao, K. Miyano, T. Kendelewicz, I. Lindau and W.E. Spicer, J. Vac. Sci. Technol. A **6** 1571 (1988).
19. M.K. Kelly, A. Kahn, N. Tache and G. Margaritondo, Sol. State Comm. **58** 429 (1986).
20. K. Stiles, A. Kahn, D.G. Kilday and G. Margaritondo, J. Vac. Sci. Technol. A **6** 1511 (1988).
21. K. Stiles, Ph.D. Thesis, Princeton University, 1988 (unpublished)
22. K. Stiles, D. Mao and A. Kahn, J. Vac. Sci. Technol. B **6** 1170 (1988).
23. J. Ihm and J.D. Joannopoulos, Phys. Rev. **47** 679 (1981).
24. J.Y.F. Tang and J.L. Freeouf, J. Vac. Sci. Technol. B **2** 459 (1984).
25. C.R. Bonapace, K. Li and A. Kahn, J. Physique Colloq. **45** C5 409 (1984).
26. J.J. Joyce, M. Grioni, M. del Giudice, M.W. Ruckman, F. Boscherini and J.H. Weaver, J. Vac. Sci. Technol. A **5** 2019 (1987).
27. G.K. Wertheim, S.B. DiCenzo and D.N.E. Buchanan, Phys. Rev. B **33** 5384 (1986).
28. L.J. Brillson, J. Vac. Sci. Technol. **40** 260 (1978).
29. Lange, in *Handbook of Chemistry*, (13th edition McGraw-Hill, New York 1985).
30. M.KH. Karapet'yants and M.L. Karapet'yants, in *Thermodynamic constants of inorganic and organic compounds*, (Ann Arbor Humphrey Science Publisher, Ann Arbor, 1970), p.58.
31. D. Troost, L. Koenders, L.-Y. Fan and W. Mönch, J. Vac. Sci. Technol. B **5** 1119 (1987).
32. D.J. Frankel, Y. Yukun, R. Avci and G.J. Lapeyre, J. Vac. Sci. Technol. A **1** 679 (1983).
33. D.J. Frankel, J.R. Anderson and G.J. Lapeyre, J. Vac. Sci. Technol. B **1** 763 (1983).
34. L.J. Brillson, Surf. Sci. Repts. **2** 123 (1982).
35. N. Newman, W.E. Spicer, T. Kendelewicz and I. Lindau, J. Vac. Sci. Technol. B **4** 931 (1986).
36. M. Prietsch, M. Domke, C. Laubschat, T. Mandel, C. Xue and G. Kaindl, Zeitschrift F. Physik B (to be published).
37. M. Prietsch, Ph.D. Thesis, Freie Universität Berlin, 1988.
38. G. Landgren, R. Ludeke, Y. Jugnet, J.F. Morar and F.J. Himpsel, J. Vac. Sci. Technol. B **2** 351 (1984).

39. W. Mönch, Appl. Surf. Sci. **22/23** 705 (1985).
40. W.E. Spicer, I. Lindau, P. Skeath, C.Y. Su and P. Chye, Phys. Rev. Lett. **44** 420 (1980).
41. S. Baidyaroy, W.R. Bottoms and P. Mark, Surf. Sci. **29** 165 (1971).
42. W. Mönch, J. Vac. Sci. Technol. B **6** 1270 (1988).
43. M. Prietsch, M. Domke, C. Laubschat and G. Kaindl, Phys. Rev. Lett. **60** 436 (1988).
44. R.M. Feenstra and J.A. Stroscio, J. Vac. Sci. Technol. B **5** 923 (1987).
45. L. Koenders, M. Blömacher and W. Mönch, J. Vac. Sci. Technol. B **6** 1416 (1988).
46. V. Heine, Phys. Rev. **138** A1689 (1965).
47. S.G. Louie, J.R. Chelikowsky and M.L. Cohen, Phys. Rev. B **15** 2154 (1977).
48. C. Tejedor, F. Flores and E. Louis, J. Phys. C **10** 2163 (1977).
49. J. Tersoff, Phys. Rev. B **30** 4874 (1984).
50. I. P. Batra and S. Ciraci, Phys. Rev. B **33** 4312 (1986).
51. W. Mönch, Phys. Rev. Lett. **58** 1260 (1987).
52. R. Ludeke, G. Jezequel and A. Taleb-Ibrahimi, Phys. Rev. Lett. **61** 601 (1988).

THERMAL EFFECTS IN SILICON-METAL INTERFACE FORMATION: A PHOTOEMISSION STUDY OF Si/Gd AND Si/Yb

L. Braicovich

Istituto di Fisica
Politecnico di Milano
P.za Leonardo da Vinci 32
20132 Milano, Italy

E. Puppin*

Stanford Electronics Laboratories
Stanford University
Stanford CA 94305, USA

INTRODUCTORY REMARKS

In the field of metal-semiconductor interfaces it has been experimentally established that many interfaces are reacted along the scale of several atomic layers when they are grown at room temperature (RT) or even at lower temperatures, such as around 80 ^{o}K (conventionally called LNT, Liquid Nitrogen Temperature). This fact resulted intriguing in consideration of the rather high energy needed to break a bond in many semiconductor substrates. For instance, the spontaneous reaction of Si with Pd at RT, in which a Pd_2Si-like interfacial compound forms over several atomic layers, was unexpected when it was observed [1,2]. A similar reaction was also observed at LNT [3]. The discussion of the reaction mechanisms became one of the central issues in interface physics due to the interest in the reaction mechanisms "per se" and for the very important connections with Schottky barrier physics . In fact, this last problem is well defined only if one takes into account the interface chemical processes which determine the real nature of the solids constituting the interface. Moreover, a better understanding of interface chemistry can be greatly useful in order to identify those systems in which the reaction compounds have a well defined stoichiometry. A well defined chemical composition, along with a knowledge of interface morphology, would make these systems the best candidates for a theoretical interpretation of their electrical properties. In this perspective the problem of interface reactivity is, in our opinion, to a large extent still open and deserves future attention from spectroscopical and structural investigations. A good example is a recent Scanning Tunneling Microscopy (STM) work on the Si(111)(7x7)-Pd interface [4] in which the authors extensively use the available knowledge, obtained through

electron spectroscopy, on the chemical nature of the interface reaction products. In this respect we belive that the role of synchrotron radiation (SR) photoemission in interface reaction studies must be regarded in a new way. Instead of using photoemission data in order to model interface growth, photoemission should be devoted to study in detail the role of some key parameter in determining the nature of the interface electron states. This approach would increase the chance of a cross fertilization with structural investigations. In this perspective an important possibility consists in studiing the role of thermal effects on interface formation. The present paper is a step forward in this direction and has two main purposes. The first is to stress the usefulness of photoemission studies vs. temperature when the low temperature range is covered, i.e., the usefulness of preparing and measuring the interfaces at LNT, and to subsequently cycle the samples between LNT and RT. We will show that this approach is very interesting in discussing of the relative weight of the possible reaction mechanisms. The second is to show the interest of the comparison between the thermal behavior of the Si(111)(2x1)-Gd interface compared to the Si(111)(2x1)-Yb interface, as seen with photoemission. Our results show interesting differences between these two cases and point out these systems as good candidates for future structural investigations.

In the present research the choice of Si, i.e. of an elemental semiconductor, comes from the need to simplify the problem by avoiding the difficulties connected with selective atom removal which is typical of interface reaction in most compound semiconductors. The choice of rare earths (RE) as metals is mainly due to the fact that reacted silicon in these interfaces, as well as in bulk silicides [5,6,7], shows very large shifts of the 2p core level (typically around 1 eV): this circumstance makes the interpretation of core level results more reliable compared to other cases. Another important reason is the possibility of carriing out a variety of significant comparisons between different atomic species along the RE family. In the present paper we discuss the effects of valence and size of the rare earth ion. Gd is trivalent and his ionic radius is 0.938 Å, roughly 7% smaller than Yb, which is divalent with an ionic radius of 1 Å [8]. It must be observed that, in the present experiment, there are no complications coming from valence fluctuations of Yb. Infact, on cleaved Si (111) surfaces the deposition of Yb at LNT does not originate valence fluctuations and also at RT valence fluctuations, if any, are very marginal [5]. Only upon heating above RT valence fluctuations are present, with a consequent variation of the average atomic dimension. In the case of Yb another advantage is that 4f spectroscopy is simpler with respect to the other REs [9]. On the other hand, Gd offers the possibility to observe a rather extended window below the Fermi level (about 6 eV wide) with no 4f emission. In this way the upper valence states are directly accessible with photoemission.

In the following we present a wide selection of data from a work in progress on the thermal behavior of these interfaces. The largest fraction of the material presented in this paper is unpublished and covers the Si/Gd and Si/Yb interfaces below RT ; to make the discussion more complete we also rely upon previous results on Si/Gd at RT [10,11] and on Si/Yb at RT and up to 450 °C [5]. In these last cases the reader is referred to the original papers for a more detailed presentation.

THE PROBLEM OF LOW TEMPERATURE REACTIVITY

Before presenting the data it is useful to clarify the frame of the discussion on low temperature reactivity, in particular of the possible processes which can trigger the reaction. We are particularly interested in the formation, if any, of a precursor situation which makes possible the further growth of silicide-like reaction products. To this end we give a very schematic summary of the main ideas which have been suggested in the past; a more detailed presentation can be found in a recent review paper by one of us [12]. A priori, two different kinds of mechanism can be considered in order to explain the reaction triggering. One is the class of processes which are capable to reduce the strenght of the Si-Si bond in the interface region. The other is the class of processes which increase the energy locally available to trigger the reaction above the level of the chemisorbtion energy of a single adatoms. We will refer to the first class as " weakening mechanisms "; these include the weakening of the Si-Si bonds originated by the incorporation of an adatom in the substrate [13] and the dielectric weakening suggested by Hiraki [14] originated by the screening effect induced by the metallic overlayer. To the second class belong those mechanisms driven by spatial inhomogeneities. An example is the suggestion that the formation of metal clusters [15] can release enough energy to disrupt the substrate. The importance of clusters has been also discussed in ref. 16,17 and 18. The problem is to establish, for each situation, the nature of the dominant process or the combination of processes which takes place at the interface under investigation. A combination of processes can also take place and this fact can be strongly influenced by morphological effects. A recent example of combination of different processes is the preferential formation of Pd_2Si in the faulted half of the unit cell of the 7x7 Si surface [4]. At present there is an increasing evidence of the importance of steric effects in the early interface formation stage. In this paper it will be shown that the comparison between the Si/Gd and the Si/Yb interface supports this view.

EXPERIMENTAL

All of the experimental data shown in this paper were collected at the Stanford Synchrotron Radiation Laboratory (SSRL) by using the monochromatic light produced by a "grasshopper" type monochromator. The experimental apparatus was the same for all of the different experiments, and this ensures the possibility to directly compare all set of data. The photoemission spectra were collected with a double pass cylindrical mirror analyzer with the axis about normal to the sample and with grazing incidence of the ligth; this geometry ensures a rather high degree of angular integration.Interfaces were prepared by cleaving Si rods and by depositing the metallic overlayers with the conventional technique of heating a piece of pure metal inside a W basket. The amount of deposited metal will be given, in the present paper, in monolayer units (ML). One ML correspond to a metal atom density equal to the surface density of Si atoms in the (111) plane. For further details on the apparatus and on the sample preparation the reader is referred to the other papers published by the authors [5].

RESULTS AND DISCUSSION

For clarity we present the data step by step with a discussion of each subset of data in order of increasing complexity; the conclusions are summarized in the next paragraph.

An important piece of physical information comes from Si 2p spectroscopy in the two interfaces (Si/Gd and Si/Yb) grown at LNT and measured at LNT without any thermal treatment. The results for Si/Gd taken with 120 eV photon energy are shown in fig 1 where we give the Si 2p spectra at increasing coverage. We normalized the spectra to the same height in order to show the lineshape modification vs. coverage.The reacted Si component at lower binding energy, in agreement with previous

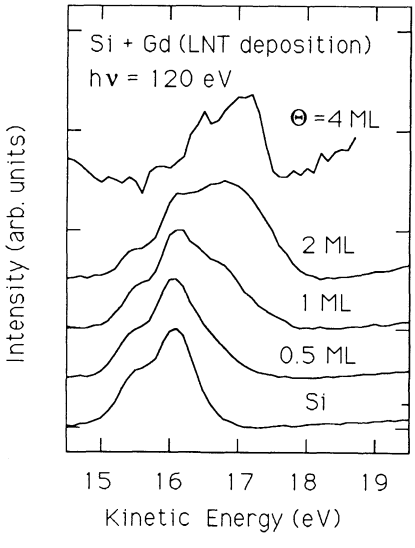

Fig. 1 Si 2p signal in the Si/Gd interface prepared by depositing Gd on cleaved Si(111) at LNT. The spectra were measured at the same temperature.

observations on RE silicides [6], is very well seen in the growth at low temperature (LNT). The striking fact to be noted before any detailed analysis is that the intensity of this reacted component is of the same order of the one found upon deposition of Gd at RT. This effect can be observed by comparing fig. 1 with fig. 2, in which the Si 2p lineshape vs. coverage is shown for the Si/Gd interface prepared at RT (data taken from ref. 11). This behavior is typical of Gd and is not observed in the Si/Yb interface grown at LNT, as we show next. This difference is one of the relevant new results presented in this paper. A summary view of the different behaviour of the two interfaces is shown in fig 3. The plot shows the results of a decomposition of the Si 2p lineshape in the two interfaces grown at LNT as a function of coverage. The upper panel of fig. 3 gives the intensities for the Si/Gd interface and the lower panel gives the analogous results for the Si/Yb case. In this

analysis we decomposed the Si 2p line in a unreacted and in a reacted component with the usual procedure [11]; we are aware of the fact that this decomposition may be very risky and for this reason we avoid any further decomposition of the reacted component. Thus, we limit ourself to discuss the gross features which are beyond any incertitude and do not depend on the deconvolution procedure. In fig. 3 we give, for each interface, the attenuation of the total Si 2p intensity, along with the intensities of the reacted and unreacted components. The difference between the two interfaces is remarkable; in particular, between 2 and 3 ML the reacted component is roughly one order of magnitude stronger in the Si/Gd interface. This difference seems to correlate significantly with the different ionic size and with the different valence of the two REs. In

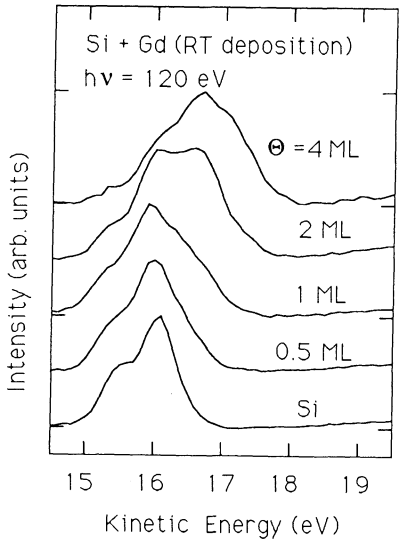

Fig. 2 Si 2p signal in the Si/Gd interface prepared by depositing Gd on Si(111) at RT. The spectra were measured at the same temperature.

effect, both the smaller dimensions and the higher valence, with a consequent tendency towards a higher coordination number, can justify the easier intrusion of Gd in the substrate in the early formation stage of the interface. This fact calls for the importance of steric effects in this stage. To be more specific we note that the attenuation of the reacted silicon component in the Si/Yb case is exponential, within the errors, after about one ML. This fact means that the growth of Si/Yb at LNT is basically a kind of chemisorbtion of the metal on top of the substrate. On the contrary a considerable intermixing is found in the Si/Gd case. In both interfaces the intensity of the unreacted component monotonically decreases in the semilogarithmic plot, with an escape depth in agreement with other Si/RE interfaces. In other words, photoemission does not indicate a substantial discovery of the substrate in any stage of the intarface growth, as expected in case of an extended

clustering. Needless to say this point requires further investigation with structural methods. We do not discuss the small escape depth difference in the two cases, since it could be partly due to some inaccuracy in the absolute calibration of the coverage scale in the two sets of measurements. In the upper panel of fig. 3 the point at 4 monolayers is slightly below the linear trend in the semilogarithmic plot and this could be due to a decrease of the escape depth when the overlayer is enriched in Gd This possible chemical effect on the escape depth may be reasonable in connection with the available knowledge on the escape depth in RE [19] and could be the subject of an interesting future research.

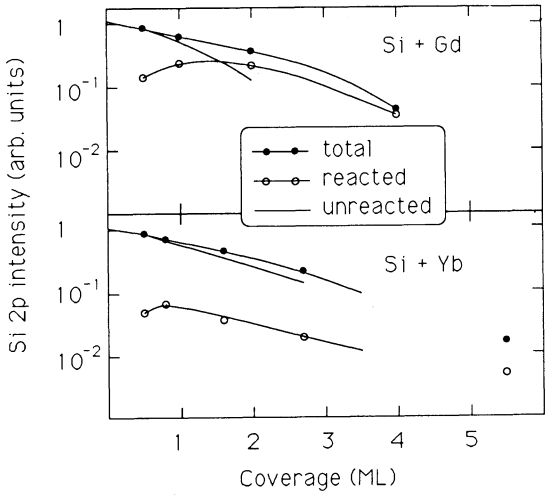

Fig. 3 Intensity of the Si 2p core level components in the Si/Gd and Si/Yb interfaces prepared by deposition at LNT. The filled dots refer to the total intensity of the peak. The empty circles to the reacted Si component whereas the solid line refers to the unreacted component coming from the substrate.

The fact that already at low temperature (LNT) a true chemical reaction takes place in the Si/Gd interface is confirmed by the shape of the valence photoemission spectra shown, vs. coverage, in fig 4. In this figure we give the spectra measured at 65 eV and also, for comparison, the spectra of the polycristalline bulk silicides along with a spectrum of metallic Gd. These spectra have been measured with the same apparatus used for the interface experiment and in strictly comparable conditions. These data show the similarity of the interface valence spectra around 2 ML with those of the bulk silicides. Another important point is the absence, within the experimental sensitivity, of a feature at the Fermi level which would be typical of the pure unreacted metal. A more detailed discussion of the average stoichiometry of the interface reaction products, on the basis of a comparison with the bulk silicides, is given later. At 4 ML the situation is very rich in metal and the valence spectum resembles the pure metal. In order to understand the nature of the reaction products at this coverage the metal core levels position is useless because the shifts of these levels are negligible, with respect to the pure metal , both in the interface and in the bulk silicides. In other words it is difficult to make any assessment, by simply reliing upon photoemission data, on the chemistry and the morphology of the interface. This is particularly true when the

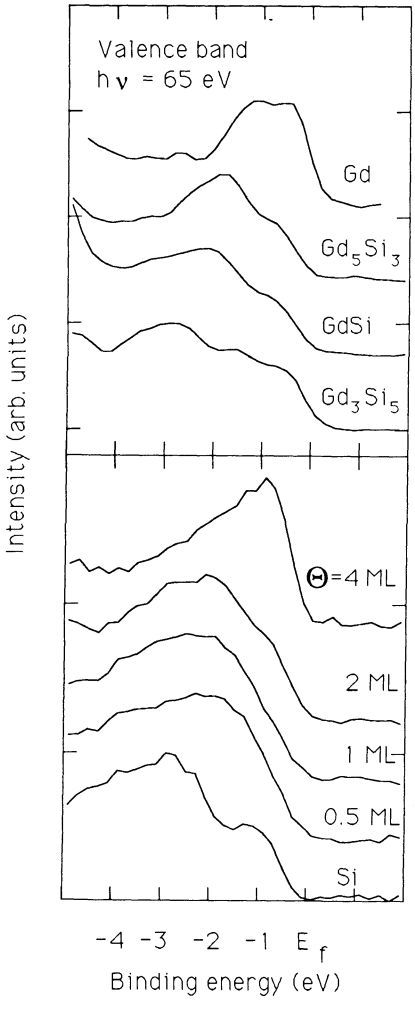

Fig. 4 Valence band photoemission spectra taken at 65 eV photon energy. In the lower panel the spectra from the Si/Gd interface prepared by deposition at LNT and measured at the same temperature. In the upper panel the spectra from the bulk silicides and from the pure metal.

thickness of the reacted layer is several times the escape depth.

The effect of heating from LNT to RT the interfaces grown at LNT is very interesting. The most important data on Si/Gd are summarized in fig 5 where we report the Si 2p lines, measured at 120 eV, from the same interfaces after preparation at LNT and after heating at RT. It must be observed that, within the time scale of the experiment (typically a few hours for each interface) no evolution of the interface spectra has been detected at constant temperature, both at LNT and at RT. The comparison of the spectra at each coverage before and after the thermal treatment is done by normalizing the signal to the Gd 4f intensity. In this way any increase of the reacted Si intensity must be regarded as indicative of an enrichment in the Si content of the reacted overlayer. Indeed, this indication must be taken only in qualitative terms since some chemical effect could be present in the escape depth, as mentioned above. Nevertheless, the general trend is clear and is beyond any incertitude: the heating effect is basically zero at submonolayer coverages, is marginal but not negligible at 2 ML, and is very strong only at higher coverages where, upon

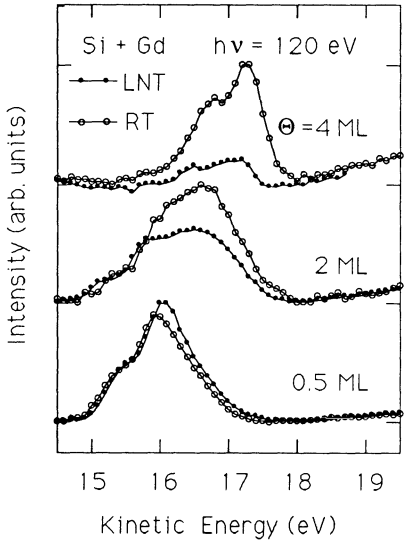

Fig. 5 Comparison of the Si 2p lineshape at different coverages for the Si/Gd interface. The dots refer to the interface grown at LNT, the empty circles to the same interface after the warm up to RT. The spectra are normalized to the Gd 4f intensity in order to give an indication of the effectiveness of the thermal treatment on the reaction. At 0.5 ML the treatment has no effect. At 2 ML there is a small increase in the amount of reacted Si and at 4 ML there is a clear indication that the warm up to RT promote a strong further reaction.

heating, the metal rich overlayer furtherly reacts with silicon. It is interesting to note that the intensity of the Si 2p line does not increase substantially in the region typical of the unreacted silicon component, which has its maximum, in the spectra taken with 120 eV photon energy, around 16 eV. The increase of the silicon intensity upon heating at RT is basically due to the increase of the reacted component without a relevant discovery of the substrate. This trend is also confirmed by the valence spectra, not reported here.

The fact that thermal treatments are effective only above some coverage (around 2 ML) is observed also in the Si/Yb interface grown at LNT and heated to RT. Only minor effects are seen at low coverages whereas a strong effect is observed at 4 ML, as shown in fig 6 where we present the Si 2p line before and after heating with the usual normalization to the 4f intensity. The need of depositing a certain amount of metal in order to make the interface sensitive to the temperature has been observed for Si/Yb also in a previous experiment on interfaces prepared at RT and heated at 300 ^{o}C and 450 ^{o}C [5]. At present all data suggest that some precursor situation forms upon deposition of metal between 1 and 2 ML. This precursor situation makes it easier to break the Si-Si bonds and allows a further progress of the reaction. An open point is the destiny of this precursor situation when the reaction proceeds. In principle two possibilities exist . The first is that the precursor situation remains at the interface and its nature is not modified by the successive reaction; if this is the case the new metal forms an overlayer whose average composition is different with respect to the precursor situation. The second possibility is that, during the progress of the reaction, the whole overlayer modify its composition, and therefore the precursor situation does not exist any more in the buried interface. As discussed above, it must be stressed that photoemission alone cannot give a reliable answer to this kind of questions, since this type of information is not directly accessible with this experimental approach. On the other hand, the occurence of a precursor situation and the fact that this situation is very stable against heating, is clearly shown by our results on temperature dependent photoemission.

We can now compare the results obtained from interfaces directly grown at RT and interfaces prepared at LNT and successively heated at RT; in other words we compare, at RT, interfaces which have different thermal histories. For Si/Gd this is done in fig 7, with the usual normalization to the 4f intensity; this is done for the interfaces at 2 and 4 ML. The data a 4 ML are redrawn in the upper part of the figure along with the Si substrate lineshape, given for reference. In this case the spectra are normalized to the same height in order to better observe the lineshape difference. It is apparent that for coverages up to 2 ML the two histories bring essentially to the same results, within the accuracy of our measuraments. On the other hand, at higher coverages, the intensity of the reacted component is considerably higher for the preparation at RT. This fact presumably means that mass transport is easier in the preparation at RT, as it is reasonable, and this originates the different final results at RT. Also in the present case the greatest fraction of the increased silicon signal comes from the region of the reacted silicon, whereas the unreacted component does not change appreciably.Again, we have the evidence that clustering is not the dominant mechanism in the reaction path. Thus, the Si-Si bond breaking is, to a great

extent, due to the effect of the previously formed overlayer, which induces a weakening action. In the Si/Yb interface, not discussed here in detail, considerable differences are seen with respect to Si/Gd. The most significant data from ref. 5 relative to the Si/Yb interface are shown in fig. 8. These data show that at low coverage, including the 2 ML case, the deposition at RT is much more effective in promoting the reaction with respect to the deposition at LNT followed by heating to RT. This fact means that, in this case, the full development of the precursor situation cannot be obtained by heating the interface prepared at LNT. this behavior is the opposite compared to the Si/Gd interface, as previously shown. Again, this calls for the importance of steric effects in the sense above discussed.

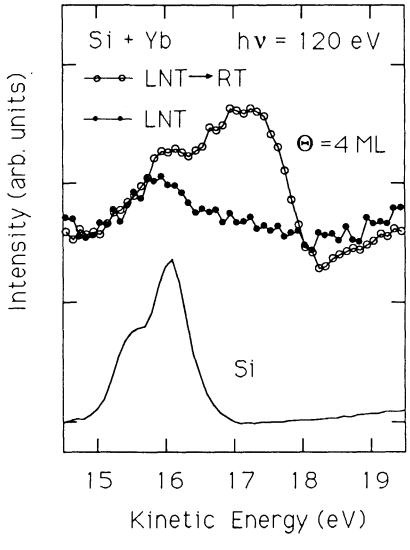

Fig. 6 As fig. 5 but referred to the Si/Yb interface grown at LNT and only for a coverage of 4 ML. The lowest spectrum represent the pure substrate 2p lineshape and is given for reference. Even in this case the warm up produces a strong increase of the amount of reacted Si.

In order to give a qualitative indication of the average stoichiometry of the interface reaction products we can rely upon the comparison of core line intensities in the interfaces and in the bulk silicides which are used as reference standards. This is done extensively for Si/Yb, at RT and at higher temperatures, in ref. 5 and for Si/Gd at RT in ref 11. The data from ref. 11 are shown in fig. 9, in which the average stoichiometry of the reacted layer is plotted vs. coverage. On the basis of the above discussion on the core line intensities it is possible to conclude that the precursor situation at LNT ends up, for the Si/Gd case, with a reacted layer whose average stoichiometry is in between Gd_5Si_3 and GdSi. In the interface

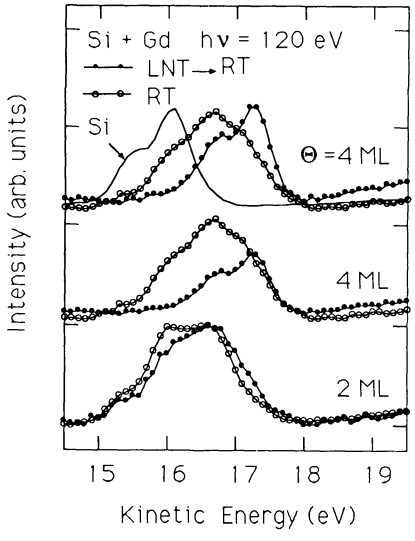

Fig. 7 Comparison of the Si/Gd interfaces prepared by deposition at LNT followed by a warm up to RT (filled circles) and by direct deposition at RT (empty circles). The lowest and mid spectra are normalized, as in fig. 5, to the Gd 4f intensity. The upper spectra are normalized to the same height in order to make it easier to observe the lineshape difference. The substrate lineshape is reported for reference.

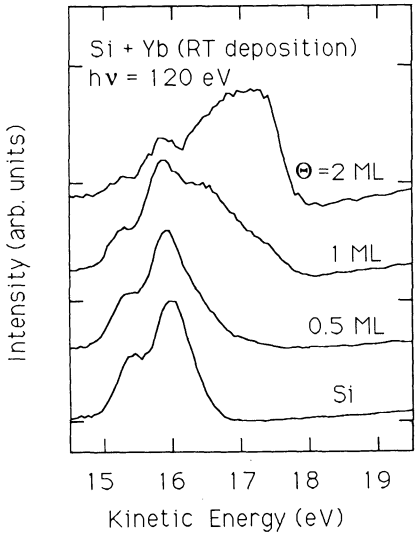

Fig. 8 Si 2p signal in the Si/Yb interface prepared by depositing Yb at RT and by measuring the spectra at the same temperature.

prepared at RT the reacted layer is connected with GdSi, as explained in ref. 11. In the Si/Yb interface grown at RT the precursor situation is related to Yb_5Si_3, as shown in ref. 5, and can be reached only upon deposition at RT. The deposition at LNT originates a kind of chemisorbtion of Yb on top of the substrate and the Yb subsequently deposited essentially grows as a pure metal.

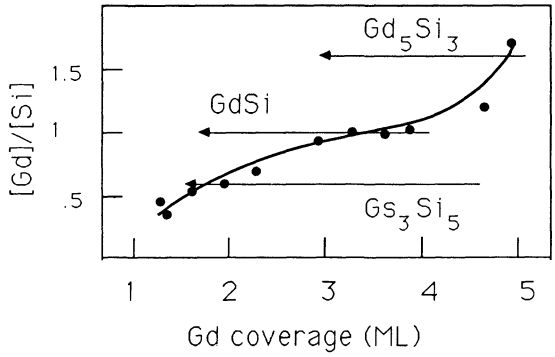

Fig. 9 Average composition of the reaction product in the Si/Gd interface grown at RT as a function of the Gd coverage. The lines corresponding to the bulk silicides are drawn for reference. (Data from ref. 11.)

The formation of a precursor phase which is stable upon heating up to the temperature in which RE diffusion into the bulk takes place with the possible formation of superstructures (for Yb diffusion is significant approximately above 450 ^{o} C [20]) could be in agreement with a concept included in a model based on core line decomposition in subcomponents [21,22] which has been extensively applied to a variety of interfaces. In effect, the precursor phase we identify could correspond to the first phase which is assumed to be formed in the model and which should to correspond to some stable silicide. From this viewpoint the present results can support the model. On the other hand, we note that this approach implies an extensive decomposition of core lines which can be very risky, in our opinion, and that this model contains many implicit assumptions (for instance on morphology and on stoichiometry as a function of lateral position and depth in the interface region) which cannot be tested directly on the basis of photoemission experiments. For this reason we do not try to discuss our results in such terms. In this connection we limit ourselves to note that the above average calibration of the compositions of the precursor phase casts some doubts on the generality of the assumption done by Del Giudice et al. in ref 23 on the fact that a monosilicide is formed as the first phase. In particular, in the case of Si/Yb the consideration of the 4f lineshape [5] makes it very hard, to say the least, to assess that the first phase formed is YbSi. As already mentioned, ref. 5 clearly shows that the first silicide-like phase to be formed is related to Yb_5Si_3.

CONCLUSIONS

Synchrotron radiation photoemission spectra taken in various moments of the thermal history of interfaces (Si/Gd and Si/Yb) prepared at low temperature shows that a kind of incubation stage exists up to about 2 ML. the presence of such stage is required, in both cases, to make the further progress of the reaction easier. The mechanisms which make the initial reaction possible are probably dominated, in these interfaces, by a weakening process. This incubation ends up with the formation of a silicide-like interfacial compound which is stable upon heating and which has a different average compositions in the two cases. In particular, it is richer in Si in the Si/Gd interface. The formation conditions of this precursor phase are very different in the two interfaces , being the formation of the precursor stage much easier in the Si/Gd interface. This is an indication of the importance of steric effects in the early interface growth which are connected with valence and ionic size. In the early interface formation trivalent Gd tends to have a higher coordination with silicon compared to divalent Yb. Moreover, trivalent Gd is smaller with respect to divalent Yb. These differences could explain the easier formation of a precursor stage in the Si/Gd interface.

The above results and discussion have some general implications. In effect, the importance of steric effects (see also ref. 4 for Si/Pd) implies, in our opinion, that the construction of a so called "unified model" for interface growth mechanism is probably an unrealistic goal. In this field the need of a unified understanding, which is one of the driving forces of physics, probably cannot be satisfied by building models. A more realistic goal is to define a general unified set of processes which are possible "a priori" and to clarify the interconnections between the single processes. These processes can be in competition or can be complementary, as shown in a tentative scheme of this kind presented in ref. 12. This set of possibilities ensures the unity of the discussion, but for each specific case the goal is to identify the particular combination of processes (i.e. the specific path within the possible ones) which is actually followed. To this end the cross fertilization between spectroscopic and structural investigations will be of paramount importance.

ACKNOWLEDGMENTS

This work has been done in the framework of a cooperation between the authors (Politecnico di Milano) and the W. E. Spicer and I. Lindau group at the Stanford University. The experiments has been perfomed at the Stanford Synchrotron Radiation Laboratory, which is supported by DOE, Department of Energy.

References

* Present address: Istituto di Fisica, Politecnico di Milano, P.za Leonardo da Vinci 32, 20132 Milano, Italy.

1. G. W. Rubloff, P. S. Ho, J. L. Freeouf, J. E. Lewis, Phys. Rev. B 23, 4183 (1981).
2. G. Rossi, I. Abbati, L. Braicovich, I. Lindau, W.E. Spicer Sol. St. Comm. 39, 195 (1981).

3. I. Abbati, L. Braicovich, B. DeMichelis, U. DelPennino, J. Vac. Sci. and Technol. 17, 1303 (1980).
4. U. K. Kohler, J. E. Demuth, R. J. Hamers, Phys. Rev. Lett. 60, 2499 (1988).
5. I. Abbati, L. Braicovich, C. Carbone, J. Nogami, I. Lindau, Surf. Sci. 168, 193 (1986).
6. I. Abbati, L. Braicovich, C. Carbone, J. Nogami, I. Lindau, I. Iandelli, G. L. Olcese, A. Palenzona, Sol. St. Comm. 62, 35 (1987).
7. M. Del Giudice, J. J. Joyce, J. H. Weaver, Phys. Rev. B 36, 4761 (1987).
8. I. Iandelli, A. Palenzona in Handbook on the Physical and Chemical Properties of Rare Earths, edited by K. A. Gschneider and L. Eyring (North Holland, Amsterdam, 1798).
9. M. Campagna, G. K. Wertheim, Y. Baer in Photoemission in Solids,, edited by M. Cardona and L. Ley (Springer, Berlin, 1978).
10. C. Carbone, J. Nogami, I. Lindau, J. Vac. Sci. and Technol. A 3. 972 (1985).
11. E. Puppin, J. Nogami, C. Carbone, Z. X. Shen, I. Lindau, B. B. Pate, I. Abbati, L. Braicovich J. Vac. Sci. and Technol. B5, 1083 (1987).
12. L. Braicovich, Absorption and Reaction of Metals on Elemental Semiconductor in The Chemical Physics of Solids Surfaces and Hteregeneous Catalysis, edited by D. A. King and D. P. Woodruff (Elsevier, Amsterdam, 1987).
13. O. Bisi, K. N. Tu, Phys. Rev. Lett. 52, 1633 (1984).
14. A. Hiraki, Surf. Sci. Rep. 3, 355 (1983).
15. A. Zunger, Phys. Rev, B 24, 4372 (1981).
16. R. Ludeke, Surf. Sci. 132, 143 (1983).
17. M. Grioni, J. J. Joyce, M. A. Chambers, D. G. O' Neill, M. Del Giudice, J. H. Weaver, Phys. Rev. Lett. 53, 2331 (1984).
18. J. F. Van Der Veen, E. J. van Loenen. Surf. Sci. 168, 701 (1986).
19. F. Gerken, J. Barth, L. I. Johansson, A. Flodstrom, Surf. Sci.117, 468 (1981).
20. I. Chorkendorff, J. Kofoed, J. Onsgaard, Surf. Sci. 153/153, 749 (1985).
21. R. A. Butera, M. Del Giudice, J. H. Weaver, Phys. Rev. B 33, 5435 (1986).
22. R. A. Butera, C. A. Hollingsworth, Phys. Rev. B 37, 10487 (1988).
23. M. Del Giudice, J. J. Joyce, J. H. Weaver, Phys. Rev. B 36 4761 (1987).

Silicon-Silicide Interfaces

STRUCTURES AND ELECTRONIC PROPERTIES OF EPITAXIAL SILICON-SILICIDE INTERFACES

D. R. Hamann
AT&T Bell Laboratories
Murray Hill, New Jersey 07974
U. S. A.

INTRODUCTION

Of all the known metal-semiconductor interfaces, those between the transition-metal silicides $NiSi_2$ and $CoSi_2$ and Si are the best characterized. This is because these silicides grow pseudomorphically on Si, and form atomically abrupt interfaces with a low defect density. Because they are pseudomorphic, they offer the opportunity to understand the atomic geometry of the interface in complete detail. This, in turn, permits detailed theoretical study of the electronic properties of these interfaces at a level not possible for other metal-semiconductor systems. These Schottky-barrier systems are on a par with, or perhaps better than, molecular-beam-epitaxy-grown semiconductor heterostructures in their degree of perfection.

$NiSi_2$ and $CoSi_2$ have cubic fluorite structures with lattice parameters which are, respectively, 0.4% and 1.2% smaller than that of Si. The fluorite structure has tetrahedrally coordinated Si, and 8-fold, cubically-coordinated metal atoms. The metal-Si bond length in these silicides is essentially equal to the Si—Si bond length in Si. Diamond and fluorite lattices have common <111> planes, and it is easy to postulate unreconstructed, undistorted interface models.

In this talk, I will summarize several theoretical investigations of various questions concerning these silicide interfaces. Ths questions can roughly be divided into two categories, those concerning atomic structure and those concerning electronic properties. In the first category, I'll discuss calculations pertaining to competing models of the initial stages of growth of $NiSi_2$ on Si, and to the different atomic structures of the (111) interfaces of $NiSi_2$ and $CoSi_2$ with Si. In the second category, I'll discuss Schottky barrier heights, the kinematics of electron transmission through these interfaces, and dynamical effects in electron transmission. I'll conclude with a discussion of future directions.

STRUCTURAL STUDIES

Theoretical Methods

The questions addressed in this section primarily concern the relative energies of different structural arrangements of atoms. There are no simple models which

give an adequate description of the cohesion of the silicides, so I have used the Local Density Functional (LDF) method[1] in all the calculations I'll be describing. The LDF method is an *ab initio* method in that it uses no input other than atomic numbers and atomic coordinates, which makes it generally applicable and frees it from the biases inherent in fitted models. When the equations governing LDF theory are solved accurately, it has been remarkably successful in yielding correct structural parameters, phonon frequencies, high-pressure phase transitions, and surface reconstructions.

I'll briefly review LDF theory, which is based on an expression for the total energy of the system as a three-part functional of the electron charge density ρ,

$$E[\rho] = T_s[\rho]+U[\rho]+E_{xc}[\rho] \ . \tag{1}$$

T_s is a kinetic energy, U is the Coulomb electrostatic energy of ρ and the nuclear charges, and E_{xc} is the exchange-correlation energy. ρ is expressed as a sum of squared-magnitudes of single-particle wavefunctions ψ,

$$\rho(\mathbf{r}) = \sum_i \psi_i^*(\mathbf{r})\psi_i(\mathbf{r}) \ , \tag{2}$$

and T_s in Eq. (1) is the sum of the single particle kinetic energies of these wavefunctions. By varying E with respect to ψ, you can show ψ satisfies a Schrödinger equation,

$$[-\tfrac{1}{2}\nabla^2+V_{eff}(\mathbf{r})]\psi_i(\mathbf{r}) = \epsilon_i\psi_i(\mathbf{r}) \ , \tag{3}$$

with an effective potential

$$V_{eff}(\mathbf{r}) = V_c(\mathbf{r})+\frac{\delta E_{xc}[\rho]}{\delta\rho(\mathbf{r})} \ . \tag{4}$$

The exchange-correlation contribution to V_{eff} is given by a functional derivative, and the Coulomb contribution by

$$V_c(\mathbf{r}) = \int \frac{\rho(\mathbf{r}')}{|\mathbf{r}-\mathbf{r}'|}d\mathbf{r}' - \sum_\alpha \frac{Z_\alpha}{|\mathbf{r}-\mathbf{R}_\alpha|} \ . \tag{5}$$

which includes the nuclear charges Z_α.

It's worth recalling that density functional theory would be an exact many-body theory if the exact functional E_{xc} were known.[1] We use the local approximation to E_{xc} because we don't have a better general form, and because it has been very successful, as I mentioned previously.

To deal with structural energies, we need to do an accurate job of solving the LDF equations. There are several methods around for doing this, but we have been using the Linear Augmented Plane Wave (LAPW) method.[2,3] With LAPW, we can handle anything in the periodic table, and it's straightforward to converge to accurate results. Briefly, LAPW is a solution of Eqs. (1-5) with an effective but

somewhat complicated form for ψ. We perform these calculations for slabs that extend to infinity parallel to their surfaces , and divide space into three kinds of disjoint regions, as shown in Fig. 1. "Muffin tin" spheres (II) are centered on each atom, and a pair of "matching planes" divide vacuum regions (III) that run to infinity from the slab interior. The region inside these planes and outside the spheres is the interstitial region (I). A unit cell is introduced which is also periodic

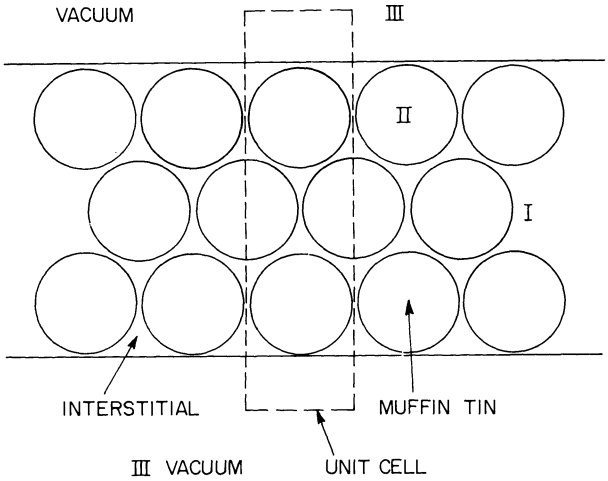

Fig. 1. Partition of space for the LAPW method.

in the slab normal direction, but this is just a trick to quantize plane waves, and does not mean the slab is periodically repeated. We then introduce basis functions for each Bloch wavevector $\mathbf{k}_{\parallel}$,

$$\chi_{\mathbf{K}}(\mathbf{x}) = \begin{cases} e^{i\mathbf{K}\cdot\mathbf{x}}, & \mathbf{x} \in \mathrm{I} \\ \sum\limits_{lm\tau} a_{\mathbf{K}nlm\tau} Y_{lm}(\hat{\mathbf{x}}_n)\, \phi_{nl\tau}(x_n), & \mathbf{x} \in \mathrm{II}_n \\ e^{i\mathbf{K}_{\parallel}\cdot\mathbf{x}} \sum\limits_{j} b_{\mathbf{K}nj}\, u_{nj}(\mathbf{x}_{\perp}), & \mathbf{x} \in \mathrm{III}_n \end{cases} \tag{6}$$

$$\mathbf{K} = \mathbf{k}_{\parallel} + \mathbf{G} \ , \ \mathbf{x}_n = \mathbf{x} - \mathbf{R}_n .$$

In these equations, n indexes various muffin tin and vacuum regions, $\mathbf{G}$ is a 3-dimensional reciprocal lattice vector, and Y_{lm} are spherical harmonics. The radial functions $\phi_{nl\tau}$ are solutions of the Schrödinger equation for the spherical average of the self consistent potential in the muffin tin at an energy centered in the valence bands ($\tau=1$), and energy derivatives of these solutions ($\tau=2$). The functions u_{nj} are solutions of the Schrödinger equation for the planar-averaged vacuum potentials, for a sequence of normal-direction energies appropriate to the range of parallel kinetic energies of the basis functions. With these choices, each basis function is already a pretty good approximation to the eigenfunctions we want for the complete potential. The muffin-tin and vacuum pieces are joined by plane waves in the interstitial region, and the coefficients $a_{\mathbf{K}nlm\tau}$ and $b_{\mathbf{K}nj}$ are

chosen to make each χ and its first derivative continuous at each boundary. The LDF wavefunctions ψ are now simply taken to be linear combinations of the basis functions,

$$\psi_{\mathbf{k}\|\nu}(\mathbf{x}) = \sum_{\mathbf{K}} c_{\mathbf{K}\nu}\, \chi_{\mathbf{K}}(\mathbf{x}). \tag{7}$$

Using this expansion, we solve Eq. (3) variationally and get a matrix eigenvalue problem for the coefficients $c_{\mathbf{K}\nu}$ and energies ϵ_i.

That's basically all there is to it. We make only one further approximation in solving Eqs. (1-5), that of using rigid spherical atom cores. The charge and potential are treated as completely general functions of $\mathbf{x}$.[3] Admittedly, the division of space makes some of the details in evaluating ρ, the self-consistent V_{eff}, and E rather complicated.

Nucleation and Growth

The growth of single-crystal $NiSi_2$ on Si(111) can be accomplished only by careful control of the growth kinetics.[4] There are two possible ways to align the Si and $NiSi_2$ structures, both of which will let common Si layers coincide. One alignment keeps all crystallographic axes coincident, and is conventionally called type A. The other corresponds to rotating the $NiSi_2$ by 180° about the interface-normal [111] axis, and is called type B. Poorly controlled growth produces polycrystalline $NiSi_2$ films with both orientations.

A "template" technique was recently developed for growing pure type A or type B.[4] A thin Ni overlayer is deposited on a clean Si substrate at room temperature, and then gently annealed. A 2-5 Å layer produces a type B $NiSi_2$ overlayer during the anneal, and an approximately 18 Å layer produces type A. Further growth through either slow Ni deposition or faster co-deposition of Si and Ni at somewhat higher temperatures continues the growth with the template orientation.

Understanding the initial reaction of deposited Ni with the Si substrate is of importance to understand the template mechanism. Two competing proposals have been put forward for the initial structure. One is that the Ni initially enters tetrahedral interstitial sites in the undisturbed Si lattice, forming a distinct surface phase up to three layers thick. This model was supported by an interpretation of growth kinetics,[5] ion channeling,[6] x-ray photoemission,[6] and ultraviolet photoemission.[6] The interstitial Ni would have 4 near-neighbor and 6 next-nearest neighbor Si's, and these 10 Si's have been dubbed the "adamantane cage". A more recent proposal is that the Ni reacts immediately to form a local arrangement with fluorite-like coordination. This is supported by surface extended x-ray absorption fine structure measurements.[9]

The disagreement between these proposals looked like a good opportunity to provide some theoretical input. The plausibility of the adamantane precursor phase depends heavily on its energy relative to a reacted structure, since even favorable kinetics won't overcome too large an energy difference.

Before applying the methods I discussed to this issue, we had to test them out and establish convergence criteria for this class of materials. We verified that we could calculate good lattice constants and bulk moduli for bulk Si and bulk Ni, both of which had previously been studied by other LDF methods. Then, we calculated the lattice constant of fluorite $NiSi_2$, which turned out to be in

excellent agreement with experiment. Finally, as a most stringent test, we calculated the heat of formation of $NiSi_2$, which involves sums and differences of the total valence energies from all three of these calculations. We found 1.1 eV,[10] compared to 0.9 eV, error bars unknown, from experiment.[11] Since this result involved differences between computed energies of approximately 1300 eV, it provides an extremely stringent test of the accuracy of our procedures and the utility of LDF theory for silicide energetics.

Since an adamantane phase at least 3 layers thick had been proposed, it was of interest to study the bulk properties of this hypothetical structure, which also has stoichiometry $NiSi_2$. The adamantane phase, which has space group T_d^2 (F43m), is technically the MgAgAs type. It can be reached from the fluorite phase be a simple pair interchange of Ni and Si neighbors. We calculated the lattice constant for adamantane $NiSi_2$ and found it to be only 0.5% expanded compared to Si.[10] A reasonable lattice match is a necessary but not sufficient condition for the occurrence of this structure as an epitaxial surface phase. The energy, however, turned out to be 1.35 eV per formula unit higher than fluorite $NiSi_2$.[10] This is such a large difference that the occurrence of this structure could effectively be ruled out.

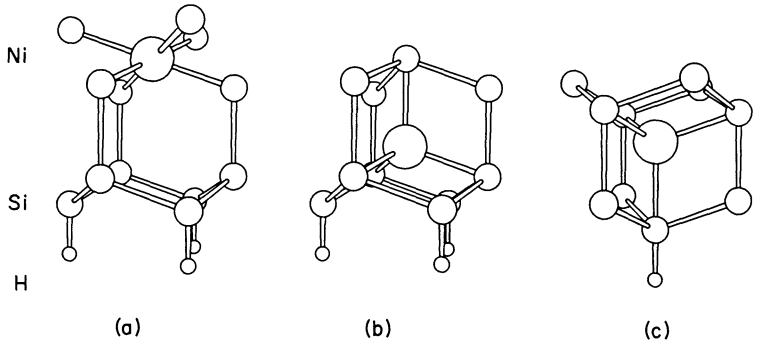

Fig. 2. Perspective drawings of unit cells from the slabs used to compare the energies of several surface structures of Ni on Si.

A further possibility needed to be investigated. At a surface, a reacted Ni wouldn't have its full 8-fold coordination, which should raise its energy compared to bulk $NiSi_2$. An adamantane Ni, however, would have Si neighbors that were not fully coordinated, and could perhaps bond more strongly to the Ni, lowering its energy compared to the bulk structure. The simplest possible geometries we could use to estimate the size of these effects are shown in Fig. 2. Using (111) slab structures of composition $NiSi_4H$, we studied a reacted structure in which the Ni is only 6-fold coordinated, shown in Fig. 2a. The adamantane structures in Figs. 2b and c have the Ni "10-fold" coordinated with one surface Si near neighbor, and with three surface Si second neighbors, respectively. The lower Si double layer is terminated by H to simulate bonding to a continued bulk in all cases. The calculations are for slabs extended periodically to infinity in two directions, not just for the small clusters shown.

The modified bonding at the surface does have an effect. However, the reacted structure remains the lowest, with the Fig. 2b structure higher by 0.79 eV, and the Fig. 2c structure higher by 0.98 eV.[10] The differences remain sufficiently large that even one monolayer of Ni in the adamantane cage sites can be effectively ruled out. While the details of template formation are not yet understood, the range of mechanisms to be examined is considerably narrowed.

Interface Structure

The fully developed (111) silicide interfaces pose another interesting problem: $NiSi_2$ and $CoSi_2$ appear to form Si interfaces with different atomic structures. While it's much more difficult to probe the structure of a buried interface than that of a surface, this fact has been established by several experimental studies. The tools that have been applied are high-resolution transmission electron

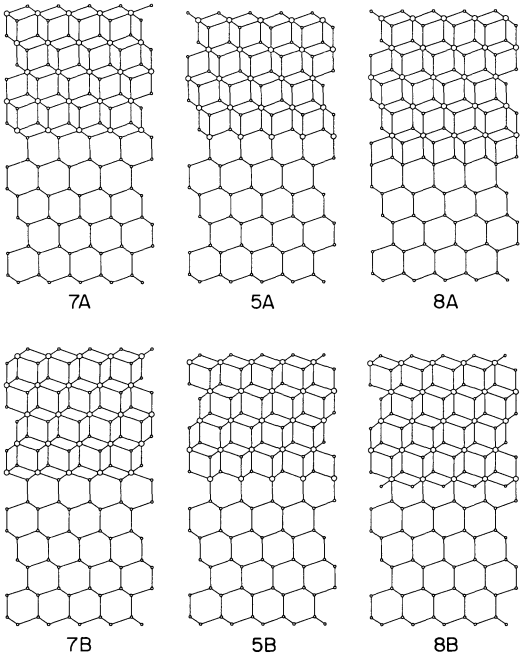

Fig. 3. Projection on the $<1\bar{1}0>$ plane of several (111) silicon-silicide interface models. The Si atoms are shown as small circles and the metal atoms as larger circles. The bonds that appear longer lie in the plane of the plot, while those that appear shorter are directed in and out of the plane.

microscopy,[12,13] x-ray standing waves,[14–16] and ion channeling-Rutherford backscattering.[17,18] All these measurements are in agreement with each other for both materials. However, they all only measure one thing, the normal displacement of the $<111>$ planes of the silicide relative to a continuation of the Si lattice.

For either A or B orientation of $NiSi_2$, the data were seen to be consistent with a bonding arrangement in which the ideal silicide lattice was terminated by a Si layer, which joined to the ideal Si lattice with bonds of nearly ideal length. This implied a 7-fold coordination of the Ni nearest the interface, and these structures are shown as 7A and 7B in Fig. 3. For $CoSi_2$, the silicide lattice planes were nearer the Si, and this was interpreted as indicating a Co termination of the silicide lattice, with the Co bonded to the Si. This results in a 5-fold coordination for the last Co. $CoSi_2$ only grows with B orientation on Si, and this structure is 5B in Fig. 3. Considering the similarity in atomic and electronic structure[19,20] of the two silicides, the different interface coordination is puzzling.

I found the low coordination of the interface Co particularly hard to believe. A close reading of the experimental papers indicated that only models with 4-fold coordinated Si throughout were considered, based on the argument that Si—Si bonds were much stronger that M—Si bonds.[12] Relaxing this assumption left open the possibility of two additional structures with 8-fold coordinated interface metal atoms, and 3-fold or 5-fold interface Si, 8B and 8A, respectively, in Fig. 3.[21] No experimental evidence could exclude 8B for $CoSi_2$. This posed a clear cut opportunity for a theoretical prediction -- to show whether the 8B $CoSi_2$ structure has a lower energy than the 5B or not. Just comparing these two energies would not have constituted a very satisfactory investigation, however. The real challenge is to examine all six geometries for both metals, and show that 7A or 7B has the lowest energy for Ni, while 5B or 8B does for Co, all within the context of completely consistent calculations.

I applied the LDF-LAPW method to superlattice structures, maintaining the true periodicity of the interface in the parallel direction, but introducing an artificial periodicity in the perpendicular direction, alternating slabs of Si and MSi_2. Since each unit cell of the superlattice contains two interfaces, the interface energy is half the supercell energy minus half the sum of the energies of a number of unit cells of each bulk material corresponding to the thickness of the respective slabs. Both bulk energies must be calculated at the supercell lattice parameter to eliminate thickness-dependent strain contributions. To minimize systematic errors in interface energy comparisons, it is important to use the same numbers of layers in all the supercells. Some "scissors and paste" study of Fig. 3 shows that superlattices with [111] periodicity require different numbers of layers for different interface geometries. These would all be hexagonal lattices, space group D^3_{3d}. The trick to solve the consistency problem was to add symmetry-preserving lateral translations to the [111] translations, forming rhombohedral supercells, space group D^5_{3d}.[21]

The calculations were done for M_2Si_8 supercells, which were thick enough to give size convergence for the interface energy, and thin enough to permit wavefunction basis size convergence. The results are shown in Table 1. We first notice that the 5A interface has a very high energy for both metals, and is in fact worse for Co. For Ni, 7A has the lowest energy, but 7B is only 0.04 eV higher. This small difference might be anticipated from the fact that only the third-neighbor coordination of the interface atoms is changed in going from 7A to 7B. The difference we calculate is approximately the same as the energy of an Si stacking fault, which has a similar rearrangement of bonds. It is consistent with the fact that either A- or B-orientation $NiSi_2$ can be grown by controlling the growth kinetics.[4] Since the 5A-5B switch involves the same type of bonding change, it did not seem worthwhile to bother with a 5B calculation. For Co, the lowest energy interface is 8B, and the next, 8A, is higher by 0.15 eV. In this case, the A-B orientational switch involves a change from an overcoordinated interface

Table 1. Interface energies for the structures in Fig. 3.

Structure	Energies (eV)	
	Ni	Co
5-fold A	1.52	2.20
7-fold A	0.35	0.86
7-fold B	0.39	
8-fold A	0.78	0.68
8-fold B	0.55	0.53

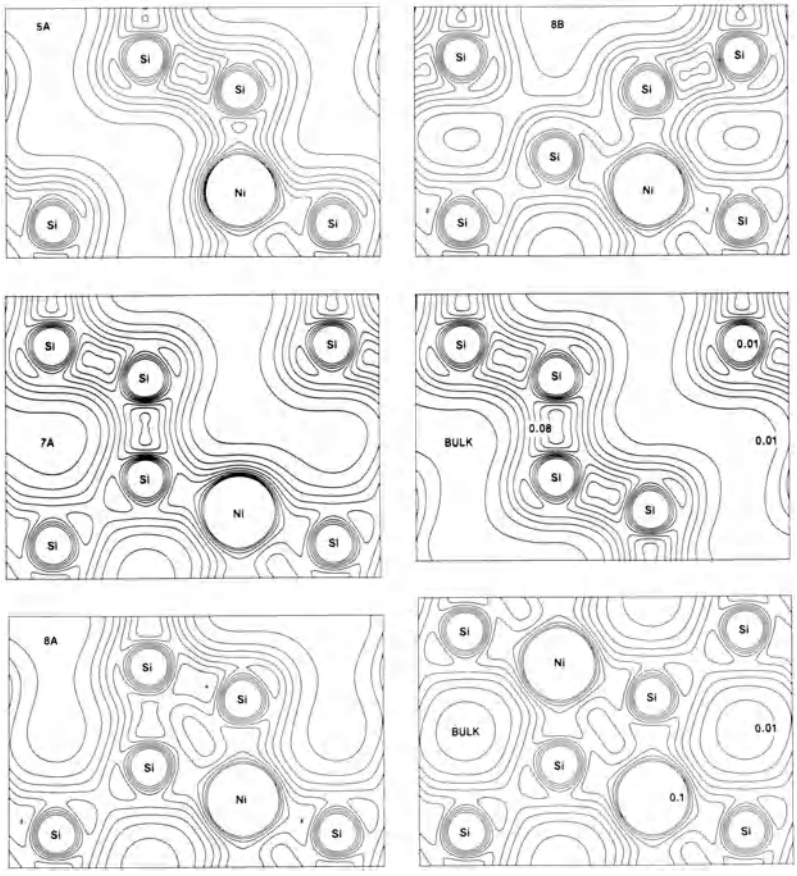

Fig. 4. Contours of constant valence charge density for the interface structures, bulk Si, and bulk $NiSi_2$. The plot is in the $<1\bar{1}0.>$ plane, and the [111] axis is vertical. Contour levels are 0.01, 0.02, ..., 0.1 au (a_{Bohr}^{-3}). Maximum and minimum values indicated near nuclei, interstitial sites, and bonds for the bulk materials are transferable to the interface structures.

Si to an undercoordinated Si, so a bigger difference could be anticipated. This is consistent with the fact that the growth of $CoSi_2$ on Si always leads to B orientation, independent of the growth kinetics.

While the relative ordering among the 5- and 8-fold structures is the same for Ni and Co, the metal-dependent reordering between 7- and 8-fold geometries remains to be explained. We can get a more detailed picture of bonding in the various interface structures by examining contour plots of the valence charge density, shown for Ni and Co in Figs. 4 and 5, respectively. For 7A, the charge densities within the MSi_2 layers and within in the Si layers are essentially identical to the corresponding bulk densities. The interface Si—Si bond appears to be the same as in Si bulk for Ni, but slightly weaker for Co, with the bond maximum 0.08 contour barely starting to develop. For 8A and 8B, the Ni—Si bonds within the interface silicide layer appear to be similar to the bulk, while the Co—Si bonds are strengthened, developing an additional contour, 0.07. The charge density in the "dangling bond" above the 3-coordinated Si in 8B barely reaches 0.05 for Co, while a large 0.05 bulge develops for Ni.

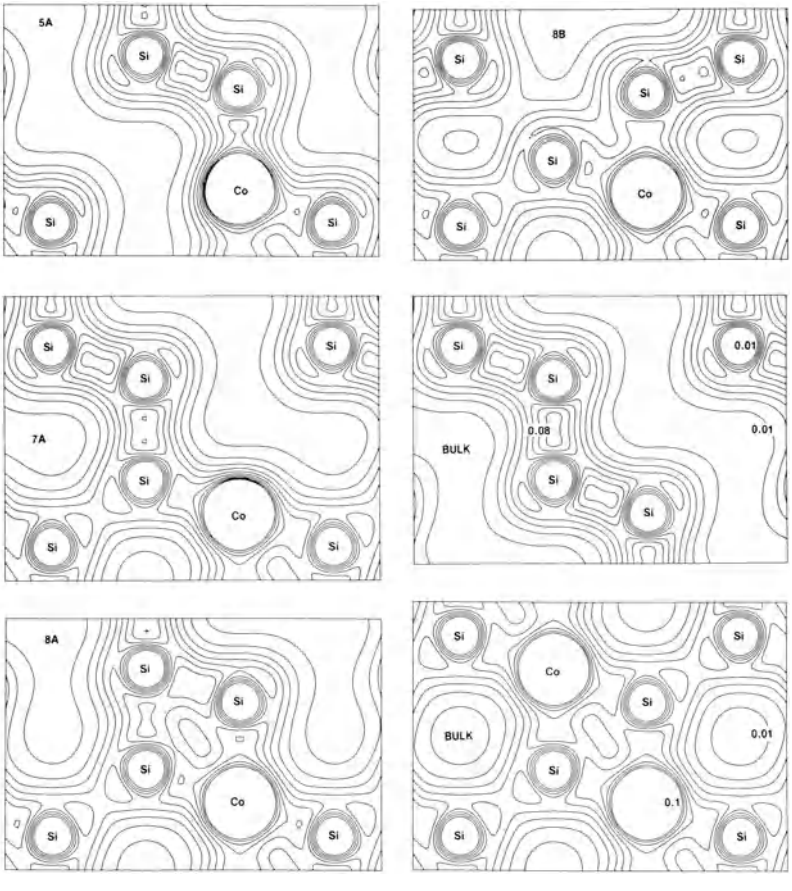

Fig. 5. Charge contours as in Fig. 4 for Co.

The above description suggests that $CoSi_2$ is more reactive at its interface than $NiSi_2$. This can be understood in terms of an analysis of the bonding in these silicides presented earlier with the aim of explaining their unique structures among transition metal silicides.[22] We pointed out the existence of a "quasigap" separating bonding and antibonding states. For $NiSi_2$, the Fermi level falls

somewhat above the gap, into the antibonding region, while for $CoSi_2$ it falls slightly below the gap. This suggests that the interface $CoSi_2$ layer can take better advantage of the extra electron made available by the 3-coordinated Si than can a $NiSi_2$ layer.

An independent study based on cluster calculations has also recently suggested an 8-fold coordinated interface Co.[23] I think the challenge now goes to the experimentalists to devise a way of distinguishing the 8-fold and 5-fold interface geometries to confirm these predictions.

ELECTRONIC PROPERTIES

Schottky Barriers

The Schottky barrier height depends on the average electrostatic dipole at a metal-semiconductor interface. It's not my intention do discuss the various possible intrinsic and extrinsic contributions to this dipole which may occur in different systems. Since the silicide-silicon interfaces appear to form with atomically abrupt and perfect geometries, however, we should be able to calculate that dipole for these systems. The dipole, after all, involves the ground state electron density, and the LDF should do a good job calculating this. The experimental results for the $NiSi_2$ - Si (111) interface are particularly intriguing, showing a significant change in barrier height between the A and B orientation.[24] The measured (n-type) barrier heights are 0.65 eV for A and 0.79 eV for B.[24] Model theories of barrier heights predict no sensitivity whatever to details of interface geometry, so this difference can only be examined with an *ab initio* approach.

The definition of the n-type Schottky barrier is the semiconductor conduction-band edge energy minus the metal Fermi level at the interface,

$$\phi = E_c(Si) - E_F(NiSi_2) \,. \tag{8}$$

There is no direct way to extract these quantities from a supercell or slab LDF calculation. Even for the thickest practical metal and semiconductor layers, "box" quantization of the energy levels in the interface-normal direction shifts the eigenstates of the model system in a way that makes accurate identification of E_c and E_F essentially impossible. Nonetheless, experience suggests that even relatively thin layers should have the correct potentials, since screening in both metal and semiconductor systems "heals" charge disturbances caused by surfaces and interfaces within a few Å's. Thus, if we can extract the potentials this far away from the interface in the metal and semiconductor parts of the supercell, we should be able to use parallel calculations of the bulk materials to identify the needed energies.

This approach is complicated by two further difficulties. One is that the zero of energy is arbitrary for bulk and supercell calculations. Another is the well know problem of the local density approximation, which significantly underestimates bandgaps in semiconductors. Recent work on many-body approaches to the bandgap problem have shown that LDF theory gives an accurate estimate of the valence band maximum energy, E_v, for Si.[25] These considerations suggest that we can get the best estimate of ϕ from LDF calculations by evaluating the following expression:

$$\phi = E_{Gap}(\text{Exp.}) + E_v(\text{Si Bulk}) - E_F(NiSi_2\ \text{Bulk})$$
$$- \overline{V}(\text{Si Bulk}) + \overline{V}(\text{Si Supercell}) \tag{9}$$
$$+ \overline{V}(NiSi_2\ \text{Bulk}) - \overline{V}(NiSi_2\ \text{Supercell}).$$

Here, Exp. refers to the experimental bandgap, and the $\overline{V}$'s are average potentials, defined in a parallel manner of course, for corresponding regions of the interface supercell or of each bulk. Note that potentials or energy levels from each of the three separate calculations needed to fill in this expression appear twice, with opposite sign, so the arbitrary and unrelated zeroes of potential are canceled out. This cancellation accomplished, the differences in the second and third line then align the respective bulk potentials with the dipole extracted from the supercell calculation.

I first attacked this problem in collaboration with Jerry Tersoff about 5 years ago, and the results were disappointing. We carried out LAPW calculations for supercells and free-standing slabs, with or without hydrogen termination, with varying numbers of layers of each material. We invariably found ϕ close to 1.1 eV, the band gap, and found no significant A-B difference.[26] This is not only a wrong result, but sort of a null result, since it indicates that the Fermi level is "pinned" as low as it can possibly be by the Si valence band states. We believed that the calculations were adequately converged, and that our unsatisfactory results were related to the band gap problem in a way we didn't really understand. When I recently learned that Das and coworkers, who used a similar strategy but a different LDF calculational method (Linear Muffin Tin Orbital - Atomic Sphere Approximation, LMTO-ASA), had obtained similar ϕ results, I wasn't surprised.[27]

A surprise came recently, however, as an incidental consequence of research I have been doing with Mark Stiles on dynamical interface transmission, which I'll discuss later. We needed to calculate the $\overline{V}$'s in Eq. (9) averaged on planes along which we planned to join bulk and interface wavefunctions. Fortunately, the potentials from the interface energy calculations I discussed had been saved, and these were what we used. We considered planes spaced one double-layer period from the interface for Si and one triple-layer period for $NiSi_2$. To our satisfaction, we found that when the averages were aligned, the rms differences in potentials between bulk and supercell were 0.001 Hartrees (1 Hartree = 27.2 eV), despite the fact that the potentials individually varied by the order of 1 Hartree over the planes. This indicates that the shape of the potentials is very effectively screened to its bulk form in this short distance. When we used these $\overline{V}$'s in Eq. (9), we found ϕ's much closer to experiment than in the previous studies.[28] The numbers we used are all shown in Table 2 to give an idea of the subtractions involved.

Our calculated orientation dependence is only half the experimentally observed value. However small geometric relaxations, which may be different for A and B, have been omitted, as has the tetragonal distortion of real pseudomorphic $NiSi_2$. Instead of elaborating further on why these numbers aren't even better, the main issue is why they are so good in light of the previous work. One answer for my new LAPW results is that the interface energy calculations[21] demanded much better convergence in the wavefunction and potential, beyond the point at which the bandstructures stabilize.

Table 2. Potentials and energies for $NiSi_2$ - Si Schottky barrier

Structure	7A	7B
E_{Gap}(Exp.)	1.12	1.12
E_v(Si B)	6.386	6.386
E_F($NiSi_2$ B)	9.639	9.639
$\overline{V}$(Si B)	0.691	0.691
$\overline{V}$(Si SC)	1.258	1.316
$\overline{V}$($NiSi_2$ B)	-3.378	-3.378
$\overline{V}$($NiSi_2$ SC)	-5.695	-5.712
ϕ(Eq. 9)	0.749	0.823
ϕ(Exp.)	0.65	0.79

The calculations I did with Jerry Tersoff used the latter criterion,[26] and may simply have not given an adequately converged dipole. I don't have personal experience with LMTO-ASA, so it's harder for me to address the difference from G. P. Das's results.[27] I can speculate that the spherical averaging of charge used in the ASA may change the interface dipole. Also, the LMTO wavefunction basis is fixed in size, and can't be extended to check convergence. As I noted, $\phi = 1.1$ eV is a pinning point, so the fact that two underconverged calculations which both tend to make the $NiSi_2$ too electronegative arrive at the same value is no coincidence. On the other side of this comparison, the Das calculations used much thicker layers of both Si and $NiSi^2$. One could argue that our new results[28] are not size converged, and that the apparent agreement with experiment is misleading. I'm afraid that responding to this point will await the next generation of supercomputers.

Transmission Kinematics

While Schottky barrier height is the most widely discussed electronic property of metal-semiconductor interfaces, especially at this workshop, there are other properties also worthy of attention. One is the transmission of electrons through such interfaces. Interest in this question has received additional stimulus from experimental programs to test the idea of a metal-base transistor using epitaxial silicides on silicon. Such a transistor consists of an n-type Si substrate collector, a thin MSi_2 base, and a further epitaxial overlayer of n-type Si serving as an emitter.[29] The device then consists of two symmetric "back-to-back" Schottky barriers. When the emitter-base barrier is forward biased, it injects electrons over the top of the barrier into the MSi_2. Hopefully most of these electrons traverse the MSi_2 without scattering, and coast across the base-collector barrier, which is back-biased to provide power gain.

In order for this all to work, both kinematical and dynamical conditions must be satisfied. There must be appropriate states in the MSi_2 to transmit the electrons, and the reflection coefficient at the interfaces must be small. To examine the kinematics, we need to know the band structure of the silicides. That of $CoSi_2$ is shown in Fig. 6.[20] The bands consist of a broad, free-electron-like manifold starting at -13 eV, formed from Si sp^3 hybrids and the Co s orbital. This is crossed by a complex of five Co d-derived bands from -5 eV to somewhat

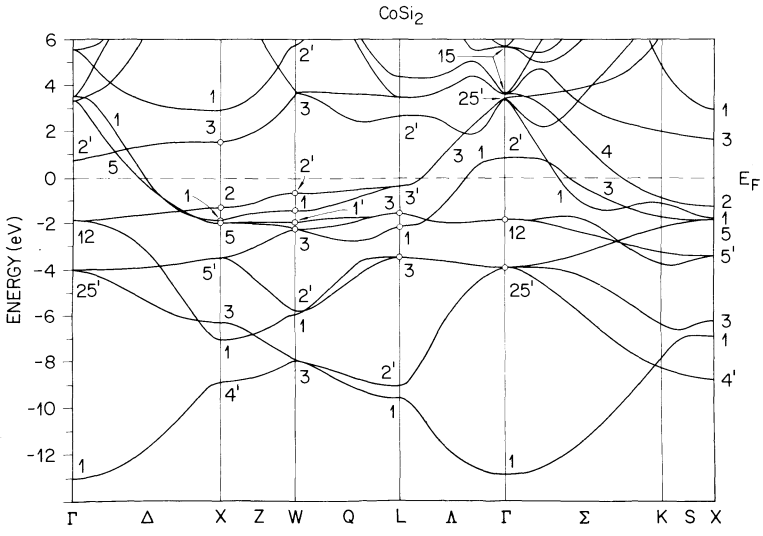

Fig. 6. Energy band structure of $CoSi_2$.

above E_F. There is a gap through much of the zone above E_F produced by a separation of bonding and antibonding states.[22] The band structure of $NiSi_2$ is very similar, with the Fermi level moved up to accommodate one extra electron.[19]

As I've discussed, the LDF method does not give accurate band gaps for semiconductors. How does it do for metals? In general, much better, at least in the vicinity of E_F. This can be understood in general terms from the analysis of the many-body approaches that have now succeeded in getting correct semiconductor bandgaps.[25] However, the most convincing evidence for the cases at hand is experimental. Extensive angle-resolved photoemission studies of $NiSi_2$ were carried out by Chang and Erskine. They were able to follow all the bands from about 0 to -5 eV along the $\Gamma-X$ and $\Gamma-L$ symmetry lines, and found them within a few tenths of an eV of the theory.[30] Recent photoemission data on $CoSi_2$ shows good general agreement, but slightly larger quantitative discrepancies.[31] However, calculated $CoSi_2$ Fermi surface areas are found to be in agreement with de Haas-van Alphen data to within a few percent.[20]

For an electron to be transmitted from Si to an epitaxial metal, the parallel Bloch wavevector and the energy must be conserved. These are the same kinematical conditions familiar in photoemission from well-ordered surfaces. An electron near the Si conduction band minimum has a wavevector (0.85, 0, 0), in units of $(2\pi/a)$. It can be transmitted through a (111) interface to any state in the silicide with wavevector (0.85+x, x, x). This defines a line in the Brillouin zone that is not one of the symmetry lines plotted in Fig. 6. The energy of the incident Si electron we know from the Schottky barrier height to be about 0.7 eV relative to E_F for both silicides. Bands along the permitted wavevector line are shown in Fig. 7 on an expanded scale near E_F. The dashed line represents the energy of an electron transmitted from the Si. We see that for $NiSi_2$, a single band satisfies the kinematical conditions. For $CoSi_2$, however, there is no available band, and the gap is sufficiently large that small errors in the band or the barrier height will not change this conclusion.

The failure of $CoSi_2$ to satisfy the kinematical conditions for electron transmission leads to the interesting question of just how the current does flow over the Schottky barrier in this system. Two possibilities are phonon or defect scattering which break the $\mathbf{k}_{\parallel}$ conservation condition, and scatter the incident electrons to silicide bands that can receive them. If phonons dominated the process, one might expect to see some unusual temperature dependence of the current-voltage characteristics, but this is not observed.[32] This suggests that either defect scattering dominates, or that the exponential dependence of the thermal excitation over the barrier swamps the observability of a temperature-dependent prefactor.

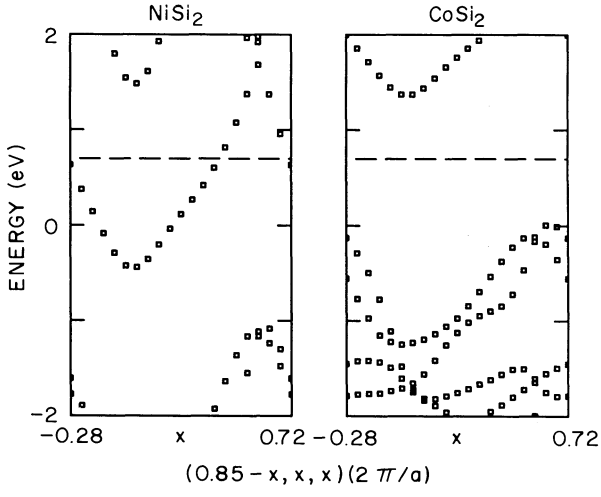

Fig. 7. Bands for kinematical matching of electron transmission from the Si conduction band minima for (111) interfaces.

The most direct evidence for the kinematical problem comes from measurements of a Si - $CoSi_2$ - Si structure that has been fabricated with a 50Å or so thick silicide layer, with apparently perfect epitaxial interfaces, and no pinholes. This is the "metal base transistor" configuration I discussed. Only about 2% of the injected current is collected, which is evidence for an indirect transition at the base - collector interface.[29] It is unfortunate that $CoSi_2$ - Si (111) is the interface for which the materials problems are under best control at present. There are kinematically allowed states for $CoSi_2$ for (100) and (110) interfaces, and for $NiSi_2$ for all 3 of these interface orientations.

Transmission Dynamics

Even in a situation where the kinematical conditions for interface transmission are satisfied, there is no easy way to estimate the transmission probability of an electron incident on the interface. For semiconductor heterostructures where the bandgap changes across the interface, but the bandstructure does not change qualitatively, the effective mass approximation is widely used, and seems to work reasonably well. For Si - MSi_2 transmission, however, the bandstructure and the

character of the wavefunctions change drastically between the two materials, and there is no reason to think that an effective mass approach would be even qualitatively correct. Mark Stiles and I have recently developed a full dynamical scattering theory for general self-consistent interface potentials.[33] The only requirement is that the interface be epitaxial, pseudomorphic to be more precise, so that there is periodicity parallel to the interface. Our methods can be applied to any pair of materials, or to more complicated multi-layer structures. The effect of the detailed atomic geometry of the interface on the electron transmission is included.

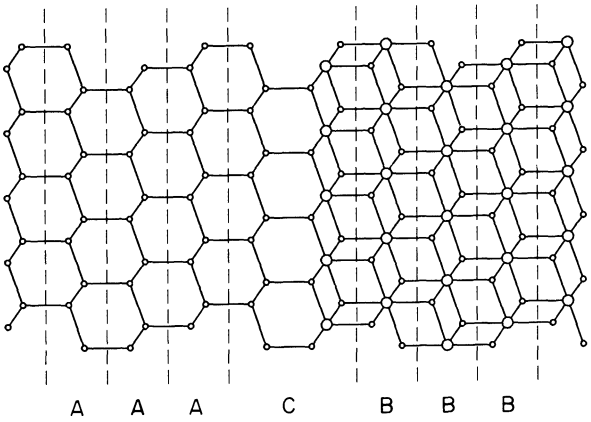

Fig. 8. Division of a Si - MSi_2 structure into layers for dynamical transmission calculations.

We deal with systems which are of infinite extent in the interface normal direction. Our method is based on dividing the system into layers, as illustrated for a 7A silicide interface structure in Fig. 8. Typically, we might have a series of identical layers of bulk material A on the left, an A-B interface layer (labeled C) in the center, and layers of material B on the right. Self-consistent potentials for each layer are obtained from several separate bulk and supercell calculations. Choosing an appropriate supercell, the potential can be made continuous across the A-C and C-B boundaries to a high degree of accuracy. Our approach is to find a set of variational wavefunctions at a specified energy E separately for each layer, with each member of the set having different values or slopes on the boundary planes. Linear combinations of the solutions in each layer may then be found which will yield value and slope continuity across all the layer boundaries.

We introduce a set of basis functions for each layer which have Bloch periodicity parallel to the layers with a selected wavevector $\mathbf{k}_{\parallel}$. We then vary their coefficients to make a functional of the trial wavefunction ϕ stationary. The functional,

$$J=\frac{1}{2}\int_{\text{cell}} d^3r\left\{\phi(\mathbf{r})^*\left[2m(\hat{H}-E)\phi(\mathbf{r})\right]+\left[2m(\hat{H}-E)\phi(\mathbf{r})\right]^*\phi(\mathbf{r})\right\}$$

$$+\frac{1}{2}\sum_X\int_{\text{IWSC}} d^2R\left\{\left[(\hat{\Lambda}+\hat{\partial}_n)\phi(\mathbf{R},z_X)\right]^*\phi(\mathbf{R},z_X)+\phi(\mathbf{R},z_X)^*\left[(\hat{\Lambda}+\hat{\partial}_n)\phi(\mathbf{R},z_X)\right]\right\}$$

$$-\sum_X\int_{\text{IWSC}} d^2R\left[t_X(\mathbf{R})^*\phi(\mathbf{R},z_X)+\phi(\mathbf{R},z_X)^*t_X(\mathbf{R})\right], \tag{10}$$

contains a volume term with Hamiltonian $\hat{H}$, and interface Wigner-Seitz cell (IWSC) boundary terms, in which $\mathbf{r}=(\mathbf{R},z_X)$, X = (left, right), $t_X(\mathbf{R})$ is an inhomogeneous term, $\hat{\partial}_n$ is the outward normal derivative, and

$$\hat{\Lambda}=\alpha\left(E_0-\frac{\partial^2}{\partial R^2}\right)^{1/2}, \tag{11}$$

where α and E_0 are arbitrary.[34] The variational principle forces the boundary value

$$b_X(\mathbf{R})=\hat{\Lambda}\phi(\mathbf{R},z_X)+\hat{\partial}_n\phi(\mathbf{R},z_X), \tag{12}$$

to converge to equal the inhomogeneous boundary term $t_X(\mathbf{R})$, and ϕ to satisfy Schrödinger's equation at energy E, in the limit of a complete basis.[33,34]

To apply the method, we expand t_X in N parallel plane waves, and find stationary solutions for the 2N t_X's formed by setting one Fourier component at a time to 1 and the rest to 0 for X = left, right. The variational Euler equation for ϕ based on J is linear, so its solution for any linear combination of these t_X's is simply the same linear combination of these solutions. We find the corresponding 2N $b_X(\mathbf{R})$, and 2N complementary boundary values

$$c_X(\mathbf{R})=\hat{\Lambda}\phi(\mathbf{R},z_X)-\hat{\partial}_n\phi(\mathbf{R},z_X). \tag{13}$$

Having found 2N solutions for each of two layers, we can find 2N solutions for a composite of the two layers by using 2N value and slope continuity conditions to constrain linear combinations those 4N solutions. For each of these combinations, we now have a new set of b's and c's, which can be used to join the next layer to this pair, etc. Unlike supercell calculations, we perform our variational calculations separately in each layer, so the basis size (and matrix dimensions) do not grow in proportion to the size of the system.

We can simplify the problem of joining many identical layers with a physically useful shortcut. Setting up the algebraic requirement that values and slopes on the two sides of a layer be identical within a factor λ, we are led to a linear eigenvalue problem whose 2N solutions are generalized Bloch states. The eigenvalues

$$\lambda=e^{-i(k_z+i\kappa)(z_L-z_R)} \tag{14}$$

give the normal Bloch wavevector k_z for propagating waves, and the growth or decay rate κ for the evanescent waves. Given the wavefunction in any layer as a linear combination of these eigenfunctions, we can trivially specify it in any other layer of a bulk-like region by taking powers of the λ's. With this approach, we construct scattering states of the A-B interface problem by finding solutions that consist only of incident, reflected, and transmitted propagating waves far from

the interface. Decaying evanescent waves must be included to satisfy matching conditions at the interface layer, and have significant amplitudes only in nearby bulk layers.

We have implemented this approach using LAPW eigenfunctions, Eqs. 6 and 7, of the bulk and supercell potentials as our basis states. We typically take two k_z values for a bulk layer, one for a supercell (where the layer may represent only half the supercell), and the lowest 1/3 to 1/2 of the band states. We test convergence by monitoring how closely b_X approaches t_X, and by comparing the dispersion relations of the propagating bulk Bloch states calculated by the layer method with those calculated directly by the LAPW method. I should stress that these are completely independent calculations. In the LAPW or any standard band method, we specify k_z and calculate an energy, while in the layer method, we specify an energy and calculate k_z.

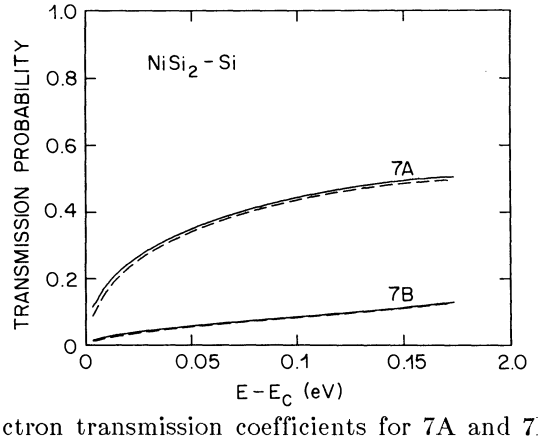

Fig. 9. Electron transmission coefficients for 7A and 7B Si - $NiSi_2$ interfaces in the vicinity of the Si conduction band minimum.

We have applied this method to the Si - $NiSi_2$ interface, and our preliminary results are shown in Fig. 9.[35] The solid and dashed curves represent electrons incident from the $NiSi_2$ or from the Si, respectively. The extent to which these curves are coincident is another convergence test, since detailed balance must come out of the scattering dynamics - it is not enforced by any symmetry in our formulation. The transmission goes to zero at the conduction band minimum. This is not too surprising, because we previously found that it goes to zero here even for a Si twist boundary. This is like a B orientation interface of Si to Si, and is a much milder perturbation of the electronic structure than that presented by the silicide. In that case, however, transmission recovered to unity (the effective mass result) within 0.1 eV.[33] Here, the transmission remains very small for the 7B interface up to 0.2eV above E_c. For the 7A interface, it is considerably larger, but the value of 0.5 near 0.2 eV is still much too small to make this a favorable case for the metal base transistor. We don't yet understand the reason for the large 7A-7B difference.

The results shown used the LDF supercell potential which I discussed when I talked about Schottky barriers in this system. This produces an error in the alignment of the Si conduction band with the $NiSi_2$ states because of the LDF band gap problem. To produce the correct alignment, we added a smoothly

varying offset potential to the supercell LDF potential (a poor man's version of the actual self-energy operator for the full interface system), but found only small changes in the transmission results.

FUTURE DIRECTIONS

There are some loose ends to be cleaned up from the work I've described. One is the $CoSi_2$ Schottky barrier. The supercell calculation we used for the 8B structure, which we believe to be the experimental structure, doesn't have any Si double layer with bulk-like coordination. We don't think the potential is well enough size-converged in this case to compare with experiment, and a further calculation with a thicker Si layer is clearly needed. It would be satisfying to have qualitative physical explanations for several of the results we already obtained, in particular the 7A-7B Schottky barrier difference and transmission probability difference for $NiSi_2$. The former is particularly tough, but we have some ideas for further analysis that may shed some light on the latter.

Control of the growth of $CoSi_2$ on Si (100) is improving, and there may soon be high-quality data available on this system. There are suggestions in the literature of 6-fold structures for the silicide (100) interfaces, based mainly on speculation. In light of our results on (111), this seems unlikely for Co at least, and we need to take a hard look at the range of possibilities that exist once quantitative data on interplanar separations is available. Structural energy and electronic structure and transmission studies should follow. We note that ballistic transmission is kinematically allowed for this interface.[20] Definitive experimental tests of our transmission probability results will certainly be welcome, and may in fact come sooner on $CoSi_2$ - Si (100) than on $NiSi_2$ - Si (111). While I know of no active program on $NiSi_2$ - Si (100), it would be interesting to establish theoretically if any structural difference between Ni and Co is expected in this case.

Looking further ahead, it would be very useful to broaden the range of materials studies. The metallic compound $CaSi_2$ has recently been shown to grow high-quality pseudomorphic interfaces on Si (111),[36] and this material should provide an interesting contrast. It has a rhombohedral crystal structure rather than a cubic fluorite structure, and the occurrence of a group II metal rather than a transition metal should produce a rather different electronic structure. Understanding this interface in the detail we understand those discussed here will considerably increase our knowledge base of well-characterized interface behavior.

Abrupt, pseudomorphic growth of elemental or compound metals on III-V's or II-VI's would provide an extremely valuable reference point for the large body of work on non-epitaxial "amorphous" metal interfaces on these semiconductors. However, the materials problems will be difficult. The systems discussed here are stable, fully-reacted two-phase "mixtures" of Si and the most stable Si-rich compound. Achieving such a situation in a phase diagram with 3 or 4 components, with structure and lattice constant matching, is a daunting challenge, which I leave to my experimental colleagues.

ACKNOWLEDGEMENT

I would like to thank Mark Stiles for permission to include our unpublished results, Fig. 9, and for constructive comments on this manuscript.

REFERENCES

1. P. Hohenberg and W. Kohn, Phys. Rev. **136**, B 864 (1964); W. Kohn and L. J. Sham, *ibid.* **140** (1965) A1133.
2. O. K. Andersen, Phys. Rev. B **12** (1975) 3060.
3. L. F. Mattheiss and D. R. Hamann, Phys. Rev. B **33**, 823 (1986).
4. R. T. Tung, J. M. Gibson, and J. M. Poate, Phys. Rev. Lett. **50**, 429 (1983).
5. K. N. Tu, Appl. Phys. Lett. **27**, 221 (1975).
6. N. W. Cheung and J. W. Mayer, Phys. Rev. Lett **46**, 671 (1981).
7. P. J. Grunthaner, F. J. Grunthaner, A. Madhukar, and J. W. Mayer, J. Vac. Sci. Technol. **19**, 649 (1981).
8. Y. J. Chang and J. L. Erskine, Phys. Rev. B **26**, 4776 (1982).
9. F. Comin, J. E. Rowe, and P. H. Citrin, Phys. Rev. Lett. **51**, 2402 (1983).
10. D. R. Hamann and L. F. Mattheiss, Phys. Rev. Lett. **54**, 2517 (1985).
11. G. V. Samsonov and I. M. Vinitskii, *Handbook of Refractory Compounds*, translated by K. Shaw (Plenum, New York, 1980), p. 131.
12. D. Cherns, G. R. Anstis, J. L. Hutchinson, and J. C. H. Spence, Philos. Mag. A **46**, 849 (1982).
13. J. M. Gibson, J. C. Bean, J. M. Poate, and R. T. Tung, Appl. Phys. Lett. **41**, 818 (1982).
14. E. Vlieg, A. E. M. J. Fischer, J. F. van der Veen, B. N. Dev, and G. Materlik, Surface Sci. **178**, 36 (1986).
15. A. E. M. J. Fischer, E. Vlieg, J. F. van der Veen, M. Clausnitzer, and G. Materlik, Phys. Rev. B **36**, 4769 (1987).
16. J. Zegenhagen, K. G. Huang, B. D. Hunt, and L. J. Schowalter, Appl. Phys. Lett. **51**, 1176 (1987).
17. E. J. van Loenen, J. W. M. Frenken, J. F. van der Veen, and S. Valeri, Phys. Rev. Lett. **54**, 827 (1985).
18. A. E. M. J. Fischer, T. Gustafsson, and J. F. van der Veen, Phys. Rev. B **37**, 6305 (1988).
19. Y. J. Chabal, D. R. Hamann, J. E. Rowe, and M. Schlüter, Phys. Rev. B **25**, 7198 (1982).
20. L. F. Mattheiss and D. R. Hamann, Phys. Rev. B. **37**, 10623, (1988).
21. D. R. Hamann, Phys. Rev. Lett. **60**, 313 (1988).
22. J. Tersoff and D. R. Hamann, Phys. Rev. B **28**, 1168 (1983).
23. P. J. van den Hoek, W. Ravenek, and E. J. Baerends, Phys. Rev. Lett. **60**, 1743 (1988).
24. R. T. Tung, Phys. Rev. Lett. **52**, 462 (1984); J. Vac. Sci. Technol. **B2**, 465 (1984).
25. R. W. Godby, M. Schlüter, and L. J. Sham, Phys. Rev. Lett. **56**, 2415 (1986).
26. J. Tersoff and D. R. Hamann, unpublished.
27. G. P. Das, P. Blöchel, N. E. Christensen, and O. K. Andersen, to be published; Also see these proceedings, I. P. Batra, Editor.
28. M. D. Stiles and D. R. Hamann, to be published.
29. A. F. J. Levi, R. T. Tung, J. L. Batstone, and M. Anzlowar, Proc. Mat. Res. Soc. Symp. Proc. **107**, 259 (1988).
30. Y. J. Chang and J. L Erskine, Phys. Rev. B **26**, 7031 (1982).
31. G. Gewinner, C. Pirri, J. C. Peruchetti, D. Bolmont, J. Derrien, and P. Thiry, Phys. Rev. B. **38**, 1879 (1988).
32. A. F. J. Levi, private communication.
33. M. D. Stiles and D. R. Hamann, Phys. Rev. B **38**, 2021 (1988).
34. G. Wachutka, Phys. Rev. B **34**, 8512 (1986).

35. M. D. Stiles and D. R. Hamann, to be published.
36. J. F. Morar and M. Witmer, Phys. Rev. B **37**, 2618 (1988).

CALCULATED ELECTRONIC STRUCTURES AND SCHOTTKY BARRIER HEIGHTS OF (111) $NiSi_2$/Si A- AND B-TYPE INTERFACES

G .P. Das*, P. Blöchl, N. E. Christensen, and O. K. Andersen.
Max-Planck-Institut für Festkörperforschung
D–7000 Stuttgart 80, Federal Republic of Germany

INTRODUCTION

In recent years it has been proved possible to predict the valence-band offsets of lattice-matched semiconductor heterojunctions[1,2] to an accuracy of about 0.1 eV using density functional theory in the local approximation (LDA). We have investigated whether, for well-characterised metal-semiconductor interfaces, the Schottky-barrier heights can be calculated with similar accuracy. In this paper we report on our findings.

In the density functional theory, the one–electron energies obtained from the Kohn–Sham equation[3] do in principle not relate to real electronic excitations. Only one energy, namely that of the highest occupied state has physical significance: it is the ionization energy. This means that the Fermi level (E_F) of a metal and the valence band maximum (E_v) of a semiconductor can be obtained from self-consistent one-electron calculations using the density functional for the ground state. Similarly, the (p-type) Schottky-barrier height,

$$\Phi = E_F - E_v , \qquad (1)$$

of a metal in contact with a semiconductor can be calculated in this way because the electron density determines the dipole shift across the interface. Now, the *exact* density functional, and thus the effective exchange-correlation potential in the Kohn-Sham equation, are not known, and therefore we have to use the LDA. More than ten years experience has shown that the LDA yields surprisingly accurate total energies and electron densities and, as mentioned above, this approximation was recently found to yield accurate valence-band offsets at semiconductor junctions too. We shall therefore try the LDA out for the calculation of Schottky-barrier heights.

The (111) interfaces between Si and the silicides $NiSi_2$ and $CoSi_2$ represent probably the most perfect and well defined semiconductor–metal contacts. The bulk constituents have almost the same lattice constants, and it is possible to grow junctions with atomically abrupt interfaces. Hence a theoretical treatment at a realistic level of sophistication should be possible. (111) $NiSi_2$/Si is particularly intersting because two distinct interface structures, called A– and B–type have been observed. These two structures were found[4] to have different Schottky barrier heights, 0.52 and 0.38 eV, repectively.

Model theories,[5,6,7] which assume that the Fermi level of the metal adjusts to a particular midgap level of the semiconductor when the Schottky contact is formed, have been useful for many theoretical predictions. However, since these theories apply parameters derived exclusively from the bulk properties of the two constituents forming the junction, they cannot describe effects that are caused by interface specific electronic properties. They cannot, therefore, predict a difference between the A– and B– offsets in (111) $NiSi_2$/Si. One purpose of our work[8] is to use a theoretical treatment that avoids such simplifications, and which therefore would allow us to estimate this offset difference. Therefore we apply parameter-free LDA calculations which include properly the structure of the interface. Another purpose of this study is to examine the bonding properties of the two $NiSi_2$/Si interfaces.

CRYSTAL STRUCTURE

Nickel disilicide crystallizes in the fluorite structure which can be described as a simple cubic arrangement of Si atoms with one Ni atom in each alternate cube. As a consequence, the Si atoms are tetrahedrally coordinated with Ni atoms, while the Ni atoms are octahedrally coordinated with Si atoms. At the (111) interface with Si the dangling bonds of the Si surface are saturated by the Si atoms of the disilicide so that the coordination number of the interfacial Ni atom is reduced to 7 from the bulk value of 8.[9] Two different orientations, called A– and B–type, have been observed;[4] they are related by a 180° rotation about the interface normal, and they differ only in second-nearest neighbour coordinations. The difference between these two structures are clearly seen in Fig 1. The lattice constant of bulk $NiSi_2$ is 0.4 per cent smaller than that of Si. Furthermore, X–ray standing-wave data[10] for interface relaxations suggest a contraction of $\sim$ 0.1 Å within the limits of experimental error.

In our calculations, the small lattice mismatch between Si and $NiSi_2$ was neglected and the Si bulk lattice constant was used. Further, except in one calculation, the Si–Si bond lengths across the interface were not relaxed and the

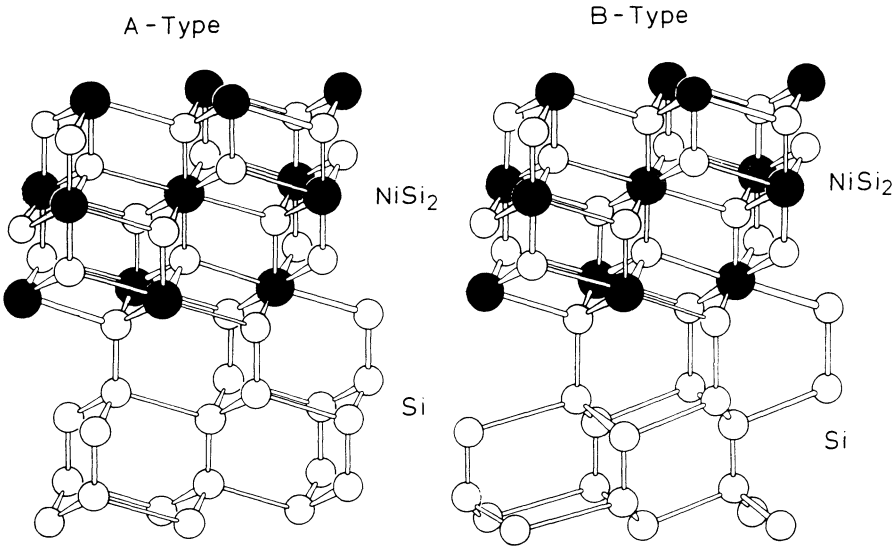

Fig. 1. The structures of the (111) $NiSi_2$/Si A and B type interfaces. The filled circles denote Ni atoms, the open cirlces are the Si atoms.

interface distance was taken to be the value calculated on the basis of the bulk bond length.

METHOD OF CALCULATION

The self–consistent scalar relativistic band structure calculations were performed with the LMTO method[11,12] and the LDA parametrization of Barth and Hedin.[13] Our calculation is based on supercell geometry with two identical interfaces buried between repeating slabs of m double layers of Si and n triple layers of silicide whereby the formula unit becomes $(NiSi_2)_n(Si_2)_m$. To ensure size convergence of the results, calculations were performed for various cell–sizes (n+m), where n varies from 2 to 8 and m varies from 3 to 9.

In most of the calculations discussed here, the LMTO method was applied within the atomic spheres approximation (ASA). In the ASA, the space is divided into volume filling, and hence overlapping, atomic spheres centered at the atoms *and* at interstitial sites. Inside these spheres the charge density and potential are approximated by their spherical averages. The use of interstitial, so-called *empty* (E), spheres allows relatively open structures, like the fluorite and the diamond structures, to be treated in the ASA. The LMTO-ASA method is highly efficient and physically transparent, especially well suited for

self–consistent calculations for large systems, as are the supercells under consideration. The ASA has recently been used successfully to estimate band–offsets for a large number of semiconductor heterojunctions.[2]

The ASA, however, neglects the polarization inside the atomic–spheres and, in order to examine the influence hereof on the Schottky barrier heights, we performed two LMTO calculation without any shape approximation, and thus went to selfconsistency in the *full potential.*[12,14] The only approximation is then due to the finite size of the LMTO basis set, and the spheres are used merely to define the augmentation of the LMTOs. In order to evaluate the full charge density from a band calculation, and in order to evaluate the matrix elements of the non-spherical part of the Hamiltonian, each LMTO is described as a smooth (pseudo) part plus a remainder, which is localized inside the spheres. The pseudo LMTO is tabulated on a regular mesh in real space and the latter is given by one–center expansions. The technique for representing the charge density without shape approximations is also used to produce contour plots of valence electron densities. Such plots help us in analysing the nature of chemical bonding.

At both levels of sophistication, we use the tight–binding (TB) representation of the LMTO basis. The *s*–, *p*–, and *d*–orbitals were included for all the atoms (i.e. 9 orbitals per atom) and the *s*–, and *p*–orbitals were included on the interstitial sites (4 orbitals per empty sphere). The *d*–partial waves in the empty spheres were included in the three–center integrals and in the spherically averaged charge density. This approximation does *not* affect our final result.[15]

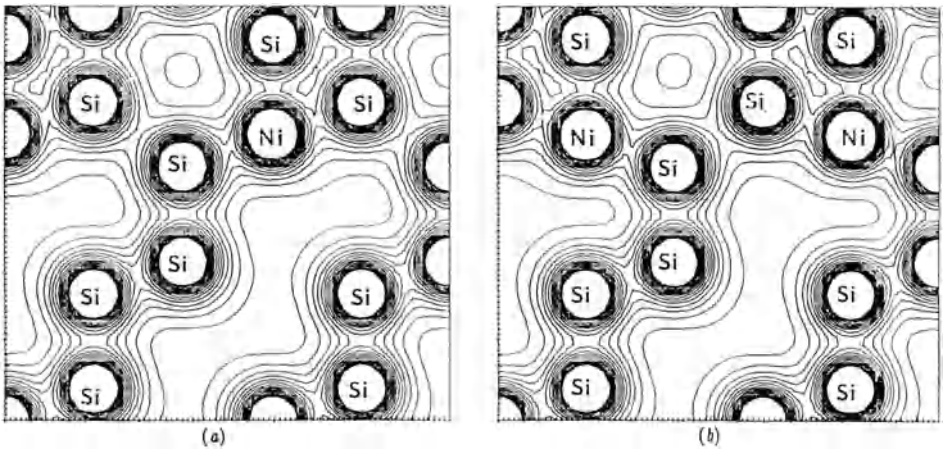

Fig. 2. Contour plots in the $(1\bar{1}0)$ plane of superposed atomic Hartree potentials for (a) type–A– and (b) type–B–type interfaces.

The Brillouin–zone integrations were performed with the tetrahedron method, using its latest version which avoids misweighting and corrects errors due to the linear approximation of the bands inside each tetrahedron.[16] The k–points were chosen on an equispaced mesh. In supercell calculations this was obtained by typically 8 divisions of each of the reciprocal-lattice vectors in the (111) plane, and one or two divisions of the reciprocal-lattice vector in the [111] direction. A specific mesh we shall denote (8,8,2), for example.

In order that the ASA works well, we must at the onset of a calculation choose the sizes of the atomic spheres, as well as the numbers, positions, and sizes of the interstitial spheres, in such a way that the perturbation introduced by spherical averaging the potential is small, and such that the overlap between the space-filling spheres is less than 15 per cent. This overlap is defined for a pair of neighboring spheres as the sum of the radii minus the distance, divided by the distance, i.e. $(s_1+s_2-d)/d$. To guide us in the choice of relative sphere sizes we generate contour plots of the atomic Hartree potentials superposed on the real structure. It is our experience that such plots give the necessary and sufficient information, and they are shown in Fig. 2 for the (111) $NiSi_2$/Si A– and B–type interfaces. On the basis of these plots, we choose for the A–type a bcc sphere-packing with equal sizes for *all* atomic and interstitial spheres ($s = 2.526$ a_0). The Snoopy–shaped interstice at the A–interface we thus describe by two neighboring (111) layers of E–spheres. For the B–type, we describe the duck-shaped interstice at the interface by condensing the two layers of E–spheres used for the A–type into a single layer of large and small interstices ($s_1/s_2 = 1.57$); their z–coordinate lies mid–way between the two silicon atoms at the interface. Including the E–spheres, the formula unit for our supercells is $(NiSi_2E)_nE(Si_2E_2)_m$.

ELECTRONIC STRUCTURE OF $NiSi_2$/Si INTERFACES

The basic features of the electronic structure in the interface region are seen in the layer–projected density-of-states functions (LDOSs). The LDOSs for type–A interface, calculated using the (8+6)–supercell, is shown in Fig. 3, and the definition of the various layers is given on the left-hand side of Fig. 4c. The LDOSs for the type–B interface differ only slightly, and the following discussion applies quantitatively to the A–type and qualitatively to both interface types.

For the 3rd and 4th $NiSi_2$-layers away from the interface, and for the 3rd Si_2-layer, the LDOSs are bulk-like.[17] The 3rd Si_2-LDOS thus clearly exhibits the band gap, whereas the 1st and 2nd Si_2–LDOS show metallic character due to the presence of metal–induced gap states. Similarly, the 3rd and 4th $NiSi_2$-LDOSs exhibit the well-known splitting-off of Ni-$d(t_{2g})$ to Si–sp^3 bonding and anti-

bonding peaks from the main Ni–*d* peak. These bonds can be clearly seen in the charge-density plot for bulk $NiSi_2$ in Fig. 4b. The bonding peak has predominantly Ni-character and is located around 5.5 eV below E_F. The anti-bonding peak has mostly Si-character and extends from slightly below the Fermi level upwards.

Turning now to the 1st $NiSi_2$-layer at the interface, we see that the bonding and anti-bonding peaks have lost weight, as was expected from the reduced Ni-coordination, and that new weight appears under– and at the high-energy side of the main *d*–peak. In addition, the whole LDOS of the interface (i.e. 1st) $NiSi_2$ layer is, crudely speaking, shifted up by $\sim$ 1 eV with respect to the bulk–like layers, an effect which can be attributed to the variation of the electrostatic potential near the interface. Around 0.7 eV *below* E_F there is a van Hove singularity from an interface band which has semi dangling-bond character. The character is mostly Ni $d(3z^2-1)$, with z perpendicular to the interface, it is dangling into the nearest interstice of the 1st Si_2-layer (i.e. into Snoopy's head), and anti-bonding with respect to the nearest Si-atom in the 2nd $NiSi_2$-layer. Since this state is occupied, it slightly weakens the bond in $NiSi_2$ between a Ni atom in the 1st layer and its nearest Si atom in the 2nd layer. This may be seen by comparison of the charge-density plots for $NiSi_2$ and $NiSi_2$/Si in Figs. 4b and 4c. The two dimensional projected band structure (Fig. 5) shows this interface

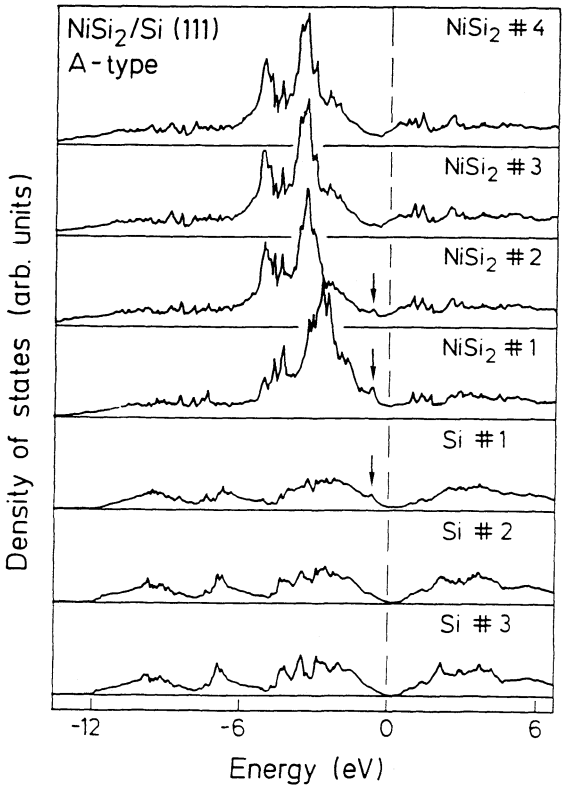

Fig. 3. Layer-projected densities-of-states for type–A interface. Definition and numbering of the layers are given in Fig. 4c. The energy is is relative to E_F. The arrows indicate the van Hove singularity, (discussed in the text). The calculation was made for the (8+6)- supercell and **k**–mesh (8,8,2).

band in the common gap of bulk $NiSi_2$ and bulk Si near the symmetry-line *MK*. The band is half full and should be observable in photoemission. In B–type $NiSi_2$/Si the interface band has a slightly lower energy than in A–type and gives rise to an even more pronounced singularity in the LDOS for the 1st $NiSi_2$ layer. In this case the state is dangling into a smaller interstice (the ducks beak; see

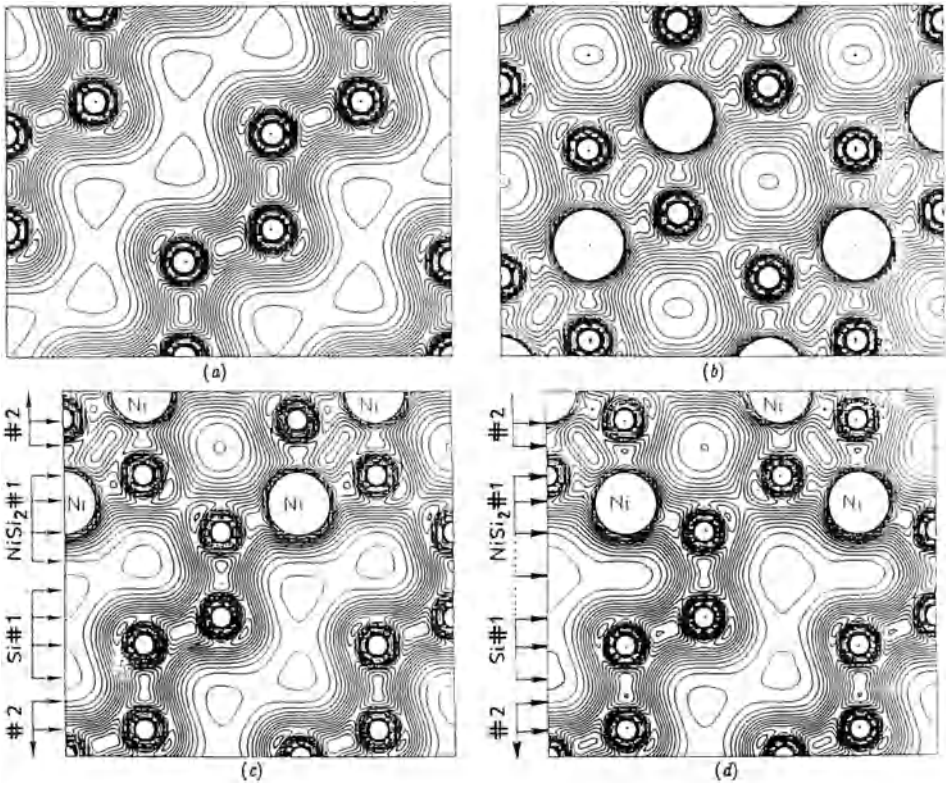

Fig. 4. Valence electron density in the $(1\bar{1}0)$–plane for (*a*) bulk Si, (*b*) bulk $NiSi_2$, (*c*) the A–interface, and (*d*) the B–interface. The charge densities were obtained by solving the wave equation for potentials self–consistent in the ASA The lowest contour-value in the Si– and in the $NiSi_2$ interstices is 0.005 e/a_0^3 (a_0 being the Bohr radius). The contour-step is 0.005 e/a_0^3. The highest contour-value in the Si-Si bond is 0.075 e/a_0^3 and that in the Ni–Si bond in $NiSi_2$ is 0.070 e/a_0^3. The cigar–shaped depletion region enclosed by the Si and Ni in $NiSi_2$ has the contour value 0.045 e/a_0^3 For the A– and B–interfaces the positions of the layers of atoms– and interstices and their grouping into $NiSi_2$– and Si-layers, as used in the projected densities-of-states and frozen-potential constructions (but not in the dipole approach), are indicated. The A–interface calculation was done for the (2+3)-supercell and **k**–mesh (8,8,2). The B–interface calculation was performed for supercell (5+3) and mesh (8,8,1).

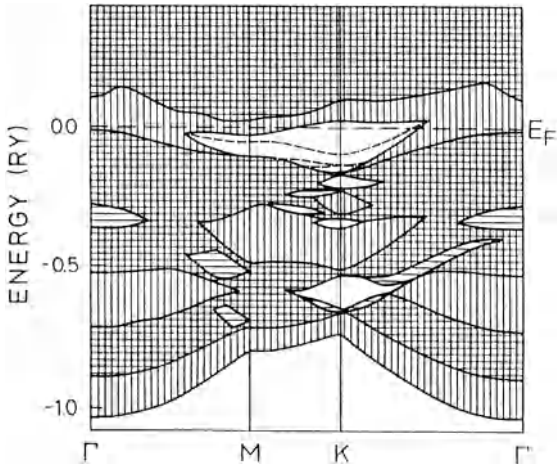

Fig. 5. Two dimensional band structure of the A–interface. The interface bands (dashed curves) were calculated using the (8+6) - supercell. The bulk band structures of $NiSi_2$ (vertically hatched) and Si (horizontally hatched) were calculated using the potentials from the bulk-like layers of the supercell.

Fig. 4d) and there is some bonding interaction across the beak with the second Si atom of the 1st Si layer.

Whereas the bonding between Ni-*d* and Si-sp^3 is lost across the interface, a Si–Si bond is being formed; this holds for the A– as well as for the B–type interface. This bond is almost as strong as in bulk Si,[18] and this is clearly seen in Figs. 4*a–d* by comparison of the valence–electron density contours for the bulk materials with those for the interfaces.

Recently, an interface structure in which the atoms at the Si-surface are in register with the transition atoms, rather than with the silicon atoms of the disilicide, was predicted to be the stable one for (111) $CoSi_2$/Si.[18,19] For this 8–fold coordinated structure we, of course, found no weakening of the bonding and anti-bonding Ni-Si peaks at the interface and, instead of Si-Si bonds, we found half-full dangling bonds on the Si-atoms of $NiSi_2$. This supports the picture given by van den Hoek et al.[19] The main reason why for the $CoSi_2$/Si interface this structure is the stable one is that, with one electron less, the dangling bonds are not occupied.

SCHOTTKY BARRIER HEIGHTS

In order to derive the Schottky-barrier height we need to know E_V and E_F. The value of E_V could, in principle, be derived from the supercell band structure; but it is complicated to extract E_V herefrom, because the states at the valence-band maximum are masked by the metal–induced gap states extending deep into the semiconductor. This method would also require extremely large supercells, so large that the states associated with the central Si– and $NiSi_2$-layers satisfy bulk

boundary conditions. We circumvent this difficulty by making use of the fact that the charge density, being the sum over the squares of all occupied states, converges much faster with the size of the cell than does some particular states, such as those at the top of the valence band of Si or those at the Fermi surface of $NiSi_2$. We thus only use the supercell calculation to generate the charge density $\rho(\mathbf{r})$ or potential $V(\mathbf{r})$ near the interface; E_F and E_v we calculate using the proper bulk boundary conditions. Two different approaches have been employed:

In one, we first perform a self-consistent supercell calculation in order to generate the one-electron potential. From this we cut bulk–like $NiSi_2$ and Si potentials from the central layers. These two potentials, which have the proper relative dipole shift, are then exported into respective bulk band calculations, which finally yield E_F and E_v. The value of the Schottky barrier height Φ follows from (1). This is the so-called *frozen-potential approach.*[20,2]

In the other – maybe more pedagogical – approach we monitor the formation of the interface dipole:

$$D \equiv 8\pi \int_{-\infty}^{+\infty} z\, \Delta\rho(z)\, dz\,, \tag{2}$$

where $\Delta\rho(z)$ is the average over the interface-induced charge density in a two-dimensional cell at the distance z from the interface. (Here, and in the following we use atomic Rydberg units). In practice, we obtain the induced charge density $\Delta\rho$ from the difference between the self-consistent charge density ρ calculated for a supercell and those calculated for the two bulk systems. The supercell, of course, has to be large enough, so that the z–integral converges. This *dipole approach* is conceptually simple, but it requires the *choice of a reference offset* Φ^o, *and a reference charge density* $\rho^o(z)$ *consistent with* Φ^o. In terms of these we then have

$$\Delta\rho(z) = \rho(z) - \rho^o(z)\,, \tag{3}$$

and for the Schottky barrier height

$$\Phi = \Phi^o - D\,. \tag{4}$$

With the signs chosen and ρ positive for electrons, the metal is at the negative–z side and the semiconductor at the positive-z side. Although the dipole approach is conceptually pleasing because it is expressed in terms of *interface-induced changes*, the choice of reference has caused a lot of confusion in the past and we shall therefore take some care in explaining it.

The reference offset Φ^o is *arbitrary*, and its choice is a matter of convenience and physical intuition. In a simplified theory one would, for instance, like to choose it in such away that the induced charge density is so small that D can be evaluated by linear-response theory.[5,6,7,21,22] To help the intuition one may express Φ^o as the difference between the two bulk levels E_F^o and E_V^o, with some choice of the absolute position of the one-electron potential and –levels in an infinite bulk crystal,[23] plus a chosen reference dipole D^o, i.e.:

$$\Phi^o \equiv E_F^o - E_V^o - D^o. \tag{5}$$

Usually one would choose Φ^o to be the difference between two bulk levels, e.g. D^o is some constant, in which case Φ^o is independent of the interface geometry.

The reference density ρ^o must go to the respective bulk densities for $z \to \pm\infty$. Near the interface, it must be consistent with the chosen Φ^o and this will imply that ρ^o may depend on the interface geometry. By comparison of the charge-density contours in Figs. *4a* and *b* with those in Fig. *4c*, we realize that the charge density calculated for the $NiSi_2$/Si A–interface is close to what would be obtained by cutting and joining the two bulk densities along a surface specified as . E Si Ni Si | E E Si Si . This is Hamann's "scissor and paste joining of the bulk densities".[18] As the basis for our reference density $\rho^o(z)$ we therefore choose to use the bulk densities cut–and–joined. Since we only need the z–dependent densities, the cut-and-join prescription can also be used for the 180°-turned B–interface and, in fact, quite generally. This cut-and-join charge density cannot be used directly as a reference charge density because it usually sets up an electric field for $z \to -\infty$, or for $z \to +\infty$. Even if this is not the case, so that far away from the interface the potential from the cut-and-join charge density becomes periodic with the shape of the bulk metal potential when $z \to -\infty$, and with the shape of the bulk semiconductor potential when $z \to +\infty$, the line-up of these two asymptotic potentials is not in general consistent with the choice of Φ^o. Therefore, before joining the two truncated semi-infinite bulk densities, we must add to each of them a fictitious surface charge density of such a magnitude that the electric field vanishes far away in the vacuum, and at such a z-position that, with the potential far away in the vaccum taken as zero, the bulk potentials have that line-up which yields the assumed reference offset. In conclusion, we shall choose the reference charge density as the cut-and-join density, plus the fictitious surface densities which make the potential far away from the interface periodic with the chosen line-up.

The dipole– and the frozen-potential approaches yield, of course, identical results, and both methods require more or less the same amount of computation, viz. a self-consistent supercell calculation in conjunction with two (self-consistent

or not) bulk calculations. We shall now use the dipole approach in connection with the ASA to calculate the Schottky barriers in A–type and B–type (111) $NiSi_2/Si$ interfaces. The frozen-potential approach will be used in the following section, both in the ASA and, with a slight modification, for the full potential.

In the ASA, the long-range (i.e. inter-sphere) electrostatics is described by point charges placed at the sphere centers, and the absolute zero of energy and potential in an infinite crystal is the average of the periodic electrostatic potential set up by these point charges. With E_F^o and E_V^o in (5) on this ASA scale, the choice

$$D^o \equiv 0 \tag{6}$$

has been used sucessfully as a zeroth-order model for band offsets at semiconductor heterojunctions.[2,20,22] This is a convenient choice also for the reference offset for the $NiSi_2/Si$ interfaces considered in the present paper. On the ASA scale, the position of Fermi level in bulk $NiSi_2$ is $E_F^o = 1.087$ eV , and the position of the valence-band maximum in bulk Si is $E_V^o = -0.786$ eV . Our *reference offset* is thus $\Phi^o = 1.87$ eV .[15] This is independent of the interface orientation and structure. The *reference charge density* is partly given by the bulk values of the point charges which are, for bulk $NiSi_2$, $Q_{Ni}^o = 0.440$ electrons, $Q_{Si}^o = -0.812$ electrons, and $Q_E^o = -2Q_{Si}^o - Q_{Ni}^o = 1.183$ electrons. For bulk Si the sphere charges are $Q_{Si}^o = -Q_E^o = -0.762$ electrons. These bulk charges are, of course, also independent of the interface. All the bulk values are listed in Table 1. Now we need to determine, for each truncated crystal of point-charges, the surface-specific fictitious plane of point charges.

Given the interface orientation, we can, for the infinite point-charge crystal, form the planar averaged electrostatic potential $V(z)$. This is a piece-wise linear function whose slope changes by the amount

$$\Delta V'(z) = -\frac{8\pi}{A}\sum Q(z) \tag{7}$$

at the planes $z = z_i$ which contain the point charges. The sum is over the point charges in the plane and in the two-dimensional cell, which has the area A . In the present case of point charges on a bcc lattice and a (111)-interface there is only one point-charge per two-dimensional cell so that $A = 12.768$ Å^2 and the spacing of the planes is $c = 0.784$ Å $[cA = (4\pi/3)s^3]$. In this case the one-dimensional Poissons equation (7) reduces to

$$-V(z_{i-1}) + 2V(z_i) - V(z_{i+1}) = \frac{8\pi c}{A}Q(z_i)\ , \text{ with } \frac{8\pi c}{A} \approx 0.81 \text{ a.u..} \tag{8}$$

The values at the planes of the bulk point-charge potentials $V^o(z_i)$ are given at the bottom of Table 1 on the ASA scale, where their average over a period in the z–direction is zero. If now the crystal is truncated, this zig-zag potential will continue in the vacuum as a straight line, which usually (polar surface) has finite slope. It is in order to bend this potential over, such that it takes the constant value zero in the vacuum, that we must add a plane of fictitious point charges before joining the semi-infinite crystal with its partner to form the reference charge density. With the above-mentioned definition of the interface, i.e. . E Si Ni Si | E E Si Si . , we must add a plane of fictitious point charges of magnitude $\frac{1}{2}Q^o_E = 0.592$ electrons to the truncated $NiSi_2$ crystal at the distance $\frac{1}{2}c\,(-Q^o_{Si})/Q^o_E = 0.343\ a_o$ outside the last Si–plane. To the truncated Si crystal, we must add a plane of fictitious charges of magnitude $Q^o_{Si} = -0.762$ electrons half a sub-layer distance, i.e. $0.5c$, outside the last E-plane. The joining of the two semi-infinite charge densities prepared in this way form our reference density and the superposition of the two point-charge potentials form the reference potential. These one-dimensional references are the same for the type A– and the type B–interfaces.

We now perform a selfconsistent supercell calculation to generate the properly screened charges for the interface. For the A-interface, the charge rearrangement $\Delta Q(z)$ with respect to the reference, and the corresponding solution $\Delta V(z)$ of the one-dimensional Poissons equation are shown in Table 2, as well as in Fig. 6b. The electron transfer is from the $NiSi_2$–side to the Si-side, which may seem natural, because for the reference E^o_F was an eV above the top of the Si gap. It is striking that this transfer is essentially limited to the 5 sub-layers

Tab. 1. Reference offset ($\Phi^0 = E_F{}^0 - E_v{}^0 = 1.87eV$) and sphere charges ($Q^0$) for bulk Si and bulk $NiSi_2$. Q^0 is the number of electrons minus protons in each sphere. The values of the resulting planar averaged point-charge potentials (V^0), as well as $E_v{}^0$ for Si and $E_F{}^0$ for $NiSi_2$ are in eV. s-, p- and d-orbitals are included in the basis set of our calculation. The interstitial (E) sphere d-orbitals are folded down as described in the text.

	Si		*$NiSi_2$*		
	$E_v{}^0 = -0.786$		$E_F{}^0 = 1.087$		
Sphere	*Si*	*E*	*Ni*	*Si*	*E*
Q^0	-0.762	0.762	0.440	-0.812	1.183
V^0	-4.405	4.405	0.199	-2.346	4.493

Tab. 2. Induced (supercell minus reference) charges (number of electrons) $\Delta Q(z_i)$ and potentials $\Delta V(z_i)$ [eV] of $NiSi_2/Si$ A- and B-type interfaces (see text for details). z_i is the distance from interface in units of c=0.784Å. The rows F_s and F_m refer to the fictitious surface charge positions of the truncated semiconductor and metal respectively.

	A-type			B-type		
	z_i	$\Delta Q(z_i)$	$\Delta V(z_i)$	z_i	$\Delta Q(z_i)$	$\Delta V(z_i)$
E	12.5	-0.001	0.000	12.5	0.000	0.000
Si	11.5	0.001	0.011	11.5	0.000	-0.003
Si	10.5	0.000	0.011	10.5	-0.001	-0.001
E	9.5	-0.001	0.007	9.5	0.001	0.009
E	8.5	0.000	0.003	8.5	0.001	0.006
Si	7.5	0.000	0.003	7.5	-0.003	-0.011
Si	6.5	-0.002	0.001	6.5	-0.001	0.003
E	5.5	0.002	0.020	5.5	0.007	0.030
E	4.5	0.001	0.015	4.5	0.015	-0.025
Si	3.5	-0.016	-0.004	3.5	-0.027	-0.242
Si	2.5	-0.067	0.158	2.5	-0.101	-0.162
E	1.5	0.021	1.070	1.5	-0.762	1.041
E_2	-	-	-	1.0	1.695	5.872
E	0.5	0.120	1.751	0.5	-0.762	1.291
F_s	0.0	0.762	1.426	0.0	0.762	0.939
F_m	-0.157	-0.592	-0.005	-0.157	-0.592	-0.500
Si	-0.5	-0.098	-0.876	-0.5	-0.128	-1.388
Ni	-1.5	-0.174	-2.325	-1.5	-0.168	-2.550
Si	-2.5	0.022	-1.847	-2.5	0.050	-1.842
E	-3.5	0.021	-1.618	-3.5	0.021	-1.684
Si	-4.5	0.009	-1.627	-4.5	0.005	-1.756
Ni	-5.5	-0.008	-1.740	-5.5	-0.009	-1.886
Si	-6.5	-0.005	-1.762	-6.5	-0.005	-1.916
E	-7.5	0.006	-1.730	-7.5	0.006	-1.890
Si	-8.5	-0.003	-1.769	-8.5	-0.002	-1.929
Ni	-9.5	-0.002	-1.781	-9.5	-0.002	-1.943
Si	-10.5	0.001	-1.770	-10.5	0.001	-1.935
E	-11.5	0.001	-1.771	-11.5	0.001	-1.938
Si	-12.5	-0.001	-1.783	-12.5	-0.001	-1.951
Ni	-13.5	0.000	-1.783	-13.5	-0.000	-1.951
Si	-14.5	0.000	-1.781	-14.5	0.000	-1.951
E	-15.5	0.000	-1.782	-15.5	0.000	-1.949

Ni Si | E E Si and that the transfer is usually less than 0.1 electron per sphere. Most of the transfer, in fact, occurs to the first E–sublayer, a layer which at the left-hand side of Fig. 4c and in Fig. 3 we even counted to the $NiSi_2$-side. The induced point-charge potential in Fig. 6b is seen to overshoot its asymptotic value, the dipole D , by a fairly large amount. This was also found in previous model studies.[24,22] For the dipole,[15]

$$D = V(\infty) - V(-\infty) = \frac{8\pi c}{A} \sum_i i\, Q(z_i) , \qquad (9)$$

we find the value D = 1.78 eV which is a much larger correction to the ASA reference offset than previously found for the lattice-matched semiconductor interfaces.[2,20,22] For the value of the Schottky barrier height at the A–interface we thus find: $\Phi = 1.87 - 1.78$ eV $= 0.09$ eV, which is 0.4 eV too low compared with experiment! We shall return to this fact, but first consider the B–interface.

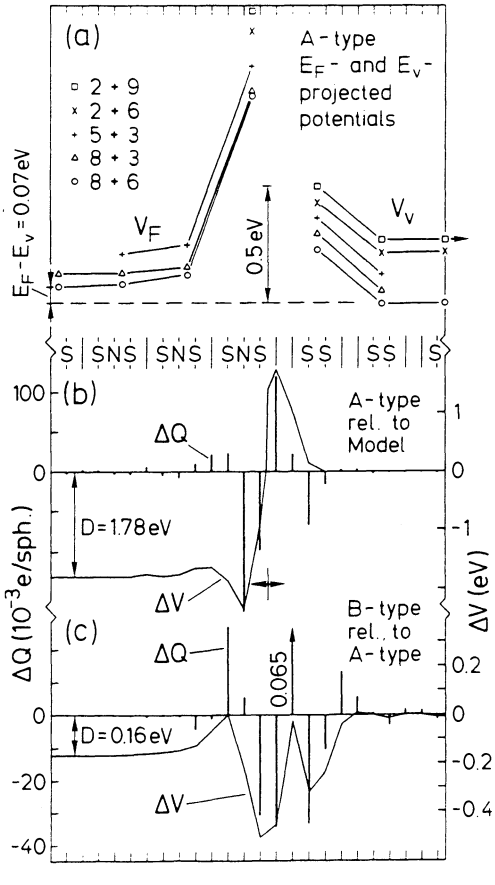

Fig. 6. Potentials and sphere charges as functions of z perpendicular to the interface. Layers of Si– and Ni–atoms are labelled respectively by S and N, and layers of interstices (E) are unlabelled. The (8,8,2) **k**-mesh was used. (*a*): Results of frozen-potential calculations for various supercells (n+m) as explained in the text. (*b*): Charges and potential calculated for the A–type (8+6) – supercell relative to those of the reference as explained in the text. The fictitious charges of the reference are not shown. The numerical values are given in Table 2 (*c*): Charges and potentials calculated for the B–type (8+6) - supercell minus those of the A–type. The charge of the double E–layer at the B-interface has been distributed onto the two E–layers of the A–interface, conserving the total charge and dipole moment.

In Fig. 6c we show the difference between the charges calculated self-consistently using A– and B–type supercells of the same size and the solution of the one-dimensional Poissons equation for this difference. The differences in charges between A and B merely amount to some hundreths of an electron per sphere (see Table 2), but they *oscillate* considerably and extend *throughout* the 1st $NiSi_2$– and Si_2-layers. This is consistent with the fact that the A– and B–interfaces only differ in the second-nearest atom coordination. The B minus A electron transfer most important for the dipole difference may even be from the Si atom in the 2nd $NiSi_2$–layer (see Figs. 4c and 4d) closest to the interface, and to the interstitial region at the interface. This would at least be consistent with the change of the interface state discussed in the previous section. The role played by this interface state for the Schottky-barrier difference between the A– and B–type is, however, not completely clear. The dipole is seen to be such as to make Φ *lower* by 0.16 eV for the B–type. This is in good agreement with the experimentally observed lowering of 0.14 eV.[25]

CORRECTIONS AND DISCUSSION OF ACCURACY

Due to the ~ 0.4 eV discrepancy found with the experimental Schottky-barrier heights, it is important to discuss the accuracy of our calculations. In order to study the cell-size convergence we made use of the frozen-potential approach described in the previous section. Application of the frozen-potential procedure, not only to the bulk-like layers but to each layer, allows us to monitor the variation across the supercell. The resulting projections of the potential, V_F for the $NiSi_2$-side and V_V for the Si-side, are shown in Fig. 6a for the A–interface and five different supercells. For clarity, the potential profiles of different supercells are displaced relative to each other. The estimate of Φ for the (8+6)-cell is seen to be 0.07 eV. Considering the fact that the frozen-potential approach needs averaging over 4 sublayers (see Fig 4) and therefore is less rapidly convergent with the size of the supercell than the dipole approach, this result is in perfect agreement with the 0.09 eV found from the dipole approach. The results of the frozen-potential approach obtained with the (8+3)- and (5+3)-cells are seen from Fig. 6a to be very similar. For the B-interface and the (8+6)-cell we find $\Phi = -0.08$ eV, a value which is also consistent with the 0.16 eV lowering found previously.

Not only the convergence with the size of the supercell, but also with the width of the **k**-mesh, must be watched in order to include properly the contributions of the Fermi-surface states to the dipole. We use the new, full-Brillouin-zone tetrahedron method[16] and, from selfconsistent calculations for the (5+3)-

supercell and for five different meshes having from 5 to 22 sub-divisions of the two primitive reciprocal lattice vectors, we extrapolate Φ to zero mesh-width (Fig. 7). Our 'corrected' estimates for E_F–E_v are now 0.16 eV for the A- and 0.00 eV for the B-interface.

A final source of numerical error is our use of the ASA which, for instance, neglects the dipole-contribution from each sphere. We have performed full-potential calculations[14] for (2+3)– and (8+6)-cells of the type–A interface. With the plane-wave expansions used in our full-potential method it is not practical to

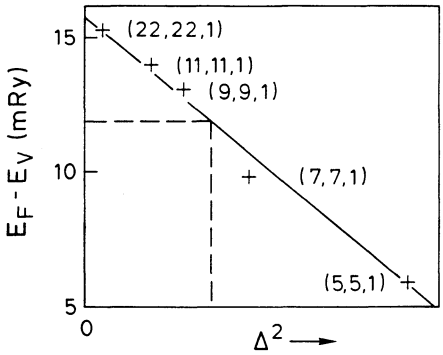

Fig. 7. **k**–mesh convergence plot : $(E_F - E_v)$ vs. Δ^2, where Δ is the width of **k**–mesh in the **k** || plane in arbitrary units. The dashed lines indicate our choice of 8 x 8 divisions of the reciprocal lattice vectors in the interface plane. Extrapolation to $\Delta^2 = 0$ yields an increase of $(E_F - E_v)$ by ≈ 0.05 eV

extract the full potential of a bulk–like cell from the supercell as was described previously. Instead, we monitor the value of the potential v_i (after subtracting the diverging nuclear part) at the centre of each atom across the interface. From selfconsistent full-potential bulk calculations we can then obtain $E_F^o - v_i^o$ and $E_v - v_i^o$, and the quantities $E_F^o - v_i^o + v_i$ and $E_v^o - v_i^o + v_i$ then form sublayer-projected Fermi-levels and valence-band maxima whose difference for the centers of the supercell gives the full-potential Φ. In order to treat the atoms in the supercell and the bulk in the same fashion (i.e. same **k**–mesh), we have described the bulk materials also in the hexagonal unit cell. The overall features of the full, frozen-potential plots resemble the ASA plots of Fig. 6a. For the

(2+3)–cell we find $\Phi = 0.4$ eV , which, however is as unconverged with respect to the size of the supercell as the similar ASA results. Like in the ASA, the (8+6)–cell gives a converged result which with the full potential is $\Phi = 0.15 \pm 0.05$ eV . The error bars reflect our difficulties in obtaining selfconsistency for this large cell. This number should be compared to the corresponding ASA estimates $\Phi = 0.07$ eV (frozen potential approach) or $\Phi = 0.09$ eV (dipole approach). Including now the 0.05 eV-correction for the (8,8,2) $\boldsymbol{k}$–mesh, we obtain

$$\Phi = 0.20 \pm 0.05 \text{ eV} \quad \text{for the A–interface.}$$

The results discussed so far were obtained for unrelaxed interfaces. X–ray standing-wave experiments indicate that the Si-Si bond lengths at the A-interface are reduced by about 4 per cent.[10] For this geometry, we calculate a *lowering* of Φ by 0.07 eV. For B-type the experimental situation is less clear but gives no basis for assuming that the relaxation differs from the one in type A.

We have considered different LDA-parametrizations,[13] and also applied an external, orbital-dependent potential to the Si-layers so as to yield the correct gap in bulk Si.[26] In the latter case, Φ changed by less than 0.01 eV. We even applied an external potential of –1.4 eV to all the Si-layers of the (5+3)-cell and found Φ to increase by merely 0.007 eV, corresponding to an effective dielectric constant of the superlattice $\epsilon_{eff} \approx 50$.[27] Therefore, the calculated *difference* between the A and B Schottky-barrier heights remains as in Fig. 6c, i.e. 0.16 eV.

SUMMARY

Our theoretical estimates of $\Phi = E_F - E_v$ for the A– and B–type interfaces are thus 0.20 ± 0.05 eV and 0.05 ± 0.05 eV , respectively. This is 0.3 eV lower than the respective experimental values, and we are inclined to ascribe this discrepancy to the use of LDA.

This LDA error is not totally unexpected : GW calculations[28] indicate that the LDA causes E_v for sp^3–bonded semiconductors to be 0.1 to 0.2 eV *too high.* This agrees very well with a recent LDA calculation of the photo-threshold for a (relaxed) GaAs surface [29], which is found to be at least 0.2 eV lower than measured [30]. In the study of Schottky contacts one compares energies (E_F and E_v) of states with very different orbital nature, and which therefore may be affected quite differently by the LDA. Now, LDA calculations of work–functions for Ni and for simple metals[31] seem to yield Fermi levels that are 0.1 to 0.3 eV *too low.* Consequently, despite recent success of LDA calculations in reproducing the

valence–band off–sets for a large number of semiconductor heterostructures within 0.1 eV,[2] errors of –0.3 to –0.5 eV in E_F–E_V could occur when treating metal–semiconductor interfaces in the LDA.

Acknowledgements : We have enjoyed discussions with O. Bisi, D. R. Hamann, W. R. L. Lambrecht, J. Tersoff, and J. Werner. We also thank J. Zegenhagen for communicating his results prior to publication.

* **Permanent Address** : *Solid State Physics Section, Nuclear Physics Division, Bhabha Atomic Research Centre, Bombay 400 085, India.*

REFERENCES

[1]C.G. Van de Walle and R.M. Martin, Phys. Rev. B35, 8154 (1987).

[2]N.E. Christensen, Phys. Rev. B37, 4528 (1988).

[3]L.J. Sham and W. Kohn, Phys. Rev. 145, 561 (1966); J.P. Perdew, R.P. Parr, M. Levy, and J.L. Balduz, Phys. Rev. Lett. 49, 1691 (1982).

[4]R.T. Tung, Phys. Rev. Lett. 52, 462 (1984); J. Vac. Sci. Technol. B2, 465 (1984).

[5]C. Tejedor, F. Flores, and E. Louis, J. Phys. C 10, 2163 (1977).

[6]J. Tersoff, Phys. Rev. Lett. 52, 465 (1984).

[7]M. Cardona and N.E. Christensen, Phys. Rev. B35, 6182 (1987).

[8]G.P. Das, P. Blöchl, N.E. Christensen and O.K. Andersen, to be published.

[9]D. Cherns, G.R. Anstis, J.L. Hutchinson, and J.C.H. Spence, Phil. Mag. A46, 849 (1982).

[10]E. Vlieg, A.E.M.J. Fischer, J.F. van der Veen, B.N. Dev, and G. Materlik, Surf. Sci. 17, 36 (1986); J. Zegenhagen, K.–G. Huang, W.M. Gibson, B.D. Hunt, and L.J. Schowalter, Phys. Rev., to be published. Note that these two works show opposite trend in the magnitude of the interface contraction for A– and B–type $NiSi_2$/Si interfaces, which is presumably due to different thicknesses of the samples used . However, the average value of the contraction can be taken to be ≈ 0.1 Å for both A– and B–type structures within the experimental error.

[11]O.K. Andersen, Z. Pawlowska, and O. Jepsen, Phys. Rev. 34, 5253 (1986).

[12]P. Blöchl, Ph. D. Thesis (University of Stuttgart, 1988) unpublished; and P. Blöchl and O. K. Andersen, to be published.

[13]U. von Barth and L. Hedin, J. Phys. C 5, 1629 (1972); D.M. Ceperley and B.L. Alder, Phys. Rev. Lett. 45, 566 (1980).

[14]P. Blöchl, G.P. Das, O.K. Andersen, and N.E. Christensen, unpublished.

[15]We have also performed some calculations with a basis of *s*–, *p*– *and d*–LMTOs on all atomic *and* empty sites. This reduces the bulk values of E_F^o and E_V^o by about 0.2 eV. But the zeroth order band offset $\Phi^o = E_F^o - E_V^o$, as well as the interface dipole remain unchanged.

[16]O. Jepsen and O.K. Andersen, Phys. Rev. B 29, 5965 (1984); O.K Andersen, P. Blöchl, and O. Jepsen, Bull. Am. Phys. Soc. 33, 804 (1988).

[17]D. Glötzel, B. Segall and O.K. Andersen, Solid State Comm. 36, 403 (1980); W.R.L. Lambrecht, N.E. Christensen, and P. Blöchl, Phys. Rev. 36, 2493 (1987). We repeated these bulk calculations for obtaining E_F^o and E_V^o relative to the ASA zero.

[18]D.R. Hamann, Phys. Rev. Lett. 60, 313 (1988).

[19]P.J. van Hoek, W. Ravenek, and E.J. Baerends, Phys. Rev. Lett. 60, 1743 (1988).

[20]O.K. Andersen and N.E. Christensen, unpublished.

[21]A. Baldereschi, S Baroni and R. Resta , Phys. Rev. Lett. 61, 734 (1988).

[22]W. Lambrecht, B. Segall and O.K. Andersen, to be published; and W. Lambrecht and B. Segall, Phys. Rev. Lett. 61, 1764 (1988).

[23]D.M. Bylander and L. Kleinman, Phys. Rev. Lett. 59, 2091 (1987).

[24]W.A. Harrison, Phys. Rev. B31, 2121 (1985); *ibid.* B37, 864 (1988)

[25]The fact that our estimate of E_F–E_V for the B–interface is now negative, and apparently unphysical, does not mean that the supercell charge density has holes in the valence band, but simply that the energy of the highest valence-band state of the (8+6)-supercell lies below E_V for the semi-infinite system, and below E_F. In terms of the thickness $L = 5.9\ a_0\ m$ of the 'm'–layer Si-slab of the supercell (in our case $m = 6$), an estimate of this energy-lowering due to confinement is $(\pi/L)^2$ Ry ≈ 0.1 eV . The order of magnitude is thus reasonable.

[26]This correction amounts essentially to shifting the energies, C, of the Si and E s–orbitals upwards by respectively 0.22 and 1.88 eV.

[27]W. Lambrecht, B. Segall and O.K. Andersen, to be published; and W. Lambrecht and B. Segall, Phys. Rev. Lett. 61, 1764 (1988).

[28]M.S. Hybertsen and S.G. Louie, Phys.Rev. B34, 5390 (1986); S.B. Zhang, D.T. Tomanek, S.G. Louie, M.L. Cohen and M.S. Hybertsen, Sol. St. Comm. 66, 585 (1988).

[29]G.–X. Qian, R.M. Martin, and D.J. Chadi, Phys. Rev. B37, 1303 (1988).

[30]Note that the GW calculations of the valence band maximum in GaAs differ, depending on the approximation in which it is treated; e.g. a recent calculation [R. Godby, M. Schlüter and L.J. Sham, Phys. Rev. 37, 10159, (1988)] yields $\Delta E_v = E_v^{GW} - E_v^{LDA} = +0.13$ eV, while the calculation of Zhang et al in Ref. 28 gives $\Delta E_v \approx -0.15$eV. For Si, on the other hand, the GW calculations of Godby et al and of Hybertsen and Louie (Ref. 28) give identical results viz. $\Delta E_v = +0.07$ eV.

[31]O. Jepsen, J. Madsen, and O.K. Andersen, Phys. Rev. B26, 2790 (1982); Y.K. Vekilov, V.D. Verner, and M.B. Samsonova, Sov. Phys. Usp. 30, 172 (1987).

ELECTRICAL CHARACTERIZATION OF INTERFACE STATES AT SCHOTTKY CONTACTS AND MIS TUNNEL DIODES

Jürgen H. Werner

Max-Planck-Institut für Festkörperforschung,
Heisenbergstr. 1
7000 Stuttgart 80, Federal Republic of Germany

I. INTRODUCTION

Schottky[1] ascribed the barrier $\Sigma = \Phi_m - \chi$ at rectifying metal/semiconductor contacts to the difference between the work function Φ_m of the metal and the electron affinity χ of the semiconductor. Bardeen explained deviations from this model by charged states within the band gap of the semiconductor.[2] Since that time, the characterization and description of interface states has become a major task for the understanding of Schottky barrier formation. These states are thought to originate either from intrinsic semiconductor surface states,[1] metal-induced gap states,[3-5] defects induced by metal deposition,[6] interface dislocations,[7] or a combination of these effects. Deviations from the Schottky model[2] are then understandable on the basis of trapped interface charge which maintains a dipole at the interface between the metal and the semiconductor.[8]

When one ascribes deviations from the Schottky model to interface states then the Schottky barrier problem is apparently reduced to the task of interface state measurements. Measured state densities might then be correlated with contact technology and, finally, if contacts with low state densities could experimentally be selected, one might compare the electronic properties of such 'ideal' contacts to theoretical predictions.

For about fifteen years conclusions about interface states have been drawn from the analysis of so-called *excess capacitances* which occurred at Schottky diodes under forward bias in addition to the space charge capacitance C_{sc} of the semiconductor.[9-15] The interpretation of such measurements refers usually to a classic admittance model[16,17] for interface state measurements at metal-oxide-semiconductor (MOS) interfaces. This classic model describes carrier trapping at the interface between the oxide and the semiconductor with an equivalent circuit which puts an interface state conductance G_{ss} and a capacitance C_{ss} in parallel to the space charge capacitance C_{sc} of the semiconductor and in series to the oxide capacitance C_{int}.[16,17] For the analysis of measurements on Schottky contacts the same circuit is usually modified by omission of the oxide capacitance C_{int}.[9-15]

Unfortunately, it seems that the numerous capacitance studies[9-15] on Schottky diodes suffered from at least two fundamental inconsistencies:

i) In the case of Schottky contacts *with* an interfacial layer (MIS tunnel diodes) the observed excess capacitances might indeed have been caused by interface states but for such contacts the evaluation scheme on the basis of a modified MOS-circuit was inconsistent. This was the case because Gauss's law was violated as previously pointed out by us[18] and recently confirmed by Muret.[19] Information about interface states may nevertheless still be obtained by our novel transistor-like evaluation scheme.[18]

ii) In Schottky diodes *without* an interfacial layer (intimate Schottky contacts) we found, on the other hand, no excess capacitance at all which could be ascribed to interface states. Instead, the only observable excess capacitances are induced by the ohmic back-contacts and stem from the diffusion of minority carriers within the bulk semiconductor.[20]

The present contribution discusses interface state measurements on MOS-interfaces, Schottky diodes and MIS tunnel structures. In particular the question of the measurability of interface states at Schottky contacts with the help of ac-admittances is addressed. The problem is here attacked from a fundamental physical standpoint in order to clarify at least part of the confusion that seems to exist in the literature.[9-15] Part II sheds therefore light on the principles which underlie the analysis of interface state measurements at MOS-structures with thick insulating oxides. The well-known equivalent circuit of Nicollian and Goetzberger[17] is re-derived from Maxwell's electrodynamic equations. The development given here for the MOS circuit deviates from the original derivation[17] but leads to the same results. Part III shows then that it is indeed possible to use ac-admittances to draw conclusions about interface states at Schottky contacts. However, the postulation of an interfacial layer is an unavoidable prerequisite for a self-consistent analysis of ac experiments. Moreover, the analysis cannot be performed simply by omitting elements from the classic equivalent circuit[17] for MOS-interfaces, as previously assumed.[9-15] Instead, the physical principles which lead to this circuit have to be reconsidered. In particular the current of majority carriers across the interface has to be carefully analyzed within a transistor-like model[18], which then yields the density of interface states and their capture cross section in MIS tunnel diodes; an appropriate equivalent circuit is here proposed for the evaluation. Our analysis deviates from previous evaluation schemes which neglected excess capacitances due to majority carrier currents across the interfacial layer. The thickness of this layer is of major importance in order that the charged interface defects be measurable: A density of states of $10^{12}/cm^2eV$ requires a layer thickness of at least 10nm in order to induce a observable effect in measured current/voltage curves or in the frequency dependence of the conductance. Part IV gives further evidence that at *intimate* Schottky contacts there is no admittance due to interface states. Observed excess capacitances which were earlier ascribed to interface states[9-15] stem instead from the diffusion of minority carriers within the bulk semiconductor as previously shown by us.[20] Part V discusses therefore minority carrier injection into Schottky contacts.

II. INTERFACE STATE MEASUREMENTS AT MOS-INTERFACES

Figure 1 shows the band diagram of the interfacial region of a MOS-device with a thick insulating oxide; Figure 2 displays the equivalent circuit which is used for the evaluation of ac-experiments in order to gain information about interface states.[16,17] This circuit is here re-derived in order to illustrate that interface states can only be detected because their charge fluctuations influence the electric fields and thus the band bending within the semiconductor.

II.1 Charge Neutrality and Gauss's Law

There are two basic equations from which the ac-admittance of the MOS interface with interface states can be derived: Charge neutrality (Gauss's law) and Ampère's law. Overall charge neutrality requires the charge trapped within the interface states Q_{ss} to be compensated by the charge Q_m at the metallic side of the interface and the charge Q_{sc} within the space charge region of the semiconductor:

$$eQ_{ss} = -\left(eQ_m + eQ_{sc}\right) = \epsilon_{int}E_{int} - \epsilon_{sc}E_{sc} = D_{int} - D_{sc} \qquad (1)$$

The second part of Eq.(1) is obtained with the help of Gauss's law and demonstrates that the trapped charge Q_{ss} is responsible for the discontinuity of the dielectric displacement. Without trapped interface charge (Q_{ss}=0) the displacements

$$D_{int} = \epsilon_{int}E_{int} \qquad (2a)$$

$$D_{sc} = \epsilon_{sc}E_{sc} \qquad (2b)$$

would be continuous across the interface. Here ϵ_{int}, ϵ_{sc} denote the dielectric constants and E_{int}, E_{sc} are the (maximum) electric fields at the oxide and semiconductor side of the boundary. Equation (1) states that any change of the charge Q_{ss} *must* result in a change of the fields. Interface states at MOS-interfaces are only detectable in ac-measurements because their charging and discharging changes the electric fields E_{int}, E_{sc} and results therefore in displacement currents. This fundamental insight was obviously overlooked when evaluation methods for ac measurements at MOS-interface were previously transferred to Schottky diodes.[9-15]

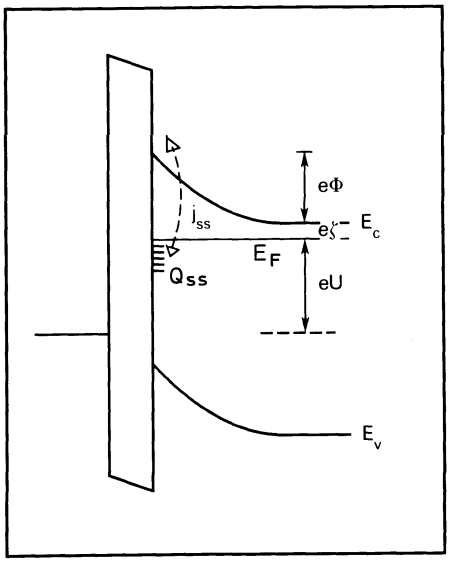

Fig.1. Band diagram of a MOS-capacitor with a thick insulating oxide under bias voltage U. Interface states with charge Q_{ss} within the semiconductor band gap are negatively charged below the Fermi level. The trapping current j_{ss} represents the exchange of electrons between the conduction band and the interface traps.

Under a dc bias voltage U_{dc}, the band diagram in Fig.1 adjusts in a way to guarantee charge neutrality (see Eq.(1)) with the consequence of a band bending Φ_{dc} and a space charge region within the semiconductor. There is no carrier flow in the oxide and within the space charge region. The Fermi level of free electrons and holes is therefore flat throughout the space charge region and the same up to the interface. The current j_{ss} at the interface in Fig.1 represents the stochastic exchange of electrons between the conduction band and the traps due to electron capture and emission.[I] Under dc-conditions the electron capture and emission rates are equal and the mean value of j_{ss} is zero. For a perfect insulating oxide there is therefore no dc-current flowing between the metallization of the oxide and an ohmic back-contact of the semiconductor.

An ac-voltage

$$\delta U = U_{ac} e^{i\omega t} \tag{3}$$

with frequency ω and amplitude U_{ac} (assumed to be small compared with the thermal voltage kT/e) is now applied to the MOS-interface in addition to the dc bias U_{dc}. The ac-voltage divides into a voltage drop $\delta\Delta$ over the oxide and a voltage drop $\delta\Phi$ over the space charge region which causes a time periodic change of the band bending

$$\Phi(t) = \Phi_{dc} - \delta\Phi \tag{4a}$$

with

$$\delta U = \delta\Delta + \delta\Phi . \tag{4b}$$

The relative magnitude of the ac-change of the band bending, i.e. the distribution of the ac-voltage between oxide and the space charge region is, however, exclusively determined by charge neutrality, Eq.(1).

[I]Only capture of electrons as majority carriers is considered here in order to illustrate the basic physical principles and the derivation of the equivalent circuit in Fig.2 from Ampère's law (Eqs.(5),(7)). Exchange with the conduction band prevails as long as the electron concentration at the interface is large compared with the concentration of free holes. Equivalent circuits which consider also *minority* carrier capture are more complicated[21] but they could also be derived along the same lines.

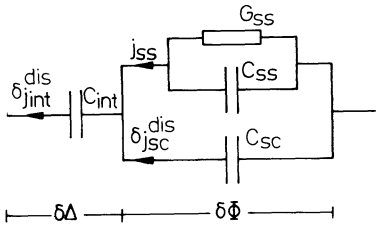

Fig.2. Equivalent ac-circuit for interface state measurements at MOS-interfaces. The applied ac-voltage δU divides in a drop $\delta\Phi$ over the space charge region and a drop $\delta\Delta$ over the oxide.

II.2 Admittance Y and Ampère's Law

The total current j through a semiconductor device consists of an electron current j_n, a hole current j_p, and a displacement current dD/dt according to Ampère's law

$$j = \nabla \times H = j_n + j_p + \frac{dD}{dt}. \tag{5}$$

The current j is spatially constant according to

$$\nabla \cdot j = \nabla \cdot (\nabla \times H) = 0. \tag{6}$$

The measured ac-admittance[II]

$$Y = G + i\omega C = \frac{\delta j}{\delta U} = \frac{\delta j_n + \delta j_p}{\delta U} + \frac{\frac{d}{dt}\delta D}{\delta U} = \frac{\delta j_n + \delta j_p}{\delta U} + i\omega \frac{\delta D}{\delta U} \tag{7}$$

consists of a conductance G and a capacitance C and is given as the ratio of the total ac-current which flows under the application of the ac-voltage. Spatial invariance of the current j allows the admittance Y to be calculated at *any* site within the device.

II.3 Displacement Current within the Oxide

For an MOS-device it is most convenient to calculate the admittance Y_{MOS} from the current j_{int} within the oxide. There are no electron and hole currents (j_n=j_p=0) and j consists therefore only of the displacement current dD_{int}/dt. Equations (2a),(7) yield therefore for the total ac-current

$$\delta j_{MOS} = \delta j_{int}^{dis} = \frac{d}{dt}\delta D_{int} = i\omega \epsilon_{int} \delta E_{int} \tag{8a}$$

and the admittance

$$Y_{MOS} = \frac{\delta j_{int}^{dis}}{\delta U} = i\omega \frac{\epsilon_{int} \delta E_{int}}{\delta U}. \tag{8b}$$

The last part of Eq.(8b) illustrates that the admittance Y_{MOS} consists merely of imaginary parts (capacitances) when the oxide field is exactly in phase with the applied ac-voltage. The displacement current (the time derivative of the field) is then exactly 90° out of phase with the applied voltage and thus capacitive. As shown below, the finite duration of the capture in interface states results, however, in a phase shift of the field E_{int} and thus in displacement currents which are also conductive. Gauss's law and the definition of the oxide capacitance C_{int} allow one rewrite Eq.(8a):

[II]Throughout the paper the symbol δ denotes an ac-change.

$$\delta j_{int}^{dis} = i\omega \epsilon_{int} \delta E_{int} = i\omega e \delta Q_m = i\omega C_{int} \delta \Delta \tag{9}$$

On the other hand, the first part of Eq.(9) can be transformed with the help of Eq.(1) to yield:

$$\delta j_{int}^{dis} = i\omega \epsilon_{sc} \delta E_{sc} + i\omega e \delta Q_{ss} \tag{10}$$

The first term at the right hand side of Eq.(10) represents the displacement current which flows within the space charge region of the semiconductor due to the change of the electric field E_{sc}. Using Gauss's law and the definition of the space charge capacitance C_{sc} one obtains

$$\delta j_{sc}^{dis} \equiv i\omega \epsilon_{sc} \delta E_{sc} = i\omega e \delta Q_{sc} = i\omega C_{sc} \delta \Phi \tag{11}$$

The second current at the right hand side of Eq.(10) can be rewritten to obtain the time-derivative of the charge Q_{ss}. One obtains then from Eqs. (9),(11)

$$\delta j_{int}^{dis} = i\omega C_{sc} \delta \Phi + e \frac{dQ_{ss}}{dt} = \delta j_{sc}^{dis} + j_{ss} \tag{12}$$

where the current

$$j_{ss} \equiv e \frac{dQ_{ss}}{dt} \tag{13}$$

has been defined.

Equations (9),(12) reveal the physical meaning of the current j_{ss}: The displacement current flowing over the oxide capacitance C_{int} (left hand side of Eq.(12)) has to be equal to the sum which consists of the displacement current flowing over the space charge capacitance C_{sc} (first term at right hand side of Eq.(12) and the current j_{ss} which is equal to the time-derivative of the interface charge Q_{ss}. The current j_{ss} must therefore stem from *moving* carriers (j_n, j_p) which flow between the space charge region and the interface due to the charging and discharging of the interface defects.

In the equivalent circuit of Fig.2 the current j_{ss} must thus be in parallel to the displacement current through the space charge capacitance C_{sc}. Both currents add up to yield the displacement current across the oxide capacitance C_{int}. *Interface states at MOS interfaces are therefore measurable because the trapping current j_{ss} induces a displacement current within the oxide.*

As in Fig.2 the current j_{ss} can *formally* be represented by an admittance Y_{ss} with an conductance G_{ss} and a capacitance C_{ss} by writing

$$j_{ss} = e \frac{dQ_{ss}}{dt} = Y_{ss} \delta \Phi = \left(G_{ss} + i\omega C_{ss} \right) \delta \Phi . \tag{14}$$

With Eq.(14) one can then rewrite Eq.(12):

$$\delta j_{int}^{dis} = i\omega C_{sc} \delta \Phi + \left(G_{ss} + i\omega C_{ss} \right) \delta \Phi = \delta j_{sc}^{dis} + j_{ss} . \tag{15}$$

Equation (15) shows that the dependence $\delta\Phi(\delta U)$ as well as the conductance G_{ss} and capacitance C_{ss} control the phase and magnitude of the measured displacement current. However, up to now G_{ss} and C_{ss} were only *formally* introduced to describe the trapping current j_{ss} with the help of Eq.(14) and Fig.2. For specific models of trapping (monoenergetic centers, interface state continua, majority or minority carrier trapping etc.) the *physical* description of the capture processes has then to yield equations for G_{ss} and C_{ss}. An example is given in section II.6.

II.4 Band Bending Modulation

The dependence $\delta\Phi(\delta U)$ is obtained by equating the currents from Eqs.(9),(15) with the result

$$\frac{\delta \Phi}{\delta U} = \frac{i\omega C_{int}}{G_{ss} + i\omega \left(C_{ss} + C_{\Sigma} \right)} \tag{16}$$

with

$$C_{\Sigma} = C_{int} + C_{sc} . \tag{17}$$

Equation (16) demonstrates that only for $G_{ss}=C_{ss}=0$ is the band bending in phase with the applied voltage.[III] Under these conditions the ac voltage divides simply over the series connected capacitances of the oxide and the space charge region.

II.5. Admittance Y_{MOS} of MOS-Interfaces

Equations (8b),(15),(16) yield the admittance Y_{MOS} of the MOS interface:

$$Y_{MOS} = \frac{\delta j_{int}^{dis}}{\delta U} = i\omega C_{sc} \frac{\delta \Phi}{\delta U} + \left(G_{ss} + i\omega C_{ss}\right) \frac{\delta \Phi}{\delta U} \tag{18a}$$

$$= \frac{i\omega C_{int}\left\{G_{ss} + i\omega\left(C_{ss} + C_{sc}\right)\right\}}{G_{ss} + i\omega\left(C_{ss} + C_{\Sigma}\right)} . \tag{18b}$$

Equation (18b) describes simply the total admittance Y_{MOS} of the equivalent circuit of Fig.2 with

$$Y_{MOS} = \frac{Y_1 Y_2}{Y_1 + Y_2} \tag{18c}$$

and

$$Y_1 = i\omega C_{int} \tag{18d}$$

$$Y_2 = G_{ss} + i\omega\left(C_{ss} + C_{sc}\right) \tag{18e}$$

II.6 G_{ss} and C_{ss} for Majority Carrier Capture

In order to use the admittance Y_{MOS} of Eq.(18) for interface state characterization, the ac-change of the interface charge Q_{ss} has to be described with the help of Shockley-Read-Hall statistics. For the special case of the capture of majority carriers in an interface state continuum one obtains then for the conductance G_{ss} and the capacitance C_{ss} of an MOS interface:[16,17]

$$G_{ss} = \frac{e^2 N_{ss}}{2\tau} \ln\left(1 + \omega^2 \tau^2\right) \tag{19a}$$

$$C_{ss} = \frac{e^2 N_{ss}}{\tau} arctan(\omega\tau) \tag{19b}$$

Here N_{ss} denotes the density of states around the dc Fermi level and the time constant

$$\tau = \frac{1}{v_{th}\sigma n} \exp\left(\frac{e\Phi_{dc}}{kT}\right) \tag{20}$$

depends on the electron's thermal velocity v_{th}, their concentration n within the bulk semiconductor, and on the interface states' capture cross section σ.

II.7 Analysis of MOS interfaces

For the analysis of traps at MOS interfaces the conductance G_{ss} and the capacitance C_{ss} are extracted from the measured admittance, Y_{MOS}.[17] The obtained G_{ss}, C_{ss} are then compared with the theoretical behavior (e.g. Eqs.(19)) in order to obtain information about the density of states N_{ss} and the capture cross section σ.

[III] G_{ss} and C_{ss} become zero if there are either no interface states at all, or, when at high frequencies the trapping process cannot follow the applied ac-voltage.

III. INTERFACE STATE MEASUREMENTS AT MIS TUNNEL DIODES

III.1. Inconsistencies in Previous Work

Previous publications[9-15] used the equivalent circuit of Fig.2 to deduce information about interface states at Schottky contacts and MIS tunnel diodes from measured low-frequency capacitances. The oxide capacitance C_{int} was omitted from the circuit and measured capacitances in excess of the space charge capacitance C_{sc} were ascribed to the interface state capacitance C_{ss}.[9-15] At low frequencies one obtains from Eq.(19b)

$$C_{ss}^{dc} = e^2 N_{ss} \tag{21a}$$

and within this model the measured total low-frequency capacitance C_{dc} is then given by

$$C_{dc} = e^2 N_{ss} + C_{sc} . \tag{21b}$$

Measured low-frequency capacitances C_{dc} seem thus to yield a direct information of the interface state density N_{ss}. This seemingly elegant evaluation method suffers, unfortunately, from severe inconsistencies:[18] The omission of the oxide capacitance violates charge neutrality, Eq.(1). Moreover, one cannot understand at all how an interface state capacitance develops when there is no oxide or interfacial layer between the metal and the semiconductor: Interface states at MOS interfaces are measurable in ac-experiments because the time-delayed change of the trapped interface charge causes the electric field E_{int} within the oxide to be out of phase with the applied voltage. This out-of-phase modulation of the fields E_{int}, E_{sc} and - according to Eq.(16) - of the band bending $\delta\Phi$ induces for example conductive components in the displacement current across the oxide as mathematically expressed by Eq.(15). The field E_{sc} within the space charge region and the band bending $\delta\Phi$ can, however, only be out of phase with the applied voltage δU because there is a voltage drop over the oxide. It seems therefore impossible to ascribe excess capacitances to interface states if one omits the oxide, making therefore the band bending change $\delta\Phi$ *equal* to the applied ac-voltage δU and *fixing* thus the field E_{sc} within the space charge region by the applied voltage.

Any model which ascribes excess capacitances at Schottky diodes to interface states should in our opinion include an interfacial layer. The postulation of such a layer as shown in Fig.3 is not only necessary to fulfill charge neutrality (Gauss's law, Eq.(1)) but to explain a measurable interface state related current on the basis of Ampère's law (Eqs.(5),(8b)). It is thus hard to imagine how excess capacitances[9-15] at *intimate* Schottky contacts (without interfacial layers) could be explained at all in terms of interface states. On the other hand, the MOS-model of section II seems to be appropriate for Schottky contacts *with* an interfacial layer (MIS tunnel diodes). However, even in this case measured admittances cannot simply be explained with the equivalent MOS-circuit of Fig.2. Instead the physical analysis of the currents which lead to this circuit has to be carefully reconsidered.

A model which is capable of deducing information about interface states at Schottky contacts with an interfacial layer was recently proposed by us.[18] Our description focuses on the major difference between a Schottky contact and an MOS-interface with a thick insulating oxide: Carrier flow across across the interface. The ac-current within the interfacial layer consists therefore not only of displacement currents as in Eq.(8a) for the MOS interface. Instead, the contributions of *flowing* electrons and holes to measured admittances have to be taken into account.

III.2 Experimental Results

Figure 4 shows experimental values for the measured conductance G and the capacitance C of an Au/Oxide/GaAs tunnel diode.[18] The MBE-grown 3.5μm thick GaAs sample was doped with a Si donor concentration of $2 \times 10^{16} cm^{-3}$. After MBE-growth on a highly doped substrate the samples were exposed to air to obtain an oxide. Scanning Auger measurements[IV] yield an oxide thickness around 12nm. Circular Au-dots were evaporated on the oxide to fabrication the diodes. The dc-characteristics yield a zero-bias Schottky barrier Σ_o=0.92eV and an ideality n_{dc}=1.35 up to about 0.4V in bias voltage. The ac-admittances of Fig.4 are taken with an HP 4192A LCR meter with a special circuit to apply an external bias current with a constant current source.

[IV] I am indebted to Joachim Clabes for his help with these measurements.

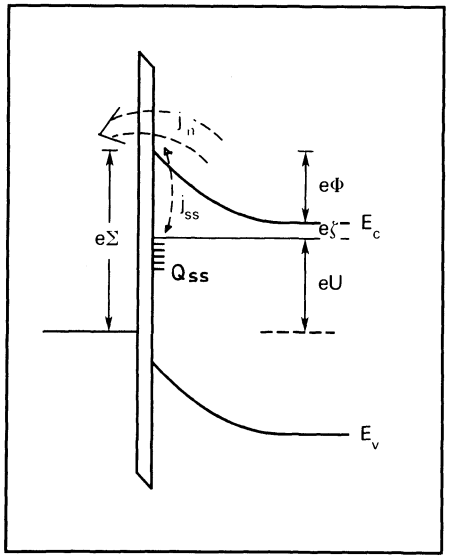

Fig.3. Band diagram of an MIS tunnel contact with a thin interfacial layer. The trapping current j_{ss} controls the interface charge Q_{ss} and modulates thus the band bending Φ and the current j_n across the interface (trap transistor model). This transistor-like effect of j_{ss} on j_n results in the frequency dependent admittances of Fig.4 with capacitive components in j_n.

III.3 Trap Transistor Model

The frequency dependence of the admittance as well as the dc current/voltage-curve can be quantitatively explained with the change of the band bending Φ within the semiconductor due to the change of the charge Q_{ss} within interface states. The following assumptions are made in our analysis which is here presented in more detail than in a previous publication:[18]

i) The majority carrier current j_n across the interfacial layer is described by a combined thermionic/emission-tunneling theory with a flat quasi Fermi level within the space charge region. This assumption should be fulfilled for GaAs.[22,23]

ii) The contribution of minority carriers to the total current of Schottky diodes is usually less than 0.1%.[24] In the following[V] holes in the MIS structure of Fig.3 are therefore neglected and the total current is approximated by the sum of the majority carrier current of electrons, j_n, and the displacement current dD/dt.

iii) It is assumed that under dc-conditions

$$\sigma_n n_{dc} \gg \sigma_p p_{dc}$$

holds where σ_n, σ_p denote the interface states' capture cross sections for electrons and holes and n_{dc}, p_{dc} are the dc carrier concentrations at the interface. Under these conditions the dc quasi Fermi level of the interface states is equal to the quasi Fermi level of free electrons even when there is a split of the quasi Fermi levels of free electrons and holes. Only capture of electrons must then be considered.[25,26]

With these assumptions the description of the capture/emission processes contributing to the current j_{ss} can be performed with the same equations as at for an MOS interface with a thick insulating oxide.

a) Electron current j_n and ideality n

A voltage U results in a current density j_n of electrons across the interfacial layer with

$$j_n = \Theta A^* T^2 \exp(-e\Sigma/kT)\{\exp(eU/kT) - 1\} \qquad (22)$$

[V]Compare, however, the discussion in section V.

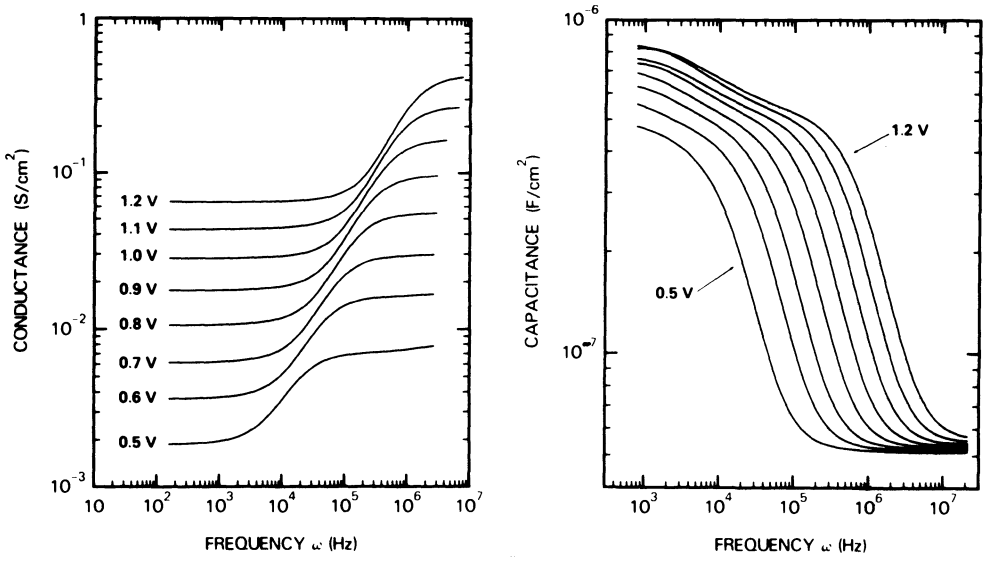

Fig.4 Experimental results for the admittance of an Au/Oxide/GaAs diode at 300K. Measurements were taken with an ac-amplitude of 10mV. The frequency dependence is used to derive information about states at the oxide/GaAs-interface. Different bias voltages correspond to different energies of the Fermi level at the interface.

where Θ denote the tunneling factor[23], and A^* the Richardson constant. The change of bias voltage results in change of interface charge because the Fermi level at the interface moves through the energy distribution of the interface states. The Schottky barrier Σ depends thus on voltage U because the band bending Φ adjusts in a way so that charge neutrality according to Eq.(1) is fulfilled. From Fig.3 one obtains with the bulk Fermi level $e\zeta$

$$e\Sigma = eU + e\zeta + e\Phi \tag{23}$$

which yields for j_n

$$j_n = \Theta A^* T^2 \exp(-e\zeta/kT)\exp(-e\Phi/kT)\{1-\exp(-eU/kT)\}. \tag{24}$$

The voltage dependence of the Schottky barrier Σ is often neglected and an equation with an 'ideality' n and a voltage *independent* barrier Σ_o is fitted to the current/voltage-curve according to

$$j_n = \Theta A^* T^2 \exp\left(-e\Sigma_o/kT\right)\{\exp(eU/nkT)-1\} \tag{25}$$

The voltage dependence of Σ is then hidden in the ideality and for eU>>kT one obtains from Eqs.(22),(25)

$$\frac{1}{n} = -\frac{d\Phi(U)}{dU} = 1 - \frac{d\Sigma(U)}{dU}. \tag{26}$$

b) Electron current j_n under ac-conditions

An ac-voltage δU is divided between the interfacial layer and the space charge region as described by Eqs.(3),(4),(16) for the MOS-interface. The finite duration of the capture/emission processes in interface traps results then in an out-of-phase modulation of

the field E_{int} within the interfacial layer and influences the displacement current. However, the phase shift of the band bending $\delta\Phi$ modifies in addition the current j_n of flowing electrons:

With $\delta\Phi \ll kT$ one obtains from Eq.(24) for a bias $U_{dc} \gg kT$

$$j_n = j_n^{dc}(1 + e\delta\Phi/kT) = j_n^{dc} + \delta j_n \tag{27}$$

with the dc-current

$$j_n^{dc} = \Theta A^* T^2 \exp(-e\zeta/kT)\exp\left(-e\Phi_{dc}/kT\right) \tag{28}$$

and the ac-current of moving electrons

$$\delta j_n = \frac{j_n^{dc}}{kT/e}\delta\Phi . \tag{29}$$

Equation (29) demonstrates that the ac-current δj_n of moving electrons is sensitively influenced by the out-of-phase modulation of the band bending $\delta\Phi$. Indeed, this effect is responsible for the large capacitances at low frequencies which arise from carriers which move out of phase with the applied voltage and not only from displacement currents as one assumes implicitly if one uses previous[9-15] evaluation schemes.

c) Total ac-current in MIS tunnel diodes

When one neglects minority carriers then the total ac-current δj_{MIS} across the interfacial layer of an MIS tunnel diode consists of the sum of the electron current δj_n and the displacement current dD_{int}/dt, according to Eq.(5). From Eqs.(8a),(15),(29) one obtains thus:

$$\delta j_{MIS} = \delta j_n + \delta j_{int}^{dis} = \delta j_n + \delta j_{sc}^{dis} + j_{ss} \tag{30a}$$

$$= \gamma\delta\Phi + \left\{G_{ss} + i\omega\left(C_{ss} + C_{sc}\right)\right\}\delta\Phi \tag{30b}$$

where

$$\gamma = \frac{j_n^{dc}}{kT/e} \tag{31}$$

has been defined.

Equation (30a) reveals that the current j_{ss} enters twofold in the measured ac-current: The trapping current j_{ss} is (as for the MOS-interface) *directly* measurable because it changes the trapped charge Q_{ss}, the band bending Φ, the electric field E_{int} within the interfacial layer and induces therefore displacement currents. There is, however, a second *indirect* effect of j_{ss} on the ac-current due to the change of the band bending Φ influencing the current j_n of flowing electrons. The trapping current j_{ss} acts thus on j_n in a similar way as the base current in a transistor acts on the emitter current. This action lead us to the name of our evaluation scheme: Trap transistor model.

III.4 Admittance Y_{MIS} of MIS Tunnel Diodes

a)Conductance G and capacitance C

The admittance Y_{MIS} of the tunnel diodes is obtained by dividing Eq.(30b) by the applied ac-voltage. The last two terms originate from the displacement current within the interfacial layer and yield thus just the admittance Y_{MOS} from Eq.(18b) for the MOS-diode. One thus obtains

$$Y_{MIS} = \gamma\frac{\delta\Phi}{\delta U} + Y_{MOS} \tag{32}$$

$$Y_{\mathrm{MIS}} = \gamma \frac{i\omega C_{\mathrm{int}}}{G_{\mathrm{ss}} + i\omega(C_{\mathrm{ss}} + C_{\Sigma})} + \frac{i\omega C_{\mathrm{int}}\{G_{\mathrm{ss}} + i\omega(C_{\mathrm{ss}} + C_{\mathrm{sc}})\}}{G_{\mathrm{ss}} + i\omega(C_{\mathrm{ss}} + C_{\Sigma})} \tag{33}$$

$$= \frac{i\omega C_{\mathrm{int}}\{\gamma + G_{\mathrm{ss}} + i\omega(C_{\mathrm{ss}} + C_{\mathrm{sc}})\}}{G_{\mathrm{ss}} + i\omega(C_{\mathrm{ss}} + C_{\Sigma})}. \tag{34}$$

Equation (34) is identical to Eq.(18b) apart from the γ in the numerator. The following equations for the MIS tunnel diodes can therefore also be applied to MOS structures by setting γ=0.

Splitting Eq.(34) into real and imaginary parts yields the measured conductance G and the capacitance C with the results:

$$G = \frac{\gamma C_{\mathrm{int}}(C_{\mathrm{ss}} + C_{\Sigma}) + C_{\mathrm{int}}^2 G_{\mathrm{ss}}}{(G_{\mathrm{ss}}/\omega)^2 + (C_{\mathrm{ss}} + C_{\Sigma})^2} \tag{35a}$$

$$C = C_{\mathrm{int}} \frac{\gamma(G_{\mathrm{ss}}/\omega^2) + \{(G_{\mathrm{ss}}/\omega)^2 + (C_{\mathrm{ss}} + C_{\mathrm{sc}})(C_{\mathrm{ss}} + C_{\Sigma})\}}{(G_{\mathrm{ss}}/\omega)^2 + (C_{\mathrm{ss}} + C_{\Sigma})^2} \tag{35b}$$

The conductances and capacitances which remain in Eqs.(35a,b) for γ=0 are caused by the displacement current and describe thus the behavior of the MOS-interface. The terms which disappear for γ=0 stem from the current j_n of *flowing* electrons within the interfacial layer.

b)High and low-frequency behavior of G and C

For the special case of majority carrier capture within an interface state continuum one obtains with Eqs.(19a,b) for the low-frequency (dc) and high-frequency (HF) values of the conductances and capacitances:

$$G_{\mathrm{dc}} = \frac{\gamma C_{\mathrm{int}}}{e^2 N_{\mathrm{ss}} + C_{\Sigma}} \tag{36a}$$

$$C_{\mathrm{dc}} = \frac{\gamma C_{\mathrm{int}} e^2 N_{\mathrm{ss}} \tau/2 + C_{\mathrm{int}}(e^2 N_{\mathrm{ss}} + C_{\mathrm{sc}})(e^2 N_{\mathrm{ss}} + C_{\Sigma})}{(e^2 N_{\mathrm{ss}} + C_{\Sigma})^2} \tag{36b}$$

$$G_{\mathrm{HF}} = \frac{\gamma C_{\mathrm{int}} C_{\Sigma} + G_{\mathrm{ss}} C_{\mathrm{int}}^2}{C_{\Sigma}^2} \tag{37a}$$

$$C_{\mathrm{HF}} = \frac{C_{\mathrm{int}} C_{\mathrm{sc}}}{C_{\mathrm{int}} + C_{\mathrm{sc}}} \tag{37b}$$

III.5 Equivalent Circuit for MIS Tunnel Diode

Equation (32) explains how the equivalent circuit of Fig.5 can be understood: The total admittance $Y=Y_{MOS}+Y_n$ consists of the admittance Y_{MOS} of the MOS-interface and the admittance

$$Y_{\mathrm{n}} \equiv \gamma \frac{\delta \Phi}{\delta U} = G_{\mathrm{n}} + i\omega C_{\mathrm{n}} \tag{38}$$

of the current j_n of *moving* electrons with

$$G_n = \frac{\gamma C_{int}(C_{ss} + C_\Sigma)}{(G_{ss}/\omega)^2 + (C_{ss} + C_\Sigma)^2} \tag{39a}$$

and

$$C_n = \frac{\gamma C_{int}(G_{ss}/\omega^2)}{(G_{ss}/\omega)^2 + (C_{ss} + C_\Sigma)^2}. \tag{39b}$$

The main difference between our new equivalent circuit in Fig.5 and earlier models[9-15] is the proposal to represent the current j_n across the interface not only by a conductance G_n but also by a capacitance C_n.

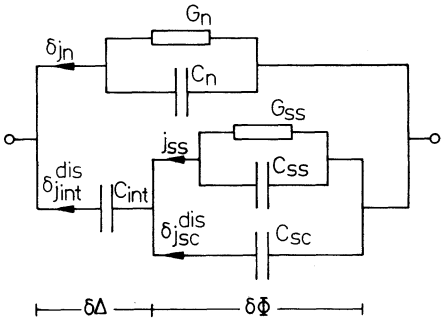

Fig.5. Equivalent circuit for MIS tunnel diodes. The current j_n of moving electrons is represented by the conductance G_n and the capacitance C_n. The equivalent MOS-circuit is in parallel and carries the displacement current within the interfacial layer.

III.6 Extraction of G_{ss} and C_{ss}

In order to obtain information about the interface states the conductance G_{ss} and/or the capacitance C_{ss} of the trapping current j_{ss} have to be extracted from the measured G and C of Fig.4. To that purpose the measured admittance Y is written as

$$Y = G + i\omega C = \gamma \frac{\delta \Phi}{\delta U} + i\omega C_{int} \frac{\delta \Delta}{\delta U} \tag{40}$$

which yields with Eq.(4b)

$$\frac{\delta \Phi}{\delta U} = \frac{Y - i\omega C_{int}}{\gamma - i\omega C_{int}}. \tag{41}$$

Equation (41) is set equal to Eq.(16) and solved for the admittance Y_{ss} with the final result

$$G_{ss} = \frac{C_{int}\{\gamma(C - C_{int}) + G C_{int}\}}{(G/\omega)^2 + (C - C_{int})^2} \tag{42a}$$

$$C_{ss} = \frac{C_{int}\{\gamma G/\omega^2 + C_{int}(C_{int} - C)\}}{(G/\omega)^2 + (C - C_{int})^2} - C_\Sigma. \tag{42b}$$

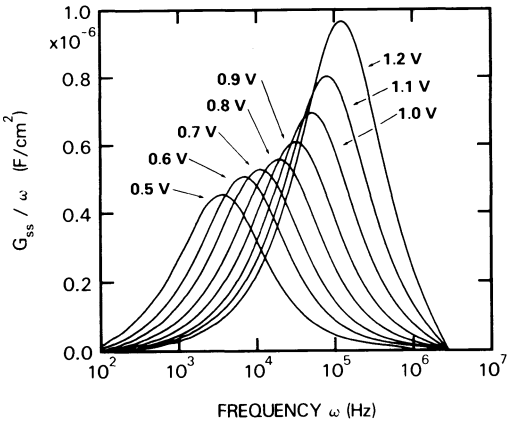

Fig.6. The values G_{ss}/ω as calculated from Eq.(42a) for the different bias voltages of Fig.4. The heights and the frequencies of the maxima yield the values in Fig.7 for the density of states N_{ss} and the capture cross section σ of the interface traps.

The extraction of G_{ss}, C_{ss} from the measured G, C, and $\gamma=ej_{dc}/kT$ requires the precise knowledge of the capacitance C_{int} of the interfacial layer. In the case of MOS devices with a thick insulating oxide one obtains C_{int} from the high-frequency capacitance in accumulation. This procedure seems not possible for MIS tunnel diodes because the high parallel conductance G_n of moving electrons results in much too small phase angles in admittance measurements. There are, however, at least three possibilities for the determination of C_{int} for a tunnel diode:

i) When the thickness d and the dielectric constant ϵ_{int} of the interfacial layer are known then the capacitance C_{int} may be calculated from $C_{int}=\epsilon_{int}/d$.

ii) Equation (28) yields the band bending Φ from the measured dc-current; the space charge capacitance C_{sc} may then be calculated. The capacitance C_{int} is then obtained from Eq.(37b) with the help of the measured value of the high-frequency capacitance C_{HF}.

iii) When the major contribution to the conductance stems from moving electrons through the conductance G_n then the high-frequency conductance of Eq.(37a) can be approximated by

$$G^{n}_{HF} = \gamma \frac{C_{int}}{C_{\Sigma}} . \qquad (43)$$

The measured values of G_{HF}, C_{HF} and γ yield then C_{int}.

III.7 Results for Au/oxide/GaAs

Figure 6 shows[18] the G_{ss}-data for the measurements from Fig.4.[VI] The capacitance C_{int} which was used in Eq.(42) was obtained from the saturation value of the high-frequency conductances G_{HF} in Fig.4 and Eq.(43). Equation (19a) predicts the maxima of the curves in Fig.6 to occur at $\omega\tau=1.98$ with a value of $0.4e^2N_{ss}$. The frequency and the height of the maximum yield therefore the time constant τ and the density of states N_{ss}. The capture cross section σ is then obtained from Eq.(20). The energy position of the (flat) Fermi level at the interface can be calculated from the band bending Φ_{dc} which follows from the dc-current or from the capacitance C_{HF}. Figure 7 displays the results which were earlier obtained for the Au/Oxide/GaAs diode.[18]

[VI]In our first evaluation in Ref.18 we approximated the direct contribution of the capture current j_{ss} on measured admittance via displacement currents by adding the high-frequency capacitance C_{HF} to the circuit elements of the current j_n. For our Au/Oxide/GaAs-diode we found the results to depend only weakly on this approximation.

III.8 Excess Capacitances: Displacement Current versus Current j_n of Flowing Electrons

The main difference between our model and previous evaluation schemes[9-15] is the postulation of a capacitive part in j_n due to electrons which move out of phase with the applied voltage across the interfacial layer. It is therefore interesting to compare the low-frequency capacitance which originates from this current with previous models[9-15] which ascribed the excess capacitances - according to Eq.(21b) - entirely to the displacement current. Both currents are described by Eq.(36b) where the capacitance of the current j_n is represented by the term which contains γ. The pure displacement current model is again obtained for γ=0.

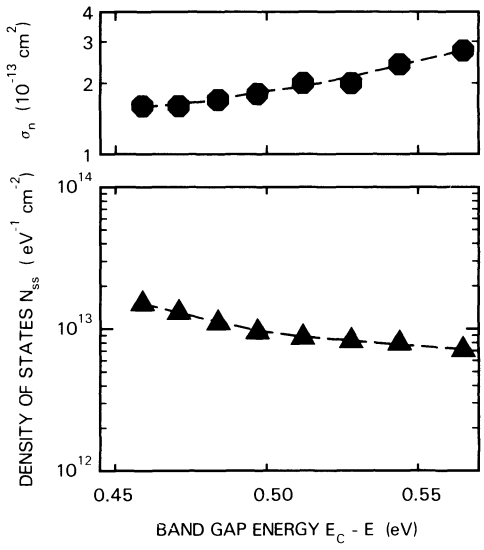

Fig.7. Density and capture cross section of states at the oxide/GaAs boundary of a Au/oxide/GaAs diode. Results stem from the analysis of Fig.6.

We start with the assumption that the measurements on a Schottky diode revealed a low-frequency capacitance which exceeded[9-15] the value at high frequencies. If one ascribes the capacitance to interface states then one may indeed use Eq.(21b) but only to describe the capacitance part which is *directly* caused by the capture processes at the interface via displacement currents. Equation (21b) follows from Eq.(36b) for $C_{int} \gg C_{sc}$ which means that the interfacial layer must be very thin when compared to the width of the space charge region; the high-frequency capacitance C_{HF} is then equal to C_{sc}. Since the low-frequency capacitance is much larger than C_{sc} the following equation must hold within this traditional interpretation[9-15] of excess capacitances:

$$C_{int} \gg e^2 N_{ss} \gg C_{sc} \tag{44a}$$

which yields from Eqs.(21) for the low-frequency capacitance

$$C_{dc}^{tradit} = e^2 N_{ss} . \tag{44b}$$

Under the same assumptions one obtains for the capacitance of the current j_n from Eq.(36b)

$$C_{dc}^{n} = \frac{e^2 N_{ss} \gamma \tau / 2}{C_{int}} . \tag{44c}$$

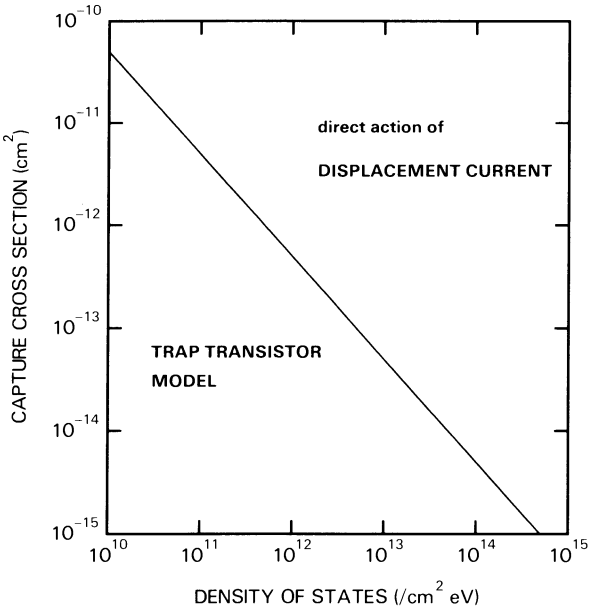

Fig.8. Interface states below the border line have their main influence on excess low-frequency capacitances via capacitive parts in the electron current j_n. Excess capacitances should thus be analyzed with the trap transistor model here described. States above the border line with unusually large capture cross sections may also show up via displacement currents.

Within our complete trap transistor model the excess low-frequency capacitance is caused by the sum of the capacitances from Eqs.(44b,c). We compare therefore the relative importance of these contributions and investigate the ratio

$$R = \frac{C_{dc}^{n}}{C_{dc}^{tradit}} = \frac{\gamma\tau}{2C_{int}}. \tag{45}$$

From Eqs.(20),(28),(31) and with $A^*T^2=eN_cv/4$ with the effective density of states N_c, the velocity $v=v_{th}(8/3\pi)^{1/2}$, and a tunnel factor $\theta=1$ one obtains then

$$R = \frac{e^2/kT}{8\sigma C_{int}}. \tag{46a}$$

For R=1 the electron current j_n and the displacement current dD_{int}/dt within the interfacial oxide are of equal importance in the observable excess capacitance. For R>1 the current j_n prevails and R<1 represents a domination of excess capacitances due to displacement currents. Equation (46a) defines therefore a border line between the two extremes. They are divided according to the interface states' capture cross section σ for majority carriers.

With $C_{int}=\alpha e^2N_{ss}$ and $\alpha>>1$ one obtains from Eq.(46a) the border line which marks the border line between the two regions

$$\sigma\left(cm^2\right) = \frac{5}{\alpha N_{ss}\left(eV^{-1}cm^{-2}\right)} \tag{46b}$$

Figure 8 displays the border line for $\alpha=10$. States with a density of $N_{ss}=10^{12}/cm^2eV$ and a capture cross section $\sigma<5x10^{-13}cm^2$ are, for example, located below the border line; they influence therefore the excess capacitances via the current j_n. The same density of states N_{ss} requires much larger capture cross sections in order to result in excess low-frequency capacitances via displacement currents. Only interface states with unusually large capture

cross sections σ are located *above* the border line.[VII] The indirect action of the capture emission current j_{ss} via the control of the electron current j_n is thus much more effective in the creation of excess capacitances than its direct influence on capacitances via displacement currents.

Equations (46a,b) hold only under the prerequisites of Eq.(44a) which requires that $C_{int} >> e^2 N_{ss}$ holds. The higher the density of states the thinner the interfacial layer should thus be. The maximum capacitance $C_{int,max}$ which could be obtained with an interfacial layer of 1nm thickness and a (relative) dielectric constant of 10 corresponds to a density of states of $10^{14}/cm^2eV$ and allows thus to fulfill Eq.(44a) for a maximum density of states around $2x10^{13}/cm^2eV$.

III.9 The Influence of Interface States on Capacitance, Ideality and Conductance

a) Excess capacitances

The preceding paragraph showed that the evaluation of excess capacitances for interface state measurements requires a precise description of the currents across the interface. The analysis always requires *frequency-dependent* data in order to verify that the excess capacitances are indeed caused by interface states and not by completely different effects as for example minority carrier injection which is discussed in section IV. Admittances can then be evaluated with the trap transistor model of section III.3. The conductance G_{ss}/ω is analyzed as shown in Fig.6. On the basis of this figure one can also demonstrate that the data from Fig.4 are really caused by interface states:

According to Eq.(41) the frequency of the maxima is proportional to the inverse time constant which is described by Eq.(20) and depends exponentially on the electron concentration $n_b = n \exp(-e\phi_{dc}/kT)$ at the interface. With the help of Eq. (28) one thus predicts the frequency of the maxima in Fig.6 to be directly proportional to the flowing dc-current. This behavior is indeed observed as shown in Fig.9.

b) Ideality n_{dc} of dc-current/voltage curve

The ideality n is defined in Eq.(25) and combined with Eqs.(4a),(26) one obtains

$$\frac{1}{n} \equiv \frac{\delta \Phi}{\delta U} \tag{47}$$

where the real and imaginary parts of n are described by Eq.(16). The ideality n_{dc} which enters the dc current/voltage curve, Eq.(25), is obtained from the real part of Eq.(47) for $\omega = 0$ with the result

$$n_{dc} = \frac{y}{G_{dc}} = 1 + \frac{C_{sc} + e^2 N_{ss}}{C_{int}} . \tag{48}$$

Equation (48) is identical to Eq.(18) in the paper of Card and Rhoderick[24] and their classic dc-model follows therefore from our trap transistor model as a special case for $\omega = 0$. The density of states which we obtain from Eq.(48) for our Au/oxide/GaAs diode agrees with the results from the analysis of Fig.6.

The minimum density of states $N_{ss,min}$ which can be detected in the ideality n_{dc} of a tunnel diode with a thin interfacial layer with $C_{int} >> C_{sc}$ is here derived from the requirement $n_{dc} > 1.1$. One obtains then from Eq.(48)

$$N_{ss,min} = \frac{\epsilon_{int}}{10 e^2 d} . \tag{49}$$

[VII] Most results of previous publications[9-15] are located *below* the border line in Fig.8 although the evaluation was carried out with the help of Eq.(44b). All these results seem therefore inconsistently evaluated even if one assumes that the observed excess capacitances were caused by interface states.

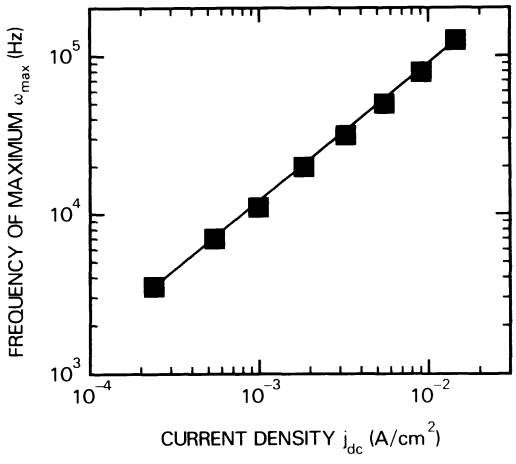

Fig.9. The frequency ω_{max} of the maxima in Fig.6 depends linearly on dc-current j_{dc} because the time constant for capture processes at the interface depends exponentially on the band bending Φ as described by Eq.(20). The observed dependence demonstrates that the low-frequency capacitances in Fig.4 are really caused by interface states.

Figure 10 shows the results which derive from the equation

$$N_{ss,min}\left(cm^{-2}eV^{-1}\right) = 6x10^{13}/d(A) \tag{50}$$

for a (relative) dielectric constant of 10 and an interfacial layer of thickness d.

c) Ratio of conductances G

For diodes in which the main influence on conductance G stems from j_n one observes a step in the frequency dependent G as shown in Fig.4. Equations (36a),(40) give for the ratio of the low- and high-frequency saturation values G_{dc}, G_{HF}

$$\frac{G^{n}_{HF}}{G_{dc}} = 1 + \frac{e^2 N_{ss}}{C_{\Sigma}} \tag{51}$$

which yields together with Eq.(48)

$$\frac{G^{n}_{HF}}{G_{dc}} = 1 + \frac{(n_{dc} - 1)C_{int} - C_{sc}}{C_{int} + C_{sc}}. \tag{52a}$$

For the case of a very thin interfacial layer with $C_{int} >> C_{sc}$ one obtains

$$\frac{G^{n}_{HF}}{G_{dc}} = n_{dc}. \tag{52b}$$

The ratio of the plateau heights in the frequency-dependent conductance G is thus equal to the ideality n_{dc} of the current/voltage curve. A minimum detectable conductance ratio of 1.1 leads thus to the same minimum density of states as already estimated in Eqs.(49),(50) and shown in Fig.10 for the ideality n_{dc}.

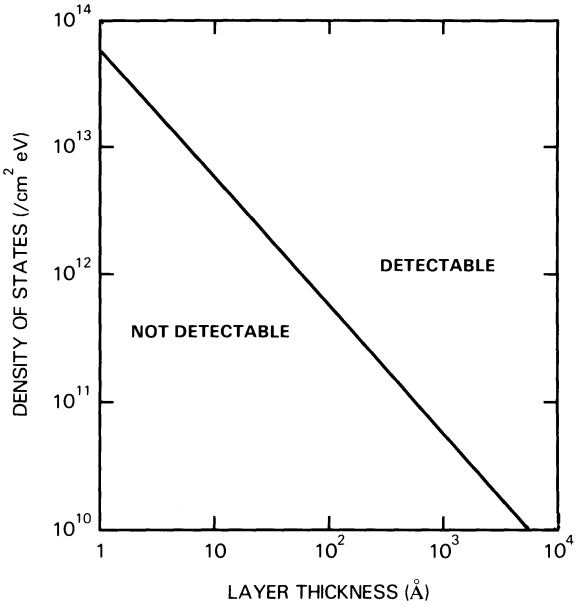

Fig.10. Detectability of interface states at MIS tunnel diodes with the help of the ideality n_{dc} in current/voltage curves or of the ratio G_{HF}/G_{dc} of frequency dependent conductances. The border line represents the minimum density of states N_{ss} which causes an ideality $n_{dc}>1.1$ in dc-current/voltage-curves or a step $G_{HF}/G_{dc}>1.1$ in the frequency dependent conductance like in Fig.4. The border line holds only for interfacial layer thicknesses which allow tunnel currents.

IV. EXCESS CAPACITANCES AT INTIMATE SCHOTTKY CONTACTS

The evaluation of measured admittances with the help of the methods described here requires the proof - as for example shown in Fig.9 - that the observed effect is *really* caused by interface states. In addition, the measurements have to be evaluated within a selfconsistent model which describes the dc as well as the ac properties. Our trap transistor model is based on the description of an out-of-phase modulation of the field E_{int} within the interfacial layer by the trapping current j_{ss}. One then observes displacement currents as well as a modulation of the majority carrier current j_n across the interface. The postulation of an interfacial layer is thus the cornerstone of our model and it cannot be applied to Schottky contacts *without* interfacial layers, i.e. to intimate Schottky contacts.

It is hard to imagine how states at intimate metal/semiconductor contacts could be detected at all in electrical experiments with a time scale of milliseconds to nanoseconds or in the corresponding frequency range: At intimate interfaces one should expect that the defect states equilibrate rather with metal electrons than with the majority carrier quasi Fermi level in the semiconductor. The equilibration should take place on a picosecond time scale and is hardly detectable in dc or low-frequency experiments. For silicon it was shown that a layer of at least 2nm thickness is required to separate the interface states from the metal and to bring them into equilibrium with the semiconductor.[32] *Theoretically* one should then not expect that metal induced gap states at intimate Schottky contacts result in frequency dependent capacitances or conductances at frequencies below 1GHz. On the other hand, excess low-frequency capacitances have been often were *experimentally* observed at intimate Schottky contacts even below 1kHz. These capacitances were ascribed to interface states and analyzed with the help of Eqs.(21b),(44b).[9-15]

Particularly interesting are epitaxial $NiSi_2$/Si-diodes: $NiSi_2$ grows in two distinct orientations (termed type A and B) on silicon (111)-surfaces.[28] The A-type and B-type interfaces are twin related and display a difference of at least 140meV between the two Schottky barriers.[29] Tung's[28] result of *different* Schottky barriers for A-type and B-type $NiSi_2$ samples was subjected to a controversial discussion for more than two years[30,31] when Liehr et al. found - probably due to a different sample preparation - *equal* barriers for their samples.[30] Liehr's results were supported by apparently strong arguments of Ho et al.[13] who claimed to have measured a similar number and energy position of interface states for samples of type A and B. Meanwhile Ospelt et al.[32] confirmed Tung's[28] original result

of *different* barriers and we showed recently[20] that the excess capacitances of Ho et al.[13] were not related to interface states but to imperfect back-contacts and *minority* carrier injection: The back-contacts extract minority carriers from the bulk semiconductor and support thus strong injection at the front Schottky diode with the consequence of strong diffusion capacitances like those in pn-junctions.[20]

Figure 11 displays experimental results for an A-type $NiSi_2$/Si-diode which is grown in UHV by the evaporation of Ni on a (111) surface of an n-type substrate. The sample has an ohmic n^+-contact at the backside which is fabricated by laser annealing an evaporated Sb-layer; the dc current/voltage curve yields a (voltage independent) Schottky barrier Σ =0.63eV and an ideality n_{dc}=1.02. The ac-measurements in Fig.11 show that we do not observe any excess capacitances in agreement with our earlier results.[20] Instead, we find at low frequencies the well-known inductances due to minority carrier conductivity modulation of the substrate resistance.[20,33,34] At higher frequencies the capacitance is independent of frequency and equal to the space charge capacitance C_{sc} within the semiconductor. The conductance (not shown) is also independent of frequency and equal to the slope of the current voltage curve. Our experiments on silicide/silicon diodes do not indicate any admittance which could be ascribed to interface states. In particular we cannot find an excess capacitance as long as we use low-resistance ohmic back-contacts.[20]

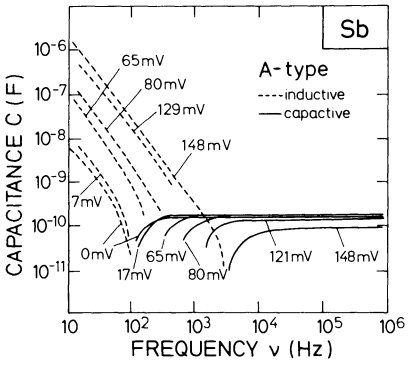

Fig.11. Only inductances (instead of excess capacitances) are observable at $NiSi_2$/Si-diodes (area $10^{-2}cm^2$) with perfect Sb back-contacts.

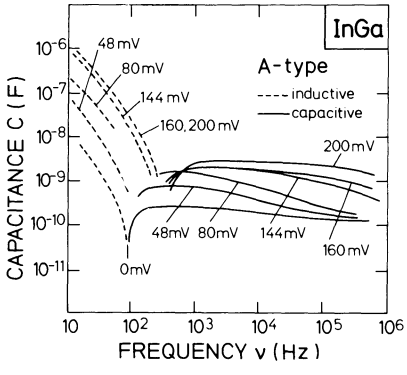

Fig.12. Diodes with InGa or other imperfect back-contacts display excess diffusion capacitances due to excessively injected minority carriers.

We find excess capacitance only if we use imperfect backside contacts. Figure 12 shows results for a diode which is identical to the one in Fig.11 apart from the back-contact: The use of an InGa-alloy for the fabrication of back-contacts results in large excess capacitances up to a few nF at frequencies above about 1kHz. These capacitances stem, however, from minority carriers which are injected into the bulk semiconductor and not from interface states.[20]

Minority carrier injection seems in fact the *only* possibility to explain excess capacitances at Schottky contacts without an interfacial layer: Without such a layer, the whole ac-voltage must drop over the space charge region within the semiconductor. The electric field E_{sc} and the band bending Φ are therefore always exactly in phase with the applied voltage and cause thus a frequency-*in*dependent displacement current dE_{sc}/dt which has only capacitive components; this capacitance is just the space charge capacitance C_{sc}. *Majority* carrier currents j_n can also not be made responsible for the excess low-frequency capacitance because they follow the band bending without time delay. Ampère's law, Eq.(5) leaves, therefore, only the *minority* carrier current j_p which may give rise to excess capacitances in intimate Schottky diodes. Indeed, holes in n-type material are phase shifted with respect to the band bending Φ because their transport through the bulk semiconductor is diffusion limited. One observes thus excess *diffusion capacitances* C_{diff} which are parallel to the space charge capacitance C_{sc} whenever Schottky diodes display excess injection.

V. MINORITY CARRIER INJECTION IN INTIMATE SCHOTTKY DIODES

Minority carriers are usually neglected in the description of current transport in Schottky diodes. The tacit disregard of minority carriers seems to be justified in most cases because their contribution to the total current is usually less than 0.1%.[24] Other transport processes such as tunneling of *majority* carriers or the combined theory of thermionic emission and drift/diffusion receive therefore much more attention than the effect which is the basis of transistor physics: Minority carrier injection.

Neglecting minority carriers is, however, only justified if it is either experimentally or theoretically verified that they *really* play no role in the specific experiment. Even in *dc*-experiments on low-barrier Schottky diodes minority carriers may show up because they modulate the resistance of the substrate.[35] This effect is particularly severe in case of thin epitaxial layers, but even for thick substrates instead of epi-layers there may still be some influence of minority carries on dc-experiments.[36-40] There are, however, still theoretical as well as experimental problems which have not yet been solved. The two main problems concern the influence of the *backside* contact and of the *area* of the Schottky diode on minority carrier injection under dc and ac-conditions.

V.1 Backside contact

The problem of the back-contact was originally (and since then practically exclusively) discussed by Scharfetter.[24] He calculated the injection of holes from the Schottky contact into the bulk semiconductor and demonstrated a sensitive dependence on the properties of the back-contacts: An imperfect back-contact extracts minority carriers via recombination and increases therefore the injection of minority carriers at the front Schottky diode considerably. Systematic *experimental* studies on the influence of the back-contact on minority carrier injection under dc- and ac-conditions of Schottky contacts are, however, very rare.[41,20]

Recombination enhancing, imperfect back-contacts are probably hard to detect in dc-experiments alone: When the contribution of minority carriers to the total current, i.e. the injection ratio, remains below about 1% then the increased injection is probably hardly detectable in the ideality n_{dc}. In the best case one detects the faulty back-contact (as for example induced by the popular InGa or Al-contact to n-type Si) because it induces a *contact* resistance. The situation is even worse when such an additional resistance cannot be detected because it is too small in comparison with the substrate resistance. Spatially homogenous ohmic back-contacts with vanishing contact resistance but different levels of n^+-doping could, for example, all appear as similar and perfect. Nevertheless their influence on minority carrier injection at the front diode may be quite different because their different doping results in different minority carrier reflecting barriers in the valence band edge of the nn^+-backside contact. A lower doped back-contact supports injection at the front Schottky diode because more minority carrier can overcome the barrier in the valence band and recombine at the backside of the wafer. Patchy defective, inhomogeneous back-contacts seem particularly dangerous because they may create *local* recombination sinks with the consequence of increased injection at the front contact. Nevertheless the contact resistance for majority carriers could be small due to adjacent highly doped regions.

The influence of the back-contact should be more severe when the sample thickness is smaller than or comparable to the minority carrier diffusion length because under these circumstances the recombination at the back-contact outstrips bulk recombination. However, for silicon one should always expect an influence of the back-contact since the typical diffusion length around 100μm is *always* comparable to sample thickness. Silicon samples require therefore implanted or laser annealed back-contacts for the characterization of interface states at the front Schottky diode.

V.2 Area dependence

The second problem concerns the dependence of the minority carrier injection on the *area* of the Schottky diode. Even when one somehow prevents excess minority carrier injection due to recombination at the back-contact there may still be substantial injection. The minority carrier current can even *equal* the majority carrier current, when the diameter of the Schottky contact is small compared to the diffusion length: Clarke et al[42] showed that under such geometrical conditions the injection ratio can reach values of up to one because the Schottky diode serves as a point source and the bulk wafer as a three-dimensional diffusion sink. This area dependence and three-dimensionality of the problem should therefore be studied in systematic experiments.

Minority carrier injection in Schottky contacts is therefore only a partially solved problem in semiconductor device physics. Only dc-effects have been studied.[35-40] Experimental data concerning the influence of the back-contact on dc-properties are very rare[41] and the situation for ac-properties and noise experiments is even worse. It is thus to some extent understandable that observed excess capacitances at intimate Schottky contacts were erroneously ascribed to interface states.[9-15]

VI. CONCLUSIONS

The present article has shown that it is possible to measure interface states at Schottky diodes via ac admittances and current/voltage curves. The postulate of an interfacial layer between the metal and the semiconductor is, however, a necessary prerequisite for a consistent analysis. For the evaluation we have described our trap transistor model which yields a unified description of the dc current/voltage-curve as well as of the frequency dependent conductances and capacitances of MIS tunnel diodes and MOS interfaces. The density of states as well as the capture cross section for majority carriers can be deduced with the aid of our methods. The main difference between our model and previous analysis[9-15] schemes is that we postulate capacitive components in the majority carrier current. These currents across the interface are responsible for the excess capacitances at low frequencies. A new equivalent circuit for the ac-properties of MIS tunnel diodes has here been proposed.

Intimate Schottky contacts with low resistance, ohmic, minority carrier reflecting n^+-backside contacts show neither excess capacitance nor any other effect in admittance which could be ascribed to interface states. Excess low-frequency capacitances are only observable with imperfect back-contacts which result in excess minority carrier injection with the consequence of diffusion capacitances. Minority carrier *extracting* back-contacts facilitate *injection* at the front Schottky diode. Previously reported excess capacitances at intimate Schottky contacts were therefore probably not caused by interface states but by imperfect back-contacts and minority carrier injection.[13,20]

ACKNOWLEDGMENTS

The author gratefully acknowledges fruitful collaboration with Michael Anzlowar, Joachim Clabes, Tony Levi, Michael Liehr, Hans Queisser, Mark Pinto, Klaus Ploog, AnnaLena Thilderkvist, and Raymond Tung. It is a pleasure to thank Alan Fowler, John Freeouf, Projnan Chattopadhyay, Bob Dimitriadis, Herbert Güttler, Paul Ho and Manfred Hügle for valuable discussions as well as Simon Bending for a critical reading of the manuscript.

REFERENCES

1. W. Schottky, Naturwissenschaften 26, 843 (1938) and Z. Physik 118, 539 (1942)
2. J. Bardeen, Phys. Rev. 71, 717 (1947)
3. V.Heine, Phys. Rev. A 138, 1689 (1965)
4. C. Tejedor, F. Flores, and E. Louis, J. Phys. C 10, 2163 (1977)
5. J. Tersoff, Phys. Rev. Lett. 52, 465 (1984)
6. W.E. Spicer, I. Lindau, P. Skeath. and C.Y. Su, J. Vac. Sci. Technol. 17, 1019 (1980)
7. J.M. Woodall, G.D. Petit, T.N. Jackson, C. Lanza, K.L. Kavanagh, and J.W. Mayer, Phys. Rev. Lett. 51, 1783 (1983)
8. A. Zur, T.C. McGill, and D.L. Smith, Phys. Rev. B 28, 2060 (1983)
9. A. Deneuville, J. Appl. Phys. 45, 3079 (1974)
10. C. Barret and A. Vapaille, Solid-State Electron. 18, 25 (1975)
11. For a review about the work before 1983 see for example:
    C. Barret, F. Chekir, and A. Vapaille, J.Phys.C.: Solid State Phys. 16, 2421 (1983);
    F. Chekir, C. Barret and A. Vapaille, J. Appl. Phys. 54, 6474 (1983)
12. F. Chekir and C. Barret, Appl. Phys. Lett. 45, 1212 (1984)
13. P.S. Ho, E.S. Yang, H.L. Evans, and X. Wu, Phys. Rev. Lett. 56, 177 (1986)
14. H.L. Evans, X. Wu, E.S. Yang, and P.S. Ho, J. Appl. Phys. 60, 3611 (1986)
15. H.Y. Chen, Y.C. Kao, Y.J. Mii, and K.L. Wang, Mat. Res. Soc. Proc. 91, 439 (1988)
16. K. Lehovec, Appl. Phys. Lett. 8, 48 (1966)
17. E.H. Nicollian and A. Goetzberger, Bell Syst. Techn. J. 46, 1055 (1967)
18. J. Werner, K. Ploog, and H.J. Queisser, Phys. Rev. Lett. 57, 1080 (1986)
19. P. Muret, Semicond. Sci. Technol. 3, 321 (1988)
20. J. Werner, A.F.J. Levi, R.T. Tung, M. Anzlowar, and M.Pinto, Phys. Rev. Lett. 60, 53 (1988)
21. See for example E.H. Nicollian and J.R. Brews, *MOS Physics and Technology*, (John Wiley and Sons, New York 1982), chapter 5
22. E.H. Rhoderick, *Metal Semiconductor Contacts*, (Clarendon Press, Oxford 1978),page 95
23. H.C. Card and E.H. Rhoderick, J. Phys. D: Appl. Phys. 4, 1589 (1971)

24. D.L. Scharfetter, Solid-State Electron. 8, 299 (1965)
25. J.H. Werner, Thesis, University of Stuttgart 1983
26. J.G. Simmons and G.W. Taylor, Phys. Rev. B 4, 502 (1971)
27. H.C. Card and E.H. Rhoderick, Solid-State Electron. 15, 993 (1972)
28. R.T. Tung, J.M. Gibson, and J.M. Poate, Phys. Rev. Lett. 50, 429 (1983)
29. R.T. Tung, Phys. Rev. Lett. 52, 461 (1984)
30. M. Liehr, P. E. Schmid, F. K. LeGoues, and P. S. Ho, Phys. Rev. Lett. 54, 2139 (1985)
31. R. T. Tung, K. K. Ng, J. M. Gibson, and A. F. J. Levi, Phys. Rev. B33, 7077 (1986)
32. M. Ospelt, J. Henz, L. Flepp, and H. von Känel, Appl.Phys.Lett. 52, 227 (1988)
33. T. Misawa, J. Phys. Soc. Jpn. 12, 882 (1957)
34. M. A. Green and J. Shewchun, Solid-State Electron. 16, 1141 (1973)
35. H. Jäger and W. Kosak, Solide-State Electron. 16, 357(1973)
36. C.T. Chuang, Solid-State Electron. 27, 299 (1984)
37. C.T. Chuang, IEEE Trans. Electron Dev. ED-30, 700 (1983)
38. H.C. Card and E.H. Rhoderick, Solid-State Electron. 16, 365 (1973)
39. J.C. Manifacier and H.K. Henisch, Phys. Rev. B 17, 2640 (1978)
40. B.Elfstein and P.A. Tove, Solid-State Electron. 28, 721 (1985)
41. M. Alavi, D.K. Reinhard, and C.C.W. Yu, IEEE Trans. Electron Dev. ED-34, 1134 (1987)
42. R.A. Clarke, M.A. Green, and J. Shewchun, J. Appl. Phys. 45, 1442 (1974)

Band Offsets and Barriers

RELATION BETWEEN SCHOTTKY BARRIER HEIGHTS, BAND OFFSETS AND THE ENERGY LEVELS OF TRANSITION METAL IMPURITIES

M. Lannoo C. Priester, G. Allan, I. Lefebvre, C. Delerue

Laboratoire de Physique des Solides - L.A. 253 CNRS
I.S.E.N., Boulevard Vauban
59046 Lille Cedex, France

INTRODUCTION

It is first shown that the Schottky barrier heights and the band offsets can be related through the energy of dangling bonds. At Schottky barriers, they become resonant states and the Friedel sum rule imposes that the dangling bond energy aligns with the metal Fermi energy. For heterojunctions the condition of negligible charge transfer corresponds to an alignment of the same dangling bond energies. The proposed theory thus allows the identification of Tersoff's midgap level with the everage dangling bond energy. Detailed calculations are worked out in a charge dependent tight binding scheme and show good correlation with experimental data.

The second part concerns the justification of the empirical rule connecting the energy levels of transition impurities in semiconductors and the band offsets at heterojunctions. This is first dicussed on the basis of a defect molecule model combined with a local neutrality condition which is then confirmed by a full Green's function calculation. The complete analysis shows that the transition metal levels are pinned to the average dangling bond energy, this one also playing the role of the charge neutrality level which controls the band offset.

I. SCHOTTKY BARRIER HEIGHTS AND HETEROJUNCTIONS BAND OFFSETS

Tersoff [1] has shown that there is a relation between the pinning position of the Fermi level at some Schottky barriers and the value of the band offset at semiconductor heterojunctions. His theory of Schottky barrier heights is based on the existence of metal-induced gap states (M.I.G.S.) [2] and on the concept of a charge neutrality level E_B (introduced by Tejedor et al. [3]) which plays, for the semiconductor, a role analogous to the Fermi level E_F in a metal. The Schottky barrier height is then determined by aligning E_F and E_B while the band offset is obtained by aligning the two levels E_B characteristic of each semiconductor. Tersoff has also proposed a Theoretical rule to determine E_B [1] from the bulk semiconductor band structure. Although this rule works remarkably well, its physical origin is not clear. It has been proposed previously that E_B should be related to the average sp^3 hybrid energies [4] or to the energy of dangling bonds [5,6]. It is this relation which is examined here and we provide arguments in favor of the identification

of E_B with the average energy of dangling bonds, as shown in ref. [7].

At the interface between a metal and a covalent semiconductor, the semiconductor surface dangling bonds are coupled to the continuum of metallic states. The coupling between dangling bonds is small compared to the direct coupling with the metal states (typical bandwidths of surface states are of order 1 eV). Each individual dangling bond state is then treated separately and becomes a resonant state. This can be described by the Hamiltonian

$$H = E_d \; |d\rangle\langle d| + \sum_k \epsilon_k \; |k\rangle\langle k| + \sum_k (V_{dk} \; |k\rangle\langle d| + cc) \tag{1}$$

where $|d\rangle$ is the individual dangling bond state of energy E_d, $|k\rangle$ are the metal eigenstates whose energies ϵ_k form a pseudocontinuum and V_{dk} are the coupling terms. We proceed as in the treatments of chemisorption on metals [8] and define the change $\delta N(E)$ in total number of states of energy lower than E. Using Green's function theory one has

$$\delta N(E) = - \frac{1}{\pi} \, \mathrm{Im} \, \mathrm{Log} \det (I - gV) \tag{2}$$

where g is the Green's function of the uncoupled systems and V is the coupling matrix of elements V_{dk}. This leads to

$$\delta N(E) = - \frac{1}{\pi} \, \mathrm{Arctg} \, \frac{I(E)}{E - E_d - R(E)} \tag{3}$$

where one has

$$R(E) + i \, I(E) = \lim_{\eta \to 0} \sum_k \frac{|V_{dk}|^2}{E - \epsilon_k + i\eta} \tag{4}$$

We now apply the Friedel sum rule which states that $2\delta N(E_F)$ must be equal to the number of chemisorbed electrons, i.e 1 for neutral dangling bond at a covalent semiconductor surface. Using (3) one gets

$$E_F = E_d + R(E_F) \tag{5}$$

Let us consider the case of a half-filled metallic band which corresponds to the "s" band of Au. If this band is symmetric with respect to E_F, then $R(E_F)$ is zero. If not, $R(E_F)$ will be a small fraction of V^2/W (where $V^2 = \sum_k |V_{dk}|^2$ and W is the metal band width) and will be negligibly small when W is reasonably large compared to V. Thus, even if the resonance is broad and the dangling bond states do not exist any more, it is their energy E_d which is aligned with the metal Fermi energy E_F. As the relative position of E_d with respect to the top of the valende band is an constant E_d, the Schottky barrier height is simply equal to this value.

The argument can be extended to the case of an nonpolar face of a compound semiconductor. The total $\delta N(E)$ contains equal contributions of cation and anion dangling bonds. Thus $\delta N(E_F)$ per pair of dangling bonds is a sum of two temrs like (3) which must equal 1, half the number of electrons per neutral pair. If the couplings between a cation (V_{ck}) or an

anion (V_{ak}) dangling bond with the metal states are equal, one easily gets

$$E_F = \frac{E_A + E_c}{2} + R(E_F) \tag{6}$$

meaning that E_F is aligned with the average dangling bond energy $\frac{E_A + E_c}{2}$ of the anion and of the cation. If V_{ck} and V_{ak} are not equal, their difference remains small as V_{ck} and V_{ak} mainly depend on the interatomic distances between the semiconductor and the metal and not on the nature of the atoms. In any case the error in (6) will be negligible as it is of the order of $(V_{ak} - V_{ck})^2 / (V_{ak} + V_{ck})^2$. To check the validity of our conclusion that E_F should be aligned with the average dangling bond

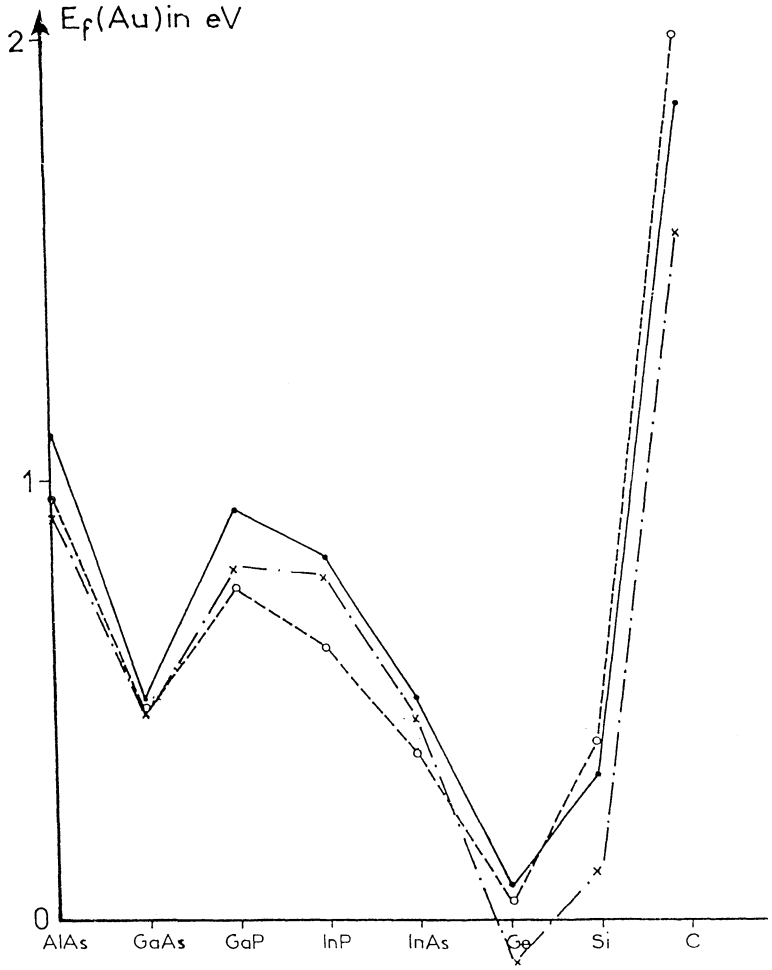

Fig. 1. Surface Fermi energy for Au on different semiconductors. Comparison between the experimental value (solid line) and the average dangling bond energy obtained with parameters of ref. [11] (dotted line) or ref. [12] dashed-dotted line).

energy we have computed the individual dangling bond states of covalent and III-V semiconductors by a charge dependent tight binding technique analogous to that used for the vacancy in Si [9] and at heterojunctions [10]. We have used two sets of tight binding parameters, the sp^3s^* nearest neighbors scheme of [11] and the second nearest neighbors sp^3 one of [12]. In this calculation, we have shifted the atomic levels of the undercoordinated atoms in such a way that local neutrality is obtained on this atom (as discussed in [9] and [10], such a condition is close to true self-consistency).

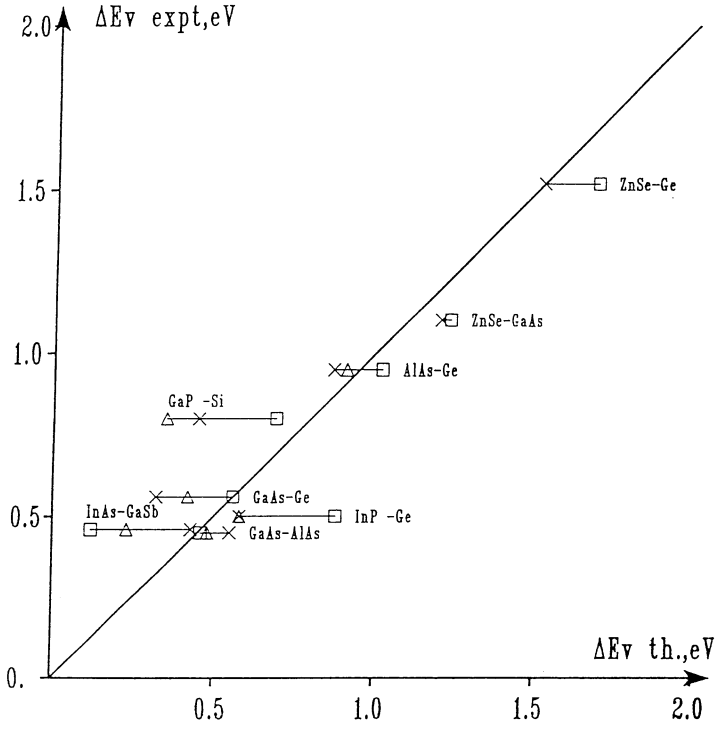

Fig. 2. Plot of the exprimental valence offsets $\Delta E_{v\ exp}$ versus predicted values $\Delta E_{v\ th}$ as deduced from average dangling bond energies (Δ obtained from [11], □ from 2nd neighbors tight binding or X Tersoff's work).

In fig. 1 the results are compared to the experimental E_F(Au) at the interface. The agreement is impressive and the trend is clearly reproduced for both sets of parameters (the differences between the two sets of results are only indicative of the error bars inherent to empirical tight bindind theory).

It remains to show why band offsets at heterojunctions should be related to E_d . For lattice matched systems dangling bond states will couple by pairs across the interface to form bonding and antibonding states as in any diatomic molecule. The contribution of one such bond i

to charge transfer across the interface is given by

$$\Delta q_i = \frac{\Delta E_{di}}{\sqrt{(\Delta E_{di})^2 + V_i^2}} \tag{7}$$

where ΔE_{di} is the difference in dangling bond levels and V_1 their covalent coupling. Our general self-consistent requirement will be that the global charge transfer is screened in such a way that a good approximation is to take it equal to zero. This is in line with Tersoff's arguments [1] and local neutrality conditions.

If we apply the zero charge transfer condition to the heterojunction between two covalent semiconductors, one directly gets $\Delta E_d = 0$, i.e the dangling bond levels E_d must align. For the case of two different bonds one must add two contributions like (7) and it is easy to show that the zero charge transfer condition is equivalent to

$$V_2 \Delta E_{d1} + V_1 \Delta E_{d2} = 0 \tag{8}$$

As $V_1 \sim V_2$ for the same reasons that $V_{ak} \sim V_{ck}$, we again get the condition that the two average dangling bond levels must align. This is likely to occur for lattice matched systems where nearest neighbors bonds have similar lengths. The theoretical offsets determined from the alignment of E_d are compared to experiment on figure 2. Again the agreement is very good.

In conclusion of this part we have shown that the equivalent of the Fermi level for a nonpolar semiconductor surface is the average energy of dangling bonds. Such a quantity is an intrinsic characteristic of a given semiconductor, and its lineup leads to a direct connection between Schottky barrier heights and band offsets. This formal relation has also been confirmed by charge dependent empirical tight binding calculations.

II. TRANSITION METAL IMPURITIES AND HETEROJUNCTION BAND LINEUPS

Very recently, a novel empirical approach, offering surprising accuracy in the prediction of canonical band-offsets (BO) for semiconductor heterojunctions (HJ), has been proposed [13,14]. This approach is based upon the assumption that a reference level, which seems to exist for transition-metal (TM) impurities in semiconductors, may be used in the band alignment procedure in HJ's. It has been observed that the relative ordering of the ionization energies for the whole series of TM's is preserved when the isovalent host is changed. It is therefore possible, by a shift in the valence band edges of two isovalent semiconductors, to align all the respective TM ionization levels. An explanation for this has been proposed by Tersoff and Harrison [15] who have concluded, on the basis of a defect molecule model previously introduced by Picoli et al [16], that TM impurity levels are pinned to bulk cation vacancy levels. On the other hand, it was also proposed [17], and then argued [18], that the reference level is simply the vacuum level.

The alignment of TM ionization levels allows one to express the ionization energy of the i-th TM in an AB semiconductor (values referred to the top of the valence band) as a simple sum :

$$E_i(AB) = E_i(TM) + E(AB) \tag{9}$$

Table 1. Comparison of the positions of the top of the valence band (GaP and ZnSe are taken as references in III-V and II-VI compounds respectively) obtained by : a) estimation from the TM averaging procedure (ΔE_{exp} and ΔE_{th} from experimental data and theoretical values respectively) b) difference between measured photothresholds $\Delta\chi$ (from ref. 29 for II-VI compounds, from ref. 30 for GaAs and InP, from ref. 31 for GaP, and from ref. 32 for AlAs) c) difference between average dangling bond energy levels $\overline{\Delta E_{db}}$ (see text) (all the energies are in eV).

III-V					II-VI				
	ΔE_{exp}	ΔE_{th}	$\Delta\chi$	$\overline{\Delta E_{db}}$		ΔE_{exp}	ΔE_{th}	$\Delta\chi$	$\overline{\Delta E_{db}}$
GaAs	+0.33	+0.39	+0.57	+0.34	HgTe	+1.10			
InP	+0.17	+0.11	+0.37	+0.03	CdTe	+0.80	+0.96	+1.04	+0.89
GaP	0	0	0	0	CdSe	+0.09		+0.20	
AlAs	-0.12		-0.15	-0.11	ZnSe	0	0	0	0
					CdS	-0.37		-0.44	
					ZnS	-0.56		-0.68	

where the first term E_i(TM) is characteristic of the TM, and the second term E(AB) of the host AB. With GaP and ZnSe as references (E(GaP) = E(ZnSe) = 0) , a global least-square minimization was performed to extract the averaged E(AB) parameters. For consistency of treatment, all the energies for a given TM impurity charge state were extracted from the same type of measurement, by following the same procedure (e.g. only photoionization, etc.). The results obtained in this way for E(AB) are given in Table 1. If one assumes that there is TM vacuum level pinning [17], then the quantity E(AB)-E(CD)=ΔE should be equal to the difference $\Delta\chi$ between the corresponding electron affinities. Table 1 presents a comparison of the two quantities (again taking GaP and ZnSe as references) which shows that differences of affinities $\Delta\chi$ produce significantly larger valence band separations than the use of ΔE derived from our TM averaging procedure. This gives some experimental indication that T.M. vacuum level pinning is not verified on the scale of 0.1 eV.

The observed alignment of TM impurity levels has led Langer and Heinrich to postulate [13] that the valence band discontinuity in a HJ is given by the difference in the energy level positions of a TM impurity in the two compounds forming the HJ, or by the difference in the ΔE if one can use an average procedure. This proposal was proven to reproduce most accurately the band offsets in GaAlAs/GaAs [19], InGaAsP/InP [19,20], InGaP/GaAs [21] and CdHgTe/CdTe [19] HJ's. A similar impressive agreement is obtained for the $In_{0.49}Ga_{0.51}P$/GaAs lattice matched pair for which a valence BO of 0.24 eV was determined [21] in accordance with the value of 0.25 eV predicted from the difference in ΔE in the respective binary compounds (see table 1). This agreement is not easy to explain if TM levels are pinned to a vacuum level, since this would imply the existence of a similar vacuum level pinning rule for HJ (i.e. the electron affinity model) which does not seem to work satisfactorily [19,22,23].

The problem of band alignment in HJ's has already been analyzed in terms of the existence of a certain internal reference level [1,24] which was identified with the neutrality level E_B by Tersoff. Following the conclusions of section I, we shall present arguments for the identifi-

cation of this level with the average self energy of dangling bonds $\overline{E_{db}}$. This rule will be confirmed by the charge dependent tight binding calculation of $\overline{E_{db}}$ for several compounds.

Some physical insight concerning the relation between TM levels and band offsets can be gained from the defect molecule model recently formulated by Picoli, Chomette and Lannoo [16]. Tersoff and Harrison [15] have recently shown, using this model, that the TM impurity levels follow the t_2 cation vacancy level at a distance independent of the bulk material, because of the strong intradefect Coulomb interaction U_d. In the defect molecule approach, one only considers the interaction between the "d" states of the transition metal impurity and the sp^3 dangling bonds of the four nearest neighbors anions (these characterize the cation vacancy in the same approach). The five "d" states transform as the E and T_2 representations of T_d point group while the sp^3 dangling bonds transform as A_1 and T_2 . The two "d" states of E symmetry will remain uncoupled and the three "d" states of T_2 symmetry will couple to the T_2 cation vacancy states leading to bonding and antibonding triply degenerate states, solutions of the 2 x 2 matrix

$$\begin{bmatrix} E_d & V \\ V & E_v \end{bmatrix} \tag{10}$$

where E_d is the atomic level, E_v the cation vacancy level and V the covalent coupling. It is easy to show that the fraction of "d" character in the bonding and antibonding states is $1/2\ (1 - \delta/\Delta)$ and $1/2\ (1 + \delta/\Delta)$ respectively, with $\delta = 1/2\ (E_d - E_v)$ and $\Delta = \sqrt{\delta^2 + V^2}$. As there are 6 electrons in the bonding state, n_E in the E state and n_A in the antibonding state, the total "d" electron population n_d is given by

$$n_d = 3\left(1 - \frac{\delta}{\Delta}\right) + n_E + n_A\left(\frac{1}{2} + \frac{\delta}{\Delta}\right) \tag{11}$$

In the limit of strong screening, i.e when the intraatomic Coulomb term U_d is large a very good approximation is provided by the local neutrality condition which states that n_d given by equ. (11) must be equal to its value n_{d0} for the neutral atom which is independent of the host. From (11) this means that δ is independent of its nonselfconsistent value δ_0 and practically takes the same value for all III-V or all II-VI semiconductors. In other words the transition metal impurity level E_d is pinned, within a constant, to the cation vacancy level.

Following this argument, Tersoff and Harrison have then tried to relate the cation vacancy level to the neutrality level E_B but this is the weakest part of their argument. The problem is that, although the molecular approach offers a transparent explanation, its numerical accuracy on the required scale of 0.1 eV is not sufficient to provide a clear-cut picture of these properties. In fact, a validation of the twofold TM and HJ connection would require TM energy level pinning not to the cation vacancy level but to the average dangling bond energy, for reasons explained in part I.

Let us show that this is indeed the case. For this, we make use of a Green's function calculation [25] based on a tight-binding formalism where the TM atom is represented by its five d orbitals and the bulk atoms by an sp basis. The band structure of the perfect crystal is obtained by the procedure of Talwar and Ting [12] (for II-VI, we have

derived our own set of parameters). We then remove an atom to replace it by a TM ion, using for this purpose the Dyson equation:

$$G = G_0 + G_0 \; V \; G \tag{12}$$

where G_0 is the perfect crystal Green's function, G the final Green's function, and V the perturbation induced by the defect. For the interatomic terms of the matrix V, the first neighbor's interaction parameters are deduced from Harrison's rules [26], the others are neglected. The energy E_d of the d orbitals of the TM ion is dependent on the electron population n_d on the atom. Proceeding as in ref. 25, we write in a spin-unrestricted formalism:

$$\begin{aligned} E_{d\uparrow} &= E_d^0 + U_d \; (n_d - n_{d0}) - \frac{J}{2} (n_{d\uparrow} - n_{d\downarrow}) \\ E_{d\downarrow} &= E_d^0 + U_d \; (n_d - n_{d0}) + \frac{J}{2} (n_{d\uparrow} - n_{d\downarrow}) \end{aligned} \tag{13}$$

where $E_{d\uparrow}$ is the d energy for the spin up, J an average exchange interaction, U_d an average Coulomb interaction and E_d^0 the d atomic energy for the configuration with $n_d = n_{d0}$.

As discussed in ref. 25, we take U_d = 8 eV and $J = \gamma \left(\frac{5}{2} B + C \right)$, where B and C are the well-known Racah parameters and γ is a reduction factor (γ=0.72). The final results are found to be insensitive to the exact value of U_d, provided it is large. The reason for this was given first by Haldane and Anderson [27]. It comes from the fact that, when U_d is large (i.e $U_d \gg 1$ eV here), the screened potential is small and independent of U_d, as shown analytically in the defect molecule model [16]. Finally, selfconsistency is achieved by applying a potential U_1 on the first neighbors of the defects. For a defect with charge state q, we impose a net charge q/ϵ, where ϵ is the dielectric constant. In the spirit of the empirical tight binding approximation the atomic energies, i.e E_d^0 and the average sp^3 energy of the bulk crystal are taken to be the free atom values, deduced from Herman and Skillman [28]. As any empirical theory its justification lies in the fact that it is successful for predicting a broad range of physical properties as demonstrated in ref. [25]. As it is the model is completely free of adjustable parameters. The ionization energies are calculated with the Slater transition state for the maximum spin configuration. We have calculated the relative valence BO's using the same TM averaging procedure as described above. As shown in Table 1 they are in excellent agreement with the values deduced from experiment [1].

To clarify the relation between TM levels and band offsets, we have also calculated the energy differences between the computed TM energy levels with : i) the t_2 cation vacancy level and ii) the average dangling bond energies determined by the same Green's function calculations. The results, depicted in fig. 3 show that the TM impurity level is connected more to $\overline{E_{db}}$ than to the vacancy level. This behavior is due to the potential U_1 on the first neighbors, introduced to impose global neutrality, and to delocalization of the impurity states included in our description, factors which increase the influence of the second nearest neighbors cations. Comparison between valence BO predicted by the TM average procedure [13] and by differences between average dangling bond energies [7] is also impressive (see table 1).

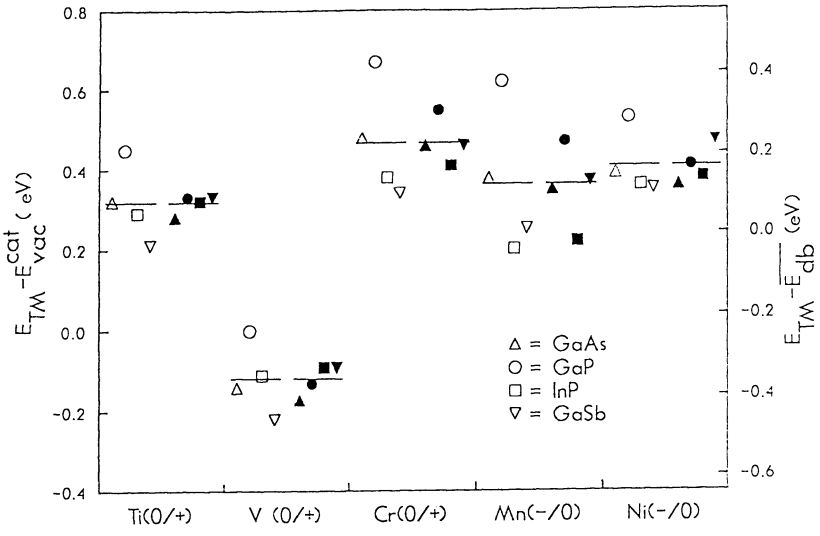

Fig. 3. The energy difference between some of the calculated TM energy levels, and the calculated t_2 cation vacancy (open symbols), and the average dangling bond (filled symbols) energy levels in several III-V semiconductors.

The physical origin of TM level alignment is thus transparent : because of strong Coulomb interactions (U_d >> 1 eV) in the 3d shell, the TM impurity level position becomes independent of U_d and is pinned to a bulk level, the latter being related to the average dangling bond energy and not just to the cation vacancy level because of long range effects (delocalisation, screening). This calculation gives sound theoretical support for the empirical rule connecting causally TM's and HJ's [13,14], and shows again the importance of the concept of a dangling bond state in description of HJ's and defects in semiconductors.

In conclusion the central physical quantity which relates Schottky barrier heights, heterojunction band lineups and transition metal impurity levels is the average dangling bond energy which also plays the role of Tersoff's neutrality level. We have demonstrated this by using defect molecule models and charge dependent tight binding calculations.

REFERENCES

1. J. Tersoff, Phys. Rev. Lett., 52, 465 (1984); Phys. Rev.B 30, 4874 (1984); J. Vac. Sci. Technol. B 3 (4), 1157 (1985).
2. V. Heine, Phys. Rev. A 138, 1689 (1965).
3. C. Tejedor, F. Flores and E. Louis, J. Phys. C 10, 2163 (1977).
4. W.A. Harrison and J. Tersoff, J. Vac. Sci. and Technol., B 4, 1068 (1986).
5. O.F. Sankey, R.E. Allen, S.F. Ren and J.D. Dow, J. Vac. Sci. Technol. B 3, 1162 (1985).
6. H. Hasegawa, Sol. State Comm., 58, 157 (1986).
7. I. Lefebvre, M. Lannoo, C. Priester, G. Allan and C. Delerue, Phys. Rev. B 36, 1336 (1987).
8. G. Allan, Handbook of Surfaces and Interfaces, Ed. L. Dobrzynski, Garland STPM (1978), 368.

9. P. Pêcheur, E. Kauffer and M. Gerl, Inst. Phys. Conf. Ser., 46, 174, The Institute of Physics, Bristol, London (1979).
10. C. Priester, G. Allan and M. Lannoo, Phys. Rev. B 33, 7386 (1986).
11. P. Vogl, H.P. Hjalmarson and J.D. Dow, J. Phys. Chem. Sol., 44, 365 (1983).
12. D.N. Talwar and C.S. Ting, Phys. Rev. B 25, 2660 (1982).
13. J.M. Langer and H. Heinrich, Phys. Rev. Lett., 55, 1414 (1985), and Physica 134B, 444 (1985).
14. A. Zunger, Ann. Rev. Mater. Sci., 15, 411 (1985) and Solid State Physics, 39, 275 (1986).
15. J. Tersoff and W.A. Harrison, Phys. Rev. Lett., 58, 2367 (1987), and J. Vac. Sci. Technol., B 5, 1221 (1987).
16. G. Picoli, A. Chomette and M. Lannoo, Phys. Rev. B 30, 7138 (1984).
17. L.A. Ledebo and B.K. Ridley, J. Phys. C, 15, L961 (1982).
18. M.J. Caldas, A. Fazzio and A. Zunger, Appl. Phys. Lett., 45, 671 (1984), and A. Zunger, Phys. Rev. Lett., 54, 849 (1985).
19. H. Heinrich and J.M. Langer, in Festkörperprobleme, edited by P. Grosse (Vieweg, Braunschweig, 1986), Vol. 26, 251, and H. Heinrich in Lecture Notes in Physics (Springer Berlin, 1988) (in print).
20. D.V. Lang, M.B. Panish, F. Capasso, J. Allan, R.A. Hamm, A.M. Sergent and W.T. Tsang, Appl. Phys. Lett., 50, 736 (1987).
21. M.A. Rao, E.J. Caine, H. Kroemer, S.I. Long and D.I. Baci, J. Appl. Phys., 61, 643 (1987).
22. D.W. Niles and G. Margaritondo, Phys. Rev. B 34, 2923 (1986).
23. J.M. Langer, C. Delerue, M. Lannoo and H. Heinrich, to be published.
24. C. Tejedor and F. Flores, J. Phys. C 11, L19 (1978), and F. Flores and C. Tejedor, ibid. 12, 731 (1979).
25. C. Delerue, G. Allan and M. Lannoo, Mat. Sci. Forum, 10-12, 37 (1986) ; Z. Liro, C. Delerue and M. Lannoo, Phys. Rev. B 36, 17 (1987) ; C. Delerue, M. Lannoo and G. Allan, to be published.
26. W.A. Harrison, Electronic Structure and the Properties of Solids (Freeman, New York, (1980).
27. R.D.M. Haldane and P.W. Anderson, Phys. Rev. B 13, 2553 (1976).
28. F. Herman and S. Skillman, Atomic Structure Calculations (Prentice Hall, New York, 1963).
29. Landolt-Bornstein : Numerical data and functional relationships in Science and Technology, edited by O. Madelung, M. Schultz, and H. Weiss (Springer-Verlag Berlin, 1982), Group 3, Vol. 17, Parts a and b.
30. G.W. Gobeli and F.G. Allen, Semicond. Semimetals, 2, 263 (1966).
31. G.M. Guichar, C.A. Srbene and C.D. Thuault, Surf. Sci., 86, 789 (1979).
32. M.K. Kelly, D.W. Niles, E. Colavita, G. Margaritondo, M. Henzer, Appl. Phys. Lett., 46, 768 (1985).

SCREENING NEAR SEMICONDUCTOR HETEROJUNCTIONS AND VALENCE BAND OFFSETS

C. Priester, G.**Allan** and **M. Lannoo**

Institut Supérieur d'Electronique d'Electronique du Nord
Laboratoire d'Etudes des Surfaces et Interfaces
41, Boulevard Vauban - F-59046 Lille Cedex (France)

INTRODUCTION

Semiconductor superlattices and quantum wells are nowadays commonly used in optoelectronic and high speed semiconductor devices [1]. The band gap value can be chosen by varying the quantum well widths or by alloying the semiconductors. However a good knowledge of the VBO (Valence Band Offset) is necessary to design the devices. The required accuracy is less than 20 meV. Recent theories which consider charge transfer effects at the heterojunction interface provide reasonable agreement with the experimental results at least for unstrained systems. This includes ab-initio self-consistent calculations in the local density approximation (with or without d states) [2] or beyond, i.e. including self-energy corrections [3], midgap neutrality point theory by Tersoff [4],dielectric midgap energy theory by Cardona and Christensen [5] and also tight-binding calculations [6-7].

Strained heterojunctions like $In_x Ga_{1-x} As$ / GaAs (with $x \simeq 0.1$) or $In_x Ga_{1-x} As$ / $In_y Ga_{1-y} As$ are also used for device applications. With our self-consistent tight-binding scheme, we have calculated the VBO and also get good agreement with the different experiments [8].

The linearity, the transitivity and the anisotropy of many experimental results have suggested that the VBO can be expressed as the difference of bulk quantities. Such a lineup of bulk characteristic energies is a consequence of the electronic screening near the heterojunction. So any accurate self-consistent model must correctly describe the material dielectric functions. In the next section, we develop a self-consistent tight-binding model which takes into account the screening in the semiconductors. To zero-th order, this suggests a zero dipole model. A first-order correction in terms of the static dielectric constant is then calculated in the third section. In section

4, we introduce the "natural" VBO defined as the VBO for isolated materials. This implies an absolute energy scale common to both materials of the heterojunction. Such a scale has been tested by the comparison of the core level shifts in CdTe and HgTe to experimental values. Finally in the last section we compare our calculated VBO to experimental values for strained and unstrained heterojunctions.

THE ZERO DIPOLE APPROXIMATION

The bulk semiconductor band structures are obtained in the tight-binding approximation using a sp^3s^* basis [9]. Such a procedure accurately fits the semiconductor valence bands and the bottom of the conduction band. The surface Green functions have been calculated by the decimation technique [10]. The electronic charge on an atom is obtained by integration of the local Green functions in the complex energy plane and a few special points [11] are used for integration over the two-dimensional Brillouin zone. We have checked that such a procedure provides accurate charge values necessary to reach the required accuracy for the VBO.

Let us define Q_i the net charge on an atom i. Such charges create a potential V_j on atom j. We can write:

$$V_j = \sum_{\text{all atoms}} \gamma_{ij} \, Q_i \tag{1}$$

where

$$\gamma_{ii} = U_i \tag{2.a}$$

$$\gamma_{ij} = 1 / R_{ij} \tag{2.b}$$

with R_{ij} is the distance betweens atoms i and j and U_i the intraatomic Coulomb energy. Due to translation symetry along the interface the charges and the potentials are equal for all atoms in a given plane parallel to the hetrojunction. Then one gets:

$$V_j = \sum_{\text{all planes}} (C^{-1})_{ji} \, Q_i \tag{3}$$

where i and j now run over planes parallel to the interface. Equation (3) can also be written under a matrix form:

$$V = C^{-1} \, Q \tag{4}$$

The charges Q_i calculated from the electronic structure are non linear functions of the potentials V_j:

$$Q_i = f_i(V_1, V_2, \ldots) \tag{5}$$

Equations (2) and (5) can be solved by iteration.Starting from charges Q^0 and potentials V^0 such as:

$$Q_i^0 = f_i(V_1^0, V_2^0, \ldots\ldots) \tag{6}$$

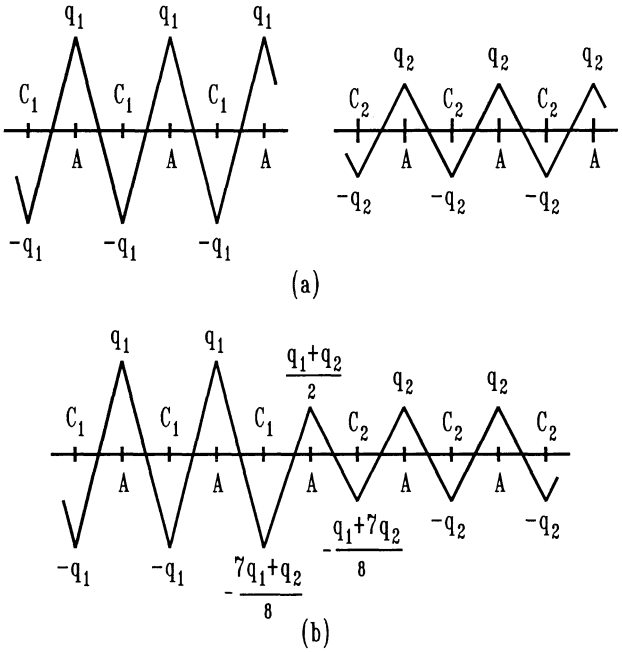

Figure 1. Potential and charges in bulk separated semiconductor compounds (a) or near an interface in the approximation of zero dipole (b). The potentials have been for this figure calculated with a continuous charge spreading in planes parallel to the surface. This approximation also gives the exact macroscopic potential step across the interface.

Equation (5) is then linearized:

$$Q = Q^0 + \chi\,(V - V^0) \tag{7}$$

where we have used the susceptibilities:

$$\chi_{ij} = \left(\frac{\partial Q_i}{\partial V_j}\right)_{V_1^0, V_2^0, \ldots} \tag{8}$$

We now have to solve a set of linear equations to get a new potential V^1:

$$V^1 = V^0 + (I - C^{-1} \chi)^{-1} C^{-1} Q^0 - (I - C^{-1} \chi)^{-1} V^0 \qquad (9)$$

If V^0 is close to the self-consistent solution or if equation (5) is almost linear, then V^1 is a very good approximation of the exact solution and can be used to calculate the macroscopic dipolar layer across the heterojunction ΔV equal to $(V_{i=+\infty} - V_{i=-\infty})$. Let use choose a charge repartition $Q^0 = Q_{ZD}$ (Zero Dipole) such as it does not give rise to any dipolar potential: i.e. $(C^{-1}Q_{ZD})_{i=+\infty}-(C^{-1}Q_{ZD})_{i=-\infty}$ is equal to zero. Such a charge repartition is obtained with a potential V^0 equal to V_{ZD} and ΔV_{ZD} is the corresponding macroscopic step potential at the interface. We must remark that V_{ZD} is determined only from equation (6) and *is not a solution of equation (4)*. If we neglect the contribution of the last two terms in (9), we obtain the "zero dipole" approximation to the dipole barrier height. We now have to choose a charge repartition Q_{ZD} which used in (4) does not give any macroscopic potential across the heterojunction. The solution is not unique but we know that the screening in these materials occurs over very short distances (less than one bond length) [12] so we retain the most localized charge disturbance Q_{ZD} . For instance , figure 1a shows for planes (100) the potential and the charges in each semiconductor. The most localized charge distribution which exactly cancels the dipole layer is given on figure 1b and corresponds to our zero dipole charge Q_{ZD} .

CORRECTION TO THE ZERO DIPOLE APPROXIMATION [8]

We can iterate equation (9) until self-consistency. We also have tried to simply estimate a "first-order" correction to the zero dipole approximation. Let us assume that the screening properties of the two materials are identical so that the dielectrix matrix $\epsilon = (I-C^{-1}\chi)$ is homogeneous. Let us also use the Fourier components V_q of the potential:

$$V_q = \sum_n V_n \exp(-inqd) \qquad (10)$$

and Q_q of the charges. The summation in (10) is performed over a large supercell of N planes containing the interface and used with periodic boundary conditions. With these assumptions, the dielectric matrix becomes diagonal when Fourier transformed. Equation (10) is reduced to:

$$V_q^1 = V_q^0 + \frac{1}{\epsilon(q)} \left[C_q^{-1} Q_q^0 - V_q^0 \right] \qquad (11)$$

The dipole layer ΔV^1 is equal to:

$$\Delta V^1 = \sum_n (V^1_{n+1} - V^1_n) \tag{12}$$

or if we use the inverse transform $V_n = N^{-1} \sum_q V_q \exp(iqnd)$:

$$\Delta V^1 = \sum_q [\exp(iqd)-1] V^0_q \delta_{q,0} \tag{13}$$

i.e.

$$\Delta V^1 = \lim_{q \to 0} iqd V^0_q \tag{14}$$

As $\mathbf{Q}^0$ is choosen to give a zero dipole layer:

$$\Delta V^1 = \Delta V_{ZD} \left[1 - \frac{1}{\epsilon(0)} \right] \tag{15}$$

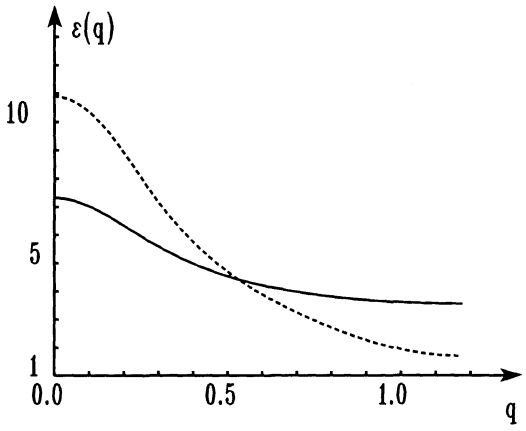

Figure 2. GaAs dielectric constant as a function of the wave vector (in Å $^{-1}$) .The full line is obtained with a continuous charge repartition in planes (100) normal to the wave vector. This also gives the same value at zero wave vector than a point charge model as the one we use. The dotted line is the scaled dielectric function we used.

Although this expression is not rigorously exact as it assumes that screening is the same in the two semiconductors, it gives the order of magnitude of the error when one uses the zero dipole approximation. As $\epsilon(0)$ is close to 10, this error remains small and in any case, this is a good starting point for the complete iterative scheme.

The potentials calculated in the preceeding section must be added to the natural VBO ΔE_v^0 (which is the band offset when the materials are separated) to get the heterojunction VBO ΔE_v:

$$\Delta E_v = \Delta E_v^0 + \Delta V \tag{16}$$

If we call $\Delta E_V^{ZD} = \Delta E_v^0 + \Delta V_{ZD}$, we get as long as (15) is valid:

$$\Delta E_v = \Delta E_v^{ZD} - \frac{\Delta E_v^{ZD} - \Delta E_v^0}{\epsilon(0)} \tag{17}$$

The second term in (17) depends on the natural VBO and on the static dielectric constant. The dielectric constant $\epsilon(0)$ calculated in the tight-binding approximation is generally too small [13]. For GaAs and a sp^3s^* basis, we find a value close to 7 instead of the experimental value equal to 10.9. Several corrections like orbital non orthogonality may enhance the tight-binding dielectric constant. As Harrison[13], we have scaled the inverse capacitance C^{-1} in order to get the experimental value.

If we want to determine the natural VBO for separated materials, we have to define a common energy level. Let us consider the case of a common anion. The anion s, p and s^* atomic levels $E_{A\alpha}^i$ (α=s, p or s^* and i=1 or 2 for each semiconductor) can be written as the sum of common atomic levels $E_{A\alpha}^0$ plus a Madelung energy related to the charge transfer in a material between anions and cations:

$$E_{A\alpha}^i = E_{A\alpha}^0 + \left(U_A^i - \frac{\beta e^2}{R_i} \right) q_i \tag{18}$$

where U_A^i is the anion intratomic Coulomb integral, β the lattice Madelung constant, q_i the bulk semiconductor anion net charges and R_i the material interatomic distance. In the fits used to determine the tight-binding bulk parameters, $E_{A\alpha}^i$ is referenced to the top of the material valence band. As we calculate the net charge q_i from the band structure, we can determine the position of the common energy level $E_{A\alpha}^0$ if we know U_A^i. We have used this Coulomb intraatomic integral to fit a Thomas-Fermi approximation of the dielectric constant[10]:

$$\frac{1}{\epsilon(q)} = \left[1 - \frac{1}{\epsilon_0} \right] \frac{1}{1+\lambda^2/q^2} + \frac{1}{\epsilon_0} \tag{19}$$

where λ is the inverse Thomas-Fermi screening length.

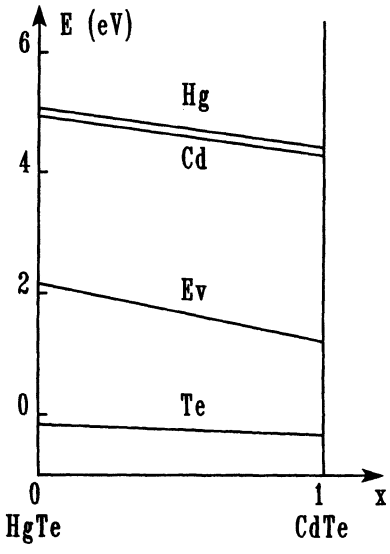

Figure 3. Variations of the sp^3 levels of the cations Hg and Cd and of the the anion Te in a $Hg_{1-x}Cd_xTe$ alloy. The common energy level Te^0 for the neutral anion is taken as the zero energy. The variation of the top of the valence band E_v is also shown. Its difference between x=0 and x=1 gives a natural VBO equal to 0.970 eV.

Table 1. Comparison of the self-consistent result with the approximation given by equation (17) and the experimental values. The dielectric constants are taken from reference 18.

	$\epsilon(0)$	ΔE_v^0	ΔE_v^{ZD}	Corrected ΔE_v^{ZD}	ΔE_v	Exp.
AlAs	8.16	-0.157	0.618	0.537	0.496	0.50±0.05[a]
GaAs	10.9					
CdTe	7.2	0.970	0.305	0.364	0.390	0.35±0.05[b]
HgTe	15.2					
AlSb	10.2	0.264	0.465	0.449	0.451	0.45±0.05[c]
GaSb	14.4					

a) Ref. 15; b) Ref. 16; c) Ref.17.

If we assume that the core electrons feel the same potential as the valence ones, we can calculate the shift of the common anion core level in different semiconductor compounds. The Te 4d level energy has been measured relative to the top of the valence band [14] in HgTe and CdTe. The difference between the experimental binding energies (0.6±0.15 eV) is in good agreement with the value we have calculated (0.80 eV). On figure 3, we plot the variation of the sp^3 atomic levels in these materials and in their alloy $Hg_{1-x}Cd_xTe$ we describe in a virtual cristal approach when x~0.5. For x~0 (x~1), the Cd (Hg) atom is treated by the Green function method as an isolated impurity in a bulk HgTe (CdTe) infinite material. The variation of the levels is linear and parallel. This gives a difference between the binding energies of the 4d Cd level and the 5d Hg one in $Hg_{1-x}Cd_xTe$ equal to 0.30 eV very close to the experimental one (0.35 eV).

SOME RESULTS AND CONCLUSION

Such a model has been first [8] applied to unstrained heterojunction like: GaAs/AlAs, HgTe/CdTe and GaSb/AlSb. Table 1 shows that the Calculated VBO agree very well with the experimental values. The zero dipole model gives values lying within 0.1 eV from the self-consistent value. One must also notice that the corrected value obtained with a mean dielectric constant and equation (17) is much closer to the exact result. The calculated values very well agree with the experimental results. Some differences exist for the zero dipole approximation with other tight-binding calculations[6]. As the band structure parameters are equal in both calculations, this seems to be due to slightly different numerical accuracy. We have carefully checked that point in our calculation. Our numerical accuracy for the zero dipole band offset is better than 1 meV. Reference 6 also uses different screening to calculate the self-consistent result and the dielectric constant they used is shown on figure 2. In the preceeding section we have notably shown that the full selfconsistent treatment must also use an accurate description of the dielectric constant.

For strained hetrojunctions, one must also include the variation of the valence band edge due to the strain [8]. Such variations must be consistent with the band edge deformation potentials one can also calculate and check for bulk materials[16]. For the heterojunction $In_{.15}Ga_{0.85}As$/GaAs strained to GaAs, our predictions are in good agreement with the experimental results. We notably get a VBO equal to +56 meV for the heavy holes and to -15 meV for the light holes [8] when the experiment respectively gives +52 meV and -15 meV. For several other configurations, comparison with available data is quite satisfactory.

In conclusion, we have presented a tight-binding treatment of band offsets for heterojunctions with a common anion. We have shown that

a correct screening of the charge transfer near the interface is necessary in order to get accurate VBO. The accuracy of a zero dipole approximation seems to be of the order of .1 eV, still larger than the one required to simulate a device heterojunction. But to get better accuracy, any model must correctly describe the variation of the dielectric function with the wave vector and also the valence band deformation potentials in the case of strained hetrojunctions.

ACKNOWLEDGEMENT

The Laboratoire des Surfaces et Interfaces is "Unité Associée au Centre National de la Recherche Scientifique No.253".

REFERENCES

1. F. Capasso Band-gap engineering and interface engineering: from graded-gap structures to tunable band discontinuities in Heterojunction band discontinuities: Physics and Device applications, F. Capasso and G. Margaritondo Eds, North Holland, Amsterdam (1987).

2. C.G. Van de Walle and R.M. Martin, Phys.Rev. B35:8154 (1987); D.M. Bylander and L. Kleinman, Phys.Rev. B36:3229 (1987); S. Massida, B.I. Min and A.J. Freeman, Phys.Rev. B35:9871 (1987) ; S.-H. Wei and A. Zunger, Phys.Rev.Lett. 59:144 (1987);

3. S.B. Zhang, D. Tomanek, S. Louie, M.L. Cohen and M.S. Hybertsen, Solid State Commun. 66:585 (1988).

4. J. Tersoff, Phys.Rev. B30:4874 (1984) ; Phys.Rev.Lett. 56:2755 (1986).

5. M. Massida and N.E. Christensen, Phys.Rev. B35:6182 (1987).

6. A. Munoz, J.C. Duran and F. Flores, Phys.Rev. B35:6468 (1987); Phys.Rev. B35:7721 (1987).

7. C. Priester, G. Allan and M. Lannoo, Proc. 15th Intern.Conf. on Physics and Chemistry of Semiconductors Interfaces, J.Vac.Sci. Technol. B4:1290 (1988).

8. C. Priester, G. Allan and M. Lannoo Phys.Rev. (To be published).

9. P. Vogl, H.P. Hjalmarson and J.D. Dow, J.Phys.Chem.Solids 44:365 (1983).

10. F. Guinea, J. Sanchez-Dehesa and F. Flores, J.Phys. C16:6499 (1983); F. Guinea, C. Tejedor, F. Flores and E. Louis, Phys.Rev. B28:4397 (1983).

11. S.L. Cunningham, Phys.Rev. B10:4988 (1974).

12. M. Lannoo and G. Allan, Solid State Commun. 33:293 (1980).

13. W.A. Harrison in Electronic Structure and the Properties of Solids, W.H. Freeman and Company, San Francisco (1980), p.113.

14. C.LK. Shih and W.E. Spicer, Phys.Rev.Lett. 58:2594 (1987).

15. Recent measurements of GaAs/AlAs VBO give 0.49 eV [W.I. Wang, T.S. Kuan, E.E. Mendez and L. Esaki, Phys.Rev. B31:6890 (1985)], 0.45 eV [M. Heiblun, M.I. Nathan and M. Eizenberg, Appl.Phys.Lett. 47:503 (1985)], 0.55 eV [J. Batey and S.L. Wright, J.Appl.Phys. 59:200 (1986)], 0.54 eV [P. Dawson, B.A. Wilson, C.W. Tu and R.C. Miller, Appl.Phys.Lett. 48:541 (1986)] and 0.53 eV [G. Danan, B. Etienne, F. Mollot, R. Planel, A.M. Jean-Louis, F. Alexandre, B. Jusserand, G. Le Roux, J.Y. Marzin, H. Savary, B. Sermage Phys.Rev. B35:6207 (1987)].

16. Tran Minh Duc, C. Hsu and J.-P. Faurie, Phys.Rev.Lett. 58:1129 (1987).

17. J. Menendez, A. Pinczuck, D.J. Wender, J.P. Valladares, T.H. Chiu and W.T. Tsong, Solid State Commun. 61:703 (1987).

18. Landolt-Börnstein: Numerical Data and Functional relationship in Science and Technology, O. Madelung Ed. (Springer-Verlag, Berlin 1982).

Metallization Review

THE THEORY OF SCHOTTKY BARRIERS:

CONTROVERSY OR CONSENSUS?

J. Tersoff

IBM Research Division, T. J. Watson Research Center
Yorktown Heights, NY 10598

INTRODUCTION

During the past decade, the theory of Schottky barrier formation at metal-semiconductor (M-S) interfaces has been viewed as highly controversial. The central issue in this subject[1] is the mechanism causing "pinning" of the Fermi level, whereby the barrier height is only weakly dependent on the metal workfunction, in contrast to the original Schottky[2] model. Review articles on this subject invariably begin by noting the disagreement among workers in the field, regarding even the fundamental mechanisms involved in Fermi-level pinning.

The purpose of this paper is to point out that, in fact, there is a considerable degree of consensus regarding the theory of Schottky barrier formation. Virtually all theorists[3–10] who have considered the question have concluded that, at a M-S interface, the Fermi level is pinned by states intrinsic to the interface. Moreover, this pinning can be described reasonably well by quite simple models, which have shown considerable predictive power.

One alternative view, that the Fermi level is pinned by states associated with native defects at or near the interface, has also gained some acceptance. However, as discussed below, that view has some profound conceptual problems.

This paper begins by attempting to define the scope of the problem, emphasizing the connection with real devices. The history of the theory of Schottky barriers is then briefly reviewed, followed by a sketch of theoretical progress in understanding pinning by intrinsic states of the M-S interface. The connection between the Schottky barrier problem, and the simpler problem of band lineups at semiconductor heterojunctions, is emphasized. Finally, the hypothesis of pinning by defects is examined.

DEFINING THE PROBLEM

Interfaces can be arbitrarily complex and "dirty", with different structures, reaction products, and defects distributed inhomogeneously. This complexity can lead to confusion unless one is careful in defining the problem initially. In particular, a general theory of Schottky barriers cannot and should not attempt to describe all possible interfaces. It is therefore necessary to restrict discussion to those interfaces for which the barrier height is both well-defined and relevant.

It is crucial to bear in mind that the interest in Schottky barriers stems almost entirely from their role in semiconductor devices. In particular, it is the transport of free carriers through the interface which is central. The Schottky barrier is important only because it is a major factor determining this transport.

From this point of view, only a stringently restricted set of interfaces are relevant here. For the Schottky barrier to determine the transport in a simple way, it is necessary that the semiconductor be essentially unperturbed (e.g. no electrically active defects except for intentional doping at ordinary densities) up to the interface. The more complex region at the interface in which the "pinning" of the Fermi level occurs, whether by defects or intrinsic states, must be sufficiently thin as to have little effect on transport other than by determining the band bending. Moreover, the "pinning" and band-bending must be laterally homogeneous.

In practise, these conditions can be checked for real devices by confirming that the transport obeys thermionic emission theory, and that the barriers determined by different methods (I-V, C-V etc) are identical. Unfortunately, in surface-science-type experiments, while the position of the Fermi level may be accurately determined, it is often not feasible to verify directly that the interface has the necessary properties to be of interest.

One must therefore be cautious in interpreting experiments where the Fermi level position is not consistent with that measured in real devices. While such experiments may reveal important effects, their *direct* relevance to Schottky barrier formation is problematic. Many devices end up in the trash, because their interfaces do not meet the conditions described above. It is not such interfaces which a theory attempts to describe, and so we must be equally selective in which experiments we compare with theory.

HISTORY OF THE THEORY OF SCHOTTKY BARRIERS

While the theory of Schottky barriers is often viewed as not only controversial but chaotic, a brief review reveals that there are, at most, two basic views regarding the mechanism of Fermi level pinning. Moreover, if we consider theories advocated by theorists (an admittedly sociological rather than scientific distinction), we see virtually no evidence of controversy.

Table 1 gives a very schematic and incomplete summary of the history of the theory of Schottky barriers. This table lists seminal work,[3–19] in chronological order, in three catagories. The first catagory, shown in the first column and labeled "mainstream theories", consists of work which follows the tradition of focusing on pinning mechanisms *intrinsic to an ideal M-S interface*, neglecting the possible role of extrinsic or collective effects.

The second catagory consists of alternative theories. These can be further divided into two subcatagories. The first two items in this column fall within the spirit of the "mainstream" work, but differ in focusing on the possible role of collective excitations. While intriguing, these qualitative suggestions have not led to specific predictions, and so are not considered further here.

The other two items in this column reflect two truly different views. The proposal of Spicer *et al.*[12] attributes Fermi-level pinning to states of native defects at the interface. The popularity of this proposal is in fact the *only* real reason for considering Schottky barriers controversial. The proposal of Freeouf and Woodall[13] amounts to the original Schottky model, i.e. no pinning of the Fermi level, with the important twist that the appropriate metal workfunction is that of some interfacial phase. However, this theory has not gained significant popularity.

The third catagory lists empirical correlations. These have played a prominent role in the discussion of Schottky barriers. Moreover, their variety (including many not listed here) has contributed to the impression of chaotic controversy in the field. However, these correlations are not theories, in

the sense that they do not propose a microscopic mechanism for Fermi level pinning. They are therefore not discussed further here.

The controversy regarding the mechanism of Schottky barrier formation thus has a very simple statement. There are basically two conflicting views. The first is that Fermi level pinning is an intrinsic property of the M-S interface. The second is that such pinning is an extrinsic effect, associated with native defects at or near the interface. These views are discussed in the sections below.

INTRINSIC MECHANISMS OF SCHOTTKY BARRIERS FORMATION

Any attempt to understand Schottky barrier formation at M-S interfaces must begin by considering the M-S interface itself. For example, the effect of defects at the interface can only be assessed if we know what the behavior the the interface would be in the absence of defects.

Most studies of the M-S interface have necessarily been based on idealized models, leading to relatively simple pictures of barrier formation. However, the accuracy of simple models is a separate question from whether the pinning is intrinsic or extrinsic. While theorists generally agree that the Fermi level is pinned by states intrinsic to the M-S interface, the assumptions involved in calculating this pinning without a microscopic knowledge of the interface structure are more problematic. Nevertheless, some of these simple models are quite successful in predicting the properties of real diodes.[6–8]

Bardeen[3] was the first to point out that surface states in the semiconductor band gap could "pin" the Fermi level, accounting for the relative insensitivity of barrier height to metal workfunction. Heine [4] noted that at a M-S interface, these surface states would be broadened into a continuum. Heine still called these states "surface states", since they are indeed closely related, but they were later called[6] "metal induced gap states" (MIGS).

Louie, Cohen and Chelikowsky[6] performed explicit calculations for ideal interfaces between a model metal and various semiconductors, and obtained barrier heights in good agreement with ex-

Table 1. Schematic history of the theory of Schottky barriers.

date	mainstream theories	other theories	empirical correlations
1947	Bardeen[3]		
1965	Heine[4]		
1969			Kurtin *et al.*[16]
1974		Inkson[14]	Andrews & Phillips[17]
1976	Louie *et al.*[6]	Harrison[15]	McCaldin *et al.*[18]
1977	Tejedor *et al.*[7]		
1978			Brillson[19]
1980		Spicer *et al.*[12]	
1981		Freeouf & Woodall[13]	
1984	Tersoff[8]		
1986	Harrison & Tersoff[9]		
1987	Lefebvre *et al.*[10]		

periment. They also inferred, less directly, the pinning strength, i.e. the degree of dependence on the metal workfunction, and again found good agreement with experiment. These calculations demonstrated that an idealized model interface has properties which are very similar to real Schottky barriers, and put the Bardeen/Heine picture on a quantitative footing.

By considering an even more idealized picture, Tejedor and Flores[7] were able to isolate the essential ingredient in Fermi-level pinning. The MIGS tend to pin the Fermi level at the "neutrality point" of the interface, to maintain local charge neutrality in the semiconductor in the region where MIGS have significant amplitude (a couple of atomic layers at the interface). Moreover, this neutrality point falls, at least within a simple one-dimensional model, essentially in the center of the semiconductor band gap.

Unfortunately, this insightful work received little attention at the time. However, these same principles were later discovered independently by the present author,[8] who also proposed a very simple technique for calculating the "neutrality point" from the bulk semiconductor bandstructure. The resulting predictions, which involve no adjustable parameters whatever, are in excellent agreement with measured barrier heights at gold contacts for all group IV and III-V semiconductors, with an accuracy of about 0.1 eV.

Further work by this author[20] provided a simple and reasonably accurate estimate of the "pinning strength" in terms of the bulk dielectric constant, and provided a very intuitive understanding of where the "neutrality point" falls in the band gap. In addition, at least two groups have reformulated the theory in a tight-binding approach,[9,10] whose great simplicity permits additional insight into the mechanism of pinning at ideal M-S interfaces.

It may be surprising that a model which neglects the structure of the interface should be so successful in calculating barrier heights. One possibility is that, while the barrier height may be somewhat structure-sensitive, the disorder present in real interfaces results in an averaging out of this dependence. For example, Sanchez-Dehesa *et al.*[21] found in tight-binding calculations that, if Ag on GaAs(110) is assumed to bond only to Ga or only to As, the resulting barrier heights differ by ± 0.2 eV. In a real interface, Ag presumably bonds to both types of atoms, and this sensitivity is lost.

Thus natural extensions of the Bardeen/Heine picture, considering only features intrinsic to any M-S interface, are able to account for both Fermi-level pinning at M-S interfaces, and the quantitative dependence of the barrier upon metal and semiconductor. This can be done either through microscopic calculations or simple models, with similar results.

It might seem strange that such a successful model should be controversial. However, experimental advances have increasingly focused attention upon the possible role of the microscopic structure of the interface, including effects of reaction products, defects, etc, and in particular upon the initial stages of barrier formation at submonolayer metal coverage. Since the traditional view was formulated strictly within an idealized interface model, its relevance to these questions was unclear, leading to some skepticism.

While it is not possible to address all of these complex issues, many of which are not entirely understood, one example suffices to demonstrate the risks of using poorly understood experiments to criticize the idea of intrinsic Fermi-level pinning at M-S interfaces.

Experiments at low metal coverage were originally interpreted[12] as inconsistent with the ideas of Heine[4] and Louie *et al.*,[6] because they showed Fermi level pinning when much less than a monolayer of metal is present. On the basis of a variety of experiments,[26–28] however, it is now understood that in that early work a metal was in fact present. The deposited atoms clustered at room temperature, and inhomogeneous pinning by those metal clusters suffices to explain the observed behavior. In fact, individual metal atoms exhibit completely different behavior, which is fascinating, but which has no obvious relevance to real interfaces. Moreover, pinning consistent with real interfaces

appears to begin simultaneously with the onset of metallic character in the overlayer. This has been interpreted[27,28] as evidence for pinning by MIGS.

THE CONNECTION BETWEEN SCHOTTKY BARRIERS AND HETEROJUNCTION BAND LINEUPS

A major obstacle in studying Schottky barriers directly is that the M-S interface is in most cases structurally complex, and relatively inaccessible spectroscopically. However, to the extent that the Schottky barrier problem is closely related to other simpler problems, studying the latter may shed light on the former.

The interface between two semiconductors is in many ways closely analogous to the M-S interface. Both interfaces have important device applications. In both, the difficult problem, both experimentally and theoretically, is to determine the lineup of the two bandstructures at the interface. For Schottky barriers, this reduces to knowing the position of the metal Fermi level relative to the semiconductor band edges at the interface. For heterojunctions, the analogous problem is to determine the lineup of the respective band edges at the interface. This problem, like that of Schottky barriers, has been analysed in considerable detail.[29]

It was theoretically predicted, from fairly general considerations, that there should be a close connection between the band lineup at semiconductor heterojunctions, and the Schottky barrier heights at intrinsically-pinned metal interfaces with the respective semiconductors.[22] Specifically, the band lineup for lattice-matched heterojunctions can be obtained by aligning the energy at which the Fermi level is pinned in diodes formed from the respective semiconductors.

Thus the conduction band offset, for example, would equal the different in barrier heights for Au contacts on the two n-type semiconductors. This prediction was subsequently verified experimentally,[29] and although it requires no calculation, it has proven to be one of the most accurate methods available for predicting band offsets.

This very close connection between band lineups and Schottky barrier heights places severe constraints on theories of either phenomenon. In particular, for heterojunctions it is well known that defects play no role in determining the band offset.[29] Thus heterojunction band offsets are recognized to be an intrinsic property of the interface. It is difficult to see how these offsets can agree so quantitatively with Schottky barrier heights, both for group IV and III-V semiconductors, unless the Schottky barrier is also an intrinsic property of the semiconductor interface.

It is worth also mentioning a third related problem, that of transition-metal (TM) impurity levels in semiconductors. A recent analysis shows[30] that TM impurity levels (of T_2 symmetry) have their position in energy in the semiconductor band gap "pinned" by an electrostatic mechanism which is closely analogous to that at M-S interfaces and heterojunctions. This explains[30] the earlier observations that such impurity levels correlate closely with measured Schottky barrier heights[31] and heterojunction band lineups.[32] Thus the correlation between calculated defect levels and measured Schottky barrier heights does not imply any causal relationship, as has been argued.[33]

EXTRINSIC PINNING: THE ROLE OF DEFECTS

As discussed above, the intrinsic properties of the ideal M-S interface lead to Fermi level pinning, with a position and strength which is quantitatively consistent with experiments on real devices. Nevertheless, at real interfaces one must expect some deviations from ideality, including native or extrinsic defects, and these will of course have some effect on the barrier height.[1]

However, Spicer and coworkers[12] proposed that in fact native defects are the actual primary cause of Fermi-level pinning, at least in the case of GaAs and a few other III-V semiconductors. This

view has gained considerable popularity, and has been elaborated and extended to include all semiconductors by Allen, Dow, and coworkers.[33]

It would be beyond the scope of this paper to criticize the specific details of models proposed for pinning by native defects. However, all of these models share a very fundamental problem. Proposals of pinning by defects invariably begin by *neglecting* the pinning which is *already present* at the M-S interface. Thus defect models contain an *implicit* assumption, which is rarely stated, that the Fermi level would not be pinned at a M-S interface, were defects not present.

However, virtually no proponent of defect pinning has explicitly argued that the Fermi level is not pinned at a defect-free M-S interface; instead, they have simply neglected this fundamental issue. I know of only two exceptions. Harrison initially argued[23] that pinning at the M-S interface was negligible; but he subsequently recognized that this was incorrect,[9] and that defects must play at most a minor role. Duke and Mailhiot[24] described a simple model for a M-S interface in which there was no Fermi-level pinning. However, the absence of pinning was built into the model, by the use of a completely local energy functional, and so the model has nothing to say on this issue.

The hypothesis that defects are responsible for Schottky barrier formation must be viewed as unscientific, if it relies on intentionally ignoring the pinning which is universally agreed to already exist at the ideal M-S interface. If, alternatively, advocates of this view wish to argue that the defect-free interface is in fact unpinning, or that defects will generally overwhelm any prior pinning, then this argument must be made explicit, and supported with concrete evidence, whether theoretical or experimental.

In addition, a defect model has little predictive value until the number and spatial distribution of defects are specified. It is particularly important to know whether the defects are concentrated right at the interface, or spread over a substantial region.

If the defects are spread over some distance, they can be treated as dopants in the usual way. In this case, defects certainly do not determine the Fermi level position *at the interface*. Then we must still know what if any pinning takes place right at the interface, in order to determine the barrier profile and transport characteristics of the interface in the presence of these defects. Moreover, such a distribution can lead to unacceptable device characteristics. For example, depending on the detailed distribution, barriers for n- and p-type doping generally will not add up to the band gap, and C-V measurements will be distorted by the excess capacitance associated with these deep levels. We can therefore restrict consideration to models which have the defects concentrated very near the interface.

It is well known[3] that, at a semiconductor surface, a hundredth of a monolayer of states is more than sufficient to pin the Fermi level. Originally, the idea of pinning by defects was attractive in part because it seemed very reasonable that a small number of defects would be present at any M-S interface, and could account for the observed pinning.

However, more careful analyses[24,25] reveal that, at a metal-semiconductor interface, because of screening by the metal, the number of defects required to pin the Fermi level approaches a monolayer, depending on the specific assumptions. Moreover, these analyses completely neglect the fact that the Fermi level is already pinned at the M-S interface, so they still overestimate the effect of defects. Including this fact would presumably render even large number of defects relatively ineffective in pinning the Fermi level.

Finally, the defect model as applied in practise generally relies on identifying the Fermi level position with the energy level of a defect. Such an identification is certainly not always valid. For example, a major point of the original defect model[12] was the observation of two distinct pinning positions, for n- and p-type GaAs, as metals were deposited. The two positions were taken to correspond to a donor and an acceptor level. However, it now appears likely[26–28] that these distinct levels were merely due to incomplete pinning by metal clusters, and have no physical significance.

REBUILDING A CONSENSUS

Because of the complexities of real interfaces, Fermi level pinning may at worst reflect a morass of competing effects. However, to understand what is happening at a fundamental level, it is obviously desirable to focus on well-characterized systems and well-posed questions.

Theorists, by focusing on a relatively well-defined although limited question, the pinning intrinsic to the "ideal" M-S interface, have attained a striking unanimity of opinion, despite the vaunted controversiality of the field. At the same time, experiment in this field has to a striking extent focused on the regime of low metal coverage, where the interface is spectroscopically accessible. As this avenue of investigation matures, it appears to be leading also to a consensus regarding Schottky barrier formation.

Much of the impetus for the defect model originally came from experiments in this low-coverage regime. Regardless of its conceptual shortcomings, that model offered a framework for understanding these early experiments, which theories of the ideal M-S interface alone did not. However, the low-coverage regime has proven to be more complex than was originally recognized, and this complexity no doubt played a large role in generating the current level of controversy.

However, recently several authors have found that, by controlling clustering at the surface, they obtained much more interpretable results.[26–28] The clustering can be controlled either through the metal reactivity, or through the substrate temperature.

In either case, the result is striking. At very low coverage, isolated metal atoms act as donors, in a manner which bears little resemblance to real interfaces. Then, at a coverage which apparently corresponds to the onset of metallic behavior, the Fermi level abruptly shifts to its final pinned position,[27,28] which agrees well with the position obtained for real devices.

Understanding the abrupt transition with coverage will presumably give additional insight into the pinning mechanism, and has already been interpreted by several groups[27,28] as supporting the traditional view of pinning by states intrinsic to the M-S interface (MIGS).

The experimental situation is evolving rapidly at present, and it is too early to draw definitive conclusions. However, it appears that a more complete experimental understanding of the low-coverage regime is leading back to the same conclusions reached by theorists considering ideal interfaces. Thus the consensus regarding the mechanism of Schottky barrier formation, which was shattered a decade ago, may already be in the process of rebuilding.

REFERENCES

1. For a brief review, see for example M. Schluter, Thin Solid Films *93*, 3 (1982); or W. Mönch, in *Festkörperprobleme: Advances in Solid State Physics*, ed. P. Grosse (Vieweg, Braunschweig, 1986), Vol. 26, p67.
2. W. Schottky, Phys. Z. *41*, 570 (1940).
3. J. Bardeen, Phys. Rev. *71*, 717 (1947).
4. V. Heine, Phys. Rev. *A138*, 1689 (1965).
5. F. Yndurain, J. Phys. C *4*, 2849 (1971).
6. S. G. Louie and M. L. Cohen, Phys. Rev. B *13*, 2461 (1976); S. G. Louie, J. R. Chelikowsky, and M. L. Cohen, Phys. Rev. B *15*, 2154 (1977).
7. C. Tejedor, F. Flores and E. Louis, J. Phys. C *10*, 2163 (1977).
8. J. Tersoff, Phys. Rev. Lett. *52*, 465 (1984). For a more complete tabulation of results, see also Phys. Rev. Lett. *56*, 2755 (1986).
9. W. A. Harrison and J. Tersoff, J. Vac. Sci. Technol. B *4*, 1068 (1986).
10. I. Lefebvre, M. Lannoo, C. Priester, G. Allan, and C. Delerue, Phys. Rev. B *36*, 1336 (1987).

11. See for example J. E. Rowe, S. B. Christman, and G. Margaritondo, Phys. Rev. Lett. *35*, 1471 (1975).
12. W. E. Spicer, P. W. Chye, P. R. Skeath, C. Y. Su, and I. Lindau, J. Vac. Sci. Technol. *16*, 1422 (1979); W. E. Spicer, I. Lindau, P. R. Skeath, C. Y. Su, and P. W. Chye, Phys. Rev. Lett. *44*, 420 (1980); W. E. Spicer, Z. Liliental-Weber, E. Weber, N. Newman, T. Kendelewicz, R. Cao, C. McCants, P. Mahowald, K. Miyano, and I. Lindau, J. Vac. Sci. Technol. B *6*, 1245 (1988).
13. J. L. Freeouf and J. M. Woodall, Appl. Phys. Lett. *39*, 727 (1981).
14. J. C. Inkson, J. Vac. Sci. Technol. *11*, 943 (1974).
15. W. A. Harrison, Phys. Rev. Lett. *37*, 312 (1976).
16. S. Kurtin, T. C. McGill, and C. A. Mead, Phys. Rev. Lett. *22*, 1433 (1969).
17. J. M. Andrews and J. C. Phillips, Phys. Rev. Lett. *35*, 56 (1975).
18. J. O. McCaldin, T. C. McGill and C. A. Mead, Phys. Rev. Lett. *36*, 56 (1976).
19. L. J. Brillson, Phys. Rev. Lett. *40*, 260 (1978).
20. J. Tersoff, Phys. Rev. B *32*, 6968 (1985).
21. J. Sanchez-Dehesa, J. D. Dow, and F. Flores, Bull. Am. Phys. Soc. *29*, 334 (1984).
22. J. Tersoff, Phys. Rev. B *30*, 4874 (1984).
23. W. A. Harrison, J. Vac. Sci. Technol. B *3*, 1231 (1985). See however Ref. 9 above for a subsequent re-evaluation.
24. C. Mailhiot and C. B. Duke, Phys. Rev. B *33*, 1118 (1986).
25. A. Zur, T. C. McGill, and D. L. Smith, Phys. Rev. B *28*, 2060 (1983).
26. S. Doniach, K. K. Chin, I. Lindau, and W. E. Spicer, Phys. Rev. Lett. *58*, 591 (1987).
27. M. Prietsch, M. Domke, C. Laubschat, and G. Kaindl, Phys. Rev. Lett. *60*, 436 (1988).
28. K. Stiles and A. Kahn, Phys. Rev. Lett. *60*, 440 (1988).
29. J. Tersoff, in *Heterojunction Band Discontinuities: Physics and Device Applications*, Ed. F. Capasso and G. Margaritondo, North-Holland 1987; and references therein.
30. J. Tersoff and W. A. Harrison, Phys. Rev. Lett. *58*, 2367 (1987).
31. J. Tersoff, Phys. Rev. Lett. 56, 675 (1986).
32. J. M. Langer and H. Heinrich, Phys. Rev. Lett. *55*, 1414 (1985).
33. Much of this work is cited and summarized by O. F. Sankey, R. E. Allen, S. Ren, and J. D. Dow, J. Vac. Sci. Technol. B *3*, 1162 (1985).

METALLIZATION OF SEMICONDUCTOR SURFACES AS A FUNCTION OF COVERAGES

G. P. Srivastava[‡]* and Inder P. Batra[†]

[‡]Physics Department, University of Ulster, Coleraine, N. Ireland BT52 1SA, U.K.
[†]IBM Research Centre K33/801, San Jose, California 95120, U.S.A.

INTRODUCTION

When a metal is deposited on a semiconductor surface, various kinds of interaction take place between the metal and the semiconductor and as a result quite often there are generated occupied states in the energy band gap of the semicondor. The Fermi level is then said to be pinned in the band gap of the semiconductor and is considered to be an important property of metal-semiconductor systems. Two types of Fermi level pinning are possible:
(i) The position of the Fermi level above the valence band edge is the same for both n- and p- types of a semiconductor in contact with a given thickness of metal overlayer.
(ii) There is no change in the Fermi level position with increase in metal coverage (a few layers at most) on a given semiconductor.
In this review we will be concerned with the second type of pinning.

The position of the Fermi level can shift with increasing metallic coverage, because the nature of interaction between metal and semiconductor is coverage dependent. At some critical coverage (may or may not be achievable experimentally) the overlayer metallizes. In such a situation the position of the Fermi level for the (thick) metal in contact with the semiconductor lies in the band gap of the semiconductor and one speaks of the Schottky barrier $\Phi^n{}_B$ as the energy difference between the conduction band edge of the semiconductor (n-type) and the Fermi level of the metal. If the Fermi level is completely pinned (no movement with metal coverage) by the introduction of a very small amount of metal then intrinsic surface states, defects and/or metal clustering are likely mechanisms for the pinning. We will discuss a case where intrinsic surface states are indeed responsible for the Fermi level pinning. On the other hand, we shall show that for Al-Ge the nature of the states determining the Fermi level continues to evolve until the overlayer metallization sets in around a monolayer coverage.

---

* Present address: Department of Physics, University of Exeter, Stocker Road, Exeter EX4 4QL, U.K.

WHAT IS MEANT BY METALLIZATION?

The density of states at the Fermi level usually increases with the amount of metal coverage on the semiconductor surface. When there is sufficient increase in the density of states at the Fermi level such that, for example, 'Fermi-edge photoemission' can be observed, we speak of 'metallization' of the metal-semiconductor system. Another signature is the appearance of plasma losses but an unambiguous identification of these requires an extremely careful analysis. The metallization of the overlayer should be distinguished from the metallization of the semiconductor surface where the Fermi level position is determined by partially occupied intrinsic surface states as proposed by Bardeen in 1947. The overlayer metallization will eventually stabilize the Fermi level required for the traditional view of Schottky barrier formation. Thus the phenomena of Fermi level pinning in the semiconductor band gap and Schottky barrier formation can be said to be linked via the concept of overlayer metallization.

In order to substantiate the aforementioned we produce evidence that Fermi level position is highly dependent on metal coverage θ (measured in monolayer) on a semiconductor surface. We suggest that for $\theta < \theta_c$, where θ_c is of the order 0.5 , the Fermi level is determined mainly by defect induced states and residual surface dangling bond states. For $\theta_c \leq \theta \leq 1$ residual surface states and chemical bonds between the metal and the semiconductor play a dominant role in determining the Fermi level. In this limit of the coverage the metal-semiconductor interaction may produce metallization of the semiconductor surface (partially occupied surface states). For $\theta > 1$ overlayer-overlayer interaction becomes quite important and metal-induced-gap-states (MIGS) play a very important role in Fermi level pinning. Such an effect can be evidenced by a big increase in the density of states at the Fermi level, and produces the onset of metallization of the overlayer. In general, for a given coverage it is possible that two or more factors can jointly control Fermi level pinning. Only in the high coverage limit ($\theta > 1$) one can realize the traditional view of Schottky barrier formation on a defect free semiconductor surface with no surface states in the band gap.

SUMMARY OF EXPERIMENTAL RESULTS

We first review some interesting experimental results for Fermi level position as a function of metal coverage θ on semiconductor surfaces.

Metal / IV Semiconductors

Fig. 1 shows the high resolution electron energy loss (HREEL) spectra for Si(111)7x7-(Al,In) for different coverages θ of (Al,In) [1]. The clean surface ($\theta = 0$) exhibits a large density of surface states inside the forbidden gap of Si. For $\theta < 0.1$ the density of gap states is reduced to zero, indicating that the surface states at the Fermi level are removed completely. For the range of coverages $0.1 \leq \theta \leq 1$ there is evidence of reappearance of the Fermi level in the gap. For $\theta > 1$ the Fermi level pinning is suggested to be due to the formation of MIGS, leading to metallic character of the overlayer.

Metal / III-V Semiconductors

Fig. 2 shows the position of the Fermi level in the gap of n- and p-GaAs(110) as a function of (Al,Au) coverage at room temperature and low temperature determined from soft-X-ray photoelectron spectroscopy

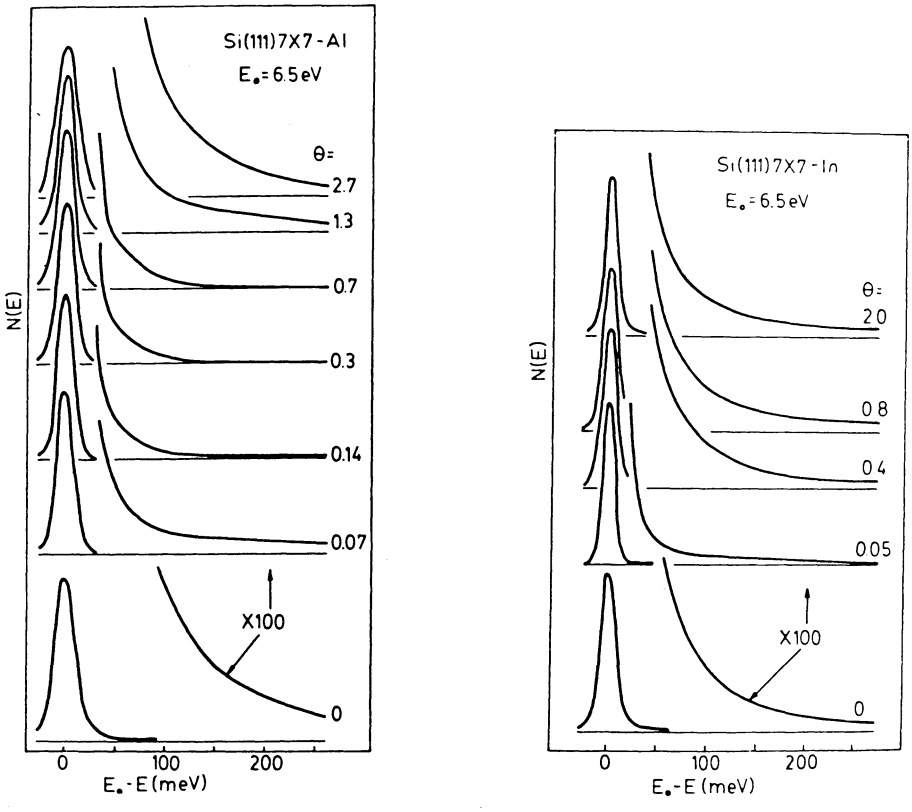

Figure 1. HREEL spectra for Si(111)7x7 - (Al,In) wi0th different coverages θ. The asymmetric tail of the primary peak disappears for low θ and is restored at θ ≈ 1 (Kelley et al [1]).

(SXPS) [2]. A few observations can be made from this study:

(i) The Fermi level is a well defined concept even for a very low coverage (θ as low as 0.01). However, the position of the Fermi level changes with increasing θ.

(ii) Both for simple metals (e.g. Al) and noble metals (e.g. Au) the movement of the Fermi level position with coverage θ on n- as well as p-GaAs is symmetric at room temperature and asymmetric at low temperature.

(iii) In general for $0 < \theta < 1$ the low temperature movement of the Fermi level on n-GaAs is considerably slower compared to that at room temperature. The low temperature results tend to merge into the room temperature results for $\theta \geq 1$.

(iv) The initial (low θ) movement of the Fermi level on p-GaAs is more rapid at low temperature than at room temperature, with the low temperature results merging into the room temperature results for $\theta \geq 0.5$.

(v) The difference between the room temperature and the low temperature results could be considered mainly to be due to different rates of defect formation at the interface, adatom-substrate bonding, adatom clustering, and interdiffusion.

(vi) The asymmetry of the Fermi level movements on the low temperature n- and p- substrates indicates that the Fermi level position is controlled by more than one specific mechanism, specially at low coverages ($\theta < 1$).

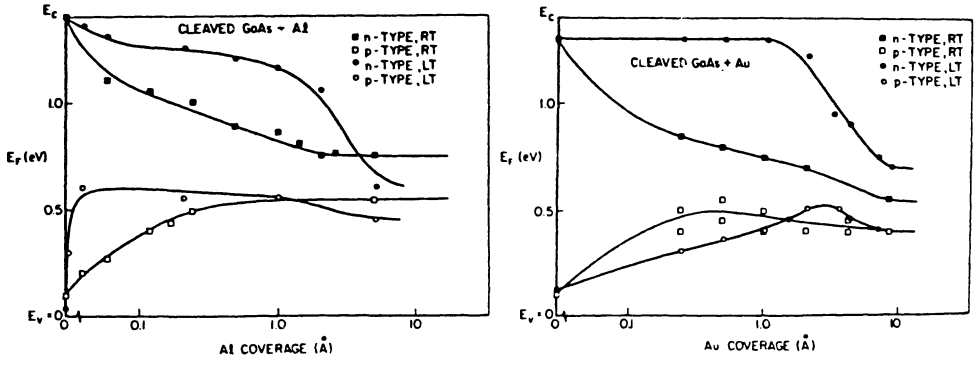

Figure 2. Fermi level position in the gap of n- and p- GaAs (110) as a function of Al and Au coverages at room temperature and low temperature (Stiles et al [2]).

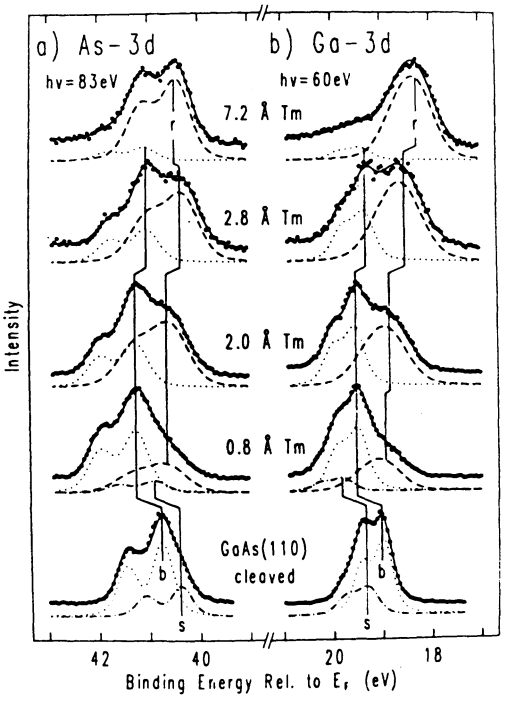

Figure 3. Abrupt changes in As - 3d and Ga - 3d core-level photoemission spectra of p-GaAs(110) - Tm as a function of Tm coverage. b and s represent, respectively, signals from the bulk GaAs and substrate surface atoms. r represents spectra originated from atoms in reacted phases (Priestsch et al [3]).

Detailed photoemission studies (Fig. 3) of the GaAs(110)-Tm interface by Prietsch et al [3] give clear evidence of an abrupt change in the Fermi level position for $\theta = 1$, suggesting that for that coverage the overlayer assumes metallic character and the Schottky barrier is fully established.

Metal/II-VI Semconductors

In general metals exhibit significantly more pronounced chemical reactions when deposited on II-VI semiconductors than on III-V's [4]. Thus, while most metal/IV and metal/III-V systems exhibit Schottky barrier height variation within a range of around 0.4 eV, metals on II-VI compounds yield a wide range of Schottky barrier heights [5].

THEORETICAL MODELS FOR FERMI LEVEL PINNING AND SCHOTTKY BARRIER FORMATION

Most of the theoretical models put forward for Fermi level pinning and Schottky barrier formation at metal-semiconductor contacts can be arranged into three categories:

(A) Generalized Bardeen model, (B) Inkson's many body theory, (C) Schottky model.

We briefly review some of these models and point out the limits of their assumptions and applicability. A detailed review of the subject is presented by Flores and Tejedor [6].

(A) Generalized Bardeen Model

A number of different theories can be grouped into this model:

(1) Intrinsic surface states — Bardeen's original model

Bardeen [7] proposed that the Fermi level is pinned in the band gap of a semiconductor by surface states, either intrinsic or extrinsic, regardless of the nature of the metal deposited on the surface. The Schottky barrier is formed when the Fermi energies of the bulk semiconductor and the bulk metal align with the Fermi level pinning at the interface.

It is now well known that cleaved surfaces of many semiconductors, especially most III-V surfaces, do not have any appreciable density of surface states in the band gap. However, metal deposition may remove surface relaxation appreciably to bring intrinsic surface states back into the band gap.

(2) MIGS — Heine's model

Heine [8] considered the situation of a thick metallic slab in contact with a semiconductor. In order to maintain continuity at the interface metal wave functions extend (or tunnel) into the semiconductor and thus give rise to metal-induced-gap-states (MIGS). This model, therefore, requires an ideal bulk like situation on both metal and semiconductor sides, and an abrupt interface. A real metal-semiconductor interface may not be abrupt, and it is also possible that there is an interplay between MIGS and interface or step states.

The metal wavefunctions tunnelling into the semiconductor gap induce a dipole D at the interface. Tejedor et al [9] estimated that D can be given by

$$D = \frac{(E_F - \Phi_0)}{S} \qquad (1)$$

where **S** is a parameter related to the dilectric constant of the semiconductor [10], and Φ_0 is the semiconductor charge neutrality level. Tersoff [11] has suggested that the neutrality level can be taken as the cation-substitutional transition metal impurity energy level in the semiconductor.

(3) Unified defect model — Spicer's model

From a range of experimental results performed with highly controlled deposition of clean metals on atomically clean cleaved semiconductor surfaces, it has become clear that the simple geometrical models of totally ordered and atomically abrupt interface is not particularly appropriate for many situations [12,13]. Further, the position of the Fermi level does not depend very much on the metal deposited on III-V semiconductors. This led Spicer et al [12,14] and Williams [13] to suggest that the existence of defects near a metal-semiconductor interface can, in many cases, dominate Fermi level pinning and that MIGS are of less importance. Support for this hypothesis comes from the theoretical calculations of defect levels in the band gap of a number of semiconductors [15-17].

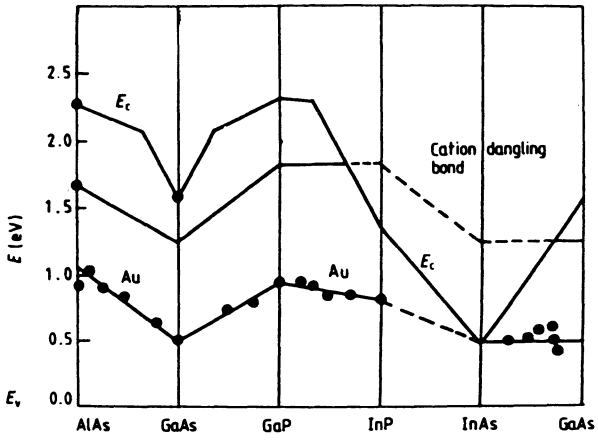

Figure 4. Trend for cation dangling-bond level (full curve) for various III-V semiconductors and their alloys and the Fermi level for Au contact on those semiconductors (dashed curve) (Sankey et al [19]).

Not only simple defects, such as a vacancy, but a whole range of complicated defects (including antisites), impurities and defect-impurity complexes can be created at metal-semiconductor contacts. Thus a wide range of Fermi level positions (presumably within a narrow energy width) can be accommodated by the defect model. Also, one can safely include metal-semiconductor compound formation as a part of the unified defect model. Such microscopic interactions at the interface, which can be introduced by the energy released from metal atoms aggregate, are considered to be more relevant than bulk thermodynamic parameters of either the metal or the semiconductor [18].

Presence of void, vacancy, or disorder at the interface can also create dangling bonds, which can be cation, anion, or antisite derived. Reactive and nonreactive metals are most likely to produce, respectively, "intrinsic dangling bonds" (due to vacancies) and "antisite dangling bonds" (due to antisite defects). Sankey et al [19]

have shown that the calculated levels for both intrinsic cation derived dangling bonds and antisite dangling bonds follow the trend of the Fermi level energy for Au contact on a number of n-type III-V semiconductors and their alloys (Fig. 4). These authors also suggest that the anion dangling bond state would determine the Fermi level position in p-type III-V's.

(4) Concomitant-mechanism model

It is now believed that several mechanisms of generalized Bardeen type can jointly control the pinning of Fermi level at metal-semiconductor interfaces. For example, Monch [20] has successfully explained the chemical trends of the Schottky barrier heights for metal- and silicide-silicon contacts by considering both MIGS and defect levels. It is suggested by Monch that if the density of defects at metal- and silicide-silicon interfaces drops approximately below 10^{13} cm^{-2} then the Schottky barrier is determined by the MIGS model. For highly defective interfaces the MIGS model is expected to explain the Schottky barrier height when all the defects are either charged or neutral (Fig 5). Another support comes from the experimental work of Stiles et al [2] who suggest that an explanation of low temperature barrier formation at metal-GaAs would require involving several independent but concomitant mechanisms.

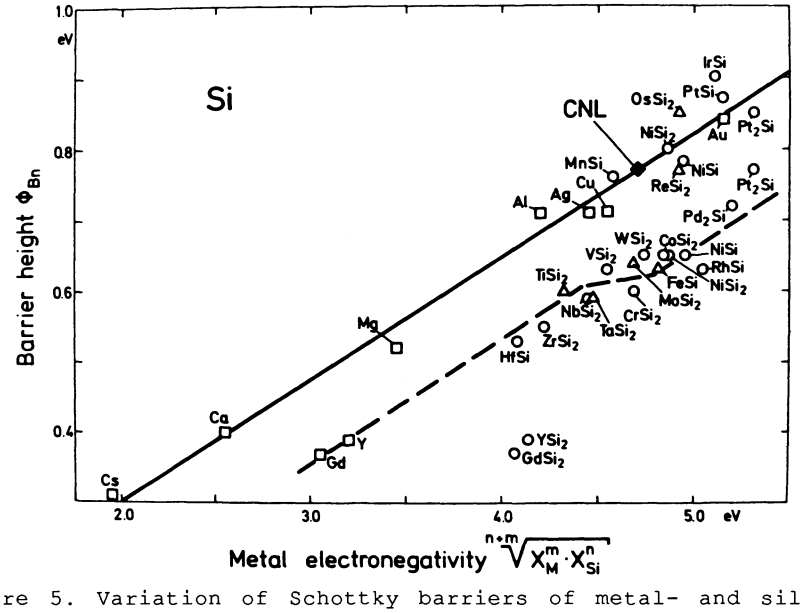

Figure 5. Variation of Schottky barriers of metal- and silicide-silicon with the effective Miedema electronegativities. Such a correlation reveals that both MIGS and defects are needed to explain the complete set of experimental data (Monch [20]).

It would be worth pointing out that in general the MIGS and other interface theories would require a thick metal overlayer, while theories related to defects or dangling bonds can be realized for submonolayer thickness of adatoms.

(B) Inkson's many body theory

Inkson [21] proposed that the behaviour of electrons at a metal-semiconductor interface requires a many body approach. According to this proposal, many body effects produce different screening of the valence and conduction bands of the semiconductor near the interface. This causes the valence band to bend up and the conduction band to bend down, with the Fermi level pinning established due to eventual narrowing of the semiconductor band gap at the interface. However, using an identical screening potential for both the valence bands and conduction bands, Louie and Cohen [22] concluded from a self-consistent calculation that there is no narrowing of the band gap near the jellium Al-Si interface. The many body theory of Fermi level pinning has yet to be supported by other theoretical or experimental works.

(C) Schottky model

(1) The original Schottky model

The classical (macroscopic) model of Schottky [23] assumes an ideal metal-semiconductor interface, with no surface or induced interface states in the band gap of the semiconductor. Schottky proposed that charge transfer takes place between the semiconductor and metal, which results in a depletion layer in the semiconductor and a common Fermi energy in the metal-semiconductor system. Accordingly, there develops an electrical barrier (called Schottky barrier) for electrons given by

$$\Phi_B^n = W - \chi \qquad (2)$$

where $\Phi^n{}_B$ is the Schottky barrier height for an n-type semiconductor, **W** is is the metal work function, and χ is the electron affinity of the semiconductor. Thus for a given semiconductor $\Phi^n{}_B$ should have a linear variation with the metal work function **W**. As is now well known, this relationship is violated for most IV, III-V, and II-VI semiconductors. However, eq. (2) seems to account well for measured Schottky barrier heights for nonreactive metals (e.g. Au and Ag) on GaSe – a layered material which is relatively free of defects.

(2) The effective work function model

A modified version of the Schottky approach – called the effective work function model – has been suggested by Freeouf and Woodall [24]. This model considers a mixture of microclusters of different interface phases resulting from either oxygen contamination or metal-semiconductor reactions which occur during metal deposition. Accordingly the Fermi level at the interface is related to the work functions of the microclusters. Eq. (2) is thus modified to

$$\Phi_B^n = W_{eff} - \chi \qquad (3)$$

where W_{eff} is an appropriate weighted average of the work functions of the different interface phases.

The concept of metal work function used in the Schottky model would require a bulk like situation on the metal side of the contact (i.e. thick overlayer of metal adatoms).

THEORY OF METALLIZATION

In the previous sections we have pointed out that the initial stages of barrier formation at metal-semiconductor contacts are generally

associated with the role of defects, dangling bonds, and chemisorbed bonds and require submonolayer coverages of metal adatoms. On the other hand, the Schottky barrier formation can be realized for semiconductor interfaces with thick metal overlayers. One fundamental question raised recently in a critical review of the subject [18] is: "to what extent the Fermi level position measured at submonolayer coverages has any relevance for the barrier height at thick metal coverages, independent of the fact that the measured value is often the same". In our view the two limits of the barrier formation can be bridged by the concept of metallization. In this section we are most concerned with an understanding of metallization as a function of coverages θ.

The phenomenon of metallization can be understood at two levels: metallization of the semiconductor surface and metallization of the metal overlayer. Here we present evidence of both types of metallization, discuss their origin, and describe factors which control their relative strength.

(i)Alkali metal/semiconductor : Metallization of substrate?
A thorough investigation of alkai metal/semiconductor interfaces will be presented in a number of contributions in this workshop. Here we present a critical assessment from the point of view of bonding and metallization. The concept of substrate metallization is somewhat controversial. This can best be described by considering adsorption of alkali metal atoms on semiconductor surfaces [25-29].

The experimental work (photoelectron spectroscopy and LEED) of Murata and co-workers [25,26] proposes that at high coverages chemisorption of K on Si(001) 2x1 and Cs on Si(111)2x1 is due to a weak attractive Coulomb interaction between partially ionized alkali metal atoms and partially negatively charged Si surface atoms. At a monolayer coverage the alkali metal atoms form 1D metallic chains, leading to Mott-type insulator-metal transition in the adlayer. Whereas at low coverages the valence electrons of alkali metal atoms are transferred into the vacant surface states of Si, at high coverages such a transfer is inhibited by the depolarization force. The coverage dependence of the interaction between the adatoms and the substrate is reflected in the behaviour of the work function which decreases steeply at low coverages, goes to a minimum, and then increases with increasing metal coverage. The SEXAF measurements of Soukiassian [29] for K/Si(100)2x1 also suggest that the K-Si bond is weak. However, valence band studies suggest a covalent K-Si bond.

To understand the microscopic nature of bonding between alkali metal and Si surface first-principles band structure calculations have been carried out by Ishida et al [27] and Ciraci and Batra [28] for K/Si(001)2x1. Ishida et al employed a non-empirical LCAO-X_α method and used the K-Si distance equal to the sum of the K and Si atomic radii. Ciraci and Batra used a repeated slab geometry and norm-conserving nonlocal pseudopotentials, and performed the self-consistent field calculations within the frame work of the local density functional theory. Ciraci and Batra determined the equilibrium position of the K atom on the Si(001) 2x1 surface by using the total energy method.

The reconstructed Si(001) - (2x1) surface, with asymmetric dimer model is known to be a semiconductor [30]: two dangling bond bands, D_1 and D_2 separated by a gap, appear in the fundamental band gap of silicon. The band structure of Si (001)(2x1) - K, with a monolayer

coverage of potassium [θ = 1, i.e. one K atom per (2x1) surface unit cell] in the Levine structure [31], is shown in Fig. 6(a) (after Ishida et al) and Fig. 6(b) (after Ciraci and Batra). In general, there are three surface derived states in and/or around the band gap of Si (labelled a, b, c in Fig. 6(a); and D_1, D_2, R in Fig. 6(b)). A detailed discussion on the nature of the states (a,b,c) or (D_1, D_2, R) is presented in this workshop by Tsukada and Shima, and by Ciraci and Batra. The main observation is that the dangling bond states D_1 and D_2 do not significantly change their position and dispersion upon the adsorption of K. However, the surface becomes metallic with the Fermi level crossing the band D_2.

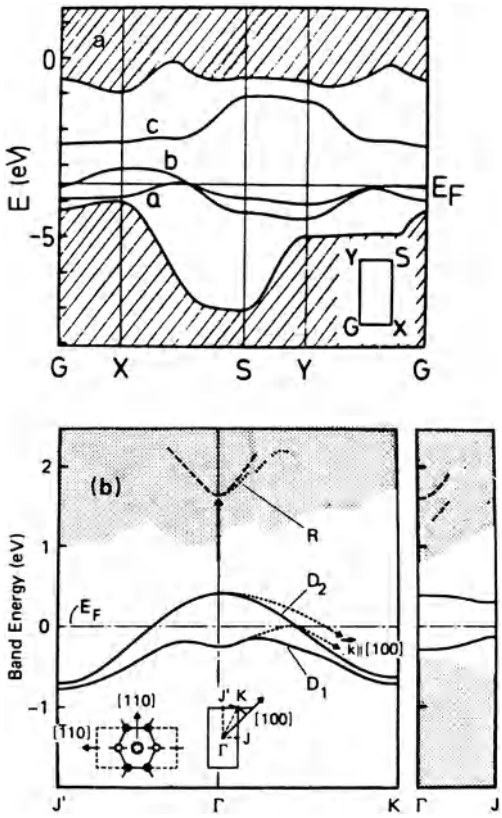

Figure 6. Calculated energy band structure of Si(001)2x1 - K for θ = 1: (a) after Ishida et al [27] using a LCAO-X_α method, (b) after Ciraci and Batra [28] using the pseudopotential method. The states (a,b,c) or (D_1, D_2, R) are silicon surface derived. Dotted curves in (b) show gap states for the clean Si surface.

Ishida et al have shown that the a -> b inter-surface-band plasmon mode reproduces the observed angle-resolved electron energy loss spectrum (AREELS) very well. The excitation energy D_1 -> R in the work of Ciraci and Batra agrees well with the observed EELS peak [32].

According to the work of Ciraci and Batra the adsorption of K on Si(001)2x1 creates no new states in the band gap of Si. No charge accumulation is observed in the proximity of the K atom. However, there is a slight polarization, and a slight change in the value, of the charge maximum for both D_1 and D_2 gap states. The empty state R has somewhat changed its character but still remains a resonance state. The K 4s electron is completely donated to fill the empty surface dangling bond state D_2, making it partially occupied and

causing the metallization of the Si surface. The bonding between the overlayer K atom and the substrate Si atoms is ionic.

Batra and Ciraci [33] also considered the adsorption of K on the ideal and the π-bonded 2x1 structure of Si(111) surface. At the monolayer coverage of the metal the bonding between K and Si is found to be ionic for both the structures, with no evidence of overlayer metallization. Northrup [34] , using the same theoretical machinery as used by Batra and Ciraci, has also predicted an ionic bonding for Na adsorbed on the ideal Si(111) surface.

There may be two sources of disagreement on 'what is metallized' between the work of Batra and Ciraci and that of Ishida et al. Firstly, the calculations of Ishida et al are not fully self-consistent and lack total-energy minimization. Indeed their choice of K-Si distance is much larger than the prediction made by Batra and Ciraci using the total energy minimization procedure. This may to some extent explain the difference between the band structure results in Figs. 6(a) and 6(b). It should be interesting in this connection to note some differences in the earlier band structure results of Tsukada and co-workers [27] and their band structure results presented in these proceedings. Secondly, it is possible that Ishida et al have somewhat inadequately interpretted their experimental data: they choose to interpret the K-Si bonding in terms of a strong polarization of K-charge and not as an ionic interaction.

The prediction of surface metallization (rather than overlayer metallization) in the work of Ciraci and Batra for θ=1 coverage of K on the Si surfaces is verified by the more recent angle-resolved photoemission results of Enta et al [35]: they observed that for higher coverage θ = 2 the metallic surface becomes insulating, because the surface-state D_2 becomes fully occupied.

From the foregoing discussion it can also be concluded that for the alkali metal — covalent semiconductor system, at a monolayer coverage the Fermi level is pinned completely by the intrinsic surface states as proposed by Bardeen, and not by chemisorption states or MIGS.

(ii) Simple metal/covalent semiconductor : Metallization of overlayer

For a microscopic understanding of metallization and Schottky barrier formation it is essential to study the electronic structure of a metal/semiconductor system with different coverages of metal. Such a study was undertaken by Batra and Ciraci [36] who studied coverage dependence of the electronic structure of Al deposited on Ge. Self-consistent calculations were made using norm-conserving nonlocal pseudopotentials and the local-density approximation. The total energy results suggest that for θ = 0.5 Al is adsorbed on Ge (001) in the bridge site. For θ = 1 additional Al atoms go in an epitaxial form. The distance of Al from Ge along [001] is R_z = 1.2 Å for θ = 0.5 and R_z = 1.8 Å for θ = 1. The total charge density for the Ge (001) - Al system is shown in Fig. 7(a) for θ = 0.5 and in Fig. 7(b) for θ = 1.

For θ = 0.5 the Al-Ge bonding is a strong directional chemisorption bonding (the maximum charge in the middle of the Al-Ge bond being 0.079 au). The Fermi level is determined by the chemisorption states, which are the Ge-Al-Ge bridge bond states produced by the combination of Ge-dangling bonds and Al sp2 orbitals.

For θ = 1 the Al-Ge chemisorption bond has weakened (the maximum charge in the middle of the Al-Ge bond being 0.056 au) and more charge has oozed out into the vacuum. This indicates that the directional covalent bonds (seen clearly for θ = 0.5) begin to be replaced by more delocalized metallic-type interaction. The local density of states for θ = 1 may be interpreted as a modulated ladder type density with an increase at the Fermi energy. For higher coverages of Al the local density of states is expected to exhibit a quasi two-dimensional, free-electron like, behaviour appropriate to a thick metallic film

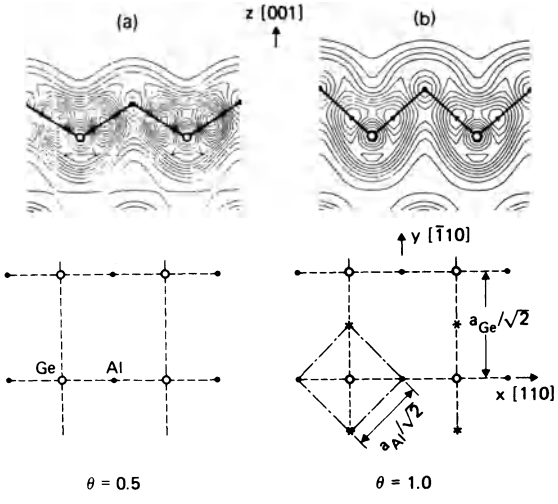

Figure 7. Contours in the ($^{-}$1 1 0) plane of the total charge density for Ge(001)-Al for (a) θ = 0.5, (b) θ = 1. Note that for θ = 1 the Al-Ge directional bond has weakened and more delocalized metallic bonding has increased (Batra and Ciraci [36]).

[37], with a larger relaxation in the value of R_z [38]. The Fermi level pinning at 1 or 2 monolayer coverage of Al on Ge can be thought of as a hybrid of two pictures: chemisorbed states and Heine's MIGS. For thicker metal overlayer the MIGS are expected to practically control the Fermi level pinning. Thus the Schottky barrier, at least for simple metal-covalent semiconductors, is fully developed only for θ ≥ 1.

These theoretical predictions are in good qualitative agreement with the experimental works of Kelley et al [1], Stiles et al [2], and Stlies and Kahn [39] on metal/semiconductor systems with both simple and transition metal adatoms. In particular, recent SXPS and UPS studies of Stiles and Kahn [39] suggest that the Fermi level pinning at the Ag/GaAs(110) interface is correlated to the appearance of metallicity in the Ag layer. The Schottky barrier is fully formed by MIGS at high Ag coverages (> 2 Å).

(iii) Factors controlling metallization behaviour and growth of overlayer

It has been suggested above that for a monolayer coverage the adsorption of K (monovalent atom) is dominated by a strong ionic bonding between the adatom and Si, and that there is no metallic bonding between the alkali-metal atoms . The system undergoes an insulator -metal transition, mainly due to two factors: (i) presence of active surface states on the Si surface, and (ii) very weak alkali metal - alkali metal interaction. Such a transition, therefore, is different from a Mott-type transition. Deposition of thick coverage (θ > 1) of the alkali metal on Si surfaces is not expected to form a thick metallic layer.

Deposition of Al (a trivalent atom) on Ge, on the other hand, is dominated by metal-substrate chemisorption bonding (covalent type) for $\theta = 0.5$, and strong metal-metal interaction for $\theta = 1$. Thus for such a system the metallization of the overlayer must compete with the formation of metal-semiconductor bonds [40].

These findings can shed light on possible epitaxial growth modes of metal overlayers on semiconductor surfaces. Let us define γ as the ratio of the interfacial bonding energy to the binding energy of the overgrowth particles. If $\gamma \approx 1$ and the lattice mismatch is not too severe, a type I or layer-by-layer (pseudomorphic) growth (also known as Frank-van de Merwe (FVDM) mode) occurs. If $\gamma > 1$ but there is a large lattice mismatch, the growth follows the Stranski-Kranstanov (SK) or type II mode. For $\gamma < 1$ the Volmer-Weber , or type III, growth occurs.

From a self-consistent pseudopotential calculation of the energetics of an epitaxial growth of Al on Ge (001), Batra [38] has concluded that the FVDM growth sequence is likely to commence at the bridging sites. The experimental studies of Stiles and Kahn [39] suggest that the room temperature growth of Ag overlayers on GaAs(110) follows the Volmer-Weber growth mode. However, at low temperature the first monolayer of Ag grows as a quasi 2D layer, but at higher coverages Ag atoms nucleate and form 3D metallic clusters.

The parameter γ may also play a significant role in controlling the type of metallization on a semiconductor surface. Considering the example of Al on Ge (001), it can be said that for low coverages (e.g. for $\theta = 0.5$) $\gamma \approx 1$ and the Fermi level pinning is dominated by the formation of chemisorption bonds. For a monolayer and thicker coverages the overlayer metallizes and relaxes, resulting in $\gamma < 1$. The K/Si system with $\theta = 1$ results into $\gamma > 1$ and provides an example of surface metallization.

SUMMARY

We have presented a short review of the existing theoretical models for Fermi level pinning and Schottky barrier formation at metal-semiconductor interfaces. A brief review of experimental results is given which produce evidence that the Fermi level position for a metal-semiconductor system is highly dependent on metal coverage θ and can be controlled by more than one mechanism. From the discussion produced in this review the following suggestion can be made. For very low coverages (for example $\theta < 0.5$) it is most likely that defect induced states and intrinsic surface states would determine the Fermi level position. For coverages in the range $0.5 \leq \theta \leq 1$, it is likely that the situation would be controlled by a competition between metal-semiconductor bonding (chemisorbed states) and intrinsic surface states. For higher coverages, $\theta \geq 1$, the position of the Fermi level can be controlled either by metal-semiconductor bonding leading to metallization of the semiconductor surface (due mainly to presence of active surface states),or by metal-metal bonding leading to metallization of the overlayer.

From the foregoing summary it can also be concluded that the barrier formed at metal-semiconductor contacts with submonolayer metal coverages is of very different nature than the barrier formed with

thick metal coverages. The phenomena of barrier formation in the limits of submonolayer and thick coverages of metals on semiconductors can be bridged by the concept of overlayer metallization. In the limit of overlayer metallization the barrier formation is practically controlled by MIGS. The traditional view of a fully established Schottky barrier can only be realized in the limit of overlayer metallization, provided that the semiconductor surface is free of defects and there are no surface states in the band gap.

REFERENCES

[1] M K Kelley, E Colavita, G Margaritondo, J Anderson, L Papagno, D J Frankel, and G J Lapeyre, Phys. Rev., B**32**: 2693 (1985).

[2] K Stiles, A Kahn, D Kilday and G Margaritondo, J. Vac. Sci. Technol., B**5**: 987 (1987).

[3] M Prietsch, M Domke, C Laubschat and G Kaindl, Phys. Rev. Lett., **60**: 436 (1988).

[4] L J Brillson, Surf. Sci. Rep., **2**: 123 (1982).

[5] I M Dharmadasa, W G Herrenden-Harker and R H Williams, Appl. Phys. Lett., **48**: 1802 (1986); and references therein.

[6] F Flores and C Tejedor, J. Phys. C: Solid State Phys., **20**: 145 (1987).

[7] J Bardeen, Phys. Rev., **71**: 717 (1947).

[8] V Heine, Phys. Rev., **138**: 1689 (1965).

[9] C Tejedor, F Frores and E Louis, J. Phys. C: Solid State Phys. **10**: 2163 (1977)

[10] W Mönch, Festkorperprobleme, **XXVI**: 67 (1986)

[11] J Tersoff, Phys. Rev. Lett., **56**: 675 (1986)

[12] W E Spicer, P W Chye, P R Skeath, C Y Su and I Lindau, J. Vac. Sci. Tech. **16**: 1427 (1979)

[13] R H Williams, J. Vac. Sci. Technol., **18**: 929 (1981).

[14] W E Spicer, I Lindau, P R Skeath and C Y Su, J. Vac. Sci. Technol., **17**: 1019 (1980).

[15] G P Srivastava, Phys. Stat. Sol., **(b) 93**: 761 (1979).

[16] M S Daw and D L Smith, Phys. Rev., B**20**: 5150 (1979).

[17] R E Allen and D J Dow, J. Vac. Sci. Technol., **19**: 383 (1981).

[18] I Lindau and T Kendelewicz, Crit. Rev. Solid State Mater. Sci. **13**: 27 (1986).

[19] O F Sankey, R E Allen, S F Ren and J D Dow, J. Vac. Sci. Technol., B**3**: 1162 (1985).

[20] W Mönch, Phys. Rev. Lett., **58**: 1260 (1987).

[21] J C Inkson, J. Phys. C: Solid State Phys., **6**: 1350 (1973).

[22] S G Louie and M L Cohen, Phys. Rev., B**13**: 2461 (1976).

[23] W Schottky , Z. Phys., **113**: 367 (1939).

[24] J L Freeouf and J M Woodall, Appl. Phys. Lett., **39**: 727 (1981).

[25] T Aruga, H Tochihara and Y Murata, Phys. Rev. Lett **53**: 372 (1984)

[26] H Tochihara, M Kubota, M Miyao and Y Murata, Surf. Sci. **158**: 497 (1985)

[27] H Ishida, N Shima and M Tsukada, Surf. Sci. **158**: 438 (1985); Phys. Rev. **B32**: 5246 (1985).

[28] S Ciraci and I P Batra, Phys. Rev. Lett., **56**: 877 (1986); Phys. Rev. **B37**: 2955 (1988). [29] P Soukiassian, these proceedings and references therein.

[30] J Ihm, M L Cohen and D J Chadi, Phys. Rev. B**21**: 4592 (1980).

[31] J D Levine, Surf. Sci. **34**: 90 (1973).

[32] H. Tochihara, Surf. Sci. **126**: 523 (1983).

[33] I P Batra and S Ciraci, Phys. Rev. B**37**: 8432 (1988).

[34] J E Northrup,J Vac Sci Tech A**4**: 1404 (1986).
[35] Y Enta, T Kirwshita, S Suzuki and S Kono, Phys. Rev. B**36**: 9801 (1987).
[36] I P Batra and S Ciraci, Phys. Rev. B**33**: 4312 (1986)
[37] I P Batra, S Ciraci, G P Srivastava, J S Nelson and C Y Fong, Phys. Rev., B**34**: 8246 (1986).
[38] I P Batra, Phys. Rev., B**29**: 7108 (1984).
[39] K Stiles and A Kahn, Phys. Rev. Lett. **60**: 440 (1988).
[40] A Zunger, Phys. Rev., B**24**: 4372 (1981).

Applications of Tunneling to Metal-Semiconductor Interfaces

FERMI-LEVEL PINNING BY OXYGEN AND ANTIMONY ADSORBATES ON THE GaAs(110) SURFACE BY SCANNING TUNNELING SPECTROSCOPY

R. M. Feenstra, P. Mårtensson, and J. A. Stroscio*

IBM Research Division, T. J. Watson Research Center
Yorktown Heights, New York, USA 10598

INTRODUCTION

It is well known that at many metal-semiconductor or oxide-semiconductor interfaces the Fermi level is pinned somewhere near the middle of the semiconductor band gap. This phenomenon has been studied in detail for both thick and thin (sub-monolayer) coverages.[1] The position of the Fermi level at the interface determines the height of the Schottky barrier formed between a metal and the semiconductor. For a thin, ordered metal overlayer on a semiconductor, the position of the Fermi level can, in principle, be determined simply by filling the surface states up to a level at which the surface charge exactly balances the bulk space-charge in the semiconductor. In reality, the situation is often more complicated, since the surface may be nonmetallic and/or the overlayer may be disordered. In those cases, the pinning of the Fermi level is generally attributed to the existence of electronic states within the band gap, although a structural identification of such states remains lacking. Indeed, various models describing Fermi level pinning hypothesize completely different types of pinning mechanisms, ranging from isolated point defects on the surface[2] to a continuum of gap states produced by the metal overlayer.[3]

With the scanning tunneling microscope (STM),[4] we have a powerful and proven tool for studying the spectroscopy of surface states. The spectrum of surface state-density is given by the measurement of conductivity, dI/dV, versus tip-sample voltage.[5] Such measurements can be performed at specified spatial locations on the surface. Furthermore, for the GaAs(110) surface in which no band gap states are found on the clean surface[6] the position of the surface Fermi level within the band gap can be directly obtained from the observed spectrum.[7]

In this paper, we discuss the properties of two overlayer systems, oxygen and antimony, on the GaAs(110) surface. These systems display quite different growth characteristics on the surface, leading to somewhat different behaviors which have been characterized with the STM. At low coverage the oxygen is observed to adsorb on the surface as individual adsorbates (as opposed to large clusters of atoms). Using voltage-dependent imaging we can directly observe the charge of these adsorbates, and we find for *n*-type GaAs that the oxygen is negatively charged.[7] The negative charge gives rise to a reversal in the STM contours of empty and filled states, with the filled states appearing as surface protrusions and the empty states as surface depressions. The negative surface charge produces band bending on *n*-type material, as observed here using tunneling spectroscopy. We find a steady increase in band bending with exposure to oxygen, for coverages up to 10^5 L (L = Langmuir = 10^{-6} Torr-sec). The band bending is understood as arising from the transfer of electrons from the conduction band into adsorbate-induced states at the surface. The energy position of these states remains unknown; they may exist in the band

gap, or they may be resonant with the valence-band. On *p*-type material, the oxygen adsorbates are observed to be neutrally charged.[8] We interpret this neutral behavior in terms of screening of the negative adsorbates by an accumulation of holes at the surface.[8]

Antimony adsorbates behave quite differently than the oxygen adsorbates. At low coverage, the antimony tends to form two-dimensional islands. These islands are observed to be charged, leading to band bending, on both *n* and *p*-type material. The islands are ordered, and with increasing coverage they grow together to form a 1x1 ordered monolayer. For the complete monolayer, we observe in tunneling spectroscopy a band gap region with width almost equal to the bulk gap.[9] The surface Fermi level lies near the edge of the observed gap. These observations are consistent with photoemission results which find, for the ordered monolayer, a relatively small amount of band bending on the surface.[10] For disordered or partial coverages however, enhanced band bending is observed, with the surface Fermi level pinned near the center of the band gap.[10,11] Using spatially resolved tunneling spectroscopy, we have directly observed the states responsible for the Fermi level pinning.[9] We find that these states are localized near the edges of Sb terraces, thereby providing an identification of the structural origin of the pinning.

EXPERIMENTAL DETAILS

The experimental details of this work have all be presented elsewhere,[7-9] and are briefly summarized below. The tunneling microscopes used in these studies are contained in ultra-high vacuum chambers, with base pressures less than 6×10^{-11} Torr. Tungsten probe-tips were prepared by electro-chemical etching, and cleaned *in situ* by electron bombardment. GaAs(110) surfaces were prepared by *in situ* cleaving of *n* or *p*-type wafers, with doping concentrations in the range $1 - 4 \times 10^{18}$ cm^{-3}. Oxygen exposures were performed by leaking high-purity oxygen into the chamber. Antimony was deposited using either a filament type evaporator or an effusion cell, with typical deposition rates of 0.2 and 0.05 ML/min respectively. During deposition the samples were held at room temperature. The total antimony coverages were estimated both from the STM images and using quartz-crystal thickness monitors assuming a sticking coefficient of unity. The pressure never exceeded 2×10^{-10} Torr during evaporation with the filament, or 1×10^{-9} Torr during evaporation with the effusion cell. The acquisition and normalization of our spectroscopic results are described in detail in Ref. 12.

OXYGEN ADSORBATES

In Fig. 1 we present STM images obtained from the GaAs(110) surface exposed to varying amounts of oxygen. Fig. 1(a) shows the clean surface, in which we see the corrugation of the surface atoms. Fig. 1(b) shows the surface exposed to 3000 L of oxygen. The oxygen atoms appear as isolated adsorbates, with typical lateral extent of ~ 15 Å. The GaAs corrugation is visible between the adsorbates. By counting the number of adsorbates on the surface, we roughly estimate the oxygen coverage to be about 0.02 ML (ML = monolayer = 8.85×10^{14} cm^{-2}) . Fig. 1(c) shows the surface exposed to 10^5 L of oxygen. The surface now appears to be quite disordered, with only a hint of the GaAs corrugation visible. It is difficult to determine the coverage directly from the image (especially since the sharpness of the STM tip will affect the appearance of the images), although a rough estimate is 0.1 ML.

In Fig. 2 we show tunneling spectra obtained from the same samples as pictured in Fig. 1. The spectrum for the clean surface, Fig. 2(a), is characteristic of tunneling from a heavily doped semiconductor. We observe three components in the tunneling current, as depicted in the inset of the figure. At large negative voltages, we observe tunneling out of the valence band (V component). Similarly, at positive voltages, tunneling occurs into empty conduction band states above the Fermi level (C component). Nonzero current is also observed within the band gap region, between -1.5 and 0 V. Since there are no surface states in the band gap on cleaved GaAs(110), we identify this latter component as tunneling out of dopant-induced filled states in the conduction band (D component).

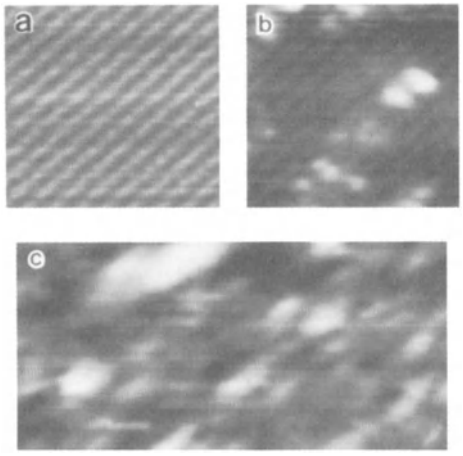

FIG. 1. STM images of oxygen adsorbed on n-GaAs(110) for exposures of (a) 0, (b) 3×10^3, and (c) 10^5 L. The images extend over (a) 60×60, (b) 60×60, and (c) 120×60 Å^2.

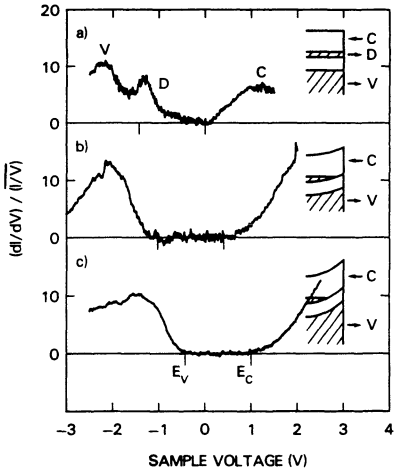

FIG. 2. Normalized conductivity spectra for the surfaces pictured in Fig. 1(a) – (c) respectively. The various components of the tunneling current are indicated in the insets - C, conduction band; V, valence band; and D, dopant induced.

These states are filled due to the n-type doping. This identification is verified by similar measurements on p-type material,[13] and by theoretical calculations of the tunneling characteristics.[13]

When oxygen is adsorbed onto the surface, the D component of the current disappears, producing a gap in the spectrum as shown in Figs. 2(b) and (c). We associate the formation of this gap with band bending in the semiconductor, which effectively pinches-off the D component of the current, as pictured in the insets of Fig. 2. The spectra are relatively homogeneous over the surface for exposures above about 200 L, corresponding to a coverage of about 0.005 ML.[7] At this coverage, the separation between adsorbates is roughly equal to the Debye length of 50 Å. At higher exposures, we find that the observed band gap shifts to higher energies as the exposure increases, with the surface Fermi level approaching the top of valence band, as seen in Fig. 2(c). This indicates a progressive increase in the surface band bending with increasing oxygen coverage.

From the spectra in Fig. 2, we can obtain a measure of the position of the surface Fermi level as a function of coverage. As demonstrated elsewhere,[7] the effect of band bending in the semiconductor due to the presence of the probe tip is small, so that the location of the valence band maximum and conduction band minimum can be determined by the onset voltages in the spectra. We mark these onset voltages in Fig. 2 by E_V and E_C respectively. (For the clean surface, Fig. 2(a), the valence band maximum is determined by the inflection point in the spectrum.) The observed gaps are generally within a few tenths of an eV of the actual gap of 1.4 eV; we attribute any small difference to residual band bending in the tip or sample. The surface Fermi level corresponds to zero volts on the plot. We obtain results for the Fermi level relative to the conduction band of 0.0, 0.4, and 1.0 eV for Figs. 2(a) - (c) respectively, with an uncertainty of about 0.1 eV. These results are quite close to those previously obtained using a slightly different analysis technique,[7] and they are also comparable to measurements of the same quantity performed by photoemission spectroscopy.[14]

As mentioned above, band bending effects are observed to be uniform over the surface for sufficiently high oxygen coverage. The spectra have also been examined directly on, and off, the oxygen adsorbates. Such data is shown in Fig. 3. In the image, the oxygen adsorbates appear as white protrusions in the image. Spectra were acquired at the

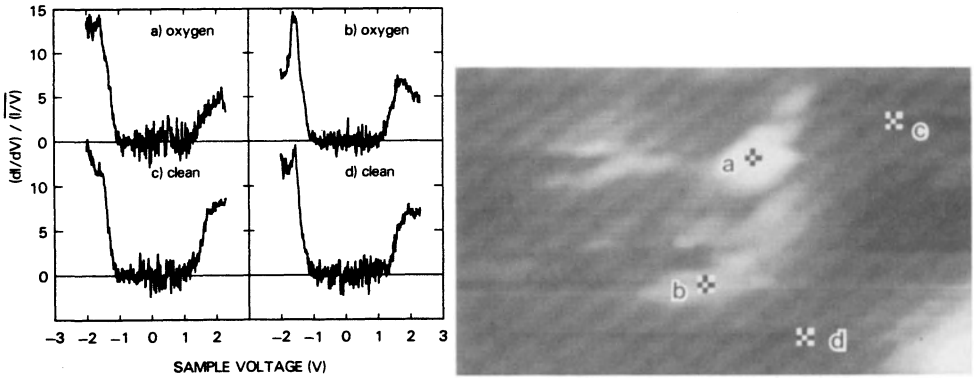

FIG. 3. Normalized conductivity spectra measured on and off an oxygen adsorbate on *n*-GaAs(110). Oxygen coverage is 800 L. The associated 90 × 55 Å² STM image is shown, with the locations indicated at which the spectra were acquired.

locations marked in the image, as shown in Fig. 3(a)–(d). We see that all of the spectra display a band gap region, with width close to 2 eV (this gap is somewhat larger than the bulk gap of 1.4 eV; we attribute this difference to some residual band bending in the tip or sample). Fig. 3(a) was acquired on an oxygen adsorbate, (b) was acquired on a disordered region near the adsorbate, and (c) and (d) were acquired on the clean surface. Comparing the spectra, we see that the ratio of valence-band to conduction-band conductivity is greater on the oxygen adsorbate than on the clean surface. This enhancement in valence-band conductivity relative to the conduction-band is reproducibly observed on the oxygen adsorbates, and is the same effect which gives rise to the positive or negative contours in the STM images. Within the band gap region of the spectra, we do not observe any conductivity. Previously, we have reported spectroscopic results on an oxygen adsorbate which did display nonzero current within the band gap region.[7] However, our new results illustrated in Fig. 3, together with the high coverage data shown in Fig. 2(c), leads us to conclude that these previous results were exceptional. In general, we do not observe any tunneling current within the band gap for the oxygen covered *n*-GaAs surfaces, independent of spatial position.

The observation of zero conductivity regions in the spectrum may imply that the oxygen adsorbates do not posses any states within the gap. If gap states are present, our spectroscopy should have enough sensitivity to detect them, as demonstrated by the observation of band gap states for Sb/GaAs discussed in the following section. One possible problem in the measurement arises from the transport of carriers through gap states. To observe a tunnel current of 0.1 nA, we must pass 10^9 electrons/sec through a state, and that current must somehow come into equilibrium with the semiconductor. For a state within the band gap, the current cannot flow directly into the bulk due to the presence of the gap (tunneling through the gap is, in general, too slow[13]). Surface conduction provides an alternate path for the tunnel current. However, for widely separated adsorbates this transport mechanism may also be limited. In the present case, it is difficult to assess whether or not the surface conductivity is sufficient to permit observation of gap states. Thus, we cannot definitively determine whether the oxygen adsorbates posses any states within the gap. Experiments at higher coverage may permit a resolution of this issue.

ANTIMONY ADSORBATES

Unlike oxygen, antimony adsorbates on the GaAs(110) surface tend to cluster together, forming islands. The islands have a height corresponding to one monolayer, and

they increase in size as the coverage is increased. At about 0.7 ML, the islands merge together and form a continuous network over the surface. In Fig. 4 we show a typical STM image of the GaAs surface covered with 1.0 ML antimony. Most of the Sb forms a 1×1 ordered terrace, as seen most clearly in the lower portion of the image. Some missing Sb atoms are always observed in these terraces. Excess Sb forms small protrusions on top of the terraces. The GaAs substrate is seen as the dark portion of the image, located 2.5 Å below the Sb overlayer.

In Fig. 5 we show typical conductivity spectra acquired from a clean, unpinned GaAs surface, and from a large ordered Sb terrace located nearby the terrace shown in Fig. 4. In these spectra, the sample voltage equals the energy of the surface states measured relative to the surface Fermi level (0 V). For the clean surface, we observe broad peaks for the valence-band states (V component) and for the conduction-band states (C component). In the band gap region, between 0 and 1.4 V, we observe a weak feature which is identified, as in Fig. 2, as tunneling into dopant-induced empty states of the valence-band (D component). For the Sb overlayer, shown in Fig. 5(b), we observe two peaks on the filled state side. This two-peaked feature is characteristic of the Sb overlayers. The amplitudes of the peaks do vary from experiment to experiment, although their location in energy is constant to within a few tenths of an eV. From their location in energy, we identify these peaks as the S_5 and S_6 surface states, associated with filled dangling bonds on two inequivalent Sb atoms in the overlayer.[15–18] On the empty state side, we observe a peak which we assign to the $S_{7,8}$ states of the overlayer.[15,16,19]

The position of the surface Fermi level relative to the band gap can be seen directly in the spectra of Fig. 5. The valence- and conduction-band edges are marked by E_V and E_C respectively, separated by the band gap of 1.4 eV. The Fermi level occurs at 0 V. Fig. 5(a) corresponds to near flat-band conditions, with $E_V = 0$ V. The Sb spectrum of Fig. 5(b) displays a band gap equal in size to the bulk gap, indicating that the surface states do not extend significantly into the bulk gap. The band edges in Fig. 5(b) are shifted to the left by 0.2 eV relative to Fig. 5(a), indicating a shift in the position of the surface Fermi level of this amount. This small amount of band bending probably arises from residual disorder on the surface. Our value of 0.2 eV is comparable to photoemission studies, which find 0.3 eV band bending on annealed (ordered) p-type samples.[10] These

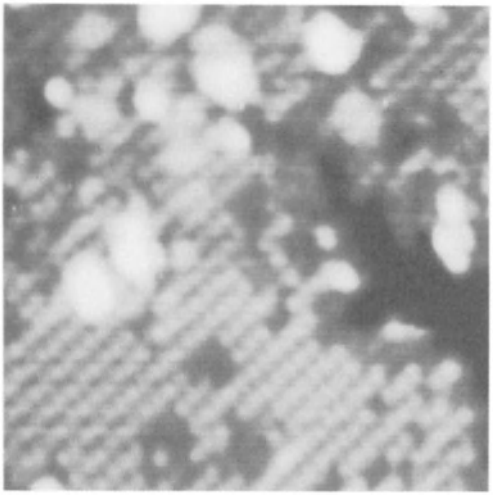

FIG. 4. 120×120 Å^2 STM image of antimony on p-GaAs(110), acquired with a sample voltage of -2 V. The Sb coverage is 1.0 ML . The topographic height is displayed by a grey-scale, ranging from 0 Å (black) to 5 Å (white).

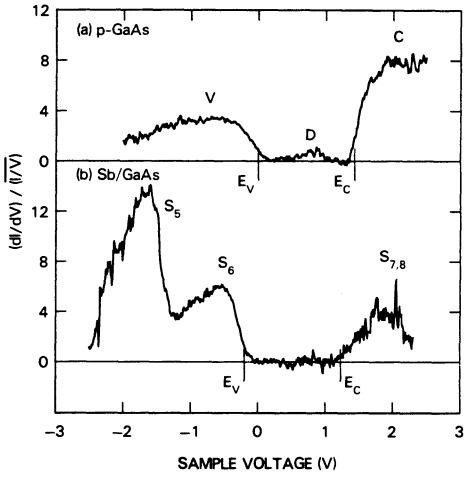

FIG. 5. Normalized conductivity versus voltage, for (a) a clean p-type GaAs(110) surface, and (b) an ordered region of an Sb overlayer on p-GaAs. The valence and conduction band edges are denoted by E_V and E_C respectively. The Fermi level corresponds to 0 V.

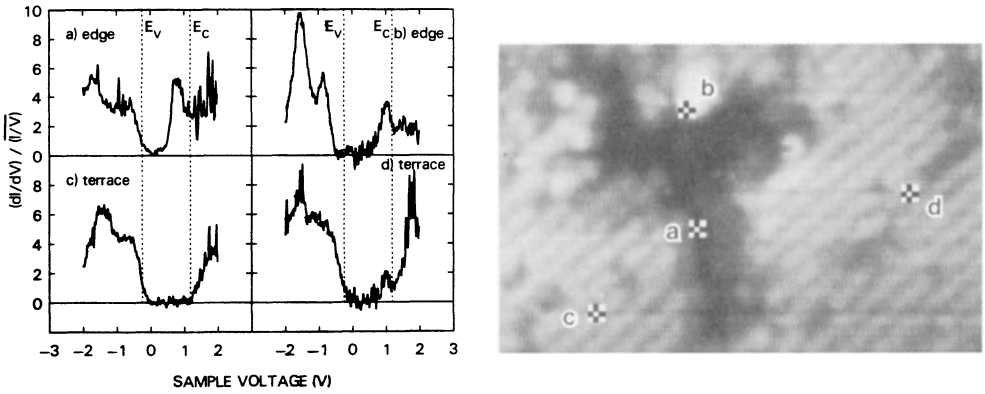

FIG. 6. Normalized conductivity versus voltage, measured on top and on the edge of an Sb terrace. The associated 120 × 80 Å² STM image is shown, with the locations indicated at which the spectra were acquired.

studies found much greater band bending on unannealed (disordered) samples, with Fermi levels pinned closer to mid-gap.[10]

To understand the enhancement in the band bending on disordered Sb overlayers, we have studied two types of samples. First, we examined small Sb clusters, prepared by deposition of typically 0.02 monolayer of Sb on the GaAs(110) surfaces. In voltage-dependent imaging we find that the clusters are charged, for both *n* and *p*-type material.[20] Spectroscopic measurements reveal the presence of a band gap region, both on and off the clusters. Band bending is a maximum on the clusters, falling off as one moves away from the cluster due to electrostatic screening from the space-charge in the semiconductor. Generally, we do not directly observe any band gap states associated with the isolated clusters. However, in many cases the spectra display "glitches" or discontinuous jumps in the current. Such effects have been previously observed on oxidized Si surfaces,[21] and were interpreted as electron hopping into localized gap states. As discussed in the previous section, the transport through such gap states may be limited, giving rise to such discrete events changes in the tunnel current.

One way to increase the conductivity through gap states is to increase the adsorbate coverage until the states overlap and form a network over the entire surface. This occurs on the Sb/GaAs(110) surface at about 0.7 ML coverage, at which point the Sb islands merge and form a continuous network over the surface. Tunneling spectra from a sample covered with 0.7 monolayer of Sb are shown in Fig. 6, along with their associated STM image. We show spectra acquired on top of the Sb terrace, and near the edge of terrace. On top of the terrace, the spectrum is consistent with that shown in Fig. 5(b), with a band bending close to 0.2 eV. Now, at the edge of the terrace, we find a much different spectrum, with a large spectral peak occuring in the gap-region near 0.8 eV. In some cases, a shoulder of states has also been seen extending into the gap from the valence-band side.[9] The Fermi level is pinned between these two sets of states. These edge-induced band gap states are thus responsible for the enhanced Fermi level pinning seen on the disordered Sb overlayers.

CONCLUSIONS

We conclude this paper with a discussion of the relevance of our observations on the O/GaAs(110) and Sb/GaAs(110) systems with the various proposed models for Fermi level pinning. First, we note that none of our observations relate to the formation of metal-induced gap states[3] on the surface, since the overlayers we have studied are non-metallic. Our observations are mainly relevant to the initial stages of Fermi level pinning on the surface, for which the most commonly discussed model is that of surface defects.[2]

It is believed that the defects give rise to band gap states of both acceptor and donor character, leading to band bending on both *n* and *p*-type material.

For oxygen adsorbates, we have studied the exposures in the range 30 – 10^5 L, corresponding to coverages of about 0.002 – 0.1 monolayers. We observe band bending on *n*-type material, and no band bending on *p*-type material. Associated with the band bending we observe a negative charge of the adsorbates on *n*-type material, and a neutral behavior on *p*-type material. In general, we can associate the negative charge with some adsorbate-induced electronic state. Since it is either negatively charged, or neutral, the state is called an acceptor. Energetically, the position of the acceptor state is unknown; it may be inside the band gap, or it may be resonant with the valence-band. In spectroscopy we do not find any evidence for the state within the band gap, but these observations may be limited by a lack of conductivity through the states. Band bending on *n*-type material is understood to occur by the transfer of electrons from the conduction band to the acceptor level. On *p*-type material the acceptor level is effectively neutralized by the presence of holes at the surface.

Thus we interpret our oxygen results in terms of simple charge transfer from the bulk semiconductor to the electronegative oxygen adsorbates. Increasing oxygen coverage produces more charge transfer and more band bending. Band gap states are not required in such a picture, although they may occur. At higher oxygen exposures, above 10^5 L, the situation changes. Photoemission indicates that the band bending behavior changes, with the surface Fermi level on both *n* and *p*-type material approaching mid-gap.[14] Such a behavior definitely indicates the existence of states within the gap. At present, we have not investigated this exposure regime with the tunneling microscope.

For the case of antimony on GaAs(110), we have studied coverages in the range 0.02 – 1.0 ML. At low coverage, we find small clusters of antimony atoms. These clusters are negatively charged on *n*-type material, and positively charged on *p*-type material, leading to band bending in both cases. Band gap states associated with the isolated clusters have not been seen in spectroscopy, and it is believed that a lack of conductivity through such states prohibits their direct observation. At higher coverage, when the Sb clusters merge together and form a continuous network over the surface, we do directly observe the gap states which are responsible for Fermi level pinning. These states are found to be spatially localized near the edge of Sb terraces. It has been suggested that intrinsic defects such as antisites may be universally responsible for such Fermi level pinning.[2] In our case, it is very difficult to imagine how such defects could be concentrated only at the edge of the Sb terraces. The states observed here arise from dangling bonds localized near the edge of Sb terraces. The precise structure of these bonds is not known at present; they could be associated with either the Sb atoms, or the Ga and/or As atoms, or both. The relevance of the edge states to pinning at Sb coverages above 1 ML depends on the amount of incomplete bonding occuring at the Sb/GaAs interface.

ACKNOWLEDGEMENTS

Expert technical assistance throughout the course of these experiments was provided by A. P. Fein.

REFERENCES

* Present address: National Bureau of Standards, Gaithersburg, MD 20899

1. For a review, see L. J. Brillson, Surf. Sci. Rep. 2, 123 (1982).
2. W. E. Spicer, I. Lindau, P. R. Skeath, C. Y. Su, and P. W. Chye, Phys. Rev. Lett. 44, 420 (1980); J. Vac. Sci. Tech. 16, 1422 (1979).
3. J. Tersoff, Phys. Rev. Lett. 52, 465 (1984).
4. G. Binnig and H. Rohrer, Helv. Phys. Acta 55, 726 (1982); Surf. Sci. 152/153, 17 (1985); Rev. Mod. Phys. 59, 615 (1987).

5. J. Tersoff and D. R. Hamann, Phys. Rev. Lett. 50, 1998(1983); Phys. Rev. B31, 805 (1985).
6. J. Van Laar and J. J. Scheer, Surf. Sci. 8, 342 (1967).
7. J. A. Stroscio, R. M. Feenstra, and A. P. Fein, Phys. Rev. Lett. 58, 1668 (1987); J. Vac. Sci. Tech. B 5, 923 (1987); J. Vac. Sci. Tech. B 4, 1472 (1988).
8. J. A. Stroscio, R. M. Feenstra, and A. P. Fein, Phys. Rev. B36, 7718 (1987).
9. R. M. Feenstra and P. Mårtensson, Phys. Rev. Lett. 61, 447 (1988).
10. F. Schäffler, R. Ludeke, A. Taleb-Ibrahimi, G. Hughes, and D. Rieger, Phys. Rev. B 36, 1328 (1987); J. Vac. Sci. Tech. B 5, 1048 (1987).
11. K. Li and A. Kahn, J. Vac. Sci. Tech A 4, 958 (1986).
12. P. Mårtensson and R. M. Feenstra, submitted to Phys. Rev. B.
13. R. M. Feenstra and J. A. Stroscio, J. Vac. Sci. Tech. B 5, 923 (1987).
14. G. Landgren, R. Ludeke, Y. Jugnet, J. F. Morar, and F. J. Himpsel, J. Vac. Sci. Technol. B 2, 351 (1984).
15. C. M. Bertoni, C. Calandra, F. Manghi, and E. Molinari, Phys. Rev. B27, 1251 (1983).
16. C. Mailhiot, C. B. Duke, and D. J. Chadi, Phys. Rev. Lett. 53, 2114 (1984). Phys. Rev. B31, 2213 (1985).
17. P. Mårtensson, G. V. Hansson, M. Lähdeniemi, K. O. Magnusson, S. Wiklund, and J. M. Nicholls, Phys. Rev. B33, 7399 (1986).
18. A. Tulke, M. Mattern-Klosson, and H. Lüth, Solid. State Comm. 59, 303 (1986).
19. W. Drube and F. J. Himpsel, Phys. Rev. B37, 855 (1988).
20. R. M. Feenstra and P. Mårtensson, Proceeding of the 19th International Conference on the Physics of Semiconductors, Warsaw, 1988.
21. R. H. Koch and R. J. Hamers, Surf. Sci. 181, 333 (1987).

INITIAL STAGES OF METAL-SEMICONDUCTOR INTERFACE FORMATION

F. Salvan, F. Thibaudau, Ph. Dumas and A. Humbert
Groupe de Physique des Etats Condensés, UA CNRS 783
Faculté des Sciences de Luminy, Case 901 - 13288 Marseille Cedex 9, France

INTRODUCTION

For more than 20 years, metal-semiconductor interfaces have been the object of various studies concerning the geometric and electronic structure revealed in the initial stages of metal condensation on the semiconductor substrate. The early stages of the interface formation condition the further growth of the metallic film and the properties of the Schottky barrier. Thus knowledge of the atomistics of the initial stages appears necessary since new insights on the formation mechanism of abrupt or mixed interfaces could thus be gained, as well as many other points like the influence of defects, the determination of electronic states responsible for Fermi-level pinning, etc.

Surface physicists are thus looking for the correlations between the structural, chemical and electronic properties of the interface during its formation and further constitution. For this program, they used complementary surface sensitive techniques (SST) like electron diffraction, ion scattering cross TEM, Auger spectroscopy, direct and inverse photoemission which probe structural, chemical and electronic properties of the system. The use of these integrated techniques has already provided us a lot of decisive data on a large number of systems but in many cases local probing at the atomic or nanometric scale is needed. A powerful technique for this purpose is of course STM [1] and it has been successfully used for the fine scale characterization of the geometric and electronic properties of metal overlayers on semiconductor substrates.

The aim of this paper is to illustrate how the combined use of STM and integrated SST techniques has provided to the scientific community new informations on the early stages of metal condensation on 7x7Si(111) surfaces. The main problems addressed here concern the adsorption sites available for metal atom condensation and the correlations between the

geometric and electronic properties revealed by different kinds of techniques.

Since in the case of 7x7Si(111) surfaces different kinds of interfaces are obtained according to the substrate temperature during metal deposition, our paper is divided in two parts. We first consider the case of low substrate temperature condensation where no new superstructure is observed, whereas LEED characterization shows only a progressive blurring of the 7x7 reconstructed substrate surface up to about 1 monolayer deposit. This is the case for room temperature (RT) deposition or for substrate temperatures around 100°C. If the substrate temperature is higher (a few 100°C), or if the system is annealed after RT deposition, at temperatures in the same range, one often observes new superstructures, revealing a change in atomic ordering at the surface. These conditions concern systems which are described in the second part of this paper.

EXPERIMENTAL

Interfaces are prepared and characterized in UHV conditions. A preparation chamber and a STM chamber are connected through a rack and pinion mechanism. The overall pressure is $2x10^{-10}$ torr. Si samples cut from Si(111) wafers are introduced via an air-lock system and annealed at 950°C, after careful disgassing at 700°C, in the preparation chamber which is equipped with Auger, LEED and metal evaporation facilities. Amounts of deposited metal is controlled with a quartz microbalance and can be estimated from the ratio of the Si and metal Auger peaks. Metal coverages are measured in equivalent monolayers (mL) of the Si(111) substrate (1 mL corresponds to a density of 7.8 10^{14} atoms/cm^2). Samples are then introduced in the STM chamber equipped with a pocket-size STM. STM images are obtained in the constant current mode ; we have also used the simultaneous double imaging procedure which has been proposed by Stroscio and Feenstra [2]. This method allowed us to compare STM images obtained by probing simultaneously filled and empty electronic states in reversing the gap voltage polarity at the end of each scan line.

ROOM AND LOW TEMPERATURE CONDENSATION

We first review some very important results on the early stages of LT metal deposition by two different groups, one at IBM Yorktown Heights in the case of Pd [3], and the other at the University of Bochum concerning Cu [4] and Ag [5] condensation.

Since we are interested in the adsorption sites offered by the substrate in the early stages of metal deposition, let us first recall some properties of the 7x7 unit cell which constitutes the basic unit for atomic ordering at the surface. The conjunction of STM [6] and transmission electron diffraction [7] characterizations has given the clue for understanding the properties of this fairly large unit cells in terms of the dimer adatom stacking fault (DAS) proposed by Takayanagi. A schematic view of the cell can be seen in the lower part of Fig.1,

where a striking consequence of the existence of the stacking fault is seen in the top view of the faulted half of the unit cell. This faulted part appears as an open surface when compared with the unfaulted one where Si atoms of the second bi-layer are visible. This is an important geometric feature but another important property concerns the electronic density of states which is higher for both empty and occupied electronic surface states, as this has been revealed in both tunneling microscopy and spectroscopy. These features probably play an important role in determining the nucleation sites of the initial substrate as they could be visualized in the case of Pd, Cu and Ag on 7x7Si(111) surfaces.

Pd/Si(111

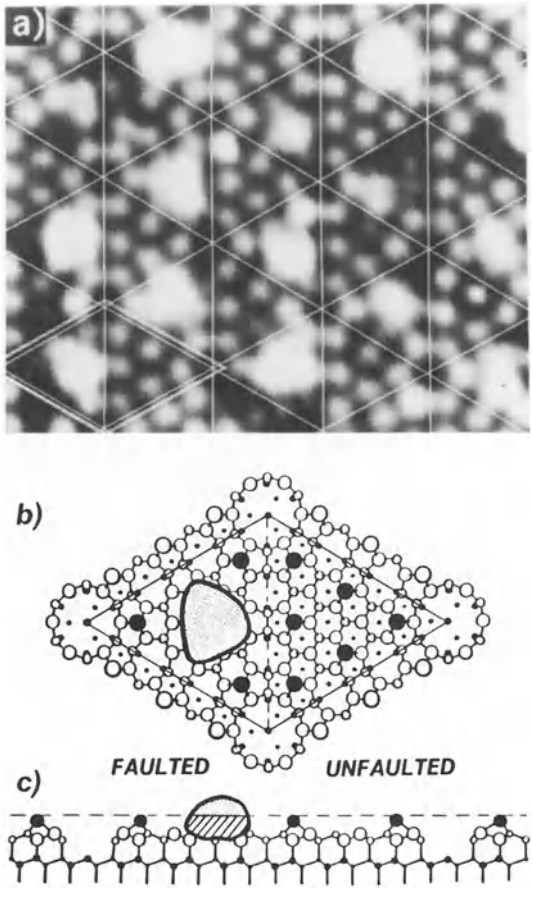

Figure 1
(a) S.T.M. image of a 115x95 Å^2 area of Si 7x7 with 0.25 ML Pd. The overlaid grid indicates the 7x7 lattice.
Pd-silicide clusters occur within the faulter part of the unit cell, whose main characteristics are distinguished on the schematic top view (b) and on the cut view through the long diagonal of the 7x7 cell (c).

Courtesy of the authors : U.K. Köhler, J.E. Demuth and R.J. Hamers.

For many years this system has been investigated by means of different surface sensitive techniques, so that many of its properties are already known. In particular, RT deposition gives rise to the growth of a Pd_2Si film, whereas in the monolayer range one the 7x7 LEED

pattern is still visible and only blurs progressively. The question we address here concerns the nucleation sites offered by the substrate. The answer is beautifully illustrated in the STM image of Fig. 1 which shows that at 0.5 mL the Pd_2Si islands occupy almost exclusively the faulted halves of the 7x7 unit cells of the initial substrate, whereas the unfaulted parts display their characteristic features (adatoms, corner holes...). Further growth of the $Pd\sqrt{3}Si$ proceeds in a Volmer-Weber mode and this has been clearly shown in STM studies reported by the IBM Yorktown group [3]. These observations lead to some comments about the role played by the stacking fault in early nucleation. It also implies that even at RT surface diffusion of the Pd atoms is quite important.

Similar observations have been reported recently by Tosch and Neddermeyer [4] on the RT growth of Cu films on 7x7 reconstructed Si(111) surfaces. Cu islands grow first on the faulted parts of the unit cells whereas the overall features of the DAS model are still observed in the STM images, accordingly to LEED observations.

When silver is deposited at substrate temperature about 100°C, one observes a progressive blurring of the 7x7 LEED pattern, while the fractionnary spots are still visible up to about 1 mL coverage. STM images show that silver condensation occurs principally at the faulted parts of the 7x7 unit cells [5]. Moreover it can be seen that the smallest visible nuclei appear in aring like configuration around the centers of the triangles, almost at the location of the rest atom dangling bonds.

HIGH TEMPERATURE CONDENSATION

A striking feature of the modifications due to metal deposition on a 7x7Si(111) surface in these conditions is the appearance of new atomic ordering at the surface, thus giving rise to different reconstructions. We will concentrate here on the $\sqrt{3}x\sqrt{3}$ structure which is rotated from 30° with respect to the orientation of the 1x1 or 7x7 cell of the substrate. This structure is observed in many cases of metal condensation and the points we are dealing with here concern the structural and electronic properties of this 2D phase. Is it metallic or semiconductor-like ? What are the location sites of the adsorbed atoms ? We will discuss these points for two kinds of $\sqrt{3}$ phases, the ones which are observed with group 3 elements first, and then consider the case of Au/Si(111)$\sqrt{3}$.

(Al,In,Ga)/Si(111)$\sqrt{3}$ structures

These systems have been investigated by means of various surface sensitive techniques like direct and inverse photoemission [8,9], scanning tunneling microscopy [10] and spectroscopy [11]. On the basis of these data and of theoretical calculations, a structural model of the $\sqrt{3}$ structure is proposed which is illustrated in Fig. 2a.

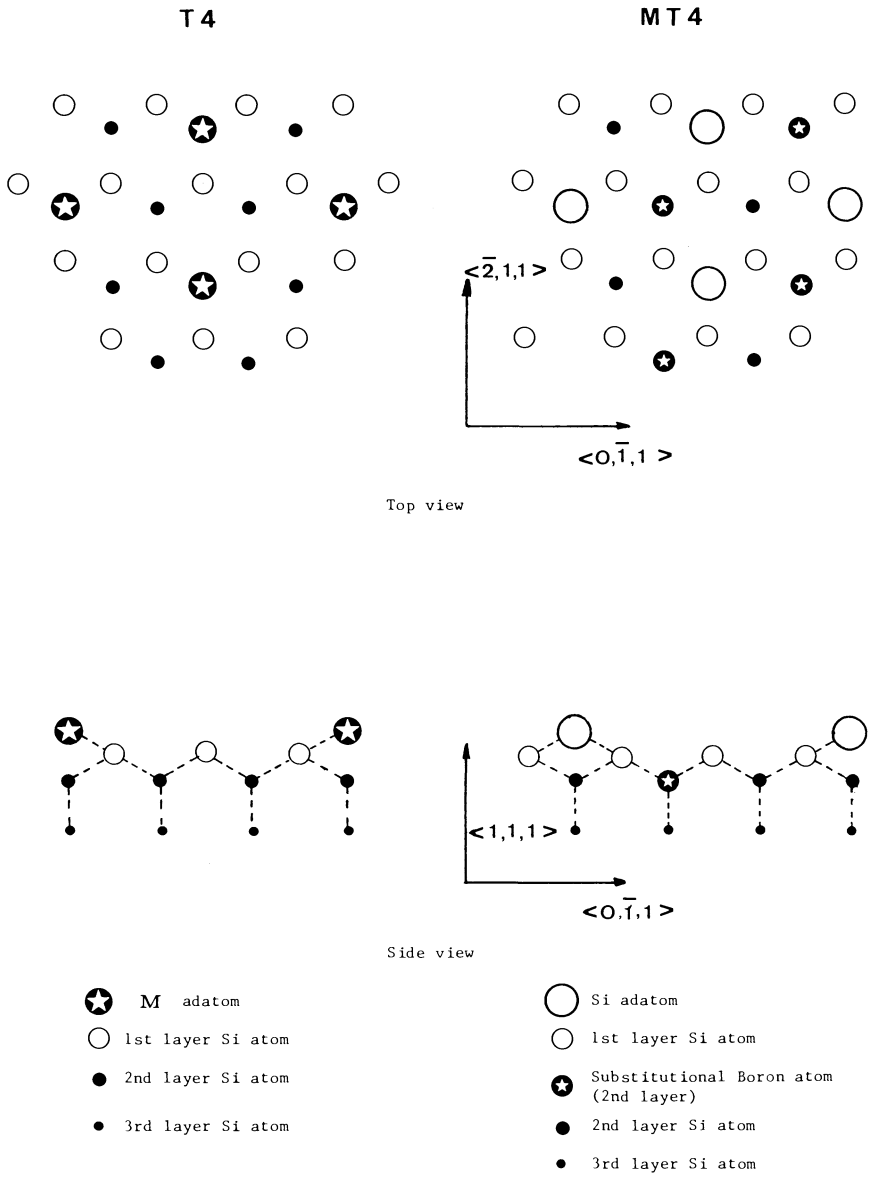

Figure 2

Schematic model of the T_4 (a) and MT_4 adatom model of the $\sqrt{3}$ reconstruction.

Before discussing the characteristics of this model, we would like to make a few remarks. First of all, the appearance of this new 2D phase corresponds to a decrease of the surface energy and, since the 7x7 ordering is drastically modified, the available adsorption sites are referred to the 1x1 surface lattice. The coupling of adsorbed atoms M should leave a minimum number of remaining dangling bonds (DB) of the silicon top layer. Finally we notice that the observed $\sqrt{3}$ structures correspond to a maximum coverage of 1/3 mL. In these conditions, the most favorable configuration would imply a symmetric coupling of the 3 valence electrons of M adatoms with 3 (DB) of the Si first layer. If this is realized, we have a system with no remaining DB, no half filled electron bands, so that we expect a semiconducting phase as effectively revealed by photoemission data. The last point to be solved concerns the assignment of the threefold hollow sites available for the M atoms. Northrup's calculations [12], as well as the ones which have been presented in this meeting by Nelson and Batra for the case of Al [13], favour the T_4 model, where the M adatom is coupled with three 1st layer Si atoms and one 2nd layer Si atom below (see Fig. 2a). This site is energetically more favourable than the empty H_3 site. This is the same location site which is occupied by the Si adatoms in the 7x7 reconstruction. We are thus in a quite simple situation for describing the structural model. One important remark concerns the mirror symmetry along $[\bar{2}11]$ plane. It is clear from inspection of Fig. 2a that the cell has a perfect mirror symmetry across the short diagonal.

Let us compare now these properties with the ones encountered while investigating the $\sqrt{3}$ structure obtained with the first group III element, boron.

B/Si(111)$\sqrt{3}$

Outdiffusion of boron atoms at the surface of highly boron doped Si samples (10^{19} cm^3) is observed after long time annealing [14,15]. We have investigated the conditions of boron presence at the surface and of the apparition of the $\sqrt{3}$ structure, in relation with the annealing times and temperatures [16]. We then have prepared $\sqrt{3}$ structures for which a rough estimation of the boron concentration, on the basis of the ratios of the Si and B Auger peaks, leaded to an average of about one B atom per $\sqrt{3}$ unit cell, i.e. a coverage of 1/3 of monolayer. Such surfaces were then characterized in STM [16].

Fig. 3 shows a 3D STM image of the centered hexagonal pattern of protrusions 6.65 Å apart. Simultaneous double imaging at different voltages or polarities, a method proposed by Stroscio and Feenstra [2], allowed us to probe both the occupied and unoccupied electronic states on the same part of the surface. Fig. 4a and 4b correspond respectively to the empty

states and filled states corrugation profiles along the large diagonal $(1\bar{1}0)$ direction for ± 0.5 V applied to the sample. Examination of these profiles shows that there is no mirror symmetry across equivalent $(\bar{2}11)$ directions and that 3 kinds of sites, 3.84 Å apart, i.e. the neighbor Si-Si distance, are present. The disymmetry of the unit cell is thus clearly visible. An analysis of the characteristic features of STM images is reported elsewhere [17]. This leads us to propose a modification of the T_4 model, hereafter called MT_4. Site 2 in the schematic diagram of the cell in Fig. 6 corresponds to a boron atom located in a substitutional site of the 2nd Si atom layer, whereas site 1 is occupied by a Si adatom in a T_4 site. The corresponding model is illustrated in Fig. 2b. Site 3 is an empty T_4 site. With these assignments all the electronic features revealed in the images can be explained since boron

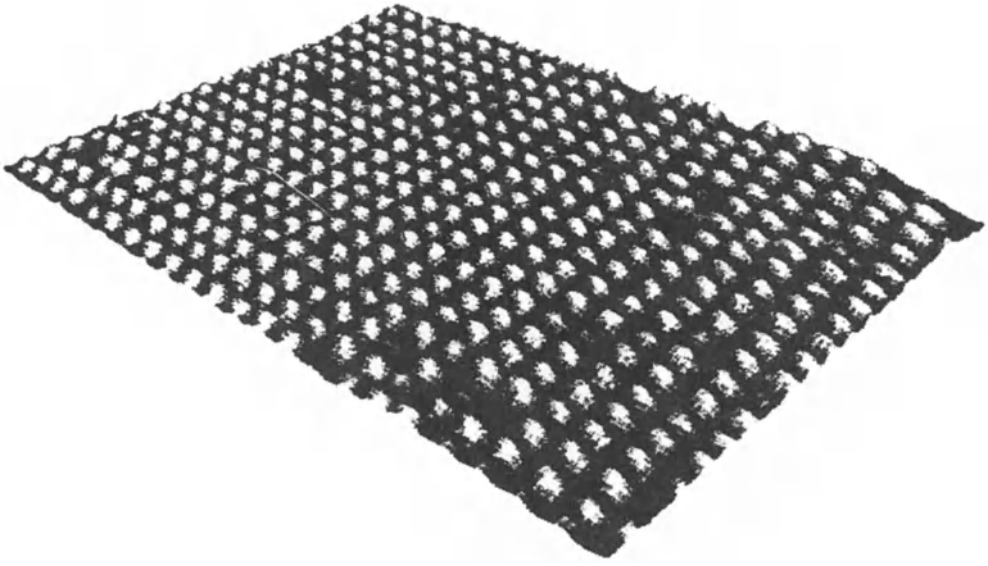

Figure 3 . 3D STM image of 120x80 $Å^2$ area of the B/Si(111)$\sqrt{3}$.

atoms are expected to show a hole in the filled image, due to a smaller density of filled electronic density, whereas they give a secondary maximum in the empty states image. The observation of antiphase domains where site 2 and 3 are interchanged provides a strong support of this model. Unfortunately there is, at the present time, no spectroscopic data on this system, neither from direct or inverse photoemission, nor from tunneling spectroscopy, so that it is difficult to conclude about the metallic or semiconducting properties of this 2D phase. Such spectroscopic data appear thus as highly wishable.

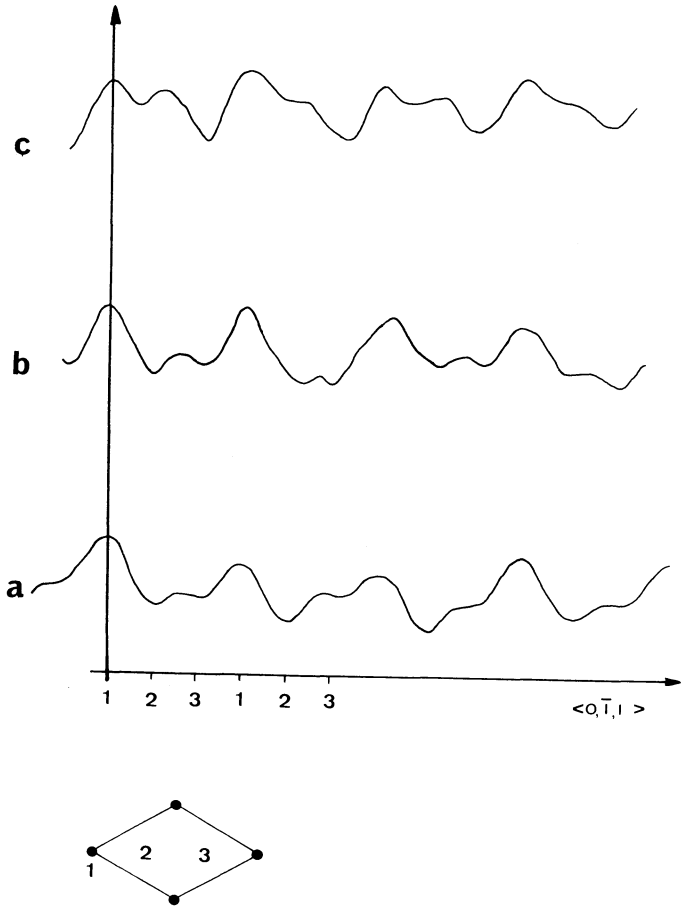

Figure 4 .

Corrugation profiles across the long diagonal of the $\sqrt{3}$ unit cell, $<1\bar{1}0>$ direction, for different sample voltages. a) -1,5 V and for simultaneously acquired images at -0.5 V (b) and +0.5 V (c) : the distances between adjacent sites labelled 1 2 3 is a.

Au/Si(111)$\sqrt{3}$

We finally discuss a more complicated case of 2D phase structure, since it involves a noble metal, so that coupling of the Si DB with both s,p and d Au orbitals prevents us to make simple considerations as the ones we have mentioned in the afore mentioned case.

Condensation of Au atoms on a heated (700°C), 7x7 reconstructed Si(111) substrate gives rise to different phases, according to the amount of deposited metal [18]. We concentrate here on the $\sqrt{3}$ structure which is obtained for a coverage ranging from 2/3 to 1 mL. This $\sqrt{3}$ structure has been investigated by means of various surface sensitive techniques [19] and various structural models have been proposed. In particular, on the basis of ICISS data reported by two different groups [20,21], different structural models which are schematized on Fig. 6 have been proposed. In both models, Au atoms are placed in the top layer, whereas different motives are deduced for the analyzed structures. A centered hexagonal pattern of Au trimers distant from a $\sqrt{3}$ constitutes the essential feature of the model proposed by Oura et al. [20], whereas the model proposed by Huang and Williams [21] is based on a mixing of honeycomb structures , as illustrated in Fig. 5b. On all the samples which have been examined, STM images have only reaveled centered hexagons of large protrusions distant from a $\sqrt{3}$, as shown on the right part of Fig. 5c, and this in both sample polarities. It has thus been concluded that the large protrusions could be assigned to Au trimers on top of the Si surface. Au atoms within the trimers could not be resolved. This assignment is supported on the basis of tunneling spectroscopy [22] and inverse photoemission [23] data which show that Au induced features in the electronic density of empty states dominate Si features revealed on the 7x7 Si substrate. It is to be noted that these results illustrate very well the correlations which exist between local characterizations with tunneling spectroscopy and that provided by integrated techniques.

We could not assign the location sites of the trimers in the Si lattice, but examination of defects in the structure like the one visible in Fig. 5c reveals that smaller protrusions which could be assigned to individual Au atoms can be registered in location sites different that the ones corresponding to the largest protrusions. This is clearly seen on this figure where a straight line has been traced which crosses this structural defect. If large protrusions are arbitrarily positionned in the centers of H_3 sites of the 1x1 lattice, then the defect on the left shows smaller protrusions which register with T_4 sites. One can also notice a few cells of a honeycomb structure in this defect. We do not expect to make general conclusions from the observation of such local defects. However, this stresses the fact that even for surfaces which display sharp $\sqrt{3}$ LEED patterns, different local atomic arrangements could occur. It has also been reported [24] that the Au/Si $\sqrt{3}$ structure can be observed with various features in LEED observations, depending on the Au coverage. It is thus of primary importance in this case to compare data provided by averaging surface sensitive techniques and STM which come from measurements on the same samples. In all the samples we have examined here and on different places on the surface, centered hexagonal patterns of protrusions are in quite good agreement with the existence of Au trimers on top of the surface.

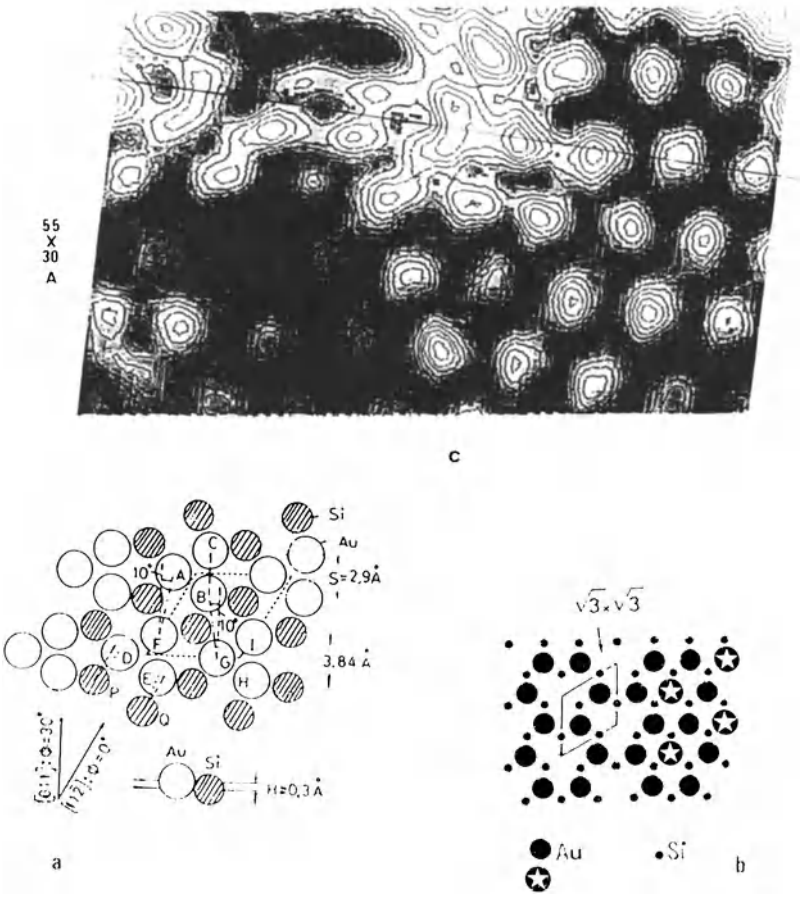

Figure 5 .

Top view STM image of Au/Si(111)$\sqrt{3}$ cells showing the coexistence of different types of unit cell with different local coverages Θ.

(a) Trimer model as suggested by Oura ($\Theta = 1$).

(b) 2 honeycomb $\sqrt{3}$ cells for $\Theta = 2/3$ (left part) and $\Theta = 1$ (right part).

(c) Equal height contours of a top view STM image with a superposed line going across a defect. Two types of $\sqrt{3}$ unit cells can be recognized on the left and right parts of the defect. The change in Au adsorption sites is also clearly visible.

We have shown in this short review that STM provides in most cases an atomic view of the surface ordering at the early stages of metal condensation. Considerable progresses have been obtained in the cases reported here. This new vision at the atomic scale is of considerable help for developing structural models of the 2D phases which have been proposed on the basis of averaging surface sensitive techniques. One has also to be aware of the necessity of performing cross characterizations by local and integrated techniques on the same samples.

Acknowledgement : The authors are grateful to U.K. Köhler, J. Demuth and R.J.Hamers for communication of the Pd/Si image.

References

1. G. Binnig and H. Röhrer, Scanning Tunneling Microscopy, Helv. Phys. Acta 55 : 726 (1982).
2. J.A. Stroscio, R.M. Feenstra, D.M. Newns and A.P. Fein, Voltage dependent scanning tunneling microscopy imaging of semiconductor surfaces, J. Vac. Sci. Technol. A6 : 499 (1988).
3. U.K. Köhler, J.E. Demuth and R.J. Hamers, Surface reconstruction and the nucleation of palladium silicide on Si(111), Phys. Rev. Lett. 60 : 2499 (1988).
4. St. Tosch and H. Neddermeyer, Nucleation of Cu on Si(111)7x7 and atomic reconstruction of theCu/Si(111) interface, Proceedings of ECOSS 10 (Bologna, sept. 1988),to be published in Surface Science.
5. St. Tosch and H. Neddermeyer, Initial stage of Ag condensation on Si(111)7x7,Phys. Rev. Lett. 61 : 349 (1988).
6. G. Binnig, H. Röhrer, Ch. Gerber and E. Weibel, 7x7 reconstruction on Si(111) resolved in real space, Phys. Rev. Lett. 50 : 120 (1988).
7. K. Takayanagi, Y. Tanishiro, S. Takahashi and M. Takahashi, Dimer adatom stacking fault model of the 7x7 reconstruction of Si(111), Surf. Sci. 164 : 367 (1985).
8. R.I.G. Uhrberg, G.V. Hansson, J.M. Nicholls, P.E.S. Persson and S.A.Flodström, Photoemission study of the surface and bulk electronic structures of Si(111)7x7 $\sqrt{3}$x$\sqrt{3}$ Al, Phys. Rev. B 31 : 3805 (1985).
9. J.M. Nicholls, B. Reihl and J.E. Northrup, Unoccupied surface states revealing the Si(111)$\sqrt{3}$x$\sqrt{3}$-Al-Ga and In adatom geometries, Phys. Rev.B 35 : 4137 (1987).

10. J. Nogami, Sang Il Park and C.F. Quate, Indium induced reconstructions of the Si(111) surface studied by S.T.M., Phys. Rev. B 36 : 6221 (1987).
11. R.J. Hamers and J.E. Demuth, Atomic structure and bonding of Si(111)$\sqrt{3}$x$\sqrt{3}$ Al, J. Vac.Sci. Technol. A 6 : 512 (1988).
12. J.E. Northrup, Si(111)$\sqrt{3}$x$\sqrt{3}$ Al : an adatom induced reconstruction, Phys. Rev. Lett. 53 : 683 (1984).
13. J.S. Nelson and I.P. Batra, Metallization, bonding and energetics of ordered phases of Al on Si(111), Proceedings of the NATO workshop on metallization (Garching, Germany - August 1988), Plenum, New York, I. P. Batra, Editor.
14. H. Hirayama, T. Tatsumi and N. Aizaki, RHEED and Auger electron spectroscopy study on B/Si(111) surfaces, Surf. Sci. 193 : L 47 (1988).
15. V.V. Korobotsov, V.G. Lifshits and A.V. Zotov, Formation of Si(111)$\sqrt{3}$x$\sqrt{3}$ B and Si epitaxy onSi(111)$\sqrt{3}$x$\sqrt{3}$: LEED and AES study, Surf. Sci. 195 : 466 (1988).
16. F. Thibaudau, Ph. Dumas, F. Salvan, Ph. Mathiez, A. Humbert and D. Satti, $\sqrt{3}$ structure of B enriched Si(111) surfaces investigated by Auger, LEED and S.T.M., Proceedings of the ECOSS 10 Conference (Bologna, Sept. 1988), to be published in Surf. Sci.
17. Ph. Dumas, F. Thibaudau and F. Salvan, STM of B/Si(111)$\sqrt{3}$x$\sqrt{3}$, Proceedings of the 3rd Intern. Conference on STM (Oxford, 1988), to be published in Journal of Microscopy.
18. Ph. Dumas, A. Humbert, G. Mathieu, Ph. Mathiez, C. Mouttet, R. Rolland, F. Salvan and F. Thibaudau, STM studies on Au/Si(111) interfaces, J. Vac.Sci. Technol. A6 : 517 (1988).
19. G. Le Lay, Physics and electronics of the noble metal semiconductor interface formation, a status report, Surf. Sci. 132 : 169 (1983).
20. K.Oura, M. Katayama, F. Shoji and T. Hanawa, Real-space determination of atomic structure of the Si(111)$\sqrt{3}$. Au Surface by low energy alkali ion scattering. Phys. Rev. Lett. 55 : 1486 (1985).
21. J.H.Huang and R.S. Williams, The atomic structure of the Si(111)$\sqrt{3}$x$\sqrt{3}$ and 6x6 Au surfaces by low-energy ion scattering, J. Vac. Sci. Technol. A6: 689 (1988).
22. F. Salvan, H. Fuchs, A. Baratoff and G. Binnig, Au/Si(111) overlayer : characterization by tunneling microscopy and spectroscopy, Surf. Sci. 162: 634 (1985).
23. J.M. Nicholls, F. Salvan and B. Reihl, Surface states of Au, Ag and Cu overlayers on Si(111) studied by inverse photoemission, Phys. Rev. B 34 : 2945 (1986).

24. K. Higashiyama, S. Kenzo and T. Sagawa, Structural disorder of Si(111) $\sqrt{3}$x$\sqrt{3}$-Au surface studied by LEED, Japan. J. of Appl. Phys. 25 : L 117 (1986).

TUNNELING SPECTROSCOPY AND POTENTIOMETRY ON CLEAVED (Al)GaAs MULTILAYERS

H. W. M. Salemink

IBM Research Division
Zurich Research Laboratory
8803 Rüschlikon, Switzerland

The continuity of the energy band structure at nanometer resolution is of considerable interest in semiconductor physics [1]. Data on the electronic density of surface states can be obtained with the scanning tunnel microscope (STM) at atomic resolution [2, 3]. Most of the STM experiments are performed on uniform low-index semiconductor surfaces or surfaces with partial coverage [4, 5].

In this paper we report on two types of spectroscopic studies on heterostructure III-V multilayers, which are MBE grown along the ⟨001⟩ orientation and measured on the (110) cleavage plane. The experiments provide data on the continuity on the energy band and its spatial dimensions in the material interfaces. The GaAs(110) face is of special interest, because its surface is 1×1 constructed and hence lacks the innergap surface states, which are present on most reconstructed semiconductor surfaces [4]. Thus, it might be expected that the density of states at the surface more closely resembles that of the bulk.

The heterostructures are cleaved in a UHV preparation vessel ($P < 5 \times 10^{-8}$ Pa) and transferred to a connected STM analysis chamber ($P < 5 \times 10^{-9}$ Pa). This chamber is equipped with a high-resolution SEM, which is used to position the tunneling tip in the region of interest (Fig. 1). In the first type of experiment the STM tip operates in a local 'potentiometric' mode, measuring the voltage potential between the tip and one of the outer contacts of the sample [6]. In this way, a cross sectional electric potential in the sample is scanned at a tunneling distance from the surface. The lower traces in Fig. 1(b) show the potentiometric response with about 1.5 V applied bias over the p-n junction in the sample. A potential drop is traced over the (unintentionally) doped GaAs layer, but some discontinuities arise at the GaAs-AlGaAs interface. A steeper potential gradient is seen in Fig. 2 on a similar sample: it shows a 15 nm wide transition which implies a field strength of 1.0×10^6 V/cm. The position of the gradient shifts with junction voltage, which is probably due to displacement of the recombination region.

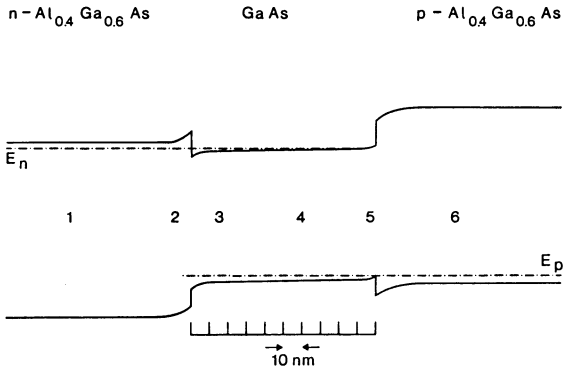

Fig. 1. (a) Schematic energy diagram of heterostructure, used for potentiometric experiments. The STM tip is positioned close to the junction using the SEM. (Adapted from [6a])

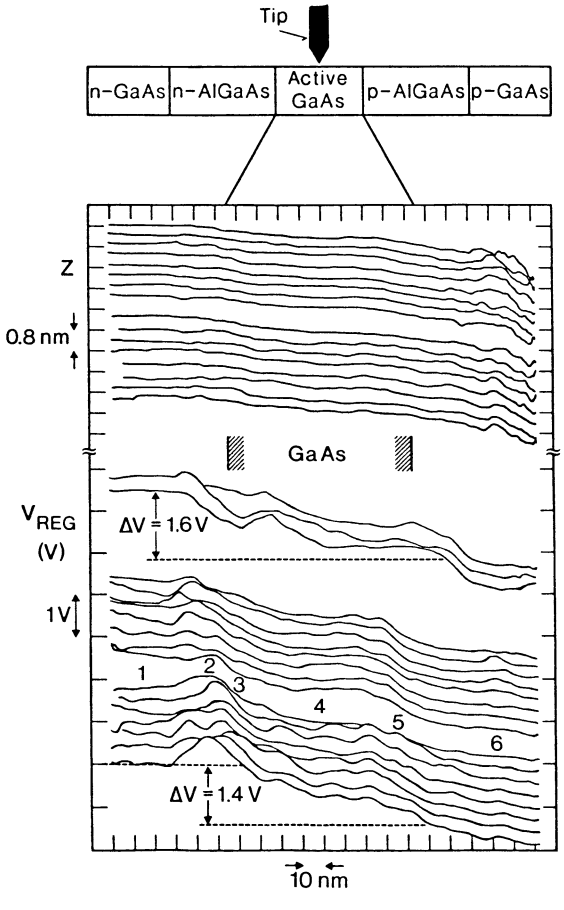

Fig. 1. (b) Topographic (upper traces) and potentiometric data (lower traces) over the cleaved p-n structure. The voltage ΔV is applied over the junction. Two different electronic circuits are used to separate topography and potentiometry. (From [6b], © 1986 Academic Press (London) Limited)

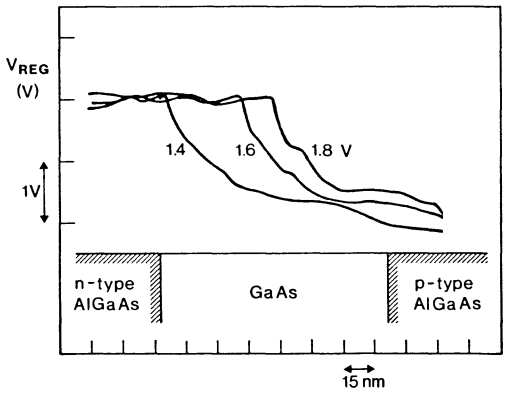

Fig. 2. The potential difference in the recombination region for several junction voltages. Note the potential drop over a range of about 15 nm. (Adapted from [6a])

The second type of experiment employs an STM spectroscopy mode to measure the local current-voltage (I-V) characteristic in cleaved sections of similar structures (Fig. 3). The I-V curves are recorded during short (10 msec) interruptions of the tip-position feedback loop. During these interruptions, local I-V curves are recorded during scans over the structure at a typical spatial separation of 1 nm.

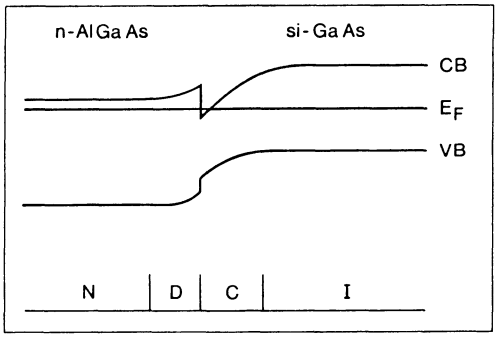

Fig. 3. Energy band scheme of the structure used for the spectroscopic studies. Growth is along ⟨001⟩, the exposed face is (110); si refers to semi-insulating GaAs region (I).

With the tip positioned close to the D-C interface (Fig. 3), the local I-V curves are acquired as a function of position, perpendicular to the interface. Four distinct zones are identified by their different conductivity. From these I-V curves, the tunneling current at a sample voltage of +1.5 V is drawn in Fig. 4. The local minimum and maximum are assigned to the depleted (D) and electron-confined (C) region, respectively. A depletion width of 15 to 20 nm is deduced, which is typical for such interfaces.

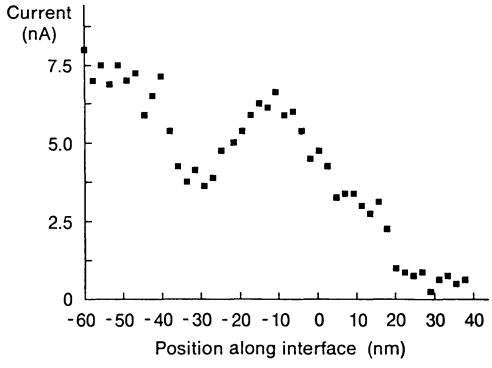

Fig. 4. Tunnel current for sample voltage of +1.5 V as a function of position over the junction.

Two local I-V curves in regions D and C (taken at a separation of 30 nm) display a band offset of 0.35 ± 0.03 eV when tunneling out of the sample [7]. This offset is attributed to the step in the valence band and compares well with the photo-emission data on a similar interface [8].

In conclusion, we have shown spectroscopic data on III-V heterojunctions, which allows the electronic properties of interfaces to be traced in real space; further work could clarify the energy positions of conduction and valence bands in such junctions.

References

1. F. Capasso and G. Margaritondo, *Heterojunctions and Band Discontinuities*, North-Holland, Amsterdam, 1987.
2. G. Binnig, H. Rohrer, Ch. Gerber and E. Weibel, *Phys. Rev. Lett.* **50**, 120 (1983).
3. R. J. Hamers, R. M. Tromp and J. E. Demuth, *Phys. Rev. Lett.* **56**, 1972 (1986).
4. R. M Feenstra and J. A. Stroscio, *J. Vac. Sci. Technol.* **B5**, 923 (1987).
5. R. M. Feenstra and P. Martensson, *Phys. Rev. Lett.* **61**, 447 (1988).
6. (a) P. Muralt, H. Meier, D. W. Pohl and H. W. M. Salemink, *Appl. Phys. Lett.* **50**, 1352 (1987). (b) P. Muralt, H. Meier, D. W. Pohl and H. Salemink, *Superlattices and Microstructures* **2**, 519 (1986).
7. H. W. M. Salemink and P. Muralt, to be published.
8. M. Heiblum, M. I. Nathan and M. Eizenberg, *Appl. Phys. Lett.* **47**, 503 (1985).

Alkali Metals-Semiconductors Interfaces

METALLIZATION OF METAL-SEMICONDUCTOR INTERFACES

S. Ciraci* and Inder P. Batra†

*IBM Research Division, Zurich Research Laboratory,
8803 Rüschlikon, Switzerland
†IBM Research Division, Almaden Research Center, 650 Harry Road,
San Jose, CA 95120-6099, USA

1. INTRODUCTION

The intimate contact of two electronic materials, and the electronic properties generated thereof, has been widely used in electronics. Increasing complexity and versatility in new device concepts have made metal-semiconductor (MS), metal-oxide-semiconductor (MOS), and semiconductor-semiconductor junctions an essential ingredient of electronic circuitry. With the recent progress in growth techniques these junctions can now be fabricated coherently according to the desired structure and degree of perfection.[1] When a metal is put in intimate contact with a semiconductor, the bands of semiconductor are aligned to have a common chemical potential with metal. This may lead to a shift of the semiconductor bands forming a barrier (Schottky barrier) so that electrons are prevented from entering into the semiconductor.

Because of the rectifying properties and the importance of Ohmic contacts in the integrated circuits this barrier has been studied extensively. Presently, the quantum size effect in the metal contacts seems to be one of the serious limitations which bars further miniaturization of these devices. A great deal of effort has been expended towards developing a microscopic understanding of the metal-semiconductor interaction and Schottky barrier formation.[2-14] Since the Schottky barrier is determined by the height of the conduction band edge (in an n-type semiconductor) above the Fermi level it is crucial to know how the Fermi level is fixed at the metal-semiconductor interface. The precise nature and origin of the electronic states responsible for the Fermi level pinning are still not fully known due to a large number of factors which influence the Fermi level position. Bardeen[4] gave a plausible explanation of the barrier height in the metal-elemental semiconductor junctions, which happen to be rather insensitive to the work function of the metal. According to his model the charge redistribution takes place within these high-density surface states of a semiconductor lying in the band gap, and fixes the relative position of the conduction band at the interface. However, it is known that these intrinsic surface

*Permanent address: Department of Physics, Bilkent University, Bilkent 06533 Ankara, Turkey

states are eliminated from the gap region owing to the reconstruction [as in the GaAs(110) surface] or bond formation with the metal atoms. Then, metal-induced gap states, which propagate in the thick metal film but become evanescent in the semiconductor, have been proposed as states responsible for the pinning.[5] Later, the existence of metal-induced gap states was confirmed by the self-consistent field (SCF) pseudopotential calculations.[6] Theories[7,8] derived from the idea of Heine have developed the charge neutrality concept at the interface. Recent experiments, however, have come to different conclusions, namely that the Fermi level can be pinned and thus the Schottky barrier is formed even at submonolayer coverage.[9,10] Different kind of states, such as intrinsic surface states, defect states,[10] adatom and chemisorption bond states[11-14] have been postulated to determine the Fermi level at submonolayer coverage. Bardeen's and Heine's theory are combined in the theory of Lannoo,[11] and the resonance states originating from the dangling bonds surface states are proposed to be responsible for the pinning. A similar mechanism was proposed earlier, based on the SCF local density of states calculated for an ideal metal-semiconductor interface.[14]

The pinning mechanism at the monolayer and multilayer metal coverage have been the subject matter of our recent studies[12-14] pointing out interesting coverage-dependent effects. After studying a prototype, nearly lattice-matched metal-semiconductor interface [i.e. Al on Ge(001) surface] from submonolayer to multilayer coverages, we found that at submonolayer coverage the chemisorption bond states and Al-atom states dominate the energy spectrum near the band-gap region and determine the Fermi level. However, above the monolayer coverage the overlayer changes into a (quasi-) two-dimensional metal characterized by a (modulated) ladder-type density of states. Concomitant with the metallization, the overlayer relaxes outwards away from the semiconductor surface, and the metal-semiconductor bonds are delocalized. At this stage the 2-D metal states (which decay in the semiconductor) together with the delocalized metal-semiconductor bond states determine the Fermi level. The pinning states at one and two metal-monolayers can also be thought of as the combination of Bardeen's and Heine's picture, in which intrinsic as well as the metal-induced states play a crucial role.[14] The delocalization of the metal-semiconductor bond corresponds to the resonance states originating from the dangling bonds postulated by Lannoo.[11]

For those semiconductors which have active surface states, the metallization of the overlayer must compete with the formation of metal-semiconductor bonds. In fact, depending on the relative value of the metallic cohesive energy and the metal-substrate interaction energy, the overlayer metallization may be suppressed altogether. In this respect, the adsorption of alkali atoms on semiconductor surfaces is rather special, and presents very fascinating conceptual ideas about bonding, metallization and collective excitations.[15-23] In contrast to the Al+Ge(001) system, we have found that the Fermi level of the alkali-elemental semiconductor system (K on Si surfaces) is determined (but not pinned) by the intrinsic surface states at monolayer coverage.[20-23] In spite of the fact that the adatom is a metal, the resulting bonding is strongly ionic, and the insulating substrate surface changes into a metallic state.

In this paper, we treat two basic interactions (i.e. metal-metal and metal-semiconductor) at the ideal metal-semiconductor interface, and discuss their role in determining the Fermi level. We show how and under what conditions the overlayer is metallized. As exemplified by two specific interfaces (i.e. Al-Ge and K-Si), we demonstrate that in the former case the Fermi level is rapidly stabilized concomitant with overlayer metallization. In the later interface the overlayer metallization does not take place up to a monolayer coverage, and thus the Fermi level continues to move as a function of the alkali atom coverage. Another important

conclusion emerging from our study points to the fact that the diverse physical phenomena taking place at the interface (charge transfer, screening, delocalization of bonds, interface reconstruction, metal-island formation and finally the Fermi level pinning etc.) have to be considered within the minimization of the total energy. In this way not only the ideal, but also the strained interface can be incorporated in a unified fashion, and the position of the Fermi level of a metal-metal or semiconductor-semiconductor junction lying at a local minimum of the Born-Oppenheimer surface can be calculated. Theories which overlook this aspect of the problem, especially the self-consistency of the charge density ensuring that the given system remains at the Born-Oppenheimer surface, are able to disclose only a small portion of the physical phenomena.

Our results are based on the *ab-initio* total energy, electronic structure and force calculations performed within the repeating slab geometry. We use the SCF-pseodopotential method in momentum representation within the local density approach.[24] The normconserving, nonlocal ionic pseudopotentials given by Hamann and Schlüter,[25] and the exchange-correlation potential of Ceperly and Alder[26] are used in our calculations. The binding energy E_b of the adsorbed atom

$$E_b = E_T[S] + E_T[M] - E_T[M + S]$$

is obtained from the total energies of the metal-semiconductor (M+S) system, the bare semiconductor (S) and the metal atom (M). Here $E_b > 0$ means that the binding of the adatom is energetically favorable. Other details of calculations can be found in Refs. [14,21].

2. Al-Ge INTERFACE

The pseudomorphic growth of Al(001) film on the Ge(001) substrate can be achieved using the molecular beam epitaxy. To assure the lattice match the Al(001) film is rotated 45° with respect to the ideal Ge(001) lattice. In this case the lattice mismatch is 1.2%. The SCF-total energy calculations have been carried out for five layers of the ideal Ge(001) substrate and adsorbed Al atoms.[14] For $\theta = 1$ [i.e. one Al atom adsorbed on each Ge(001) surface unit cell], the geometry optimization favors the bridge site providing a natural hybridization of Al-sp^2 orbitals with the surface dangling bonds. Whereas the height from the surface is $h = 2.3$ a.u. and the binding energy is $E_b = 3$ eV, the lowest binding energy of the Al(001) layer [$\theta = 2$, and two Al atoms are adsorbed per Ge(001) cell] occurred at the height of 3.4 a.u. leading to a significant increase in the interplanar distance. As a result, the strongly directional Al-Ge bond is elongated, and becomes delocalized. This can be seen from the charge density plots presented in Fig. 1. The maximum charge density for $\theta = 1$ reaches a value of 0.079 a.u. at the center of the Al-Ge bond; the corresponding value for $\theta = 2$ is 0.056 a.u. It is clear that the directional covalent bonding changed into a more delocalized metallic type of interaction.[27] The metallization of the Al overlayer is illustrated by the contour plots of the total charge density on the overlayer plane. For $\theta = 1$, the charge density forms a row along the [110] direction displaying a 1-D character. The complete metal overlayer ($\theta = 2$) shows a more isotropic charge density. In this case a 2-D metal is formed leaving less charge at the interface. The effect of the overlayer metallization in the electronic structure and the Fermi level pinning is clearly seen in the local density of states (LDOS) shown in Fig. 1. New major peaks appear in addition to the usual structure of the bulk Ge and are connected with the interaction at the interface. The chemisorption states forming the Ge-Al-Ge bonds appear near the Fermi level, and also 3 eV below it. The states connected with the dangling sp^2 orbital of Al overlap with the chemisorption band of

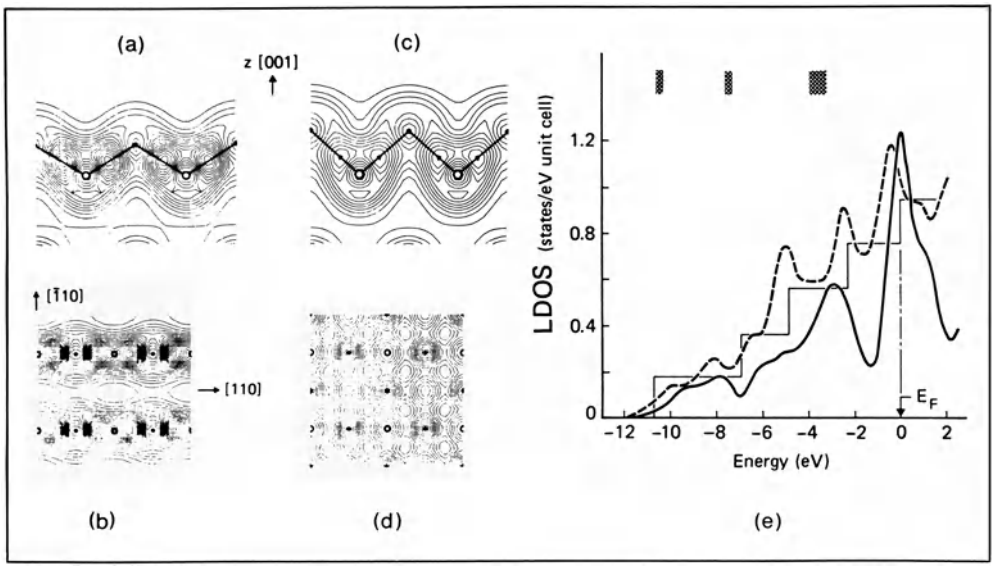

Fig. 1. Charge density contours: (a) Vertical plane, $\theta = 1$; (b) Horizontal plane passing through Al atoms, $\theta = 1$; (c) and (d) same for $\theta = 2$. The contour spacings $\delta\rho$ (in electrons per a.u.^{3}) are 0.005, 0.0025, 0.005, 0.0025, respectively. The local density of states at the Al layer calculated for $\theta = 1$ (dashed curve), and $\theta = 2$ (solid curve). The ladder-type density of states is for the quasi 2-D electron system with the same areal charge density as for $\theta = 2$. The shaded zones indicate the major structure of bulk Ge (reproduced from Ref. 14).

Al, and contribute to the pinning at this coverage. States having Al-3p_y character would couple the metal atoms along the [110] direction, but since these states are unoccupied, the overlayer displays a nearly 1-D character. For $\theta = 2$, the local density of states may be viewed as a modulation on top of the ladder-type density of states of a quasi 2-D electron gas.[28] This implies that the states of the overlayer are free electron-like in the plane parallel to the interface, and hence consistent with the definition of the overlayer metallization.

In view of the above results we propose that the Schottky barrier is fully developed only after a deposition of one to two layers of metals, and not at submonolayer coverage. With this ansatz we make the following observations. The macroscopic metallic properties of a thin metal layer, e.g. work function, are significantly different from the bulk. At one to two monolayers, on the other hand, we see an evolution towards the bulk properties. Also in those cases where nondirectional interactions are sought, a metallized phase is a more likely candidate than a chemisorbed layer. In a recent study,[28] we found that a seven-layer thick Al film exhibits a quasi 2-D character, with the states having free electron-like solutions in the *(x,y)* plane, but decaying into the vacuum from both surfaces of the film. The local density of states suggests similar behavior in the metal overlayer. The metal states may decay into the semiconductor, when they cannot find any matching partner. Therefore, without invoking either defect states or metal-induced states of a thick overlayer,[5] even a single metal layer is capable of providing enough gap states leading to the delocalization of the metal-semiconductor bond, and thus the pinning of the Fermi level.[14] The justification of this model is evident in the experimental work[29] indicating that in the Al-Si case the metallic character appears above one layer.

3. ALKALI ATOM-INDUCED METALLIZATION OF SILICON

Coverage-dependent properties of the alkali adsorption on metal surfaces have been reported for various metal surfaces.[30] The common trend is that at the initial stage of the alkali adsorption the work function Φ decreases rapidly. It is argued that at low coverage, ionic bonding between the alkali atoms and the metal surface occurs through donation of the alkali valence electrons. This creates a surface dipole which is responsible for lowering the work function. Further alkali atom deposition near the monolayer coverage ($\theta \simeq 1$) causes Φ to pass through a minimum and an energy loss peak to grow in intensity. Eventually, at high ($\theta >> 1$) Φ saturates at the work function of the alkali metal. The second stage of adsorption corresponding to relatively higher coverage is related to the metallization of the alkali overlayer.

The interesting features of alkali adsorption on the Si-surfaces have been revealed by the pioneering work of Tochihara et al.,[15-17] and have attracted much attention recently. Their experimental observations on the potassium-covered Si(001) surface pointed to the fact that the alkali atoms on the semiconductor surfaces lead to practically the same features as observed on transition metals. At the monolayer coverage [$\theta = 1$, i.e., one K-atom per (2×1) surface unit cell] the surface shows a clear (2×1) LEED pattern but with a different intensity as compared to the bare surface. The work function decreases rapidly at submonolayer coverage ($\theta << 1$), and later ($\theta \simeq 0.5$) concomitant with the onset of an electron-energy loss peak (EELS) at 2 eV, it decreases slowly. Similar to the conclusions drawn for the alkali-metal adsorption on metal surfaces[30] these observations were interpreted to imply a metal-insulator (Mott) transition. It was proposed that up to $\theta = 0.5$, K-atoms donate their 4s valence electrons to the substrate and become ionic as evidenced by a higher core excitation energy and lower work function. Continued deposition of alkali atoms causes the internuclear distance of the potassium atoms to decrease and, beyond a threshold adatom density, the smaller K-K distance allows the metallic bands to form which, in turn, results in a back transfer of charge to the alkali-metal overlayer. Accordingly, the growing intensity of the peak in the electron-energy-loss spectra (EELS) with increasing θ was attributed to a collective excitation of the metallic electrons of the overlayer. Similar results were obtained also for the Cs-covered Si(001) surface.[16] The analysis of this plasmon loss by the angle-resolved EELS[17] indicated an anisotropic and positive dispersion in contrast to the plasmon dispersion of an alkali-metal overlayer on a metal surface. In view of the interband and intraband (zero-sound) plasmon modes calculated[18] for a simple model, these $|\vec{q}$ –dependent loss peaks were attributed to the 1-D plasmons associated with the K-chains on the surface. Similar to the conclusions drawn for the alkali metal-adsorbed Si(001)-(2×1) surface, the ultraviolet photoemission spectrum (UPS) taken from the Cs-covered Si(111)-(2×1) surface[19] has been interpreted to imply the metallization of the alkali overlayer beyond the adatom coverage of $\theta = 1$.

We carried out total energy and electronic structure calculations for the unsupported K-layers, clean and K-covered Si surfaces at $\theta = 1$ and $\theta = 2$ by using the repeating slab geometry. The top surface is either clean or covered with alkali atoms, but the bottom surface is always saturated with hydrogen atoms. Due to this asymmetric termination of the two surfaces one may get some small artifact on the slab-computed work function. The Bloch states are represented by a basis set of ~1000 plane waves corresponding to $|\vec{k} + \vec{G}|^2 < 6.5$ Ry, whereby the degree of convergence compatible with the desired accuracy in the calculation of properties (such as the binding energy and charge density) is achieved.

3.1. K-adsorbed Si(001)-(2×1) surface

We searched the equilibrium structure among the plausible adsorption sites by comparing the calculated binding energies. Our analysis of the optimum binding structure for $\theta = 1$ within the (2×1) reconstructed Si(001) surface (with symmetric dimer bond) yielded the lowest total energy for the K-atom located at the center of the six-fold hollow site, between two parallel dimer bonds, and at 2.4 a.u. above the surface.[20,21] The Si-K interatomic distance $d_{(K-Si)} = 4.9$ a.u. may be underestimated due to the form of the exchange-correlation potential given in the local density approximation and also due to the core pseudopotential used in these calculations. The calculated binding energy is $E_b \simeq 3$ eV per K-atom. According to this equilibrium structure the adsorbed K-atoms form a chain along the [110] direction with an interchain distance of $2a/\sqrt{2}$ (a being the lattice parameter of Si). Along the chain each K-atom has two nearest neighbors with an internuclear distance of 7.26 a.u. The small and symmetric forces on the surface silicon atoms indicate that at $\theta = 1$ the asymmetric dimer bond changes into the symmetric one (as initially assumed), and is lowered towards the surface. Moreover it contracts to yield a slightly smaller bond length relative to that of the bare surface. The equilibrium structure of the adsorbed potassium atoms is presented in Fig. 2. It is also worthwhile to mention that our structure optimization identifies other sites (i.e. the hollow sites above the third and fourth-layer Si atoms) which yield binding energies comparable to that of the equilibrium site. This implies the possibility that at room temperature K atoms can be adsorbed at the equilibrium site as well as at these secondary sites forming a disordered structure at $\theta = 1$.

Since the first hollow-site between two dimer bonds was already occupied by the K-atoms (denoted by K_1), an appropriate position for the second K-atom (denoted by K_2) at $\theta = 2$ is the second hollow site above the third-layer Si atom. The optimum structure of $\theta = 2$ is determined by minimizing the interatomic forces and total energy through simultaneously varying the height of K_1 and K_2 (h_1 and h_2). The equilibrium structure is found for $h_1 = 2.5$ a.u. (slightly higher than $\theta = 1$) and $h_2 = 1.2$ a.u. The

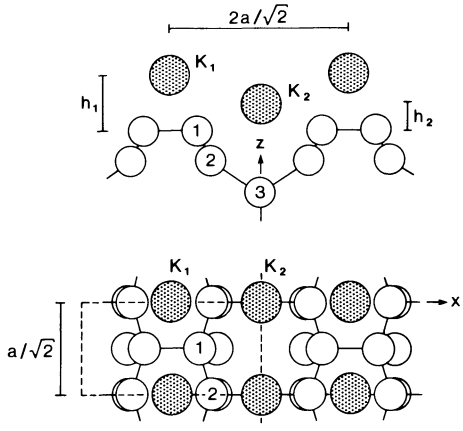

Fig. 2. Side and top views describing the positions of adsorbed potassium atoms on the Si(001)-(2×1) surface at $\theta = 2$. Shaded large and empty small circles denote K and Si atoms, respectively. Numerals in the circles indicate the atomic layers. At $\theta = 1$ only the K_1 site is occupied; a = 10.26 , $h_1 = 2.5$ and $h_2 = 1.2$ a.u.

internuclear distance between K_2 and surface Si is 6.3 a.u., and that between K_2 and second-layer Si is 5.3 a.u. The binding energy corresponding to this equilibrium structure at $\theta=2$ is found to be 2.7 eV per K-atom. The decrease of the binding energy of 0.3 eV per K-atom at high coverage is associated with the enhanced K-K interaction and Coulomb repulsion in the surface state bands. It is noted that the calculated binding energy is large for either coverage, and is in fact three times larger than the cohesive energy of the bulk potassium. This indicates a rather strong interaction between Si surface and adsorbed atom even for $\theta=2$. Comparing the value of binding energy with the adhesion energy[31] between two potassium jellium surfaces separated by ~1 a.u. (which is ~0.2 eV per K-atom) one concludes that the metallization of the K-chain on the Si(001)-(2×1) cannot occur because of the strong Si-K interaction.

The character of this strong interaction underlying the large binding energy is clarified by studying the electronic structure and the total and state charge distributions. It is known that the Si(001)-(2×1) surface has two bands confined to the band gap; the first one, D_1, is filled and the second, D_2, is empty, leading to an insulating surface with an asymmetric dimer bond. The unsupported, fully metallized K-chain has a half-filled band with a width of 2.5 eV along the chain direction. Our calculated band structures for both values of K-coverage ($\theta=1$ and 2) do not depict a band picture significantly different from that of the bare Si(001)-(2×1) surface. Potassium-covered surfaces have again two bands in the gap with the upper band, D_2 half filled for $\theta=1$, but both bands are completely filled and the Fermi level is located between the conduction band and D_2 for $\theta=2$ (see Fig. 3). It also becomes clear that the bands which would form upon metallization of the K-chain are almost totally discarded, and are merged in the conduction band of the substrate. Surface states or resonances in the conduction band are found in the energy region where the interband plasmon dispersion is measured.[17] These states are accessible by the excited electrons in the EELS experiment, which samples mainly the surface region, and are likely to be responsible for collective and individual excitations. For example, the resonance state R, which originates from the antibonding dimer bond state, hybridizes with different bulk-conduction band states along the [100] direction. At the center of the surface Brillouin zone this state is located 1.9 eV above the filled D_1 band. The individual excitation energy inferred from D_1 and R state energies is in fair

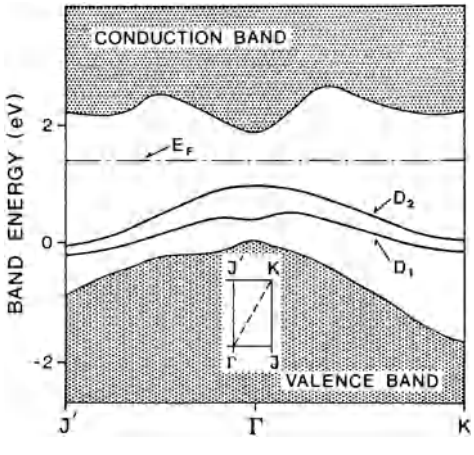

Fig. 3. Calculated energy band structure of K-covered Si(001)-(2×1) surface at $\theta=2$. D_1 and D_2 are dangling bond surface states. Surface Brillouin zone is shown by the inset.

agreement with the observed EELS peak.[17] It should be noted that the clean Si(001)-(2×1) surface exhibits an EELS peak in the same energy region.[32,33] The backbonding and dimer bond states can be identified in the valence band, indicating that the effect of the adsorbed alkali layer on the surface states is insignificant. The calculated work function of the K-covered surface at $\theta = 1$ is found to be 2.3 eV lower than the work function of the clean surface. This value is in fair agreement with the observed lowering of the work function upon K-adsorption.[15] The local density of states calculated above the lateral plane intersecting the spacing between the first and second Si atomic layers is comparable with the bulk density of states, except that the peak due to D_1 and D_2 appears in the band gap of Si (see Fig. 4). The integration of this distribution up to E_F yields 9.7 (but not 10) electrons. No structure is seen near E_F that can be associated with the metallized overlayer.

The character of these two bands in the gap is unveiled by examining their charge distribution before and after the K-adsorption presented in Fig. 5 for $\theta = 1$. The contour plots of D_1 and D_2 for the bare surfaces are not much affected by the alkali adsorption, and they nearly preserve their dangling bond character. Therefore, not only the metallization of the K-chain, but also any significant contribution of K-orbitals in the states near the Fermi level are rejected by these plots. Certainly, the slight modifications of the intrinsic surface bands and their charge distribution due to the change in the surface potential are not ruled out. The character of states forming the completely filled band in the gap for $\theta = 2$ is examined by the difference of the total charge densities

$$\Delta\rho_T(\vec{r}) = \rho_{T,\,\theta=2}(\vec{r}) - \rho_{T,\,\theta=0}(\vec{r})$$

of the $K_1 + K_2 + Si$ and the bare Si surface. Figure 6 illustrates the contour plots of $\Delta\rho_T$ on two vertical planes, one passing through the dimer bond, and other containing K_1 and K_2. It is seen that the valence electrons of the adsorbed K-atoms (two electrons per cell) are essentially accommodated by the dangling bond surface state band, D_2. However, the difference plot on the second plane has a small amount of charge accumulated between K_2 and second-layer atoms, implying some covalent nature in the binding. Also from the charge distribution one can sense a minute interaction set between K_1 and K_2. Of course, this interaction is much weaker than that of the fully metallized, unsupported K_1 and K_2 layer presented in Fig. 6 (c). However, in view of the energy gap between D_2 and the conduction band, one concludes that the alkali overlayer is not metallized, but only the D_2 state is modified in the presence of K_2. One should keep in mind that the intra-atomic Coulomb repulsion (Hubbard U) may become effective when both D_1 and D_2 are fully occupied. This may alter the electronic structure somewhat, but is beyond the scope of present calculations, which are based on LDA.

The above results provide clear evidence that the interaction between adsorbed K and the Si(001)-(2×1) surface is strong (three times the bulk cohesive energy of K) and the resulting bonding is ionic. For $\theta < 2$, the 4s valence electron of the alkali atom is donated into the empty dangling bond band D_2 of the bare Si(001)-(2×1) surface. Accordingly, starting from $\theta << 1$ this band accommodates the alkali electron, and thus the insulating semiconductor surface becomes metallic, as opposed to the overlayer metallization. Since this band is completely filled at $\theta = 2$, the semiconductor surface regains the insulating character. This behavior is a decisive criterion distinguishing two seemingly immaterial, but fundamentally subtle cases: overlayer or substrate surface metallization. In contrast to the present situation the metallization would be enhanced at $\theta = 2$ if the overlayer is already metallized at $\theta = 1$. For $\theta > 2$, the main issue is whether additional potassium can be bound on the surface and form a thick overlayer of alkali atoms.

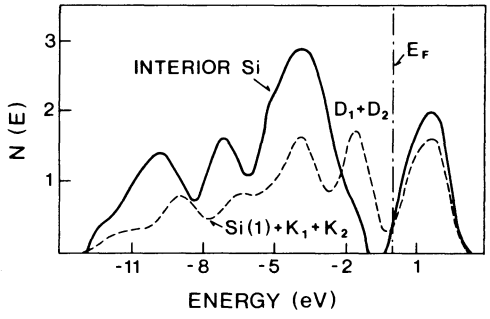

Fig. 4. Layer density of states calculated above the plane bisecting the distance between the surface and subsurface Si layers (dashed line), and at the fourth Si layer of the K-covered Si(001)-(2×1) slab (solid line) at $\theta = 2$. The states originating from the dangling bond surface states are indicated by $D_1 + D_2$.

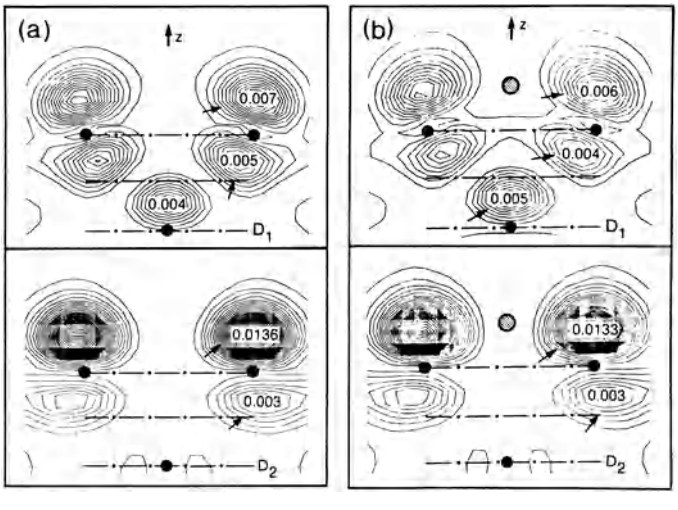

Fig. 5. Charge density contour plots of D_1 and D_2 states in a vertical plane calculated for the clean (a), and K-adsorbed Si(001)-(2×1) surface (b). $\theta = 1$ and $\vec{k} = (0.0;0.108;0.0\ \text{a.u.}^{-1})$. The atomic (001) planes of Si substrate are shown by dash-dotted lines. Charge density increases in the direction of small arrows. Contour spacings are 5×10^{-4} in a.u. (Reproduced from Ref. 21).

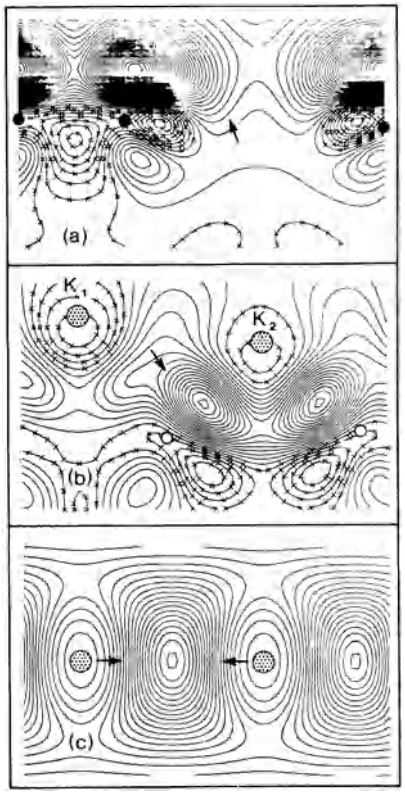

Fig. 6. Contour plots of the difference charge density $\Delta\rho$, in a vertical plane passing through the dimer bond (a), and K_1 and K_2 (b). $\theta = 2$ and $\delta\rho = 5\times10.^{-4}$ Contours with crosses indicate the region of charge depletion. (c) Contour plots of unsupported potassium layer on a vertical plane passing through K_1 and K_2 with $\delta\rho = 2\times10^{-4}$ a.u. Positions of surface Si, subsurface Si, and K-atoms are indicated by filled, empty, and large shaded circles, respectively.

3.2. K-adsorbed Si(111)-(2×1) structure

The π-bonded Si(111)-(2×1) surface[34] has two surface state bands denoted π and π^*. Because of the chain structure these bands are almost flat along the KJ-direction of the surface BZ, but have a large dispersion along the chain direction. The π^*-band is empty and separated from the filled π-band by a small superlattice gap. The surface unit cell has two (low-charge density region) hollow sites at the centers of two adjacent hexagons of surface bonds. These features are very similar to what we have seen in the Si(001)-(2×1) surface. However, as far as the adsorption of K is concerned, the dramatic difference between these two surfaces is that the π^*-band overlaps with the conduction band continua. Also, the (negative) formation energy of the π-chain relative to the ideal surface is smaller than that of the dimer bond structure of the Si(001)-(2×1) surface. This makes the stability of the K-adsorbed surface an important issue.

The minimum total energy configuration at $\theta = 1$ is found for the K-atom at 2.8 a.u. above the center of the tilted hexagon. In this configuration the height is $h_1 = 1.8$ a.u. above the surface corresponding to $d_{(K-Si)} \simeq 5$ a.u., and the binding energy is 2.8 eV per K_1. By placing the second K-atom (K_2) above the second hollow site we calculate the binding energy 2.5 eV per K-atom. Because of the strong interaction with the Si(111)-(2×1) surface the metallization of the K-overlayer does not take place. Otherwise, it would cause K-atoms to relax by regaining their electrons, so that they would lose ~2 eV per atom, but gain only ~1 eV through metallic cohesion. These assertions are evidenced by the band and charge density calculations.

The band structure results of the K+Si(111)-(2×1) system show that at $\theta = 1$ the Fermi level rises by 0.7 eV with respect to the valence band edge, and the π^*-band becomes partially occupied by the valence electrons donated from the adsorbed K-atom. As identified from an extensive charge density analysis over the BZ of the K-covered and the bare surface, the overall form of the gap states does not change in the presence of the adsorbed potassium. Since the π^*-band overlaps with the conduction band continua, the electrons donated by the adsorbed K-atom are accommodated by the bulk conduction band states above a threshold coverage of $\theta \simeq 0.9$, and the Fermi level stays in the conduction band (see Fig. 7). This situation related with the upward shift of the Fermi level is obtained from the present calculations which uses a thin Si(111) slab. In a semi-infinite slab one expects, however, the Fermi level to stay almost pinned near the conduction band minimum. Only at $\theta \simeq 2$ are the states above the Fermi level modified to have an admixture from K-4s orbitals. As seen in the dimer bonded Si(001)-(2×1) surface the presence of the active surface states plays a crucial role and prevents the alkali overlayer from becoming metallized. However, an important phenomenon here is that above a threshold coverage, alkali metal valence electrons are accommodated by the substrate conduction band states. This gives rise to a change in the dimensionality of the metallic system from one (at $\theta < 0.9$) to two (at $\theta > 0.9$), and enhances the conductivity perpendicular to the substrate surface. Of course, owing to the band bending effects the occupied conduction band states are prevented from extending over the entire semi-infinite substrate, but are confined to a quantum well between the vacuum and thick substrate.

Finally we would like to address the stability of the K-covered Si(111)-(2×1) surface. The above analysis is based on the assumption that this surface is stable (or

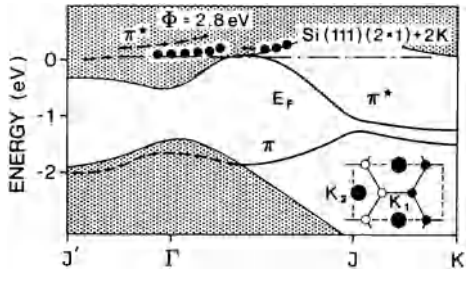

Fig. 7. Energy band structure of K-covered π-bonded Si(111)-(2×1) surface at $\theta = 2$. The conduction and valence band continua are shown by shaded areas. The positions of K_1 and K_2 atoms are given in the inset.

metastable). In the UPS spectrum of the Cs+Si(111)-(2×1) system[19] the peak appearing in the gap is attributed[35] to the π^*-band, indicating the fact that the chain structure endures after adsorption. In this experimental data, the evolution of the state distribution, and finally the pinning of the Fermi level, are consistent with our findings based on the π-bonded chain structure. Moreover, we find small forces exerted on the chain atoms. Whether the chain structure under the adsorbed K-atoms is only a local minimum of the Born-Oppenheimer surface, however, requires an extensive search among all possible structures. Such an optimization of the equilibrium structure is not feasible. On the other hand, it is known[36] that the barrier against going from the ideal Si(111) surface to the π-bonded chain topology is only 0.03 eV per surface atom, but the latter is energetically favorable by 0.6 eV. Interestingly, our calculations indicate that the K-adsorbed Si(111)-(1×1) structure is more stable than the the π-bonded chain structure by a total energy difference of ~0.3 eV. Even on the ideal Si(111) surface the alkali atoms are ionically bonded by donating their valence electrons to the half-filled, dangling bond surface band in the band gap. The resulting binding is 0.9 eV stronger than what we calculated for the reconstructed surfaces. The adsorption site is again the center of the hollow site (the hexagon formed by three surface and three subsurface Si atoms). As far as the stability of the chain structure is concerned, one has to keep in mind that the flat surface state band of the ideal surface yields stronger intra-atomic Coulomb repulsion. This certainly affects the stability of the K-covered ideal surface relative to that of the chain structure in the reverse direction. In this respect, the transition from the metastable to stable structure may be an interesting phenomenon to observe experimentally.

3.3. Comparison with other experimental and theoretical results

The unexpectedly strong interaction between the Si surface and the K-overlayer, and the results indicating the metallization of the Si surface, have attracted a great deal of interest, both experimentally and theoretically. Based upon the relatively larger $d_{(K+Si)}$ measured by SEXAFS, Kendelewicz et al.[37] have argued that the bonding is not ionic, but has to be covalent indicating the overlayer metallization. As mentioned earlier, our bond distances have an error bar due to the local density approach. This becomes evident by earlier total energy calculations of K-bulk underestimating the cubic lattice constant by 0.6 a.u., but making an excellent prediction of the binding energy.[38] It is also known that the nonlocal pseudopotential used in this study yields reliable total energies, but seems to underestimate the bond distances. One may conclude that $d_{(K+Si)}$ is underestimated in our calculations due to the nonlocal pseudopotential and LDA formalism. This becomes evident with an independent Hartree-Fock calculation,[39] which finds the bonding energy in the range of what we are finding, but with larger $d_{(K+Si)}$. Interestingly in this study, practically the same results are obtained when the K-atom is replaced by a single positive charge confirming the strongly ionic nature of the bonding. In agreement with the present conclusions, the SCF Hartree-Fock calculations predict that 94% of the K electrons are transferred to Si. SCF-pseudopotential calculations of Northrup[40] also find Na adsorbed on the Si(111)-(2×1) surface in the ionic state.

Based on the charge density analysis and the charge allocation obtained from their pseudofunction calculations Kasowski and Tsai[41] have proposed that the overlayer is metallized. Unfortunately, the binding energy they calculated was not stated. Their arguments on the charge allocation and density of states are based on an arbitrary charge partitioning, and thus are not conclusive.[42] Based on their experimental data strengthened by an empirical calculation, Oelling et al.[43] have challenged our theory. Their empirical tight binding calculation with an ad hoc self-consistency scheme and charge allocation predict that ~0.3 electrons are

transferred from K to Si, implying an ionic bonding. Using Topping's expression[44] they predict $\Delta\Phi$ in agreement with their measured value. Since the weak interaction is indigenous to the Hamiltonian they have constructed, one cannot expect to have a strong K-Si interaction from their empirical calculations. The energy parameters incorporated in this Hamiltonian are obtained from different fittings to the LDA bands, and thus are not unique. For example, the energy of the K-monolayer in their calculations corresponds to the structure and electron density, which is rather different from that on the Si(001) surface. This may give rise to a significant uncertainty in the value of the charge transfer. The calculation of the K-Si interaction by using a transfer Hamiltonian approach and omitting the matrix element of the potential cannot be justified. The use of the Topping expression with an ad hoc charge transfer procedure may give rise to erroneous conclusions.[45] Moreover, it appears that their measured data are also in disagreement with the recent experiments by Enta et al.[46] and by Papageorgopoulos.[47] In contrast to their previous LCAO band picture,[18] the improved LCAO and SCF pseudopotential calculations by Tsukada et al.[48] yield the binding energy and band structure in agreement with our results. However, they attribute some covalency to the K-Si bond at the SEXAFS height.

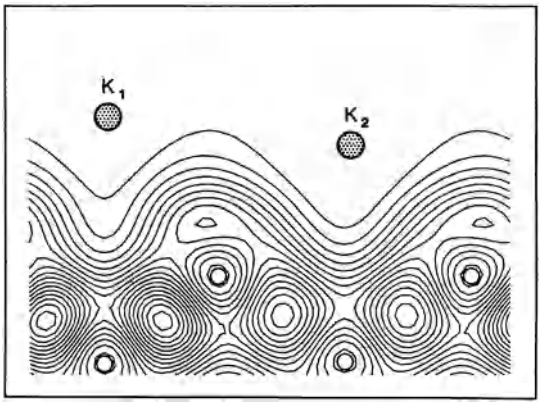

Fig. 8. Contour plots of the total charge density on a vertical plane passing through and K_1 and K_2; $\theta = 2$ and $\delta\rho = 5\times10^{-3}$ a.u.

The bands obtained by the angle-resolved inverse photoemission spectroscopy[49] confirms the band structure we obtained for the K+Si(001)-(2×1) surface. Moreover, angle-resolved photoelectron spectroscopy,[46] which reveals an insulating surface at $\theta = 2$, rules out previous band models, but supports our theory of metallization. A pictorial description of how the Si surface differs from the metal and why the binding is ionic is given in Fig. 8. The empty surface states, and the large corrugations of the surface charge density with the hollow sites arising thereof, are capable of accommodating the potassium atoms in their ionic state. Obviously, such a binding structure cannot yield an unexpectedly large work function lowering effect as presumed by Oelling et al.[43] This is the main difference between the metal and semiconductor surface as far as the interaction with K is concerned.

4. CONCLUSIONS

In this paper we investigated two basic interactions for determining the Fermi level of the metal-semiconductor systems at low coverage. For the metal atoms, which can form strong bonds with the semiconductor atoms, the surface states are replaced by the chemisorption states. The electronic energy spectrum in the gap region is dominated by these chemisorption and metal atom states, which determine the Fermi level at monolayer coverage. Depending upon the metal—metal-adatom distance the metallization of the overlayer can set in even below the monolayer by the formation of metal clusters. Upon metallization the metal-semiconductor bonds weaken. At multilayer coverage, the metal induced gap states combined with the delocalized metal-semiconductor bond states are responsible for the pinning.

The situation with the alkali overlayer on Si surfaces is found to be rather unusual. The intrinsic surface states continue to exist and up to $\theta = 2$ (one alkali atom per surface Si) they participate in determining the Fermi level by capturing electrons from alkali atoms. In this case, while the metal overlayer is changing to an ionic state, the insulating semiconductor surface is metallized. Since the surface state band is completely filled for $\theta > 2$, whether the metal induced gap states form to screen the K-Si bonds depends on whether the multilayer K can grow on the Si(001) surface, or the adsorption saturates at $\theta = 2$ as proposed by Etna et al.[46] However, as we pointed out earlier[20] and as verified experimentally by Papageogopoulos[47] the multilayer coverage as well as diverse experimental data[43] are strongly dependent on the cleanliness of the surface.

REFERENCES

1. L. Esaki and R. Tsu, *IBM J. Res. Develop.* **14**, 61 (1970).
2. R. H. Williams, *Contemp. Phys.* **23**, 329 (1982).
3. L. J. Brillson, *Surf. Sci. Rep.* **2**, 123 (1982).
4. J. Bardeen, *Phys. Rev.* **71**, 717 (1947).
5. V. Heine, *Phys. Rev.* **138**, A1689 (1965).
6. S. G. Louie and M. L. Cohen, *Phys. Rev.* **B13**, 2461 (1976).
7. E. Louis, F. Yndurain, and F. Flores, *Phys. Rev.* **B13**, 4408 (1976).
8. J. Tersoff, *Phys. Rev. Lett* **52**, 465 (1984).
9. G. Margaritondo, J. E. Rowe, and S. B. Christman, *Phys. Rev.* **B14**, 5396 (1976).
10. W. E. Spicer, I. Lindau, P. Skeath, C. Y. Su, and P. Chye, *Phys. Rev. Lett.* **44**, 420 (1980); *idem, J. Vac. Sci. Technol.* **17**, 1019 (1980).
11. M. Lannoo, these proceedings.
12. I. P. Batra and F. Herman, *J. Vac. Sci. Technol.* **A1**, 1080 (1983); I. P. Batra, *J. Vac. Sci. Technol.* **B1**, 558 (1983).
13. S. Ciraci and I. P. Batra, *Solid State Commun.* **51**, 43 (1984), I. P. Batra and S. Ciraci, *Phys. Rev.* **B29**, 6419 (1984); *idem, J. Vac. Sci. Technol.* **B3**, 427 (1984).
14. I. P. Batra and S. Ciraci, *Phys Rev.* **B33**, 4312 (1986).
15. H. Tochihara, *Surf. Sci.* **126**, 523 (1983).
16. H. Tochihara and Y. Murata, *J. Phys. Soc. Jpn.* **51**, 2920 (1982).
17. T. Aruga, H. Tochihara, and Y. Murata, *Phys. Rev. Lett.* **33**, 372 (1984).
18. M. Tsukada, H. Ishida, and N. Shima, *Phys. Rev. Lett.* **53**, 376 (1984); H. Ishida, N. Shima, and M. Tsukada, *Phys. Rev.* **B32**, 6236 (1985).
19. H. Tochihara, M. Kubota, M. Miyao, and Y. Murata, *Surf. Sci.* **158**, 497 (1985).
20. S. Ciraci and I. P. Batra, *Phys. Rev. Lett.* **56**, 877 (1986).
21. S. Ciraci and I. P. Batra, *Phys Rev.* **B37**, 2995 (1988).
22. S. Ciraci and I. P. Batra, *Phys. Rev. Lett.* **58**, 1982 (1987).
23. I. P. Batra and S. Ciraci, *Phys Rev.* **B37**, 8432 (1988).

24. J. Ihm, A. Zunger, and M. L. Cohen, *J. Phys.* **C12**, 4409 (1979).
25. C. B. Bachelet, D. R. Hamann, and M. Schluter, *Phys. Rev.* **B26**, 419 (1982).
26. D. M. Ceperley and B. J. Alder, *Phys. Rev. Lett.* **45**, 566 (1980).
27. A. Zunger, *Phys. Rev.* **B24**, 4372 (1981).
28. S. Ciraci and I. P. Batra, *Phys. Rev.* **B33**, 4294 (1986).
29. M. K. Kelly et al., *Phys. Rev.* **B32**, 2693 (1985).
30. A. U. MacRae, K. Muller, J. J. Lander, J. Morrison, and J. C. Phillips, *Phys. Rev. Lett.* **22**, 1048 (1969); U. Jostell, *Surf. Sci.* **82**, 333 (1979); S. A. Lindgren and L. Wallden, *Phys. Rev.* **B22**, 5967(1980).
31. J. Ferrante and J. R. Smith, *Phys. Rev.* **B31**, 3427 (1985).
32. J. E. Rowe and H. Ibach, *Phys. Rev. Lett.* **32**, 451 (1976).
33. S. Ciraci, R. Butz, E. M. Oelling, and H. Wagner, *Phys. Rev.* **B30**, 711 (1984).
34. K. C. Pandey, *Phys. Rev. Lett.* **47**, 1913 (1981).
35. P. Soukiassian, *Surf. Sci.* **172**, L507 (1986).
36. N. E. Northrup and M. L. Cohen, *Phys. Rev. Lett.* **49**, 1349 (1982).
37. T. Kendelewicz, P. Soukiassian, R. S. List, J. C. Woicik, P. Pianetta, I. Lindau, and W. E. Spicer (*to be published*).
38. V. L. Moruzzi, J. F. Janak, and A. R. Williams, *Calculated Electronic Properties of Metals* (Pergamon, New York, 1978).
39. I. P. Batra and P. S. Bagus, *J. Vac. Sci. Technol.* **A6**, 600 (1988).
40. J. E. Northrup, *J. Vac. Sci. Technol.* **A4**, 1404 (1986).
41. R. V. Kasowski and M. H. Tsai, *Phys. Rev. Lett.* **60**, 546 (1988).
42. S. Ciraci and I. P. Batra, *Phys. Rev. Lett.* **60**, 547 (1988).
43. E. M. Oelling, E. G. Michel, M. C. Asensio, R. Mirnada, J. C. Duran, A. Munoz, and F. Flores, *Europhys. Lett.* **5**, 727 (1988).
44. J. Topping, *Proc. R. Soc. London* **114**, 67 (1927).
45. I. P. Batra, *Progress in Surf. Sci.* **25**, 175 (1987).
46. Y. Enta, T. Kinoshita, S. Suzuki, and S. Kono, *Phys. Rev.* **B36**, 9801 (1987).
47. C. A. Papageorgopoulos, these proceedings.
48. M. Tsukada and N. Shima, these proceedings.
49. I. P. Batra, J. M. Nicholls, and B. Reihl, *J. Vac. Sci. Technol.* **A5**, 898 (1987).

ELECTRONIC STRUCTURE AND EXCITATIONS OF METAL OVERLAYER ON SEMICONDUCTOR SURFACES

M. Tsukada, N. Shima, Z. Zhu, H. Ishida* and K. Terakura*

Department of Physics, Faculty of Science, University of Tokyo
Hongo 7-3-1, Bunkyo-ku
Tokyo 113, Japan

*Institute for Solid State Physics, University of Tokyo
Roppongi 7-22-1, Minato-ku
Tokyo 106, Japan

1. INTRODUCTION

Monolayer of metal atoms on clean substrate surfaces forms interesting material phase with a wide variety of properties. The structure and electronic properties of the overlayer depend remarkably on the initial substrate structure as well as atom kinds of both overlayer and substrate. Especially overlayer of alkali atoms reveals remarkable properties such as large reduction of work function and enhanced chemical activity. Because of this much interest has been attracted to the alkali overlayer systems. Particularly important systems are the alkali overlayers on semiconductor surfaces, because atomic arrangement on clean surface of semiconductors have now been clarified for many systems and the overlayer with characteristic structure can be formed on such well characterized surfaces.

The most typical example is found in the Levine model [1] of Si(100)2×1/alkali surface, in which atomic chains of alkali are formed on the dimer rows of the Si(100)2×1 surface as shown in Fig.1. As shown in this example, one might expect that a very unique artificial material phase can be fabricated utilizing the special reconstructed structure of substrate. Moreover, since the electronic structure of alkali atoms is much simpler than that of other metals, the semiconductor/alkali overlayer system is appropriate as the starting point of the study of generally more complicated metal overlayer system.

Recently there have been some controversies on the electronic structure of K overlayer on Si(100)2×1 surface. The hitherto accepted model of Si(100)2×1/alkali surface is that proposed by Levine [1]. DV(Discrete

Variational)-Xα-LCAO calculations by the group of present authors [2,3] revealed metallic overlayer bands which are characterized by a considerable hybridization between the states of the alkali atom and substrate. On the other hand, Ciraci and Batra[4] concluded almost ionic character of the overlayer K atom based on their pseudopotential calculation. The two theories seem to give different pictures of the electronic structure of Si(100)2×1/K surface.

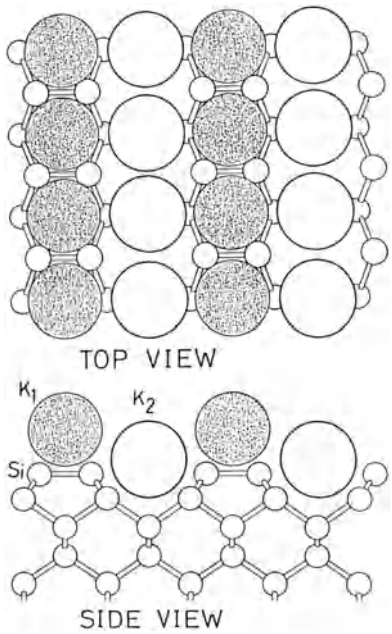

Fig. 1 Models of Si(100)2×1/alkali surface. Alkali atom is chemosorbed only at the K_1 site for the Levine model, while it is chemisorbed at both the K_1 and K_2 site for the double layer model.

The other issue of the controversy concerns the atomic structure of the overlayer. By the analysis of photoelectron diffraction, Abukawa and Kono [5] proposed recently a new model depicted in Fig.1. In their model K atoms are also chemisorbed in the trough between the dimer rows, as well as the row of K atoms on the ridge, therefore this model is called as "double layer model"; the coverage is twice as large as the Levine model. One naturally expects that the electronic structure of the double layer model is quite different from that of the Levine model. Actually Enta et al [6] observed by ARUPS (Angle-Resolved Ultraviolet Photoemission Spectroscopy) that the band structure of the overlayer shows semiconducting character. This feature is different from that of the metallic overlayer band theoretically predicted for the Levine model [1-4]. It is not yet certain whether, according to the quality of substrate, both structures of Si(100)2×1/K, i.e., Levine model and double layer model can be formed, or only either of them can exist. Thus at the present stage, it is very significant

to calculate the overlayer electronic structures for both the models and compare them with experimental informations.

To resolve the first issue of the controversy, we perform in this work detailed calculations of the overlayer bands of the Si(100)2×1/K surfaces by the two complementary methods, 1) DV-Xα-LCAO method applied to the isolated slab model [3], and 2) norm conserving pseudopotential method [7] applied to the repeated slab model. The orbital characters of the overlayer bands and the adatom charge are analysed in full detail. The methods and the results for the Levine model are described in Section 2. In Section 3, we also present the calculated overlayer bands for the double layer model, and make comparative study with those of Levine model. In Section 4 characteristics of the overlayer plasmon for the alkali chains of Si(100)2×1/K Levine model are described and the possible mechanism of the EELS (Electron Energy-Loss Spectroscopy) peak on this surface is discussed. To see that the overlayer bands depend remarkably on the substrate structure, we discuss in Section 5 the alkali overlayer bands on Si(111)2×1 surface and compare them with those on Si(100)2×1.

2. ELECTRONIC STRUCTURE OF Si(100)2×1/K SURFACES --LEVINE MODEL--

2-1) Models and methods of calculation

Different numerical results on the electronic structure of Si(100)2×1/K have been recently reported in literatures [2-4,8]. Some differences might be caused by the method of calculations and models, but some are concerned with the physical interpretation of the results. To clarify this point, we calculate the energy bands of Si(100)2×1/K surface with the following two complementary methods.

In the method I, calculations are performed by the DV-Xα-LCAO band method, the details of which have been reported elsewhere [3]. As for the atomic basis functions, the numerically generated minimal bases, Si 1s-3p, K 1s-4p are used. These basis functions are self-consistently recalculated in each iteration step, so that they have enough degree's of freedom to adjust their shape according to the potential around the respective atoms [9]. The structure model used in method I is the isolated slab with 10 atomic layers as shown in Fig.2(b). Hydrogen atoms are attached to the Si atoms on the back side surface to eliminate the dangling bonds.

The method II uses the norm conserving pseudopotential method and adopts the repeated slab model as shown in Fig.3. Substrate layer includes 10 layers and K atoms are chemisorbed on both sides of the substrate surfaces. The separation between the overlayers on the adjacent slabs is 16 Å. The number of plane waves included are ~1800 which corresponds to the cut-off energy of 88 eV.

2-2) Si(100)2×1 clean substrate surface

Substrate structure is assumed to be the symmetric dimer model and the Si-

Si distance of the dimer is chosen to be the same as the bond length in the bulk. The dispersions of the π and π^* surface state bands originated from the dimer dangling bonds are essentially the same as reported before [3,10]. There are no significant differences between the results of the two methods, except that method I gives a wider gap between the valence and the conduction band of substrate.

2-3) Dependence of the overlayer band structure on the adatom-surface distance

We calculated the overlayer bands of Si(100)2×1/K for three different geometries specified by the Si-K distance;(a) d(Si-K) = 3.5Å, (b) d(Si-K)=3.1Å, and (c) d(Si-K)=2.6Å. The Si-K distance for the case (a) is equal to the sum of atomic radii. The geometry of the case (b) corresponds to the Si-K distance determined by SEXAFS (Surface Extended X-ray Absorption Fine Structure) [11] and that of the case (c) corresponds to the optimized geometry by the pseudopotential calculations by Ciraci and Batra [4].

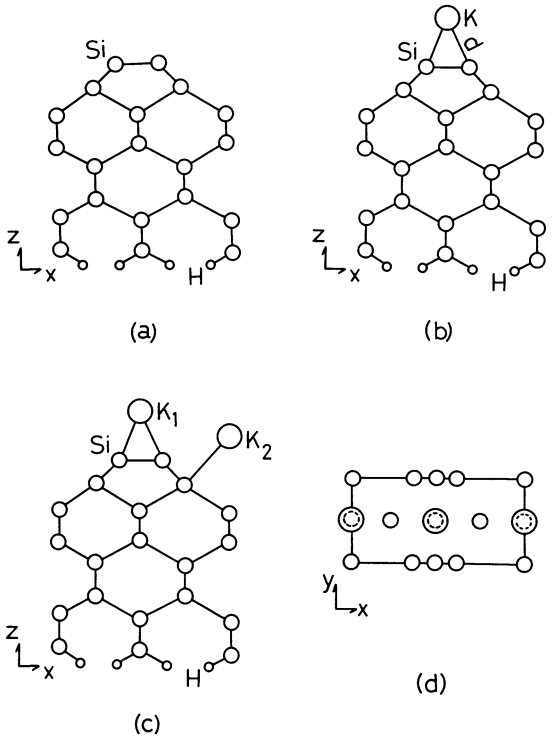

Fig. 2 Isolated slabs used in the calculation of method I. (a) substrate surface (b) Levine model (c) the double layer model (d) the double layer model (top view). Only atom arrangement in the unit cell is shown.

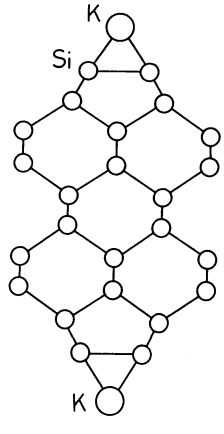

Fig. 3 Slab used in the calculation of method II.

The obtained overlayer band structures by the method I are shown in Fig.4(a)~(c) for the three geometries, respectively. In Fig.4(a), which corresponds to the case d(Si-K)=3.5Å, three overlayer bands a,b,c appear which have significant orbital character of the K valence states. If the thickness of the layer is increased to be infinite, most part of the band a and b appear as the surface gap state, but some part of the band c might be merged into the continuum of the bulk states. The Fermi level crosses with the band b, while the band a (c) is completely occupied (unoccupied). The orbital character of the three bands near the Γ point is shown in Fig.5. The band a has the bonding character of K 4s−dimer π as well as a slight admixture of the bonding combination of K $4p_z$−dimer π. The bonding combination between K $4p_x$−dimer π^* dominates the orbital character of the band b. Here the x axis is chosen along the dimer axis. The upper overlayer band c has the antibonding character of K 4s−dimer π with a slight admixture of the antibonding component of K $4p_z$−dimer π.

It is observed in Fig.4(a)~(c) that the band b is pushed down and the band c is raised with the approach of K atoms toward the substrate surface. Such behavior can be understood by the orbital characters mentioned above. On the other hand, the energy position of the band a shows only very slight shift with the change of the Si-K distance. The downward shift of the band a seems hindered at the valence band top, as is usually the case for the deep impurity states. Anyhow we observe that the relative overlayer band energies depend remarkably on the distance of K atom from the surface. The direction of the shift of each band can be explained by the orbital components.

2-4) Comparison between the energy bands by the method I and those by the method II

The overlayer bands by the method II, i.e., the pseudopotential calculation applied to the repeated slab model is shown in Fig.6. The Si-K distance is chosen as 3.1Å as in the case of Fig.4(b). The overlayer band structure of Fig.6 is similar to that of Fig.4(b) except that the overlayer bands by the method II split slightly into two due to the interaction with the bands on the back surface. The overlayer band c and the substrate conduction bands by the method II are located at relatively lower positions compared with the corresponding ones in Fig.4(b). But otherwise the dispersions of the three bands and the separation between the a and b bands (~0.5eV by the method I, ~0.8eV by the method II) are similarly obtained by the two methods.

The overlayer band structure for d(Si-K)=2.6Å by the method I is almost the same as that obtained by Ciraci and Batra by the pseudopotential method [4]. Therefore it may be concluded that both methods, i.e., DV-Xα-LCAO and the pseudopotential method give roughly the same results, except the unoccupied bands are located at a somewhat higher position in the former method.

2-5) Charge of K adatom and the work function

The net charge of the K adatom estimated by the Mulliken population analysis by the method I is +0.10, +0.06, +0.12 for the case of d(Si-K)=3.5, 3.1,

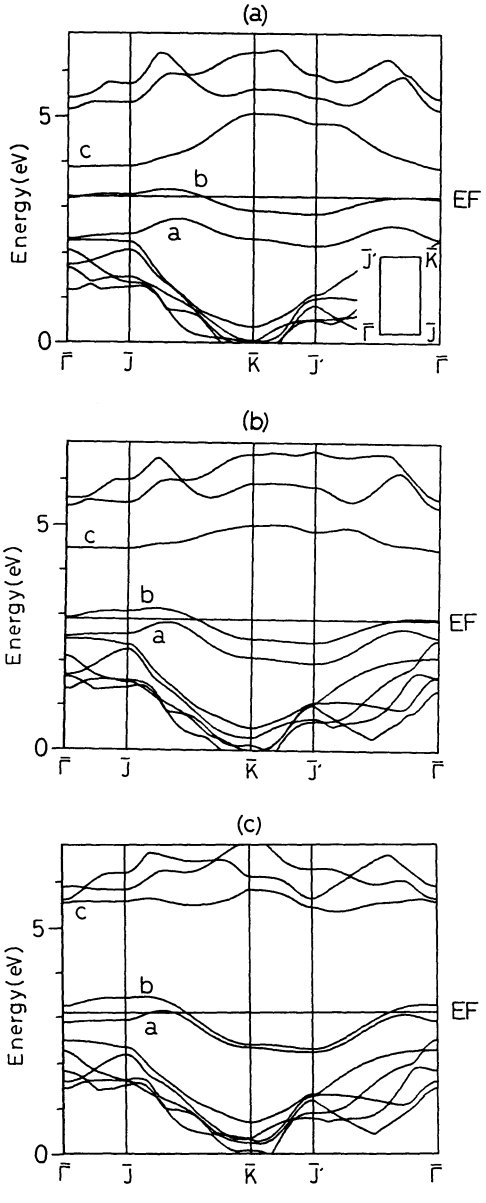

Fig. 4 Overlayer band structure of Levine model obtained by the method I. (a), (b), (c) correspond to the nearest K-Si distance 3.5Å, 3.1Å and 2.6Å, respectively.

2.6 Å, respectively. The orbital hybridization and the difference of electron negativity tend to decrease and increase the positive net charge on K, respectively, with the decrease of the K-Si distance. The net charge of K is determined by a delicate balance of these effects, which causes its non-monotonous change with the K-Si distance in the wide range. The important point, however, is that the net charge on K estimated by the method I is remarkably small. The calculation by the method II also reveals that the number of electrons induced within K atomic spheres upon chemisorption is very close to that in the same spheres for isolated K layers as seen in Table I and II. Though the tables show the case of the double layer model, almost the same feature is observed for the Levine model. This property is understood from the local DOS at the K atom spreading deep below E_F as shown in Fig.7.

Then how is the large decrease of the work function induced by the alkali atom chemisorption? Recently a new mechanism of the work function reduction of the metal/alkali system has been proposed by Ishida and Terakura [12]. Based on it, the large dipole moment of alkali adatom is induced by the adatom polarization due to strong hybridization between adatom and substrates, which results in the reduction of the electron density on the vacuum side region of the

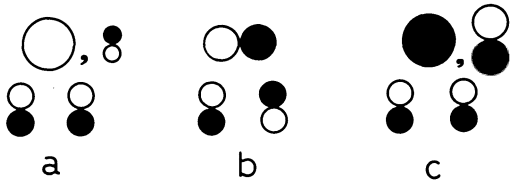

Fig. 5 Major orbital components of the overlayer bands a, b, c for the Si(100)2×1/K Levine model.

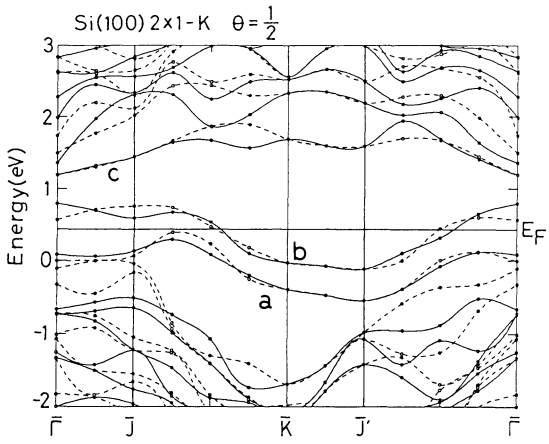

Fig. 6 Overlayer band structure of Levine model obtained by the method II. The nearest K-Si distance is assumed as 3.1Å.

Table I. Electron numbers within atomic spheres around K_1 site for the double layer model.

System R(Å)	Si/K	Si	Si/K−Si	$K_{isolate}(\theta=1/2)$
1.3	0.1427	0.0703	0.0724	0.0810
1.6	0.3591	0.1793	0.1798	0.1796
1.9	0.7942	0.4362	0.3580	0.3264
2.1	1.5994	0.9880	0.6114	0.5101

Table II. Electron numbers within atomic spheres around K_2 site for the double layer model.

System R(Å)	Si/K	Si	Si/K−Si	$K_{isolate}(\theta=1/2)$
1.3	0.1542	0.0807	0.0735	0.0810
1.6	0.3941	0.2138	0.1803	0.1793
1.9	0.8799	0.5248	0.3551	0.3253
2.1	1.7813	1.1837	0.5976	0.5077

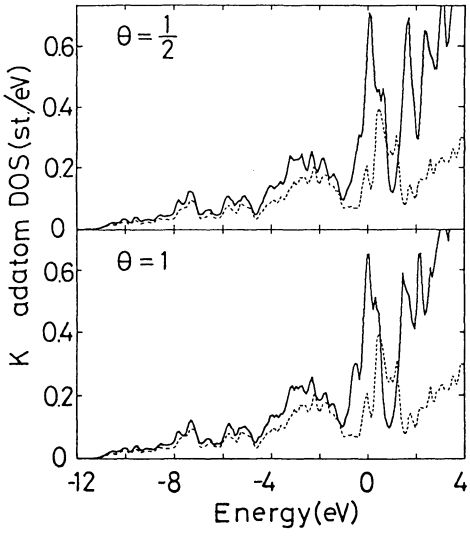

Fig. 7 Density of states within atomic sphere around K_1 site (full line) for the Levine model (upper curve) and the double layer model (lower curve). The dashed lines show density of states within atomic sphere around (empty) K_1 site for the bare Si(100)2×1 surface.

adatom and its accumulation over the intermediate region between the adatom and the substrate. As opposed to usual Gurney's picture [13], the alkali adatom is not ionized, but its electron distribution is distorted in the wide spatial region. And this is just the mechanism to cause the large dipole moment.

The same picture can be applied here. As seen in the contour map of Fig.8, the difference charge distribution

$$\Delta\rho = \rho(\mathrm{Si/K}) - \rho(\mathrm{Si}) - \rho(\mathrm{K}) \tag{1}$$

shows the accumulation and the depletion of the electrons in the K-Si intermediate region and in the vacuum side of adatom, respectively. This is the same characteristics as found in metal/alkali system. This property does not depend so much on the distance of the adatom from the substrate. The reduction of the work function by the chemisorption of the alkali layer is calculated to be 2.8eV for the case of d(Si-K)=3.1Å, which explains roughly the value observed by the experiment.

3. ELECTRONIC STRUCTURE OF Si(100)2×1/K SURFACE --DOUBLE LAYER MODEL--

Recently Kono's group measured the dispersion of the overlayer bands of the Si(100)2×1/K, Cs surfaces by ARUPS experiment [6]. As opposed to the theoretical expectation on Levine model [1-4], they did not observe the metallic

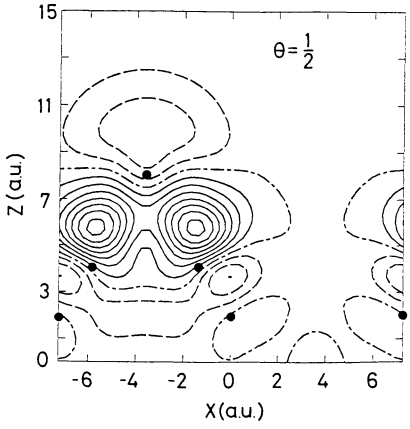

Fig. 8 Difference charge density map of $\Delta\rho = \rho(\mathrm{Si/K}) - (\rho(\mathrm{Si}) + \rho(\mathrm{K}))$ in the x-z plane passing through the midpoint between K atom and the dimer center for the Levine model by the method II. The geometry is the same as that in Fig. 6. Black small circles are projeted positions of atoms. Contour spacing is 0.005 electrons/(a.u.)^3. (—— for $\delta\rho > 0$, - - - - for $\delta\rho < 0$, —·—·- for $\delta\rho = 0$).

overlayer bands. Because the electron number per surface unit cell is odd, it is rather obvious that the Levine model is incompatible with the semiconducting band structure of the overlayer. Based on the photoelectron diffraction measurement, Abukawa and Kono [5] proposed a new structure model shown in Fig.1. Since this structure includes even number of electrons per surface unit cell, this does not contradict with the non-metallic electronic structure of the overlayer.

To clarify the overlayer bands of the double layer model, we calculated the electronic structures of the slab models by the two methods in the previous section. As for the geometry of the K adatoms, the following model is used: the position of the outer K atom K(1) is chosen as that of Fig.4(b), i.e., d(Si-K(1))=3.1Å, and the second K atom (K(2)) is further approached by 1.1Å toward the substrate. This difference of the height is determined by the photoelectron diffraction experiment.

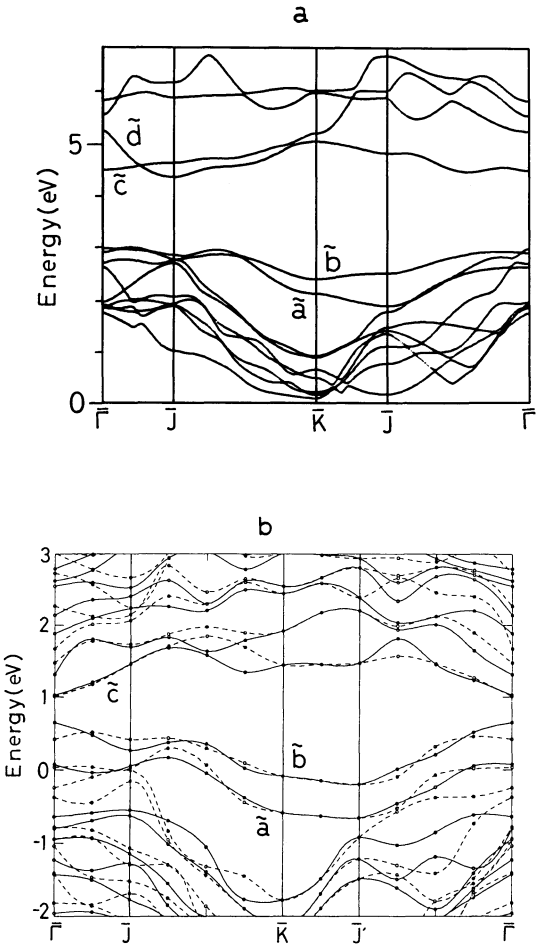

Fig. 9 The overlayer band structures of the double layer model calculated by (a) the method I and (b) the method II.

The overlayer bands of the double layer model calculated by the method I and II are depicted in Fig.9(a),(b), respectively. Both results reveal two completely occupied bands $\tilde{a}$, $\tilde{b}$. The two uncoccupied overlayer bands $\tilde{c}$, and $\tilde{d}$ are obtained by the method I, but the band $\tilde{d}$ is not found by the method II. The band $\tilde{d}$ may be merged in the continuum of the inner layer conduction band in the method II. The theoretical energy band structure is semiconducting in accord with the ARUPS experiment. As shown in Fig.9 there are two occupied overlayer bands with the separation less than 0.7eV. According to the very recent ARUPS data with the use of the single domain Si(100)2×1 substrate, two distinct overlayer bands are observed. Their maximum separation is about 0.8eV. The overall dispersions seem to correspond to those two occupied bands obtained by the theoretical calculations. But further study is needed for both experiment and theory, to get a definite conclusion.

At the present stage we cannot say which models, Levine model or double layer model are more appropriate for the Si(100)2×1/K surface. It may be possible that either of the model is realised according to the preparation method and the quality of the substrate surface. It should be remarked that the chemisorption energy is calculated to be about the same, 2.5eV, for both the models. Reason of the negligibly small difference of the chemisorption energies between the two models is not clear. Moreover the work function change is calculated as $\Delta\phi$=2.8eV for both the models. No significant differences can be found between the two models. This means that the K adatom in the second layer (K(2)) induces only very small dipole moment in contrast to the large dipole moment of the outer K adatom.

4. OVERLAYER PLASMON

A characteristic peak of EELS has been observed by Tochihara and Murata [14], and Aruga et al [15] for Si(100)2×1/alkali overlayers. The peak energy depends considerably on alkali atom species; it is about 1.7eV and 1.2eV for the K overlayer and Cs overlayer, respectively. The intensity of the peak grows rapidly with the alkali coverage θ in the region, $\theta \geqq 0.3$. The dispersion of the peak energy observed by the angle resolved EELS shows the following features. 1) The main peak energy is finite for the zero wave number **Q**=0, and the energy increases with **Q** linearly for the small wave number regions. Here **Q** means the 2-dimensional wave number. 2) The dispersion is anisotropic and largest for the perpendicular direction to the dimer row. 3) A weak shoulder structure is observed at the low energy side of the main peak for some region of **Q**.

Qualitative features of the dispersion of the EELS peak can be explained by the overlayer plasmons of the parallel rod model [3,16], which mimics the alkali adatom chains of the Levine model. The parallel rod model is a system of free electrons confined in thin rods placed on a dielectric substrate. There are three modes of the collective excitations in the parallel rod model; 1)The s→s intraband mode which is a collective electron motion along the rod axis, 2)The s→p_z interband mode with the polarization perpendicular to the surface, and 3) the s→p_x interband mode with the polarization parallel to the surface and

perpendicular to the rod axis. The dispersion relations of the three modes obtained by the random phase approximation (RPA) are expressed as

$$\omega^2(\mathbf{Q}) = \frac{2k_F}{ma}\left\{\frac{2}{\kappa+1} + \left[\frac{5}{4\pi^2} - \frac{1}{3} + \frac{\kappa-1}{\kappa+1}\right]\ell Q\right\} Q\cos^2\theta \tag{2}$$

(for intraband mode)

$$\begin{aligned}\omega^2(\mathbf{Q}) &= \omega_{sp}^2 + 4\pi N_s \omega_{sp} e^2 \\ &\times \left\{\frac{S}{2\pi}\int d\mathbf{r}_1 \int d\mathbf{r}_2 \Phi^*(\mathbf{Q}=0,\nu,\mathbf{r}_1)|\mathbf{r}_1-\mathbf{r}_2|^{-1}\Phi(\mathbf{Q}=0,\nu,\mathbf{r}_2)\right. \\ &+ \frac{2}{Q(\kappa+1)}\left|\int d\mathbf{r}\phi_s^*(\mathbf{r})(Q_x x + Q_y y)\phi_p(\mathbf{r})\right|^2 \\ &- \left.\frac{2\kappa Q}{\kappa+1}\left|\int d\mathbf{r}\phi_s^*(\mathbf{r}) z\phi_p(\mathbf{r})\right|^2\right\}\end{aligned} \tag{3}$$

(for interband mode).

In the above a, S, l, κ, N_s are the separation between adjacent rod, area of the surface unit cell, the diameter of the rod, the dielectric constant of the substrate and the electron density per surface area, respectively. y and z directions are parallel to the rod axis and the surface normal, respectively. The angle between the 2-dimensional wave vector $\mathbf{Q}$ and the rod axis is denoted as θ. $\Phi(\mathbf{Q},\nu,\mathbf{r})$ is the induced charge density associated with the interband transition of the mode ν, and ϕ_s, ϕ_p are the wave functions of the initial and the final state, respectively, whose single electron transition energy is denoted as ω_{sp}.

The energy of the intraband mode goes to zero as Q with the decrease of the wave number, $Q = |\mathbf{Q}|$. Therefore this mode cannot be the origin of the main peak appeared in the EELS. Ishida and Tsukada [17] showed that the intensity of the intraband mode of the overlayer plasmon is generally strongly suppressed due to the screening by the substrate electrons. It might be possible that the weak shoulder structure observed in the EELS is due to the intraband mode [15].

It is easily verified by eq.(3) that the $s\rightarrow p_z$ interband mode has isotropic negative linear dispersion, while the $s\rightarrow p_x$ interband model has anisotropic positive linear dispersion. The positive linear dispersion of the $s\rightarrow p_x$ mode is explained by the fact that the depolarization field of each rod is most canceled by that of the adjacent rod for the case of Q=0. On the other hand it is most enhanced for the $s\rightarrow p_z$ mode for the zero wave number.

The dispersion of the observed main EELS peak shows the same behavior as the $s\rightarrow p_x$ mode of the rod model, i.e. it has positive slope which depends on the azimuthal angle of $\mathbf{Q}$ vector. For the overlayer band of the Levine model, the collective excitation associated with the a→b interband transition has the same character as the $s\rightarrow p_x$ mode of the rod model. Ishida et al [3] calculated the dispersion relation of the a→b interband overlayer plasmon based on the band structure for the case of d(Si-K)=3.5Å. The theoretical dispersion relation

of the a→b plasmon mode shows similar feature as that of the main EELS peak. The peak energy of the a→b overlayer plasmon is very close to the experimental value, for the bridge chemisorption site (see Fig.10). However the agreement of the peak energy should not be taken seriously, since it depends considerably on the method of the calculation and the geometry of the adatom.

It is important to examine whether the peak of the EELS can be also explained by the single particle transitions. In such a case, the second term on the right hand side of eq.(3) does not contribute so much to the dispersion relation. The main feature of the EELS peak, then, should be caused by the **Q** dependence of the single particle transition energy, $\omega_{sp}(\mathbf{Q})$. Based on the calculated band structures by the pseudopotential method, the possibility cannot be discarded that the anisotropic positive dispersion can be obtained by the a→c single particle transition, which overcomes negative contribution to the dispersion by the second term. Anyhow the detailed calculation of the electron loss spectrum both for the Levine model and the double layer model should be necessary, to clarify the mechanism of the characteristic EELS structure.

5. ELECTRONIC STRUCTURE OF Si(111)2×1/ALKALI SURFACES

Alkali overlayers on semiconductor surfaces show different features depending on the substrate structure. As an example, we discuss here the electronic structures of Si(111)2×1/K,Cs surfaces and compare them with the alkali overlayer on Si(100)2×1 surface.

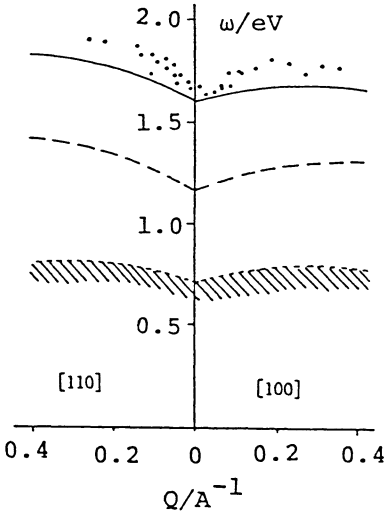

Fig.10 The dispersion relation of the a→b interband overlayer plasmon for the bridge site (full line) and the hollow site (dashed line) Levine model. The calculations are performed by the method I with six layer slab.

Tochihara et al [18] measured the change of the photoemission spectrum with Cs coverage on Si(111)2×1 substrate. Main result is that the structure of the occupied surface states of the substrate persists with the unchanged shape for all the coverage, and a new surface state peak appears around the Fermi level for higher coverages. The intactness of the substrate electronic structure indicates the weak interaction between alkali adatom and substrate, which makes a contrast to the situation in the Si(100)2×1/alkali overlayer. It is crucial in establishing the general picture of semiconductor/alkali overlayers to clarify the reason of the different way of the overlayer band formation between the two Si substrate surfaces, (111)2×1 and (100)2×1.

We have performed the DV-Xα-LCAO band calculation of the slab model for the Si(111)2×1/K,Cs overlayers [19]. The substrate surface is assumed as the π-bonded chain model and the slab of the substrate consists of eight Si layers. Hydrogen atoms are attached to the back surface to eliminate the dangling bonds. The alkali atoms are placed on the tilted hexagon and the distances from the two neighboring Si atoms in the π bonded chain are chosen as the same and equal to the sum of the atomic radii, 3.5Å and 3.8Å for K and Cs, respectively.

The calculated overlayer bands are shown in Fig.11. The band dispersions of the K and Cs overlayer are remarkably similar. The lowest overlayer band shown in the figure are mainly contributed by the bonding π dangling bond band of the substrate. By the overlayer formation, the dispersion of the lowest band is slightly distorted, but this effect is not significant. This is the reason why the occupied surface states of the substrate is observed unchanged in the UPS.

The orbital components of the antibonding π^* surface band dominate the second and the third overlayer band along K-J and Γ-J' line of the surface Brillouin zone, respectively. The second band is mostly composed of K 4s or Cs 6s orbitals along Γ-J' line, and the orbital character is sharply changed around a certain point along the Γ-J line. Except the band crossover region, the dispersion of the substrate surface states are not much influenced by the overlayer formation.

The second band crosses the Fermi level. One might conceive that the metallization of Si(111)2×1/alkali overlayer is mainly caused by the electron

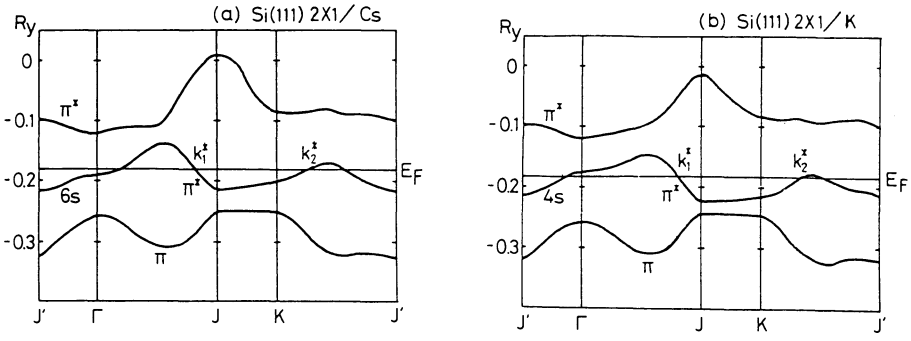

Fig.11 Overlayer band structures of (a) Si(111)2×1/Cs and (b) Si(111)2×1/K.

donation to the π^* band, since the electron pocket surrounding the K-J line has dominantly the π^* band character. The wave functions of electrons in the region around Γ-J' line have strong alkali orbital character. However, as is the case for the general alkali overlayers, these electrons distribute over wide region surrounding the alkali atom and rather concentrates around the intermediate region between the adatom and the substrate. The surface state peak around the Fermi level observed for higher coverage is assigned to the electron pockets around K-J and Γ-J' line.

Batra and Ciraci [20] obtained a similar band structure for Si(111)2×1/K surface, although in their optimized geometry, K-Si distance is 2.6Å, much shorter than that assumed here. Their assignment of the partially occupied band along Γ-J' line is different from the present results.

The reason of the intactness of the substrate surface bands is attributed to their large dispersion. In other words, the interaction between the dangling bond in the π bonded chain is stronger than that between the dangling bond and the alkali s orbital. In this respect, the overlayer bands on the Si(100)2×1 substrate show different property. The dispersion of the π, π^* band and their average separation in Si(100)2×1 are much smaller than those of Si(111)2×1 surface. This means interaction between the dangling bonds in the dimer model is smaller than that in the π bonded chain. Reflecting this, the band crossover behavior is not found in Si(100)2×1/alkali overlayer, but the energy of the overlayer bands are relatively shifted from those of the substrate surface band.

6. DISCUSSIONS AND CONCLUSIONS

From the calculations by the two complementary methods, DV-Xα-LCAO and norm conserving pseudopotential method, a detailed picture of the electronic states of the Levine model of Si(100)2×1/K surface has been clarified. There are three overlayer bands with considerable admixture between the K and Si orbital components. The middle overlayer band b with the character of the bonding admixture of K $4p_x$ and dimer π^* crosses the Fermi level, which causes the metallization in the Levine model. The electron distribution around K atom is remarkably polarised, which induces a large dipole moment. The reduction of the work function by the K monolayer formation in the Levine model is calculated to be 2.8 eV, which roughly agrees with the experimental value. The electron numbers within an atomic sphere surrounding K nucleus is almost unchanged by the chemisorption, which requires modification of the simple picture of "ionic" chemisorption. This feature is the same as that recently verified for alkali overlayer on simple metal surfaces [7,12].

The electronic structure of the double layer model is revealed by the two calculational methods. There are four overlayer bands, of which two are occupied and the others are unoccupied. Therefore Si(100)2×1/K overlayer is not metallised in the double layer model, and remains to be semiconductor. This character of the overlayer band agrees with the ARUPS result by Kono's group, as well as the presence of the two distinct occupied overlayer bands.

Important features of the collective excitation of the linear metal chain overlayer are discussed based on the parallel rod model. Owing to the simplification of the model, the result can predict qualitative characteristics of the metallised overlayer system with quasi-one-dimensional structure. The dispersion of the EELS peak of the Si(100)2×1/alkali surface has the same characteristics as the $s \rightarrow p_x$ interband overlayer plasmon. However, to make clear the origin of the EELS peak, detailed calculations of the loss functions for both the a→b, a→c interband modes are necessary. The change of the shape and the intensity of the EELS peak with the coverage would afford an important clue to this problem.

The character of the alkali overlayer depends considerably on the substrate structure. The interaction of the alkali layer and Si(111)2×1 substrate causes only slight change of the dispersion of the substrate surface states. And this theoretical result explains the observed intactness of the surface states upon alkali chemisorption.

ACKNOWLEDGEMENTS

The numerical calculations were performed at the Computer Center of the University of Tokyo and that of the Institute for Molecular Science. This work was supported by a Grant-in Aid from the Ministry of Education, Science and Culture, Japan.

REFERENCES

1. J.D. Levine, Surface Sci. **34** (1973) 90
2. H. Ishida, N. Shima and M. Tsukada, Surface Sci. **158** (1985) 438
3. H. Ishida, N. Shima and M. Tsukada, Phys. Rev. **B32** (1985) 6246
4. S. Ciraci and I.P. Batra, Phys. Rev. Lett. **56** (1986) 877,
   Phys. Rev. **B37** (1988) 2955
5. T. Abukawa and S. Kono, Phys. Rev. **B** (1988) in press
6. Y. Enta, T. Kinoshita, S. Suzuki and S. Kono, Phys. Rev. **B36** (1987) 9801
7. H. Ishida and K. Terakura, Phys. Rev. **B36** (1987) 4510
8. R.V. Kasowski and M.H. Tsai, Phys. Rev. Lett. **60** (1988) 546
9. H. Adachi, M. Tsukada and C. Satoko, J. Phys. Soc. Jpn. **45** (1978) 875
10. J. Ihm, M.L. Cohen and D.J. Chadi, Phys. Rev. **B21** (1972) 469
11. T. Kendelewsicz, P.Soukiassian, R.S. List, J.C. Woicik, P. Pianetta, I. Lindau and W.E. Spicer **B37** (1988) 7115
12. H. Ishida and K. Terakura, Phys. Rev. **B38** (1988) 5752
13. R.W. Gurney, Phys. Rev. **47** (1935) 479
14. H. Tochihara and Y. Murata, J. Phys. Soc. Jpn. **51** (1982) 2920
15. T. Aruga, H. Tochihara and Y. Murata, Phys. Rev. Lett. **53** (1984) 372
16. M. Tsukada, H. Ishida and N. Shima, Phys. Rev. Lett. **53** (1984) 376
17. H. Ishida and M. Tsukada, Surface Sci. **169** (1986) 225
18. H. Tochihara, M. Kubota, M. Miyano and Y. Murata, Jpn. J. Appl. Phys. **23** (1984) L271
19. H. Ishida, K. Terakura and M. Tsukada, Solid State Commun. **59** (1986) 365
20. I.P. Batra and S. Ciraci, Phys. Rev. **B37** (1988) 8432

ALKALI-METAL OVERLAYERS ON SILICON SURFACES

Yoshitada Murata, Hiroshi Tochihara and Masakazu Kubota

The Institute for Solid State Physics
The University of Tokyo,
7-22-1, Roppongi, Minato-ku, Tokyo 106, Japan

Alkali-metal overlayers on the Si(001)-(2x1) surface at saturation coverage form a one-dimensional metal which is verified with observing dispersion relation of an overlayer plasmon for Si(001)-(2x1)-K. The metallization is considered to take place in the K chains as the results of photoelectron-spectroscopic measurements. Then, we tried to find the Peierls transition for Si(001)-(2x1)-K and Cs but have not found it. The Li atom adsorption on Si(001)-(2x1) is very different from the other alkali-metal atoms. The Li overlayer has no metallic character and seems to form lithium silicide. It is also emphasized that the surface preparation is important.

INTRODUCTION

Alkali-metal atom adsorption on metal surfaces has been extensively studied and its mechanism can be interpreted by Gurney's scheme in the low coverage region.[1] That is, the valence level of a single alkali-metal atom is broadened and shifted upward in energy, as the adsorbing atom approaches a surface. Almost one valence electron for each adatom is transferred to the substrate, when adsorption takes place. As the coverage increases, the depolarization field causes a downward shift of the valence level of the adsorbates in energy, and hence one valence electron comes back from the substrate to each adsorbed alkali-metal atom.[2] Then, neutralization takes place on the alkali-metal atom overlayer.

For alkali-metal atom adsorption on semiconductor surfaces, however, a new picture was recently proposed.[3] The interaction of alkali metals with the surfaces can give a different scheme due to the dangling-bond surface states of semiconductors. Actually the alkali-metal overlayer on the Si(001)-(2x1) surface makes a one-dimensional metal in the adsorbed (2x1)-structure surface (Fig. 1), which is based on the anisotropic property due to dimer-bond formation of the topmost atoms on the Si(001)-(2x1) surface. The one-dimensional-metal formation is verified with observing dispersion relation of an overlayer plasmon.[5] However, this overlayer plasmon is doubted by the new scheme, where it is concluded that metallization takes place not in the alkali-metal overlayer but in the dangling-bond states of the Si substrate.[3] In the present paper, we will discuss this problem and present related phenomena from the experimental standpoint.

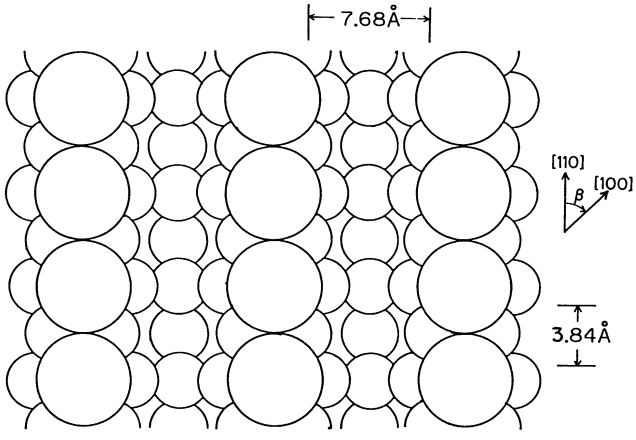

Fig. 1. A structure model of the linear-chain arrangement of adsorbed alkali-metal atoms (large circles) on Si(001)-(2x1) (small circles).

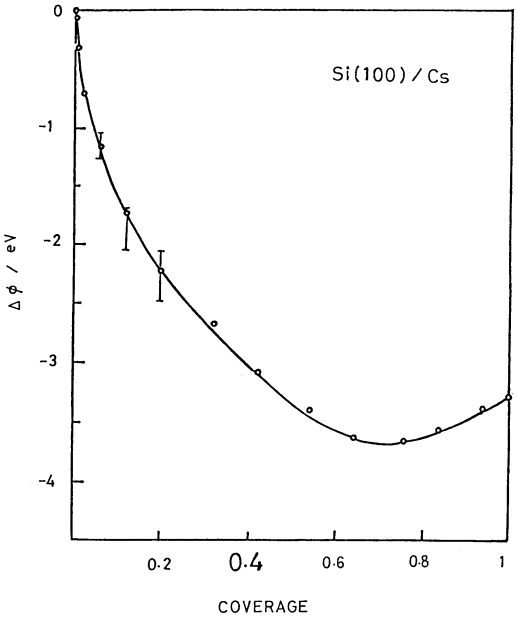

Fig. 2. Work function change as a function of Cs coverage on Si(001).

OVERLAYER PLASMON OF THE ONE-DIMENSIONAL SYSTEM

At first, we will shortly review the experimental results of alkali-metal overlayers on the Si(001)-(2x1) surface. The work function change as a function of Cs coverage is shown in Fig. 2. The abscissa shows the relative coverage Θ of Cs. Unity of Θ, at which the surface gives a clear (2x1) low-energy electron diffraction (LEED) pattern, shows the saturation coverage at room temperature as determined by Auger electron spectroscopy (AES). The minimum point of the work function appears at $\Theta \sim 2/3$. When the surface at $\Theta=1$ is exposed to oxygen atmosphere by 0.7 L (1 L=1x10^{-6} Torr·sec), the minimum work function of the negative electron affinity is obtained, at which the work function is reduced by 3.9 eV as compared with that of the clean surface. On the other hand, we have reexamined the work function change for the K-covered surface. The minimum point did not appear in the work function vs. coverage curve, which was very similar to that reported by Enta et al.[4]

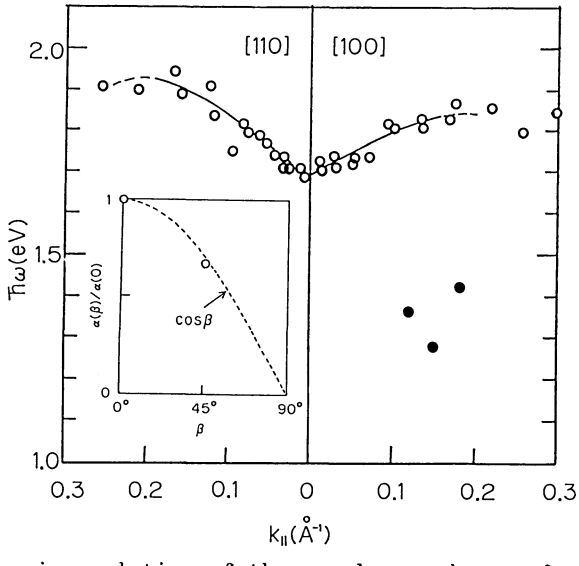

Fig. 3. Dispersion relation of the overlayer plasmon for Si(001)-(2x1)-K. The inset shows the azimuth dependence of the gradient of the dispersion. (From ref. 5.)

The dispersion of the overlayer plasmon for Si(001)-(2x1)-K was observed by using angle-resolved electron energy-loss spectroscopy (AREELS) and was found to show the linear relation with a positive gradient in the region of small surface-parallel momentum $\hbar k_{\parallel}$, which is a momentum transfer associated with the energy loss, as shown by open circles in Fig. 3.[5] This relation is clearly different from the dispersion relations of the bulk plasmon and the isotropic two-dimensional plasmon. The former is parabolic with respect to the momentum and the latter is linear with a negative gradient.[6] The linear and positive dispersion relation is characteristic of the one-dimensional or the anisotropic two-dimensional plasmon[7] and can be interpreted with the depolarization field effect from the nearest neighbor chains in the array of one-dimensional atomic chains shown in Fig. 1.[8] Moreover, the gradients in the linear dispersion relation are different in the [100] and the [110] azimuth, as seen in Fig. 3, and satisfy the cosine relation with respect to the azimuthal angle, as shown in the inset of Fig. 3.[5] Hence, the observed dispersion relation shows that the overlayer plasmon has clearly the one-dimensionality.

This mode of the overlayer plasmon is related to the inter-band transition from the K 4s to the K 4p state, since the energy loss takes a finite value at $k_{\parallel}=0$. The polarization vector of this mode is parallel to the surface and perpendicular to the K-atom chain. If the K-atom chains have a metallic property, it is expected to observe a mode parallel to the K-atom chains. The parallel mode has an energy loss of 0 eV at $k_{\parallel}=0$ and is related to an intra-band transition in the metallic (K 4s) band. This collective intra-band mode was observed as the shoulder in the [100] azimuth and the broadened shoulder in the [110] azimuth, as seen in Fig. 4. The dispersion relation of this mode is shown by full circles in Fig. 3. This result clearly indicates that the K 4s band is partially occupied by electrons. The intensity of this mode in the electron energy-loss spectrum is significantly reduced due to the screening effect from valence electrons of the substrate[9] and not due to a small amount of electrons occupied in the K 4s band.

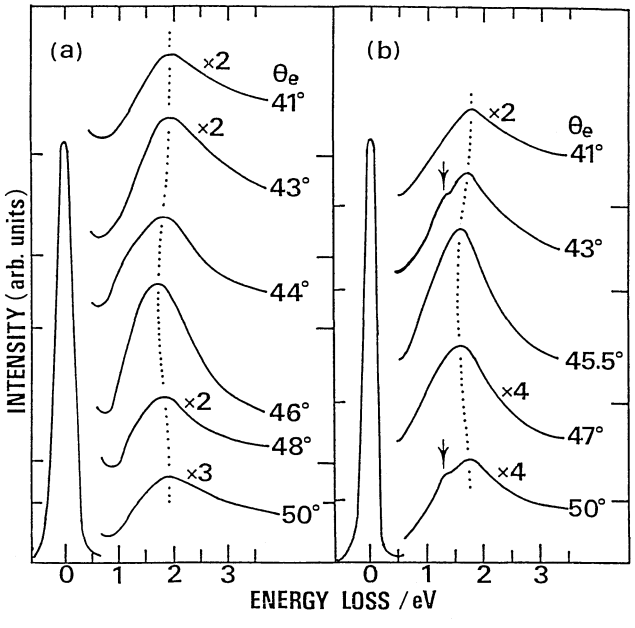

Fig. 4. Typical AREEL spectra for Si(001)-(2x1)-K. θ_e: emission angle. Incidence angle $\theta_i=45.5°$. (a) Incident energy $E_p=43.8$ eV, [110] azimuth. (b) $E_p=39.8$ eV, [100] azimuth. The arrow indicates a shoulder. (From ref. 5.)

We have also observed AREELS for Si(001)-(2x1)-Cs. The energy loss due to the overlayer plasmon excitation was constant for the emission angle, as shown in Fig. 5. The constant dispersion relation might be caused by the insufficient surface cleanliness, as discussed below. However, we believe it to be of different origin, since the Cs overlayer deviates from the K overlayer in various aspects.

PHOTOEMISSION MEASUREMENTS

We tried to observe the electronic structure of the K overlayer on the Si(001)-(2x1) surface by ultra-violet photoelectron spectroscopy (UPS) using synchrotron radiation from two different sources. One was performed at the SOR-Ring (the storage ring of our Institute at Tanashi) at the BL-3 beam line.[10] The photon energy was 20 eV with a total energy resolution of 0.8 eV. The angle-resolved spectra were observed as a function of emission angle for the Si(001)-(2x1)-K surface and were very similar to

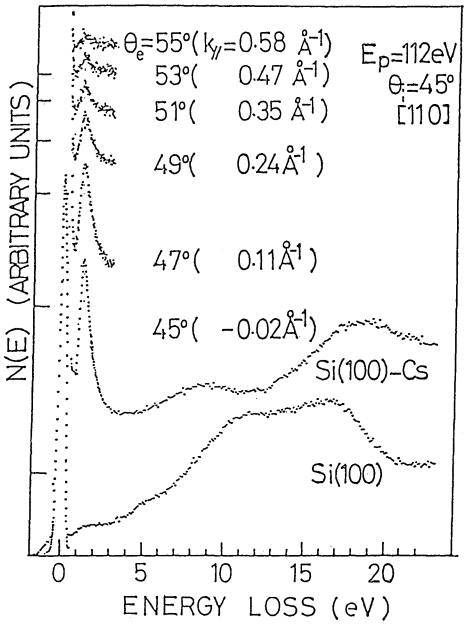

Fig. 5. AREEL spectra for Si(001)-(2x1)-Cs. [110] azimuth, E_p=112 eV, and θ_i=45.0°.

those for the clean surface. The photoemission intensity of the Si surface state of the K-covered surface was slightly reduced as compared to that of the clean surface, as the polar angle increased. This result shows that the K atom interacts very weakly with the dangling bond state of Si(001). That is to say, the surface state is hardly affected by K adsorption. However, photoelectrons emitted from the K 4s level of Si(001)-(2x1)-K could not be detected. This result is considered to be due to a small photoemission cross section from the K 4s state at this photon energy.

The second study was performed with a better energy resolution using synchrotron radiation of the PF-RING (the storage ring of the National Laboratory for High Energy Physics at Tsukuba).[11] The monochromator used was a Seya-Namioka type mounted at the BL-7B beam line. The photon energy was 8 eV, since the photoemission cross section of the K 4s state is expected to increase with decreasing photon energy. The electron spectrometer was a cylindrical-mirror type, the axis of which was set at 90° from the incident light, so that s- and p-polarized lights could be used in the UPS measurements. The former satisfies the condition that photoemission from the Si(001) surface state is strongly reduced. At low photon energies a strong photoemission intensity of the surface state is usually observed in the overlapping region with the photoemission of the K 4s state.

Figure 6 shows the K-coverage dependence of the photoemission spectra near the Fermi level of the K-covered Si(001)-(2x1) surface. The electric vector of the linearly polarized incident light was directed to the [110] azimuth. The energy resolution was about 0.1 eV. In s-polarization the binding energy of the valence band top increases by 0.2 eV at the initial stage of K adsorption and next decreases gradually, as shown in Fig. 6(a).

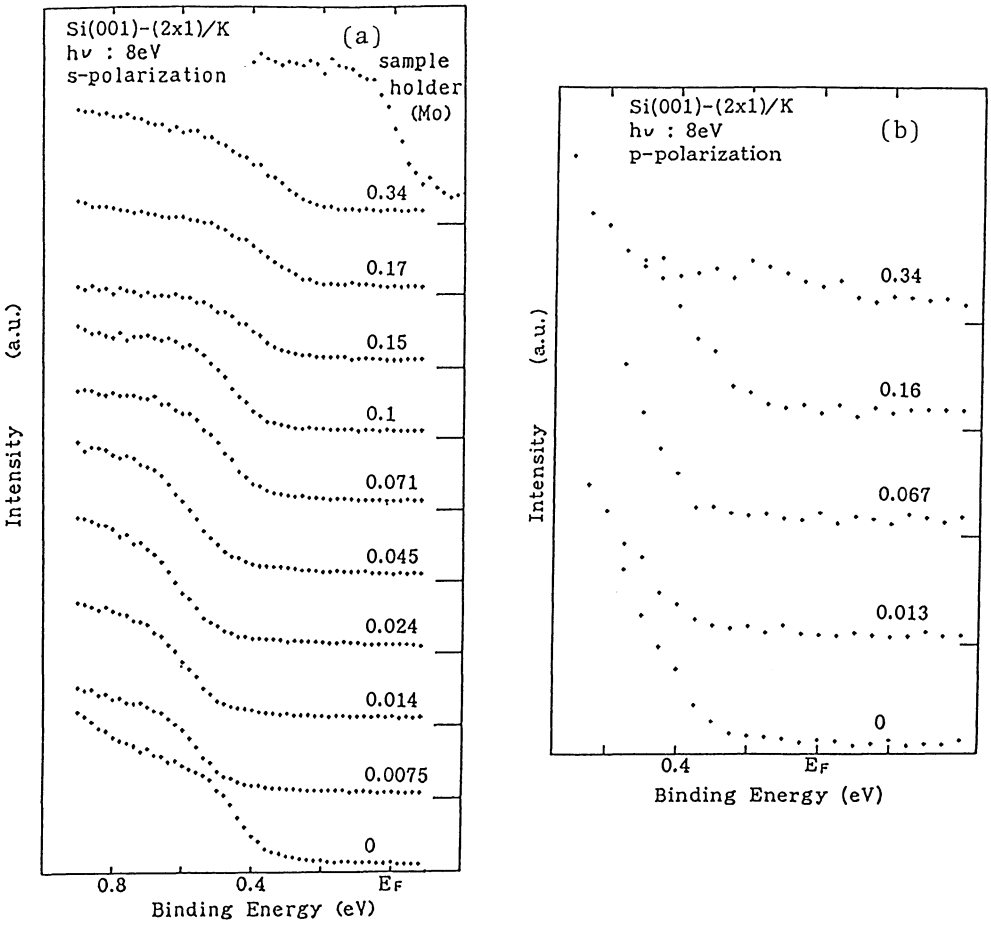

Fig. 6. Typical UPS spectra near the Fermi level for K on Si(001)-(2x1) (a) in s-polarization and (b) in p-polarization. hν=8 eV. The inset gives the Fermi-level onset obtained from the Mo sample holder. Numbers written in the right side of each curve show the Auger electron intensity ratio I(K-LVV)/I(Si-LVV).

A similar tendency was observed in the peak position of photoemission from the surface state of Cs on the Si(111)-(2x1) surface, as shown in Fig. 7.[12,13] This result can be explained as follows. The initial shift to the higher binding energy is caused by electron transfer from the Cs 6s state to the empty surface state of the substrate and by the upward shift of the Fermi level pinned near the bottom of the empty Si surface state. The following shift of the peak position towards lower binding energies is attributed the appearance of the Cs 6s peak. The Cs 6s peak is better visible by subtracting the spectrum of the Si surface state and the Si bulk band, as shown in Fig. 8.[12] The Fermi level is considered to be pinned in the Cs 6s state from this model. The spectra were measured by using a cylindrical-mirror analyzer at photon energy of 50 eV and hence an angle-integrated spectrum was observed. Therefore, the Fermi edge due to the Cs 6s state is expected to be observed, but it could not be seen. It is considered that the Fermi edge cannot be detected owing to the low energy resolution in these spectra.

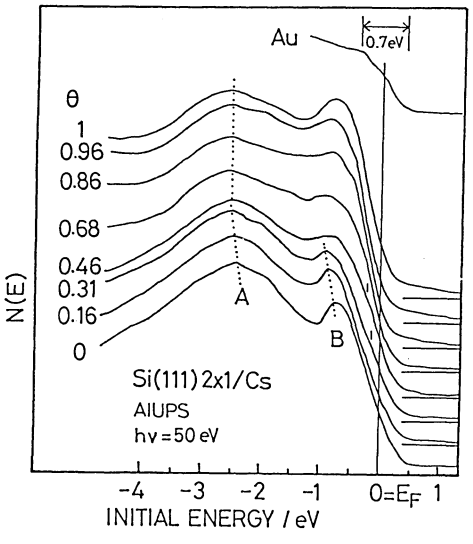

Fig. 7. Photoelectron spectra for Cs on Si(111)-(2x1). hν=50 eV. (From ref. 12.)

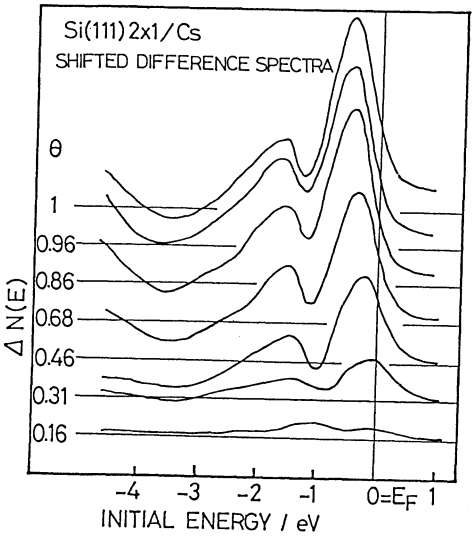

Fig. 8. Photoemission shifted difference curves between the clean and Cs-covered energy distribution curves. (From ref. 12.)

The interpretation for the level shift mentioned above is considered to be similarly satisfied in the K adsorption on the Si(001)-(2x1) surface. The Fermi level is pinned in the K 4s level located in the substrate band gap at the saturation coverage. The unoccupied surface state thus expected to appear just above the Fermi level was observed at 0.25 eV above the Fermi level at $\bar{\Gamma}$ by the k-resolved inverse photoemission study of the Si(001)-(2x1)-K surface.[14] However, the experimental result at the saturation coverage shown in Fig. 6(a) implies that the Si(001)-(2x1)-K is semiconductor-like because the binding energy of the valence band top has a finite value of 0.2 eV. In the present experimental condition the observed region in momentum space is limited near $\bar{J}'$-$\bar{K}$-$\bar{J}'$ and the second zone of $\bar{\Gamma}$-$\bar{J}'$ in spite of using the cylindrical-mirror energy analyzer, because the photon energy is as low as 8 eV. Considering the polarization vector of the incident light, the spectrum obtained by s-polarized light has a dominant contribution near the $\bar{J}'$ point. The calculated band structure with the LCAO-Xα method of the thin film models shows a finite binding energy for the occupied state at $\bar{J}'$ (LCAO denotes linear combination of atomic orbitals).[8] The self-consistent and geometry-optimized band structure has also a finite value at $\bar{J}'$.[3]

On the other hand, the p-polarized light gives different behavior. The shift of the valence band top shows a similar tendency in the low coverage region. As the K coverage approaches the saturation, however, a small peak appears close to the Fermi level and the onset of the high intensity peak shifts to the higher binding energy, as shown in Fig. 6(b). In the present experimental condition, the contribution from the near normal emission is contained in the spectrum that is the photoemission from the near $\bar{\Gamma}$ point is contributed to the spectrum. The calculated band structure with the LCAO-Xα method shows that the occupied state is close to the Fermi level at $\bar{\Gamma}$ and that the K overlayer is metallic.[8] Therefore, the metallic property of the K overlayer on the Si(001)-(2x1) surface is acceptable at the saturation coverage. On the other hand, the self-consistent and geometry-optimized band structure, which results in the metallization of the Si(001) substrate surface, has a clear band gap around the $\bar{\Gamma}$ point.[3] However, the clear conclusion cannot be obtained because the present experimental condition is angle-integrated.

Another important result for the Cs overlayer on the Si(111)-(2x1) surface is that the Si surface state remains unchanged even at the Cs saturation coverage[12] that is the interaction between the Cs atoms and the Si(111)-(2x1) surface does not affect the π-bonded Si surface chains. A similar result seems to be obtained for K on Si(001)-(2x1) in the present study as shown in Fig. 6(a).

LEED OBSERVATIONS AT LOW TEMPERATURES

We tried to find the Peierls transition expected in the one-dimensional metal system. If the valence state of the overlayer for the one-dimensional metal of Si(001)-(2x1)-A (alkali metal) is occupied by one electron for each alkali-metal atom, every atom is displaced and a couple of adjasent atoms close up in pairs due to the ordered arrangement for spin below the transition temperature.[15] Therefore, the surface structure is expected to change from the (2x1) to the (2x2) structure when the sample is cooled down. We designed and constructed a cooling stage for LEED observation at low temperatures and the temperature dependence of LEED was observed for Si(001)-(2x1)-K and Cs.[16] Schematic drawings of the cooling stage are shown in Figs. 9(a) and 9(b). Liquid helium is continuously supplied through a transfer tube from a liquid helium reservoir during the measurements. The minimum temperature was 15 K in the case of the Si specimen. The temperature was measured by a thermocouple, which was placed on a side of the sample holder and removed in preparing the sample, and corrected by the temperature difference

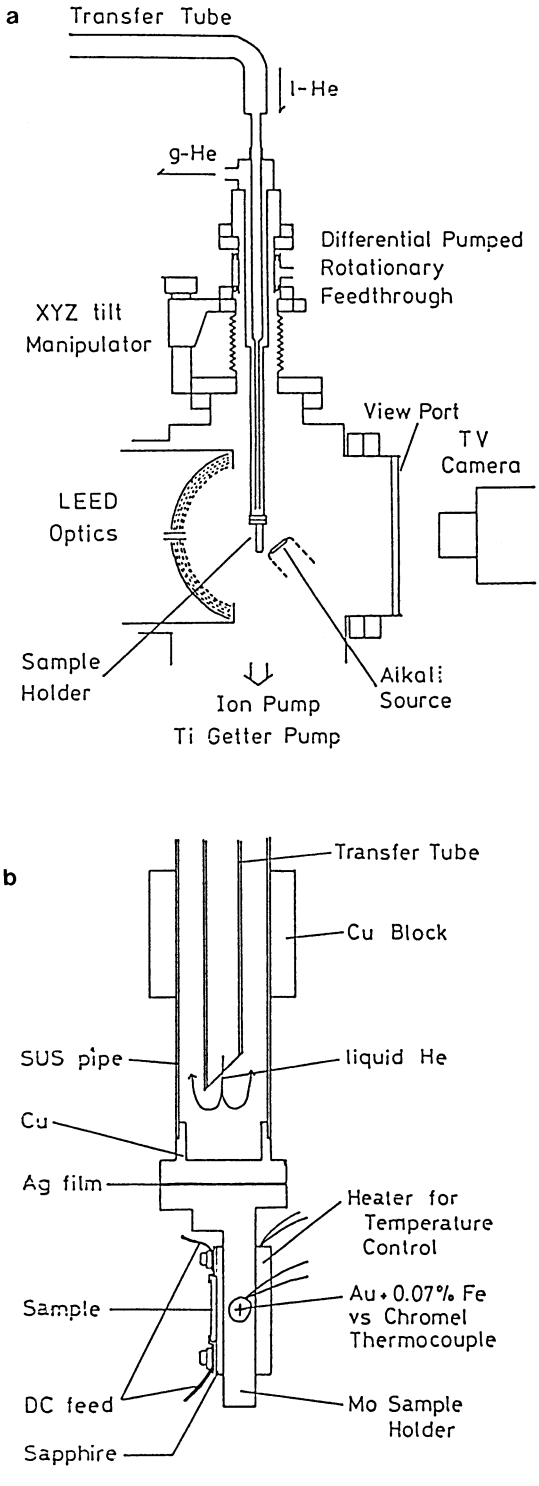

Fig. 9. Schematic drawings of a cooling stage for the LEED observation. (a) Total arrangement and (b) sample-surrounding part.

previously measured between the sample position and the side of the sample holder.

The LEED patterns were observed over the temperature range from room temperature to 15 K at several incident energies. The 1/2 1/2 spot could not be found in both surfaces. Moreover, the LEED pattern of the K-adsorbed surface did not change except for the effect of the Debye-Waller factor. On the other hand, in case of Si(001)-(2x1)-Cs the relative intensity of the diffraction spots was clearly changed upon cooling to low temperature. Figure 10 shows the LEED I-V curves for several spots at 23 and 300 K. A surface-structural change is clearly found. Since we have not performed LEED structural analysis, we cannot conclude what kind of structural change takes place. This will be done in the near future.

LITHIUM OVERLAYERS ON Si(001)

From the following standpoint we have carried out an experiment of Li atom adsorption on the Si(001)-(2x1) surface.[17] It is very interesting to know whether monolayers of alkali-metal atoms have metallic characters or not, when the diameter of the alkali-metal atom becomes smaller than the nearest neighbor distance of dimers on Si(001), 3.84 Å, while the nearest-neighbor atomic distance in lithium metal is 3.02 Å. The Li atom adsorption on Si(001) was studied by using EELS, AES, LEED and work function change. This case is very different from the other alkali-metal atoms (Na, K, Rb and Cs). The AES intensities of Li KLL and Si LVV Auger transitions as a function of Li deposition time clearly exhibited a break in slope of each curve at the same deposition time. After the break point the Li AES intensity increased gradually and finally saturated with increasing coverage. On the contrary, the intensities of the other alkali-metal atoms increase linearly and saturated suddenly. In the Li system the work function decreased almost linearly stopping at the same deposition time as the break point observed by AES. After that time the work function remained almost constant. The observed LEED patterns changed into a (1x1) structure around the break point passing through a new (2x1) structure. It is reasonable to say that one monolayer of Li is completed at the AES break point.

The overlayer plasmon was not observed in the Li EEL spectra at monolayer coverage and also at the surface of the new (2x1) LEED patterns. This means that the Li overlayer has not a metallic character contrary to other alkali-metal atoms in the (2x1) structure. Furthermore, we speculate that Li atoms intermix with the Si substrate after monolayer formation and form lithium silicide. This conclusion is supported by the fact that the (311) facetted Si(001) surface is formed after repeated annealing of the Li-covered surface. Li atoms form rather strong covalent bonds with Si atoms like H atoms.

DISCUSSION

The UPS results described in this article are clearly different from those reported by Enta et al.[4] In their observed UPS spectra there is a prominent peak close to the Fermi level for the clean (2x1) surface and the K-adsorbed surfaces in the low coverage region. In the present data this structure, which is caused by vacancies, was not found. Enta et al.[4] made a clean Si(001) surface by repeated Ar^+ bombardment and annealing at 900°C. In the present experiments, the Si(001) surfaces were carefully cleaned only by heating Si(001) wafers covered with carbon-free oxide layers. Missing-dimer defects on the Si(001) surface are frequently created, because the number of dangling bonds is reduced by missing-dimer creation, and found by scanning tunneling microscopy.[18] Ar^+ bombardment and/or high temperature annealing are considered to create a high density

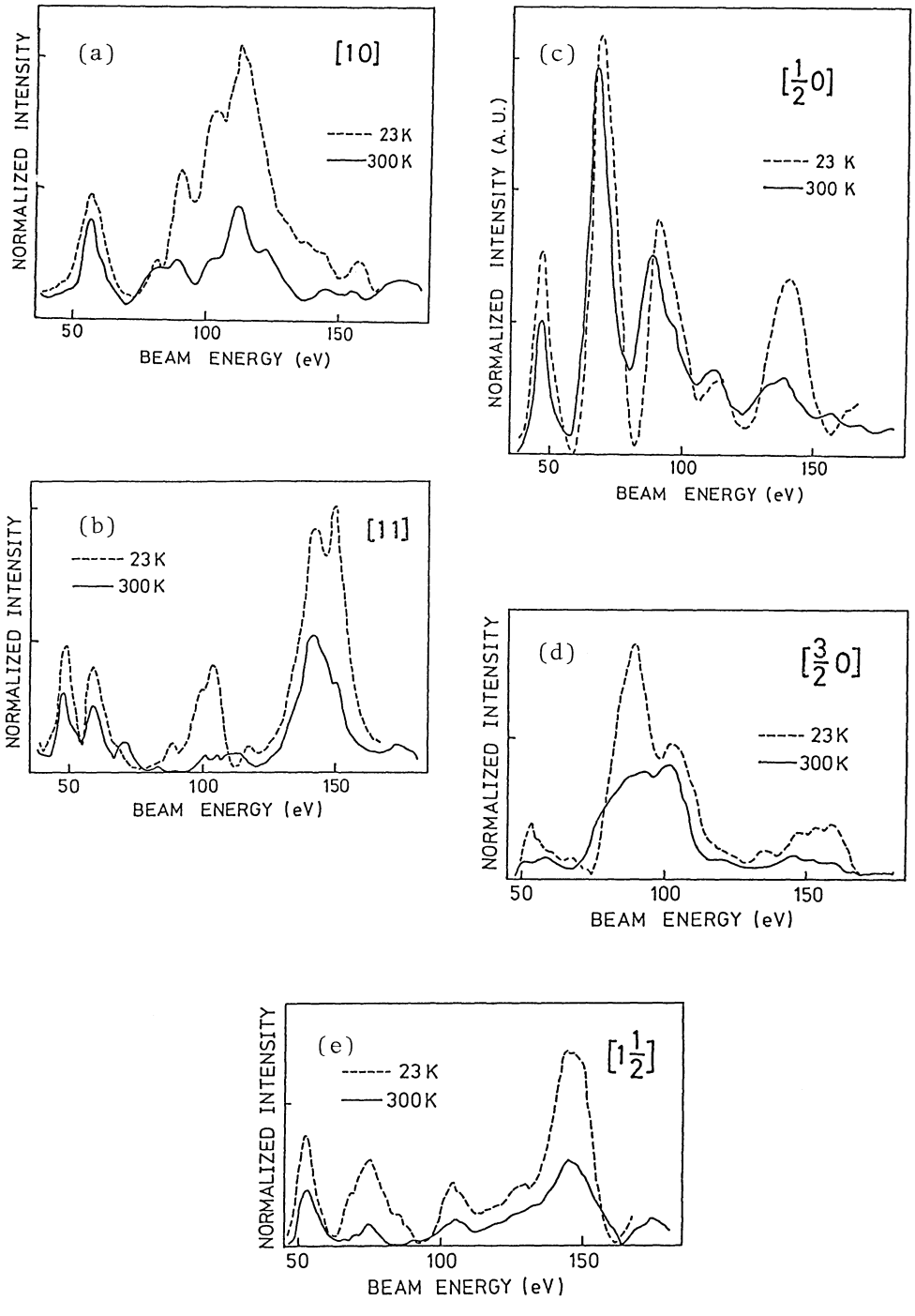

Fig. 10. LEED I-V curves of normal incidence for Si(001)-(2x1)-Cs at T=23 K (broken lines) and at T=300 K (solid lines). (a) 1 0, (b) 1 1, (c) 1/2 0, (d) 3/2 0, and (e) 1 1/2 spots.

of missing-dimer defects. Actually the (2x8) structure of the Si(001) surface, which is explained by the ordered missing-dimer defect model, is formed by annealing at high temperature (1400-1600 K) without any contamination.[19] Prolonged annealing at lower temperatures (1200-1300 K) and slow cool-down sometimes gave a small portion of the (2x8) domains coexisting with the (2x1) structure.[19]

On the other hand, Tabata, Aruga and Murata found by LEED that a transition from a low-temperature c(4x2) phase to a high-temperature (2x1) phase takes place on the clean Si(001) surface at the critical temperature $T_c \sim 200$ K.[20] This transition was concluded to be an order-disorder transition of the buckled dimers. The basic atomic arrangement in the (2x1) unit mesh is conserved during transition. These results were in good agreement with a renormalization-group calculation by Ihm et al.[21] and a Monte Carlo simulation by Saxena et al.[22] However, this transition could not be observed in the Si(001)-(2x8) surface and the (2x1) surfaces with high density of missing-dimer vacancies. In these surfaces the photoemission intensity from the surface state in UPS measurements using Ne I is not so high in comparison with the carefully prepared clean surface.[23] Therefore, the density of missing-dimer vacancies is serious for the various properties of the clean Si(001) surfaces and is also considered to be serious for the one-dimensional chain system such as Si(001)-(2x1)-K. Actually the potassium density at saturation coverage strongly depends on the sample treatment, since the number of vacancies is strongly dependent on the sample-cleaning method. The Auger electron intensity ratio I(K-LVV)/I(Si-LVV) at saturation coverage is 0.34 in our data shown in Fig. 6, while 0.49 in the specimen of Enta et al.[4] This intensity ratio is not seriously affected by the measuring conditions.

The surface preparation is also very important for measuring the dispersion relation of the overlayer plasmon. The dispersion relation is obtained from the emission angle dependence in AREELS, as shown in Fig. 4. Electrons reflected from the surface are detected for these measurements. Energy loss processes take place in double scattering events after elastic scattering of the incident electron beams, i.e. the diffraction-loss process. The experimental condition is schematically shown in Fig. 11. In the elastic scattering process, the incident electron energy is set at the maximum intensity position of the 00 spot (specular reflection) in the LEED I-V curve.

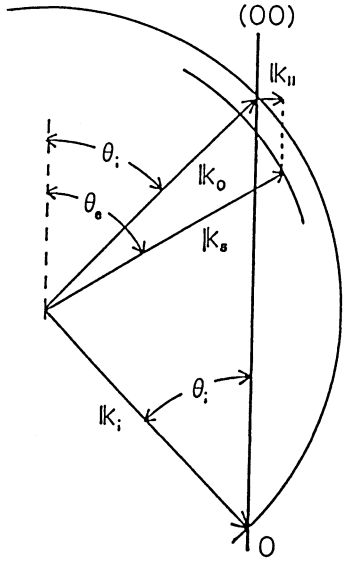

Fig. 11. Ewald construction of experimental condition for measuring the dispersion relation of overlayer plasmon by AREELS using low energy electron. **k** , $\mathbf{k}_0$ and $\mathbf{k}_s$ are wave vectors of the incident beam, the elastic-scattering beam (00 spot) and inelastic-scattering electrons corresponding to a plasmon with the surface parallel momentum hk , respectively. θ : incidence angle and θ_e : emission angle.

When the surface preparation is improper and the background intensity of a LEED pattern is high, a flat dispersion relation of the overlayer plasmon is occasionally observed and shows an erroneous electronic property. When the plasmon loss is observed at θ_e of an off-specular reflection, the plasmon excitations corresponding to $k_{\parallel} \neq 0$ shown in Fig. 11 as well as to $k_{\parallel}=0$ take place. The latter is the inelastic scattering of electrons forming the background at 0° scattering angle. As the background intensity increases, the latter process becomes dominant as compared with the former because the inelastic-scattering intensity with the plasmon excitation steeply decreases with $k_{\parallel}$. Then, the apparent energy loss should be the plasmon loss at $k_{\parallel}=0$ and shows a constant value in case of the insufficient surface cleanliness such as the formation of high-density missing-dimer defects. In the preliminary observation of the overlayer-plasmon dispersion relation for Si(001)-(2x1)-K, a flat dispersion relation was incorrectly obtained. After careful sample treatment, the clear dispersion was observed, as shown in Fig. 4. On the other hand, a flat dispersion relation was obtained for Si(001)-(2x1)-Cs after careful sample treatment, as shown in Fig. 5.

The alkali-metal overlayers on Si surfaces show metallic characters except for Li atoms, which make a strong covalent bond with Si atoms. Though the K overlayer on Si(001)-(2x1) at the saturation coverage, Si(001)-(2x1)-K, has a one-dimensional metallic character, it is a significant problem whether this character is caused by the metallization of K chains or the Si(001) surface. In the present UPS study the origin of metallization seems to be K chains, but this conclusion is not so clear. Detailed ARUPS measurements for a carefully prepared surface at low photon energy are important.

Recently, Nishigaki et al. observed metastable-atom deexcitation spectroscopy for Cs on Si(111)-(7x7).[24] The Cs 6s peak was clearly observed close to the Fermi level. This result is consistent with that of UPS measurements for Cs on Si(111)-(2x1)[12,13] described in this article. However, interaction of alkali-metal atoms with the Si surfaces seems to be different between K and Cs and also depends on the surface structures. Especially, the surface state of Si remains unchanged even at the monolayer coverage for Cs overlayer on Si(111)-(2x1). This result might be characteristic of the Si(111)-(2x1) surface, on which the dangling bond density is much reduced by making π-bonded chains[25] and interaction of Cs atoms with Si atoms must be weaker than that of K. We think that experiments at low temperatures are effective for the study of the difference among alkali-metal atoms about the interaction with silicon, as seen in LEED observations at low temperatures.[16]

ACKNOWLEDGEMENTS

This work is supported by the Grant-in-Aid for the Scientific Research from the Ministry of Education, Science and Culture.

REFERENCES

1. R. W. Gurney, Phys. Rev. 47, 479 (1935).
2. T. Aruga, H. Tochihara, and Y. Murata, Phys. Rev. B 34, 8237 (1986).
3. S. Ciraci and I. P. Batra, Phys. Rev. Lett. 56, 877 (1986); S. Ciraci and I. P. Batra, Phys. Rev. B 37, 2955 (1988).
4. Y. Enta, T. Kinoshita, S. Suzuki, and S. Kono, Phys. Rev. B 36 9801 (1987).
5. T. Aruga, H. Tochihara, and Y. Murata, Phys. Rev. Lett. 53, 372 (1984).
6. D. M. Newns, Phys. Lett. 39A, 341 (1972).
7. M. Nakayama, T. Kato, and K. Ohtomi, Solid State Commun. 50, 409 (1984).

8. H. Ishida, N. Shima, and M. Tsukada, Phys. Rev. B 32, 6246 (1985).
9. H. Ishida and M. Tsukada, Surf. Sci. 169, 225 (1986).
10. M. Kubota, T. Koyama, and Y. Murata, unpublished.
11. M. Kubota, Y. Murata, N. Namba, and H. Kuroda, to be published.
12. H. Tochihara, M. Kubota, M. Miyao, and Y. Murata, Surf. Sci. 158, 497 (1985).
13. H. Tochihara and Y. Murata, Surf. Sci. 172, L509 (1986).
14. I. P. Batra, J. M. Nicholls, and B. Reihl, J. Vac. Sci. Technol. A 5, 898 (1987).
15. R. E. Peierls, "Quantum Theory of Solids," Oxford University Press, London (1956) p. 111.
16. T. Tabata, T. Aruga, and Y. Murata, unpublished.
17. H. Tochihara and Y. Murata, to be published.
18. R. M. Tromp, R. J. Hamers, and J. E. Demuth, Phys. Rev. Lett. 55, 1303 (1985).
19. T. Aruga and Y. Murata, Phys. Rev. B 34, 5654 (1986).
20. T. Tabata, T. Aruga, and Y. Murata, Surf. Sci. 179, L63 (1987).
21. J. Ihm, D. H. Lee, J. D. Joannopoulos, and J. J. Xiong, Phys. Rev. Lett. 51, 1872 (1982).
22. A. Saxene, E. T. Gawlinski, and J. D. Gunton, Surf. Sci. 160, 618 (1985).
23. M. Kubota, T. Koyama, and Y. Murata, to be published.
24. S. Nishigaki, et al., to be published.
25. K. C. Pandey, Phys. Rev. Lett. 47, 1913 (1981).

PRESENT UNDERSTANDING OF A MODEL METAL/SEMICONDUCTOR JUNCTION: K/Si(001)2x1

Enrique G. Michel, María C. Asensio, and Rodolfo Miranda

Dto. de Física de la Materia Condensada
Universidad Autónoma de Madrid, 28049-Madrid, Spain

Introduction

The formation of metal/semiconductor interfaces is a topic of the utmost interest since more than a century [1]. In spite of the continuous effort our understanding of the microscopic aspects of this problem is far from being satisfactory [1]. These studies have been plagued with complications arising from interdiffusion, mixing and complex chemical reactions taking place at the metal-semiconductor interface. Thus, most of the transition and noble metals when deposited in Ultra-High-Vacuum onto semiconductive surfaces diffuse locally into the substrate rendering almost impossible the task of determining the geometry of the interface by laterally-averaging techniques. Recent work using Scanning Tunneling Microscopy (STM) has unraveled the beauty and complexity of the geometry and electronic structure at the metal/semiconductor interfaces [2].

Recently, a widespread belief arose that most of these difficulties could be overcome by using alkali metals as the deposited adspecies. Thus, it was suggested that the alkali metals (except Li) when deposited on Si or GaAs substrates do not react or interdiffuse with the substrate. They could thus provide an almost ideal playground where problems such as metallization, Schottky-barrier formation or bonding at interfaces could be tackled by experimentalists and theoretitians. The technological implications of this type of interfaces (infrared detectors, image intensifiers, Negative Electron Affinity Photocathodes [3], spin-polarized electron guns [4], promoted oxidation of semiconductors [5,6], etc) have given an additional boost to the proliferation of experiments and calculations in the alkali metal/semiconductor system.

In the following we will report the results of a multi-technique approach to the much debated K/Si(001)2x1 system which has been considered an alkali metal/semiconductor prototype. We will address some unsettled issues in this problem in an effort to clarify the basic physics involved in metallization, charge transfer and bonding at metal/semiconductor interfaces. The experimental details have been reported elsewhere [6].

Surface geometry and adsorption site

Early Low Energy Electron Diffraction(LEED)studies revealed that the clean (001) surface of Si presents a (two-domain) 2x1 reconstruction [7]. It was proposed that the microscopic origin of this reconstruction was the formation of dimers along the [110] direction in order to minimize the surface energy associated with the dangling bonds [7]. Furthermore, the dimers were supposed to be asymmetric, i.e tilted in the surface plane, which would explain the semiconductor character of this surface [8]. Actually, the surface electronic structure is determined by two surface state bands, one completely occupied and the other completely empty. The energy position and dispersion of the surface state bands have been mapped by Angle Resolved Ultraviolet Photoelectron Spectroscopy [9]. Recent Scanning Tunneling Microscopy (STM) work [10] has confirmed the validity of the dimer model and has shown as well the existence of a large density of extended surface defects (~10 %) and dimers of both symmetric and buckled type associated with regions of local c(2x2) and p(2x2) symmetry as previously suggested by He diffraction experiments [11]. In Fig. 1 we show a schematic picture of an ideally ordered 2x1 reconstruction of the Si(001) surface at 300 K. It should be noted that there has been some experimental evidence [12] as well as calculations [13] that suggest that the equilibrium reconstruction of Si(001) at low temperature has a c(4x2) symmetry and that the room temperature phase consists of randomly oriented dimers.

Adsorption of K on this surface produces no change in the symmetry of the LEED pattern [14,15] but results in a different distribution of the diffracted intensity among the LEED spots. Three possible adsorption sites consistent with the LEED observations are shown in Fig. 1. Total energy calculations have favored so far the A-site as the energetically preferred adsorption site [16]. Experimentalists and theoretitians have accepted this adsorption site for further subsequent work without clear experimental evidence of its preeminence. With this geometry, adsorption of 0.5 monolayers (ML) of K (1 ML of K is defined in this work as a number of K adatoms equal to the atomic density of the Si(001)2x1 surface, i.e $n_K = 6.78 \times 10^{14}$ atoms/cm^2) would produce one-dimensional chains of K riding on the dimer rows.

Coverage calibration and multilayer growth

In the system at hand the calibration of the coverage deserves a careful treatment as it is related to some basic aspects of the problem. The adsorption of alkali atoms on transition metal surfaces produces a noticeable decrease of the work function followed by a slight increase at higher coverages. This behavior is generally interpreted considering that the first alkali adatoms transfer to the substrate an amount of charge that decreases as the coverage increases due to depolarization effects. The minimum in work function corresponds to the most ordered structure and usually occurs at submonolayer coverages [17]. The charge transfer at completion of the alkali monolayer is small and a complete transfer of the alkali valence electron does not take place even during the first stages of the adsorption [18]. This picture is not yet accepted to describe properly the alkali metal/semiconductor interface. Two conflicting models have been put forward and a strong debate exists in the literature [16,19-21]. On one side, upon alkali deposition, a similar behavior of the work function should be observed in the case of semiconductor substrates if the qualitative evolution of the charge transfer would be parallel to the one outlined above for metal substrates. Accordingly, the bonding between K and Si at saturation would be mainly covalent, the

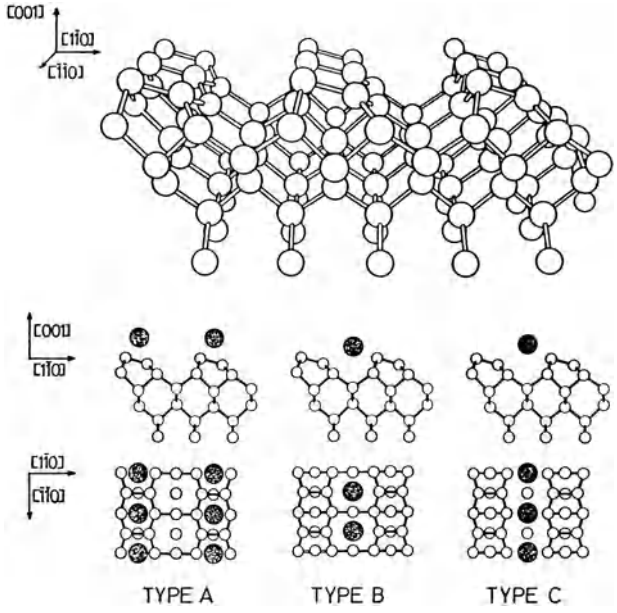

Figure 1. Scheme of the ideally reconstructed Si(001)2x1 showing asymmetric dimers at the topmost layer (upper part). In the lower part, schematic models depict the three different adsorption sites for the K/Si(001)2x1 surface. K atoms are represented by shaded circles and open circles denote Si atoms in the surface of the crystal. The K-Si distance is 3.1 Å as determined by SEXAFS [25] (Figure from Ref. 36).

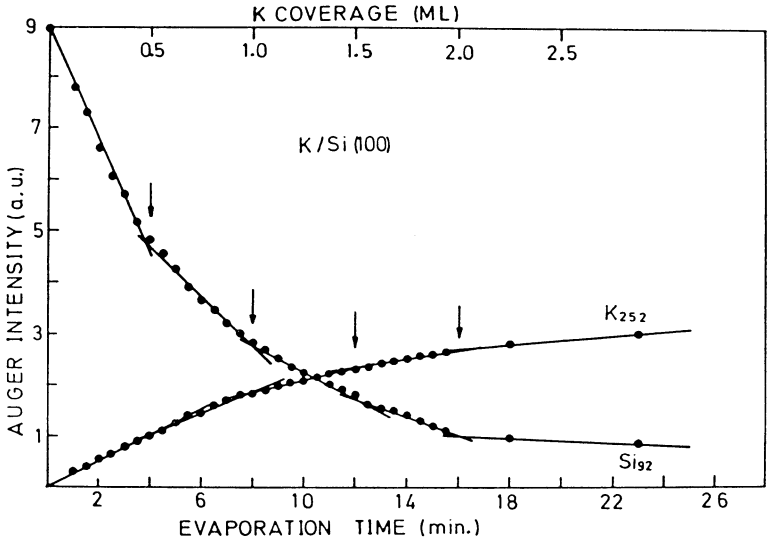

Figure 2. Auger peak-to-peak intensities of the Si(LVV) and the K(LMM) transitions versus evaporation time and K coverage in monolayers. The arrows indicate completion of each layer (Fig. from Ref. 15).

overlayer would metallize below saturation coverage and further deposited K could form bonds with the first deposited layer strong enough for multilayer growth to occur at temperatures close to room temperature (R.T.)[15].

The second model proposes, on the basis of pseudopotential calculations, a whole charge transfer to the substrate at all coverages (up to $\theta_K = 0.5$ ML) which results in purely ionic bonding [16], a semiconducting surface at 1 ML coverage [19] and the impossibility of growing multilayers at temperatures around 300 K, as bonding of further deposited K would not be possible [16]. This point of view was apparently supported by early measurements at 300 K which suggested that the K coverage saturates at $\theta_K = 0.5$ ML and that the work function decreases without passing through a minimum [14]. Later, the saturation coverage at 300 K was reported to be 1 ML [19]. On the contrary, the thorough Auger calibration reproduced in Fig. 2 first indicates that multilayer growth was in fact possible at temperatures close to R.T. [15]. The first break in the AES intensity versus evaporation time curve was assigned to $\theta_K = 0.5$ ML. An independent confirmation of the accuracy of this calibration has been provided recently by a simultaneous Auger and Xe Thermal Desorption study [22]. In this work Xe adsorption has been used to titrate the coverage of K. In the chosen conditions pre-adsorption of K blocks adsorption sites for Xe (see also Fig. 9). The area of the thermal desorption spectrum of Xe for a K coverage of 0.5 ML (as given by AES) is only half of the Xe desorption peak for the clean surface. These data prove that at $\theta_K = 0.5$ ML half of the Si surface is not covered by K adatoms.

Recent Thermal Desorption (TDS) data [22] depicted in Fig. 3 show that for $\theta_K > 0.5$ ML the desorption of K is first order with a desorption peak at $T_p = 343$ K. Adsorption of K at 60 K where multilayers are easily grown produces a desorption peak at the same temperature. For $\theta_K < 0.5$ ML the maximum of desorption occurs at ~ 700 K (not shown in this T range, see the lowest coverage of K in Fig. 3) with only traces of K being desorbed at 343 K.

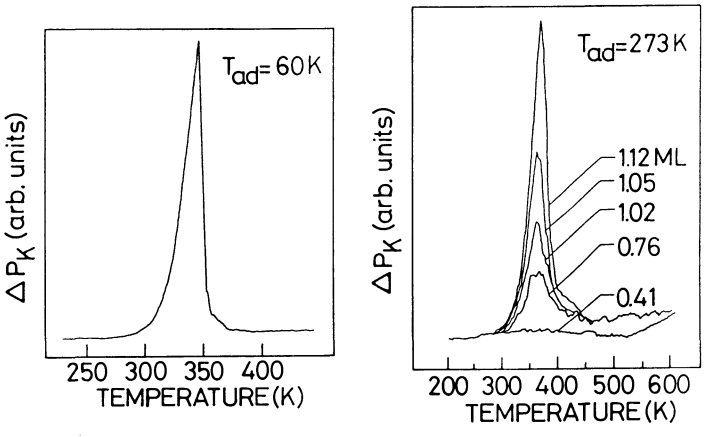

Figure 3. TDS of potassium from a Si(001)2x1 surface for different conditions. The left pannel shows the K-TDS for multilayer deposited at 60 K (heating rate = 0.4 K/s). The right panel shows K-TDS for increasing amounts of adsorbate deposited at 273K (heating rate = 1.0 K/s).

The bonding energy of K to the Si surface can be obtained from the desorption peak temperature by using the known Redhead expression, $E_d = k_B T_p [\ln (\nu T_p/\beta) - 3.64]$, where k_B is the Boltzmann constant, T_p is the temperature of the desorption peak, ν is a preexponential factor (10^{13} s^{-1}), and β is the heating rate (K/s). Analysis of the TDS data yields $E_d = 1.8$ eV/atom for $\theta_K = 0.5$ ML and $E_d = 0.95$ eV/atom for $\theta_K > 0.5$ ML. These results disagree with the calculated bonding energy of half-a-monolayer K to the Si substrate of about 3 eV/atom [16]. On the other hand, the cohesive energy of K in the bulk metallic state is of the order of 1 eV/atom in nice agreement with our results for $\theta_K > 0.5$ ML. This suggests that above $\theta_K = 0.5$ ML the overlayer can be considered as metallic. These data prove that the growth of K multilayers at 273 K is undoubtedly feasible. Nevertheless the maximum of desorption is so close to 300 K that small variations of the actual surface

temperature produce a completely different situation. In order to illustrate this point Fig. 4 shows the Auger peak ratio (K_{252}/Si_{92}) and the work function changes produced by K adsorption on Si (001)2x1 at a temperature slightly above RT, i.e. 325 K. In this case a saturation of the K coverage at θ_K = 0.65 ML and a small work function minimum are observed in agreement with data obtained by other groups [14,19]. In conclusion multilayer growth is definitively possible close to R.T. but small changes in the sample temperature results in growth of only submonolayer amounts of K. Careful determination of the actual K coverage is, thus, essential in this system for any meaningful measurement close to R.T. For instance, the data shown in Fig. 1 of Ref. 19 indicate that the K coverage was 0.8 ML in the particular conditions of that experiment.

Band bending, work function and charge transfer

The adsorption of K on Si(001)2x1 produces a charge transfer to the empty surface states of the substrate which modifies the initial band bending of the clean surface. For n-type Si(100)2x1 the Fermi level is pinned 0.4 eV above the valence-band maximum by the high density of surface defects present in this surface [23]. The band-bending changes during K adsorption have been determined by temperature-dependent surface photovoltage effect

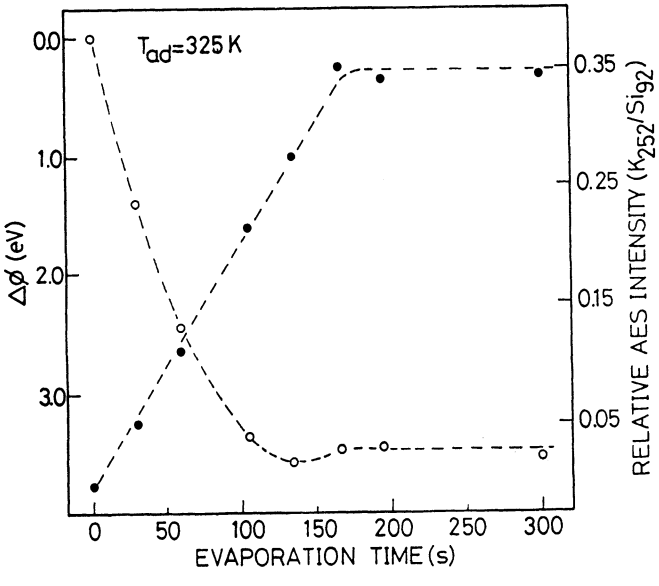

Figure 4. Work-function change (left hand scale, open circles) and relative AES intensity for the peaks K_{252} and Si_{92} (right hand scale, shaded circles), upon adsorption of K on a Si(001)2x1 surface at 325 K, versus evaporation time. The flattening of the curves from ~170 s of evaporation indicates coverage saturation at a value of θ_K = 0.80ML.

during photoemission [24]. This method is based on the Ultraviolet Photoelectron Spectra of the sample taken respectively at 300 K and at 60 K, which are shifted in Kinetic energy by an amount $V_D = V_{BB} + \Delta - \Delta'$ where V_{BB} is the band-bending, and Δ (Δ') the distance in energy between the Fermi level, (E_F), and the conduction band edge, E_c, at 300 K (60 K) [25]. The reason for this shift is a flattening of the bands at low temperature during photon irradiation as schematically depicted in Fig. 5. The resulting Schottky barrier height (or Fermi level movement) versus K coverage as determined by the method outlined above [24] is plotted in Fig. 5. At $\theta_K = 0.5$ ML (completion of the rows) the Fermi level has shifted 0.3 eV upwards. The shift of E_F is almost completed at $\theta_K = 0.15$ ML . The experimental value is in excellent agreement with the Fermi level shift calculated by Flores and coworkers (0.28 eV) [21].

Work function changes in semiconductors include two contributions: the band-bending changes and the surface dipoles produced upon adsorption [1,26]. The work function changes measured by a Kelvin probe during deposition of K on Si(001)2x1 at 300 K are

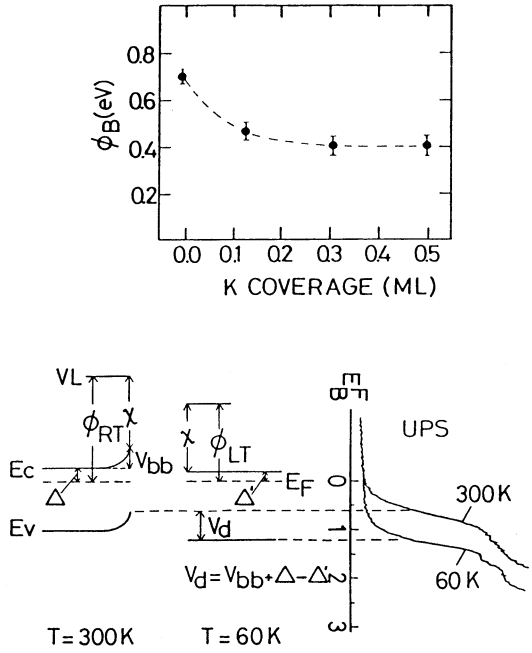

Figure 5. The upper part of the figure shows the Schottky-barrier height versus K-coverage. The lower part shows a scheme or the process involved in the measurement of the Schottky-barrier height. E_c is the bottom of the conduction band, E_v the top of the valence band, ϕ_{RT} (ϕ_{LT}) the work function at room temperature (low temperature), Δ (Δ') the distance between the bulk Fermi level (E_F) and the bottom of the conduction band at room temperature (low temperature), χ is the electron affinity, V_{bb} is the band bending and V_d the shift in the UPS spectrum observed upon lowering the temperature (right hand part of the lower scheme) (Figure from Ref. 24).

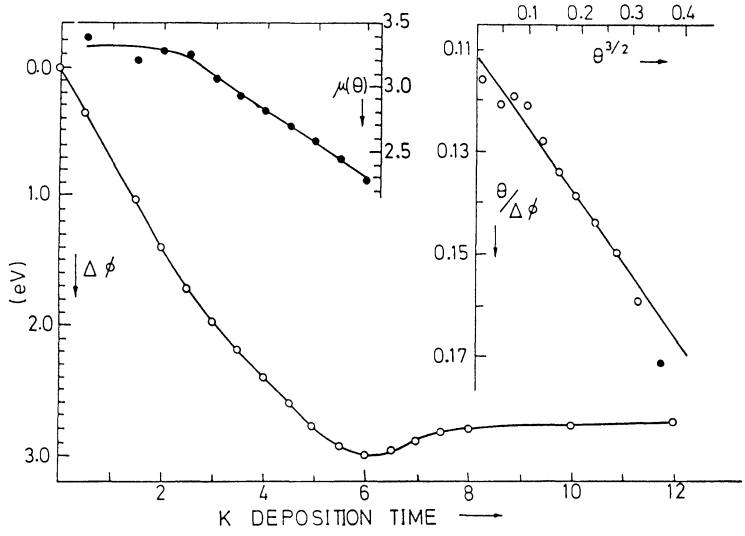

Figure 6. Work-function changes for K deposition on Si(001)2x1. The data have been taken at 300 K with a Kelvin probe. The left inset depicts the dipole moment per K adatom $\mu(\theta)$ as a function of θ. The right inset show the same data points plotted as $\theta / \Delta\phi$ vs. $\theta^{3/2}$ The linear behavior indicates that $\Delta\phi(\theta)$ can be described by the Topping model. (Figure from Ref. 21).

shown in Fig. 6. A clear minimum is observed at $\theta_K = 0.5$ ML [15] followed by a rise to the work function of bulk metallic K in close similarity to K adsorption on metals. In this particular case the final coverage of K is 1.9 ML. The work function dependence with coverage deviates from linearity indicating that the average dipole moment per K adatom, $\mu(\theta)$, decreases with θ as shown in the inset. The same data points plotted as $\theta/\Delta\phi$ versus $\theta^{3/2}$ (see the inset in Fig. 6) display a linear behavior indicating that the evolution of $\Delta\phi$ with θ can be described by the Topping model [19]. This suggests that mutual depolarization is the main cause of the $\Delta\phi$ changes with θ as previously found for alkali metal adsorption on metallic substrates.

These data can be easily interpreted by assuming that the charge transfer decreases with K coverage as occurs for alkali metals adsorbed on metals. Simple estimations of the degree of charge transfer at $\theta_K = 0.5$ ML result in 0.22 electrons per K atom [21] in nice agreement with the results of Mönch in Cs/GaAs(110) [26]. Self-consistent tight binding calculations give 0.28 electrons/K atom at $\theta_K = 0.5$ ML and 0.41 electrons/K atom at low K coverage [21]. Furthermore, these calculations yield a shift of E_F of 0.3 eV and 3.1 Å for the K-Si bond length in excellent agreement with our data described above and recent SEXAFS measurements [27] respectively, but in disagreement with predictions of a very short (2.6 Å) K-Si bond length [16]. The existence of a polarized Si-K bond rather than a purely ionic one could be indirectly inferred from the crystal structure and physical properties of bulk potassium silicides such as KSi [28] and K_8Si_{46} [29] which are not typical from strong ionic compounds.

The image presented here profoundly contradicts the conclusions of previous calculations which also predict a constant transfer of charge up to $\theta_K = 0.5$ ML [16]. Were this prediction true, the binding energy of a K electronic core level e.g. the K 2p level, would be constant independently of coverage as long as the overlayer is not metallic and the screening of the photohole does not change its character which is a safe assumption for $\theta_K < 0.5$ ML . The data shown in Fig. 7 indicate that this is not the case. The binding energy of the K 2p core level as obtained from XPS measurement decreases by almost 1 eV from the first stages of K deposition to $\theta_K = 0.5$ ML as illustrated in Fig. 7. The evolution with θ of the K 2p binding energies can easily be rationalized as due to a larger degree of charge transfer at lower K coverages.

Metallization of the overlayer

Strictly speaking, metallization of the surface occurs whenever the density of states at E_F is nonzero. However, from an experimental viewpoint it is a non-trivial task to decide when it is metallic. An emission at E_F can be clearly observed in angle-integrated photoemission experiments at $\theta_K = 1$ ML as shown in the left-hand inset of Fig. 7, but it starts to grow at lower K coverages. In the same sense, plasmons from a metallic K overlayer can be easily detected in the K 2p core level spectrum at $\theta_K = 1.37$ ML (see the right-hand inset in Fig. 7), although with an energy somewhat smaller (3.3 eV) than the bulk plasmon energy (3.8

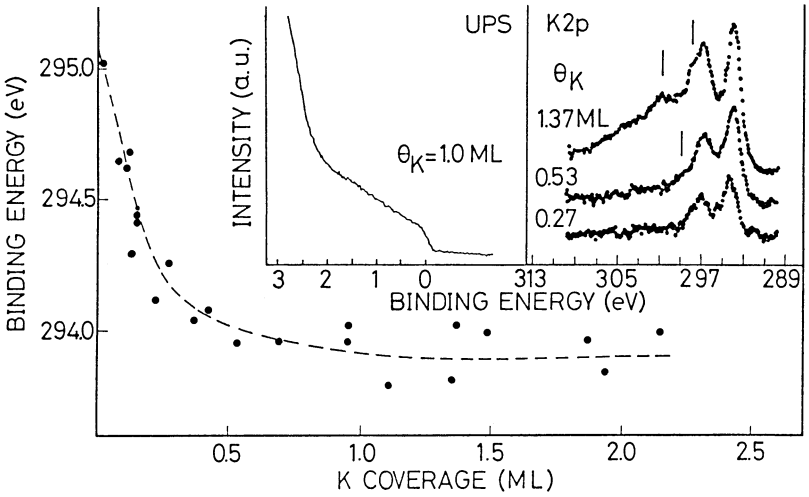

Figure 7. Binding Energy of the K 2p core level as a function of the K-coverage. The energies are referred to the Fermi level. The right hand inset shows representative K 2p core level spectra, where the presence of plasmons (indicated by tic marks), signalling the metallization of overlayer can be seen only from coverages above $\theta_K = 0.5$ ML. The left inset shows intense Fermi level emission as observed with angle-integrated UPS for $\theta_K = 1.0$ ML. The emission starts to appear at coverages between 0.5 and 1.0 ML.

eV). Plasma losses with the energy of the bulk plasmon are observed in the K 2p and Si 2p core levels from $\theta_K = 2$ ML. A similar increase in plasmon-loss energy with alkali coverage has been reported for Cs, Rb and Na deposited on GaAs(110) [30]. Since the plasmon energy is proportional to the square root of the density of valence electrons, the increasing plasmon energy indicates an increasing density of delocalized electrons in the overlayer. It should be mentioned that the interband transition at 1.8 eV observed with ELS [20] can already be detected in the K 2p emission at $\theta_K = 0.53$ ML.

These data reveal that the overlayer metallization is complete at $\theta_K = 1$ ML and suggest that it may begin already at $\theta_K = 0.5$ ML. Actually, this view is strongly supported by an indirect observation, namely, the completely different reactivity of the K-covered Si surface with respect to O_2 adsorption above and below $\theta_K = 0.5$ ML [31]. An eventual metallization of the overlayer at $\theta_K = 0.5$ ML would explain two experimental facts: i) the additional decrease of the work function upon O_2 adsorption [31,32] above $\theta_K = 0.5$ ML (only a work function increase is observed for $\theta_K < 0.5$ ML and ii) the formation of oxygen species (e.g. KO_2) that are characteristic of O_2 adsorption on thick K metallic films [31,33].

Local work function changes

The strong decrease in $\Delta\phi$ observed in Fig. 6 for submonolayer K coverages is not laterally homogeneous. The ideal technique to reveal lateral inhomogeneities of the surface potential is the Photoemission of Adsorbed Xenon Atoms (PAX) as developped by Wandelt and coworkers [34]. The binding energy of the Xe 5p levels is pinned to the local vacuum level, shifting in energy with the local work function of the adsorption site.

Representative PAX measurements of 5p Xe levels in the K/Si(001)2x1 system as a function of the K coverage [22,24] are shown in Fig. 8. For the clean Si(001)2x1 surface, only one Xe state (A) is observed at 7.8 eV below EF. Deposition of only 0.03 ML of K results in the appearance of a second Xe state (B) at larger B.E., which is ascribed to Xe atoms adsorbed in the vicinity of the K adatoms. The intensity of state B increases with K dosage while that of state A (Xe adsorbed on clean patches of the Si surface) steadily decreases and finally disappears between 0.12 and 0.35 ML. For a comparison with the average decrease of the work function see Fig. 6. The B.E. difference between state A and B, ~ 0.45 eV, stays constant independently of θ_K

These data indicate that the adsorption of K modifies the potential with a long range effect. Thus, even patches of clean Si have a reduced work function. This long-range effect produces the overall shift in Xe B.E.'s observed in PAX. Additionally, the detection of two Xe states implies that there is a further, local, decrease of the work function in the vicinity of the K adatom, i.e. a short-range effect affecting only those Xe atoms adsorbed in direct

contact with the K adatoms. This mixture of short and long-range effects could shed some light into the microscopic mechanisms of the alkali-promoted oxidation of Si [31-33].

The K adsorption site revised

So far we have assumed that the adsorption geometry of K on Si(001)2x1 was known, i.e. the K adsorption site is the sixfold hollow site between two parallel dimer bonds (site A in Fig. 1). Only this adsorption site would be occupied below $\theta_K = 0.5$ ML. However, some doubts have been cast on the correctness of this assumption. Recent X-ray Photoelectron Diffraction (XPD) data by Abukawa and Kono [35] show a large azimuthal anisotropy in the K 2p emitted intensity that was interpreted as reflecting a K double layer. At saturation (at RT) the K coverage would be 1 ML and K rows would cover not only the A sites but also the C (or B) sites [35]. In the experimental conditions of Abukawa and Kono [35] the K coverage is 0.8 ML according to our calibration (see above) which explains why two adsorption sites are detected. However, the point that should be addressed is which one (A, B or C) is the equilibrium adsorption site at $\theta_K = 0.5$ ML when 1D rows are formed. Two

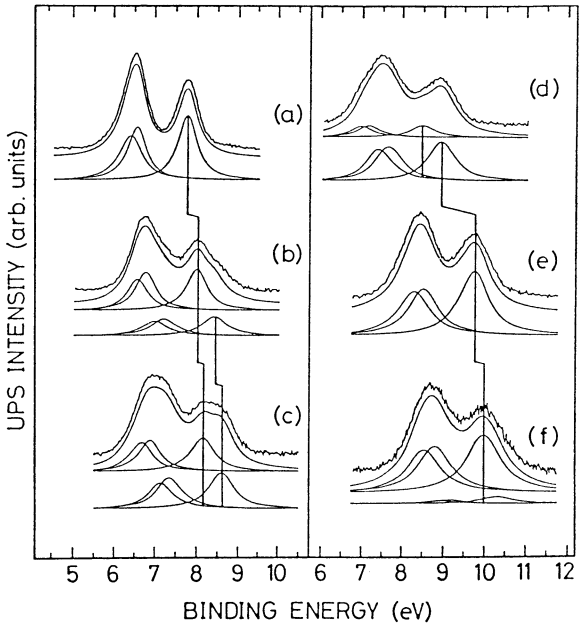

Figure 8. Photoemission of adsorbed Xenon (PAX) ($h\nu = 21.2$ eV) for increasing K-coverages on a Si(001)2x1 surface exposed to 1 L Xe. The coverages are: (a) clean Si(001)2x1 surface, (b) 0.03 ML, (c) 0.09 ML, (d) 0.12 ML, (e) 0.35 ML, and (f) 0.55 ML. Two Xe states (A and B) are observed at this exposure. A corresponds to clean Si patches and B to the sites on the surface in the vicinity to K adatoms. Observe that the B.E. scales from left and right-hand panels are different. (Figure from Ref. 24).

recent pieces of experimental evidence point to the cave positions (B or C) as the preferred sites. The first comes from desorption of Xenon.

TDS data for 30 Langmuir (L) of Xe adsorbed at 60 K on clean and K-covered Si(001) surfaces are plotted in Fig. 9 [20]. In order to avoid kinetic problems associated with low surface diffusion the K adlayer was deposited at 60 K and annealed at 325 K for 1 min prior to lowering again the temperature for Xe adsorption. On the clean Si surface two Xe desorption peaks with almost equal weight are detected. The bonding energies for Xe are respectively 0.21 eV/atom and 0.24 eV/atom. The desorption peaks correspond to Xe adsorbed on both dimer (A) and cave (C) sites. Upon K adsorption, the peak at higher bonding energy is suppressed while the other remains unaffected, suggesting that the K adatoms occupy preferentially the sites with higher bonding ener gy for Xe, blocking them for further Xe adsorption. Since the adsorption energy of Xenon is mainly determined by the coordination with the substrate atoms [30] this might indicate that the preferred adsorption site for K is the C site, i.e. in the caves instead of the A site.

Further indication of the C site being the microscopic adsorption site comes from recent Auger Electron Diffraction experiments[36]. This technique is based on enhanced forward scattering of the outgoing Auger electrons by overlying atoms in the lattice resulting in peaks in the angular distribution of electrons located along the major axes of the crystal.

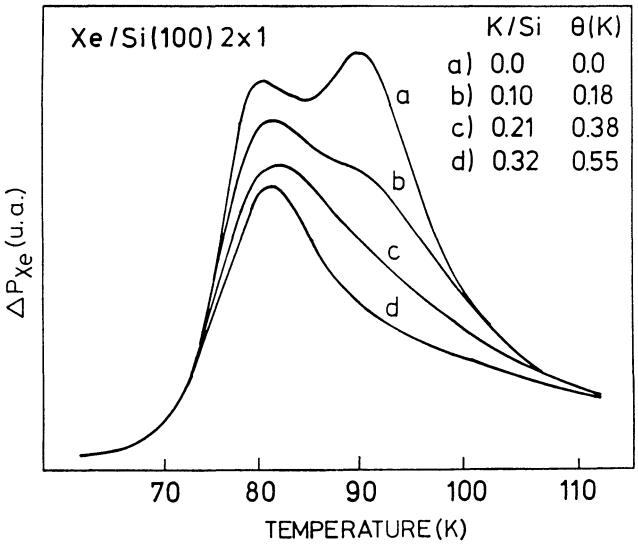

Figure 9. TDS of Xe for increassing K coverages. The clean surface shows two adsorption states. Upon deposition of K (annealed 1 minute at 300 K), one of these states is quenched. (Figure from Ref. 22)

The maxima in the experimental polar-angle distribution of emitted electrons are not consistent with K rows on top of the Si dimers, rather they suggest that K adsorbs forming rows in the caves of the Si(001)2x1 surface [36].

Acknowledgement

The authors are deeply indebted to Eva M. Oellig, J.E. Ortega, P.Pervan, Prof. G.R. Castro, Prof. K. Wandelt, Prof. F. Flores and coworkers, Dr. C. Laubschat and Dr. M. Prietsch, who have contributed in a collaborative effort to our present understanding of this problem.

References

1. For a short, excellent review see W. Mönch in Festkörperprobleme **XXVI**, 67 (1986), Advances in Solid State Physics, (Vieweg, Braunschweig).

2. U.K. Köhler, J.E. Demuth and R.J. Hamers, Phys. Rev. Lett. **60**, 2499 (1988).

3. A.H. Somer, "Photoemissive Materials", Wiley, New York (1968).

4. B. Reihl, M. Erbudak and D.M. Campbell, Phys. Rev. B **19**, 6358 (1979).

5. P. Soukiassian, T.M. Gentle, M.H. Balshi and Z. Hurych, J. Appl. Phys **60**, 4339 (1986).

6. E.M. Oellig, E.G. Michel, M.C. Asensio and R. Miranda, Appl. Phys. Lett. **50**,1660 (1987).

7. R.E. Schlier and H.E. Farnsworth, J. Chem. Phys. **30**, 917 (1959).

8. D.J. Chadi, Phys. Rev. Lett. **43**, 43 (1979).

9. R.I.G. Uhrberg, G.V. Hansson, J.M. Nicholls and S.A. Flödström, Phys. Rev. B **24**, 4684 (1981)

10. R.M. Tromp, R.J. Hamers and J.E. Demuth, Phys. Rev. Lett. **55**, 1303 (1985).

11. M.J. Cardillo and G.E. Becker, Phys. Rev. Lett. **40**, 1148 (1978).

12. T. Tabata, T. Aruga and Y. Murata, Surface Sci. **179**, L63 (1987).

13. J. Ihm, D.H. Lee, J.D. Joannopoulos and J.J. Xiong, Phys. Rev. Lett. **51**, 1872 (1982).

14. H. Tochihara, Surface Sci. **126**, 523 (1983).

15. E.M. Oellig and R. Miranda, Surface Sci. **177**, L947 (1986)

16. S. Ciraci and I.P. Batra, Phys. Rev. Lett. **56**, 877 (1986).

17. J.L. Morán-López and A. Ten Bosch, Phys. Rev. B **18**, 2555 (1978).

18. B. Woratschek, W. Sesselmann, J. Küppers, G. Ertl and H. Haberland, Phys. Rev. Lett. **55**, 1231 (1985).

19. Y. Enta, T. Kinoshita, S. Suzuki and Kono, Phys. Rev. B **36**, 9801 (1987).

20. T. Aruga, H. Tochihara and Y. Murata, Phys. Rev. Lett. **53**, 372 (1984).

21. E.M. Oellig, E.G. Michel, M.C. Asensio, R. Miranda, J.C. Durán, A. Muñoz and F. Flores, Europhys Lett. **5**, 727 (1988).

22. P. Pervan, E.G. Michel, G.R. Castro, R. Miranda and K. Wandelt, Verhandl. DPG(VI) **23**, 5 (1988) and J. Vac. Sci. Technol. (submitted).

23. F.J. Himpsel, P. Heimann, T.C. Chiang, and D.E. Eastman, Phys. Rev. Lett. **45**, 1112 (1980).

24. P. Pervan, E.G. Michel, G.R. Castro, R. Miranda and K. Wandelt, Phys.Rev. Lett. (submitted).

25. J.E. Demuth, W.J. Thompson, N.J. diNardo and R. Imbihl, Phys. Rev. Lett. **56**, 1408 (1986).

26. W. Mönch, J. Vac. Sci. Technol. B **4**, 1085 (1986).

27. T. Kendelewicz, P. Soukiassian, R.S. List, J.C. Woickik, P. Pianetta, I. Lindau, and W.E. Spicer, Phys. Rev. B **37**, 7115 (1988).

28. E. Busmann, Z. Anorg, Chem. **313**, 90 (1961).

29. J. Gallmeier, H. Schäfer and A. Weiss, Z. Naturforsch. B **24**, 665 (1969).

30. M. Prietsch, M. Domke, C. Laubschat, T. Mandel, C. Xue, and G. Kaindl, Z. für Physik (in press).

31. E.G. Michel, E.M. Oellig, J.E. Ortega, M.C. Asensio, J. Ferrón, and R. Miranda, Phys. Rev. B. (in press).

32. J.E. Ortega, E.M. Oellig, J. Ferrón and R. Miranda, Phys. Rev. B **36**, 6213 (1987).

33. E. G. Michel, E.M. Oellig, M.C. Asensio, and R. Miranda, Surf. Sci. **189/190**, 245 (1987).

34. K. Wandelt, J. Vac. Sci. Technol. A,**2**, 802 (1984).

35. T. Abukawa and S. Kono, Phys. Rev. B 37, 9097 (1988).

36. M.C. Asensio, E.G. Michel, J. Alvarez, C. Ocal, R. Miranda, and S. Ferrer, Surface. Sci. (submitted).

INVERSE-PHOTOEMISSION STUDIES OF CLEAN AND METAL-COVERED SEMICONDUCTOR SURFACES

B. Reihl, K.O. Magnusson, J.M. Nicholls*, P. Perfetti# and F. Salvan**

IBM Research Division, Zurich Research Laboratory
8803 Rüschlikon
Switzerland

I. INTRODUCTION

In this article we are summarizing our experimental bandstructure results on clean and metal-covered semiconductor surfaces, which we obtained employing the technique of inverse-photoemission spectroscopy (IPES). The paper is organized as follows. Within the introduction chapter we will give a short description of the inverse-photoemission technique with special emphasis on the angle-resolved measurement capabilities. Also it will become clear why IPES is particularly suited to study the metallization of semiconductor surfaces and what its limitations are. Experimental details are following. Then we will present case studies. The systems specifically mentioned are the ordered noble-metal structures $\sqrt{3} \times \sqrt{3}$ R30°-Ag and -Au, "5×5"-Cu, and 6×6-Au on Si(111), the ordered simple-metal structures $\sqrt{3} \times \sqrt{3}$ R30°-Al, -Ga, and -In on Si(111), the clean Si(111)7×7 and 2×1, Ge(111)2×1, GaAs(110), and GaP(110) surfaces, the potassium-covered Si(100)2×1 and the cesium-covered Si(111)2×1 surfaces, and finally the xenon-covered Ag(110) and (100) metal surfaces. Details of these studies may be found in our original publications [1-11].

In an IPES experiment [12] a well-prepared sample surface is bombarded with monoenergetic electrons of kinetic energy E_k. These electrons occupy empty states, but subsequently lose their energy by radiative transitions to lower empty states. The intensity of emitted photons is a measure of available initial and final empty states. There are two modes of operation: (i) In the fluorescence mode E_k is kept fixed and the spectral distribution of the emitted photons is being measured using a grating monochromator. (ii) In the isochromat mode E_k is being swept and the photon intensity at a fixed energy $h\nu_0$ is monitored. Here we have used only the latter mode. The emission onset which in case of a metal surface defines the Fermi energy E_F occurs when E_k exceeds $h\nu_0 - \Phi$ (Φ denotes the sample workfunction). The low-energy regime ($h\nu < \sim 100$ eV) is often called IPES in contrast to bremsstrahlung isochromat spectroscopy (BIS) which is reserved for the high-energy regime. This is similar as with photoelectron spectroscopy, where the corresponding notations are UPS and XPS. The reasons are historical and may even be misleading, since IPES is a "photon-emission technique" in contrast to photoemission where electrons are emitted. In fact, better terms would be [13] electron-subtraction spectroscopy for UPS and XPS and electron-addition spectroscopy for IPES and BIS, since it became clear that both techniques do not a priori measure the ground state of the system, but part of the excitation energy is being eaten up by the response of the electronic system to the photohole or the additional electron, in other words screening and relaxation

energies shift the measured result with respect to its true ground-state value. This is strongly sample dependent, i.e. more localized electronic states require bigger screening energies for the non-neutral charge distribution during the excitation process than more itinerant states. As examples we mention f electrons in rare-earth and actinide systems versus 5d's in transition metals, respectively. We also point out that surface electronic states could be more localized than the corresponding bulk states, and certainly valence states are more itinerant than core states in the same sample.

Although direct photoemission (UPS) and inverse photoemission (IPES) are the time-reversed processes of each other as shown by Pendry [14], there are distinct differences: (a) In light of the above mentioned final-state character of both spectroscopies, it is interesting to realize that in a simple picture a photohole in UPS acts as an additional core charge, deepens the potential and therewith increases the localization of the surrounding electrons. In contrast, electron addition in IPES flattens the potential and therewith the surrounding electrons become more itinerant. This implies that in the same system screening energies could be bigger in UPS than in IPES. (b) The cross-section ratio $\sigma_{IPES}/\sigma_{UPS}$ is given by the respective phase-space ratio for photon creation as opposed to electron creation, since the matrix elements cancel. It equals $(\lambda_{electron}/\lambda_{photon})^2$, and for an energy of 10 eV results in $(4/1000)^2 \sim 10^{-5}$. Hence the quantum yield in IPES is very low. As an estimate we remember that in UPS good-quality negative-electron affinity GaAs has a yield (outgoing electrons per incident photon) of as high as 0.5, while in a typical metal electron-electron interaction reduces this number to 10^{-3}. Thus on average we get a quantum yield of as low as 10^{-7} in IPES. Such low a yield requires very efficient photon-detection techniques as well as high-flux low-energy electron guns. (c) This last point of difference between UPS and IPES is more of a practical nature. For the reasons just explained in (b) sample currents ought to be high. They range from $\sim$1 μA to more than 1 mA depending if a Geiger-Müller-type photon detector or a grating monochromator is used. The former has a large solid angle of acceptance but no photon-energy tunability. In UPS on the contrary sample currents stay smaller than 10 nA. As a consequence sample charging and sample contacting are a severe problem in IPES experiments, in particular for semiconductors. The low count rate is also the reason for the worse energy resolution in IPES (typically 0.3 eV) as compared to UPS (better than 0.1 eV).

Figure 1 illustrates why IPES is particularly suited to study the metallization of semiconductor surfaces. Unoccupied bulk and/or surface states are not available anymore as final states in the inverse-photoemission process once they become filled by charge flowing from the metal atom into the surface states forming the bond. As we shall discuss below, this picture of semiconductor metallization indeed describes alkali deposition on Si(100) and Si(111) surfaces [15]. The change of the IPES signal from the clean to the metal-covered surface is a monitor of the semiconductor-metal interaction. Now the surface states which are mostly affected by any deposition onto the surface usually form bands with very well-defined E(**k**) dispersion relationships. Their knowledge allows to identify the surface states, i.e. distinguish them from bulk states, find a possible crossing of the Fermi energy, which is a necessary condition for metallization, and in comparison to electronic-structure calculations even allows to derive surface-atom configurations.

The wavevector **k** of surface states as two-dimensional entities has only a component parallel to the surface $k_{||}$ which can be related [12] to the kinetic energy E_k and polar angle θ of the incident electron beam by $k_{||} = 0.512 \sin\theta \ (E_k)^{1/2}$, where $E_k = h\nu_0 - \Phi + E_B$ is the measureable kinetic energy of a spectral feature in the IPES spectra with binding energy E_B relative to $E_F \equiv 0$. Energies are in electronvolts and wavevectors in reciprocal Ångströms.

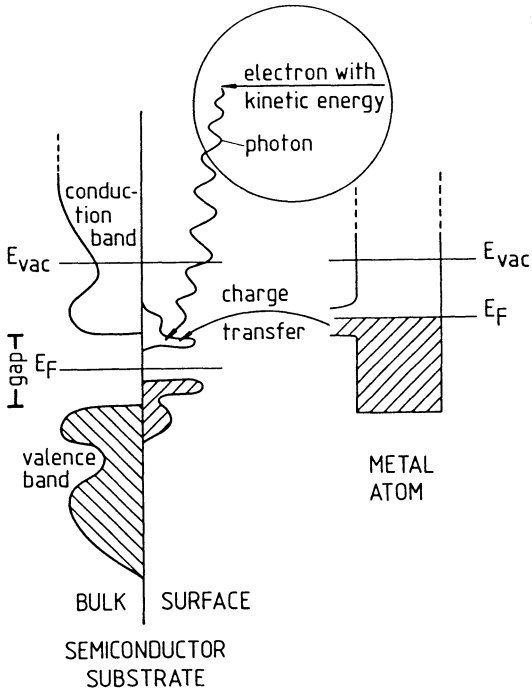

Figure 1. Illustration of inverse photoemission as a monitor of metal-atom interaction with a semiconductor surface.

Before we discuss our spectrometer and the sample preparation in detail, we present in figure 2 as illustration IPES spectra of clean Si(111)7×7 as well as covered with two different amounts of gold (from ref. 2) and with germanium (from ref. 8). Plotted here are the intensity of the outcoming photons at $h\nu_0 = 9.7$ eV versus the kinetic energy of the incident electrons with zero energy arbitrarily defined by the onset of photon emission of a metallic reference sample in contact with the Si sample. This defines our Fermi energy. All spectra of figure 2 were measured in normal incidence, i.e. $k_{||} = \theta = 0$. The spectral features A and B are present in all four spectra and reflect Si bulk conduction-band states. For comparison we show in figure 3 the calculated density of unoccupied states of Stukel and Euwema [16]. Two peaks which can be associated with critical points of the conduction bands are clearly present. Not accounted for in these bulk calculations are the structures denoted S in figure 2. They represent electronic states which are localized at and/or near the surface and are therefore called surface states. Experimentally the surface-state character of a spectral feature can be checked by exposing the surface to some chemically active gas. This is demonstrated for the germanium covered Si(111) surface (bottom panel of figure 2), where peaks S_4 and S'_4 are quenched by hydrogen (dashed spectrum). The bulk features become enhanced with hydrogen coverage owing to the reduced surface umklapp sçattering from less surface lattice vectors. This can also be observed in going from the clean 7×7 to the Au covered surfaces in figure 2. Otherwise the Ge-covered surface bears strong similarity to the clean 7×7 silicon surface, in particular with respect to the surface states near E_F, S_4 versus S_1. They originate from dangling-bond orbitals or weaker adatom bonds and are very sensitive to contamination. Indeed, this state is immediately quenched when gold is deposited onto the surface to form a $\sqrt{3} \times \sqrt{3}$ R30° (also denoted $\sqrt{3} \times \sqrt{3}$) ordered overlayer. Instead a new state S_2 occurs, which we interpret as a true interface state, since it cannot be quenched by activated hydrogen or oxygen [2]. In addition, the k-resolved study revealed [2] that this state disperses into the silicon bulk state A. To further verify that the S_2 peak corresponds to an interfacial state of the ordered Si(111)$\sqrt{3} \times \sqrt{3}$-Au surface, spectra were also recorded from the surfaces of thick room-temperature Au deposits. These spectra showed only a

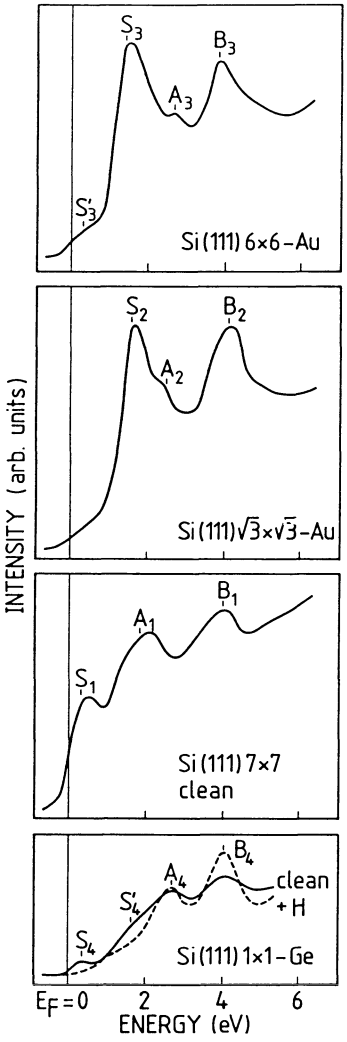

Figure 2. Normal-incidence inverse-photoemission spectra of clean Si(111)7×7, Si(111) $\sqrt{3} \times \sqrt{3}$-Au and 6×6-Au, at $h\nu$ = 9.7 eV (top three spectra from ref. and 1×1-Ge at 9.5 eV (bottom spectrum from ref. 8). Surface states are denoted by S_i, bulk states by A_i and B_i.

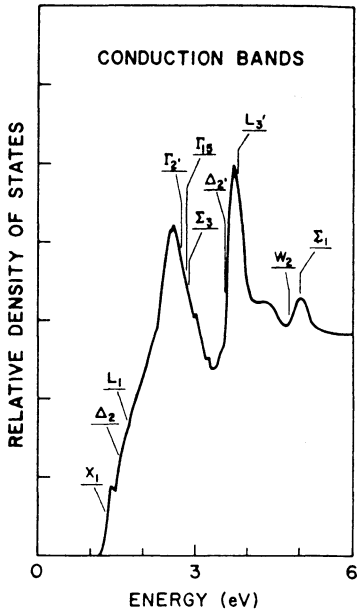

Figure 3. Bulk density of uncoccupied states of silicon calculated by Stukel and Euwema, ref. 16.

uniform distribution down to the Fermi-level cut-off, and no features similar to S_2 were present. Hence it reflects the bonding properties of the gold atoms to the silicon substrate. With increasing coverage a 6×6 ordered structure is formed and the interface state S_3 moves to lower energies as compared to the position of S_2. Furthermore we observe an increase of spectral intensity denoted S'_3 at the Fermi level. This new surface state indicates the onset of metallization of the gold overlayer and therewith reflects the Au-Au interaction.

II. EXPERIMENTAL

The experiments were performed in a two-chamber UHV system with fast entry air lock. See reference [1] for more details. The system houses facilities for ultraviolet-photoemission spectroscopy (UPS) and k-resolved inverse-photoemission spectroscopy (KRIPES). The Fermi-level positions of both spectroscopies were

determined from the emission onsets of a polycrystalline Ta foil which was frequently interchanged with the sample during the experiments. UPS experiments with $h\nu$ = 21.2 eV and 40.8 eV were performed in an angle-integrated mode (~20° cone of acceptance angle) using a hemispherical electron-energy analyzer (energy resolution of 0.2 eV). For the inverse-photoemission experiments we used Geiger-Müller-type photon detectors which were equipped either with a CaF_2 or a SrF_2 window. With the former, photons of energy 9.7 eV were filtered with a total-energy resolution (electrons and photons) of 0.7 eV, whereas with the latter, photons of energy 9.5 eV were filtered and a total-energy resolution of 0.35 eV obtained. The electrons impinging on the surface at polar angle θ were produced by a custom-built electron gun [17] with a measured beam divergence of 3° resulting in a $k_{||}$-resolution of $\Delta k_{||} < 0.1$ Å^{-1}.

We used <111>-oriented p-type Si, and <110>-oriented n-type GaP and GaAs bars with ohmic contacts (In and Au-Ge-Ni, respectively) alloyed along one side to avoid any undesirable charging of the sample. The samples were cleaved in situ using a knife-and-anvil technique. Clean and well-ordered Si(111)7×7 surfaces were produced by resistive heating of the wafer (p-doped ~0.03 Ωcm) up to ~ 1000°C. The clean and metal-deposited surfaces were characterized with low-energy electron diffraction (LEED), Auger electron spectroscopy (AES) and UPS. The ordered metal overlayers were produced by evaporating ultra-pure metals from well out-gassed Ta filaments, with the sample at room temperature, followed by careful annealing where necessary. Alkali metals were evaporated from SAES dispenser ovens. The evaporation rate was calibrated and monitored during evaporation using a quartz crystal oscillator. Independently the coverages were determined from AES signal ratios, workfunction measurements and UPS signals in the respective cases. The base pressure in the UHV system was $\leq 5\times10^{-11}$ Torr, and remained below 3×10^{-10} Torr during evaporation and annealing. To check for surface-state contributions we exposed our samples either to oxygen or hydrogen activated by a hot Ta filament in the vicinity of the sample.

III. RESULTS AND DISCUSSION

III.1 Ordered Cu, Ag, and Au overlayers on Si(111)

Another technique besides IPES, which can unravel unoccupied electronic states, is tunneling spectroscopy using the scanning tunneling microscope [18]. Here the tunnel conductance dI/dV is measured as function of bias voltage between tip and sample. Since the electrons tunnel from the tip into unoccupied electronic states at the sample surface, a spatially very local density of unoccupied states is obtained. In figure 4 this technique is applied [19] to clean Si(111)7×7 and the $\sqrt{3}\times\sqrt{3}$ R30° and 6 × 6 ordered Au overlayer structures on Si(111), which we have already discussed in the introduction chapter. In general, two groups of conductance features are observed. Below 4 Volt, peaks can directly be associated with the surface and interface states, S_1, S_2, and S_3 revealed in the inverse-photoemission spectra of fig. 2. The characteristic series of peaks seen above 4 Volt is attributed to image/field resonance states [18]. They are of a general nature in tunneling spectroscopy and less dependent on particular electronic properties of the surface. Rather their shape and energy separation is determined by the applied voltage, i.e. the electric field. In contrast, the more localized surface and interface states are hardly affected by the applied field. We find them at their IPES positions and even observe the shift to lower energy in going from the $\sqrt{3}\times\sqrt{3}$ R30° to the 6×6 gold overlayer structure as in figure 2.

There are two related noble-metal structures on Si(111), which occur [20] after the deposition of copper and silver, respectively, and careful annealing. These are

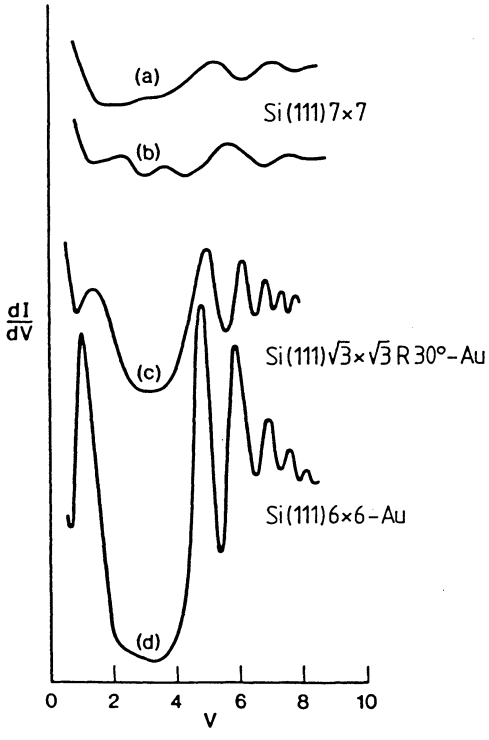

Figure 4. Tunneling spectroscopy, dI/dV versus tip-sample voltage V, at constant DC tunneling current (I = 0.7 nA). (a), (b) Si(111)7×7, (c), (d) ordered Au/Si(111) overlayers, from ref. 19.

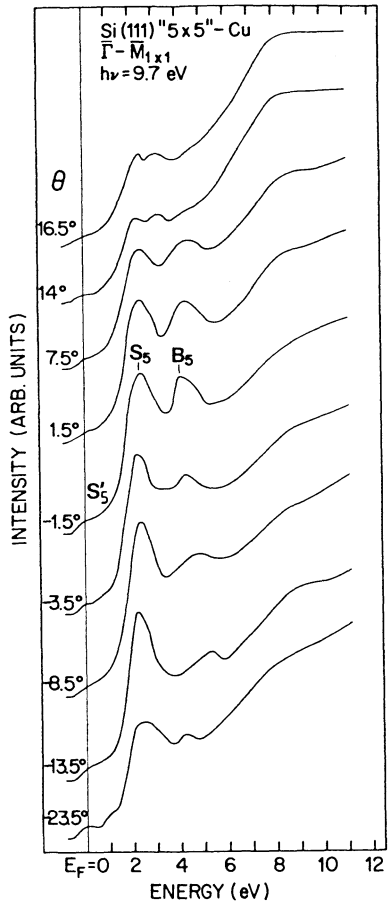

Figure 5. Inverse-photoemission spectra of Si(111)"5 × 5"-Cu as function of polar angle θ, from ref. 2.

the quasi-"5×5"-Cu [21,22] and the $\sqrt{3} \times \sqrt{3}$ R30°-Ag [23] ordered overlayers. One of the questions concerning all these surfaces is the local atomic geometry and the type of bonding involved. Do the noble metals form similar local bonds on the Si(111) surface in analogy with what is observed for group-III metals on Si(111), see chapter III.2 below? The $\sqrt{3} \times \sqrt{3}$ R30°-Ag surface has recently attracted considerable interest because of a controversy about the position of the Ag atoms (top versus sub surface) [24,25].

The spectra of the Si(111) "5×5"-Cu surface are shown in figure 5 as a function of polar angle θ along the $\bar{\Gamma} - \bar{M}_{1x1}$ symmetry direction. Similar as in the Au/Si(111) spectra of figure 2 we note the interface state S_5 at about 2.5 eV above E_F, although it is wider and remains with a high intensity and hardly any dispersion for a wide region of angles. With additional evaporation of Cu onto the "5×5"-Cu surface, S_5 disappears again while the bulk peak B_5 is still visible. This further indicates the

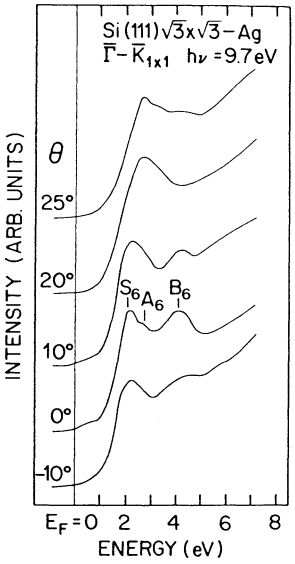

Figure 6. Inverse-photoemission spectra of Si(111)$\sqrt{3} \times \sqrt{3}$-Ag. as function of θ, from ref. 2.

surface-state character of the S_5 peak, and that it corresponds to the Cu-Si interface formation. However, S_5 may also contain some contribution from the lower-lying bulk state A (cf. fig. 2), if the structure is composed of two features. The quasi-metallic emission feature S'_5 visible for all polar angles in figure 5 suggests a similarity of the "5×5"-Cu surface to the 6×6-Au surface with respect to the bonding properties. In contrast, the IPES data of th Si(111)$\sqrt{3} \times \sqrt{3}$ R30°-Ag surface shown in figure 6 lack the Fermi-level emission. This together with the observed dispersion of the interface state S_6 as well as a clearer distinction of the A bulk state connect the $\sqrt{3} \times \sqrt{3}$ silver surface with the $\sqrt{3} \times \sqrt{3}$ gold surface.

As metal-induced unoccupied-state features can be observed on all four ordered noble-metal overlayer surfaces, but at different energies relative to the bulk states, there is little doubt that these features are really surface states. It is suggestive that the surface features are so similar in shape and in energy position for the small-size $\sqrt{3} \times \sqrt{3}$ unit cells and the larger 6×6 and "5×5" unit cells. It indicates that the observed surface states originate from a similar bonding mechanism, and are predominantly local in nature. This is in analogy with the group-III metals on Si(111), where good agreement with existing band calculations is observed (see next chapter III.2), and the strong surface features can be assigned to the local chemical bonding of the interface. In contrast, the weak contributions at the

Fermi level for the 6×6-Au and "5×5"-Cu surfaces can be attributed to the long-range order of the reconstructions. It is evident that such bandstructure calculations of energy-minimized geometries are also needed to quantitatively compare to measured energy dispersions of occupied and unoccupied surface/interface states.

III.2 Ordered Al, Ga, and In overlayers on Si(111)

The simple metals Al, Ga, and In form ordered-metal overlayers on the Si(111) surface, which exhibit a $\sqrt{3} \times \sqrt{3}$ R30° LEED pattern which occurs at 1/3 monolayer coverage of the metals. Several models have been suggested for this reconstruction [23,26,27]. In the two most likely geometries, the metal adatom is placed in either the filled site above the second Si-layer atoms (T_4) or in the hollow site above the fourth Si-layer atoms (H_3). Both adatom models, T_4 and H_3, are illustrated in fig. 7. Using the pseudopotential method and the local-density approximation, Northrup has performed total-energy calculations for the two geometries of the Si(111)$\sqrt{3} \times \sqrt{3}$-Al [27], -In [29], and -Ga [3] surfaces. In all three cases it was found that the T_4 geometry has the lowest total energy for the energy-minimized geometries. For Si(111)$\sqrt{3} \times \sqrt{3}$-Al, -Ga, and -In, the resulting total energy for the T_4 model is 0.3 eV/adatom, 0.38 eV/adatom, and 0.2 eV/adatom lower, respectively, than for the

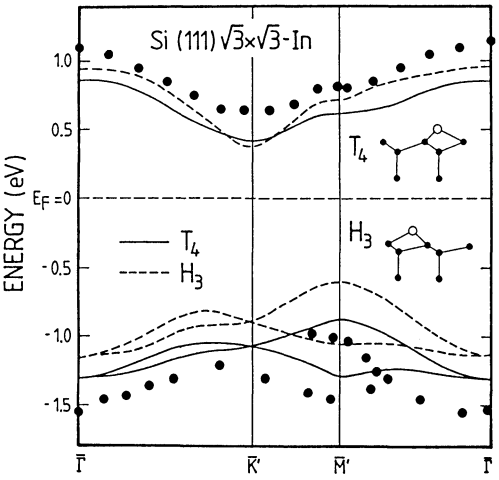

Figure 7. Comparison between experimental dispersion plots obtained by KRIPES (ref. 3) and UPS (ref. 29) and surface-state bands calculated for energy-minimized geometries of the T_4 and H_3 models (after ref. 29) for the Si(111)$\sqrt{3} \times \sqrt{3}$-In surface.

H_3 model [3]. However, these energy differences are small to conclusively exclude the H_3 model. Therefore angle-resolved UPS was used to determine the occupied surface-state band dispersion of these surfaces [23,29-33] and compare them to the calculated surface-state bands. Again it was not possible to obtain conclusive experimental evidence for either geometry, since the experimental bandstructures were found to be in equally good agreement with the occupied surface-state bands calculated [27-29] for the two different models. Now, as we shall see, KRIPES is able [3] to distinguish the two surface structures.

The k-resolved IPES spectra of the $\sqrt{3} \times \sqrt{3}$ R30°-In surface show a very sharp and pronounced surface-state peak at ~1 eV above E_F (see reference 3 for the original data). It is separated by more than 1 eV from the bulk state A and exhibits a downward dispersion, i.e. towards E_F, with increasing θ along the $\bar{\Gamma}$-$\bar{K}'$ and $\bar{\Gamma}$-$\bar{M}'$ directions of the $\sqrt{3} \times \sqrt{3}$ R30° surface Brillouin zone (SBZ). At the same time its intensity decreases in going from the center ($k_{||} = 0$) of the SBZ towards its boundaries.

In fig. 7, the experimental energy positions of the empty and filled adatom-induced states of the Si(111)$\sqrt{3} \times \sqrt{3}$-In surface are plotted as a function of

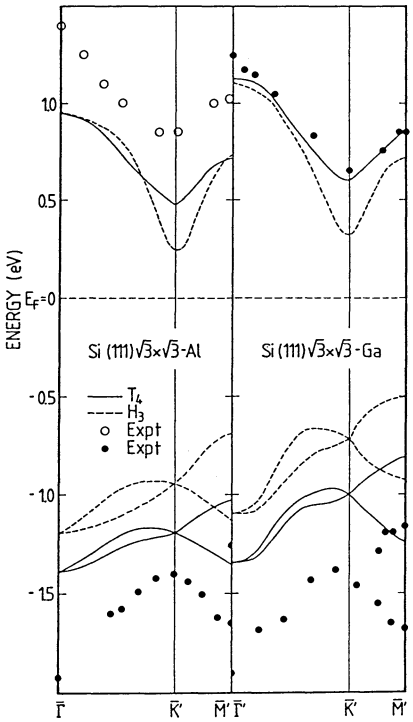

Figure 8. Comparison between experimental dispersion plots and surface-state bands calculated for the T_4 and H_3 models for the Si(111) $\sqrt{3} \times \sqrt{3}$-Al surface (left panel) and the Si(111)$\sqrt{3} \times \sqrt{3}$-Ga surface (right panel). The occupied surface-state dispersions are from refs. 32 and 33, the unoccupied ones from ref. 3.

$k_{||}$ for the $\bar{\Gamma}$-$\bar{K}'$-$\bar{M}'$ and $\bar{\Gamma}$-$\bar{M}'$ directions. In this figure, surface-state dispersions $E(k_{||})$ are compared with surface-state bands from the pseudopotential calculations [29] for the two energy-minimized geometries (H_3, T_4) of this surface. In comparing the shape of the bands, the empty surface-state band determined experimentally is in better agreement with that of the T_4 model (full line) as the energy difference between them is almost constant along the directions probed. Considering the total bandwidth of the unoccupied bands of the two models, that of the T_4 geometry is slightly smaller, and that of the H_3 slightly larger than the experimental one. The angle-resolved UPS data on the filled surface-state bands from a previous study [29] are in good agreement with the bands of both models, since they are very similar.

In fig. 8, the bands calculated for the energy-minimized geometries of the T_4 and H_3 models of Si(111)$\sqrt{3} \times \sqrt{3}$-Al [27] and -Ga [3] surfaces are shown. The calculated surface-state bandstructures are compared with the occupied bands obtained in UPS studies by Kinoshita *et al.* [32,33] and with the unoccupied bands from the KRIPES measurements of ref. [3]. Again for the $\sqrt{3} \times \sqrt{3}$-Al surface, the shape of the T_4 band is in better agreement with experiment, and after a rigid shift of 0.3 eV the bands almost overlap each other completely. The measured bandwidth (0.55 eV) of the unoccupied bands favors the T_4 model with 0.48 eV, relative to the H_3 model with 0.70 eV. For the empty band of the $\sqrt{3} \times \sqrt{3}$-Ga surface obtained experimentally, better agreement in the shape of the dispersion and the bandwidth is again found with the band of the T_4 model (cf. fig. 8, right panel). The T_4 band can be seen to be almost identical to the experimental one, with bandwidths of 0.53 eV and 0.6 eV, respectively, while the H_3 band is much wider (0.78 eV).

In all cases, the calculated energy splitting between the occupied and unoccupied surface-state bands is larger for the T_4 model, as here the substrate deforms so that the dangling-bond orbitals of the silicon atoms point more directly to the adatom, most probably yielding the lower total energy of the T_4 geometry. Considering the band gaps of the surface-state bands and, in particular, the

indirect-minimum gaps in the outer parts of the SBZ (cf. figs. 7 and 8), the T_4 bands are considerably more separated than the H_3 bands and closer to experiment. In general, the bulk and surface-state band gaps are underestimated in local-density calculations, as it is also the case for Si(111)2×1 with a gap calculated [34] to be 0.25 eV too small (for a further discussion see III.4). Therefore, we cannot rely on a comparison of the band gaps of the surface-state bands. Like for the $\sqrt{3} \times \sqrt{3}$-In surface, the calculated occupied bands of the T_4 and H_3 models of $\sqrt{3} \times \sqrt{3}$-Al and -Ga surfaces are too similar and hence too difficult to be discriminated by angle-resolved UPS, although in general an adatom model is supported where the surface overlayer is completed ideally for 1/3 monolayer of the metals. In contrast, the unoccupied bands calculated for the two models are significantly different from each other in shape and bandwidth. The probable adatom geometry of the $\sqrt{3} \times \sqrt{3}$ surfaces as energetically favored by the T_4 model is then corroborated by the dispersions of the empty surface-state bands measured by KRIPES for all three surfaces. Recent scanning tunneling microscopy work [35] directly prove the T_4 geometry for the Si(111)$\sqrt{3} \times \sqrt{3}$-Ga surface.

The conclusive picture now obtained on the geometries of group-III metal-adatom systems on Si(111) may lead to an increased understanding of the adatom systems in general. Recently, T_4 and H_3 models have been applied to the Si(111)7×7 surface [36], which according to Takayanagi et al. [37] contains 12 Si adatoms per unit cell. For a Si(111)$\sqrt{3} \times \sqrt{3}$-Si surface with the adatoms in T_4 geometry, the total energy is again found to be much lower than for the H_3 geometry. This will be discussed in the next chapter.

III.3 The annealed Si(111)7×7 surface

Based on transmission-electron diffraction [37] and scanning tunneling microscopy [38] results, the geometric reconstruction of the Si(111)7×7 is widely accepted to be described by the dimer-adatom-stacking-fault (DAS) model [37]. Despite its intriguing beauty this model is yet to complex to allow for total-energy calculations to find the energy-minimized surface-atom geometry. This fact has led Northrup [36] to construct a much simpler adatom model resulting in a Si(111) $\sqrt{3} \times \sqrt{3}$ R30°-Si structure, which is feasible for the calculations and similar to the group-III metal overlayers discussed in chapter III.2. His simplification step is illustrated in figure 9 where the DAS model of Takayanagi et al. is shown in the center (b). In panel (c) of fig. 9 a schematic drawing of the various atom positions is shown. The adatoms with equivalent positions are groupwise marked A, A′, B, and B′, the rest atoms C and C′, and the corner vacancies D and D′. The dimers are lying along the full lines, and the left half contains the stacking fault. To obtain the simpler Si(111)$\sqrt{3} \times \sqrt{3}$ R30°-Si surface-atom arrangement, the C and C′ rest atoms are removed. Then as before with the group-III metal atoms, the Si adatoms may sit in T_4 or H_3 geometry. The total-energy calculations [36] again favored the T_4 over the H_3 model by 0.64 eV per Si adatom. Indeed, the true DAS model has 12 adatoms on T_4 sites.

The calculated [36] occupied and empty surface-state bands belonging to the T_4 model are plotted in figure 10. They resemble the $\sqrt{3} \times \sqrt{3}$-Al, -In, and -Ga bands of figs. 7 and 8 to some extent. Again there are three bands, but the top one, Σ_1, is partly filled now. These calculated bands are compared with the experimentally obtained occupied (from ref. 39) and unoccupied (from ref. 7) bands. As illustration the normal-emission UPS and normal-incidence IPES spectra, respectively, are shown in panel (a) of figure 9. We have now chosen the peak notations S_1, S_2, and S_3 for the occupied surface states, and U_1 for the unoccupied state. Their surface-state character had been checked by exposing the clean 7×7 surface to activated hydrogen (S_1, S_2, S_3 : [40]; U_1 : [7,41]). The calculations [36] of the Si(111)$\sqrt{3} \times \sqrt{3}$ R30°-Si

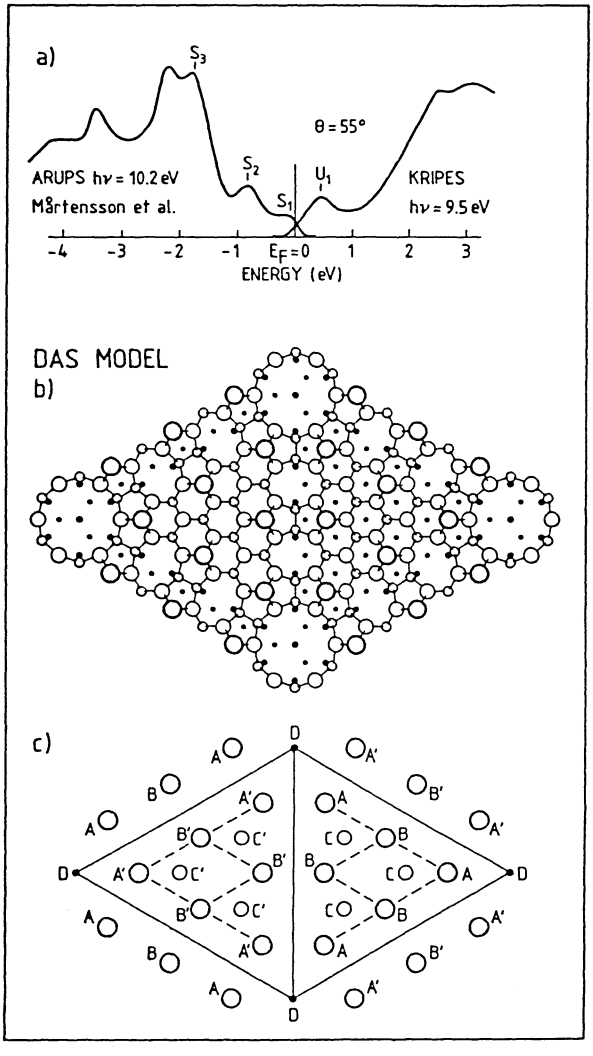

Figure 9. (a) Angle-resolved UPS and KRIPES of Si(111)7×7 from refs. 30 and 7, respectively, (b) the dimer-adatom stacking-fault model of Takayanagi et al. (ref. 37), (c) positions of different atom groups of the DAS model: adatoms A, A′, B, and B′; rest atoms C and C′; corner hole atoms D (from ref. 7).

surface and comparison with the UPS data [39] suggested that the dispersing Σ_1 band corresponded to the S_1 state. But the Σ_1 band has too large a bandwidth and the agreement with the flat S_1 state is far from good. Instead it is evident that the shape of the dispersing U_1 state in figure 10 resembles that of the Σ_1 band. Furthermore both bands, U_1 and Σ_1, are similar to the empty adatom states calculated and observed experimentally for the $\sqrt{3} \times \sqrt{3}$-Al, -Ga, and -In adatom surfaces (cf. chapter III.2). Therefore we believe that instead U_1 is the uppermost adatom state which corresponds to the Σ_1 band. Taking into account the large bandwidth calculated for the Σ_1 band (0.5 eV) and that bandgaps are usually underestimated in the local-density calculations, the agreement is much better with U_1 than with the S_1 state.

As discussed in chapter III.1 for noble-metal overlayers on Si(111), tunneling spectroscopy can also reveal surface states. Besides the first tunneling spectra on Si(111)7×7 [19] shown in figure 4 (a) and (b), there is another study [42] which goes far beyond that work. It is found, e.g., that the unoccupied state U_1 is uniformly distributed on the 12 adatoms A, A′, B, and B′ in the 7×7 unit cell. In contrast, the state around E_F exhibits an asymmetric appearance in the two triangular halfs (cf.

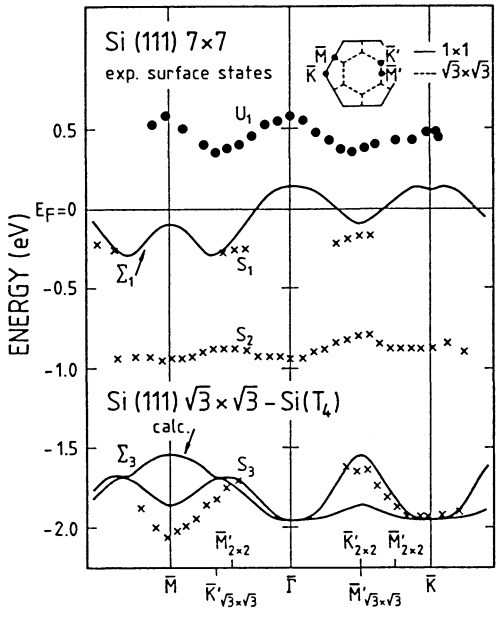

Figure 10. Dispersion plots of the empty surface state U_1 (from ref. 7) and occupied surface states S_1, S_2, and S_3 (from ref. 39). Also shown are the calculated surface-state bands for Si(111)$\sqrt{3} \times \sqrt{3}$-Si (from ref. 36).

fig. 9) for both positive and negative bias voltages. Also the conductance to or from the different adatom groups were different for this state. This together with the dispersive character of U_1 indicates a rather strong interaction in the local bonding with overlap to neighboring states, as this is the case for adatom p_z orbitals coupling to underlying dangling bonds. This is actually the origin of the calculated Σ_1 band in figure 10 [36]. The S_1 state, on the other hand, is dispersionless (cf. fig. 10) as is typical for an atomiclike state with little overlap to neighboring orbitals. Both, S_1 and U_1, have intensity maxima below and above E_F, respectively, but with metallic tails (cf. fig. 10a). Also a wide dI/dV feature is observed [42] on both sides of the Fermi level in tunneling spectroscopy. No intrinsic Fermi-level states exist on the Si(111)$\sqrt{3} \times \sqrt{3}$-Al, -Ga, and -In surfaces suggesting that for the Si(111)7×7 surface the Fermi-level states are related to the particular geometry of the whole 7×7 unit cell and not to the local bonding of the adatoms.

III.4 The cleaved Si(111)2×1 surface

Besides the annealed 7×7 reconstruction, Si(111) also exhibits a 2×1 reconstruction when it is cleaved. Essential for a KRIPES investigation is then the single-domain character of the Si(111)2×1 surface, which could be achieved [6] by cleaving <111> oriented Si rods along the bulk <$\bar{2}$11> direction and checking by LEED. LEED was also used to set the azimuthal orientation for the KRIPES measurements, i.e. polar-angle changes along or parallel to the π-bonded chains [43], which are the $\bar{\Gamma} - \bar{J}$ and $\bar{\Gamma} - \bar{J}'$ directions of the SBZ, respectively.

Two sets of inverse-photoemission spectra taken as function of θ are presented in fig. 11 along the $\bar{\Gamma} - \bar{J}'$ direction (short axis of the rectangular SBZ) and in fig. 12 along the $\bar{\Gamma} - \bar{J}$ direction (long axis). As in reference [44] we note for $\theta = k_{||} = 0$ an emission feature at $E_F + 0.9$ eV which could be quenched by exposing the clean Si(111)2×1 surface to hydrogen activated by a hot filament until a 1×1 LEED pattern was obtained (solid versus dashed curves in fig. 11). The normal-incidence spectrum is now profoundly different from the Si(111)7×7 spectrum of figs. 2 or 10a. In particular, the 2×1 surface remains semiconducting. The peak positions (tickmarks) in both figures were obtained from difference curves of the clean and hydrogen-covered spectra which for clarity are both shown as solid and dashed

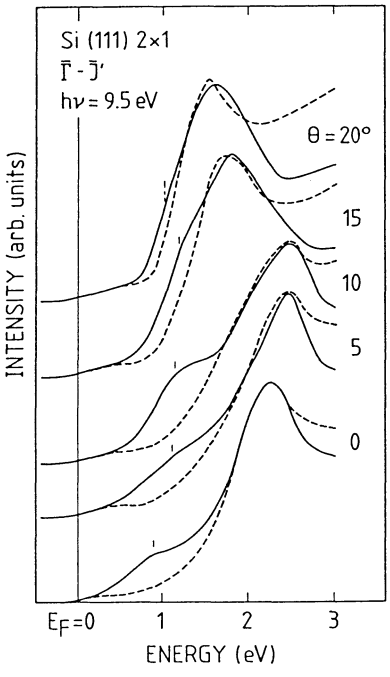

Figure 11. k-resolved inverse photoemission spectra at $h\nu$ = 9.5 eV as function of polar angle θ along the $\bar{\Gamma} - \bar{J}'$ direction. Solid curves are from the clean Si(111)2×1 surface. Dashed curves are from the Si(111)1×1-H* surface produced by exposing the clean surface to about 600 langmuirs of hydrogen activated by a hot filament. From ref. 6.

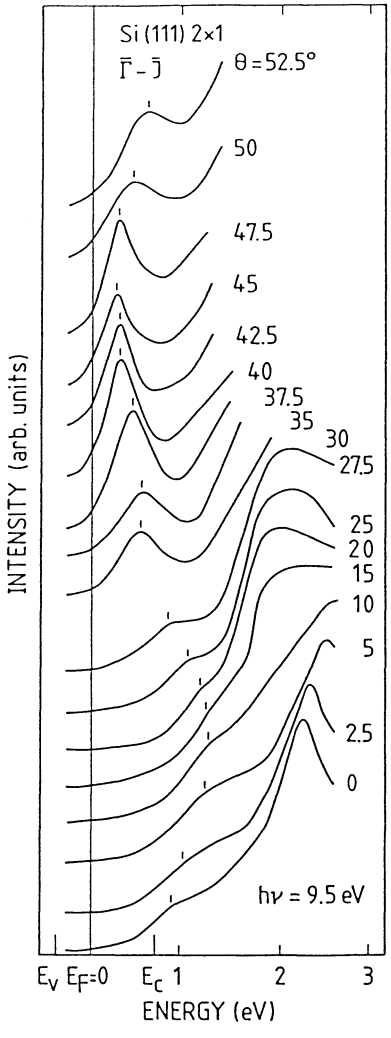

Figure 12. Same as fig. 11 for the $\bar{\Gamma} - \bar{J}$ direction. From ref. 6.

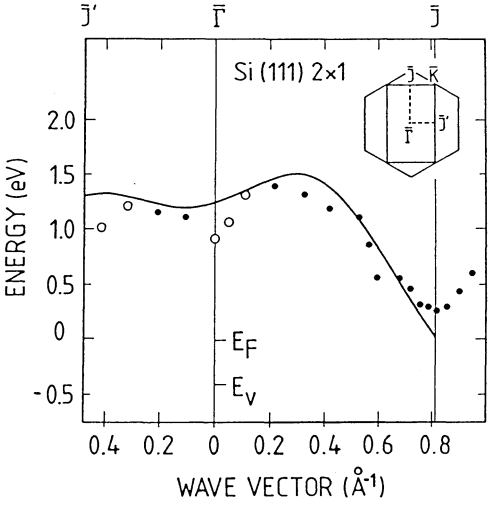

Figure 13. Plot of the experimental energy dispersion of the surface-state emission from figs. 11 and 22 (full dots and open circles). The solid line represents the calculated energy dispersion within the π-bonded chain model (from Pandey, ref. 43). From ref. 6.

curves only in fig. 11. While we observe a rather small energy dispersion of 0.2 eV along $\bar{\Gamma}-\bar{J}'$, we find a stronger dispersion of about 1 eV along $\bar{\Gamma}-\bar{J}$ as it was also the case for the occupied surface-state band [45]. The minimum energy position of 0.25 eV is found for $\theta = 45°$ correponding to the $\bar{J}$ point of the SBZ at $k_{||} = 0.82$ Å^{-1}. Around this critical point the surface-state feature exhibits the strongest spectral intensity (cf. fig. 12), as it is a true surface state, i.e. it falls within a projected bulk band gap [34]. For $\theta < 30°$ the feature becomes less pronounced, as it is becoming a surface resonance for $k_{||} < 0.6\ \bar{\Gamma}-\bar{J}$ in agreement with the calculations [34]. The maximum energy of 1.22 eV also appears in this region (see 10° spectrum in fig. 12, which correponds to 0.27 $\bar{\Gamma}-\bar{J}$). The spectral feature at higher energies, e.g. at 2.33 eV in the normal-incidence spectrum, corresponds to the bulk L_1^c critical point discussed in detail elsewhere [44].

The $E(k_{||})$ dispersion curves of the surface-state features in figs. 11 and 12 are plotted in fig. 13 where strong features are marked as solid dots and weaker features by open circles. The solid line represents the calculated surface-state band of Pandey [43] using the π-bonded chain model without any buckling. We have chosen these theoretical results, since they were done for both symmetry directions $\bar{\Gamma}-\bar{J}$ and $\bar{\Gamma}-\bar{J}'$. The agreement with our experimental disperson curves is quite good. Slightly better agreement between theory and experiment may be obtained for the $\bar{\Gamma}-\bar{J}$ direction if the calculated band of Northrup and Cohen [34] is used.

The experimentally derived unoccupied surface-state band is 0.25 eV higher at $\bar{J}$ than the calculated band (cf. fig. 13). Since the occupied surface-state band at $\bar{J}$ was determined [45] to be at E_{VBM} - 0.1 eV, where E_{VBM} denotes the valence-band maximum measured [46] to be E_{VBM} = -0.40 eV, it all together results in a surface-state band gap at $\bar{J}$ of 0.75 eV, a number which is 0.3 eV higher than the optical-transition energy [47] and the value obtained by photoemission from highly-doped silicon [48].

Owing to our limited energy and $k_{||}$ resolution of 0.35 eV and 0.1 Å^{-1}, respectively, we cannot completely rule out that the surface-state peak at $\bar{J}$ may be closer to E_F than actually measured in fig. 12. However, we believe that part of this discrepancy is real and compare with the analogous inverse-photoemission [49] study of Ge(111)2×1 where the surface-state band gap at $\bar{J}$ is deduced to be 0.15 eV larger than the 0.5 eV derived from optical-reflectivity [50] and direct-photoemission measurements [51]. Even larger discrepancies exist for GaP and GaAs (110) surfaces, as will be discussed in the next chapter.

III.5 The cleaved (110) surfaces of GaAs and GaP

For a long time there was the belief that the Fermi-level pinning at the semiconductor-vacuum interface as well as in Schottky barries is due to the presence of dangling-bond states in the semiconductor band gap [52]. Gallium arsenide was one of the first materials where this hypothesis was shown to be incorrect. It was found [53] that good cleavages of n-type samples produced flat bands on GaAs(110) surfaces indicating that surface states are not present in the fundamental gap and cannot be responsible for the pinning of the Fermi level. The absence of surface states in the band gap was then theoretically explained by a surface-relaxation model [54] which assumed rigid-bond lengths for the surface atoms but a rotation of these fixed bonds moving the surface As and Ga atoms outward and inward, respectively, relative to their unrelaxed geometrical positions. This surface relaxation strongly affects the energy positions of the surface states, moving the filled As-derived surface-state band into the bulk valence band and the empty Ga-derived surface-state band into the bulk conduction band with respect to the energy positions for the ideally truncated surface.

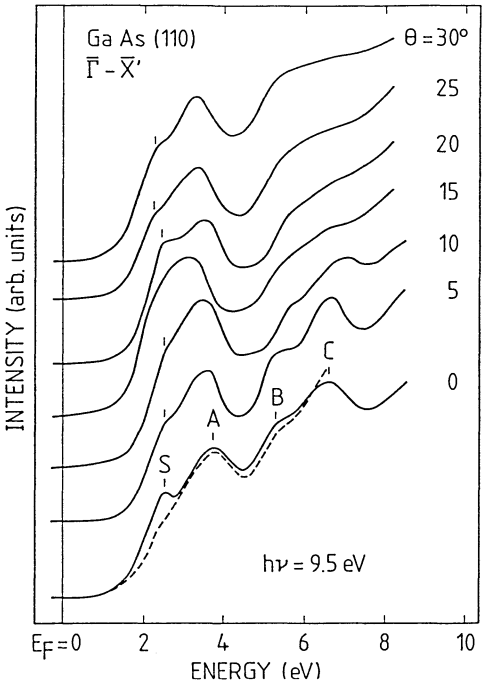

Figure 14. KRIPES spectra at $h\nu$ = 9.5 eV of cleaved GaAs(110) for polar angles θ along the $\bar{\Gamma}-\bar{X}'$ azimuth. The bottom dashed curve belongs to the same surface exposed to 1000 langmuirs of oxygen activated by a hot Ta filament. The tickmarks indicate the position of the surface-state emission S and bulk conduction-band states A, B, and C. From ref. 9.

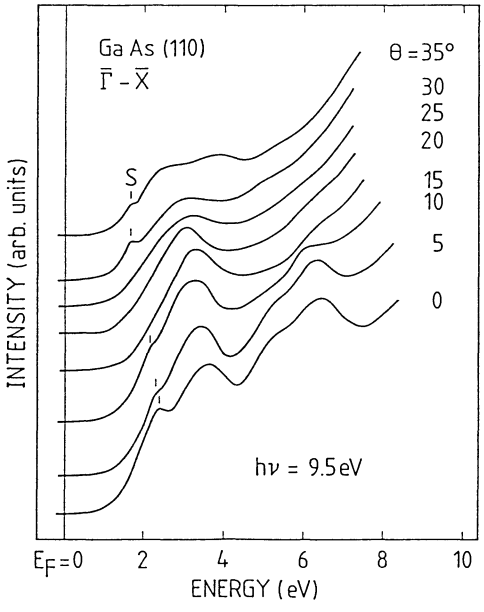

Figure 15. KRIPES spectra as in fig. 14 but along the $\bar{\Gamma}-\bar{X}$ azimuth. Tickmarks denote the dispersing surface-state emisssion S. From ref. 9.

The occupied bulk and surface electronic structure has been the subject of several studies [55-59] in the past. There is now general agreement regarding the energy positions and E(k) dispersion relationship of the topmost surface-state band. Only recently there have been efforts to study unoccupied electronic states below the vacuum level using new techniques like inverse photoemission [60,61], photoemission with laser pumping [62], and cathodo-luminescence [63]. We now present here the $E(k_{||})$ dispersion relationhip. Two sets of k-resolved inverse photoemission spectra [9] are shown in figs. 14 and 15 for the $\bar{\Gamma}-\bar{X}'$ and $\bar{\Gamma}-\bar{X}$ directions, respectively. At E_F + 2.3 eV there is a peak denoted S in fig. 14, which can be quenched when the surface is exposed to 1000 langmuirs of activated oxygen (cf. dashed curve in fig. 14). We associate it with the Ga-derived unoccupied surface-state band of the GaAs(110) surface. This surface state has previously been observed by inverse photoemission at some critical points only [61]. Here we present the complete energy-band dispersion $E(k_{||})$ along the two main symmetry directions of the SBZ. The energy positions (tickmarks in figures 14 and 15) of the surface-state features are plotted as function of $k_{||}$ in fig. 16. The estimated accuracy

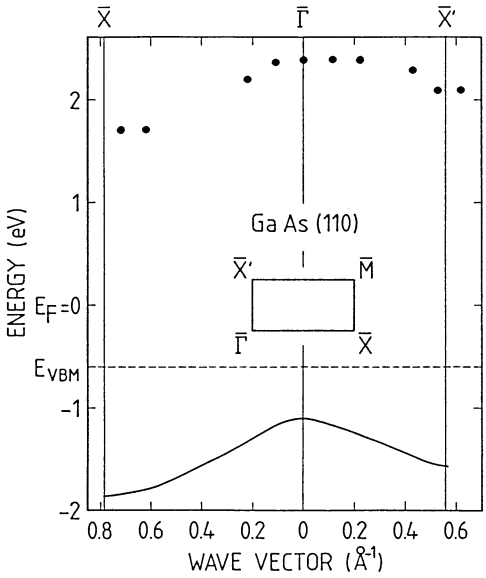

Figure 16. Plot of the surface-state dispersion of GaAs(110) (from ref. 9). The valence band maximum E_{VBM} was obtained from UPS measurements performed on the same sample after the KRIPES data taking had been finished. The solid line represents the occupied As-derived surface-state band of Huijser et al., ref. 64.

of the energy positions obtained from difference spectra of the clean cleaved GaAs and the oxygen-exposed surface is of the order of 0.1 eV. Along $\bar{\Gamma}-\bar{X}$ the surface-state band exhibits a downward dispersion with a minimum of 1.7 eV above E_F near $\bar{X}$ and a total band width of 0.7 eV. The dispersion along $\bar{\Gamma}-\bar{X}'$ is smaller (0.3 eV) and a minimum of $E_F + 2.1$ eV is reached at the zone boundary $\bar{X}'$. It is in good agreement with the theoretical results of ref. [54].

The only correct way to determine the top of the valence band E_{VBM} with respect to E_F is to measure both inverse and direct photoemission on the same sample surface under identical experimental conditions, i.e. without breaking the vacuum, and connect it to the Fermi level of some metallic reference sample in contact with GaAs. This procedure is important, since microscopic cleavage defects, also present on mirror-like surfaces obtained after cleavage, as well as defects induced by beam damage from the electron guns in LEED and/or inverse photoemission modify the position of E_F within the gap, i.e. cause a band bending at the surface. Hence in our case E_{VBM} in fig. 16 was measured by UPS just *after* the inverse photoemission measurements had been finished for *all* polar angles. Despite the apparent good quality of all our surfaces we observed differences in the Fermi-level positions relative to E_{VBM} even when initially a flat-band situation had existed. Four examples are summarized in table I. These differences could be due to

Table I. Position of E_F with respect to E_{VBM} as obtained by UPS on four different GaAs(110) surfaces together with the position E_{SS} of the empty surface-state band at $\bar{\Gamma}$ with respect to E_F and E_{VBM}. All energies in eV.

Sample No.	$E_F - E_{VBM}$	$E_{SS} - E_F$	$E_{SS} - E_{VBM}$
1	0.6	2.4	3.0
2	1.3	1.8	3.1
3	0.7	2.3	3.0
4	0.6	2.3	2.9

either microscopic cleavage defects or to electron-beam induced defects. We notice that the difference $E_{SS} - E_{VBM}$ of the empty surface-state (SS) band at $\bar{\Gamma}$ (to be discussed below in detail) to the valence-band maximum is practically constant considering the various uncertainties in the determination of the peak positions and valence-band edges. This implies that band-bending effects possibly induced by the electron beams - once they had saturated - rigidly shifted both the valence- *and* conduction-band electronic structure.

We could then also include in figure 16 as full line the As-derived occupied surface-state band measured by Huijser et al. [64]. We note that the empty and occupied surface-state bands have nearly a parallel energy-dispersion behavior along $\bar{\Gamma} - \bar{X}$ and $\bar{\Gamma} - \bar{X}'$. As a consequence possible optical transitions can arise at about the same photon energy of 3.5 to 3.6 eV for all $k_{||}$ values of the main symmetry directions. Indeed, the optical results reported by Selci et al.[65] reveal only one peak due to surface-state transitions at 2.9 eV. This number is 0.6 - 0.7 eV higher than calculated above for transitions between the measured occupied and unoccupied surface-state bands. The discrepancy is now well beyond any uncertainties in the optical data [65] as well as our KRIPES measurements [9]

Among all III-V (110) semiconductor surfaces GaP(110) was considered to be an exception [53] in the sense that surface relaxation does only partially remove the empty surface states from the gap. The empty surface state was always interpreted [53,66] as being responsible for the pinning position of the Fermi level which was found between 1.5 eV [66] and 1.7 eV [53] above E_{VBM}. The empty surface states were previously observed by angle-integrated inverse photoemission [67] and by normal-incidence KRIPES [68]. Their energy position was found to be 0.3 eV below the conduction-band minimum [68].

For the original k-resolved inverse-photoemission spectra see reference [5] Analogous to GaAs(110) the surface-state feature (1.5 eV above E_F in normal incidence) can be quenched by exposing the clean GaP(110) surface to 2000 L activated oxygen. It had been observed [68] before on GaP(110) at normal incidence. We now present the dispersion of this surface-state band along the $\bar{\Gamma} - \bar{X}'$ and $\bar{\Gamma} - \bar{X}$ symmetry directions in fig. 17. Along $\bar{\Gamma} - \bar{X}$ the surface state disperses downward in energy towards the boundary of the SBZ where it reaches a minimum of 0.9 eV above E_F. Along the $\bar{\Gamma} - \bar{X}'$ direction, the surface state is less resolved from the bulk conduction-band emission (open circles) and its dispersion appears to be quite flat.

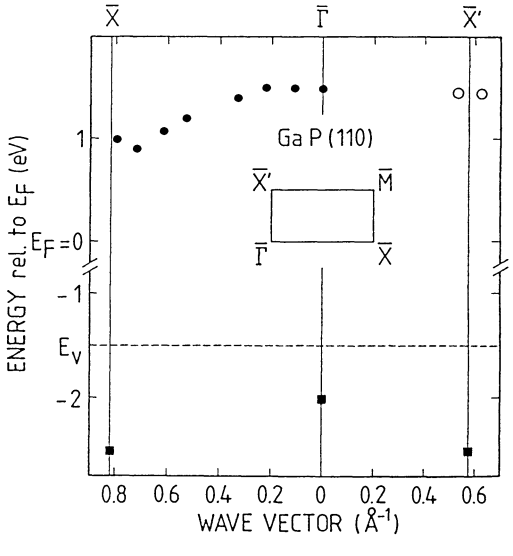

Figure 17. Plot of the surface-state dispersion of GaP(110), from ref. 5. Also indicated are the positions of the valence-band edge E_{VBM} = E_F - 1.5 eV and of the occupied surface-state band at symmetry points (full squares, from ref. 70).

This behaviour agrees quite well with recent bandstructure calculations [69]. The only significant difference is the value of the energy dispersion along $\bar{\Gamma}-\bar{X}$ which is $\sim$ 0.5 eV larger in the calculation than in our experiment.

The position of E_{VBM} shown in fig. 17 is again obtained by linear extrapolation of the leading edge of the valence band as measured by UPS. E_{VBM} is found to be 1.5 eV below E_F. The positions of the filled surface states at the critical points as obtained by angle-resolved photoemission [70] are also included in fig. 17. These data [70] show an occupied surface-state band between 0.5 and 1.0 eV below E_{VBM}, dispersing from E_{VBM} - 0.5 eV at $\bar{\Gamma}$ to about E_{VBM} - 1.0 eV at $\bar{X}'$ and $\bar{X}$. From the data presented in fig. 17, direct optical transitions between filled and empty surface states are possible along $\bar{\Gamma}-\bar{X}$ and at $\bar{X}'$ with an energy of 3.4 eV and 4.0 eV, respectively. These two values are again 0.5 - 0.6 eV higher than the two surface optical transitions observed on GaP(110) [65] at 2.8 and 3.5 eV. Since the optical results have an accuracy of better than 0.1 eV, the 0.5 - 0.6 eV discrepancy is significant and of the same order as in GaAs.

III.6 Surface Band Gaps

To summarize our findings of chapters III.4 and III.5 we compare in table II surface band-gap energies as obtained by optical reflectivity, UPS on highly-doped or laser-pumped samples, and by combining UPS and IPES. The discrepancy Δ between

Table II. Surface band-gap energies in eV as obtained by optical reflectivity, UPS on highly-doped (Ge, Si) or laser-pumped (GaAs) samples, and by combining UPS and IPES as described in III.4 and III.5. In the last column, Δ gives the difference between the optical reflectivity (column 2) and the UPS&IPES result (column4).

Sample	optical reflectivity	UPS doped/laser	UPS&IPES	Δ
Ge(111)2×1	0.5[50]	0.5[51]	0.65	0.15
Si(111)2×1	0.45[47]	0.45[48]	0.75	0.3
GaP(110)	2.8[65] 3.5[65]		$\bar{\Gamma}-\bar{X}$ 3.4 $\bar{X}'$ 4.0	0.6 0.5
GaAs(110)	2.9[65]	2.1[62]	3.5-3.6	0.7

the optical band gap (column 2) and the photoemission band gap (column 4) is significant. It must have a physical origin and could be due to either an excitonic shift in the optical data or to relaxation effects in direct and inverse photoemission. In principle, both mechanisms could be present in the different techniques at the same time. We further point out that Δ increases in going from covalent (0.3 eV for Si(111)2×1) to more ionic semiconductor compounds (0.5 eV for GaP, 0.7 eV for GaAs). We speculate that this is an indication for the presence of relaxation effects in the two photoemission techniques (see chapter I). By this we mean a different response of the surrounding electrons to the photohole in UPS and to the additional electron in IPES. The screening of such a charge perturbance is less effective the more localized the electronic system is [71]. The latter may be the case for ionic compounds as compared to covalent materials. As the occupied surface state can be associated with the more negatively charged As or P ions and the empty surface state with the more positively charged Ga ion, photoionization and inverse

photoemission locally decrease the charge on the respective ions. This possibly increases the relaxation energies involved. We had reached this conclusion already in the discussion [6] of Δ for Si(111)2×1, since there excitonic effects in the optical and energy-loss measurements of the same entity could be shown to be much smaller than the discrepancy with the photoemission results. Hence, we believe that excitonic effects are also absent for GaP(110) and GaAs(110).

Finally, we would like to give another argument for the presence of relaxation effects to explain the discrepancy between optical and photoemission results for the surface band gap. If only UPS results are considered, we expect a downward energetic shift in contrast to IPES where the screening energy for the opposite charge would cause an upward shift. The two shifts add up when the results are combined as in table II. In the experiment by Haight and Bokor [62] on GaAs(110) the empty surface-state band minimum at $\bar{\Gamma}$ is filled by intensive laser pumping. Subsequent direct photoemission of the occupied valence- and laser-filled conduction-band states reveal a surface resonance at 1.5 eV above E_{VBM}. Combining this value with the maximum of the As-derived surface-state band from ref. [64] (cf. fig. 16), an energy difference of 2.1 eV is obtained for the surface band gap. This value is indeed smaller than the optical result [65] of 2.9 eV.

III.7 Alkali-metal overlayers on Si(100) and Si(111)

The interest in the adsorption of alkali metals on semiconductor surfaces is steadily growing [72]. The nature of the bonding is distinctly different from, e.g., noble metals interacting with semiconductors (cf. chapter III.1). In addition, the tremendous decrease of the work function with alkali-metal coverage makes these systems interesting from the technical point of view as high-yield photoemitters [73] or sources of spin-polarized electron beams [74]. An important unresolved issue to date has been the ionic versus covalent bonding of K and Cs on the Si(100) and Si(111) surfaces at one-monolayer coverage. A picture [75] which in analogy to alkali metals on transition or noble metals favors a ionic bonding for low coverages and an overlayer metallization for higher coverages is at variance with calculations [15,76] of the surface electronic structure using a self-consistent pseudopotential method, where the anti-bonding π^*-state becomes partly filled by the alkali valence electrons. This metallizes the substrate and *not* the alkali overlayer, at the monolayer coverage. The reason is that semiconductor surfaces usually have active dangling bonds

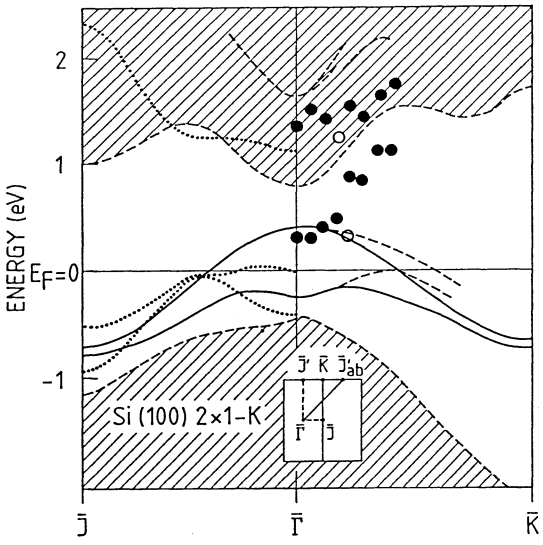

Figure 18. Surface band structure of Si(100)2×1-K. The hatched area shows the projected bulk bands, the full lines represent the calculated surface-state bands along the $\bar{J}-\bar{\Gamma}-\bar{K}$ directions, the long-dashed lines the surface-state bands along $\bar{\Gamma}-\bar{J}'_{ab}$, and the short-dashed lines surface resonances, from ref. 76. The surface states and resonances from ref. 77 are plotted as dotted lines along $\bar{\Gamma}-\bar{J}$. The experimentally obtained surface-state bands (from ref. 4) are shown as full dots and open circles for weaker spectral features.

protruding into vacuum, which interact strongly and ionically with the alkali atoms up to higher coverages than in case of a metal substrate.

As described above (chapters III.1, III.2) we have performed [4] IPES measurements on Si(100)2×1-K as function of polar angle. The surface-state character of two features in the spectra was checked by 10-L oxygen exposure. This allowed to determine the peak positions from difference curves (clean minus oxygen covered) and plot them as function of $k_{||}$ in figure 18. Owing to the inevitable two-domain character of the 2×1-K surface we measured along the only well-defined $\bar{\Gamma}-\bar{J}'_{ab}$ symmetry direction (see inset of figure 18), but compare with the $\bar{\Gamma}-\bar{K}$ and $\bar{\Gamma}-\bar{J}$ directions. Also shown are the calculated surface-state bands from refs. [76,77]. We note that the lower state exhibits very little dispersion around $\bar{\Gamma}$ and then ceases to be observable. This could be consistent with the calculated band [76] which dips below the Fermi level at 0.5 $\bar{\Gamma}-\bar{K}$ and becomes occupied. The upward dispersion at higher $k_{||}$, however, is not accounted for in the calculations at least for this symmetry direction. The surface-state bands of ref. [77] on the other hand show even less agreement except for the upper state near $\bar{\Gamma}$, which is a surface resonance, i.e. degenerate with projected bulk states. There is certainly room for an experimental improvement (coverage determination, reduced disorder of the two-domain surface structure, etc.), while theory should indeed provide the surface electronic structure along the feasable $\bar{\Gamma}-\bar{J}'_{ab}$ azimuth.

In the case of Cs adsorption on the cleaved Si(111)2×1 surface, UPS and LEED indicated [78] that Cs did not form any ordered overlayer, even at saturation coverage corresponding to one monolayer. But a new occupied surface state occurred [78] which made the system metallic. Theoretical analyses of the Cs and K/Si(111) surfaces by Ishida et al. [79] and Ciraci and Batra [15] assumed that the π-bonded chain is stable upon alkali adsorption, and that despite the findings of Tochihara et al. [78] both Cs and K go into a 2×1 structure. Recently, Batra and Ciraci [80] studied the potassium adsorption on the ideal Si(111)1×1 surface and found, within their adsorption-site model, this adsorption system to have a 0.3 eV lower total energy than what they had found for the adsorption on the π-bonded chain structure.

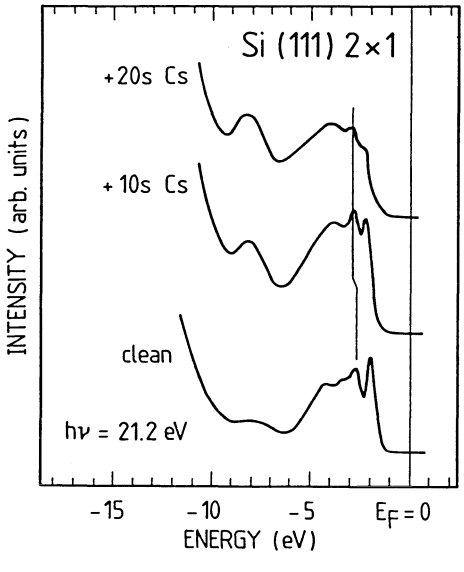

Figure 19. UPS data of the valence-band region of Si(111)2×1 as function of Cs evaporation in seconds. The vertical line reflects the downward band bending of 0.15 eV. Form ref. 10.

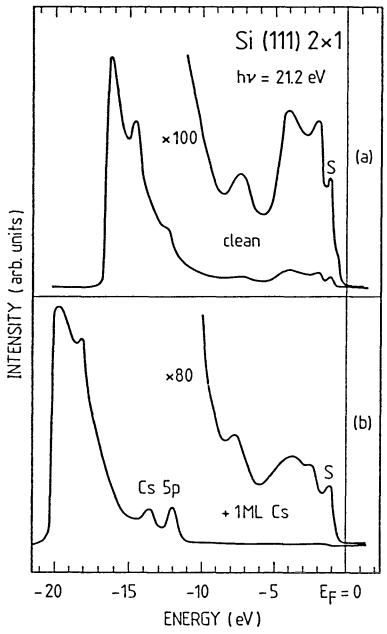

Figure 20. UPS data of (a) clean and (b) 1-ML-Cs covered Si(111)2×1. The latter corresponds to the onset of saturation of the secondary electron cut-off (total shift: -3.7 eV) as function of Cs coverage, where we observe a $\sqrt{3} \times \sqrt{3}$ R30° LEED pattern. S denotes the surface state. From ref. 10.

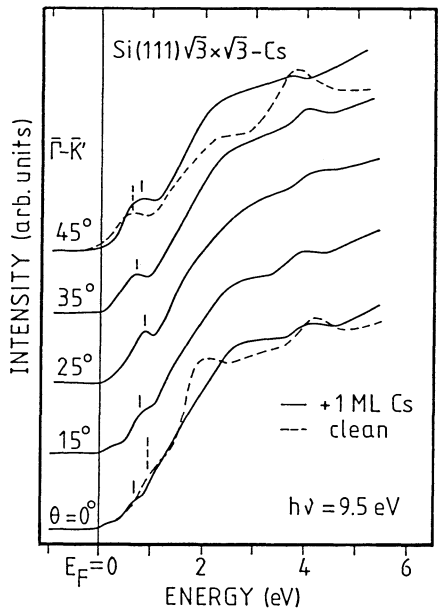

Figure 21. KRIPES results of clean (dashed curves) and 1-ML-Cs covered Si(111)2×1 as function of θ along the $\bar{\Gamma} - \bar{K}'$ azimuth of the $\sqrt{3} \times \sqrt{3}$ R30° SBZ. The tickmarks give the surface-state emission. From ref. 10.

In contrast to the analyses mentioned above, we have found [10] for the Cs/Si(111) system that one monolayer of Cs on cleaved Si(111) destabilizes the π-bonded chain structure and induces a $\sqrt{3} \times \sqrt{3}$ R30° reconstruction. The Cs evaporation was checked with a crystal monitor, but the actual coverage was determined from the change of the secondary electron cut-off energy in UPS. After the first evaporation, a downward band-bending of 0.15 eV was observed from the shift of the uppermost Si valence state. This is shown in figure 19 and in agreement with ref. [78]. The cut-off decreases almost linearly until it reaches a saturation value of -3.7 eV (shown in figure 20). In the saturation region of the cut-off which corresponds to a minimum of the work function, a well-ordered $\sqrt{3} \times \sqrt{3}$ R30° LEED pattern was observed. We interpret this coverage as the completion of the first monolayer. At lower coverages, only a 2×1 pattern of decreasing quality could be observed. This is attributed to a disordered Cs overlayer perturbing the Si(111)2×1 surface. In figure 21 we present a series of IPES spectra for different polar angles along the $\bar{\Gamma} - \bar{K}' - \bar{M}'$ line of the $\sqrt{3} \times \sqrt{3}$ SBZ. The 1-ML-Cs spectra differ from the clean spectra (dashed curves in figure 21, see also figures 11 and 12), in particular with respect to the tickmarked surface-state features. This peak moves to higher final-state energies with increasing angles, reaching a maximum at $\theta = 25°$. This corresponds to the $\bar{K}'$-point in the SBZ at $k_{||} = 0.63$ Å^{-1}. For higher incidence angles, probing the $\bar{K}' - \bar{M}' - \bar{K}'$ line, the peak moves down through a minimum with a symmetry around $\theta = 35°$ corresponding to the $\bar{M}'$-point in the SBZ.

The simple metals Al, Ga, and In (see III.2) form the $\sqrt{3} \times \sqrt{3}$ R30° LEED pattern at 1/3 monolayer coverages of the metals. However, recently the $\sqrt{3} \times \sqrt{3}$ reconstruction was also found at 1-ML coverage of Sb [81] and Pd [82] on Si(111) surfaces. One difference between the Si(111)$\sqrt{3} \times \sqrt{3}$ R30°-Cs and the -Al, -Ga, and -In surfaces is the upward dispersion of the unoccupied surface state along $\overline{\Gamma} - \overline{K}'$ in case of Cs as compared to Al, Ga and In (see figures 7 and 8). The different dispersion behavior indicates a considerably different bonding situation, the origin of which may lie in the initial substrates, 2×1 or 7×7, as well as in the differing adsorbate-substrate and adsorbate-adsorbate interactions. Finally we note that the Si(111)$\sqrt{3} \times \sqrt{3}$ R30°-Cs surface appears to be semiconducting.

III.8 Xenon adsorbed on silver (100) and (110) surfaces

Although not evident we think that the adsorption of rare-gas atoms is relevant for the problem of alkali-metal/semiconductor interfaces. In an extreme ionic picture Cs has donated its valence electron to the semiconductor substrate, and an ion with a xenon configuration is left at the surface which at least in some theories [15,76,80] has become metallic. Hence a noble-metal substrate with 1 ML of xenon coverage

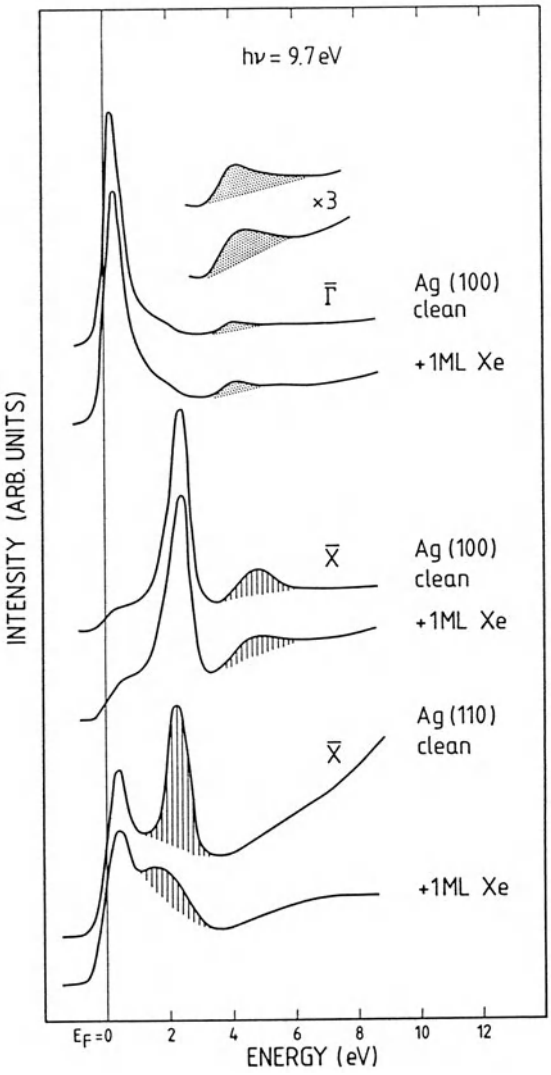

Figure 22. KRIPES results of clean and 1-ML-Xe covered Ag(100) (top and center curves) and Ag(110) (bottom curve). The data were taken at T = -35°, from ref. 11. The shaded area represents emission from image-potential surface states at $\overline{\Gamma}$, the hatched are Shockley-type surface state at the respective $\overline{X}$ points.

may shine some light on the behavior of surface states with coverage. It is known [1] that surface states on metals are quenched by hydrogen, oxygen or water exposure as likewise on semiconductor surfaces (see figures 2,11,14). However, we present in figure 22 examples (from ref. [11]) which prove that the interaction of an adsorbate may depend on the nature of the surface state, even though the interaction with the substrate is weak, as in the case of Xe. For the image-potential surface states at $\overline{\Gamma}$ on Ag(100) (top curves in fig. 22), the spectral feature around 4 eV is not affected at all, while there seems to be a small reduction of the Shockley-type surface state at $\overline{X}$ on the same surface (center curves). However, a clear reduction of the surface-state intensity occurs at $\overline{X}$ on Ag(110). The latter state is again of the Shockley type [83]. It should also be noted that the unoccupied Xe 6s and 6p states occur around 4 eV as can be seen when the coverage is increased [11]. We added this example to stimulate some discussion on the behavior of surface states in general, when the chemical surrounding of the surface is altered by the deposition of metals or semiconductors or the adsorption of various gases. It is not at all evident to derive the nature of the bond from one observation alone.

IV. Summary

This paper summarizes our inverse photoemission results on clean and metal-covered semiconductor surfaces and tries to put them in perspective to calculations as well as results obtained by different techniques. It does not at all claim to be complete. It is mostly dealing with unoccupied surface states and in this sense complements the much more elaborate review on occupied surface states on semiconductor surfaces by Hansson and Uhrberg [84].

We thank Meinrad Tschudy for his help with the experiments and the preparation of the samples. We also acknowledge Thomas Riesterer for his help with the GaAs and GaP work, and K.H. Frank and K. Horn for their cooperation on the Xe/Ag system.

References

*) Present address: Royal Institute of Technology, Material Science, 10044 Stockholm, Sweden.

#) Permanent address: Istituto di Struttura della Materia, CNR, Via E. Fermi 38, 00044 Frascati, Italy.

**) Permanent address: Faculté des Sciences du Luminy, Département de Physique, Case 901, 13288 Marseille Cedex 9, France.

1. B. Reihl, Surf. Sci. 162:1 (1985).

2. J.M. Nicholls, F. Salvan, and B. Reihl, Phys. Rev. B 34:2945 (1986).

3. J.M. Nicholls, J.E. Northrup, and B. Reihl, Phys. Rev. B 35:4137 (1987).

4. I.P. Batra, J.M. Nicholls, and B. Reihl, J. Vac. Sci. Technol. A 5:898 (1987).

5. T. Riesterer, P. Perfetti, M. Tschudy, and B. Reihl, Surf. Sci. 189/190:795 (1987).

6. P. Perfetti, J.M. Nicholls, and B. Reihl, Phys. Rev. B 36:6160 (1987).

7. J.M. Nicholls and B. Reihl, Phys. Rev. B 36:8071 (1987).

8. P. Perfetti and B. Reihl, Phys. Rev. B 37:10429 (1988).

9. B. Reihl, T. Riesterer, M. Tschudy, and P. Perfetti, Phys. Rev. B (in press).

10. K.O. Magnusson and B. Reihl, to be published.

11. K. Horn, K.H. Frank, J.A. Wilder, and B. Reihl, Phys. Rev. Lett. 57:1064 (1986) and to be published.

12. For a review see V. Dose, Surf. Sci. Rep. 5:337 (1985); F.J. Himpsel, Comments Cond. Mat. Phys. 12:199 (1986); N.V. Smith and D.P. Woodruff, Prog. Surf. Sci. 21:295 (1986).

13. W.B. Jackson and J.W. Allen, Phys. Rev. B 37:4618 (1988).

14. J.B. Pendry, J. Phys. C 14:1381 (1981).

15. S. Ciraci and I.P. Batra, Phys. Rev. Lett. 58:1982 (1987).

16. D.J. Stukel and R.N. Euwema, Phys. Rev. B 1:1635 (1970).

17. P.W. Erdman and E.C. Zipf, Rev. Sci. Instrum. 53:225 (1982).

18. G. Binnig, K.H. Frank, H. Fuchs, N. Garcia, B. Reihl, H. Rohrer, F. Salvan, and A.R. Williams, Phys. Rev. Lett. 55:991 (1985).

19. F. Salvan, H. Fuchs, A. Baratoff, and G. Binnig, Surf. Sci. 162:634 (1985).

20. For a review, see G. Le Lay, Surf. Sci. 132:169 (1983).

21. E. Daugy, P. Mathiez, F. Salvan, and J.M. Layet, Surf. Sci. 154:267 (1985).

22. S.A. Chambers, S.B. Anderson, and J.H. Weaver, Phys. Rev. B. 32:581 (1985).

23. G.V. Hansson, R.Z. Bachrach, R.S. Bauer, and P. Chiaradia, Phys. Rev. Lett. 46:1033 (1981).

24. R.J. Wilson and S. Chiang, Phys. Rev. Lett. 58:369 (1987).

25. E.J. van Loenen, J.E. Demuth, R.M. Tromp, and R.J. Hamers, Phys. Rev. Lett. 58:373 (1987).

26. J.J. Lander and J. Morrison, Surf. Sci. 2:553 (1964).

27. J.E. Northrup, Phys. Rev. Lett. 53:683 (1984).

28. H. Nagayoshi, Solid-State Sci. 59:167 (1985).

29. J.M. Nicholls, P. Mårtensson, G.V. Hansson, and J.E. Northrup, Phys. Rev. B 32:1333 (1985).

30. R.I.G. Uhrberg, G.V. Hansson, J.M. Nicholls, P.E.S. Persson, and S.A. Flodström, Phys. Rev. B 31:3805 (1985).

31. G.V. Hansson, J.M. Nicholls, P. Mårtensson, and R.I.G. Uhrberg, Surf. Sci. 168:105 (1986).

32. T. Kinoshita, S. Kono, and T. Sagawa, Phys. Rev. B 32:2714 (1985).

33. T. Kinoshita, S. Kono, and T. Sagawa, Solid State Commun. 56:681 (1985).

34. J.E. Northrup and M.L. Cohen, Phys. Rev. Lett. 49:1349 (1982).

35. J. Nogami, Sang-il Park, and C.F. Quate, Surf. Sci. Lett. 203:L631 (1988).

36. J.E. Northrup, Phys. Rev. Lett. 57:154 (1986).

37. K. Takayanagi, Y. Tanishiro, M. Takahashi, and S. Takahashi, J. Vac. Sci. Technol. A 3:1502 (1985).

38. G. Binnig, H. Rohrer, C. Gerber, and E. Weibel, Phys. Rev. Lett. 50:120 (1983).

39. P. Mårtensson, A. Cricenti, L.S.O. Johansson, and G.V. Hansson, Phys. Rev. B 34:3015 (1986).

40. F.J. Himpsel, D.E. Eastman, P. Heimann, B. Reihl, C.W. White, and D.M. Zehner, Phys. Rev. B 24:1120 (1981).

41. F.J. Himpsel and T. Fauster, J. Vac. Sci. Technol. A 2:815 (1984).

42. R.J. Hamers, R.M. Tromp, and J.E. Demuth, Phys. Rev. Lett. 56:1972 (1986).

43. K.C. Pandey, Phys. Rev. Lett. 47:1913 (1981); Physica B 117&118:761 (1983).

44. D. Straub, L. Ley, and F.J. Himpsel, Phys. Rev. Lett. 54:142 (1985); Phys. Rev. B 33:2607 (1986).

45. R.I.G. Uhrberg, G.V. Hansson, J.M. Nicholls, and S.A. Flodström, Phys. Rev. Lett. 48:1032 (1982).

46. F.J. Himpsel, G. Hollinger, and R.A. Pollak, Phys. Rev. B 28:7014 (1983).

47. P. Chiaradia, A. Cricenti, S. Selci, and G. Chiarotti, Phys. Rev. Lett. 52:1145 (1984).

48. P. Mårtensson, A. Cricenti, and G.V. Hansson, Phys. Rev. B 32:6959 (1985).

49. J.M. Nicholls and B. Reihl (to be published).

50. S. Nannarone, P. Chiaradia, F. Ciccaci, R. Memeo, P. Sassaroli, S. Selci, and G. Chiarotti, Solid State Commun. 33:593 (1980).

51. J.M. Nicholls, P. Mårtensson, and G.V. Hansson, Phys. Rev. Lett. 54:2363 (1985).

52. J. Bardeen, Phys. Rev. 71:717 (1947).

53. J. van Laar and J.J. Scheer, Surf. Sci. 8:342 (1967); A. Huijser and J. van Laar, Surf. Sci. 52:202 (1975); A. Huijser, J. van Laar, and T.L. van Rooy, Surf. Sci. 62:472 (1977); J. van Laar, A. Huijser, and T.L. van Rooy, J. Vac. Sci. Technol. 14:894 (1977).

54. C. Calandra, F. Manghi, and C.M. Bertoni, J. Phys. C 10:1911 (1977); D.J. Chadi, J. Vac. Sci. Technol. 15:631 (1978) and Phys. Rev. B 18:1800 (1978).

55. W.E. Spicer and R.C. Eden, in: Proc. IXth Int. Conf. on the Physics of Semiconductors, Moscow , 1968 (Hanks, Leningrad, 1968).

56. A. Knapp, D.E. Eastman, K.C. Pandey, and F. Patella, Bull. Am. Phys. Soc. 23:399 (1978).

57. T.C. Chiang, J.A. Knapp, M. Aono, and D.E. Eastman, Phys. Rev. B 21:3515 (1980).

58. T.C. Chiang and D.E. Eastman, Phys. Rev. B 22:2940 (1980).

59. G.P. Williams, F. Cerrina, J. Anderson, G.J. Lapeyre, R.J. Smith, J. Hermanson, and J.A. Knapp, Physica B 117&118:350 (1983).

60. V. Dose, H.-J. Gossmann, and D. Straub, Phys. Rev. Lett. 47:608 (1981); Surf. Sci. 117:387 (1982).

61. D. Straub, M. Skibowski, and F.J. Himpsel, Phys. Rev. B 32:5237 (1985).

62. R. Haight and J. Bokor, Phys. Rev. Lett. 56:2846 (1986).

63. R.E. Viturro, M.L. Slade, and L.J. Brillson, Phys. Rev. Lett. 57:487 (1986).

64. A. Huijser, J. van Laar, and T.L. van Rooy, Phys. Letters A 65:337 (1978).

65. S. Selci, A. Cricenti, F. Ciccacci, A.C. Felici, C. Coletti, Zhu Yong, and G. Chiarotti, Surf. Sci. 189/190:1023 (1987).

66. F. Sette, P. Perfetti, F. Patella, C. Quaresima, C. Capasso, M. Capozi, and A. Savoia, Phys. Rev. B 28:4882 (1983).

67. D. Straub, V. Dose, and W. Altmann, Surf. Sci. 133:9 (1983).

68. D. Straub, M. Skibowski, and F. Himpsel, J. Vac. Sci. Technol. A 3:1484 (1985).

69. F. Manghi, E. Molinari, R. Del Sole, and A. Selloni, Surf. Sci. 189/190:1028 (1985).

70. F. Solal, G. Jezequel, F. Houzay, A. Barski, and R. Pinchaux, Solid State Commun. 52:37 (1984).

71. J.C. Fuggle, M. Campagna, Z. Zolnierek, R. Lässer, and A. Plateau, Phys. Rev. Lett. 45:1597 (1980).

72. For a review see I.P. Batra, Prog. Surf. Sci. 25:175 (1987).

73. W.E. Spicer, Appl. Phys. 12:115 (1977) and references therein.

74. B. Reihl, M. Erbudak, and D.M. Campbell, Phys. Rev. B 19:6358 (1979) and references therein.

75. E.M. Oellig and R. Miranda, Surf. Sci. 177:L947 (1986); E.M. Oellig, E.G. Michel, M.C. Asensio, R. Miranda, J.C. Duran, A. Munoz, and F. Flores, Europhys. Lett. 5:727 (1988).

76. S. Ciraci and I.P. Batra, Phys. Rev. Lett. 56:877 (1986).

77. H. Ishida, N. Shima, and M. Tsukada, Phys. Rev. B 32:6236 (1985); Surf. Sci. 158:438 (1985).

78. H. Tochihara, M. Kubota, T. Aruga, M. Miyao, and Y. Murata, Jpn. J. Appl. Phys. 23:L271 (1984); H. Tochihara, M. Kubota, M. Miyao, and Y. Murata, Surf. Sci. 158:497 (1985).

79. H. Ishida, K. Terakura, and M. Tsukada, Solid State Commun. 59:365 (1986).

80. I.P. Batra and S. Ciraci, Phys. Rev. B 37:8432 (1988).

81. T. Kinoshita, Y. Enta, H. Ohta, Y. Yaegashi, S. Suzuki, and S. Kono, Surf. Sci. 204:405 (1988).

82. K. Akiyama, K. Takayanagi, and Y. Tanishiro, Surf. Sci. 205:177 (1988).

83. B. Reihl, R. Schlittler, and H. Neff, Phys. Rev. Lett. 52:1826 (1984.

84. G.V. Hansson and R.I.G. Uhrberg, Surf. Sci. Reports 9:197 (1988).

INFLUENCE OF OVERLAYER METALLIZATION ON SCHOTTKY-BARRIER FORMATION

C. Laubschat, M. Prietsch, M. Domke, E. Weschke, T. Mandel, G. Remmers, J.E. Ortega,* C. Xue, and G. Kaindl

Institut für Atom- und Festkörperphysik, Freie Universität Berlin
Arnimallee 14, D-1000 Berlin 33, Germany

1. Introduction

The investigation of metal/semiconductor interfaces has raised increasing interest in the recent past mainly due to technological aspects.[1] Despite wide-spread applications of Schottky diodes, the mechanisms of Schottky-barrier formation are still not well understood until now. It is by now well accepted that interfacial states in the semiconductor band gap play a crucial role in determining band bending and therefore the Schottky-barrier height, but there is still a considerable controversy on the nature of these states. Two types of such states are presently discussed: (i) defect states connected with vacancies or antisite defects in the interfacial layer of the semiconductor,[2,3] and (ii) virtual gap states (VGS) induced by electronic states of the overlayer that penetrate a few Å into the semiconductor;[4-8] in case of a metallic overlayer the latter states are often denoted as metal-induced gap states (MIGS).

In this context, core-level photoemission (PE) from interfaces of thin metal films with semiconductor surfaces has been proven to be a powerful technique that is capable of providing detailed information on band bending in the course of Schottky-barrier formation as well as on chemical and electronic properties of these interfaces by measurements of core-level binding energies (BE). In these PE studies it turned out to be very important to follow the BE positions of unreacted components up to relatively large thicknesses of the overlayers, in particular in the case of reactive interfaces, in order to allow a discrimination of BE shifts due to chemical reaction from those caused by band bending. Interfaces between alkali films and GaAs(110) have been found to be particularly well suited for such investigations, since they comprise both non-reactive and reactive interfaces, depending on substrate temperature and on the specific alkali metal.[9-12]

In the present paper, we present PE results on the interface formation between alkali metals (Na, K, Rb, and Cs) and GaAs(110), both for reactive and non-reactive cases, and compare these data with those of the reactive Tm/GaAs(110) interface.[13,14] It is shown that band bending at very low coverages may be assigned to defect states only in case of reactive interfaces, while for the non-reactive interfaces with alkali films a strong asymmetry between n- and p-type substrates is observed. This asymmetry reflects the influence of the donor/acceptor character of n-type/p-type GaAs with respect to the donor character of the alkali atoms. For high alkali coverages, band bending in both the reactive and non-reactive case is determined by a single Fermi-level position in the band gap defined by the influence of MIGS.

Furthermore, it is shown that a correlation between overlayer metallicity and band bending exists by switching the metallic properties of the overlayer on and off, just by successive oxidation of the overlayer and further alkali-metal evaporation. For the case of the non-reactive Cs/GaAs(110) interface it is shown that adsorption of oxygen, which affects only the alkali overlayer, results in a non-metallic Cs oxide film causing a backshift in band bending to almost the value observed for uncovered GaAs(110), while subsequent metallization of the oxide layer by further deposition of Cs reinstalls the metallic band bending. These observations provide strong support for the validity of the VGS/MIGS model and demonstrate that defect states play only a minor role in case of nonreactive interfaces.

2. Experimental

The PE measurements were performed with monochromatized synchrotron radiation from the "Berliner Elektronenspeicherring für Synchrotronstrahlung" (BESSY) or with VUV light from a He-resonance lamp, using hemispherical energy analyzers operated in normal-emission geometry. The overall system resolution (FWHM) was 0.1 to 0.25 eV, and BE changes were determined with an accuracy of ± 0.03 eV. Si-doped n-GaAs (doping concentration: $3 \cdot 10^{17}$ to $3 \cdot 10^{18}$ atoms/cm^3) or Zn-doped p-GaAs ($3 \cdot 10^{17}$ to $1.4 \cdot 10^{18}$ atoms/cm^3) served as substrates and could be cooled with liquid nitrogen. Clean GaAs(110) surfaces were obtained by cleavage, and only mirrorlike surfaces were taken for the measurements. Alkali films were evaporated from commercial chromate dispensers (obtained from SAES Getters) with deposition rates of ≈ 1 monolayer (ML) per minute. Relative alkali coverages were calibrated via evaporation time (estimated accuracy: ± 10 %), while absolute coverages were obtained with an accuracy of ± 30 % either from the relative intensities of surface components in the substrate core-level spectra or from the emission of a second layer in the alkali core levels.[11,12] Tm interfaces were prepared by evaporation of 99.99 % pure Tm metal from a tungsten basket. In this case, the evaporation rates were measured with a quartz-crystal microbalance (accuracy: ± 30 %). During oxygen exposure the ion gauge (Leybold-Heraeus IE511) was left on.

A superposition of Lorentzian lines containing lifetime broadening (FWHM = 0.2 eV), convoluted by a Gaussian for instrumental and inhomogeneous broadening was least-squares fitted to the substrate core-level spectra. These spectra consist of spin-orbit split doublets with intensity ratios very close to 3:2, and splittings of 0.67±0.02 eV (in case of As-3d) and 0.46±0.02 eV (in case of Ga-3d). The PE background was approximated in all cases by straight lines.

3. Non-Reactive Interfaces

3.1. The Band-Bending Behavior

PE spectra of the As-3d and Ga-3d core levels are shown in fig. 1 for thin Na films deposited on p-GaAs(110) at 85 K. For the freshly cleaved surface, spin-orbit split doublets due to emission from bulk (dashed) and surface atoms (dotted) are observed, separated by surface core-level shifts of -0.39 ± 0.03 eV (in case of As-3d) and +0.31 ± 0.03 eV (in case of Ga-3d). The relative intensity of the surface components is ≈ 30 %, in good agreement with the signal from an atomic surface layer expected on the basis of a photoelectron escape depth of $\lambda \approx 6$ Å.[15]

The lineshape of the As-3d PE line stays almost unchanged over the whole coverage range, while the Ga-3d lineshape shows substantial variations: With increasing Na coverage, a shoulder (dash-dotted) appears and grows at the lower-BE side of the Ga-3d spectra. The increase in intensity of the dash-dotted component is accompanied by a decrease in intensity of the dotted substrate-surface component. It is therefore reasonable to assign the dash-dotted component to former substrate-surface atoms covered by Na; consequently, it will be denoted as Na-contact component in the following. The sum of the relative intensities of the Na-contact component

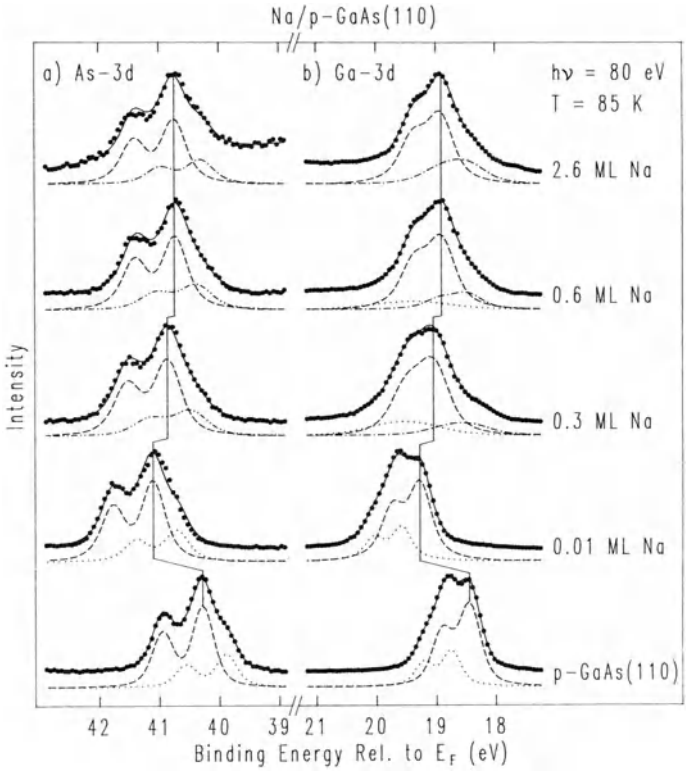

Fig. 1. As-3d and Ga-3d core-level PE spectra of the Na/p-GaAs(110) interface at 85 K for various Na coverages, together with the results of least-squares fits. Dashed subspectra represent the substrate bulk, dotted the substrate surface, dash-dotted the Na-contact component, and dash-doubledotted the sum of the contributions of substrate-surface and Na-contact components to the As-3d signals. The vertical solid bars mark the positions of the $3d_{5/2}$ components. All spectra are normalized to equal height.

and the substrate-surface component is found to be constant. This observation is consistent with the given assignments and excludes chemical reaction and/or intermixing processes at the interface. This view is further supported by the As-3d PE lineshape that remains practically unchanged with Na coverage; this observation is most probably due to a coincidence in BE of the substrate-surface and the Na-contact components. Accordingly, the sum of both components of the As-3d spectra is given by the dash-doubledotted subspectra in the intermediate coverage range (0.3 and 0.6 ML). In addition to the variations in lineshape, the spectra exhibit rigid shifts of the same magnitude for both As-3d and Ga-3d core levels, which are assigned to band bending.

A similar evolution of core-level PE lineshapes is also observed for interfaces of the alkali metals K, Rb, and Cs on n- and p-type GaAs(110) kept at 85 K. Therefore all interfaces grown at low temperatures may be considered as non-reactive.

The coinciding BE variations of the As-3d and Ga-3d substrate core level lines, which reflect the band-bending behavior, are presented in fig. 2 for interfaces of Na, K, Rb, and Cs with n- and p-GaAs(110) at 85 K as a function of alkali coverage. All interfaces exhibit a similar band-bending behavior: For p-GaAs(110), a

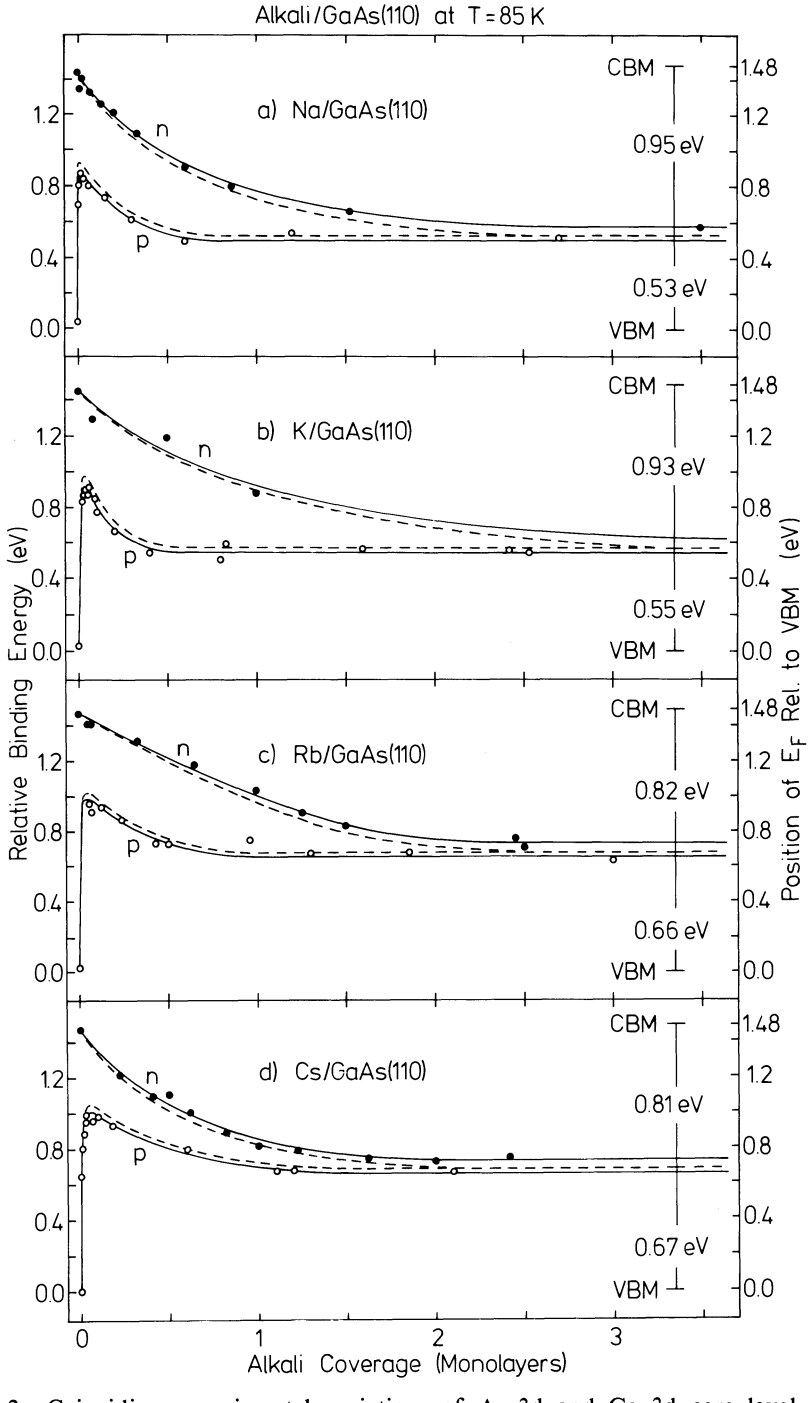

Fig. 2. Coinciding experimental variations of As-3d and Ga-3d core-level BEs of substrate atoms as a function of alkali coverage for interfaces of Na, K, Rb, and Cs with n- and p-GaAs(110) at 85 K (solid lines and left-hand scale). The dashed lines represent the Fermi-level positions at the interface relative to VBM (right-hand scale), obtained for n- and p-GaAs(110) substrates from the measured core-level BEs after correction for finite photoemission sampling depth.

large BE shift of about 1 eV is observed at $\Theta \simeq 0.01$ ML, followed by a smooth backshift at higher coverages, while for n-GaAs(110) a smooth monotonous BE variation is observed for the whole coverage range.

The differences of the core-level BEs from the values of a freshly cleaved GaAs(110) substrate represent the weighted mean values of band bending within the PE sampling depth. In order to obtain a value for the band bending directly at the interface, $|V_s|$, a correction, $\Delta|V_s|$, for the long-range variation of band bending within the PE sampling depth has to be applied.[11-14,16,17] Assuming a linear variation of band bending with distance from the interface, we obtain a correction of $\Delta|V_s| = \lambda \cdot (2ne|V_s|/\epsilon\epsilon_0)^{1/2}$ (Ref. 18). Here, n denotes the doping concentration, and $\epsilon = 10.4$ the dielectric constant of GaAs;[18] for the photoelectron mean-free path, λ, at kinetic energies of $\simeq$ 35 eV or $\simeq$ 55 eV for As-3d and Ga-3d photoelectrons, respectively, a value of $\lambda = 6$ Å was used. In this way, the correct bandbending values at the interface, which define the Fermi-level position with respect to the valence-band maximum (VBM) or conduction-band minimum (CBM) of GaAs, are obtained and given in fig. 2 by the dashed curves.

All alkali/GaAs(110) interfaces investigated exhibit a rather similar band-bending behavior as a function of alkali coverage, with similar strong asymmetries in band bending for n- and p-GaAs(110). For p-GaAs(110), an astonishingly large band bending of $\simeq$ 1.0 eV is observed for coverages as low as $\simeq$ 0.01 ML. At higher coverages, the magnitude of band bending decreases and stabilizes above $\simeq$ 1 ML at values of $\simeq$ 0.6 eV. For n-GaAs(110), on the other hand, the band bending at low coverages of $\simeq$ 0.01 ML is negligible, and it is followed by a smooth variation with increasing coverage and a saturation at coverages above $\simeq$ 2 ML. At these high coverages, a common Fermi-level position is observed for both n- and p-GaAs(110).

First, it should be noted that the observed band-bending behavior at low coverages is markedly different from a variation expected on the basis of the defect model. Assuming the same density for donor- and acceptor-type defect states, the defect model predicts a symmetric band-bending behavior for n- and p-GaAs(110), with an expected stabilization for relatively low coverages leading to a Fermi-level position close to the center of the GaAs band gap.[2,3] This is definitely not observed here. In addition, the influence of defect states are not expected to be dominant, since the interfaces grown at 85 K are non-reactive.

3.2. The Virtual-Gap-States Model

The overall band-bending behavior observed for non-reactive interfaces may be explained on the basis of the VGS model. To facilitate discussion, a schematic diagram of the density of states of the overlayer and accordingly of the induced density of states in the GaAs band gap is presented in fig. 3.

From the striking difference in band bending between n- and p-GaAs at low coverages, it is concluded that the adsorbed alkali atoms behave as electron donors, filling up the acceptor states (holes) in p-GaAs at the interface and thereby causing a strong band bending for p-GaAs(110) only. For an estimate of the magnitude of this charge transfer, the area charge density transferred to the semiconductor required to cause the observed band bending is compared with the area density of adsorbed alkali atoms. In a purely electrostatic model, the magnitude of the transferred area charge density, ρ, causing a band bending, $|V_s|$, is given by $\rho = (2\epsilon\epsilon_0 ne|V_s|)^{1/2}$ (Ref. 18). This means that with the given doping concentration of p-GaAs of $n = 1 \cdot 10^{18}/cm^3$, a band bending $|V_s| = 1$ eV is caused by an area charge density $\rho \simeq 3.5 \cdot 10^{12}$ electrons/cm^2. We find that a band bending of this magnitude is already reached for alkali coverages of only $\simeq$ 0.01 ML, corresponding to an alkali-atom area density of $\simeq 5 \cdot 10^{12}/cm^2$. Within the uncertainities of the quoted numbers, this comparison shows that a charge transfer of about one electron per alkali atom to the p-type GaAs substrate has to be considered, in agreement with the monovalency and low electronegativity of the alkali atoms. Such an almost

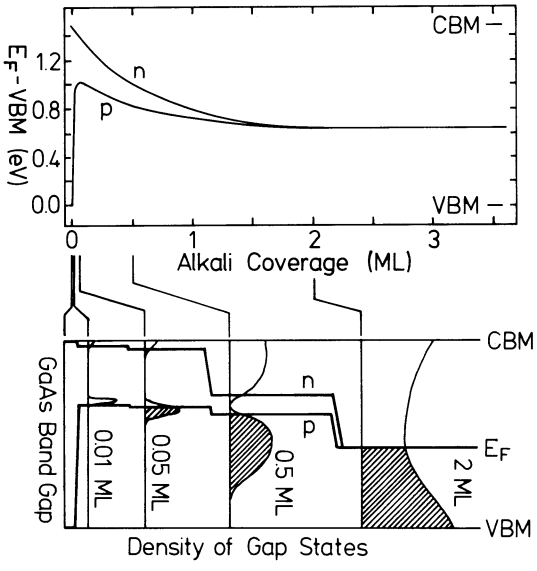

Fig. 3. Model for the density of states in the GaAs band gap for different alkali coverages. The upper part of the figure displays the typical band-bending behavior for n- and p-type substrates as a function of alkali coverage for non-reactive interfaces. In the lower part of the figure, the density of VGS is shown schematically for distinct alkali coverages. Shaded areas correspond to occupied states. Thick horizontal lines mark the actual Fermi-level positions within the GaAs band gap.

complete charge transfer, however, is expected to occur only for very low alkali coverages up to ≈ 0.01 ML. At coverages between 0.01 ML and 0.05 ML, band bending stays almost constant, showing that no further charge transfer into p-GaAs acceptor states is possible. It may therefore be concluded that the adsorbate s-derived state (with its extension into the semiconductor, the VGS) has an energetic position at ≈ 1 eV above VBM and will be gradually occupied with increasing coverage. This is schematically shown in fig. 3 for Θ = 0.01 and 0.05 ML. In the same picture, it may be assumed that the respective unoccupied adsorbate state is situated close to CBM, since nearly no band bending is observed for n-GaAs(110) at these low coverages.

The large values of maximum band bending at very low alkali coverages on p-GaAs(110) (as shown in fig. 2) illustrate the effects of the low ionization energies of the alkali atoms on band bending. For the series of alkali atoms studied, a clear systematic behavior is observed: With decreasing atomic ionization energy from 5.12 eV for Na, via 4.32 eV for K, 4.16 eV for Rb, to 3.88 eV for Cs, the maximum band-bending value increases from 0.91 eV for Na, via 0.95 eV for K, 1.02 eV for Rb, to 1.05 eV for Cs; the experimental uncertainities are estimated as ± 0.03 eV. This behavior agrees well with recent results on various other metal/GaAs(110) interfaces grown at low substrate temperatures, where a strongly reduced interfacial reactivity has been observed.[19,20] In these studies, interfaces with Al, Ag, Au, In, and Sn were investigated, which are characterized by considerably higher atomic ionization energies than the alkali metals. The observed maximum band-bending values on p-GaAs(110) were accordingly found to be lower than those observed for the alkali/GaAs(110) interfaces. A behavior reverse to the case of the electropositive alkali elements was reported for the chlorine/GaAs(110) interface, where in case of p-GaAs(110) at low coverages practically no band bending at all was observed, while a very strong band bending of ≈ 1.2 eV was found for n-GaAs(110).[21] Such a behavior is actually expected on the basis of the high electron affinity (high ionization

energy) of chlorine causing a transfer of electronic charge from n-GaAs to adsorbed chlorine.

With increasing alkali coverages, the Fermi-level positions in the band gap of GaAs are smoothly lowered both for n- and p-GaAs(110), approaching a common value of ≈ 0.6 eV above VBM for coverages of ≈ 2 ML. Below this coverage, the alkali films are considered to be non-metallic. Since the influence of defect states may be excluded, a mechanism of band alignment similar to that operating in semiconductor heterojunctions is proposed.[22] Then the alkali film acts as a semiconductor, and the observed Fermi-level positions within the GaAs band gap for n- and p-type GaAs are more or less given by the CBM and VBM, respectively, of this alkali film (Θ = 0.5 ML in fig. 3). In this model, the observed differences in Fermi-level positions for n- and p-GaAs(110) substrates approximately define the band gap of the alkali film, which obviously decreases with increasing coverage and vanishes due to overlayer metallization at $\Theta \approx 2$ ML. In this way, a continuous transition from band bending due to adsorbed alkali atoms, which is explained on the basis of VGS, to a situation dominated by MIGS is observed. It should be noted here that slight deviations of the CBM or VBM, respectively, of the alkali film from the observed Fermi-level positions may exist due to charge transfer from the alkali film to the donor or acceptor states of n- and p-type GaAs, respectively (see fig. 3). Thus the actual metallization coverage may be less than 2 ML.

The specific values of the final Fermi-level position exhibit systematic variations with the work function of the deposited metal, in an analogous way as the initial band bending in case of p-GaAs(110). We note that the final Fermi-level position increases from 0.53 eV for Na, via 0.55 eV for K, 0.66 eV for Rb, to 0.67 eV for Cs, with estimated uncertainities of ± 0.03 eV, while the work functions of the elemental metals decrease from 2.35 eV for Na, via 2.2 eV for K and Rb, to 1.8 eV for Cs.[23] This behavior reflects a systematic variation of the final Fermi-level position with respect to the charge-neutrality level of the MIGS, that is caused by charge transfer between the alkali-metal layer and the MIGS region at the interface.[4-8,24]

3.3. De-Metallization by Overlayer Oxidation

The interpretation of the final Fermi-level pinning in terms of MIGS can be further justified by erasing the metallic character of the overlayer. This may be achieved by a simple oxidation of the overlayer provided that it affects only this layer and not the GaAs(110) substrate. In this case, no further defect states are produced that could influence the band bending.

The results of such an oxidation experiment are shown in fig. 4 for the Cs/GaAs(110) interface held at a temperature of 140 K. The lower wide scan PE spectrum was obtained from freshly cleaved n-GaAs(110) that is dominated by intense emission from As-3d and Ga-3d core levels. Deposition of 2 ML Cs results in additional emission lines attributed to the Cs-5s and Cs-5p core levels as well as in strong satellites for all core lines at ≈ 2 eV higher BE (indicated by vertical arrows). These satellites are assigned to plasmon losses, which serve here as a monitor of metallization. As a consequence of band bending, both the As-3d and Ga-3d core levels shift simultaneously to lower BE by about 0.5 eV. Upon additional adsorption of 2 L oxygen, the plasmon-loss structures disappear, and a multi-peaked valence-band emission from O-2p states becomes visible. The most interesting fact is the behavior of the As-3d and Ga-3d lineshape, which do not show any features pointing to substrate oxidation, but reveal a clear backshift in BE to almost the BE values of the uncovered substrate. Annealing of the interface to 800 K leads to additional components shifted by ≈ 4 eV (As-3d) and ≈ 1 eV (Ga-3d) to higher BE, which are attributed to As and Ga atoms coordinated to 3 to 4 oxygen atoms.[25] Parallel to the appearance of these components, strong changes in the valence-band region are observed, pointing to changes in chemistry. Thus, upon annealing heavy oxidation of the GaAs substrate occurs.

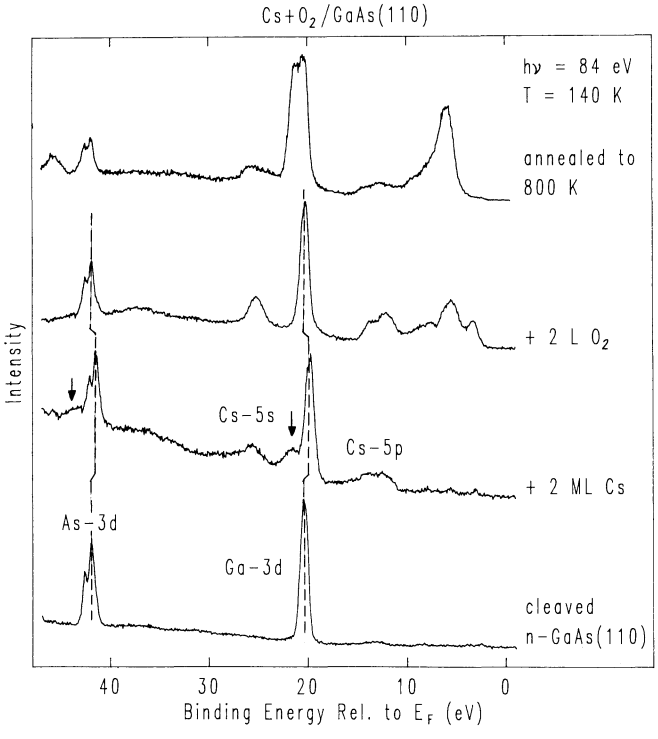

Fig. 4. Wide-range PE spectra (hν = 84 eV) of a cleaved n-GaAs(110) surface at T = 140 K, successively covered with 2 ML Cs, exposed to 2 L oxygen, and annealed at 800 K. Note the common BE variations of the As-3d and Ga-3d lines, indicated by the dashed vertical lines, and the appearance of a plasmon, marked by arrows.

The experimental data displayed in fig. 4 provide clear evidence that oxidation of thin Cs overlayers at a substrate temperature of 140 K does not affect the chemical composition of the GaAs(110) substrate. This is expressed in the absence of spectral changes in the As-3d and Ga-3d core-level PE lines after oxidation of the overlayer at this temperature. As a consequence, the multi-peaked valence-band PE spectrum in fig. 4 has to be assigned to O-2p emission from a mixture of bare Cs oxides, particularly to Cs_2O_2 and Cs_2O_4 (Ref. 26,27), in accordance with theoretical calculations of the O-2p spectra of O_2^{2-} and O_2^- ions, respectively.[28] The most interesting feature in fig. 4 is the quenching of the plasmon-loss satellites upon oxygen exposure and the parallel backshift due to a change in band bending of both the As-3d and the Ga-3d core levels to BE positions characteristic for the uncovered substrate.

For the Ga-3d lines, the experimental results for both n- and p-GaAs(110) at 140 K and after successive treatments with Cs and oxygen are shown in more detail in fig. 5. At the bottom of the figure, the PE spectra for the cleaved GaAs substrate are shown, deconvoluted into bulk (dashed) and surface (dotted) components. The different BEs of the Ga-3d emission lines for n- and p-type GaAs reflect the different Fermi-level positions in the GaAs band gap. Deposition of 2 ML Cs leads to BE shifts of the order of 0.5 eV in opposite directions for n- and p-GaAs(110), attributed to band bending. The surface component is quenched indicating that the whole surface area is covered by Cs atoms,[12] while the respective Cs-contact component is not be resolved from the bulk emission line (see also section 3.1). A plasmon-loss feature at ≈ 2 eV higher BE (shaded subspectrum) reflects an increa-

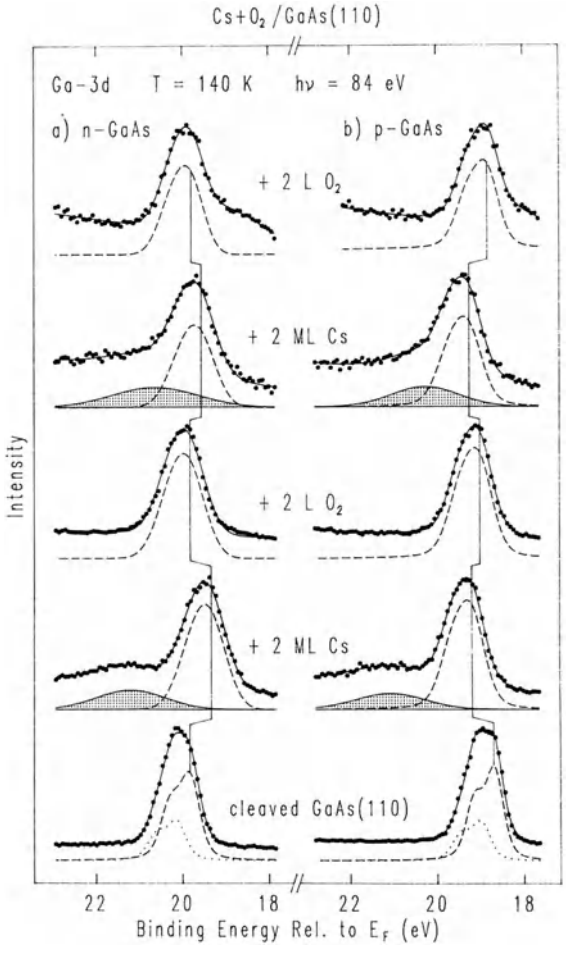

Fig. 5. Ga-3d PE spectra of cleaved n- and p-GaAs(110) surfaces, and after successive Cs evaporations and oxygen exposures. Dashed subspectra represent the substrate bulk, dotted ones the substrate surface, and the shaded subspectra correspond to plasmon-loss structures that are assigned to overlayer metallicity. The vertical solid bars mark the positions of the Ga-$3d_{5/2}$ components. Note that the ≈ 19 eV shoulder in the upper spectra stems from emission from the O-2s core-level.

sing density of delocalized electrons, signalling metallicity of the overlayer.[12] By adsorption of 2 L oxygen, this plasmon-loss satellite vanishes. At the same time, the core levels exhibit a backshift in BE towards the values determined for the pure substrates. Subsequent deposition of 2 ML Cs leads again to the appearence of a plasmon-loss satellite, however, with a lower plasmon energy reflecting a reduced density of delocalized electrons as compared to the first Cs deposition. In addition, the BEs of the Ga-3d PE lines shift back to values close to those observed after the first Cs deposition. Subsequent exposure to 2 L of oxygen leads again to a disappearance of the plasmon-loss features as well as to a backshift of the core-level PE lines towards the line positions of the pure substrate.

The data presented in fig. 5 provide strong evidence for a direct correlation between the metallization of the overlayer, as monitored by the appearance of plasmon-loss features, and a Fermi-level position close to the center of the GaAs

band gap that is typical for interfaces with metals. Suppression of the metallic character of the overlayer by oxidation leads to backshifts of the Fermi-level positions to almost the same values encountered for freshly cleaved n- and p-GaAs(110). This unambiguously rules out defect states as a possible cause for band bending in these interfaces, since defects can obviously not be removed by oxitation. On the other hand, the initial Fermi-level positions for n- and p-GaAs are also not fully reproduced by oxidation of the overlayer, reflecting the fact that the CsO_x/GaAs(110) interface represents a kind of heterojunction between two semiconductors. Therefore, Fermi-level pinning for n- and p-GaAs is expected to be governed by the energetic positions of the CBM and VBM, respectively, of the Cs oxide layer, changing with stoichiometry. Such a dependence on stoichiometry could be the cause for the slightly different Fermi-level positions observed after the first and second oxygen exposures, and will be the subject of further investigations. Different pinning positions for different Cs oxide overlayers, however, do not affect the basic results of this work, which shows that the final pinning position in case of non-reactive interfaces between alkali metals and GaAs(110) is directly correlated with the metallization of the overlayer. This finding provides strong evidence for the validity of the VGS/MIGS model, and conclusively rules out the defect model in case of non-reactive interfaces.

4. Reactive Interfaces

In case of reactive interfaces, the situation is somewhat different. Fig. 6 displays PE spectra of the As-3d and Ga-3d core levels for the Na/p-GaAs(110)

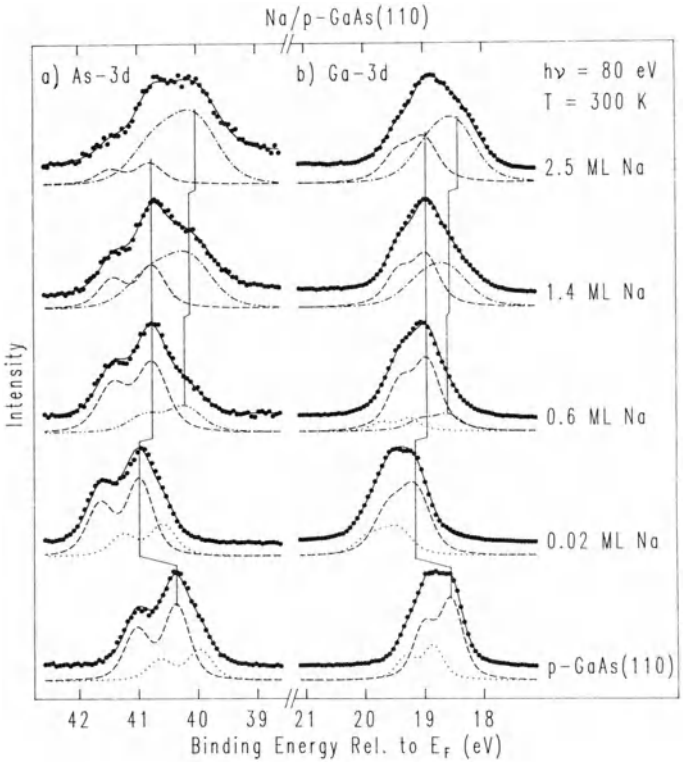

Fig. 6. As-3d and Ga-3d core-level PE spectra of the Na/p-GaAs(110) interface at 300 K for various Na coverages. The notation is the same as in fig. 1, with the Na-contact component replaced by the reacted component.

interface formed at 300 K as a function of Na coverage. Up to 0.6 ML, the overall behavior is quite similar to that found for a substrate temperature of 85 K (fig. 1). The As-3d lineshape does not change, while the Ga-3d PE signals exhibit a decrease in the relative intensity of the dotted substrate-surface component and an increase of the dash-dotted Na-contact component at lower BE. At higher coverages, however, the spectra of the room-temperature grown interface reveal substantial differences to the low-temperature case. These particularly include the relative intensity of the dash-dotted components, which exhibit a strong increase with Na coverage, considerably exceeding the maximum weights found for the non-reactive interface at 85 K. This observation signals a thermally controlled chemical reaction at the interface, accompanied by an interdiffusion of As, Ga, and Na atoms. The lower BE of the reacted components (dash-dotted) with respect to the GaAs substrate is assigned to an electron uptake upon reaction, which is also expected on the basis of the low electronegativities of the alkali atoms. The additional variation in BE of the reacted components with increasing coverage is most probably due to changes in stoichiometry and/or mean coordination number of the chemical compounds in the reacted layer.

In fig. 7, the variations in BE of the As-3d and Ga-3d substrate core levels are displayed as a function of Na coverage for interfaces grown at 85 K and at room temperature. The band-bending behavior of the reactive Na/GaAs(110) interface grown at 300 K exhibits striking differences to the non-reactive, low-temperature grown case. At coverages below 0.05 ML, a strong, almost symmetric band bending is observed for both n- and p-GaAs(110), resulting in an almost identical Fermi-level position at ≃ 0.75 eV above VBM for $\Theta \simeq 0.05$ ML. With increasing coverage,

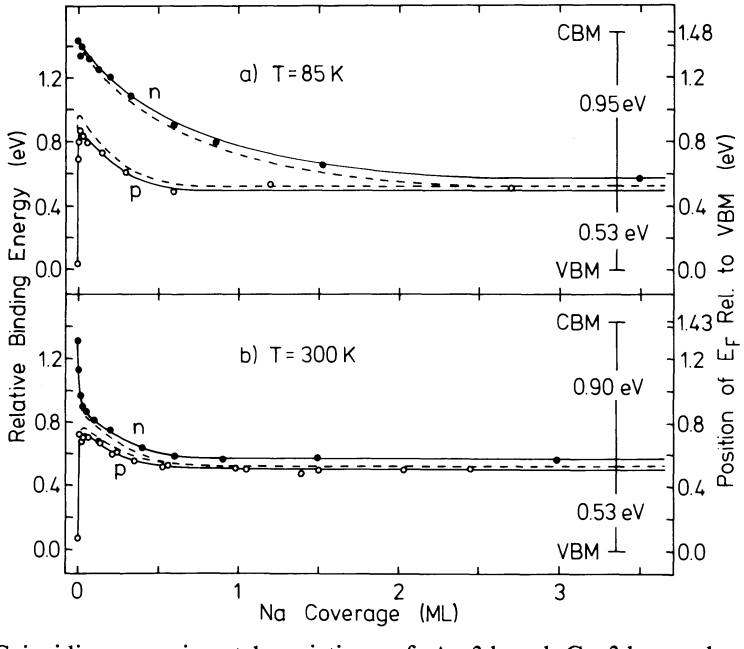

Fig. 7. Coinciding experimental variations of As-3d and Ga-3d core-level BEs of substrate atoms as a function of alkali coverage for interfaces of Na with n- and p-GaAs(110) at 85 K and 300 K (solid lines and left-hand scale), and the respective Fermi-level positions at the interface relative to VBM (dashed lines and right-hand scale). Note that the band gap of GaAs decreases from 1.48 eV at 85 K to 1.43 eV at 300 K.

the Fermi level is lowered by ≈ 0.2 eV, stabilizing at a final position of ≈ 0.53 eV above VBM for Θ > 0.6 ML. Note that the quoted absolute values of the Fermi-level positions contain an uncertainity of at most ± 0.05 eV due to a possible small initial band bending of the freshly cleaved GaAs(110) surfaces, which may arise from cleavage-related extrinsic surface states.

The band-bending behavior observed for the reactive Na/GaAs(110) interface may be explained in the region of low Na coverages by a strong influence of defect states, that are produced by the observed interfacial reaction processes. Such defect states have energetic positions close to the center of the band gap, giving rise to a pinning of the Fermi level already for rather low coverages and in practically the same way for n- and p-type substrates.[2,3] In this way, the influence of defect states explains why for n-GaAs(110) in the reactive case band bending increases steeper with coverage than in the non-reactive case, while the maximum band-bending value observed for low-temperature grown Na/p-GaAs(110) is not reached. With increasing Na coverage, the Fermi-level position is lowered towards the final value found for the non-reactive case. This observation is readily explained by a transition from band bending due to defect states to a MIGS-dominated mechanism in case of thick metallic overlayers.

A similar transition has recently been observed for the strongly reactive Tm/GaAs(110) interface.[13,14] Fig. 8 shows the corresponding BE shifts of the As-3d and Ga-3d core levels for both n- and p-type GaAs as a function of Tm coverage. Again, the dashed line represents the Fermi-level position after correction of the PE data for finite sampling depth. The most striking informations in this figure are (i) a strong initial band-bending effect, which leads to a common Fermi-level position for both n- and p-type substrates at coverages smaller than 0.5 Å, and (ii) an

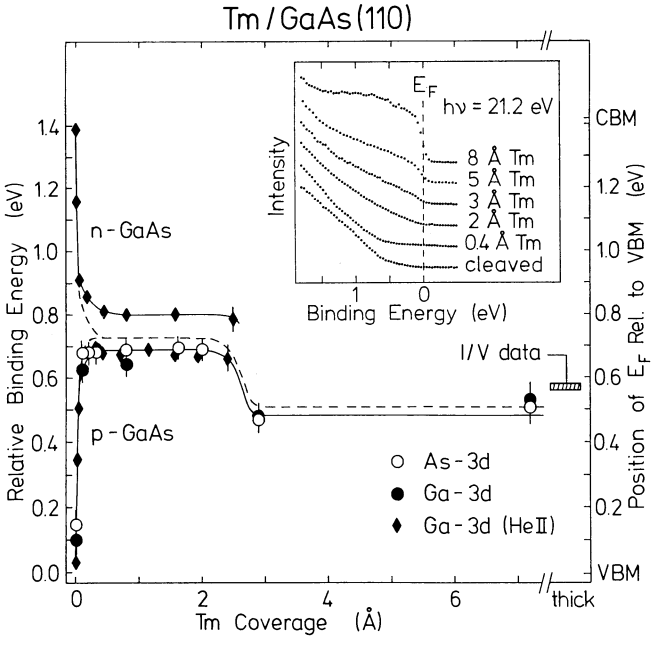

Fig. 8. Coinciding experimental variations of As-3d and Ga-3d core-level BEs of substrate atoms and of the respective Fermi-level positions as a function of Tm coverage for interfaces of Tm with n- and p-GaAs(110) at 300 K. The insert shows a selection of valence-band spectra, signalling overlayer metallization for Tm coverages between 2 and 3 Å.

additional change in band bending by ≈ 0.2 eV occurring almost abruptly at $\Theta \approx$ 2.6 Å, leading to the final Fermi-level position derived from I/V measurements.

Whereas the first, symmetric band-bending behavior at low coverages may be explained by formation of defect states, this mechanism fails to give an explanation for the second shift at ≈ 2.6 Å coverage, since such an additional change in Fermi-level position due to different defect states should be accompanied by substantial changes in the chemical composition of the reacted layer, which were not observed.[13,14] On the other hand, the shift in Fermi-level position is obviously correlated with a metallization of the overlayer. This is illustrated by the valence-band PE spectra shown in the insert of fig. 8. The spectral region around the Fermi level is displayed for various Tm coverages. As is evident from the figure, the top of the valence band shifts to lower BE with increasing Tm coverage, being intersected by the Fermi energy at coverages exceeding ≈ 2 Å. This means that the reacted overlayer turns metallic for Tm coverages between 2 and 3 Å, leading to the formation of MIGS, which overcome the defect states in terms of density and dominate the final Fermi-level position for thick metal coverages. Thus, as in the case of the reactive Na/GaAs(110) interface, we observe a transition from defect states to MIGS as the dominant band-bending mechanism.

It is interesting to note that this change is nearly abrupt for Tm/GaAs(110), while a smoother variation is observed for Na/GaAs(110). This difference may be explained by different chemical reaction processes at the interface and/or by the influence of the overlayer band structure. Na atoms are expected to be more mobile on the GaAs(110) surface than Tm atoms due to the fact that alkali atoms can be desorbed at quite low temperatures. This may result in the formation of Na islands or chains prior to chemical reaction. Such aggregates should lead to different reaction processes as compared to isolated, statistically distributed adatoms that are assumed in case of Tm. Moreover, the formation of electronic bands within these aggregates may give rise to VGS or MIGS at even lower coverages than for Tm. These are expected to compete with the defect states at lower coverages giving rise to a smooth variation of the pinning position. On the other hand, the characters of the valence bands are quite different for both metals: The spatially extended s-orbitals of Na may lead to band formation at even lower coverages, but with a lower density of states than in case of Tm with its more localized d-orbitals. Also, a transition from an insulating to a metallic behavior may occur for Tm within a smaller coverage range than for Na due to the stronger spatial localization of the radial d-wavefunction. These different properties of the metallic overlayer will be transmitted to the MIGS and could be responsible for the observed differences in pinning behavior.

5. Conclusions

In summary, we have shown that the overall band-bending behavior of non-reactive interfaces between GaAs(110) and alkali metals is well described on the basis of VGS. Metallization of the overlayer leads to a common Fermi-level position for both n- and p-type substrates, which is determined by the charge-neutrality level of the MIGS. Suppression of metallicity by overlayer oxidation results in a backshift of the Fermi-level positions to almost the same values as observed for the uncovered substrate, demonstrating a negligible influence of defect states to band bending in case of non-reactive interfaces.

In case of reactive interfaces, on the other hand, the Fermi-level position for low, non-metallic coverages is strongly influenced by defect states. For higher coverages, a transition of the dominant band-bending mechanism from defect states to MIGS is observed upon metallization of the overlayer, leading to the same final Fermi-level position as in the case of non-reactive interfaces. Thus, independent of the reactivity of the interface, the final pinning position for thick metallic overlayers is always determined by MIGS.

Acknowledgements

The authors thank Prof. R. Miranda for helpful discussions. This work was supported by the Bundesminister für Forschung und Technologie, Projekt Nr. 05 313AX B2/TP3.

References

* On leave from: Departamento de Física de la Materia Condensada, Universidad Autónoma de Madrid, Cantoblanco, E-28049 Madrid, Spain.

1. L.J. Brillson, Surface Sci. Rep. 2, 123 (1982).
2. W.E. Spicer, P.W. Chye, P.R. Skeath, C.Y. Su, and I. Lindau, J. Vac. Sci. Technol. 16, 1322 (1979).
3. I. Lindau and T. Kendelewicz, CRC Critical Rev. Solid State and Mat. Sci. 13, 27 (1986).
4. V. Heine, Phys. Rev 138, A1689 (1965).
5. E. Louis, F. Yndurain, and F. Flores, Phys. Rev. B 13, 4408 (1976).
6. M.L. Cohen, Adv. in Electronics and Electron Phys. 51, 1 (1980).
7. J. Tersoff, Phys. Rev. Lett. 52, 465 (1984).
8. F. Flores and C. Tejedor, J. Phys. C: Solid State Phys. 20, 145 (1987).
9. P.E. Gregory, and W.E. Spicer, Phys. Rev. B 12, 2370 (1975).
10. H. Clemens and W. Mönch, CRC Critical Rev. Solid State Sci. 5, 273 (1975).
11. M. Prietsch, C. Laubschat, M. Domke, and G. Kaindl, Europhys. Lett. 6, 451 (1988).
12. M. Prietsch, M. Domke, C. Laubschat, T. Mandel, C. Xue, and G. Kaindl, Zeitschrift für Phys. B, submitted (1988).
13. M. Prietsch, M. Domke, C. Laubschat, and G. Kaindl, Phys. Rev. Lett. 60, 436 (1988).
14. M. Prietsch, C. Laubschat, M. Domke, and G. Kaindl, Phys. Rev. B, in print (1988).
15. D.E. Eastman, T.-C. Chiang, P. Heimann, and F.J. Himpsel, Phys. Rev. Lett. 15, 656 (1980).
16. W. Mönch, R.S. Bauer, H. Gant, and R. Murshall, J. Vac. Sci. Technol. 21, 498 (1982).
17. J.Y.-F. Tang and J.L. Freeouf, J. Vac. Sci. Technol. B 2, 459 (1984).
18. H.F. Wolf, *Semiconductors*, Wiley (1971).
19. K. Stiles, A. Kahn, D.G. Kilday, and G. Margaritondo, J. Vac. Sci. Technol. B 5, 987 (1987).
20. R. Cao, K. Miyano, T. Kendelewicz, K.K. Chin, I. Lindau, and W.E. Spicer, J. Vac. Sci. Technol. B 5, 998 (1987).
21. D. Troost, L. Koenders, L.-Y. Fan, and W. Mönch, J. Vac. Sci. Technol. B 5, 1119 (1987).
22. R.W. Grant and J.R. Waldrop, J. Vac. Sci. Technol. B 5, 1015 (1987).
23. M. Cardona and L. Ley, *Photoemission in Solids*, Vol. 1, Springer (1978).
24. W. Mönch, J. Vac. Sci. Techn. B 6, in print (1988).
25. G. Landgren, R. Ludeke, Y. Jugnet, J.F. Morar, and F.J. Himpsel, J. Vac. Sci. Techn. B2, 351 (1984).
26. C.Y. Su, I. Lindau, and W.E. Spicer, Chem. Phys. Lett. 87, 523 (1982).
27. R. Miranda, M. Prietsch, C. Laubschat, M. Domke, T. Mandel, and G. Kaindl, Phys. Rev. B, submitted (1988).
28. B.J. Moss and W.A. Goddard III, J. Chem. Phys. 63, 3523 (1975).

VBM's. The band widths for the two cases are 10.91 eV and 10.85 eV, respectively. This confirms our early argument about the determination of VBM's – they must have bulk properties, and are not to be influenced by the surface conditions.

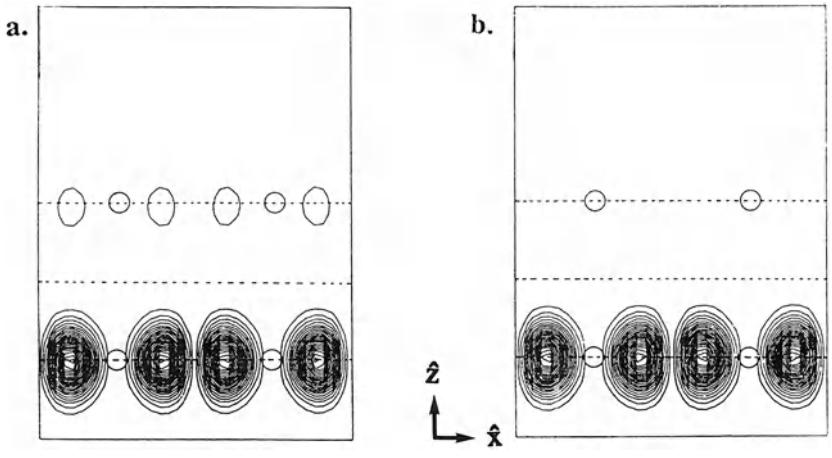

Fig. 6 The charge density contours of the VBM. (a) $\Theta_t = \frac{1}{2}$ ML. (b) $\Theta_t = 1$ ML. The position of the As atom is indicated by an open circle. The dashed lines denote the GaAs layers.

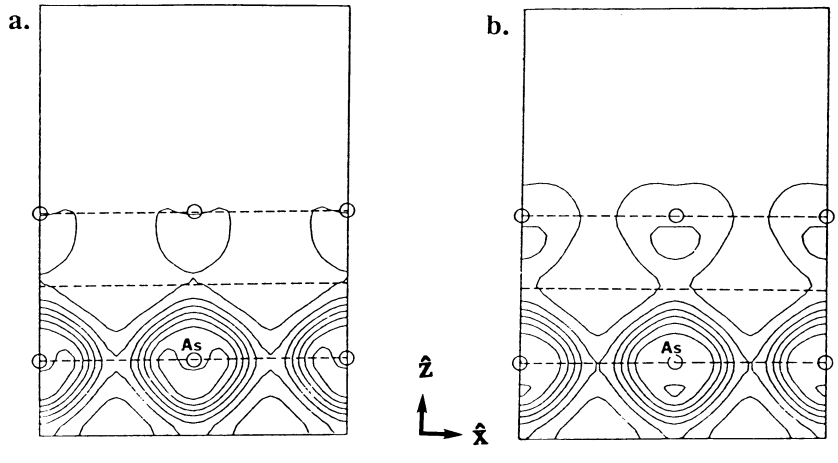

Fig. 7 The charge density contours of the bottom of the valence band. (a) $\Theta_t = \frac{1}{2}$ ML. (b) $\Theta_t = 1$ ML. The position of As is indicated by an open circle. The dashed lines denote the GaAs layers.

After we determined the VBM's for these two coverages, the shift of the corresponding Fermi levels with respect to their VBM's can then be calculated by choosing

the highest occupied energies as the Fermi levels. The Fermi level with respect to the VBM for $\Theta_t = \frac{1}{2}$ ML is 0.96 eV, while the value for $\Theta_t = 1$ ML is 0.63 eV. The resulting Fermi-level shift from $\Theta_t = \frac{1}{2}$ ML to $\Theta_t = 1$ ML is downward and is 0.33 eV. The experimental value is a down shift of 0.2 eV for the n-type semiconductor in Ref. [4]. By taking the possible systematic errors from the experiments[3,4] into accounts, the 0.13 eV discrepancy of our result with the one in the n-type semiconductor – metal interface is satisfactory. Our theoretical result is too large as compared with the shifted value (< 0.1eV) for the p-type surface. However, more importantly, the down shift behavior of E_F from $\Theta_t = \frac{1}{2}$ to 1 ML is qualitatively in good agreement with the experiment.

D. Local density of states

The LDOS calculated by Zhang et al.[13] for the thick Al layer adsorbed on GaAs(110) surface has been used to support the Fermi-level pinning due to MIGS by Tersoff.[2] In order to see whether the similar LDOS can be obtained for the Na atoms adsorbed on GaAs(110) with $\Theta_t = \frac{1}{2}$ and 1 ML, we calculated the LDOS by

$$\mathrm{LDOS}(E, z_0, \Delta z) = \frac{1}{\Delta z \cdot S} \int_{\Delta z} d^2\rho dz \sum_{n\bar{k}} |\Psi_{n\bar{k}}(\bar{\rho}, z)|^2 \delta(E - E_{n\bar{k}}), \tag{3}$$

where Δz is the thickness about z_0 and z_0 is the center of the $\hat{z}$-component about which the LDOS is calculated, that is $z = z_0 \pm \Delta z/2$. $\bar{\rho}$ is a vector in the surface and S is the surface area.

The results (solid curves) for relaxed clean, ideal clean surfaces and the Na adsorbed surfaces with z_0 at the surface layer are presented in Fig. 8. For the relaxed clean surface (Fig. 8(a)) there is essentially no state above the E_v (VBM). Since E_F is defined as the energy of the highest occupied band, it coincides with the VBM. The band gap is indicated by the region between E_v and E_c. Note that E_c is not accurate because of the local density approximation used in the calculations, but we use it as a guidence. The slightly nonvanishing states in the gap are due to the Gaussian broadening of the energy. In Fig. 8(b) the LDOS of the ideal surface shows significant states above the E_v and at E_F, those states are called gap states. These gap states originated from dangling bonds of the Ga and As atoms, with the Ga dangling bond occupied by less electron than the one of As atom. The peak below E_F is associated with As states, while Ga states are associated with the peak appearing above E_F. By comparing the results in Figs. 8(a) and 8(b) for the clean surface, we conclude that the relaxation of the surface atoms heals these gap states.

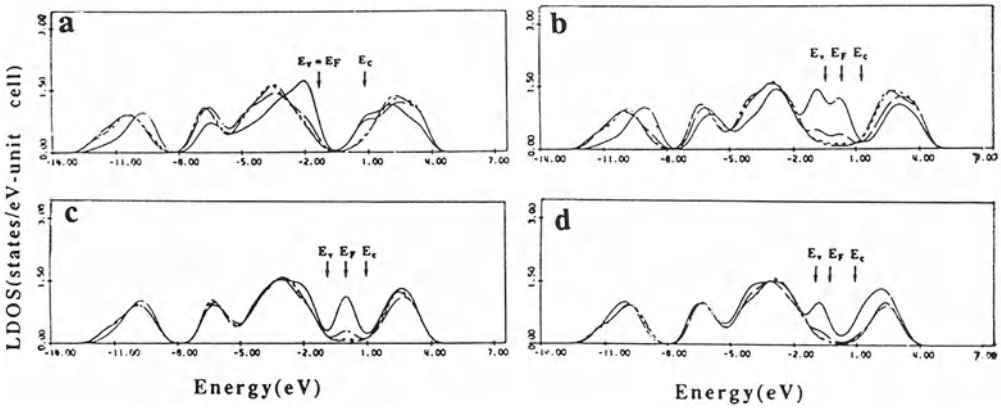

Fig. 8 The local density of states (solid lines) in the interface region. (a) The relaxed surface. (b) The ideal surface. (c) $\Theta_t = \frac{1}{2}$ ML. (d) $\Theta_t = 1$ ML. Also shown are the LDOS for the other three layers: second layer (broken solid line); third layer (dashed line); the fourth layer (center of the slab) (dotted line).

With the adsorption at $\Theta_t = \frac{1}{2}$ ML, two physical effects happen: (1) the bonding between the Na and Ga atoms; and (2) the reorientation states between the Na ion and the As atom. Effect (1) contributes to the gap states at E_F (Fig. 8(c)). The effect (2) lowers the energies of states characterizing the charge density between the Na ion and the As atom. The former shifts down the peak slightly above E_F shown in Fig. 8(b), while the latter merges the As dangling bond states to the peak located at 2.2 eV below E_v in Fig. 8(b). As discussed in Section III.B, the Ga atom needs $\frac{5}{4}$ electrons to complete the formation of a bond. However, the Na atom contributes only one electron in the case of $\Theta_t = \frac{1}{2}$ ML. Therefore, the formation of the bond is not complete in this case. Increasing the coverage to 1 ML, more charge from the additional Na atom can be transferred to the Ga and the As atoms. Consequently, the bonding states between the Na atoms and the surface atoms are formed and the energy of these states are thus lowered. The peak near E_F is shifted down in energy when the coverage increases from $\Theta_t = \frac{1}{2}$ to 1 ML (Figs. 8(c) and (d)). The small enhancement of the LDOS in the band gap region with the adsorption as compared to those for the bulk layers, MIGS do not clearly present in the range of coverages considered in this paper.

IV. Fermi-level pinning mechanism

From the above results and those presented in Table II, we now propose a mechanism of Fermi level pinning for the Na atom adsorbed on the GaAs(110) surface. As

soon as there is a small adsorption of metal atom (about 0.14 ML) on the GaAs(110) surface, the surface relaxation diminishes. Because the formation of a bond between the Na and the Ga atoms releases 2.4 eV per surface unit cell while it takes only 0.58eV per surface unit cell for the surface atoms to move back to their ideal positions, one bond formation can, therefore, restore several surface relaxations. The unrelaxed surface exhibits dangling bonds which in turn pin the Fermi level. For $\Theta_t < 1$ ML, the E_F is pinned at the energy of the Ga dangling bond. This mechanism supports the experimental results of the Sb atoms on GaAs(110)[15] – the dangling bonds at the edge of the terrace formed by Sb atoms could be the possible mechanism for the Fermi-level pinning. As the coverage increases, $\Theta_t > 1$ ML, the dangling bonds are saturated, metallic bonds can then form between the metal atoms. The Fermi level is then pinned by the MIGS.

V. Summary

We have studied the relaxed clean GaAs(110) surface and the Na atoms adsorbed surfaces. Two coverages of $\Theta_t = \frac{1}{2}$ ML and $\Theta_t = 1$ ML have been considered. We first show that with adsorption the ideal surface is energetically favorable than the relaxed surface. By choosing the energy of the VBM as reference, the E_F is down shifted by 0.33 eV for the two coverages. The local density of states provide the clue of the importance of the dangling bond states - intrinsic surface states in pinning the Fermi level. Finally, a possible pinning mechanism for the Na atom on the GaAs(110) surface was proposed.

Acknowledgements

We would like to thank Drs. M. Prietsch and C. Laubschat for many helpful discussions. LHY would like to thank the supports from the IBM Almaden Research Center. CYF and LHY would like to express their gratitude for support from the Committee on Research of the University of California at Davis.

VI. REFERENCES

1. L.J. Brillson, Surf. Sci. Rep. **2**, 123(1982); I. Lindau and T. Kendelewicz, CRC Critical Rev. Solid State and Mat. Sci. **13**, 27 (1986).
2. J. Tersoff, Phy. Rev. Lett. **52**, 465 (1984).

3. For examples, C.B. Duke, A. Paton, R.J. Meyer, L.J. Brillson, A. Kahn, D. Kanani, J. Carelli, J.L. Yeh, G. Margaritondo, and A.D. Katnani, Phy. Rev. Lett. **46**, 440 (1981); P. Soukiassian, and T. Kendelewicz, to appear in "Metallization and Metal-Semiconductor Interfaces" ed. by Inder P. Batra, Plenum, New York (1989).

4. M. Prietsch, M. Domke, C. Laubschat, T. Mandel, C. Xue, and G. Kaindl, Z. Phys., submitted; M. Prietsch, C. Laubschat, M. Domke, and G. Kaindl, Europhys. Lett. **6**, 451(1988); C. Laubschat et al., this workshop.

5. L.H. Yang, C.Y. Fong, and Inder P. Batra, Bull. Am. Phys. Soc. **33**, 571 (1988).

6. See for example, Inder P. Batra, Prog. in Surf. Sci. **25**, 175 (1987).

7. G.B. Bachelet, D.R. Hamann, and M. Schlüter, Phys. Rev. B**26**, 4199 (1982).

8. J. Ihm, A. Zunger, and M.L. Cohen, J. Phys. C**12**, 4409 (1979); erratum J. Phys. C**13**, 3095 (1980).

9. E.P. Wigner, Phys. Rev. **46**, 1002 (1959).

10. C. Mailhiot, C.B. Duke, and D.J. Chadi, Surf. Sci. **149**, 366 (1985); G.X. Qian, R.M. Martin, and D.J. Chadi, Phys. Rev. B**37**, 1303 (1988).

11. Eugene J. Mele, and J.D. Joannopoulos, Phys. Rev. Lett. **42**, 1094 (1979).

12. J. Ihm, and J.D. Joannopoulos, Phys. Rev. Lett. **47**, 679 (1981); Phys. Rev. B**26**, 4429 (1982).

13. S.B. Zhang, M.L. Cohen, and S.G. Louie, Phys. Rev. B**34**, 768 (1986).

14. Inder P. Batra and S. Ciraci, Phys. Rev. B**33**, 4312 (1986).

15. R.M. Feenstra, and P. Martensson, Phys. Rev. Lett. **61**, 447 (1988).

ELECTRONIC AND STRUCTURAL PROPERTIES AND SCHOTTKY BARRIER FORMATION OF ALKALI METAL - SEMICONDUCTOR INTERFACES

P. Soukiassian*

Commissariat à l'Energie Atomique, Service de Physique des Atomes et des Surfaces, CEN Saclay, 91191 Gif sur Yvette Cedex, France
and
Département de Physique, Université de Paris-Sud, 91405 Orsay Cedex, France.

T. Kendelewicz

Stanford Electronics Laboratory, Stanford University, Stanford, California 94305, U.S.A.

PART I

ELECTRONIC AND STRUCTURAL PROPERTIES OF THE ALKALI METAL /SILICON INTERFACES

INTRODUCTION

Because it induced an important decrease in the substrate work function, which is important in many technological applications [1-5], the chemisorption of alkali metals on surfaces has been widely studied in the recent past years. From the fundamental approach, these studies are also interesting, because the alkali metal adsorbed on surfaces represents examples of rather simple model of interfaces. The classic picture of alkali metal chemisorption was until recently derived from the Langmuir's model[6] with an adsorbate ionic at low coverages and atomic or metallic near one monolayer [7]. Unfortunately, these theoretical models, in which the surface is represented as a free electron gas or as a jellium [8], were unable to explain the behavior of cesium and other alkali metals adsorption on substrates such as transition metals [9] which present the particularity to have, near the Fermi level, highly localized "$d_{z}2$" surface states with a dangling bond character [10]. Ab-initio calculations taking in account the true electronic structure of the substrate were recently performed on Cs/W(100) and

*also: Department of Physics, Northern Illinois University, DeKalb, Illinois 60115, U.S.A.

Cs/Mo(100) [11,12]. They were found to be in excellent agreement with experiments on the same systems [9,13]. These experimental and theoritical studies brought a new insight into the understanding of the mechanisms of alkali metals adsorption on surfaces. It was shown that cesium adsorbate formed a strongly polarized covalent bonding on the surface by hybridization between "Cs 6s" and surface substrate "d_z2" electronic levels [11-13]. Is such a picture valid for alkali metal /semiconductor interfaces or should we refer to recent theoritical calculations predicting a strong ionic bond even at the monolayer coverage [14,15]. Despite the model of a weak ionic bond proposed on the footing of photoemission experiments on the Cs/Si(111)2x1 system [16], there were indications that the alkali metal/silicon bonding is covalent [17,18]. However, with a calculation [14] using a pseudopotential method on Na adsorbed on the Si(111) ideal surface, the Na-Si bond was found primarly ionic. Similar theoretical ab-initio investigations using also a pseudopotential on the K/Si(100)2x1 system [15] calculated the K-Si bond length to be 2.59 Å. This bond is so short that the potassium atoms are believed to be endenbed on the Si dangling bond (which is found to play an important role in the chemisorbed ad-atom), leading to the silicon surface metallization (in contrast with the previous conclusion of Aruga et al. of potassium adsorbate metallization in the K/Si(100)2x1 interface [19]). The nature of the alkali metal/silicon bond is therefore found to be strongly ionic [15].

However, this picture was questionned both by another theoretical work [20] and by several experimental investigations [18,21,22]. In an ab-initio self consistent total energy calculation using a pseudofunction method, Kasowski and Tsai found a K-Si bond length of 3.30 Å on the Si(100)2x1 surface [20] while in an surface extended x-ray adsorption fine structure (SEXAFS) study of the same K/Si(100)2x1 system, we measured this K-Si bond length to be 3.14 Å [22], i.e. the exact sum of both silicon and potassium covalent radii. This value, which is much larger than the one calculated using a pseudopotential (2.59 Å) [15] is in agreement with the value given by Kasowski and Tsai (3.30 Å). Furthermore, in contrast with transition metal surfaces where temperature well above 1000°C were necessary for desorption [23], the low temperature of desorption of alkali metals from the silicon (100) surfaces (550°C for Na [24], 600°C for K [22,25] and 650°C for Rb [26] and Cs [24]) clearly indicate that the bonding is weak [18,27]. Despite another theoritical tentative using Hartree-Fock technique and pseudopotential approach calculations with a cluster model of few atoms [28], it is now clear that the alkali metal/silicon bond is not strong and that its full ionicity is questionnable.

In fact, it is interesting to compare the situation of alkali metals adsorbed on silicon surfaces to the behavior of highly ionic adsorbates such as fluorine or calcium. McFeely and Morar et al. have found that the presence on silicon surfaces of a highly electronegative specie like fluorine induces a very important chemical shift of more than 1 eV at higher binding energies

on the Si 2p core level [29] of Si(111)2x1, Si(111)7x7 and Si(100)2x1 surfaces as a result of an important charge transfer from the substrate to the adsorbate. Similarly, Franciosi et al. [30] reported results on the adsorption of a low electronegative element like calcium on silicon which induces a chemical shift on the Si 2p core level to the lower binding energies by 1.1 to 1.35 eV as a consequence of a large charge transfer from the adsorbate to the substrate. This behavior is exactly what one could, in general expect from strongly ionic bonds between adsorbates and substrates. Therefore, if the alkali metal/silicon bond is strongly ionic, one would expect at least dramatic changes in the Si 2p core level such as a very large core level chemical shift (larger than 1 eV because Cs has lower electronegativity than Ca) on the low binding energies side of Si 2p core level. For comparison, one should note that, in the case of the strong covalent bonding found between alkali metals and transition metal on surfaces like the (100) face of tungsten and tantalum, the W 4f and Ta 4f are shifted towards lower binding energies by values as small as 0.06 eV and 0.1 eV respectively, indicating a very small charge transfer from the alkali adsorbate to the surface of the transition metal substrate [31]. In addition to all these fundamental issues, recent photoemission experiments have shown the role of alkali metals as highly efficient promoters of semiconductor oxidation [18,24-27,32] and nitridation [33]. In both cases, it was possible to remove the alkali metal catalyst by a flash at mild temperature. These interesting and unique properties are another motivation for the understanding of the basic mechanism of chemisorption of alkali metals on semiconductors like silicon.

Using valence band and core level photoemission experiments with synchrotron radiation and surface EXAFS measurements, we show, in this paper, that alkali metals induce interface states near the Fermi level on the Si(100)2x1 surface with hybridization between alkali metals "s" and silicon "p" valence electrons. These results bring the first evidence that the bonding between alkali metal and silicon is a covalent. This covalent bond is weak and polarized. The plasmon induced at the adsorbate core level clearly indicates that the alkali metal overlayer is metallic.

EXPERIMENTAL DETAILS

The photoemission experiments were performed on the Aladdin 1 GeV storage ring at the Synchrotron Radiation Center (SRC) of the University of Wisconsin-Madison . Grasshopper Mark II, grasshopper Mark V and toroidal grating (TGM) monochromators were used to disperse the synchrotron radiation. The experiments were performed in an ultra-high vacuum chamber with a base pressure of $3x10^{-11}$ Torr. The photoelectron kinetic energies were analyzed by a double-pass cylindrical mirror analyzer (CMA) equiped with a coaxial electron gun for Auger spectroscopy (AES). The overall resolution was better than 300 meV in the valence band. The surface EXAFS experiment was performed at the Stanford Synchrotron

Radiation Laboratory (SSRL) on the Jumbo Beam line with a ultra high vacuum chamber at a pressure of $2x10^{-11}$Torr.

In order to minimize eventual band bending effects, we only used undoped silicon samples. The Si(100)2x1 surface was cleaned by ion bombardements and thermal annealings at 950^0 C and its cleanless checked by AES. Low energy electron diffraction shows the expected 2x1 reconstruction of the Si(100) surface. Pure Cs, Rb, K, and Na was deposited on the silicon surface using SAES Getters chromates sources. As in our previous papers, we define the monolayer coverage (1ML) as the saturation coverage (Cs, K and Rb) at room temperature.

Alkali metals are known to be highly sensitive to contamination. For instance, oxygen exposures as low as 0.07 Langmuir (1 Langmuir = 10^{-6} Torr x Sec) and 0.25 Langmuir have been shown to induces dramatic changes respectively in the electronic and stuctural properties of surfaces covered with alkali metals [34]. Since the nature of the bond (ionic versus covalent) and the role of the dangling bond are major issues in the chemisorption of alkali metals on semiconductor surfaces, it is very important to work on a very clean surface. Our experience indicates that the pressure in the vacuum chamber should be better than $5x10^{-11}$ Torr to insure a sufficient surface lifetime. Furthermore, since alkali metals were found to enhance the sticking coefficient and to dissociates inorganic as well as organic gas molecules [27,35], it is important to carefully outgassed the alkali metal dispensers. A gas analysis during evaporation of alkali metal from a partially outgassed source, indicates presence of hydrogen (partially atomic) (1,2), oxygen (16) and carbon monoxide (28)[36]. While hydrogen on semiconductor surfaces is generally bonded to the dangling bond and therefore might eventually compete with the alkali atoms, oxygen and/or carbon monoxide could ionized the alkali atoms on the surface. Furthermore, a contaminated surface could also allow alkali metal deposition in excess of a monolayer at room temperature (the saturation coverage is 1ML for Cs, Rb and K at room temperature). This might eventually explain the discrepancies between various experimental results concerning the controversial question of the growth layer by layer [21,37]. Our experience shows that, during the time necessary to deposit one alkali metal monolayer, the pressure should not increase by more than $1x10^{-10}$ Torr. A pressure increase above this level results in surface contamination. In the present experiment, the pressure increases during the time necessary to deposit one alkali metal monolayer were always lower than $2x10^{-11}$ Torr for Cs and Rb, $3x10^{-11}$ Torr for K and $5x10^{-11}$ Torr for Na.

RESULTS

a) Si 2p core level

Figure 1 displays the Si 2p core level for the clean Si(100) surface and covered with one Cs, Rb, K and Na monolayer. The deposition of one monolayer of any of these alkali metals

results in the decrease by half of the Si 2p core level intensity. However, there is no significant core level chemical shift upon alkali metal deposition. A similar behavior has been observed on Si(111)7x7 surfaces covered by a Cs [32] overlayer as well as on Si(111)2x1 surfaces covered by Cs or Na [38]. This behavior is in contrast with the effect of highly electronegative species like fluorine [29] which induces important chemical shifts to the higher binding energies of the Si 2p core level and with low electronegative adsorbate like calcium which was found to provoke a chemical shift larger than 1.1 eV to the lower binding energy of the Si 2p.

b) Valence Band

Figure 2 shows the Si(100)2x1 valence band at a photon energy of 82 eV for sodium coverages between 0 and 2 monolayers. The clean spectra is in good agreement with previous studies [39]. Peak A (- 1 eV below Ef) is related to the surface p level and the silicon dangling bond, while peak B (-3.7 eV below Ef) comes from the emission of bulk 3p level. If the Na-Si bond was strongly ionic as predicted by ab-initio theoretical pseudopotential calculations [14,15], one should expect destruction of this "p" surface state (peak A, figure 2) upon sodium deposition. Instead, upon increasing sodium coverage, a new peak C grows near peak A and is likely to derive from this "p" surface state. Peak C has a binding energy of -1.8 eV below the Fermi level. Also its intensity is increasing with the coverage up to one Na monalayer. Between 1 ML and 2 ML, the energy of peak C remain constant while its intensity seems to decrease at 2 ML of Na. This behavior indicated that peak C is related to electronic emission coming from the Na/Si interface most likely involving both Si p electronic surface state and Na 3s valence electron. With increasing sodium coverages, peak B is shifted towards higher binding energies (i.e. lower kinetic energies) by 0.55 eV at 1 ML of Na. At coverages between 1 and 2 sodium monolayers, peak B keeps the same binding energy of 4.25 eV below the Fermi level while its intensity is significantly decreased.

Similarly, the continuous shift of the Si 3p level versus sodium increasing coverages indicates an hybridization with the sodium "3s" valence electronic level which is the only candidate. This hybridization also occurs with the Si p surface state giving raise to this new derived interface state (peakC). In fact, since the cross section of alkali metal "s" valence electron is very low at photon energies above 10 eV, one cannot observe, as recently suggested [16] the alkali "s" electron without a change in its character [17]. In the s-p hybridization which results in an increase of the binding energy by 0.8 eV, the Na 3s loses part of its "s" character through the "p" orbital, which therefore clearly explains why this state could be observed at photon energies as high as 82 eV. On Si(100)2x1, this state is not very sensitive to oxygen [18] or to chlorine [35] which further confirms [17] that this electronic state cannot simply be interpreted as being due to alkali metal "s" valence electron.

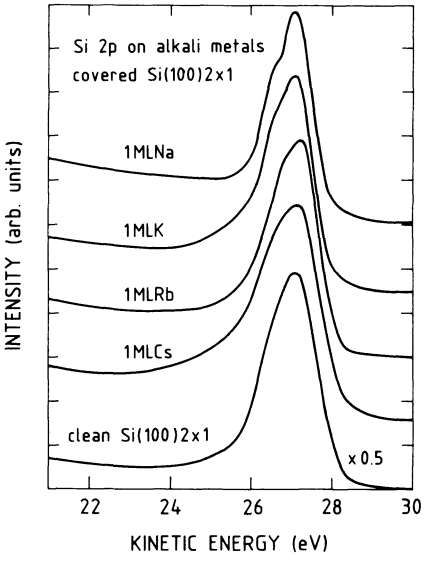

Figure 1 Si 2p core level for a Si(100)2x1 surface covered with 1 monolayer (1ML) of Cs, Rb, K and Na. The photon energy was 130 eV.

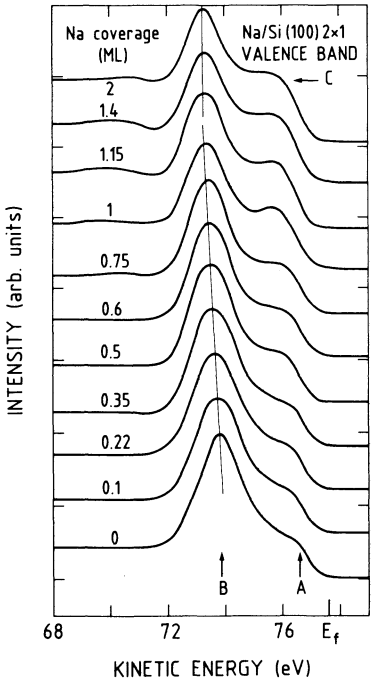

Figure 2 Valence Band spectra of the Na/Si(100)2x1 interface for sodium coverages between 0 and 2 monolayers. The photon energy was 82 eV.

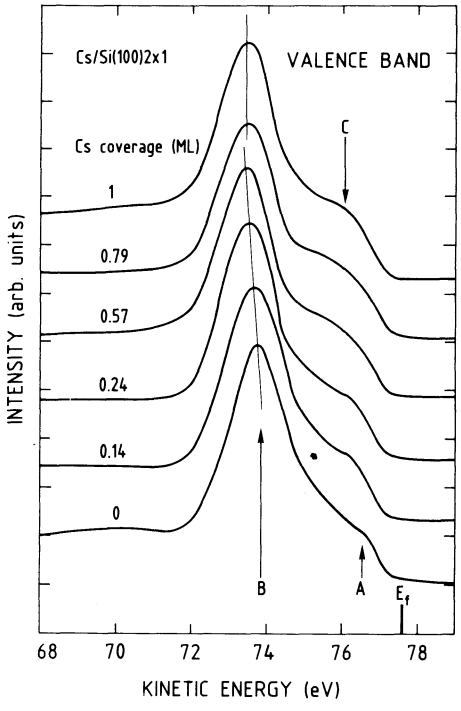

Figure 3 Valence Band spectra of the Cs/Si(100)2x1 interface for cesium coverages between 0 and 1 monolayers. The photon energy was 82 eV.

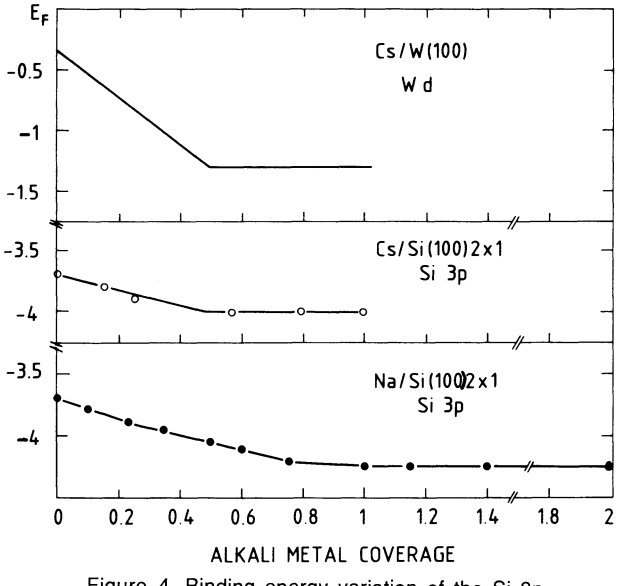

Figure 4 Binding energy variation of the Si 3p valence level versus sodium and cesium coverages on the Si(100)2x1 surface. These results are compared with the equivalent sequence on the s-d hybridized electronic state for the Cs/W(100) interface (reference 13)

Figure 3 displays the Si(100)2x1 valence band upon cesium coverages between 0 and 1 monolayer. Like with sodium, increasing Cs coverages induces a shift of the Si 3p level (peak B) towards higher binding energies by 0.3 eV at a coverage of 0.57 Cs monolayer. Between 0.57 and 1 Cs ML, peak B keeps the same binding energy at -4 eV below the Fermi level. Also, a similar electronic interface state derived from Si p surface level grows with increasing cesium coverages. Its binding energy is 0.44 eV higher (as refer to peak A) at the monolayer coverage than on the clean silicon surface. Like for the Na/Si(100) system, these results also indicate that Cs 6s valence electron hybridized with "p" surface state and "3p" electronic level of the silicon substrate. Figure 4 exhibits the binding energy variation of peak B for the various sodium and cesium coverages. These curves are compare to the similar one obtained for the coverage dependence of the W(100) "d_z2" state binding energy [13]. Here, the comparison between Cs/Si(100) and Cs/W(100) is striking: in both case, the "d_z2" state for tungsten and the "3p" state for silicon binding energy increased by 1 eV and 0.3 eV respectively up to the same half monolayer Cs coverage. Then, there are no other changes in their binding energy up to the saturation coverage of 1 monolayer. For the Na/Si(100) interface, the peak B related to the 3p level of silicon is almost continuously shifted by 0.55 eV to the higher binding energies from 0 to 1 sodium monolayer and keeps then a constant energy from 1 to 2 Na ML.

c) Cs 4d and Na 2p core levels

Figure 5 shows the Cs 4d core levels for various cesium coverage on the Si(100)2x1 surface. With increasing cesium coverages, the shape of the tail of the Cs 4d $_{5/2}$ on the low kinetic energy side changes as a result of plasmon excitation near the monolayer[40]. When the cesiated surface is subjected to low oxygen exposures, the tail existing at the monolayer coverage on the Cs 4d $_{5/2}$ on low kinectic energy side is removed for an exposure of 1 Langmuir, indicating the disappearance of the plasmon at this exposures. See figures 6 and 7. This is the results of charge transfer from the Cs adsorbate to the oxygen and is consitent with previous observations on Cu(111) surface [41]. This further confirm the existence of the plasmon within the alkali metal adsorbate. Figure 8 displays an equivalent sequence for the Na 2p on the same Si(100)2x1 surface. For increasing sodium coverages, a new broad structure appears at approximately 3.5 eV on the low kinetic energy side of the Na 2p core level at coverages above 0.6 sodium monolayer. The energy of this structure is consistent with sodium plasmon as observed on Cu(111) [41] and W(100) [42] surfaces. Further confirmation of the existence of a sodium plasmon can be found by oxygen chemisorption. Figure 9 exhibits the effect of small oxygen exposures on the Na 2p core level. An exposure

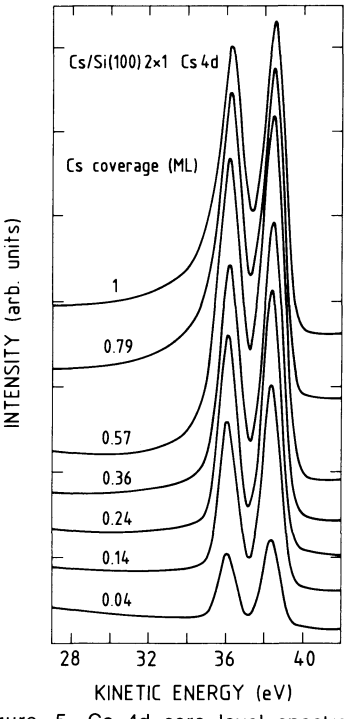

Figure 5 Cs 4d core level spectra for the Cs/Si(100)2x1 surface at cesium coverages between 0.04 and 1 monolayer. The photon energy was 120 eV

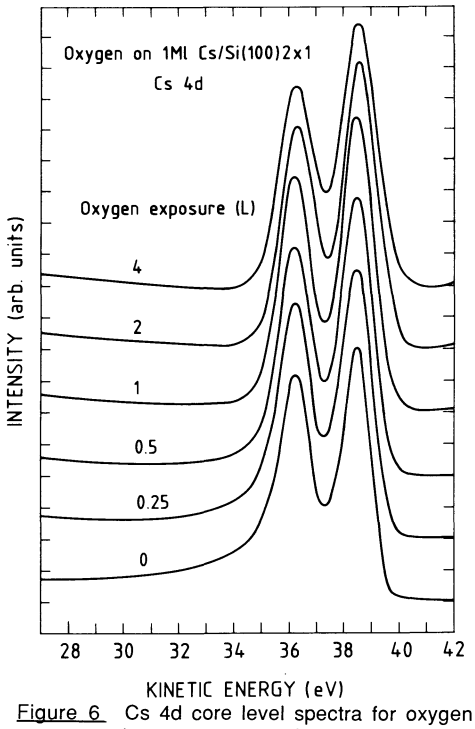

Figure 6 Cs 4d core level spectra for oxygen exposures between 0 and 4 Langmuir on the 1 ML Cs/Si(100)2x1 surface. The photon energy was 120 eV

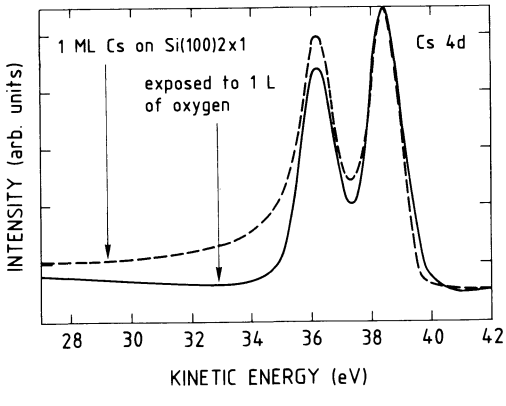

Figure 7 Comparison between Cs ad core level spectra for the 1 ML Cs/Si(100)2x1 and for the 1 Langmuir of O_2/ 1 ML Cs /Si(100)2x1 systems. The photon energy was 120 eV.

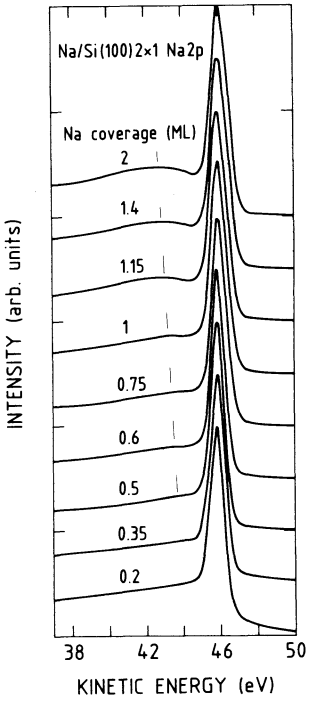

Figure 8 Na 2p core level spectra for the Na/Si(100)2x1 surface at sodium coverages between 0.2 and 2 sodium monolayers. The photon energy was 82 eV.

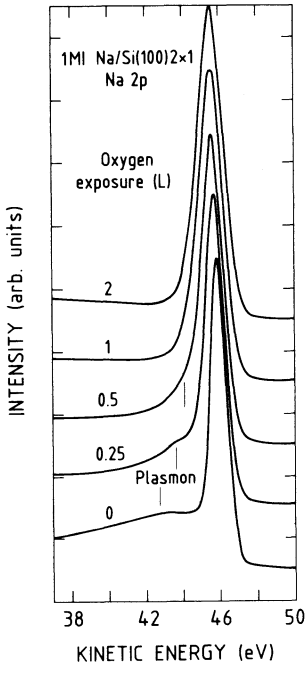

Figure 9 Na 2p core level spectra for oxygen exposures between 0 and 2 Langmuir of oxygen on the 1 ML Na/Si(100)2x1 surface. The photon energy was 82 eV.

to 0.25 Langmuir of oxygen decreases the plasma frequency, while at 1 Langmuir, the plasmon is completly removed. As for the Cs/Si(100)2x1 interface, this is the consequence of the effective charge transfer from sodium to oxygen. Above 1 Langmuir, the Na 2p core level is broadened which correspond to the onset of oxidation as previously reported [18]. This indicates that the surface metallization is remove below the oxidation threshold and further confirms [32] that surface metallization do not play a major role in the mechanism of catalytic oxidation.

DISCUSSION

It is now clear that the nature of the bonding between alkali metals and silicon system is not ionic. The absence of any significant chemical shift on the low binding energy side of the Si 2p core level for Cs, Rb, K, Na on Si(100)2x1 (fig. 1), Cs on Si(111)7x7 [32] and Cs and Na on Si(111)2x1 [38] is incompatible with a strong ionic bond [15]. Low electronegative species like calcium which give raise to significant charge transfer on silicon surface [30] induce in the monolayer range, large chemical shifts (1.1 to 1.35 eV) on the low binding side of the Si 2p core level. The absence of similar feature on alkali metal/silicon interface is also consistent with the lack of significant reaction between adsorbate and substrate and indicates that, there is no silicide formation between alkali metal and silicon, in opposition to the behavior of many other metal adsorbates like noble, transition or rare earth metals [43]. With the exception of lithium, the alkali metals do not diffuse through the silicon surface. The low temperature of desorption of sodium (550°C), potassium (600°C), rubidium and cesium (650°C) from Si(100)2x1 surfaces [24-27] unambiguously demonstrates that the alkali metal/silicon bond is weak [18,27].

Turning to the valence band results of the Cs/Si(100) 2x1 and Na/Si(100)2x1 interfaces, one could remark that alkali metals induce shift to higher binding energy of the silicon "p" levels (figures 2 and 3). The 3p electronic level of Si is shifted by 0.3 eV to higher binding upon deposition of Cs in the monolayer range while the shift reaches 0.55 eV for Na. This indicates Si 3p - Cs 6s and Si 3p - Na 3s hybridizations. Similarly, the Si p surface state located near the Fermi level and which is related to the silicon dangling bond has its intensity and binding energy increase with alkali metal deposition. It also indicates hybridization between Cs 6s or Na 3s and Si p giving raise to an electronic interface state. The fact that this interface state (peak C of figure 2 and 3) is more intense that the original Si p surface state, indicates that the alkali metal valence electron lose a part of its "s" chararacter by hybridizing with Si p. It also shows that, the silicon dangling bond play some role in the alkali metal chemisorption, which is partially in agreement with Ciraci and Batra's conclusions [15]. It is interesting to note that Cs and Na have been shown to induce new electronic structures just below the Fermi level on W(100) [13,44], Mo(100) [13] and Ta(100) [13,45] which are likely due to electronic emission coming from the adsorbate-substrate interface, and could therefore, as on alkali metal-semiconductor surfaces, be interpreted as electronic interface states. The s-p hybridization also occurs with the Si 3p bulk electronic levels as a

consequence of the rather extended wave function of alkali metal "s" valence electron. All these results also indicate that the alkali metal valence electron remain localized at the alkali metal/silicon interface. These findings clearly demonstrate that the alkali metal-silicon bond is covalent. Since alkali metal induce an important decrease of the silicon work function, this bonding is polarized which is consistent with the more localized nature of the "p" electrons. This picture is basically similar to the one described theoretically [11,12] and experimentally [13] on alkali metal/transition metal systems, where Cs and Na have been found to induce shifts of "d" electronic states on the (100) faces of tungsten [9,13,44], molybdenum [13] and tantalum [13,45] and on the (110) face of molybdenum [46] resulting in s-d hybridization. However, due to the rather low temperature of desorption the alkali metal/silicon covalent bond is weak, in contrast with transition metal surfaces. Despite the absence of any significant core level shift on the Si 2p core level which clearly eliminates the possibilty of a strong ionic bond, it is still possible that a small charge transfer might occurs below the detection limits of the present experiment. Such a small charge transfer was indeed observed on covalently bonded alkali metal/transition metal systems [31] and is compatible with the existence of a covalent bond between adsorbate and substrate. Finally, this covalent nature of the alkali metal/silicon bond is fully consistent with our recent SEXAFS experiments performed on the the K/Si(100)2x1 system. The K-Si bond length was found to be 3.14 Å, i.e. the exact sum of both K and Si atoms covalent radii.

The existence of plasmon within the Cs, Na (figures 5-9) and K [19,47] overlayers clearly indicates that the alkali adsorbate is metallic. This picture, while consistent with previous works based on electron energy losses [19] and photoemission [40] spectrocopies as well as theoretical calculations [47], is in conflict with the potassium induced silicon surface metallization predicted by the ab-initio pseudopotential calculations [15].

Very recently, Ling et al. using ab-initio FLAPW self-consistent total energy calculations (with a cluster model of 39 Si atoms) on the K/Si(100)2x1 interface [48] have determined the K-Si bond lenght for two different K adsorption models, the chain arrangement for the pedestal model [49] and for the cave model. In both cases, they found the same K-Si bond length, 3.22 Å which indeed is the closest value from our experimental measurement found using ab-initio self consistent calculations. However, their present investigations indicate that the cave model seems to be much more stable than the pedestal one, which might support the conclusions drawn in a recent photoelectron diffraction experiment on the same K/Si(100) system [50].

CONCLUSIONS

Using core level and valence band photoemission spectroscopy, we have demonstrated that the alkali metal-silicon bond is a weak and polarized covalent bonding. This conclusion is in excellent agreement with our surface EXAFS measurements on the K/Si(100)2x1 system.

The alkali metal "s" valence electron hybridizes with silicon "2p" and "3p" electronic levels and remains localized at the adsorbate/substrate interface. Also, all alkali metals were found to induce an electronic interface state near the Fermi level. Through alkali metals induce plasmon on silicon surface, the alkali adsorbate is found to be metallic. Our results are inconsistent with theoretical pseudopotential calculations predicting a very short K-Si bond length, a strong ionic bonding between potassium and silicon and silicon surface metallization. In this theoretical investigation, the maximum decrease of the work function for the K/Si(100)2x1 system was found to be of 2.2 eV instead of 3.2 eV for the experimental value [37]. This indicates that the representation used in this pseudopotential calculation seems to correspond to a potassium coverage well below half a monolayer. In this case, a more "ionic bond" could eventually be found and might partially explain the discrepancies with our conclusions. Our picture is similar to the one described for the alkali metal/transition metal interfaces [11-13].

PART II

IMPORTANT ISSUES IN THE CHEMISORPTION AND SCHOTTKY BARRIER FORMATION OF ALKALI METAL/III-V SEMICONDUCTOR SYSTEMS: EXAMPLE OF THE Na/GaAs (110) INTERFACE

INTRODUCTION AND RESULTS

There is a renewed interest in alkali metal overlayers on III-V semiconductors. These interfaces were studied in the past from the point of view of work function lowering which can lead to many important applications. Recently, new emphasis is placed on chemisorption, Schottky barrier formation and catalytic reactions. We recently studied several alkali metal/III-V semiconductor interfaces. Our results will be illustrated with the example of the Na/GaAs(110) interface. Some data for the Na/InP interface will be also presented here for comparison. Cleavable GaAs and InP crystals were used in this work. All other experimental conditions are similar to those described in part I of this paper for Si. We limit our concentration to the Na coverages of up to about 1 ML. This is to avoid effects of contamination brought forth by extensive Na exposures. We have evidence that contamination in an important way affects the physical properties of the system including band bending and chemical reactions. Below one ML at RT we see very limited reaction of Na with the substrate. Still at these coverages, very pronounced band bendings take place, which are of central interest in this part of the investigation.

Figures 10 and 11 present the evolution of the Ga 3d and As 3d core levels for n- and p-GaAs covered with increasing amounts of Na. There are no important changes of the Ga 3d lineshape, although Na induces large changes in the core level kinetic energies. These are taken

as a measure of the band bending. The changes for the As 3d are similar, although for some cleaves close to 1 ML we observed a high kinetic energy shoulder perhaps indicating some interaction with the substrate (see top spectra in Fig. 11). An example of the valence band spectra from the Na/GaAs(110) interface is shown in Fig. 12. These spectra also show no evidence of reaction. The conclusion that Na does not react to form new phases does not preclude the possibility of strong chemisorption. There is also no evidence that the overlayer is metallic by 1 ML. The VB spectra show only some broadening on the high kinetic energy side. The backshift of the spectra due to band bending is partially responsible for this. Clearly, however, the Fermi edge does not develop in this coverage range which might be due to the fact that the alkali metal "s" valence electron has a very low cross section for the photon energies used in this experiment.

In Fig.13 we plot the surface Fermi level shift deduced from the core level spectra of figures 10 and 11. One sees sharp movement of the Fermi level for both types of doping for coverages below 0.1 ML. Above this coverage the changes in the Fermi level position relative to the GaAs band edges are less pronounced and for the higher exposures for both n- and p- type GaAs a gradual shift to 0.5 eV above the valence band maximum is observed. To assess the reproducibility the data were taken on several cleaves. The scatter in the data is less than 0.1 eV and trends are idendical. At low coverage the data consistently show very strong band bending on p-GaAs followed by a gradual decrease at higher coverages ("overshoot"). These changes of the Fermi level are similar to what was reported for some other overlayers on GaAs especially at low temperatures [51,52].

Additionally, information on the alkali metal chemisorption can be provided by the overlayer core level spectra. In our previous work, we reported large splittings of the Cs 4d core levels at the initial stages of the Cs/GaAs(110) and Cs/InP(110) interface formation [53,54]. These splittings were interpreted as indication of multisite chemisorption. For the Na/GaAs(110), no such splitting has been seen. The changes in the Na 2p for one of the cleaves are illustrated in fig 14. We observe one single peak (the very small spin-orbit splitting of Na 2p is not resolved) which at higher coverages shifts to lower binding energy - a behavior typical for overlayers. The Na 2p for the Na/InP(110) interface behaves in a very different fashion. A sample of this data is seen in fig 15. In this case, we observe a multicomponent spectrum. The evolution of the intensity ratio between components is, however, somewhat different that what we reported for Cs core levels on GaAs and InP. The reasons for these apparent differences are not clear and require further work which is in progress. Anyway, it also indicates a multisite for the Na atoms at low coverages. Furthermore, as for the Cs/GaAs(110) [53] and Cs/InP(110) [54] interfaces, the difference in the binding energies for each site suggests a difference in the ionicity.

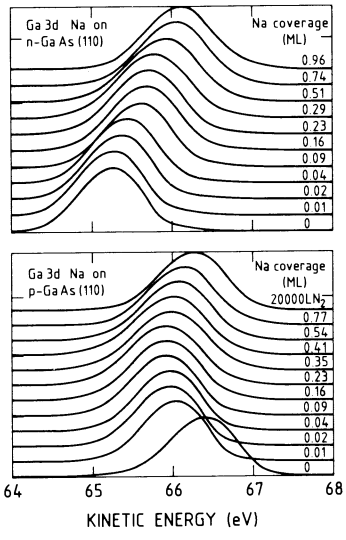

Figure10 The Ga 3d spectra of Na/GaAs(110) at room temperature.

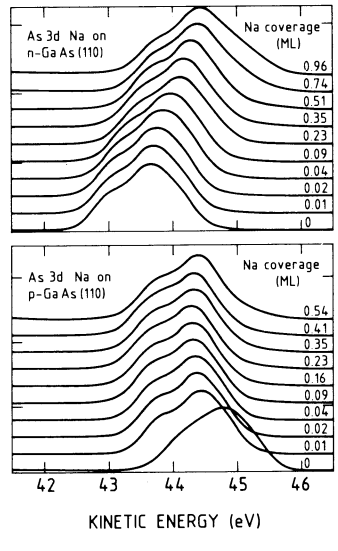

Figure11 The As 3d spectra of Na/GaAs(110) at room temperature.

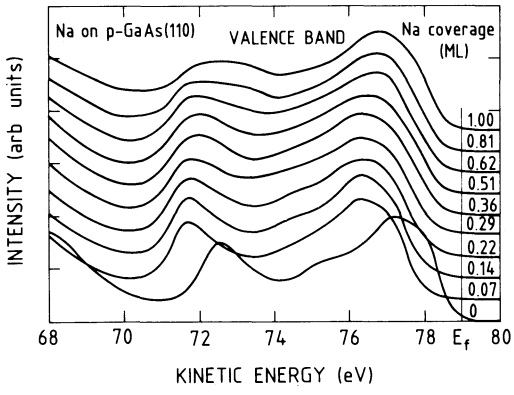

Figure12 Valence band spectra of the Na/GaAs(110) interface at room temperature.

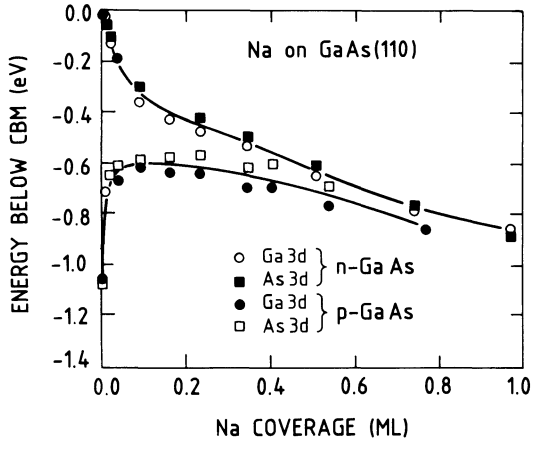

Figure13 The band bending diagrams for n- and p-type GaAs(110) at room temperature determined from the Ga 3d and As 3d core level shifts as a function of Na coverage.

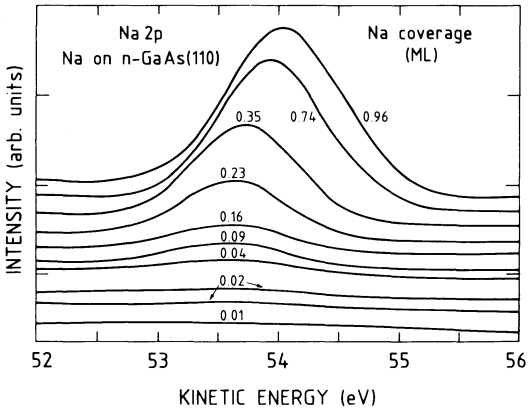

Figure14 The Na 2p spectra of the Na/GaAs(110) interface.

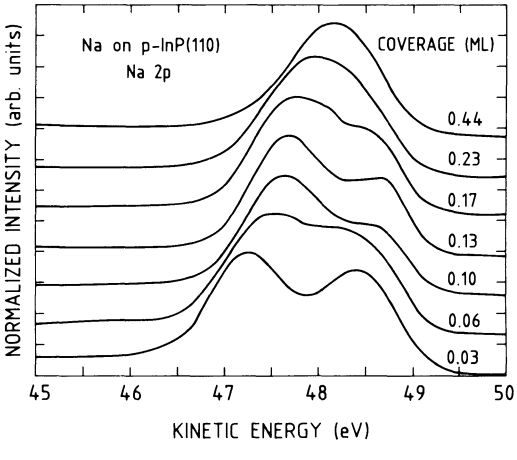

Figure 15 The intensity normalized spectra of the Na/InP(110) interface at selected Na coverages.

DISCUSSION

Recently, Na/GaAs(110) Schottky barriers with 800 Å thick Na layers were studied electrically *in situ* using conventional current-voltage (I-V) and capacitance-voltage (C-V) techniques by McLean et al. [55]. On the basis of I-V and C-V measurements the authors concluded that, contrary to what might be expected on the basis of the Schottky like models, the barrier height for Na on n-GaAs is quite high (about 0.7 (0.69-0.72) from I-V and 0.8 (0.76-0.82) from C-V data) and similar to barriers of many other metals (ex. Mn, V, Sb, Al, Cr) with much higher work functions or electronegativities. In our PES study of Cs on GaAs [53] and InP [54] we came to the same conclusions.

Very recently the Na/GaAs system has been studied at room and lower temperature by Prietsch et al. [56]. We believe that their results are in large part consistent with ours. One apparent difference is the claim made by the authors that the interface is reactive at RT. In their data, the evidence of reaction becomes clear only at high coverages. Our experience indicates that at that point, the interface can easily be contaminated. Although the pressure during exposures in our experiment was an order of magnitude better for very high exposures (not reported) we have clearly observed in some cases, evidence of contamination in the valence band spectra. Good vacuum conditions as well as very low pressure increase during alkali metal deposition are particularly important for alkali metal overlayers which act as catalysts for oxidation and other surface reactions [18,24,32]. Prietsch et al. [56] do not report VB spectra, so it is difficult to trace down if contamination might be the problem. Our band bending results resemble more closely the data Prietsch et al. report for low temperature. Despite some minor differences, very strong similarities in both studies should be emphasised. In both cases, strong overshooting (considered below) and similar stabilization energies for high coverages are documented. These sets of data and electrical results of McLean et al. [55] clearly establish a consensus that the alkali metal pin the Fermi level very deep in the band gap. This observation is important because Schottky-like model for III-V are still being considered [57].

The data on band bending presented in Fig. 13 require more detailed analysis. We argue that much of the data for very small coverages on p-GaAs can be explained in terms of the chemisorption of the metallic atoms. Monch was the first to suggest that metals on GaAs are likely to act as donors and thus induce large band bendings on the p- but not on the n-type GaAs crystals [58]. This mechanism, which explains the asymmetry of band bending for low temperature grown interfaces, gets strong support from the photoemission results on RT alkali metal studies. These atoms have the lowest first ionization potentials of any species and are very likely to be donors and yield particularly large band bendings (overshootings) on p-type substrates at the initial stage of the chemisorption (the isolated alkali metals donate the external "s" electrons to the substrate producing a barrier proportional to the square of the charge transfer). For the Na/GaAs interface, we find a large band bending of 0.8 eV. In the data presented by Spicer et al. elsewhere in this proceedings, a shift as large as 1.1 eV is reported for the Cs/GaAs(110) interface. This is in good agreement with our independent study. We

studied also the K/GaAs(110) and Rb/GaAs(110) systems for which intermediate values (0.9-0,95 eV) were observed [59]. Thus, as expected for the discussed mechanism, the maximum of the band bending on the p-GaAs is indeed inversely proportional to the ionization potential of the alkali metal. This mechanism is probably important only at small coverages, and another mechanism has to be invoked to explain Schottky barriers in the thick overlayer regime. A closer look at the data indicate, however, that yet another mechanism needs to be considered even at the low coverages. The alkali metal can act as donors but not as acceptors, and therefore it is not clear how to account for the band bending present from the very beginning of the interface formation on n-GaAs. We tentatively assign this to a defect mechanism [60]. In some previous studies at low temperature the band bending could be fully supressed for a relatively large range of coverages. This was explained by inhibition of the formation of island which were sought to be responsible for the kinetics of the defect formation. For alkali metals the island formation even at RT is not likely due to the very nature of the alkali metal-alkali metal interaction (dipolar repulsion). We argue that defects could be formed because of large heats of condensation of alkali metals (as proposed by Spicer in first papers introducing the defect model [60]). With this mechanism, one can explain easily why defects could be formed even at the very beginning of metal deposition.

The mechanism of the high coverage Fermi level pinning is of particular interest because it determines characteristics of practical devices. Recently, several authors reported important changes in the Fermi level movement close to, what they believed, was the onset of the metallicity [61,62]. The claim was made that these data provide a clear-cut evidence in favor of the MIGS mechanism [63]. The defects, even if present earlier, would be screened by formation of the metallic overlayer. A very recent work of Ludeke et al. [64] cast some doubt that these data are conclusive. As a matter of fact, they show that changes similar to these observed by Kaindl's and Kahn's group could be explained by a defect mechanism. Interestingly, the exposition of the Na/p-GaAs interface to an acceptor specie like nitrogen (Fig. 10) induce an additionnal shift to higher kinetic energies of the Ga 3d core level indicating thereby band bending reduction. A similar band bending reduction was observed on the Cs/n-GaAs and K/n-GaAs systems exposed to nitrogen as well as on the K/n-GaAs [53] and the Cs/n-InP ones exposed to oxygen [65]. This suggests removal of the MIGS mechanism. We believe that both the MIGS and defect mechanisms are important and which one is more important depends on how disrupted is the interface. The MIGS mechanism seems to be more appropriate for the nonreactive interfaces. The defect mechanism has to be seriously considered for the strongly reactive interfaces where a large density of defect states are not likely to be screened by the metallic overlayer (the calculations by Zhang and Cohen [66] are particularly illuminating on this). Going back to the results for the Na/GaAs interface we notice that Prietsch et al. find their data to be consistent with MIGS model at high coverages [56]. We, however, argue that the pinning at the energy in close agreement with electrical data is established for thicknesses at which the overlayer is not yet metallic. The conclusive evidence on this is yet to be given. The work of Spicer et al. in this proceedings elaborates more on this subject.

ACKNOWLEDGEMENTS

We are grateful to Professor Ye Ling and to Professor Art Freeman for informing us of their theoritical investigations on the K/Si(100)2x1 system prior to publication. This work was supported by the NATO, the U.S. National Science Foundation under contracts DMR 84-05173 & 88-07754 through the Northern Illinois University and DMR 83-13523 through the University of Wisconsin-Madison, the U.S. Office of Naval Research under contract No. N00014-83-K-0073 through the Stanford University and by the Dow Corning Corporation. We thank the technical staff of the Synchrotron Radiation Center of the University of Wisconsin-Madison for its expert and outstanding technical assistance.

References

1. G.N. Hatsopoulos and E.P. Gyftopoulos, Thermionic Energy Conversion, Cambridge, Massachusetts, MIT Press, (1979).

2. Chen Chou Wang, J. Appl. Phys. 48, 1477 (1977).

3. M.E. Dry, T. Shingles, L.J. Boshoff and G.J. Ousthuizen, J. Catalysis15, 190 (1969); J.G. Van Ommen, W.J. Bolink, J. Prasad and P. Mars, ibid, 38, 120 (1975).

4. J.R. Hiskes and P.J. Schneider, Phys. Rev. B 23, 949 (1980); K.N. Leung and K.W. Ehlers, Rev. Sci. Instr. 53, 803 (1982).

5. F. Capasso, Science 235, 172 (1987).

6. I. Langmuir, J. Am. Chem. Soc. 54, 2788 (1932); Phys. Rev. 43, 224 (1933)

7. J. Topping, Proc. Roy. Soc. A 114, 67 (1927).

8. J.D. Levine and E.P. Gyftopoulos, Surf. Sci. 1, 171 (1964); A.J. Bennett and L.M. Falicov, Phys. Rev. 151, 512 (1966); J.W. Gadzuk, Surf. Sci. 6, 133 (1967); J.P. Muscat and D.M. Newns, ibid, 74, 355 (1978).

9. P. Soukiassian, R. Riwan and Y. Borensztein, Sol. State Commun. 44, 1375 (1982); P. Soukiassian, R. Riwan, C. Guillot, J. Lecante and S. Zuber, Phys. Scr. T 4 (Sweeden), 110, (1983).

10. S.L. Weng, E.W. Plummer and T. Gustafsson, Phys. Rev. B 18, 1718 (1978); W. Drube, I. Straub, F.J. Himpsel, P. Soukiassian, C.L. Fu and A.J. Freeman, Phys. Rev. B 34, 8989 (1986).

11. E. Wimmer, A.J. Freeman, J.R. Hiskes and A.M. Karo, Phys. Rev. B 28, 3074 (1983); S.R. Chubb, E. Wimmer, A.J. Freeman, J.R. Hiskes and A.M. Karo, Phys. Rev. B 36, 4112 (1987).

12. Ruqian Wu, Kailai Chen, Dingsheng Wang and Ning Wang, Phys. Rev. B 38, 3180 (1988).

13. P. Soukiassian, R. Riwan, J. Lecante, E. Wimmer, S.R. Chubb and A.J. Freeman, Phys. Rev. B 31, 4911 (1985).

14. J.R. Northrup, J. Vac. Sci. Technol. A 4, 1404 (1986).

15. S. Ciraci and I.P. Batra, Phys. Rev. Let. 56, 877 (1986); ibid, 58, 1982 (1987); Phys. Rev. B 37, 8432 (1988).

16. H. Tochihara, M. Kubota, M. Miyao and Y. Murata, Surf. Sci. 158, 497 (1985).

17. P. Soukiassian, Surf. Sci. Let. 172, L507 (1986).

18. P. Soukiassian, T.M. Gentle, M.H. Bakshi, A.S. Bommannavar and Z. Hurych, Phys. Scr. 35 (Sweeden), 757 (1987).

19. T. Aruga, H.Tochihara and Y. Murata, Phys. Rev. Let. 53, 372 (1984).

20. R.V. Kasowski and M.H. Tsai, Phys. Rev. Let. 60, 546 (1988).

21. E.M. Oellig and R. Miranda, Surf. Sci. Let. 177, L947 (1986).

22. T. Kendelewicz, P. Soukiassian, R,S, List, J.C. Woicik, P. Pianetta, I. Lindau and W.E. Spicer, Phys. Rev. B 37, 7115 (1988).

23. J.L. Desplat and C.A. Papageorgopoulos, Surf. Sci. 92, 97 (1980).

24. P. Soukiassian, T.M. Gentle, M.H. Bakshi and Z. Hurych, J. Appl. Phys. 60, 4339 (1986).

25. E.M. Oellig, E.G. Michel, M.C. Asensio and R. Miranda, App. Phys. Let. 50,1660 (1987); E.G. Michel, E.M. Oellig, M.C. Asencio and R. Miranda, Surf. Sci. 189/190, 245 (1987).

26. H.I. Starnberg, P. Soukiassian and Z. Hurych, to be published.

27. P. Soukiassian, M.H. Bakshi, Z. Hurych and T.M. Gentle, Phys. Rev. B 35, 4176 (1987).

28. I.P. Batra and P. Bagus, J. Vac. Sci Technol. A 6, 600 (1988).

29. F.R. McFeely, J.F. Morar, N.D. Shinn, G. Landgren and F.J. Himpsel, Phys. Rev. B 30, 764 (1984); J.F. Morar, F.R. McFeely, N.D. Shinn, G. Landgren and F.J. Himpsel, Appl. Phys. Let. 45, 174 (1984).

30. A. Franciosi, J.H. Weaver and D.T. Peterson, Phys. Rev. B 31, 3606 (1985).

31. P. Soukiassian, R. Riwan, J. Cousty, J. Lecante and C. Guillot, Surf. Sci.152/153, 290 (1985).

32. H.I. Starnberg, P. Soukiassian, M.H. Bakshi and Z. Hurych, Phys. Rev. B 37, 1315 (1988).

33. P. Soukiassian, M.H. Bakshi, H.I. Starnberg, Z. Hurych, K.P. Schuette and T.M. Gentle, Phys. Rev. Let. 59, 1488 (1987); P. Soukiassian, T.M. Gentle, K.P. Schuette, M.H. Bakshi and Z. Hurych, Appl. Phys. Let. 51, 346 (1987).

34. P. Soukiassian, R. Riwan and J. Lecante, Surf. Sci. 152/153, 522 (1985); R. Riwan, P. Soukiassian, S. Zuber and J. Cousty, Surf. Sci 146, 382 (1984).

35. T.M. Gentle, P. Soukiassian, K.P. Schuette, M.H. Bakshi and Z. Hurych, Surf. Sci. Let. 202, L 568 (1988).

36. P. Soukiassian and R. Riwan, unpublished results (1981)

37. Y. Enta, T. Kinoshita, S. Suzuki and S. Kono, Phys. Rev. B 36, 9801 (1987).

38. A. Franciosi, P.Soukiassian, P. Philip, S. Chang, A. Wall, A. Raisanen and N. Troullier, Phys. Rev. B 35, 910 (1987).

39. G. Hollinger and F.J. Himpsel, Phys. Rev. B 28, 3651 (1983).

40. H. Tochihara, K. Kubota and Y. Murata, Sol. Stat. Commun. 57, 437 (1986).

41. S.A. Lindgren and L. Wallden, Phys. Rev. B 22, 5967 (1980) and references therein.

42. J. Cousty, R. Riwan and P. Soukiassian, J. Physique (Paris) 46, 1693 (1985).

43. J. Derrien and F. Ringeisen, Surf. Sci. Lett. 124, L235 (1983); A. Franciosi , S. Chang, P. Philip, C. Caprile and J. Joyce, J. Vac. Sci. Technol. A 3, 933 , (1985); F.U. Hillebrecht, M. Ronay, D. Rieger and F.J. Himpsel, Phys. Rev. B 34, 5377 (1986).

44. J. Cousty, R. Riwan, P. Soukiassian and F. Mila, J. Phys. C, 19, 2889 (1986).

45. J. Cousty and R. Riwan, Europhysics Lett. 3, 1119 (1987).

46. P. Soukiassian, P. Roubin, J. Cousty, R. Riwan and J. Lecante, J. Phys. C 18, 4785, (1985).

47. H. Ishida, N. Shima and M. Tsukada, Phys. Rev. B 32, 6236 (1985).

48. Ye Ling, A.J. Freeman and B. Delley, private communication and to be published.

49. H. Tochihara, Surf. Sci. 126, 523 (1983).

50. T. Abukawa and S. Kono, Phys. Rev. B 37, 9097 (1988).

51. R. Cao, K. Miyano, T. Kendelewicz, K. K. Chin, I. Lindau and W. E. Spicer, J. Vac. Sci. Technol. B 5, 998 (1987); R. Cao K. Miyano, T. Kendelewicz, I. Lindau, and W. E. W. Spicer, Appl. Phys. Let. 53, 210 (1988).

52. K. Stiles, A. Kahn, D. G. Kilday and G. Margaritondo, J. Vac. Sci. Technol. B5, 987 (1987).

53. T. Kendelewicz, P. Soukiassian, M. H. Bakshi, Z. Hurych, I. Lindau, and W.E. Spicer, Phys. Rev. B 38, 15 October, (1988) and J. Vac. Sci. Technol. A6, 1569 (1988).

54. T. Kendelewicz, P. Soukiassian, M. H. Bakshi, Z. Hurych, I. Lindau, and W.E. Spicer, J. Vac. Sci. Technol. B6, 1331 (1988).

55. A. B. McLean, D. A. Evans, and R. H. Williams, to be published in Semicond. Sci. Technol.

56. M. Prietsch, C. Laubschat, M. Domke, and G. Kaindl, Europhys. Let. 6, 451 (1988).

57. L.J. Brillson, R.E. Vitturo, M.L. Slade, P. Chiaradia, D. Kilday, M.K. Kelly and G. Margaritondo, Appl. Phys. Lett. 50, 1379 (1987); L. J. Brillson, M. L. Slade, R. E. Vitturo, M.K. Kelly, N. Tache, G. Margaritondo, J. M. Woodall, P. D. Kirchner, G, D. Pettit, and S. L. Wright, Appl. Phys. Let. 48, 1458 (1986).

58. W. Monch, J. Vac. Sci. Technol. B6, 1270 (1988).

59. T. Kendelewicz and P. Soukiassian, unpublished

60. W. E. Spicer, I. Lindau, P. Skeath, C. Y. Su, and P. Chye, Phys. Rev. Let. 44, 420 (1980).

61. M. Prietsch, M. Domke, C. Laubschat, and G. Kaindl, Phys. Rev. Let. 60, 436 (1988).

62. K. Stiles, A. Kahn, Phys. Rev. Let. 60, 440 (1988).

63. S. G. Louie, J. R. Chelikovsky, and M. L. Cohen, Phys. Rev. B15, 2154 (1977); J. Tersoff, Phys. Rev. Let. 52, 465 (1984).

64. R. Ludeke, G. Jezequel, A. Taleb-Ibrahimi, Phys. Rev. Let. 61, 601 (1988), and J. Vac. Sci. Technol. B6, 1277 (1988).

65. P. Soukiassian, M.H. Bakshi and Z. Hurych, J. App. Phys. 61, 2679 (1987).

66. S. B. Zhang, M. L. Cohen, and S. B. Louie, Phys. Rev. B32, 3955 (1985).

ADSORPTION OF Cs ON HYDROGENATED W(110) SURFACES

C.A. Papageorgopoulos

Department of Physics
University of Ioannina
P.O. Box 1186
GR-452 10 Ioannina, Greece.

I. INTRODUCTION

The coadsorption of cesium and gases on semiconducting and metallic substrates is a subject of great interest.

Cesium and O_2 on metallic and semiconducting substrates provide low work function surfaces,[1-3] which are appropriate for photocathodes and thermionic energy converters.[4,5] Submonolayers of Cs can be used as catalysts in the oxidation of semiconductors, especially in the formation of $Si-SiO_2$ interfaces of high technological importance.[6,7] Cesium is also used in many other chemical reactions such as $H_2O+CO \rightarrow CO_2+H_2$ for H_2 production.[8] Recently, cesiated transition metal surfaces as those of tungsten and molybdenum are used for the production of negative hydrogen ions.[9] These systems are characteristic by low work function, low H sticking coefficient[10,11] and high yield of backscattered and sputtered negative ions.[12,13] Beams of energetic H^- ions are needed for neutral beam heating of future fusion plasma.[14] The formation of H^- ions in the H-Cs/W surface collision is affected strongly by the adsorption of hydrogen atoms.[15] However, the actual mechanism of this effect has not been explained completely. This is reasonable since the coadsorption of Cs and H_2 on metallic substrates has not been yet understood.

According, to our previous reports of Cs and H_2 coadsorption on W(100),[11] the work function at maximum coverage of Cs on W(100), Φ_{max}, was increasing with increasing amount of preadsorbed hydrogen.[10] These

data also showed that the work function minimum, Φ_{min}, which was measured before the completion of a Cs monolayer on clean W(100) was shifted to smaller values of Cs coverage with increasing amount of preadsorbed hydrogen. The increase of Φ_{max} was correlated to the increase of work function during hydrogen adsorption on clean W(100).[10] Unlike W(100), the work function of W(110) was decreasing upon hydrogen adsorption at 300 K.[16,17] This basic difference of the behavior of H on clean W(100) and W(110) surfaces raises questions which initiated the present work of Cs and H_2 coadsorption on W(110) surface. Moreover, a W(110) surface covered with a submonolayer of Cs has promising characteristics for negative ion formation.[14]

The present paper refers the study of Cs deposition on H precovered W(110) surfaces. These studies prerequire detailed knowledge of the separate adsorption of H_2 and Cs on clean W(110). The results are compared with relevant reported studies.

2. EXPERIMENTAL

The experiments were performed in an UHV system equipped with surface analysis techniques for Auger electron spectroscopy (AES), thermal desorption spectroscopy (TDS) and work function (WF) measurements. The TDS measurements were made with a quadrupole mass spectrometer capable of detecting mass to charge ratios up to 300. The WF changes were measured with a Kelvin probe. Absolute work functions were obtained by assuming a clean W(110) work function value of 5.3 eV.[18]

The W(110) specimen (15x6x0.15) mm could be resistively heated up to 2500 K. The crystal temperatures were measured by a W-Re thermocouple attached at the back side of the crystal. The specimen was cleaned in the vacuum system by heating to ~1300 K in O_2 at 10^{-7} torr with intermediate flashings to 2500 K. Auger measurements were used to follow the cleaning of the crystal.

Spectroscopically pure H_2 was admitted to the system through a bakable leak-valve. Atomic cesium was deposited from a Knudsen fusion cell containing metallic cesium (99.99% pure). A leak valve prevented the spreading of cesium over the rest of the chambers. While a shutter was used to accurately dose the specimen with Cs. A rotatable surface ionization detector with a Pt ionizer could be moved into a position in front of the Cs source to determine the Cs flux which was kept constant at 7.4×10^{12} $cm^{-2}s^{-1}$.

3. SEPARATE ADSORPTION OF HYDROGEN AND CESIUM

3.1 H_2 on clean W(110)

As we mentioned in the introduction, the study of the coadsorption of H_2 and Cs on W(110) prerequires detailed knowledge of the behavior of each adsorbate alone on clean W(110).

Adsorption of hydrogen on W(110) has been reported in many instances.[16,17,19]

Thermal desorption results indicate that hydrogen on clean W(110) has two adsorption states β_1 and β_2. These results will be shown later in this paper in correlation with the hydrogen desorption spectra for Cs/H/W(110). The first adsorption state, β_2, of hydrogen on W(110) corresponds to θ_H=0.5 (which requires about 3L of hydrogen exposure) and the H atoms occupy 3-fold sites of the W(110) substrate. Above 0.5 ML, the hydrogen atoms reside on top of the W atoms of the susbstrate and constitute the second adsorption binding state , β_1.[17]

As it is mentioned in the introduction adsorption of hydrogen on a W(110) surface causes a decrease in WF, in contrast to W(100) surface where the work function increases with hydrogen adsorption.[17] This basic difference may result a different behavior of Cs on H/W(100) and H/W(110) surfaces and probably help to understand the mutual effects of Cs and H on W substrates.

3.2 Cs on clean W(110)

Figure 1 shows the Auger peak height of Cs (560 eV), W(170 eV) and WF versus Cs deposition time at RT. Initially, the Auger peak height of W substrate decreases linearly while that of Cs increases linearly with Cs deposition and both approach a plateau at the time when the WF reaches its maximum value. This indicates that Cs is deposited uniformly in a single monolayer and does not form a second layer on W(110) at RT, in contrast to W(110) at low temperatures (LT) where Cs grows a second layer.[2,20] As it is seen in fig. 1, deposition of Cs on W(110) gives the characteristic WF curve of Cs on metal surfaces.[1,2] Initially the WF decreases with Cs deposition, it goes through a minimum value Φ_{min} = 1.4 eV at θ_{Cs} = 0.22 ML and subsequently increases to a maximum value Φ_{max} = 2.15 eV at θ_{Cs} = 0.37 ML, saturation coverage of Cs. The Cs coverage could be calculated from the Cs flux. The calculations agree quite well with the correlation of AES and WF measurements and also with published work.[2]

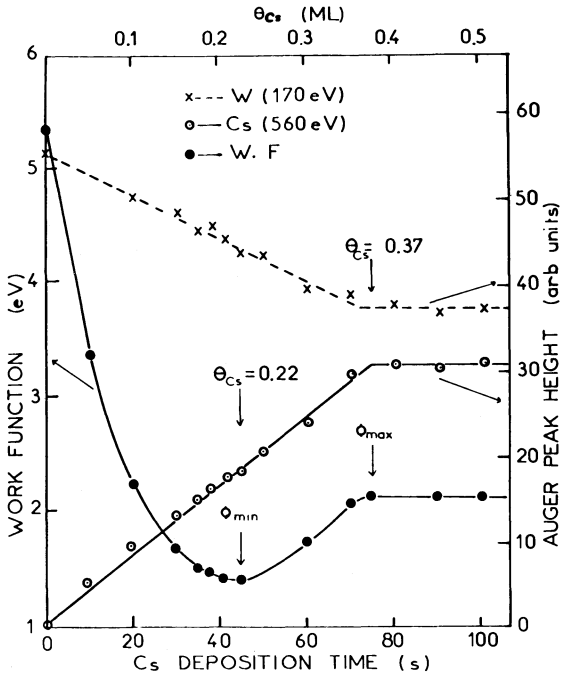

Fig. 1. Work function and Auger peak heights of Cs (560 eV) and W(170eV) versus Cs deposition time on W(110) surfaces at RT.

4. CESIUM ADSORPTION ON HYDROGENATED W(110)

4.1 WF Measurements

Figure 2 shows the WF versus Cs deposition on clean W(110) and H-covered W(110) surfaces.

In each of these curves there is an initial WF minimum, Φ_{min}, and a subsequent maximum, Φ_{max}, at saturation Cs coverage. As it is seen in this figure, the Φ_{min} is lowered and shifted to smaller Cs coverage with increasing amount of preadsorbed hydrogen. Moreover, the increase of the initial hydrogen coverage causes the Φ_{max} to increase. These measurements are quite similar to those of Cs on H-covered W(100) surfaces.[10] However, due to the lack of other correlated techniques such as AES and TDS, the explanation of the WF results was difficult. An explanation of the lowering of Φ_{min} with increasing amount of preadsorbed H was based on the theory of work function by Lang and Kohn.[22] However, it has not been given any satisfactory explanation in Ref. 10. for the increase of the Φ_{max} and the shift of Φ_{min} to lower Cs coverage with increasing amount of preadsorbed

H. A possible cause of the Φ_{min} shift could be an increase of the sticking coefficient of Cs with increasing amount of preadsorbed H on W(110). However, this possibility should not be considered, because, first, it is generally believed that the sticking coefficient of Cs on metals is very close to one and second, the following AES and TDS meaurements do not indicate any change of Cs sticking coefficient in the presence of H on W(110).

4.2 AES measurements

Figure 3 shows the variation of Cs(560 eV) peak height versus deposition time of Cs on H-covered W(110) surfaces as compared to that on clean W(110). The almost linear variation of these curves suggest that the adsorption of Cs on H/W(110) is uniform, in agreement with LEED observations. The important message of this figure is that the presence of H on the W(110) surfaces does not cause any substantial change of the sticking coefficient of Cs on the surface. This is important because it precludes the attribution of the shift of Φ_{min} (fig. 2) to a change in sticking of Cs with increase amount of preadsorbed H. Near saturation coverage, the peak height decreases slightly as the amount of preadsorbed H increases. This may indicate a decrease of the maximum amount of Cs that can be deposited on W(110) at RT with increasing amount of predeposited H.

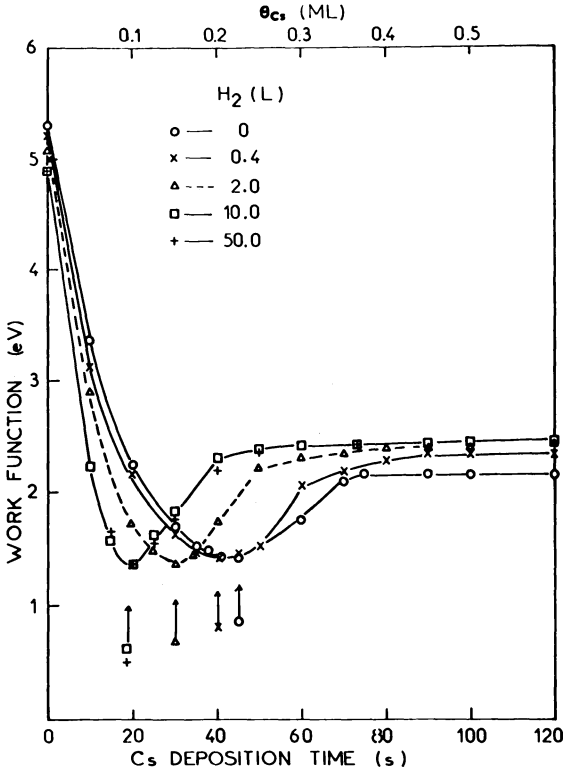

Fig. 2. Work function versus Cs deposition time on clean and H-covered W(110) surfaces.

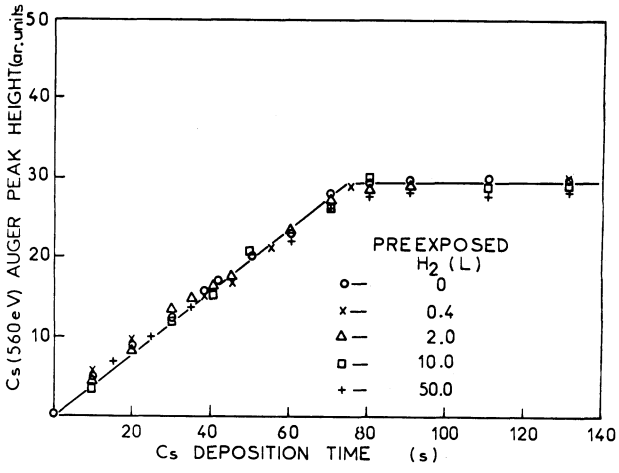

Fig. 3. Auger peak height of Cs(560 eV) versus Cs deposition time on H-covered W(110) surfaces.

4.3 TDS Meaurements

(a) TDS of Cs

Figs 4a and 4b show two series of thermal desorption spectra of Cs from Cs/W(110) and Cs-covered H/W(110) surfaces, respectively. The spectra in Fig. 4a are similar to those reported previously.[2] The heating rate of the substrate during Cs desorption was ~300 K s^{-1}. The relatively fast heating rate was necessary to minimize diffusion of Cs out of the specimen area sampled by the mass spectrometer. Neutral desorption spectra from Cs/W(110) indicate rather a continuous decrease of the desorption energy as the Cs coverage increases. These spectra are shown for comparison with those of Cs from hydrogenated W(110) surfaces (Fig. 4b). In Fig. 4b, the coverage of the preadsorbed hydrogen is about 0.5 ML, which correspond to β_2 adsorption state. Except of a shift to lower temperatures, the preadsorbed hydrogen does not cause any substantial change of the Cs-peak shapes. When the amount of preadsorbed H increases, the Cs-peaks are shifted farther to lower temperatures, while, the peak-shapes are about the same. The shift of Cs-peaks to lower temperature suggests that the presence of hydrogen on W(110) decreases the binding energy of the subsequently deposited Cs. This decrease is greater with increasing amount of preadsorbed H. However, the areas under the curves in in Fig. 4b are not substantially different than those of the corresponding curves in Fig. 4a. This indicates that the preadsorbed H does not influence the sticking coefficient of Cs on W(110), which is in agreement with the fact that all the curves in Fig. 3 have almost the same initial slope.

(b) TDS of H_2

Figs 5a and 5b show two series of hydrogen TDS spectra from

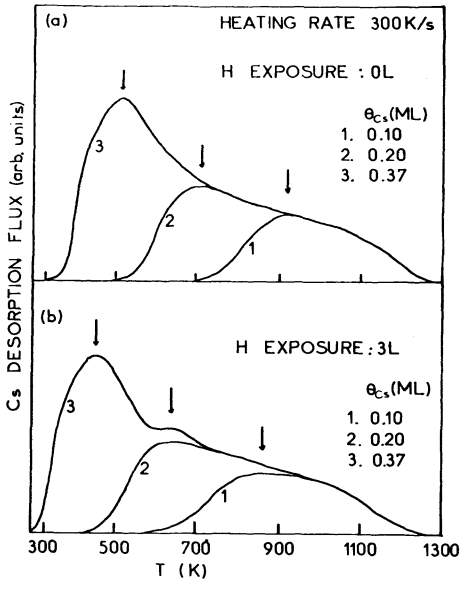

Fig. 4. TDS of Cs from (a) Cs/W(110) and (b) Cs-covered H/W(110) surfaces.

Cs-covered H/W(110) and H/W(110), respectively. As it is seen in this figure, the presence of the Cs overlayer does not change substantially the H-peak shape. The β_1 and β_2 adsorption states remain at about the same positions. Most likely, the presence of the Cs overlayer does not form any complex with the H underlayer and does not cause any obvious change in binding energy of it on W(110). The most probable configuration is one in which the small H atoms remain in their normal adsorption sites on W(110) and the subsequently deposited Cs atoms reside on top.

4.4 Discussion

As we mentioned in the introduction, one of the initiators of this work was the difference in WF variation of hydrogen on W(100) and W(110) surfaces. Adsorption of H_2 on clean W(100) surface causes an increase of the WF,[1] while adsorption of H_2 on W(110) decreases the WF of the surface. According to the literature of the preceding decade,[16] hydrogen on W surfaces behaves as electropositive. The increase of the WF on W(100) was attributed to a submergence of H atoms into the bulk of W, whereas the decrease of the WF on W(110) was attributed to a deposition of H atoms on top of the outermost layer of W(110) substrate.[16] However, in a recent study of hydrogen adsorption on W(100) and W(110) surfaces, it has been found that H atoms reside on top of the outermost plane of both W(100) and W(110) surfaces. Specifically, the H-W distance normal to relaxed surfaces

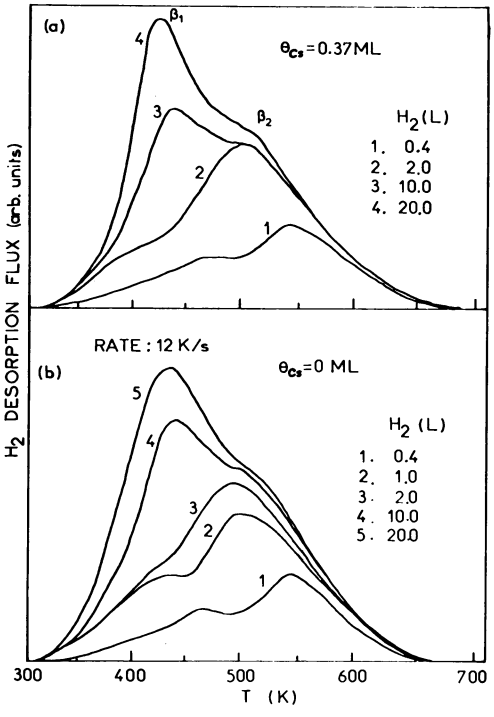

Figure 5. TDS of H_2 from (a) Cs-covered H/W(110) and (b) H/W(110) surfaces.

are 1.15 Å for H/W(100) and 1.25 Å on threefold site and ≥2.1 Å on top site for H/W(110).[17] According to a theoretical work by Shustorovich,[23] chemisorption of electropositive adsorbates (such as alkali metal) will always decrease the Φ on all transition-metal surfaces. While, chemisorption of electronegative adsorbates (such as H or halogens) can either increase or decrease the Φ, depending on the nature of the adsorbate and the type of the metallic substrate. The least electronegative adsorbates on the most highly dense surfaces are most favorable to produce the paradoxical decrease of WF ($\Delta\Phi<0$). The smallest difference in adsorbate versus metallic substrate electronegativity prove to be most likely to produce such a decrease in WF. Shustorovich's theoretical model [23] suggests that, under chemisorption of an electronegative adatom on a transition-metal surface the contributions to work function change, $\Delta\Phi$, is given by

$$\Delta\Phi = \Delta\Phi_{ext} + \Delta\Phi_{int} \qquad (1)$$

where $\Delta\Phi_{int}$ is the internal change of WF, which is due to changes in surface dipole moment (surface polarization) of the substrate under chemisrotpion, and $\Delta\Phi_{ext}$ is the external change in WF due to dipole moment

of the adsorbate. For an electronegative adsorbate $\Delta\Phi_{ext}>0$, under chemisroption of H (the least electronegative adsorbate) the charge transfer between H atoms and metal substrate is very small, i.e., very small magnitude of $\Delta\Phi_{ext}>0$. For the most highly dense W(110) surface $\Delta\Phi_{int}<0$ and if $|\Delta\Phi_{int}|>\Delta\Phi_{ext}$ then

$$\Delta\Phi = \Delta\Phi_{int} + \Delta\Phi_{ext} < 0 \qquad (2)$$

This is an explanation for the WF decrease ($\Delta\Phi<0$) during adsorption of H_2 on W(110) surface. Therefore the small electronegativity of H adsorbate and especially the small difference in electronegativity between H and W (2.20 and 2.36 on the Pauling scale, respectively) implies that the electronic charge transfer from W substrate to H adsorbate is very small. Also, the small electronegativity of H does not favor a strong interaction and/or a transfer of electronic charge between Cs and H underlayer, in contrast to the case of Cs and oxygen coadsorption on W surfaces.[1] Moreover, the H layer decreases the interaction between the Cs overlayer and W substrate, thus weakens the bond of Cs on W(110). This is consistent with the TDS measurements (section 4.3) which suggest that the presence of hydrogen on W(110) decreases the binding energy of the subsequently deposited Cs. Therefore the main contribution of the almost neutral preadsorbed H on W(110) to the initial dipole moment of Cs adsorbate may be due to a displacement of the Cs overlayer towards the vacuum and consequently, to an increase of Cs adsorbate-W substrate interlayer distance d.

According to a theoretical work by Wimmer et. al.,[24] for a fixed coverage of Cs on W, but for different values of d, there is a strong dependence of $\Delta\Phi$ on d. This dependence has been recently studied more systematically by Muscat and Batra.[25] This study suggests that the initial change of the WF in the Φ versus θ of alkali on metal substrates curves is more drastic with increasing adsorbate-substrate interlayer distance d. This implies that the initial dipole moment p_0 increases with increasing Cs-W interlayer distance d. As it is seen in Fig. 6, the initial dipole moment of Cs on H/W(110), p_0, increases linearly with increasing area of H_2 TDS peak of preadsorbed H_2 on W(110), which is proportional to θ_H. Above 10 L of hydrogen exposure, which corresponds to about 1 ML of H on W(110) (where all the available sites are occupied) the change of p_0 is almost negligible. The induced dipole moment and depolarization effect of these dipoles with increasing Cs coverage (θ_{Cs}) play an essential role to the initial decrease of $\Phi(\theta_{Cs})$.[26] The increase of the initial dipole moment with increasing amount of preadsorbed H may cause an earlier dipolarization effect. This could be a reason of the shift of Φ_{min} to lower Cs coverages

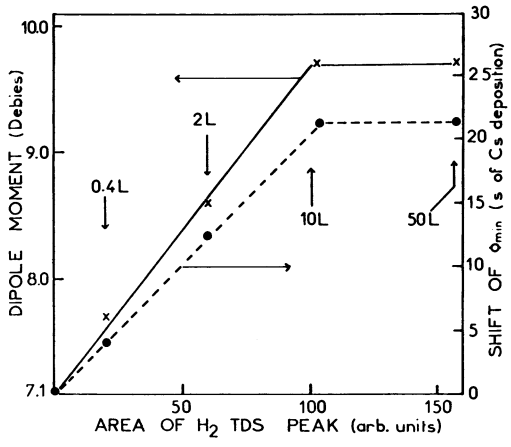

Fig. 6. Initial dipole moment p_0 and the shift of the Φ_{min} of Cs on H-covered W(110) surfaces (calculated from Fig. 5) versus the area under the TDS peak of preadsorbed H_2 W(110).

(Fig. 2). However, this is not the case, because the deviation from the initial constant slope of the WF curves in Fig. 2, which might be due to depolarization, occurs at about the same Cs coverage independently of the amount of H.

Muscat's and Batra's theory suggests that the onset of metallization of an alkali overlayer is accompanied by an increased alkali-substrate interlayer distance d. The regain of charge by the overlayer is certainly facilitated if d increases at the coverage where metallization sets in. Therefore, for the same θ_{Cs}, the increase of the Cs-W interlayer distance by the H is accompanied by an increase of the electron density in the Cs overlayer. Increasing electron density in the Cs overlayer with increasing amount of preadsorbed H may cause an earlier metallization in the Cs overlayer and thus an earlier occurence of Φ_{min}. Observed plasmons at coverages of alkali on metals right above the Φ_{min} suggest the appearance of nearly free electrons in the alkali overlayer. This finding is in a good agreement with the assumption about a metal-like overlayer.[27,28] Therefore, the shift of the Φ_{min} to lower Cs coverages with increasing amount of preadsorbed H on W(110) (Fig. 2) could be attributed to an early metallization in the Cs overlayer with increasing amount of preadsorbed H on W(110). An increase of the rate of metallization in the Cs overlayer with increasing amount of preadsorbed H on W(110) can be seen in Fig. 2, where above the Φ_{min}, the rate of WF increase with increasing Cs coverage is higher when the amount of preadsorbed H is greater. Figure 6 shows that the shift of Φ_{min} increases almost linearly with increasing amount of preadsorbed H on W, up to the completion of 1 ML (~10 L).

Analogous shifts of Φ_{min} have been reported. This shift occured with increasing size of deposited alkali atoms (Na, K, Cs) on metal surfaces, such as Ni(001) and Ru(001).[29,27] Specifically, the Φ_{min} of the WF curves of Na, K and Cs on Ni and Ru surfaces are shifted to lower coverage in the sequence of Na-K-Cs. Characteristic of the above measurements is that the initial dipole moment increase from Na to Cs.[27] The surface dipole distance is greater for the bigger Cs adatoms than for the smaller Na. The observed shift of Φ_{min} in the sequence of Na-K-Cs adsorbates on metals may be attributed to an early metallization of the layer with the bigger alkali adatoms. Most likely, the greater size of Cs atoms than that of Na atoms makes the electron communication to start earlier in the Cs layer than in the Na layer.

Now let us discuss the increase of the Φ_{max} of Cs with increasing amount of preadsorbed H on W(110) (Fig. 2). According to Lang's theory,[22] this could be attributed to an increase in the density of the saturated alkali layer N_{max}. However the AES and TDS measurements in sections 4.2 and 4.3 respectively, indicate that N_{max} of Cs does not increase with increasing amount of preadsorbed H on W(110). Considering again Muscat's and Batra's theory, the electron density of a saturated Cs layer on W(110) must be greater with increasing Cs-W interlayer distance d. As we mentioned earlier in this section, above the Φ_{min} the Cs overlayer starts to become a metal-like. Therefore, the electron density of the Cs overlayer is greater in the presence of H underlayer than without it. As the amount of preadsorbed H increases, the electron density in the saturated Cs overlayer becomes greater with a result the increase of the Φ_{max}.

Figure 7 shows the variation of Φ_{min} and Φ_{max} of the WF curves of Cs on H/W(110) (Fig. 2) versus the area under the TDS peak of preadsorbed H_2 on W(110) (the area is proportional to the preadsorbed θ_H). The small linear decrease of Φ_{min} is mainly due to the increase of p_0 with increasing θ_H. The Φ_{max} increases almost exponentially with increasing θ_H. This curve is quite similar to that of Φ versus electron density, n_e, in the adsorbed alkali layers on a metal substrate, which has been reported by Wojciechowski.[26]

At this point it is appropriate to correlate the present increase of the initial dipole moment of Cs versus increasing amount of preadsorbed H on W(110) with the model proposed by Wimmer et. al.[24] According to this

model, the initial WF lowering upon cesiation of W arises from a complex multiple dipole formation mechanism. Essentially, the Cs valence electrons are polarized towards the W surface leading to an increase of electronic charge in the interface region between the Cs and surface W atoms. We believe that, at early stages of Cs deposition, the increase of Cs-W distance by the almost neutral H layer provides a spatial extension of the polarized Cs adatoms toward W substrate. As a result is the increase of the initial dipole moment and further lowering of the Φ_{min}. Probably, at higher coverages, when the electronic communication between Cs adatoms occurs, the increase of Cs-W distance by H weakens the Cs-W covalent bond, thus more electronic charge from the Cs-W interface is shifted into the Cs overlayer. The result is the enhancement of metallization in the Cs overlayer, with a consequence, the shift of Φ_{min} and increase of Φ_{max}.

Finally, the increase of the initial dipole moment p_0, the shift of Φ_{min} and the increase of Φ_{max} of the Φ vs θ_{Cs} on H/W curves (Fig. 2), do not disagree with the simple model which at low θ_{Cs} ionizes the Cs overlayer atoms by electron transfer into W surface. As the θ_{Cs} increases, a progressive metallization of the Cs overlayer takes place. According to this model, the presence of the almost neutral H between the Cs-W interlayer, at low θ_{Cs}, increases the surface dipole distance and thus increases the p_0. Also, the H interlayer decreases the transition probability of electronic charge from the Cs overlayer into the W substrate and therefore increases the electron density in the Cs overlayer causing the shift of Φ_{min} and increase of Φ_{max}.

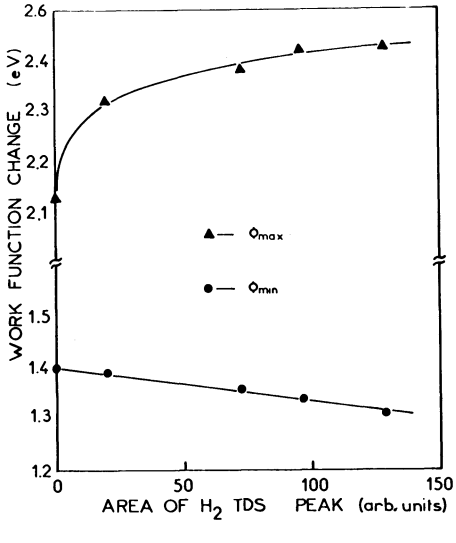

Fig. 7. Variation of Φ_{min} and Φ_{max} of the WF curves of Cs on H/W(110) surfaces (from Fig. 5) versus the area under the TDS peak of the preadsorbed H_2 on W(110).

As it has been mentioned in the introduction, the coadsorption of hydrogen on cesiated transition metal surfaces as those of W and Mo decreases strongly the production of negative H^- ions.[14,15] Cesiated W or Mo substrates with θ_{Cs} which corresponds to the Φ_{min} of the Φ-vs- θ_{Cs} curve are characteristic systems for the production of high yield of backscattered and sputtered negative ions. However, it has been found that, adsorption of H_2 on the above systems decreases very quickly the yield of H^- ion production. According to Gauyacq and Geerlings,[15] the hydrogen underlayer results in a decrease of the charge exchange interaction between the collisional hydrogen and the surface. Specifically, the adsorbed H atoms attract the electrons and reduce the tail of the electron wavefunction outside the metal. In contrast to the present work, they consider the adsorbed H on Cs/W as positively ionized H^+. It is noteworthy that the Φ_{min} decreases further with preadsorbed H on W(110) (Fig. 7) and thus we should expect easier escape of electrons from the metal for the ionization of hydrogen. We believe that the almost neutral H atoms (least electronegative) below the Cs layer increase the Cs-W interlayer distance. Thus, the H interlayer may result a decrease in the transition probability of electronic charge from the metal substrate to the colliding or sputter neutral hydrogen atoms, despite the low WF of the surface. Probably, the production of H^- ions takes place right above the Cs overlayer. A possible screening of the transfered electronic charge by the H interlayer may be correlated with a study of H^- production by backscattering energetic hydrogen atoms from Cs/O/W at Φ_{min}.

5. SUMMARY

The present work refers a systematic experimental study of Cs deposition on clean and H precovered W(110) surfaces . The experiment was performed in an UHV equipped with the surface techniques of AES, TDS and work function (WF) measurements.

Deposition of Cs on clean W(110) at RT produces a single layer which saturates at $\theta_{max} \approx 0.37$ ML. It gives the characteristic WF curve of alkali on metals. Initially, the WF goes through a minimum value, Φ_{min}, at θ_{Cs} = 0.22 ML and subsequently increases to a maximum, Φ_{max}, at saturation Cs coverage (θ_{Cs} = 0.37 ML).

During Cs deposition on H-covered W(110), the Cs atoms reside on top of the H-layer, while the H-atoms remain in their normal adsorption sites on W(110). The preadsorbed H causes (i) an increase of the initial dipole

moment, p_0, (ii) a lowering of Φ_{min} (iii) a shift of Φ_{min} to smaller θ_{Cs} and (iv) an increase of Φ_{max}. Hydrogen (the least electronegative) resides on top of the outermost plane of W(110) and weakens the bond of the subsequently deposited Cs with W substrate. The main effect of H on the surface structure is an increase of the W-Cs interlayer distance. According to Muscat and Batra[25], the increase of Cs-W distance by the H interlayer causes an increase of the initial surface dipole moments and of the electron density in the Cs overlayer. This finding explaines the lowering and shift of Φ_{min} and also the increase of Φ_{max}. This explanation is consistent with Wimmer's et al.[24] theoretical work and does not disagree with the models which ionize the Cs overlayer atoms by electron transfer into W surface.

6. ACKNOWLEDGMENT

we wish to thank Dr M. Kamaratos who helped for the collection and discussion of some data.

REFERENCES

1. C.A. Papageorgopoulos and J.M. Chen, Surface Sci. 39 (1973) 313.
2. J-L. Desplat and C.A. Papageorgopoulos, Surface Sci. 92 (1980) 97.
3. D. Edwards, Jr. and W.T. Peria, Appl. Surface Sci. 1 (1979) 419.
4. C.A. Papageorgopoulos, Surface Sci. 104 (1981).
5. G.N. Hatsopoulos and E.P. Gyftopoulos, Thermionic Energy Conversion, MIT Press, Cambridge, Mass., 1979.
6. M.H. Bakshi, P. Soukiassian, T.M. Gentle and Z. Hurych, J. Vac. Sci. Technol. A 5(4) (1987) 1428.
7. C.A. Papageorgopoulos S. Foulias, S. Kennou and M. Kamaratos, Submitted to Surface Science, Proc. of the 10th ECOSS.
8. C.T. Campbell and B.E. Koel, Surface Sci. 186 (1987) 393.
9. A. Pargellis and M. Seidl, Phys. Rev. B 25 (1982) 4356.
10. C.A. Papageorgopoulos and J.M. Chen, Surface Sci. 39 (1973) 283.
11. M-L. Ernst-Vidalis, M. Kamaratos and C.A. Papageorgopoulos, Surface Sci. 189/190 (1987) 276.
12. P.J. Schneider, K.H. Berkner, W.G. Graham, R.V. Pyle and J.W. Strearns, Phys. Rev. B 23 (1981) 941.
13. M. Wada, R.V. Pyle and J.S. Stearns, AIP Conf. Proc. III (1984) 247.
14. P.W. Van Amersfoort, J.J.C. Geerlings, R. Rodink, E.H.A. Granneman and J. Los, J. Appl. Phys. 59 (1986) 241.
15. J.P. Gauyacq and J.J.C. Geerlings, Surface Sci. 182 (1987) 245.
16. L.D. Schmidt, Topics In Applied Physics, Vol. 4, p. 80, Edited by R. Gomer, Springer-Verlag 1975.
17. H-J. Herlt and E. Bauer, Surface Sci. 175 (1986) 336.
18. C.J. Todd and T.N. Rhodin, Surface Sci. 42 (1974) 109.

19. P.W. Tamm and L.D. Schmidt, J. Chem. Phys. 54 (1971) 4775.
20. A.G. Fedorus and A.G. Naumovets, Surface Sci. 21 (1970) 426.
21. C.A. Papageorgopoulos, Phys. Rev. B 25 (1981) 3740.
22. N.D. Lang and W. Kohn, Phys. Rev. B 1 (1970) 4555; B 3 (1971) 1215.
23. E. Shustorovich, J. Phys. Chem. Vol. 86, No 16 (1982) 3114.
24. E. Wimmer, A.I. Freeman, I.R. Hishes and A.M. karo, Phys. Rev. B 28 (1983) 3074.
25. J.P. Muscat and I. P. Batra, Phys. Rev. B 34 (1986) 2889.
26. K.F. Wojciechowski, Surface Sci. 55 (1976) 246.
27. G. Rangelov and L. Surnev, Surface Sci. 185 (1987) 457.
28. B. Woratschek, W. Sesselmann, J. Küppers, G. Ertl and H. Haberland, Phys. Rev. Letters 55 (1985) 1281.
29. R.L. Gerlach and T.N. Rhodin, Surface Sci. 19 (1970) 403.

PARTICIPANTS

Dr. G. Allan
Lab. Phys. des Solides
Inst. Superieur d'Elec. Nord
41 Boulevard Vauban
59046 Lille Cedex, FRANCE

Dr. I. P. Batra
IBM Almaden Research Center
Mail Stop K33-801
San Jose, CA 95120 U.S.A.

Dr. L. J. Brillson
Xerox Webster Research Ctr.
800 Phillips Road, W-114
Webster, NY 14580, U.S.A.

Dr. H. P. Bonzel
Inst. Grenzflachenforschung
und Vakuumphysik
KFA Postfach 1913
D-5170, JULICH
WEST GERMANY

Dr. L. Braicovich
Istituto di Fisica
Politecnico di Milano
Milano, ITALY

Dr. P. Chiaradia
CNR-University of Rome
Istituto di Fisica G. Marconi
Piazza A. Moro 2, Rome 00185
ITALY

Prof. S. Ciraci
Bilkent University
Dept. Physics
06572 Maltepe/Ankara
TURKEY

Dr. G. P. Das
Max-Planck Inst. Festkorperforschung
Postfach 80 06 65
D-7000, Stuttgart 80
WEST GERMANY

Dr. R. M. Feenstra
IBM Watson Research Center
Dept. 461 39-020
Yorktwon Heights, NY 10598, U.S.A.

Dr. F. Flores
Dept. de Fisica del Estado Solido
Universidad Autonoma, Cantoblanco
28049 Madrid, SPAIN

Prof. C. Y. Fong
Department of Physics
University of California
Davis, CA 95616, U.S.A.

Dr. M. Z. Gedik
Department of Physics
Bilkent University
Ankara, TURKEY

Dr. D. R. Hamann
Bell Laboratories
600 Mountain Ave.
Murray Hill, NJ 07974, U.S.A.

Dr. A. Kahn
Dept. Elec. Eng.
Princeton University
Princeton NJ 08544, U.S.A.

Prof. L. F. Kaufmann
Department of Physics
Eindhoven Univ. Technology
P. O. Box 513
5600 MB Eindhoven
The NETHERLANDS

Dr. F. Koch
Physik-Department
der Technischen Universität München
8046 Garching b München
WEST GERMANY

Dr. C. Laubschat
Freie Universität Berlin
Inst. für Atom und Festkörperphysik
1000 Berlin 33
WEST GERMANY

Dr. R. Ludeke
IBM Watson Research Center
Dept. 461 40-009
P. O. Box 218
Yorktwon Heights, NY 10598, U.S.A.

Dr. R. Miranda
Dpto. Fisica Materia Condensada
Facultad de Ciencias
Universidad Autonoma de Madrid
Cantoblanco, 28049 Madrid
SPAIN

Prof. Dr. W. Mönch
Lab. für Festkorperphysik
Univ. Duisburg
D-4100 Duisburg
WEST GERMANY

Prof. Y. Murata
Institute for Solid State Physics
University of Tokyo
Roppongi, Minato-ku
Tokyo 106, JAPAN

Dr. J. S. Nelson
Sandia National Labs.
P. O. Box 969
Group 8341
Livermore, CA 94550 U.S.A.

Dr. C. A. Papageorgopoulos
University of Ioannina
Dept. of Physics
P. O. Box 1186
GR-451 10
Ioannina, GREECE

Dr. M. Prietsch
Freie Universität Berlin
Inst. für Atom und Festkörperphysik
1000 Berlin 33
WEST GERMANY

Dr. M. Lannoo
Lab. Phys. des Solides
Inst. Superieur d'Elec. Nord
41 Boulevard Vauban
59046 Lille Cedex, FRANCE

Dr. B. Reihl
IBM Zurich Research Laboratory
CH-8803 Rüschlikon
SWITZERLAND

Dr. H. Rohrer
IBM Zurich Research Laboratory
CH-8803 Rüschlikon
SWITZERLAND

DR. M. Saglam
Dept. of Physics
Ankara Universitesi
Fen Fakueltesi
Tandogan-Ankara
TURKEY

DR. H. Salemink
IBM Zurich Research Laboratory
CH-8803 Rüschlikon
SWITZERLAND

Dr. F. Salvan
Dept. Physique, Case 901
Faculte Sci. de Luminy
F-13288 Marseille
Cedex 09, FRANCE

Dr. C. A. Sebenne
Univ. Pierre Marie Curie
Lab. Phys. Solides
4 Pl Jussieu - Tour 13 E.2
75252 Paris Cedex 05
FRANCE

Dr. P. Soukiassian
Sous les Vignes
40 Route de Villebertin
Moussey, 10800
Saint Julien les Villas
FRANCE

Prof. W. E. Spicer
Electronics Laboratory
Stanford University
Stanford, CA 94305, U.S.A.

Dr. G. P. Srivastava
Physics Department
University of Exeter
Exeter EX4 1SW
U.K.

Dr. M. Tsukada
Dept. Physics
University of Tokyo
Tokyo 113, JAPAN

Dr. J. Tersoff
IBM Watson Research Center
Dept. 459 20-254
P. O. Box 218
Yorktwon Heights, NY 10598, U.S.A.

Dr. J. H. Werner
Max-Planck Inst. for
Solid State Research
D-7000, Stuttgart 80
WEST GERMANY

Dr. J. H. Wolter
Department of Physics
Eindhoven Univ. Technology
P. O. Box 513
5600 MB Eindhoven
The NETHERLANDS

Dr. R. H. Williams
Department of Physics
University College, Cardiff
P. O. Box 78
Cardiff CF1 1XL
U. K.

INDEX

Adamantane cage, 199
Adatom induced surface dipoles, 34
Adatom induced surface states, 23, 41
Adsorbate induced states, 172
Adsorption, 58
Al/GaAs, 17, 26, 148
Al/Ge, 21, 337
Alkali metals, 4, 174, 297, 339, 367, 429, 445, 465
Al/Si interface, 57
Annealing, 154
Antisite, 155
ASA, 225
Auger electron spectroscopy, 118, 164, 369, 384, 493

Band bending, 5, 17, 40, 99, 108, 167, 426
Band offsets, 274
Band structure, 207, 345, 355
Barrier heights, 1, 12, 27, 83
Ballistic transport, 130, 211

Cathodoluminescence spectroscopy, 99
CdS, 83
CdTe, 83, 105
Charge density contours, 203, 218, 343, 359, 455
Charge neutrality level, 26, 39, 41, 446
Charge transfer at semiconductor interfaces, 6, 44, 347, 357
Chemical reaction, 107, 142
Chemical reactivity, 434
Chemisorption energy, 445
Coadsorption, 490
Core levels, 185, 426
Covalent bond, 119, 346, 415, 466
Covalent ionic transition, 83
Coverage dependent effects, 114, 118, 119, 300, 336, 457, 499

Dangling bonds, 260
Deep level, 103
Defect molecule, 265
Defects, 3, 39, 40, 93, 102, 133, 285, 313, 437
Delocalization, 51
Delta function doping layers, 24
Dispersion relation, 370

EELS, 339
Electron affinities, 27
Electron transmission, 211
Electronegative, 167
Electronegativity concept, 26, 47, 48, 173
Exchange reactions, 41

Friedel sum rule, 260

Gap state at submonolayer coverages, 27
Ga/Si, 115, 116
Gd/Si, 183
Green's function, 260

Hartree-Fock, 346
Hot electron, 131
H-preadsorption, 492

Impact collision, 114
Index of interface behavior, 49
Interface dipole, 223
Interface states, 95, 236, 250
Interfacial chemistry, 155
Inverse photoemission, 398
Ionic bond, 6, 342, 384, 415, 466
Islands, 142

K-GaAs, 443
K-Si, 6, 297, 340, 351, 383

Ladder type density of states, 338
LAPW, 197
LCAO method, 352
LDOS, 66, 460
LEED, 79, 118, 166, 382
LMTO, 206, 217, 218
Local density approximation, 60, 196, 215, 337
Low temperature, 13, 142, 147, 164, 165, 182

Macroscopic dipole sheet, 125
Mesoscopic, 132
Metal induced gap states (MIGS), 2, 11, 43, 57, 80, 107, 140, 144, 283, 293
Metal induced surface states, 18, 27
Metallization, 3, 106, 120, 142, 164, 174, 175, 284, 296

Metal clustering, 42, 172
Metal silicides, 188, 195, 216
MIS tunnel diodes, 235, 244
Molecular beam epitaxy, 94, 126, 329

Na/GaAs, 450, 480

Overlayer metallization, 4, 299, 341, 385, 415, 431, 433, 454

Peierls transition, 374
Photoemission, 148, 174, 181, 342, 372, 467
Pinning, 55, 56, 87, 91, 104, 140, 170, 206, 281, 286, 293, 312, 374, 431, 461
Potentiometry, 329
Pseudopotentials, 60, 337, 353, 450

Rare earth metals, 437
Rectifying, 1, 335
RHEED, 118
Roughness, 120

Scanning tunneling microscopy (STM) applied to
(Al, In, Ga)/Si, 318
Au/Si, 320
B/Si, 320
GaAs/AlGaAs, 329
O/GaAs, 308
Pd/Si, 317
Sb/GaAs, 310
Schottky barrier, 2, 15, 40, 46, 51, 55, 57, 80, 163, 204, 222, 282, 335, 387, 471
Schottky diodes, 29, 235
Semiconductor heterojunctions, 263, 285, 330
Si(111)-(2x1), 112
Substrate metallization, 4, 297, 342, 389, 415
Superlattices, 269
SEXAFS, 354, 466
Surface molecule, 20
Surface/overlayer plasmons, 339, 361, 369, 472

Thermal desorption, 5, 385, 495
Thermal effects, 180
Tight binding method, 20, 270, 440
Total energy, 61, 196, 337, 453
Transition metal impurity level, 264
Tunnel current, 131

Unified defect model, 107, 145, 172, 294, 439
Unoccupied states, 5, 399

Virtual gap states, 12, 25, 107, 429

Work function, 357, 368, 388, 493, 497, 500

Yb/Si, 184

Zero dipole approximation, 272